THE PHYSICAL REVIEW

VOLUME 95 NUMBER 5

SEPTEMBER 1, 1954

PUBLISHED BY THE

AMERICAN PHYSICAL SOCIETY

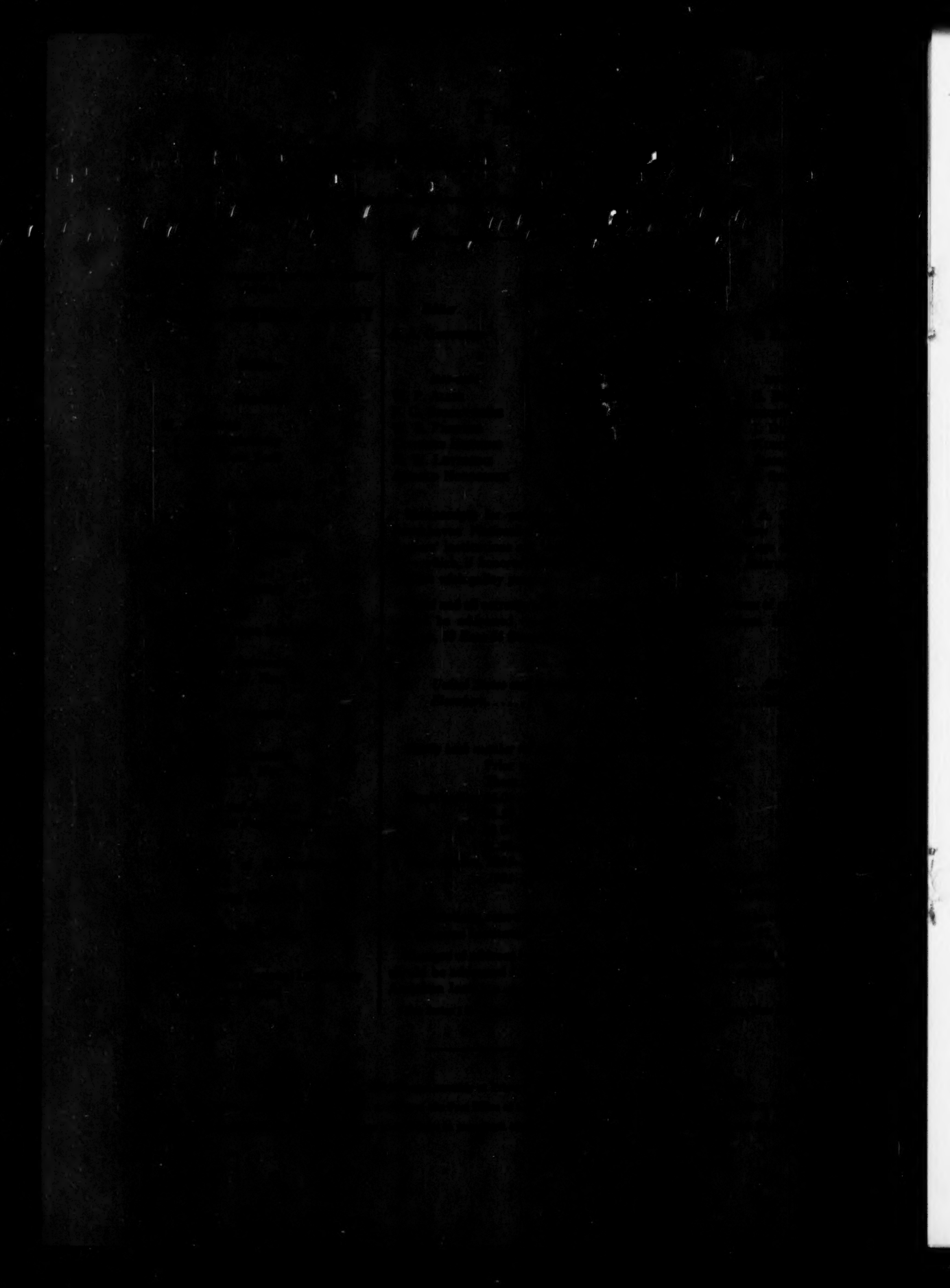

THE
PHYSICAL REVIEW

A journal of experimental and theoretical physics established by E. L. Nichols in 1893

SECOND SERIES, VOL. 95, NO. 5 SEPTEMBER 1, 1954

Harmonic Oscillator Wave Functions

I. R. SENITZKY
Signal Corps Engineering Laboratories, Fort Monmouth, New Jersey
(Received April 16, 1954)

A harmonic oscillator wave packet which oscillates sinusoidally without change in shape has been described by Schrödinger and others. It is shown in the present note that there are an infinite number of such wave packets—of which the above is a special one—having the shapes of the various eigenfunctions of the harmonic oscillator Hamiltonian. The relation of these wave packets to the classical oscillator is discussed.

DUE to the importance which the one-dimensional harmonic oscillator problem has in quantum theory, its wave functions have been given considerable attention. Several authors[1–3] have shown that there is a particular harmonic oscillator wave function in the form of a wave packet, the center of which oscillates sinusoidally about the origin and the shape of which remains constant in time. The purpose of the present note is to show that there are an infinite number of such wave packets.

The most general expression for a complex function of q and t, the absolute value of which remains constant in shape, is given by

$$\psi(q,t)=f(q-q_0(t))e^{i\varphi(q,t)}, \tag{1}$$

where f, q_0, and φ are real, arbitrary functions. Inserting (1) into Schrödinger's equation for the harmonic oscillator,

$$ih\frac{\partial\psi}{\partial t}=-\frac{\hbar^2}{2m}\frac{\partial^2\psi}{\partial q^2}+\frac{m\omega^2}{2}q^2\psi,$$

and equating real and imaginary parts separately, we obtain

$$-\frac{\hbar^2}{2m}\frac{\partial^2 f}{\partial q^2}+\frac{m\omega^2}{2}q^2 f+\left[\frac{\hbar^2}{2m}\left(\frac{\partial\varphi}{\partial q}\right)^2+\hbar\frac{\partial\varphi}{\partial t}\right]f=0, \tag{2}$$

and

$$-\frac{\partial f}{\partial q}\dot{q}_0+\frac{\hbar}{m}\frac{\partial f}{\partial q}\frac{\partial\varphi}{\partial q}+\frac{\hbar}{2m}f\frac{\partial^2\varphi}{\partial q^2}=0. \tag{3}$$

Equation (3) can easily be transformed into

$$\frac{\partial}{\partial q}\left(-\dot{q}_0+\frac{\hbar}{m}\frac{\partial\varphi}{\partial q}\right)f^2=0,$$

which yields, as the solution,

$$\left(-\dot{q}_0+\frac{\hbar}{m}\frac{\partial\varphi}{\partial q}\right)f^2=\text{constant}.$$

Now, if $\psi(q,t)$ is to be normalizable, f must vanish at infinity. The constant is therefore equal to zero, and we have

$$\varphi(q,t)=(m/\hbar)q\dot{q}_0+S(t), \tag{4}$$

where S is an arbitrary function of the time only. Substituting this expression into Eq. (2) and completing the square involving q, we obtain

$$-\frac{\hbar^2}{2m}\frac{\partial^2 f}{\partial q^2}+\frac{m\omega^2}{2}\left(q+\frac{1}{\omega^2}\ddot{q}_0\right)^2 f+\left(\hbar\frac{dS}{dt}+\frac{m}{2}\dot{q}_0^2-\frac{m}{2\omega^2}\ddot{q}_0^2\right)f=0. \tag{5}$$

This is a differential equation for f. Since we have taken f to be a function of $q-q_0$, the coefficients in this equation must be functions of $q-q_0$. We must therefore

[1] E. Schrödinger, Naturwiss. 14, 664 (1926).
[2] L. I. Schiff, *Quantum Mechanics* (McGraw-Hill Book Company, Inc., New York, 1949), Sec. 13.
[3] D. Bohm, *Quantum Theory* (Prentice-Hall, Inc., New York, 1951), Chap. 13.

have

$$\frac{1}{\omega^2}\ddot{q}_0=-q_0, \tag{6}$$

and

$$\hbar\frac{dS}{dt}+\frac{m}{2}\dot{q}_0^2-\frac{m}{2\omega^2}\ddot{q}_0^2=-E, \tag{7}$$

where E is a constant independent of the time. Equation (5) can now be written as

$$-\frac{\hbar^2}{2m}\frac{\partial^2 f}{\partial Q^2}+\frac{m\omega^2}{2}Q^2 f=Ef, \tag{8}$$

where we have put $q-q_0(t)=Q$. But Eq. (8) is just the time-reduced Schrödinger equation for the harmonic oscillator. Its solutions are the well-known harmonic oscillator eigenfunctions,[2]

$$f_n(Q)=\left(\frac{\alpha}{\pi^{\frac{1}{2}}2^n n!}\right)^{\frac{1}{2}}H_n(\alpha Q)\exp(-\tfrac{1}{2}\alpha^2Q^2), \tag{9}$$

corresponding to the eigenvalues $E_n=(n+\frac{1}{2})\hbar\omega$, where $\alpha^2=m\omega/\hbar$, H_n is the nth Hermite polynomial, and n is any non-negative integer. The solutions of Eqs. (6) and (7) can be written down immediately. These are

$$q_0=A\cos(\omega t+\theta), \tag{10}$$

and

$$S=-\frac{E_n}{\hbar}t-\frac{1}{\hbar}\int(\tfrac{1}{2}m\dot{q}_0^2-\tfrac{1}{2}m\omega^2q_0^2)dt, \tag{11}$$

where A and θ are arbitrary constants.

We see, thus, that there are an infinite number of harmonic oscillator wave packets defined by Eqs. (1), (4), (9), (10), and (11), for each of which the absolute value remains constant in shape while oscillating sinusoidally about the origin. The wave packet described in references 1–3 is obtained by setting n in Eq. (9) and θ in Eq. (10) equal to zero.

It is interesting to note that if q_0, which, in view of Eq. (9), is the expectation value of q, be regarded as the coordinate of a classical particle, then the integral in Eq. (11) is Hamilton's principle function for that particle. The energy of this classical particle, however, has no direct connection with the eigenvalue E_n, since it depends on the arbitrary constant A.

It is also interesting to obtain the expectation value of the energy of our oscillating wave packets. We have

$$\langle H\rangle=i\hbar\int_{-\infty}^{\infty}\psi^*\frac{\partial\psi}{\partial t}dq$$

$$=i\hbar\dot{q}_0\int_{-\infty}^{\infty}ff'dq-\hbar\int_{-\infty}^{\infty}f^2\frac{\partial\varphi}{\partial t}dq.$$

The first integral vanishes, since the limit of f is zero as q becomes infinite either positively or negatively. We thus have

$$\langle H\rangle=-\hbar\int_{-\infty}^{\infty}f^2\frac{\partial\varphi}{\partial t}dq$$

$$=-m\ddot{q}_0\int_{-\infty}^{\infty}Qf^2(Q)dQ$$

$$+[E_n+(\tfrac{1}{2}m\dot{q}_0^2+\tfrac{1}{2}m\omega^2q_0^2)]\int_{-\infty}^{\infty}f^2(Q)dQ$$

$$=E_n+(\tfrac{1}{2}m\dot{q}_0^2+\tfrac{1}{2}m\omega^2q_0^2), \tag{12}$$

where use has been made of Eq. (6), of the normalization of $f(Q)$, and the symmetry of $f^2(Q)$. It is seen, therefore, that the expectation value of the energy is just the sum of the quantum-mechanical energy of the wave packet when it is stationary and the classical energy of the particle with coordinate $q_0(t)$. Equation (12) can be written as

$$\langle H\rangle=m\omega^2(\langle Q^2\rangle+\langle q_0^2\rangle_{Av}),$$

where the average of q_0^2 is the time average. It is evident, then, that if the amplitude of oscillation is large compared to the width of the wave packet, the energy is predominantly of classical origin, while if the amplitude of oscillation is small compared to the width of the wave packet, the energy is predominantly of quantum-mechanical origin.

The author is indebted to Professor Julian Schwinger for helpful discussion of the foregoing subject matter.

Measurement of the Current during the Formative Time Lag of Sparks in Uniform Fields in Air*†

H. W. BANDEL
Department of Physics, University of California, Berkeley, California
(Received May 17, 1954)

The current in a parallel plane gap during the long formative time lags of sparks in air has been measured from 10^{-6} amp a few μsec after application of the voltage up to 10^{-3} amp just before breakdown, for time lags between 10 and 100 μsec. Calculations for the increase of $\exp(\int_0^d \alpha dx)$ due to field distortion by positive ions are in good agreement with an observed rapid increase of current shortly before breakdown. The Townsend discharge is shown to be spread over the whole electrode surface in contrast to the filamentary nature of the final spark. The photosensitivity of the cathode surface has been found to decrease following collection of positive ions. The conditioning of the electrodes observed by Fisher and Bederson is believed to be due to such a decrease in γ_p. Some gain has been made toward a theoretical solution for the growth of the Townsend discharge. Working with an integral equation and taking due care with integration limits, has established the range of validity of the existing solution and yielded another approximate solution; from these, exact solutions for the limiting cases of only one γ are obtained. There is over-all agreement between theory and experiment within limits of error except for an observed delay in the initial current rise. To explain this requires the consideration of mechanisms, involving creation and transmission of active photons, which could cause a delay of the order of an electron crossing time.

INTRODUCTION

PRESENT understanding of spark breakdown depends mainly on two very different processes; the Townsend discharge[1] and streamer propagation.[2] For some years it was commonly believed that spark breakdown in uniform fields in air could be explained by applying the two theories separately; Townsend theory at low values of pd (pressure×gap length), and streamer theory at high pd. In an attempt to study the transition region Fisher and Bederson[3] measured time lags with low overvoltages from atmospheric pressure down to a few cm of Hg and found no transition from streamer to Townsend mechanism. Moreover, with their improved voltage stability they were able to work at overvoltages down to 0.02 percent and observed time lags varying continuously from 1 up to 100 μsec long at atmospheric pressure. Thus they observed filamentary sparks characteristic of streamer breakdown with time lags at least a thousand times too long for a streamer crossing time. In view of the work of Varney, White, Loeb, and Posin,[4] and similar contributions by Steenbeck,[5] which had shown that $\exp(\int_0^d \alpha dx)$ could be increased by field distortion due to the accumulation of space charge, Loeb,[6] and Fisher and Bederson,[3] proposed that the discharge starts as a Townsend type mechanism which builds up space charge until the field distortion is such that a streamer can start and then the breakdown is by streamer mechanism. (α is the average number of ionizing acts by one electron traveling 1 cm in the field direction.)

The long time lags observed offered the possibility of measuring the current buildup during the formative time as a means of further studying the mechanisms involved; that was the object of this work.

APPARATUS

The purpose of the apparatus was to suddenly overvolt a parallel plane gap and then measure the current flowing in the gap while the discharge built up to a spark. To accomplish this a positive approach voltage V_a was applied to the gap while the pulser side of the 0.005-μf condenser (see Fig. 1) was held at 1000 volts negative to ground. Thus the voltage across the condenser was V_a+1000. The opening of S_1 triggered the pulser which then raised the negative side of the condenser up to ground potential so that the full voltage across it was then also across the gap; at the same time the sweep was triggered on the synchroscope. S_2 was adjusted to open about 3 μsec after the pulse was applied and thereafter the voltage developed across the signal resistor R was amplified and displayed on the synchroscope, which was photographed.

Due to the capacity of the gap a charging current had to flow to the cathode when the pulse was applied. This was 10^6 or more greater than the discharge currents to be measured just afterward and had to be prevented from blocking the amplifiers. As a switch to short it out, a hard tube has too much resistance when closed and a thyratron cannot be opened fast enough. If the nonoverloading amplifier circuit[7] had been available at the

* Work supported by the U. S. Office of Naval Research, National Science Foundation, and Research Corporation of America.

† This work has been presented in more detail, especially as regards apparatus, in the Ph.D. thesis of H. W. Bandel, Department of Physics, University of California, Berkeley, California, April 1954.

[1] L. B. Loeb, *Fundamental Processes of Electrical Discharge in Gases* (John Wiley and Sons, Inc., New York, 1939).

[2] L. B. Loeb and J. M. Meek, *The Mechanism of the Electric Spark* (Stanford University Press, Stanford, 1941).

[3] L. H. Fisher and B. Bederson, Phys. Rev. **81**, 109 (1951).

[4] Varney, White, Loeb, and Posin, Phys. Rev. **48**, 818 (1935).

[5] A. v. Engel and M. Steenbeck, *Elektrische Gasentladungen* (Julius Springer, Berlin, 1934), Vol. II, p. 48 ff.

[6] L. B. Loeb, Phys. Rev. **81**, 287 (1951).

[7] R. L. Chase and W. A. Higinbotham, Rev. Sci. Instr. **23**, 34 (1951).

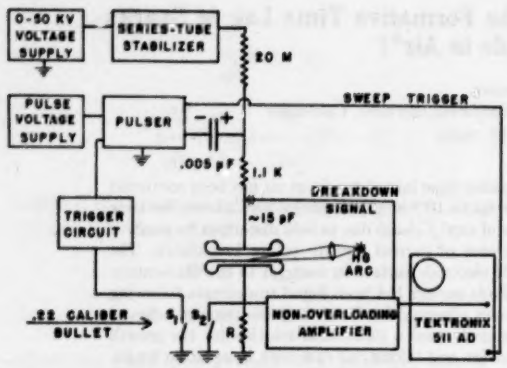

FIG. 1. Block diagram of apparatus.

start of the work a dummy system with a pulse of opposite sign might have been used, but balancing such a system to a part in a million did not seem feasible so the rifle operated switch was developed. It was completely shielded, contact separation was normal, and the motion stopped after ~1 μsec. With $R=1000$ ohms, switch noise was measured up to 1 millivolt.

The parallel plane electrodes were of brass polished with rouge and tin oxide. They were 10 cm in diameter with the edges having a radius of curvature of 1 cm. Fine fiducial lines were turned on the outer edge when they were made so that adjustments for parallelism and gap length could be made by measuring the separation of these lines with a cathetometer; accuracy was about ±0.01 mm. The cathode was mounted on a screw thread so that it could be raised or lowered while in the chamber. The threads were lubricated with graphite. Clearance between the outer edge of the electrodes and the chamber walls was about 9 cm.

The chamber was of brass with a Dural lid. The windows were of quartz and all gaskets of neoprene. The chamber was originally cleaned with nitric acid before assembly. Later, after collapse of an oil-filled lead-in insulator, it was disassembled and washed with detergent; then scoured with whiting, washed with water, and rinsed several times with distilled water before the final assembly. After this treatment a trap cooled with dry ice in alcohol was kept on at all times that the chamber was connected to the vacuum system in order to exclude mercury and stopcock greases.

Whenever the chamber was pumped it soon came down to 2×10^{-4} mm Hg and then stayed about the same for a day or more after which it would drop to 10^{-5} mm Hg. The source of this virtual leak is not known but in this work on air it didn't matter. No difference was noticed for gas fillings made before the final drop to 10^{-5} occurred, or for those left in the chamber many days and used for a number of runs. Room air was drawn in through glass wool, calcium chloride, glass wool, and then a trap made of ~4 meters of 7-mm glass tubing cooled by dry ice in alcohol.

The light from a Hanovia quartz mercury arc was focused on the cathode through a side window and a quartz lens. Intensity was adjusted by moving screens into or out of the beam. For determining i_0 the cathode could be connected to a Keithley electrometer and a set of Victoreen resistors to measure currents down to 10^{-12} amp.

The high voltage was furnished by a 0–50 kv supply which was regulated until measurements of the output showed voltage fluctuations and ripple to both be less than ½ volt at 32 kv except for thermal drifts which could not be controlled or measured.

The pulse voltage came from a 0 to −6 kv series tube regulated supply, although for the work reported here only pulses of 1000 volts were used. The pulse came from the cathode of a 677 thyratron; to reduce noise from the thyratron a capacitor was used instead of a resistor in the cathode lead. The pulse rose from −1000 volts and overshot to +1 volt in less than a μsec; it then dropped back to +½ volt at 2 μsec, rose to +¾ volt at 5 μsec, and decayed to its final value of −⅓ volt by 30 μsec. Approximate integration of the measured discharge current showed that in the worst case it would have lowered the gap voltage by only a small fraction of a volt during the time of measurement. As far as the development of the discharge was concerned, the deviations of the pulse from a perfect step function could be neglected but they did place a limitation on the measurement of small currents, because any dv/dt of the applied pulse resulted in a charging current flowing to the gap and thus a signal to the amplifier.

The non-overloading amplifier used the basic circuit of Chase and Higinbotham.[7] Its maximum output did not cause blocking of the amplifiers of the Tektronix 511 AD when using 1 stage of gain so the system as a whole was non-overloading except for the first grid and S_2 protected that until after the pulse. The amplifier input was protected from damage when breakdown occurred by first a spark gap and then an illuminated Ne bulb preceded by 2000 ohms. With 4 stages of gain the sensitivity could be varied by factors of 10 from 2.5×10^{-4} to 2.5×10^{-1} volt/cm. In addition, the signal resistor could be varied; 1000 ohms was the largest commonly used. With this, the maximum current sensitivity was 1 μa for full scale deflection of 4 cm with a noise level usually of about 2 or 3 mm and a low-frequency ripple of about twice that. Although the available sensitivity would have allowed measurement of currents from about 10^{-7} up to 1 amp the limits of measurement at both ends of the time lag were set in general by the rate of rise of the synchroscope trace being too fast to register photographically. In the early part of the time lag there was also a limit set by the dv/dt of the applied pulse.

The time of breakdown was recorded by taking a signal capacitatively from the high-voltage lead-in insulator and coupling it to the amplifier output through a germanium diode in such a way that normal operation of the amplifier was not affected by quite large fluctua-

tions of the anode potential, but when breakdown occurred the sudden drop by thousands of volts drove the amplifier output to full negative signal. This gave an indication of the time of spark that was independent of the gain of the amplifier or the value of R.

EXPERIMENTAL PROCEDURE AND RESULTS

The voltage supplies and arc were turned on and allowed to warm up for at least an hour, and the light intensity was adjusted to give the desired value of i_0. Then without firing the rifle, the pulser circuit was triggered by tripping S_1 by hand and the time lags observed visually on the synchroscope so the approach voltage could be adjusted to give the desired time lag. Then with everything adjusted the camera shutter was opened and the rifle fired. A number of such photographs were taken for different time lags at each sensitivity setting. The negatives were then projected on a screen; deflections were measured, converted to amperes, and plotted on a semilogarithmic plot. Each trace was labeled with the time lag measured from the film. When enough data was collected to have such sections of curves close together all over the plot a continuous curve for any particular time lag could be drawn in. Further, because of the statistical variations in the discharges, such a mean curve is more representative than any single one of the measured data.

In this work as in that of Fisher and Bederson,[3] i_0 was determined by measuring the multiplied current at a voltage roughly 10 percent below sparking and then using Sanders'[8] values of α in the equation $i=i_0e^{\alpha d}$. This method is not very good because $e^{\alpha d}$ varies so much for small uncertainties in α, but it seems to be the only method at present available. When the data of Harrison and Geballe[9] became available, a comparison was made between using their data for α and η (coefficient for attachment) and that of Sanders. In general, neither could be said to fit better than the other so the use of Sanders' data was continued.

Fisher and Bederson[3,10] found that each time after starting, the sparking potential kept rising until the electrodes had been conditioned by the passage of a large number of sparks, after which it became definite at any time but still changed slowly with time. Essentially the same thing was observed in this work, and it was found that the passage of sparks also decreased i_0; this was found to be a change in the photosensitivity of the cathode, probably a change in the gas film on the surface following collection of positive ions. Starting with a chamber that had been evacuated for a day or more and then filled, the photosensitivity was always high. Then even the small current passed by the approach voltage caused a gradual, measurable decrease, and sparking often caused a decrease by orders of magnitude. After the photosensitivity had been much depressed by sparking it recovered slowly by just standing idle. It seems likely that γ_p may decrease along with the photosensitivity to light from the Hg arc, and this would account for the observed increase in sparking potential as the electrodes are conditioned. (γ_p is the average number of electrons released from the cathode by photons generated in the gas per ionizing event in the gas.)

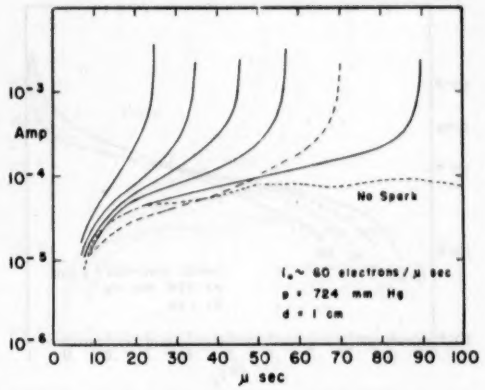

FIG. 2. Current *vs* time with large i_0. The 70-μsec curve shows maximum scatter. Curves terminate within one μsec of breakdown.

By the nature of Fisher and Bederson's apparatus,[3] it seems likely that they would have kept sparking it frequently while taking data so that some saturation of the effect might have been maintained. In this experiment, that could have been done while conditioning the electrodes, or observing time lags visually to get the voltage adjusted, but there was an unavoidable delay each time the camera, rifle switches, and voltages were all reset and the data recorded. After this idle time the first time lag was always shorter than previous ones at the same voltage, and the data taken showed a very large scatter. All of the data finally used were taken by sparking once every 5 minutes. This regular sparking was usually carried out for an hour or more until i_0 seemed comparatively constant before any data were taken, and then i_0 was checked, and if necessary the light intensity readjusted, occasionally during a run. With this, measured values of i_0 usually varied by less than ± 10 percent. There was still nearly always a drift of the sparking potential up or down, sometimes over a range of nearly 200 volts out of about 29 kv in the course of a day's run.

Figure 2 shows some plots of data taken with $i_0 \approx 60$ electrons per μsec, $d=1$ cm, and $p=724$ mm Hg. (All pressures are reduced to 22°C.) In general the current builds up rapidly in the early part of the formative time, then increases roughly exponentially in the middle of the time lag, and finally increases much faster than exponentially shortly before breakdown. The upper ends of the curves terminate within one μsec of breakdown.

[8] F. H. Sanders, Phys. Rev. **41**, 667 (1932); **44**, 1020 (1933).
[9] Melvin A. Harrison and Ronald Geballe, Phys. Rev. **91**, 1 (1953).
[10] L. H. Fisher, Elec. Eng. **69**, 613 (1950).

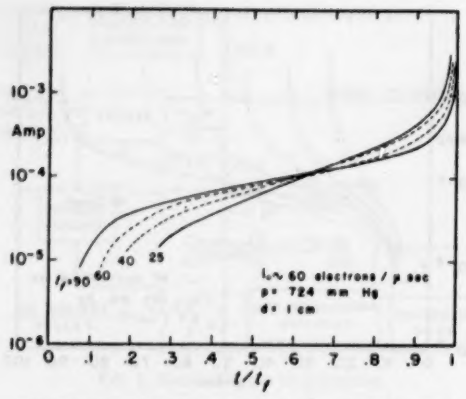

FIG. 3. Some of the same data as in Fig. 2 with current plotted *vs* fraction of the formative time lag.

A rough qualitative picture of the general shape of these curves is as follows. The current measured by the external circuit is due to the motion of all of the ions and electrons in the gap at any particular time. Because the electron velocity is so much higher, electrons make a much larger contribution to the current for the short time they are in the gap, but the positive ions remain in the gap for a correspondingly longer time. In a steady state the contribution of the positive ions and that of the electrons are in the ratio of the average distances they each travel in the field, which is approximately $(\alpha d-1)/1$. For the values of αd at onset this would be a contribution by the positive ions of about ten times as great as that of the electrons. When any change occurs in the rate of ion (and electron) production, the electron current follows the change quickly while the ion current requires an ion crossing time to adjust to the new value. Thus, whenever the measured current is increasing, a larger fraction of it is due to electrons than would be the case for steady state; and the faster it is increasing, the larger is the fraction of it due to electrons. This makes direct interpretation of the measured current difficult.

In the absence of any secondary mechanisms the measured current would increase rapidly at first as the constant rate of production increased the number of positive ions in the gap. It would level off gradually and become constant at one ion crossing time when the rate of loss became equal to the rate of creation. With secondary mechanisms acting, this initial buildup is of course greater, and the current cannot become constant by one ion crossing time. The more or less exponential increase in the middle of the time lag is due to secondary mechanisms, and the final up-curving which leads to breakdown is due to space-charge distortion of the field, as will be shown later.

Figure 3 shows some of the same data as in Fig. 2 plotted against fraction of the formative time, t/t_f. Two of the curves are dashed merely to aid the eye in following them through. This method of plotting spreads out the beginnings of the curves which were nearly the same for all time lags but it reveals the similarity in shape of all the curves.

There was always some statistical scatter in the development of the discharges but with this relatively heavy i_0 it was not very great. In general a section of curve obtained with one sensitivity would join quite smoothly onto another section for the same time lag although they had been taken for different sparks. The lower end of the dashed curve in Fig. 2 is actual data for a time lag of 70.5 μsec and is included because it was the widest variation observed in the whole run.

This variation is to be compared with Fig. 4 which presents some data for the same pressure and gap length but with i_0 an order of magnitude lower. These were all for time lags within a few percent of 40 μsec and when plotted against t/t_f should have all fallen practically on the same curve were it not for variations in the development of the discharges. The scatter here is much greater than with the heavier i_0 and the different traces do not plot smoothly together. However, a sort of mean curve drawn through the center of these (dashed line in Fig. 4) passes 10^{-6} amp at about the same time that the 40 μsec curve crosses 10^{-5} amp in Fig. 3. In general, changes in i_0 merely raised or lowered the early part of the curves, because in this work the independent variable was time lag instead of overvoltage. Voltage was always recorded but, with the sparking limited to one every 5 minutes, V_s (sparking threshold voltage) could not be checked conveniently or frequently so the overvoltage was not usually known. There can be no question that if V_s were constant, changes in i_0 would move the entire curves up or down at least up to the point where space charge distortion starts the final up-curving, and the time lag for a given overvoltage would be changed. Fisher and Bederson did not observe this because their variations in i_0 were small and the resultant changes in time lag *vs* overvoltage were less than the experimental accuracy.

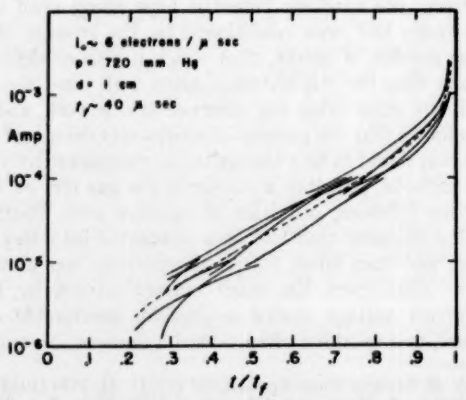

FIG. 4. Current *vs* fraction of the time lag with small i_0 for lags of ~40 μsec, showing scatter.

Figure 5 includes a set of experimental curves (dashed lines) for $d=1$ cm, $p=722$ mm Hg, and $i_0\approx 12$ electrons per μsec. The scatter in this data was appreciably less than with $i_0\approx 6$ electrons/μsec but was still considerable.

In Figs. 2 and 5, examples are included of actual data for cases in which sparks just failed to develop. These are fairly typical of many such events observed either by chance or by intentionally lowering the voltage to remain a few volts below threshold. The early build-up, which is due largely to filling the gap with positive ions, is nearly the same as for the longer time lags but then the curves level off, although there was always more or less fluctuation about the final values.

A considerable amount of data was taken at different gap lengths and pressures, but the results were inconclusive because the variations observed were all such that they could be ascribed to errors in determining i_0.

THEORY AND APPLICATION

Since the work of Fisher and Bederson, there have been three published attempts at theoretical explanation of the dependence of time lag on overvoltage which they observed. The first was that of Kachikas and Fisher[11] in the extension of the work to N_2, for which the experimental results were "almost identical" with those in air. This was a simplified and approximate theory which considered only a photon γ, and assumed all the photons to come approximately from the anode. It was not intended to apply for times greater than an ion crossing time. Although they recognized the role of space charge distortion and the streamer mechanism in the final breakdown they had no way of taking it into account so used a critical current at the cathode as the criterion for breakdown.[12] This simple theory was remarkably successful for the results in N_2 but less so in A and O_2.[13]

Dutton, Haydon, and Jones[14] showed no recognition of the streamer as the final breakdown mechanism or of the consequent necessity of expressing a true criterion in terms of the necessary field distortion by positive ions. They used an approximate solution for a Townsend discharge due to Bartholomeyczyk[15] and Davidson,[14] and took a critical current at the cathode as the criterion for breakdown. (This solution will be discussed later.) By varying the overvoltage, that is α, they obtained curves of roughly the same general shape as those of Fisher and Bederson.

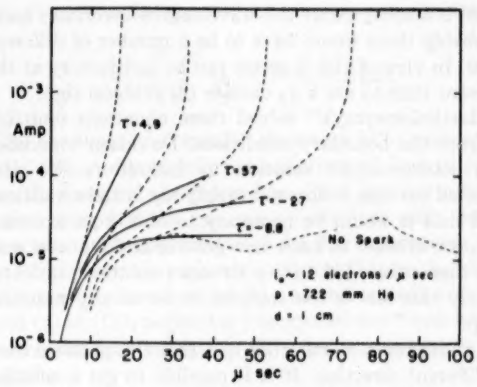

FIG. 5. Comparison of theory and experiment (dashed lines experimental).

Raether[16] has been the only one to attempt a criterion based on space charge distortion of the field. His picture of the physical situation is good (the spreading of the discharge receives verification later in this work), but he was forced to make rather crude approximations to carry the work through.

If we consider the case of a uniform field, taking $x=0$ at the cathode and $x=d$ at the anode the balance equations are:

$$\begin{aligned}\frac{1}{v_-}\frac{\partial i_-}{\partial t}&=-\frac{\partial i_-}{\partial x}+\alpha i_-,\\ \frac{1}{v_+}\frac{\partial i_+}{\partial t}&=\frac{\partial i_+}{\partial x}+\alpha i_-,\end{aligned}\tag{1}$$

where $i_-(x,t)$ and $i_+(x,t)$ are the electron and positive ion currents and v_- and v_+ the electron and ion velocities, assumed constant for the range of overvoltages involved. Considering only α, γ_p, and γ_i mechanisms the boundary conditions are:

$$\begin{aligned}&i_-(0,t)=i_0+\gamma_i\alpha i_+(0,t)+\gamma_p\alpha\int_0^d i_-(x,t)dx,\\ &i_+(d,t)=0.\end{aligned}\tag{2}$$

(γ_i is the average number of electrons released from the cathode per impinging positive ion). The γ_p term in (2) is sometimes written

$$\frac{\delta}{\omega}\int_0^d e^{-\mu x}i_-(x,t)dx$$

to include an absorption coefficient explicitly but this is likely to be more misleading than helpful. The photons do not go directly to the cathode in the minus x direction but go off in all directions so that some may reach the cathode after traveling a distance many times x. Thus μ would itself have to be a function of x. Further, very

[11] G. A. Kachikas and L. H. Fisher, Phys. Rev. **88**, 878 (1952).
[12] As published, the criterion is expressed in terms of number of electrons per electron transit time. This theory was an approximation to single electron triggering of the original theory presented in Kachikas' thesis (see reference 13) which expressed the criterion in terms of current explicitly.
[13] G. A. Kachikas, thesis, Department of Physics, College of Engineering, New York University (unpublished).
[14] Dutton, Haydon, and Llewellyn-Jones; Mathematical Appendix by P. M. Davidson, Brit. J. Appl. Phys. **4**, 170 (1953).
[15] W. Bartholomeyczyk, Z. Physik **116**, 235 (1940).
[16] Heinz Raether, Z. angew. Phys. **5**, No. 6, 211 (1953).

little is known about the wavelengths involved; quite probably there would have to be a number of different $\mu(x)$. In view of this it seems just as satisfactory at the present time to use a γ_p outside the integral sign.

Bartholomeyczyk[16] solved these equations omitting i_0 from the boundary conditions. Davidson[14] modified Bartholomeyczyk's solution to include i_0. He also pointed out that it does not satisfy the initial conditions and that it would be necessary to obtain an accurate solution in order to know how good or bad that one was. He then proceeded to get an exact solution; unfortunately this last is too complex to be of any practical help.

It has proven worth while to attack this problem from a different direction. If it is possible to get a solution for $i_-(0,t)$, the electron current at the cathode, then

$$i_-(x,t)=i_-(0,t-x/v_-)e^{\alpha x}. \tag{3}$$

The positive ion current created in dx' at x' and t is

$$di_+=\alpha i_-(x',t)dx'=\alpha i_-(0,t-x'/v_-)e^{\alpha x'}dx'.$$

This reaches x at a time $(x'-x)/v_+$ later so the current at x and t coming from dx' is

$$di_+(x,t)=\alpha i_-\left(0,t-\frac{x'-x}{v_+}-\frac{x'}{v_-}\right)e^{\alpha x'}$$

$$=\alpha i_-\left(0,t+\frac{x}{v_+}-\frac{x'}{v}\right)e^{\alpha x'},$$

where $1/v=1/v_++1/v_-$ or $v=v_+v_-/(v_++v_-)$. Then

$$i_+(x,t)=\int_x^{v(t+x/v_+)\text{ or }d}\alpha i_-\left(0,t+\frac{x}{v_+}-\frac{x'}{v}\right)e^{\alpha x'}dx'. \tag{4}$$

The upper limit on this integral assumes that no electrons leave the cathode until $t=0$ (time of application of the voltage) and then takes into account the fact that x' makes no contribution to the positive ion current at x until there has been time for an electron to go up to x' and a positive ion to go back to x. So the upper limit is $v(t-x/v_+)$ until this quantity equals d and then remains d thereafter. Similarly there can be no contribution by γ_p from any x until electrons have had time to reach x from the cathode. With this, (3) and (4) may be used in (2) to obtain the integral equation

$$i_-(0,t)=i_0+\gamma_i\alpha\int_0^{vt\text{ or }d}i_-\left(0,t-\frac{x'}{v}\right)e^{\alpha x'}dx'$$

$$+\gamma_p\alpha\int_0^{v_-t\text{ or }d}i_-\left(0,t-\frac{x}{v_-}\right)e^{\alpha x}dx. \tag{5}$$

Now, trying

$$i_-(0,t)=i_0(A-Be^{t/\tau}) \tag{6}$$

in (5) gives

$$i_-(0,t)=i_0+\gamma_i\alpha i_0\left[\frac{A}{\alpha}\{\exp[\alpha(vt\text{ or }d)]-1\}\right.$$

$$\left.-\frac{Be^{t/\tau}}{\alpha-1/v\tau}\left\{\exp\left[\left(\alpha-\frac{1}{v\tau}\right)(vt\text{ or }d)\right]-1\right\}\right]$$

$$+\gamma_p\alpha i_0\left[\frac{A}{\alpha}\{\exp[\alpha(v_-t\text{ or }d)]-1\}\right.$$

$$\left.-\frac{Be^{t/\tau}}{\alpha-1/v_-\tau}\left\{\exp\left[\left(\alpha-\frac{1}{v_-\tau}\right)(v_-t\text{ or }d)\right]-1\right\}\right]. \tag{7}$$

For times shorter than $vt=d$ this equation cannot be satisfied for any constant τ or A, and for longer times it is just the equation obtained by Davidson. However, we now know that the solution is exact for longer times and can see when it begins to fail. Unfortunately, since $v\simeq v_+$, it does not become good until one ion crossing time, so the whole solution is not of much help. On the other hand, in case $\gamma_i=0$ the remaining equation can be satisfied for times greater than one-electron crossing time. In this limiting case, A and τ are given by

$$A=\frac{1}{1-\gamma_p(e^{\alpha d}-1)}, \tag{8}$$

and

$$\gamma_pe^{\alpha d}e^{-d/v_-\tau}=1-1/\alpha v_-\tau+\gamma_p. \tag{9}$$

I am indebted to Dr. Wulf Kunkel for another solution of the integral Eq. (5). If $(di_-/dt)\cdot(d/v_-)\ll i_-$, then $i_-(0,t)$ can be used in the γ_p term instead of $i_-(0,t-x/v_-)$, and in this case he was able, by means of a Laplace transform, to obtain the solution, for $d/v_-\leq t\leq d/v$,

$$i_-(0,t)=\frac{i_0}{1+\gamma_i-\gamma_p(e^{\alpha d}-1)}\left[1+\frac{\gamma_i}{1-\gamma_p(e^{\alpha d}-1)}\right.$$

$$\left.\times\exp\left(\frac{1+\gamma_i-\gamma_p(e^{\alpha d}-1)}{1-\gamma_p(e^{\alpha d}-1)}\alpha vt\right)\right]; \tag{10}$$

and for $t\geq d/v$,

$$i_-(0,t)=\frac{i_0}{1-(\gamma_i+\gamma_p)(e^{\alpha d}-1)}-i_0Be^{t/\tau}, \tag{11}$$

where τ is the root of

$$\gamma_ie^{\alpha d}e^{-d/v\tau}=\frac{-1}{\alpha v\tau}[1-\gamma_p(e^{\alpha d}-1)]+1+\gamma_i-\gamma_p(e^{\alpha d}-1).$$

The condition $(di_-/dt)\cdot(d/v_-)\ll i_-$ says that the current change during one electron transit time is much less than the current itself. If we consider the case of $i_0=1$ electron per electron transit time (i.e., $\sim$10 electrons per μsec) this is approximately the same as saying $\gamma_p(e^{\alpha d}-1)\ll 1$. This does not hold at the sparking potential, so again the whole solution is not good for

the present case, but this solution is exact for the limiting case of $\gamma_p=0$. In this case the constant B, evaluated by equating (10) and (11) at $t=d/v$, can be written in a simple form by neglecting γ_i compared to 1 and 1 compared to $e^{\alpha d}$:

$$B\simeq\frac{\gamma_i e^{\alpha d}(1-1/\alpha v\tau)}{1-\gamma_i e^{\alpha d}}. \tag{12}$$

Moreover, this can be used to evaluate the constant B in the case of $\gamma_i=0$ above. From (5) it is seen that the integral equation for the two limiting cases is the same with only the change of subscripts on γ and v. Therefore letting $\gamma_p=0$ in (10) and then changing γ_i to γ_p and v to v_- gives the solution for $\gamma_i=0$ and $t\leq d/v_-$. It follows that with this change of subscripts (12) gives the constant B in the case of $\gamma_i=0$. Further, this solution for $t\leq d/v_-$ is good even if γ_i is not zero because the ions cannot contribute in so short a time.

At this point, solutions have been obtained for the case when both γ_i and γ_p are important for $t\leq d/v_-$ and for $t\geq d/v$, though for the latter B has not been evaluated, and for the limiting cases $\gamma_i=0$ or $\gamma_p=0$ for all times.

For $d/v_-<t<d/v$ an approximate solution for both γ's might be obtained by taking the one for $\gamma_i=0$ in the early times before many ions can reach the cathode and somehow joining it to the one for both γ's which becomes valid at $t=d/v$. If no mathematical expression could be obtained the two could still both be plotted into the intermediate region where they both lose validity and then possibly be joined graphically. However this would have to be studied carefully because there seems to be no *a priori* reason why the first derivative need be continuous at one ion crossing time. With both γ's quite unknown, both velocities a bit indefinite, and even α and the required overvoltage of doubtful applicability, as will be seen, the use of this method to try to fit the experimental data would require more trial and error calculation than seems worth while at present.

The data taken for the cases when sparks did not occur indicates that steady state (if it may be called that in spite of the fluctuations) was achieved in 50 μsec or less. To account for the steady-state value of the current with the known voltage and Sanders' data for α requires that secondary mechanisms increase the current by one or two orders of magnitude. If the major part of this were due to γ_i it would take thousands of microseconds to reach steady state, therefore calculations have been made here only for $\gamma_i=0$.

The above solutions are equally good for $\gamma e^{\alpha d}<$ or >1 because τ changes sign with the denominator.

Having once obtained an expression for $i_-(0,t)$, then (3) and (4) give $i_-(x,t)$ and $i_+(x,t)$. The current measured by the external circuit is due to the motion of all the charges in the gap, and for infinite parallel planes is

$$i(t)=\frac{1}{d}\int_0^d\{i_-(x,t)+i_+(x,t)\}dx. \tag{13}$$

The assumption of infinite electrodes is to assure not only uniformity of field but also that all lines of force from a charge in the gap end on either the electrodes or other charges in the gap, not on chamber walls, but it is a reasonable approximation for this experiment.

For the case of $\gamma_i=0$, when (8) and (12) (with change of subscripts) are used in (6) and this is used with (3) and (4) in (13), neglecting 1 compared to $e^{\alpha d}$ and taking $v=v_+$, the final result for the measured current is, for $t\leq d/v_+$,

$$i(t)=\frac{i_0}{\alpha d(1-\gamma_p e^{\alpha d})}\left[\left\{1-\gamma_p e^{\alpha d}\frac{\varphi}{\psi}(1-\alpha v_+\tau)\right\}e^{\alpha d}\right.$$
$$+\alpha v_+ e^{\alpha d}t-\left\{1-\gamma_p e^{\alpha d}\frac{\varphi}{\psi}\right\}e^{\alpha v_+ t}$$
$$\left.-\gamma_p e^{\alpha d}\frac{\varphi}{\psi}e^{\psi d}\left\{\frac{\alpha(v_+\tau)^2\varphi-1}{v_+\tau\varphi}\right\}e^{t/\tau}\right],$$

and for $t\geq d/v_+$,

$$i(t)=\frac{i_0}{\alpha d(1-\gamma_p e^{\alpha d})}\left[\alpha d e^{\alpha d}-\gamma_p e^{\alpha d}\frac{\varphi}{\psi}\right.$$
$$\left.\times\left\{e^{\alpha d}\left(\frac{\alpha(v_+\tau)^2\varphi-1}{v_+\tau\varphi}\right)-\alpha v_+\tau e^{\psi d}\right\}e^{t/\tau}\right], \tag{14}$$

where $\varphi=(\alpha-1/v_-\tau)$, $\psi=(\alpha-1/v_+\tau)$, and τ is given by (9). In order to use these expressions to plot curves for comparison with the experimental data values are needed for α, v_-, v_+, and γ_p. The expression,

$$\alpha=p\times1.048\times10^{-4}(E/p-27.38)^2, \tag{15}$$

was adjusted to fit Sanders' data at $E/p=34$ and 40, and is quite close at $E/p=50$. E_s is not definitely known because of the way the sparking potential varied, but was nearly 28.8 kv/cm for the data to be compared with it. For breakdown E/p is about 40 volts/cm$\times$mm Hg; if the work of Bradbury and Nielsen[17] for electron velocity in air is extrapolated to this E/p, it gives $v_-\simeq1.6\times10^7$ cm/sec. From Varney's[18] work on drift velocities in N_2 and O_2, $v_+=6\times10^4$ cm/sec was taken as a reasonable value for air at $E/p\simeq40$.

Using these values, and $p=722$ mm Hg and $i_0=12$ electrons/μsec, some curves were calculated for comparison with the data of Fig. 5 as follows. From E_s and p, (15) gives α. If $\gamma_p e^{\alpha d}<1$, then for long times the solution (14) goes over into the familiar steady-state expression,

[17] See reference 2, p. 191.
[18] R. N. Varney, Phys. Rev. 89, 708 (1953).

$i=i_0e^{\alpha d}/(1-\gamma_p e^{\alpha d})$. Taking the steady-state value of the current for the "no spark" curve in Fig. 5 as 2×10^{-5} amp, this equation gives γ_p. Then τ can be obtained from (9). γ_p is then assumed constant for the small range of overvoltages studied, and α and τ are calculated for successively higher voltages. The curves calculated using these values were too widely separated vertically at the first shoulder, for a given change of final slope. A better fit was obtained by taking $E_s=28.5$ kv/cm and $v_+=8\times10^4$ cm/sec. (These gave $\gamma_p=1.5\times10^{-5}$.) This change is greater than the experimental uncertainty in E_s but α is really the quantity being varied; and it is more uncertain. The curves drawn in heavy lines in Fig. 5 were calculated using these values.

The calculated curves have a similar shape and change with overvoltage in a similar manner but there are two main differences which cannot be reconciled by adjustment of the parameters. The first is a difference in time for the initial current rise; the fit of the early part of the curves would be quite good if the experimental curves could be translated 5 μsec to the left. The second is that the final slope of the calculated curves increases much faster with overvoltage than that of the experimental curves if Fisher and Bederson's data for overvoltage is applied to the time lags observed here using Sanders' data for α. The curve labeled $\tau=4.9$ μsec was calculated for an overvoltage of only 0.03 percent [percent overvoltage$=100(V-V_s)/V_s$]. From the data of Fisher and Bederson this overvoltage would give a time lag of 50 μsec. However, it is somewhat doubtful that their data applies because they probably had a lower γ_p due to "conditioning" of the electrodes by repeated sparking, as discussed above. In fact, it was noted in the course of this work that the overvoltages necessary seemed less than theirs, but with sparks 5 minutes apart and V_s as capricious as it was, it was nearly impossible to get data on this. Further, although it was argued above that positive ions cannot contribute the major portion of the secondary electrons because of the apparent leveling off of the "no spark" curves, these curves fluctuate far too much to be able to rule out the positive ion mechanism entirely. If γ_i does contribute appreciably in the longer formative times, then the overvoltage must be correspondingly larger for the short time lags since then the ions cannot contribute significantly. All in all, this point is not too serious because both theory and experiment are still too inexact and incomplete.

The difference in time at the beginning is not so easily disposed of, however. If the parameters of the calculated curves are adjusted to make the shoulder of the curve come at a late enough time the initial slope is less than the experimental; it is as though the experimental current rise were somehow delayed. The operation of the apparatus was rechecked as to start of the sweep relative to the pulse, linearity of the sweep, and rise time of the amplifiers; 1 μsec seems an outside limit for experimental error.

Anything which would delay the development of an avalanche, or of following secondary avalanches, by a time comparable to an electron transit time could slow up the whole buildup process about as observed. The delay may be due to one, or a combination, of several effects. The first is photoionization in the gas. Cravath[19] has measured absorption coefficients of 2 and 10 cm^{-1} for radiations from a discharge in air. He found the second radiation was "more effective in ionizing air than in releasing photoelectrons from brass." Dechene[20] has measured absorption coefficients from about 2 to 6 cm^{-1} for ionizing radiation in air. Now Sanders' measurements were for steady-state currents and such photoionization in the gas merely looked like a larger α, but when this α is then used to calculate transients the rise will be too fast. That is, by using Sanders' α, avalanches crossing the gap in one-electron transit time are calculated to yield a certain amount of ionization, whereas actually the original avalanches are smaller but are followed by other avalanches starting at various places in the gap and yielding their ionization at later times. Due to absorption, more of the secondary avalanches would start near the anode, but those which started near the cathode would have much greater amplification in the gas and these would be about an electron transit time late. The only estimate of yield for such photoionization in air seems to be that of Cravath for the 10-cm^{-1} radiation that there was about one such photon for every 10^4 ions created by collision. Therefore it is impossible to estimate how much average delay might be thus introduced, but it doesn't seem likely that all of the observed delay could be due to this effect.

There could also be a delay of the γ_p action by entrapment of resonance radiation, by creation of atomic excited states by metastables, by excitation of atomic states by secondary impacts, or by chemical interaction such as between N and O to yield excited states of NO, the radiation from which is not absorbed and can liberate photoelectrons but arrives at the cathode after some delay. From Holstein's[21] theory for imprisonment of resonance radiation, one would expect times for this of the order of 10^{-5} to 10^{-4} sec, which is much too long for the observed discrepancy. However, molecular radiations are much less liable to entrapment and if such occurs at all it would be for much shorter times. In O_2, photons above 6-ev energy are heavily absorbed to give dissociation to O. E. Huber (work to be published), using cylindrical geometry with a Ni cathode, has found that pure N_2 or O_2 give no γ_p pulses at pressures from 50 to 600 mm Hg, presumably because all the radiation capable of photoemission is absorbed in the gas. The addition of a little O_2 to the N_2 does give γ_p pulses, either by increasing γ_p or by decreasing

[19] A. M. Cravath, Phys. Rev. **47**, 254 (1935).
[20] G. Dechene, J. phys. et radium **7**, 533 (1936).
[21] T. Holstein, Phys. Rev. **72**, 1212 (1947).

γ_i so that some previously masked γ_p action can be observed.

A metastable process has been observed in argon by L. Colli and U. Facchini (work to be published) with lifetimes about right to account for the difference observed here. They found $A^m+2A \rightarrow A_2^*+A$ and $A_2^* \rightarrow A_2+h\nu$. The photons should have an energy of 6.5 to 11 ev and are not absorbed in the gas.

None of these processes could be expected to delay more than a small portion of the total radiation from the discharge, but the γ_p process may be entirely due to just a few such wavelengths; too little is known yet for definite conclusions.

As earlier stated, it was proposed that space charge distortion of the field is required to make streamer propagation possible; no mechanism considered in the foregoing analysis could account for the hyper-exponential increase in current observed just before breakdown. It is thus essential to see whether the observed increase in the rate of rise of the current can be shown quantitatively to be due to space charge.

In order to get an expression for the field due to space charge in the gap, consider infinite parallel plane geometry with charge distributed uniformly in the y and z directions in a slab of thickness dx' at x' and both planes at zero potential. If the volume charge density is given by $q_v(x)$, then the charge per unit area of this slab is $q_v(x')dx'$. If a Gaussian surface is taken in the form of a cylinder parallel to the field, the use of the facts that with no variation in the y and z directions the field lines must be parallel, and that the integral of $E_{sc}dx$ across the gap must be zero, yields, in mks units, $E_{sc}=-q_v(x')(d-x')dx'/\kappa_0 d$, and $E_{sc}=q_v(x')x'dx'/\kappa_0 d$ for the regions $x \leq x'$ and $x \geq x'$, respectively. Assuming the discharge to be spread uniformly over the electrodes and neglecting the few electrons present, $q_v(x)=i_+(x)/v_+A$, where A is the area of the electrodes; so, finally,

$$E_{sc}(x)=\int_0^x \frac{i_+(x')x'}{v_+A\kappa_0 d}dx'-\int_x^d \frac{i_+(x')(d-x')}{v_+A\kappa_0 d}.$$

This will be in volts/cm if we use amp, cm, sec, and $\kappa_0=8.85\times10^{-14}$ farad/cm.

Now to show whether or not space charge distortion of the field is enough to appreciably affect $\exp(\int_0^d \alpha dx)$, some expression for the current must be used in the above expression for E_{sc} and the integrations performed; then the resulting $E_{sc}(x)$ plus the applied field are used in (15) for α where the whole quantity is squared and again integrated across the gap. To do this with the rather complicated expression for $i_+(x,t)$ used above involves a prohibitive amount of labor. However, in the expression for the final steady-state current when $\gamma e^{\alpha d}<1$, i.e., $i=i_0e^{\alpha d}/(1-\gamma e^{\alpha d})$, the effect of the γ action is the same as an increased i_0, and for the longest time lags studied when the current is increasing slowly the distribution of charge in the gap should not be so very different from what it would be for a steady current of that value. Thus the expression $i_+(x)=i_0(e^{\alpha d}-e^{\alpha x})$ should give a reasonable approximation for that case. When the integrations are carried through using this expression for i_+, the final result for the increment in the exponent is

$$\Delta\int_0^d \alpha dx \simeq \frac{1.05\times10^{-4}}{p}\left(\frac{i}{v_+\kappa_0 A}\right)^2 \times\left(\frac{-1}{\alpha^6 d^4}+\frac{2.5}{\alpha^5 d^3}-\frac{1}{\alpha^2 d^2}+\frac{1}{12}\right)d^3,$$

where $i=i_0e^{\alpha d}$ is the measured current with the assumed expression for $i_+(x)$.

For the long time lags, values of α near threshold are of interest; the change in α between the lower two calculated curves in Fig. 5 was $\sim$0.015. Certainly a smaller change than this would give an appreciable change in the current. However, since the effect of a change in α on the measured current appears gradually over one ion crossing time, a change of say one-tenth this much could hardly give a visible change of slope. Something around 0.005 seems a reasonable figure. Equating the above expression to this figure and solving for i, the current at which field distortion should cause a noticeable up curving, the extent of variation in i for v_+ from (6 to 8)$\times10^4$ cm/sec and α from 11.1 to 11.8 (i.e., V_s from 28.5 to 28.8 kv) is from 2.8 to 3.7$\times10^{-4}$ amp. Experimentally, the semilog plots of current for the long time lags begin to curve upward around (2 to 4)$\times10^{-4}$ amp. This agreement not only supports the proposed space charge mechanism but also shows that the discharge is spread more or less uniformly over the electrodes as assumed in the calculations. If the discharge were localized to an electrode area of a few cm^2 the up curving would have had to appear for currents more than an order of magnitude smaller. As seen above, the dependence on v_+ and α are not critical, and since i is proportional to the square root of the value chosen as a sufficient change in α, this is not over-critical either; there cannot be any order of magnitude error. This is also in agreement with the experimental observation that when the light was focused on the center of the cathode, sparks appeared to occur randomly over the whole electrode, independent of the illuminated area.

ACKNOWLEDGMENTS

I am very grateful to Professor Loeb who suggested this problem for his continued interest and guidance, and to all of the group of students working under him for many helpful discussions, especially G. G. Hudson and C. D. Maunsell. I also wish to thank Dr. Wulf Kunkel for several discussions as well as the mathematical solution given in the text, and Norman T. Seaton for much help with the electronics.

Velocity of Sound in Superconducting Tin

CHARLES F. SQUIRE
The Rice Institute, Houston, Texas
(Received May 27, 1954)

The ultrasonic pulse method has been used to measure the velocity of 10-Mc/sec sound waves in polycrystalline tin from 295°K to 2°K. The superconducting state has no effect (±0.3 percent) on the velocity and attenuation of longitudinal and of transverse waves. The value of θ_D computed from these velocity measurements at the very low temperature is 210°K.

INTRODUCTION

THE ultrasonic pulse method[1-3] has been used in this research to measure the velocity of 10-Mc/sec sound waves in a polycrystalline tin cylinder from 295°K down to 2°K. Both longitudinal and transverse waves were measured. It is well known that ordinary pure tin enters the superconducting state at 3.735°K and, in the presence of a magnetic field, the transition occurs at lower temperatures. Measurements on velocity were made both with and without small magnetic fields and attention was given to the attenuation of the sound in crossing the superconducting transition. The experimental facts reported here show that there is no velocity change and no attenuation change observable within the limits of our equipment on crossing into the superconducting state. We had first examined these observations in a preliminary way several years ago[4] and Bommel and Olsen[5] have reported similar results using standing waves at 1 Mc/sec. The recent theory of Bardeen[6] and, independently, of Fröhlich,[7] indicates that the superconducting state is brought about by electron-lattice vibration interaction. Thus, the superconducting state might be expected to influence the velocity of longitudinal and/or transverse waves. The question of the degree to which the interaction can alter the velocity of these waves was not a matter of prediction from the existing state of the Fröhlich-Bardeen theory. The phenomenological theory by Gorter and Casimir,[8] and by Gorter and Bender[9] describes the new electronic state in terms of a two-electron fluid such that for $T<T_c$ one of the fluids is separated from the other by an energy gap and possesses superfluid properties. It was, quite frankly, our expectation that the ultrasonic waves would be completely absorbed just at the transition temperature T_c because the small energy in the waves would produce excitations of superfluid electrons to the normal conducting electrons. In superfluid liquid helium just such an energy absorption occurs[1] at the λ point. The important difference between these two superfluids, insofar as sound waves are concerned, is that the helium atoms are the particles undergoing displacement with the sound wave and are also the superfluid particles. On the other hand, the electrons in the metal do not participate in the sound wave and become more and more free from lattice interaction at low temperatures. For these reasons, the experiment seemed important at this stage of our understanding of superconductivity.

EXPERIMENTAL

Figure 1 shows the experimental arrangement of the liquid helium cryostat with the tin cylinder specimen and the quartz crystal transducer. The coaxial line feeding the 10-Mc/sec voltage to the quartz crystal was made from a ¼-inch copper-nickel alloy thin walled tube as outer conductor and a No. 36 enamel coated copper wire inner conductor. The heat leak was small and 2 liters of liquid helium served for eight hours of experimentation without having the level get below the specimen. The electronic equipment for the direct measure of the round trip time of the sound pulse has been described before[2] and very little modification of circuits has been introduced.

The quartz crystal was made to adhere to the specimen by the use of the binder,[3] Dow Corning 200 Fluid, viscosity 25 000 poises. We had previously tried a number of crystal to specimen binders, with best results[2] from an organic liquid consisting of ethyl ether, ethyl alcohol, and isopentane. The discovery by McSkimin[3] that the Dow Corning 200 Fluid would work has allowed us to bind the crystal to tin and work from 150°K down to 2°K. The technique used by us has been as follows: (a) at 290°K, put a small quantity of binder on and lightly press the quartz crystal down so that the entire crystal area is wetted but without excess fluid creeping up on its top surface; (b) put the assembly of Fig. 1 into the warm Dewar flasks and start the electronic gear sending signals to shake the crystal; (c) slowly cool to liquid N_2 temperature over a period of 2–3 hours; (d) transfer liquid helium into the inner Dewar flask and the echoes are usually still

[1] J. R. Pellam and C. F. Squire, Phys. Rev. **72**, 1245 (1947).
[2] W. C. Overton, Jr., J. Chem. Phys. **18**, 113 (1950); W. C. Overton, Jr. and R. T. Swim, Phys. Rev. **84**, 758 (1951).
[3] H. J. McSkimin, J. Appl. Phys. **29**, 988 (1953).
[4] W. C. Overton, Jr., thesis, The Rice Institute, 1950 (unpublished).
[5] H. Bommel and J. L. Olsen, Phys. Rev. **91**, 1017 (1953).
[6] J. Bardeen, Phys. Rev. **79**, 167 (1950); Revs. Modern Phys. **23**, 261 (1951).
[7] H. Fröhlich, Phys. Rev. **79**, 845 (1950); Proc. Roy. Soc. (London) **A64**, 129 (1951).
[8] C. J. Gorter and H. Casimir, Physica **1**, 306 (1934).
[9] C. J. Gorter and P. L. Bender, Physica **18**, 597 (1952).

there. For our work we did not press down hard on the quartz crystal with the electrodes of the coaxial cable. In particular for the transverse waves (Y-cut crystal), a light contact gave best results. The tin was cast as a cylinder by melting in a vacuum furnace and cooling very slowly. The ends were machined off parallel to give a length of 2.745 cm. The tin had a purity stated as 99.99 percent.

Figure 2 shows the velocity of longitudinal and transverse waves (10 Mc/sec) through the specimen of polycrystalline tin. The signals on the oscilloscope (DuMont 256-D) allowed one to reproduce the setting

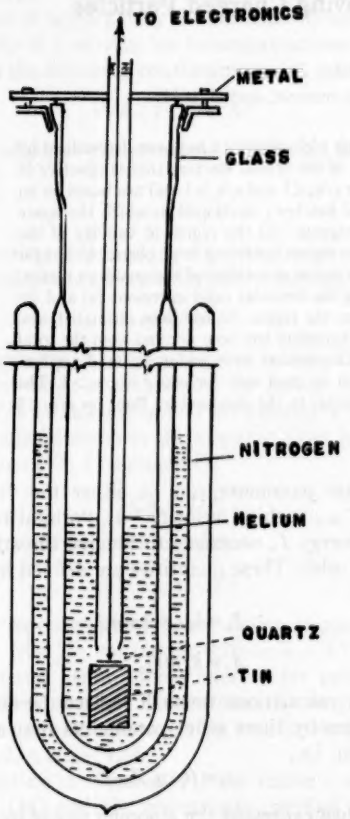

FIG. 1. Liquid helium cryostat for measuring velocity in metal specimens of 10-Mc/sec sound waves.

for the round trip time to ± 0.05 microsecond out of 17 microseconds. The echoes were not observed to change their position to within this accuracy (0.3 percent) in the liquid helium temperature range. The expansion of the tin cylinder is so small in this region that we may neglect it. We have taken into account the thermal expansion in a manner used by us on previous work.[2] The linear expansion is taken as a function of temperature to resemble the specific heat curve, i.e., it is zero at the absolute zero and rises to

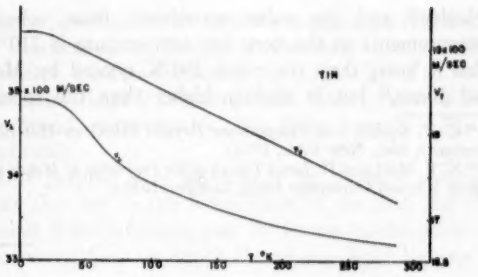

FIG. 2. The velocity *vs* temperature of longitudinal waves V_L and of transverse waves V_T in polycrystalline tin. There is no change in velocity (± 0.3 percent) at the superconducting transition.

become a linear function of temperature above 200°K and becomes quite normal with a value for the coefficient of 32×10^{-6} per degree above 250°K. The sharp fall off below the Debye characteristic temperature, 185°K for Sn, is characteristic of the expansion coefficient in most metals. The measured results at liquid nitrogen temperature and liquid helium temperature were the averaged time for the round trip signals. The calculation of velocity thus introduces the uncertainty of the length of the specimen. The absolute value of the velocity may be off several percent in the liquid helium temperature range but the relative value of the velocity is 0.3 percent in possible error. Within this latter limit the velocity of longitudinal and of transverse waves does not change when the Sn enters the superconducting state. The attenuation of the signals can be measured by the method of inserting attenuation[1] with external circuit elements. Thus, for example, one can insert one decibel of loss in the receiver circuit and watch the drop in signal height on the scope. Had there been a change as great as this amount when the Sn entered the superconducting state one would have seen such an effect directly on the face of the scope. No observable change was detected in the received signal strength on entering the superconducting state or on leaving it, i.e., raising the temperature. The constant velocity and constant attenuation was observed both with and without an applied magnetic field of 30 gauss.

CONCLUSIONS

The superconducting state has no large scale effect on the velocity and attenuation of longitudinal and transverse waves. The very high electrical conductivity of Sn just before the metal becomes superconducting should perhaps have foretold the possibility that the electrons are very little disturbed by the lattice oscillations. Conversely the elastic waves are not greatly influenced by the electron gas. The experimental results are not able to decide the merits of any existing theory of superconductivity. We may compute the characteristic Debye temperature θ_D from the measured

velocity[10] and the value we obtain from velocity measurements at the very low temperature is 210°K. This is lower than the value 260°K quoted by Mott and Jones,[11] but is slightly higher than the specific heat value 185°K computed by Keesom and Van Laer.[12]

We are indebted to Dr. W. D. Mason and Dr. H. J. McSkimin of The Bell Laboratories for calling our attention to the use of Dow Corning 200 Fluid in low-temperature work.

[10] C. F. Squire, *Low Temperature Physics* (McGraw-Hill Book Company, Inc., New York, 1953).
[11] N. F. Mott and H. Jones *Theory of the Properties of Metals and Alloys* (Oxford University Press, London, 1936).
[12] W. Keesom and P. Van Laer, Physica **5**, 193 (1938).

PHYSICAL REVIEW VOLUME 95, NUMBER 5 SEPTEMBER 1, 1954

Bohr's Theory of Energy Losses of Moving Charged Particles

JACOB NEUFELD
Oak Ridge National Laboratory, Oak Ridge, Tennessee
(Received February 4, 1954; revised manuscript received April 5, 1954)

The stopping power of a particle having charge $Z_{eff}e$ and moving with velocity v has been determined by Bohr for $\kappa=2Z_{eff}e^2/\hbar v$ and $\eta_s=2v/u_s>2$, where u_s is the velocity of the orbital electron that is effective in stopping the particle. Bohr's results are formulated differently for $\kappa/\eta_s<1$ and $\kappa/\eta_s>1$ and are based on an orbital picture of the processes involved. An alternative method has been developed in which the space surrounding the particle track has been subdivided into three regions: (a) the region of validity of the Rutherford formula (adjacent to the track), (b) the intermediate region involving large perturbations for which no adequate theory exists at the present time, and (c) the region of validity of the quantum perturbation theory (the most remote from the track). By extrapolating the formulas valid in regions (a) and (c) into the region (b), the contribution to the stopping power due to the region (b) has been estimated, and adding to it the contribution due to the regions (a) and (c) an expression has been derived from the total stopping power that is applicable whenever $\kappa>1$ and $\eta_s>1$. This expression has a wider region of applicability than the corresponding Bohr's formula since the latter can be used only for $\kappa\ll\eta_s^2$ if $\kappa/\eta_s>1$. The physical picture used for deriving this expression is somewhat similar to the one used by Bohr for $\kappa/\eta_s<1$ but is different from the one used by Bohr for $\kappa/\eta_s>1$.

I. INTRODUCTION

THE present investigation deals with Bohr's theory of energy losses due to excitation and ionization processes by moving charged particles. This theory is particularly applicable to heavy ions when

$$\kappa=2Z_{eff}e^2/\hbar v\gg 1, \tag{1}$$

where $Z_{eff}e$ is the effective charge of the ion and v its velocity. A further requirement is that

$$\eta_s=2v/u_s>2, \tag{2}$$

where u_s is the orbital velocity of the sth electron in one of the atoms of the stopping substance.

The stopping power of a moving charged particle can often be determined by separately evaluating the contribution σ_s of the sth orbital electron and then summing to get the total effect as $\sum_s\sigma_s$. In these calculations the processes resulting from the loss and capture of orbital electrons of the moving particle are not considered and a term depending on these processes should be added to $\sum_s\sigma_s$ in order to determine the total stopping power.

The contribution σ_s to the stopping power is often expressed as a function of three parameters, two of which characterize the moving particle; e.g., the effective charge $Z_{eff}e$ and velocity v, and one characterizing the orbital electron that is effective in stopping the particle. The latter parameter can be either the "cyclic frequency" ω_s, "orbital velocity" u_s, "orbital radius" a_s, or the energy I_s necessary to remove the sth electron from its orbit. These quantities are defined by Bohr as follows:[1]

$$I_s=\hbar\omega_s=\tfrac{1}{2}mu_s^2, \tag{3}$$

$$a_s=\hbar/mu_s. \tag{4}$$

In our calculations we shall replace the above three parameters by three other parameters that are nondimensional, i.e.,

$$\sigma_s=f(\kappa,\eta_s,Z_{eff}). \tag{5}$$

Bohr has expressed the stopping power by means of two formulas having different regions of applicability. The first of Bohr's formulas, derived in 1912, is as follows:[2]

$$\sigma_s=2B_s\ln\frac{km v^3}{Z_{eff}e^2\omega_s}=2B_s\ln\frac{k\eta_s^2}{\kappa}, \tag{6}$$

where

$$B_s=2\pi Z_{eff}^2e^4/mv^2=\pi I_s\kappa^2a_s^2 \tag{7}$$

and

$$k=1.25. \tag{8}$$

[1] N. Bohr, Kgl. Danske Videnskab. Selskab, Mat.-fys. Medd. **18**, No. 8 (1948), formulas (3.1.7), (3.3.1), and (3.3.2).
[2] N. Bohr, Phil. Mag. **25**, 10 (1913).

This formula is applicable in the region where

$$\kappa/\eta_s<1. \tag{9}$$

The second of Bohr's formulas, derived in 1948, is as follows:[3]

$$\sigma_s=B_\epsilon \ln\frac{2^{\frac{1}{2}}m^{\frac{1}{2}}v^4}{\hbar^{\frac{1}{2}}\omega_s^{\frac{1}{2}}Z_{\text{eff}}\epsilon^2}=B_\epsilon \ln\frac{\eta_s^3}{\kappa}, \tag{10}$$

and is applicable in the region where

$$\kappa/\eta_s>1. \tag{11}$$

We shall now consider the range of values of κ/η_s and the regions of applicability of formulas (6) and (10) if the velocity of a moving ion having an atomic number Z satisfies the following relationship:

$$\epsilon^2/\hbar<v<Z^{\frac{1}{2}}\epsilon^2/\hbar. \tag{12}$$

Then the effective charge number of the ion is roughly equal to:[4]

$$Z_{\text{eff}}\sim Z^{\frac{1}{2}}\hbar v/\epsilon^2. \tag{13}$$

Substituting (13) in (1), we find that in the velocity region considered, κ is substantially constant, i.e.,

$$\kappa\sim 2Z^{\frac{1}{2}}. \tag{14}$$

The minimum value of η_s is given by (2). The maximum value of η_s is determined by taking from (12) $v_{\max}=Z^2\epsilon^2/\hbar$ and assuming that the velocity of the most loosely bound electron in the stopping atom is roughly equal to $u_1=\epsilon^2/\hbar$. Consequently,

$$2<\eta_s<2Z^{\frac{1}{2}}, \tag{15}$$

and we obtain from (14) and (15)

$$Z^{-\frac{1}{2}}<\kappa/\eta_s<Z^{\frac{1}{2}}. \tag{16}$$

For a "representative" heavy fission fragment such as iodine ($Z=53$) we obtain $0.26<\kappa/\eta_s<3.75$. If we consider recoil heavy atoms released for instance by bombardment of solids by neutrons the range of κ/η_s may be somewhat more extended, i.e., for lead ($Z=82$) we find $0.23<\kappa/\eta_s<4.34$.

Substituting in (9) and (11) the values κ and η_s as given by (14) and (2), respectively, we find that the electronic orbital velocities for which the Bohr formula (6) is applicable are approximately given by

$$u_s<v/Z^{\frac{1}{2}}. \tag{17}$$

Similarly the Bohr formula (10) is applicable for

$$v>u_s>v/Z^{\frac{1}{2}}. \tag{18}$$

As an example of the applicability of the two Bohr formulas, consider a fission fragment moving in hydrogen. In the beginning of the range of the fission fragment, $Z_{\text{eff}}\sim 20$ and $v\sim 1.4\times 10^9$ cm/sec. Consequently, $\kappa\sim 6$ and $\eta_s\sim 10$ and the stopping power should be determined by means of the Bohr formula (6). However, close to the end of the range $Z_{\text{eff}}\sim 2$ and v is somewhat above 2.18×10^8 cm/sec. This gives $\kappa\sim 4$ and $\eta_s\sim 2$ and, consequently, the Bohr formula (10) is applicable.

Our purpose is to investigate the physical assumptions that led to the formulation of the first and the second Bohr formulas, and to discuss modification of the assumptions on which the second Bohr formula is based.

The evaluation of the stopping power involves considerations that are based partly on an orbital picture and partly on quantum mechanical arguments. We shall use an impact parameter and divide the space surrounding the track of the particle into three regions designated as (a), (b), and (c), and defined by concentric cylinders aligned along the particle track: (a) is the "region of the orbital representation" and is adjacent to the particle track; (b) is an "intermediate region" involving large perturbations, and (c) is the "region of small perturbations," the region most remote from the track. The stopping power can thus be represented as a sum of three terms:

$$\sigma_s=\sigma_s^{(a)}+\sigma_s^{(b)}+\sigma_s^{(c)}, \tag{19}$$

representing individually the contributions of each of the above three regions.

II. REGION OF THE ORBITAL REPRESENTATION

In the region of the orbital representation we neglect the binding of electrons in the stopping atom and assume that the energy transfer from the particle to an electron expressed in terms of the impact parameter is[5]

$$T^{(a)}(p)=\frac{B_\epsilon}{2\pi}\frac{8}{(4p^2+b^2)}, \tag{20}$$

where B_ϵ is defined by (7) and the quantity b is the collision diameter, i.e.,

$$b=2Z_{\text{eff}}\epsilon^2/mv^2=2\kappa a_s/\eta_s. \tag{21}$$

We assume that this region extends from $p=0$ to $p=li_s$, where $l\ll 1$ and i_s is the value of the impact parameter corresponding to the energy transfer I_s, i.e., $T^{(a)}(i_s)=I_s$. We have, approximately,[6]

$$i_s\sim\kappa a_s. \tag{22}$$

The contribution to the stopping power due to collisions in the region (a) is

$$\sigma_s^{(a)}=2\pi\int_0^{li_s}pT^{(a)}(p)dp=B_\epsilon \ln(l^2\eta_s^2+1). \tag{23}$$

[3] See reference 1, formula (3.3.11).
[4] See reference 1, formula (4.4.1).
[5] See reference 1, formula (1.1.10).
[6] See reference 1, formula (3.3.3).

III. REGION OF SMALL PERTURBATIONS

In this region the field exerted by the moving particle upon the stopping atom is sufficiently small so that the method of variation of constants can be applied. We consider the particle as moving along the z axis and assume that an isotropic oscillator having a cyclic frequency ω_s is located on the x axis at a distance p from the origin. The value p is the impact parameter and $t=0$ corresponds to the instant at which the particle passes through the origin. Since $v \ll c$, we consider the perturbation due to the scalar potential only, i.e.,

$$V_x=\epsilon(\partial\phi/\partial x)_{x=p}r_x \quad \text{and} \quad V_z=\epsilon(\partial\phi/\partial z)_{z=0}r_z. \tag{24}$$

In the above expression ϕ designates the perturbing potential, i.e.,

$$\phi=Z_{eff}\epsilon/(p^2+v^2t^2)^{\frac{1}{2}}; \tag{25}$$

r_x and r_z are the projections of the vector $\mathbf{r}$ on the x and z axes, respectively. The vector $\mathbf{r}$ represents the position of the electron with respect to the center of the oscillator.

Let $a_x^{(s)}(t)$ and $a_z^{(s)}(t)$ represent the transition probabilities for excitation of the oscillator along the x and z axes due to the moving particle at the instant t. We have[7]

$$a_x^{(s)}(t)=(i\hbar)^{-1}\int_{-\infty}^{t}\langle 1|V_x|0\rangle\exp(i\omega_s t)dt, \tag{26}$$

and a similar expression for $a_z^{(s)}(t)$.

We are concerned here with the transition probability after the particle has gone to infinity, i.e., at $t=\infty$. Substituting (24) in (26) and taking into account (1), (2), (3), and (4), we obtain

$$\begin{aligned}|a_x^{(s)}(\infty)|&=\frac{\kappa}{\eta_s}K_1\left(\frac{p}{\eta_s a_s}\right),\\ |a_y^{(s)}(\infty)|&=\frac{\kappa}{\eta_s}K_0\left(\frac{p}{\eta_s a_s}\right),\end{aligned} \tag{27}$$

where K_0 and K_1 are modified Bessel functions of the second kind, having the order 0 and 1, respectively.[8]

The method of variation of constants can be applied for those impact parameters for which the probability of transition is small, i.e.,

$$|a_x^{(s)}(\infty)|^2 \ll 1 \quad \text{and} \quad |a_z^{(s)}(\infty)|^2 \ll 1. \tag{28}$$

Taking into account that

$$K_0\left(\frac{p}{\eta_s a_s}\right)<\frac{\eta_s a_s}{p} \quad \text{and} \quad K_1\left(\frac{p}{\eta_s a_s}\right)<\frac{\eta_s a_s}{p}, \tag{29}$$

and substituting (27) in (28), we find that for

$$p \gg a_s\kappa=i_s \tag{30}$$

the method of variation of constants can be applied.

We shall, therefore, assume that the region of small perturbations extends from $p=l'i_s$ to $p=\infty$, where $l' \gg 1$.

The energy transfer at a distance p from the particle track is[7]

$$T^{(s)}(p)=\frac{B_s}{2\pi}\frac{2}{\eta_s^2 a_s^2}\left[K_0^2\left(\frac{p}{\eta_s a_s}\right)+K_1^2\left(\frac{p}{\eta_s a_s}\right)\right], \tag{31}$$

where $K^2(a)\equiv[K(a)]^2$ and the contribution to the stopping power due to the region (c) can be represented as[7]

$$\begin{aligned}\sigma_s^{(c)}&=2\pi\int_{l'p}^{\infty}pT^{(c)}(p)dp\\ &=2B_s l'\frac{\kappa}{\eta_s}K_0\left(l'\frac{\kappa}{\eta_s}\right)K_1\left(l'\frac{\kappa}{\eta_s}\right).\end{aligned} \tag{32}$$

IV. INTERMEDIATE REGION

We have determined by means of expressions (23) and (32) two of the terms entering into the stopping power σ_s. The term $\sigma_s^{(b)}$ representing the contribution of the intermediate region cannot be determined with a precision comparable to those of (23) and (32). We are dealing here with quantum mechanical systems subjected to large perturbations and no adequate theory exists for dealing with such cases.

In view of the above difficulty there is no exact theory for determining the stopping power when $\kappa>1$. Bohr has derived two approximate expressions for the stopping power which apply to cases when $\kappa/\eta_s<1$ and $\kappa/\eta_s>1$, respectively.

V. BOHR'S EXPRESSIONS FOR σ_s WHEN $\kappa/\eta_s<1$

We briefly sketch the derivation of formula (6).

Bohr treated the perturbation caused by the field of the moving particle upon a classical oscillator and obtained for the energy loss an expression somewhat different in form but equivalent to (31). He assumed that (31) is valid not only in the region of small perturbations but also in the portion of the intermediate region extending from $p=l'i_s$ to $p=i_s$. He obtained thus as a contribution to the stopping power due to (31):

$$\sigma_s^{(A)}=\frac{2\omega_s i_s}{v}K_0\left(\frac{\omega_s i_s}{v}\right)K_1\left(\frac{\omega_s i_s}{v}\right). \tag{33}$$

Furthermore, Bohr assumed that (20) is valid not only in the region of orbital representation but also in the portion of the intermediate region extending from $p=li_s$ to $p=i_s$. He obtained thus as a contribution to the stopping power due to (20):

$$\sigma_s^{(B)}=2B_s\ln(2i_s/b). \tag{34}$$

[7] J. Neufeld, Proc. Phys. Soc. (London) **A66**, 590 (1953).

[8] For tables of K_0 and K_1 functions, see for instance: British Association for the Advancement of Science, *Mathematical Tables* (Cambridge University Press, Cambridge, 1937), Vol. 6, pp. 264–271.

By adding the expressions (33) and (34), we obtain (6) provided that

$$k=\frac{\kappa}{\eta_s}\exp\left[\frac{\kappa}{\eta_s}K_0\left(\frac{\kappa}{\eta_s}\right)K_1\left(\frac{\kappa}{\eta_s}\right)\right]. \tag{35}$$

As shown in Fig. 1, k is a slowly varying function of κ/η_s confined within a relatively narrow range from 1.055 to 1.288 when κ/η_s varies from 0.01 to 1. Consequently, the constant value attributed to k in the expression (8) is within the above range.

Bohr's method is based essentially on two assumptions; first, an extrapolation of the expressions (20) and (31) from the respective regions in which they are valid into the intermediate region, and second, that the point $p=i_s$ is the boundary separating the regions of applicability of (20) and (31).

The feasibility of the above assumptions can be verified by applying the formulas (20) and (31) to the point $p=i_s$ at which they are presumably valid and comparing the values obtained. These two values of the energy transfer are $T^{(a)}(i_s)$ and $T^{(c)}(i_s)$ and should be approximately equal one to another.

We have from (20) and (31)

$$\frac{T^{(c)}(i_s)}{T^{(a)}(i_s)}=\left(\frac{\kappa}{\eta_s}\right)^2\left[K_0^2\left(\frac{\kappa}{\eta_s}\right)+K_1^2\left(\frac{\kappa}{\eta_s}\right)\right]. \tag{36}$$

As shown in Fig. 2, the expression (36) is confined within the range from 1.033 to 0.539 when κ/η_s varies from 0.02 to 1. This range is within acceptable limits and, therefore, $T^{(c)}(i_s)$ and $T^{(a)}(i_s)$ are of the same order of magnitude.

The expression (6) has also been derived by Bohr using an alternative method based on the use of an adiabatic limit. This limit corresponds to an impact parameter

$$d_s=v/\omega_s=a_s\eta_s. \tag{37}$$

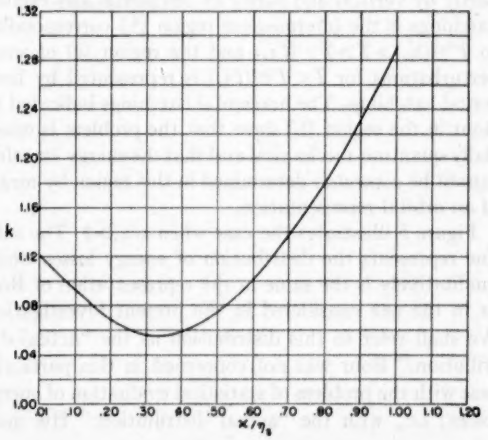

FIG. 1. Plot of $k=\left(\frac{\kappa}{\eta_s}\right)\exp\left[\left(\frac{\kappa}{\eta_s}\right)K_0\left(\frac{\kappa}{\eta_s}\right)K_1\left(\frac{\kappa}{\eta_s}\right)\right]$.

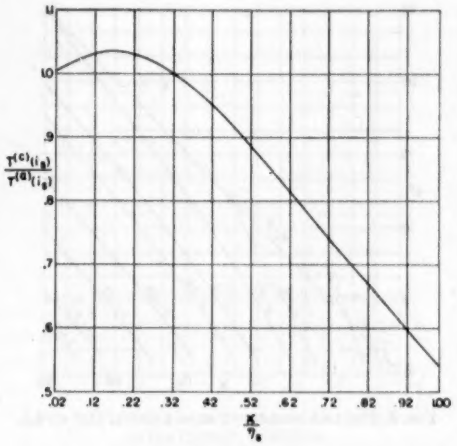

FIG. 2. Plot of $\frac{T^{(c)}(i_s)}{T^{(a)}(i_s)}=\left(\frac{\kappa}{\eta_s}\right)^2\left[K_0^2\left(\frac{\kappa}{\eta_s}\right)+K_1^2\left(\frac{\kappa}{\eta_s}\right)\right]$.

The space surrounding the particle track and comprised within the adiabatic limit (i.e., corresponding to $p\leqslant d_s$) was divided into two regions: first, the region of "free collisions" extending from $p=0$ to $p\sim i_s$, in which the energy transfer was represented by (20) and, second, the region of resonance effects extending from $p\sim i_s$ to $p=d_s$ in which the formula (31) was used in a somewhat modified form. In the region of "free collisions," the binding energy of the electrons is neglected and the energy transferred exceeds I_s. In the region of "resonance effects" the moving field interacts with the oscillator and the energy transferred is smaller than I_s.

This alternative method is based on an obvious assumption that

$$li_s<i_s<d_s. \tag{38}$$

By taking into account (22) and (37) we obtain from (38)

$$\frac{i_s}{d_s}=\frac{\kappa}{\eta_s}<1. \tag{39}$$

The inequality (39) expresses the condition of validity of (6).

VI. BOHR'S EXPRESSION FOR σ_s WHEN $\kappa/\eta_s>1$

Since $\kappa/\eta_s>1$ we obtain from (39) that $i_s>d_s$. We face here an unusual situation in which the adiabatic limit is within the region of free collisions and, therefore, the reasoning leading to (6) cannot be applied. In treating this case, Bohr did not consider resonance collisions since their aggregate effect upon stopping power is small, and assumed that the region of free collisions has been reduced in size. In the previous case (for $\kappa/\eta_s<1$) it was assumed that this region extended from $p=0$ to $p=i_s$. In this case, however, Bohr assumed that this region extended from $p=0$ to $p=d_s^*$. The new

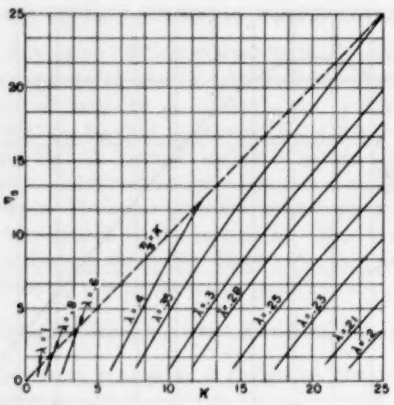

FIG. 3. Plot of λ as a function of κ and η_s (for $\kappa>\eta_s$).

limit d_s^* is smaller than i_s and was expressed as[9]

$$d_s^* = i_s^{\frac{1}{2}} d_s^{\frac{1}{2}}. \tag{40}$$

Bohr obtained the expression (10) for the stopping power by taking into account energy transfer as expressed by (20) and the maximum impact parameter as expressed by (40).

VII. PROPOSED FORMULA FOR $\kappa/\eta_s>1$

The proposed expression utilizes an extrapolation of (20) and (31) into the intermediate region: namely, we assume that (20) is valid for $0<p<\lambda i_s$ and (31) is valid for $\lambda i_s<p<\infty$. The value λ is such that

$$T^{(a)}(\lambda i_s) = T^{(c)}(\lambda i_s). \tag{41}$$

Substituting $p=\lambda i_s$ in (20) and (31), the equality (41) can be expressed as

$$K_0^2\left(\lambda\frac{\kappa}{\eta_s}\right)+K_1^2\left(\lambda\frac{\kappa}{\eta_s}\right)=\frac{\eta_s^4}{\lambda^2\eta_s^2\kappa^2+\eta_s^2}. \tag{42}$$

The relation (42) is illustrated diagrammatically in Fig. 3 by means of which we can determine λ corresponding to any pair of values (κ,η_s) for which $\kappa/\eta_s>1$.

Our expression for the stopping power becomes

$$\sigma_s = 2\pi\left[\int_0^{\lambda i_s} pT^{(a)}(p)dp+\int_{\lambda i_s}^{\infty} pT^{(c)}(p)dp\right]$$

$$= B_s\left[\ln(\lambda^2\eta_s^2+1)+2\lambda\frac{\kappa}{\eta_s}K_0\left(\lambda\frac{\kappa}{\eta_s}\right)K_1\left(\lambda\frac{\kappa}{\eta_s}\right)\right]. \tag{43}$$

In view of the absence of an exact theory of energy losses in the intermediate region, it may be feasible to use (43) as an approximate value for the stopping power when $\kappa/\eta_s>1$. This expression is based on an approach similar to that which lead to (6).

[9] See reference 1, formula (3.3.10).

VIII. DISCUSSION OF THE RESULTS

The general considerations leading to (43) are apparently in agreement with those stated by Bohr. This can be illustrated by means of Fig. 4 and 5 which correspond, respectively, to the diagrams of Fig. 7-II and Fig. 7-I of Bohr.[10] The ordinates represent the ratio between the actual differential cross section for energy transfers T and the cross section corresponding to collisions with a free electron. The abscissas represent $\log(T_m/T)$, where T_m is the maximum value of the energy transfer.

It should be mentioned that the diagrams made by Bohr are simplified; i.e., in order to avoid complications in the drawing, Bohr has eliminated in his representation the discrete resonance lines corresponding to excitation processes with $T<I_s$.[11] In order to show more clearly the analogy between the Bohr representation and the one used in this discussion the diagrams of Bohr have been completed so as to show the excitation processes.

Figure 4 illustrates the case when $\kappa/\eta_s<1$. The region represented by vertical hatchings is the region (a) of

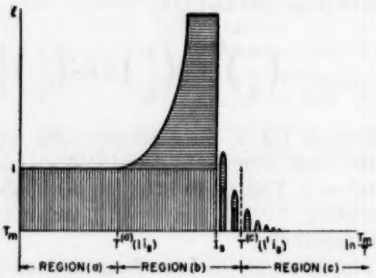

FIG. 4. Statistical distribution of energy losses for $\kappa/\eta_s<1$.

the orbital representation and it corresponds to energy transfers $T_m>T>T^{(a)}(li_s)$. The region represented partly by vertical and partly by horizontal and vertical hatchings is the intermediate region (b) corresponding to $T^{(a)}(li_s)>T>T^{(c)}(l'i_s)$ and the region (c) of small perturbations for $T<T^{(c)}(l'i_s)$ is represented by horizontal hatchings. The horizontal hatchings indicated by Bohr in the region (b) show that the problem is essentially quantum-mechanical and that the energy transfers cannot be *accurately* determined in this region by means of an orbital representation.

Figure 5 illustrates the case when $\kappa/\eta_s>1$. The solid line represents the distribution of energy losses which qualitatively is the same in the representation of Bohr as in the one considered in the present investigation. We shall refer to this distribution as the "actual distribution." Bohr was not concerned in this particular case with the problem of statistical evaluation of energy losses; i.e., with the "actual distribution." His main

[10] See reference 1, p. 89.
[11] See reference 1, p. 90.

problem was to calculate the aggregate effect of all losses, and with this purpose in mind he replaced the "actual distribution" by an equivalent distribution represented by dotted lines. His distribution comprises only energy transfers in the range $T_{\max} \geqslant T > D_s^*$, where $D_s^* = T^{(a)}(d_s^*)$ and is based on a collision with a free electron. We shall call it, therefore, the "free collision approximation."

Bohr's expression (10) contains a logarithmic term which does not have physical meaning for $\kappa \gtrsim \eta_s^3$. According to Bohr,[12] it is actually applicable if $\kappa \ll \eta_s^3$. Consequently, the expression (10) has a relatively limited region of applicability since it can be used only when

$$\eta_s < \kappa \ll \eta_s^3. \tag{44}$$

On the other hand, the expression (43) does not have this limitation since it is applicable to all those cases in which $\kappa > \eta_s$.

The physical picture used in this investigation may be helpful in evaluating the energy loss as a function of the impact parameter, and Fig. 6 illustrates two specific examples illustrating the "actual distribution."

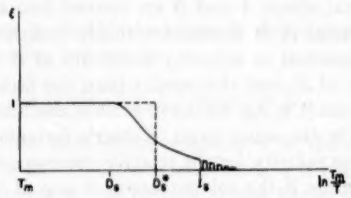

FIG. 5. Statistical distribution of energy losses for $\kappa/\eta_s > 1$.

Since Bohr was not concerned with the actual statistical distribution of the energy losses but with their aggregate effect, the "free collision approximation" was not intended to represent the behavior of the "actual distribution."

[12] See reference 1, p. 85.

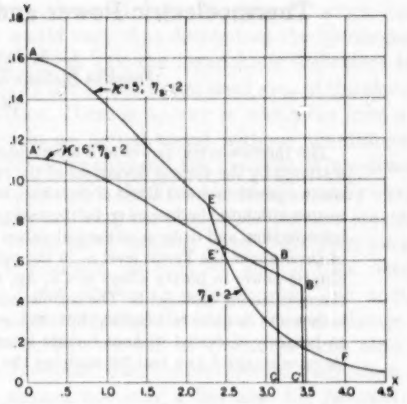

FIG. 6. Plot of the energy transfer as a function of the impact parameter.

Figure 6 shows the energy transfer at various impact parameters corresponding to the two distributions. The abscissa $X = p/a_s$ represents the impact parameter and the ordinate $Y = (\pi a_s^2/B_s)T(p)$ represents the energy transfer. The expression $T(p)$ can be represented either by (20) or (31). Two examples have been chosen:

Example 1: $\kappa = 5$; $\eta_s = 2$. For this case the stopping number σ_s/B_s, according to the Bohr formula (10), is 0.47 and according to the proposed formula (43) is 0.99. Curve ABC represents the "free collision approximation," and the curve AEF represents the distribution which is the basis of (43). More particularly, AE represents the distribution (20) and EF represents the distribution (31).

Example 2: $\kappa = 6$; $\eta_s = 2$. The stopping number, σ_s/B_s according to (10) is equal to 0.29 and according to (43) is equal to 0.83. Curve $A'B'C'$ represents the "free collision approximation" and the curve $A'E'F'$ represents the distribution which is the basis of (43).

Thermoelectric Power and Electron Scattering in Metal Alloys*†

C. A. Domenicali and F. A. Otter
Franklin Institute Laboratories, Philadelphia, Pennsylvania
(Received April 5, 1954)

The thermoelectric power of a metal depends on the details of how the current carriers in the metal are scattered by the various deviations of the crystal from a perfect lattice. A semiempirical theory of thermoelectric power in metal alloys is described, which is based on a formula due to Mott and others. The theory relates absolute thermopower to the energy dependence of the scattering cross section $Q_i(\epsilon)$ of a lattice imperfection, and deduces numerical values for the first few "scattering coefficients" in a Taylor expansion of $Q_i(\epsilon)$ about the Fermi level μ_0 in the pure solvent metal. The few known empirical "rules" of thermoelectric power in binary alloys of Cu, Ag, and Au, of alkali metals, and of Al are interpreted in terms of these scattering coefficients. The correlation with high-temperature thermoelectric properties of such alloys is shown to be quite satisfactory, but the low-temperature properties present several difficulties which cannot be properly discussed without further extensive experiments at very low temperatures. The usefulness of thermoelectricity as a tool for studying the nature of lattice imperfections is discussed briefly.

INTRODUCTION

IT has long been known[1,2] that the thermoelectric power of a metal depends upon the *details* of how the current carriers in the metal are scattered by the various deviations of the crystal from a perfect lattice. The most important of these deviations are thermal vibrations and potential perturbations caused by foreign atoms, vacancies and interstitial atoms in the lattice, and dislocations. In contrast to this the electrical resistivity of the metal is determined by the gross or "total" scattering and is relatively insensitive to the precise details of how a scattering center might discriminate between fast and slow electrons. Hence, although a number of papers have been written on the quantum kinetics of thermoelectric power, few of these have carried the theory to the point of making actual numerical calculations for a variety of metals and alloys. One of the main difficulties in the field of thermoelectricity is that there has been found very little "empirical consistency" in the variation of thermopower from metal to metal and from alloy to alloy. (Thermoelectricity has no "Matthiessen Rule," no "Wiedemann-Franz Relation.") There have been attempts to formulate "additivity rules" for thermopower, for example by Kohler,[3] and in this case the additive quantity is the ratio of thermopower to thermal conductivity. Kohler emphasizes the importance of using *absolute* thermopower instead of relative thermopower in such additivity relations. Unfortunately, a disadvantage of such relationships is that they involve other parameters besides thermopower, so that a comparison with experiment necessitates having simultaneous thermopower and thermal conductivity data for the same specimens.

Introducing the Wiedemann-Franz relation into his formulas, Kohler deduces the following rule: If two noble-metal alloys A and B are formed into a thermocouple, metal A is thermoelectrically positive against B if the residual or impurity resistivity of B is greater than that of A, and this results from the fact that the noble metals (Cu, Ag, Au) have *positive* absolute thermopowers. On the other hand, Kohler's formula predicts the reverse polarity for the relative thermopower of the thermocouple if the solvent metal is one of the alkali metals which has a *negative* absolute thermopower. It is found experimentally[4] that if almost any foreign atom is added in small amounts to Cu, Ag, or Au, the resulting alloy is thermoelectrically negative relative to the pure solvent. Manganese dissolved in copper is one exception[5,6] and the absolute thermopowers of α-phase (Cu-rich) Cu−Mn alloys attain values higher and higher above that for pure copper as the temperature increases (at least as far as data are available, namely, +700°K). Ti and Cr in Cu appear to be additional exceptions,[7] but the thermopower data available for these alloys are not extensive.[8] Apart from these three cases, we know of no other exceptions to Kohler's rule. In the *International Critical Tables* the compilation by Caswell gives the thermopower of Ag−Tl alloys as positive relative to pure silver, but the sign convention of Bernoulli,[9] from whose work Caswell's

* Supported by Signal Corps Engineering Laboratories, Fort Monmouth, New Jersey.

† During the final typing of our manuscript our attention was called to a recent paper by J. Friedel, J. phys. et radium **14**, 561 (1953), on much the same problem as we discuss here. There seems to be at least one very important difference between our two points of view. Friedel assumes that for small impurity concentrations the Fermi level of the metal remains fixed upon alloying; in contrast to this, we attribute the main features of thermopower behavior to precisely this variation of Fermi level upon alloying, even for very small impurity concentrations. It is interesting that both we and Friedel have speculated on the existence of an "internal Ramsauer effect."

[1] A. Sommerfeld, Z. Physik **47**, 1, 43 (1928).
[2] L. Nordheim and C. J. Gorter, Physica **2**, 383 (1935).
[3] M. Kohler, Z. Physik **126**, 481 (1949).
[4] G. Borelius, *Handbuch der Metallphysik*, edited by G. Masing, (Leipzig, Akademische Verlagsgesellschaft m.b.h., 1935), Vol. 1, part 1, p. 404.
[5] A. L. Norbury, Phil. Mag. **2**, 1188 (1928).
[6] J. L. Thomas, J. Research Natl. Bur. Standards **16**, 149 (1936).
[7] See W. H. Keesom and C. J. Mattijs, Physica **2**, 623 (1935).
[8] We have begun an experimental study of the systems Cu−Mn, Ag−Mn, Au−Mn, Cu−Ti, and Cu−Cr.
[9] A. L. Bernoulli, Ann. Physik **33**, 690 (1910).

data are taken, is the reverse of that commonly used nowadays.

Another fairly general trend was found by Norbury,[5] who pointed out that the initial slopes of thermopower *vs* composition curves increase with increasing valence, for various elements dissolved in copper.

We propose to show that present quantum theories for thermoelectric power can lead to interesting and important information about electron scattering in solids. The formulation of Mott[10] is particularly convenient for our purposes inasmusch as his formula for absolute thermopower is given in terms of the energy dependence of resistivity. We shall concentrate primarily on dilute, substitutional, binary alloys of various foreign atoms in Cu, Ag, or Au, but the general approach should be useful in other alloy systems as well. In fact, we hope soon to extend the study to ternary alloys, and to scattering by lattice vacancies, interstitials, and dislocations. The arguments given here should be applicable to alkali metal-base alloys, and do indeed seem to apply to very recent results of MacDonald and Pearson.[11] However, the solubility of most nonalkali atoms in the alkali metals is extremely small.

A. FORMULAS FOR ABSOLUTE THERMOPOWER AND RESISTIVITY

According to Mott[10] the absolute thermopower S of a metal or alloy is given by

$$S=(\pi^2k^2T/3|e|)[\partial \ln\rho(\epsilon)/\partial\epsilon]_{\epsilon=\mu}. \tag{1}$$

Here k is the Boltzmann constant, e is the electron charge, T is the absolute temperature, ϵ is the energy of the electrons at the surface of the Fermi distribution, and μ is the actual value of ϵ in the particular metal in question. The formula is valid for pure metals for temperatures $T\gg\Theta_D$, where Θ_D is the Debye temperature; and for $T\ll T_0$, T_0 being the "degeneracy" temperature of the free electron gas in the metal. The values of T_0 for Cu, Ag, and Au are of the order of 50 000°K, whereas for Fe, Ni, Pt, Pd, etc. (transition metals), T_0 is probably an order of magnitude smaller, roughly speaking. The formula is valid for any functional relation between energy and wave number, $\epsilon=\epsilon(\mathbf{k})$, provided that the scattering is isotropic. Finally, the formula is applicable to alloys even at low temperatures, provided that the impurity resistivity ρ_i is much greater than the resistivity ρ_T resulting from lattice vibration or phonon scattering.

The significance of the derivative in (1) is as follows. If the energy ϵ of the "surface electrons," i.e., those which actually carry the current, could be varied without otherwise altering a given metal or alloy, then the resistivity $\rho(\epsilon)$ would vary. The way in which the resistivity would vary thus determines the thermopower, according to Eq. (1), the logarithmic derivative being evaluated at the actual Fermi level $\epsilon=\mu$ of the electrons in the lattice. There is no way in which the level μ can be varied in an actual metal without simultaneously introducing other changes. For example, if one dissolves foreign atoms in Cu, the Fermi level will usually change; however, in so doing we also introduce new scattering centers whose cross sections have their own peculiar energy dependence, so that we should then need to separate these scattering effects from one another. Likewise, by squeezing the metal we can change the Fermi level, but we will at the same time alter the effective potential distribution around each atom and thereby change not only μ but also the *function* $\rho(\epsilon)$ itself. However, we can use relation (1) by postulating some reasonable energy dependence for the resistivity ρ, then comparing the deductions from the formula with the known thermoelectric properties of metals.

We write the total resistivity $\rho(\epsilon)$ of the binary alloy in the usual form,

$$\rho(\epsilon)=\rho_T(\epsilon)+\rho_i(\epsilon), \tag{2}$$

where $\rho_T(\epsilon)$ represents the "thermal" resistivity arising from phonon scattering of the electrons and $\rho_i(\epsilon)$ represents that arising from perturbations of the solvent lattice potential caused by the presence of the impurity atoms. In the cases that it is possible to speak of a mean free path one can express the impurity resistivity $\rho_i(\epsilon)$ in terms of an effective, total scattering cross section $Q_i(\epsilon)$ which is in general a function of the energy of the current-carrying electrons:[12,13]

$$\rho_i(\epsilon)=[(2m)^{\frac{1}{2}}n_i/e^2n_0]\epsilon^{\frac{1}{2}}Q_i(\epsilon), \tag{3}$$

where m, e are electronic mass and charge, n_i is the density of impurity atoms in the alloy, and n_0 is the density of "free electrons" in the lattice. It should be emphasized that Eq. (3), and therefore our entire theory, is based on the one-electron approximation. If we let x be the fraction of impurity atoms in the alloy, β be the number of conduction electrons contributed per impurity atom, and suppose for simplicity that each solvent atom (Cu, Ag, Au, Na, or K, etc.) contributes a single conduction electron per atom, then the ratio n_i/n_0 in (3) becomes $x/[1+(\beta-1)x]$ and (3) becomes

$$\rho_i(\epsilon)=21.1\frac{x}{1+(\beta-1)x}\epsilon^{\frac{1}{2}}Q_i(\epsilon),\quad \mu\Omega-\text{cm}, \tag{4}$$

[10] N. F. Mott and H. Jones, *Theory of Metals and Alloys* (Oxford University Press, London, 1936).

[11] D. K. C. MacDonald and W. B. Pearson, Proc. Roy. Soc. (London) **A221**, 534 (1954). The most often quoted experimental work on the thermopower of alkali metals is that of C. C. Bidwell, Phys. Rev. **23**, 357 (1924). More recent work is that of E. Heiber, Ann. Physik **23**, 111 (1935).

[12] F. Seitz, *Modern Theory of Solids* (McGraw-Hill Book Company, Inc., New York, 1939), p. 541.

[13] The assumption that mean free path (or cross section) is energy independent is valid only for very special scattering potentials. For example, the "hard-sphere approximation" leads to $\partial l/\partial\epsilon=0$; but for more realistic scattering potentials there results in general an energy dependence of mean free path l on energy. For simplicity we assume throughout this paper that the effective electron mass is simply the free electron mass.

the energy ϵ now being expressed in electron volts, $Q_i(\epsilon)$ in A^2 units (i.e., in units of 10^{-16} cm^2), and $\rho_i(\epsilon)$ in microhms-cm. The actual residual resistivity of the alloy is given by (4) evaluated at $\epsilon=\mu$. We assume that the alloys are relatively dilute ($x\leq 0.1$ approximately, i.e., ≤ 10 atomic percent); and since the Fermi energy μ of an ideal free-electron gas varies with the $\frac{2}{3}$ power of the electron density, we see that, if we neglect lattice parameter changes upon alloying, the Fermi level varies with composition x in the following manner for small $(\beta-1)x$:

$$\mu=\mu_0[1+(\beta-1)x]^{\frac{2}{3}}\cong\mu_0[1+\tfrac{2}{3}(\beta-1)x]. \quad (5)$$

Inserting this into Eq. (4) and again using approximations appropriate to small $(\beta-1)x$, one finds for the actual resistivity of the alloy

$$\rho_i(\mu)=21.1x[1-\tfrac{2}{3}(\beta-1)x]\mu_0^{\frac{1}{2}}Q_i(\mu)$$

$$=0.211p\left[1-\frac{\beta-1}{150}p\right]\mu_0^{\frac{1}{2}}Q_i(\mu); \quad (6)$$

the units here are of course the same as in (4), and the atomic percentage $p=100x$.

It is customary[14] to define the so-called "atomic resistivity change" ζ as the *initial* slope of the resistivity *vs* percent impurity curve, so that if we assume in Eq. (2) that ρ_T is independent of p, we find from Eq. (6) that

$$\zeta=[\partial\rho_i(\mu)/\partial p]_{p=0}=0.211\mu_0^{\frac{1}{2}}Q_i(\mu_0). \quad (7)$$

It has been found that ζ can be expressed in the form

$$\zeta=k_1+k_2z^2, \quad (8)$$

where k_1 and k_2 are nearly constant for dilute binary solid solutions of various atoms in Cu, Ag, or Au, and $z=N-11$, N being the group number (column number) of the added element in the column-of-eighteen periodic table of the elements. Equation (8) represents the empirical rule found by Norbury[15] and Linde[16] and explained by Mott.[17]

Now it is clear that what is needed is the energy dependence of the scattering cross section $Q_i(\epsilon)$. Suppose that this function be expanded in a Taylor series about the Fermi energy $\epsilon=\mu_0$ in the pure metal. We can write this expansion in the form

$$Q_i(\epsilon)=Q_0[1+\alpha_1(\epsilon-\mu_0)+\alpha_2(\epsilon-\mu_0)^2+\cdots], \quad (9)$$

where

$$Q_0=Q_i(\mu_0), \quad Q_0\alpha_1=[\partial Q_i(\epsilon)/\partial\epsilon]_{\mu_0},$$

$$2Q_0\alpha_2=[\partial^2Q_i(\epsilon)/\partial\epsilon^2]_{\mu_0}, \cdots.$$

We shall see that in most cases only the linear term (in α_1) in (9) is needed for the thermopower calculations, while in some cases the α_2 term is also necessary. In Sec. E we shall correlate the terms in (9) with an analytic expression derived by Mott[17] for calculating resistivities of binary alloys.

If we substitute Eq. (2) into (1), we find

$$(3|e|/\pi^2k^2)(S/T)=[\partial\ \ln\rho(\epsilon)/\partial\epsilon]_\mu$$

$$=(\rho_T+\rho_i)^{-1}[\partial\rho_T(\epsilon)/\partial\epsilon+\partial\rho_i(\epsilon)/\partial\epsilon]_\mu. \quad (10)$$

The second term in the brackets is $\rho_i[\partial\ \ln\rho_i(\epsilon)/\partial\epsilon]_\mu$, and from (3), (5), and (9) we find

$$\rho_i\left[\frac{\partial\ \ln\rho_i(\epsilon)}{\partial\epsilon}\right]_\mu=\rho_i\left[\frac{1}{2\epsilon}+\frac{1}{Q_i}\frac{\partial Q_i}{\partial\epsilon}\right]_\mu\cong\rho_i\left[\frac{1}{2\mu_0[1+(\beta-1)p/150]}+\frac{\alpha_1+2\alpha_2\mu_0(\beta-1)p/150}{1+\alpha_1\mu_0(\beta-1)p/150+\alpha_2\mu_0^2(\beta-1)^2p^2/(150)^2}\right]. \quad (11)$$

At temperatures $T\gg\Theta_D$ we have, from Mott's formula (1) applied to the pure metal,

$$S_0=[\pi^2k^2T/3|e|][\partial\rho_T(\epsilon)/\partial\epsilon]_{\mu_0}\cdot[\rho_T(\mu_0)]^{-1},$$

so that

$$[\partial\rho_T(\epsilon)/\partial\epsilon]_{\mu_0}=3|e|\rho_T(\mu_0)S_0/(\pi^2k^2T), \quad (12)$$

in which S_0 is the absolute thermopower of the solvent metal at temperature T. The first term in the brackets in (10) is the derivative $\partial\rho_T/\partial\epsilon$ evaluated at $\epsilon=\mu$, the Fermi level in the *alloy*, whereas in (12) this derivative is evaluated at $\epsilon=\mu_0$, the level in the *pure solvent metal*. There are several reasons for supposing that these two derivatives are almost exactly equal. First, if we make the reasonable assumption that the phonon scattering is of the same nature in the three similar metals Cu, Ag, and Au, we can suppose that the derivative $\partial\rho_T/\partial\epsilon$ is practically uniform over a large electron-energy range, since these *pure* metals have very nearly equal thermopowers despite the large differences in Fermi energy μ_0. Thus whereas the level μ_0 changes by a factor of approximately 2 in passing from pure Cu to pure Au, the Fermi level μ in noble-metal base alloys varies only slightly from μ_0 (in the pure metal) as we dissolve even up to 10 atomic percent of a foreign atom in the solvent. Secondly, the absolute thermopowers of all the *pure* metals extended over a range of only some 50 μv/deg despite the large variation in crystal structure, Fermi level, and phonon distribution functions; this indicates that the quantity $\partial\rho_T/\partial\epsilon$ does not vary rapidly with energy. This situation is to be contrasted with the very great effect on the thermopower of the noble metals when only minute amounts of impurities are added to the solvents. Thirdly, from the quantum-mechanical point of view one would expect the *purely phonon scattering itself* to be determined primarily by the distribution-in-energy of the phonons, and this

[14] G. Borelius, reference 4, p. 336.

[15] A. L. Norbury, Trans. Faraday Soc. **16**, 570 (1921); A. L. Norbury and K. Kuwada, Phil. Mag. **4**, 1338 (1927).

[16] J. O. Linde, Ann. Physik **10**, 52 (1931); **14**, 353 (1932); **15**, 219 (1932).

[17] N. F. Mott, Proc. Cambridge Phil. Soc. **32**, 281 (1936).

would surely not change radically as a result of the introduction of a small percentage of foreign atoms; it follows that the *rate of change* of this scattering with electron energy would be quite small.[18] For these reasons we feel justified in assuming that the derivatives of $\rho_T(\epsilon)$ in Eqs. (10) and (12) are equal or very nearly so; i.e., we set

$$[\partial\rho_T(\epsilon)/\partial\epsilon]_\mu=[\partial\rho_T(\epsilon)/\partial\epsilon]_{\mu_0}. \tag{13}$$

Upon substituting (11), (12), and (13) into (10) and solving for S, we find

$$S=[\rho_T+\rho_i]^{-1}\cdot\left\{S_0\rho_T+\frac{\pi^2k^2}{3|e|}\cdot\rho_iT\left[\frac{1}{2\mu_0[1+(\beta-1)p/150]}+\frac{\alpha_1+2\alpha_2\mu_0(\beta-1)p/150}{1+\alpha_1\mu_0(\beta-1)p/150+\alpha_2\mu_0^2(\beta-1)^2p^2/(150)^2}\right]\right\}, \tag{14}$$

where S is the absolute thermopower of the alloy containing p atomic percent of a foreign atom in solid solution in Cu, Ag, Au, Li, Na, $\cdots$, S_0 and ρ_T are, respectively, the absolute thermopower and resistivity of the *pure* solvent metal at temperature T°K, and ρ_i is given by Eqs. (6) and (9). Inserting numerical values for the constants in (14) one finds the formula

$$S=[\rho_T+\rho_i]^{-1}\left\{S_0\rho_T+0.0243\rho_iT\left[\frac{1}{2\mu_0[1+(\beta-1)p/150]}+\frac{\alpha_1+2\alpha_2\mu_0(\beta-1)p/150}{1+\alpha_1\mu_0(\beta-1)p/150+\alpha_2\mu_0^2(\beta-1)^2p^2/(150)^2}\right]\right\}, \tag{15}$$

in which now S, S_0 are in microvolts/deg K, ρ_T and ρ_i must be in microhm-cm in order to be consistent with Eq. (6), $\pi^2k^2/(3|e|)=0.0243$ (ev-microvolt)/deg,[2] μ_0 is in ev, α_1 in (ev)$^{-1}$, α_2 in (ev)$^{-2}$, and p is atomic percent. Equation (15) is the basis of our discussion of the thermopower of noble-metal base alloys at temperatures above the Debye temperature of the solvent metal. It should be emphasized that (15) is valid only for $T>\Theta_D$, because of our use of Eq. (12) for the pure metal. We shall discuss in Sec. F the formulas which apply at low temperatures.

B. APPLICATIONS TO DILUTE BINARY ALLOYS OF Cu, Ag, Au, Li, Na, etc., $T\gg\Theta_D$

Equation (15) for the absolute thermopower of an alloy, together with the relations (6) and (9) for ρ_i and Q_i, contains the following parameters:

(1) μ_0, the Fermi level at T°K in the pure metal. This parameter is almost temperature independent in "ideal gas" metals if there is no expansion of the lattice. We shall neglect these changes with T, although the variation resulting from thermal expansion can be very significant. In fact, this latter variation may have a great deal to do with deviations from linearity of S with T at very low temperatures.

(2) β, the number of conduction electrons contributed per atom by the solute. For this parameter one should attempt to be consistent with the arguments of Friedel,[19] Jones,[20] and Haworth and Hume-Rothery,[21] although it appears that the "best" value for β depends in many cases upon the particular physical property with which one is concerned.

(3) Q_0, the "zero-order" approximation to the scattering cross section in Eq. (9). We shall see that the terms in α_1 and α_2 in Eq. (9) are generally only very small fractions. Thus, while the resistivity[7] is determined by the "zero-order" approximation Q_0, the thermopower (15) is strongly dependent on the way in which the cross section varies with the speed of the current-carrying electrons. From Eqs. (7) and (9) we see that the atomic resistivity change ζ is determined by Q_0, and this fact allows us to deduce values of Q_0 from experimentally-found values of ζ, for example from the extensive measurements of Linde.[16] The parameter Q_0 enters into the S expression (15) through the factor ρ_i in the numerator and denominator.

(4) α_1 and α_2, the first- and second-power coefficients in the expansion for the scattering cross section (9). These parameters can in principle be computed by an elaborate program of curve fitting, in which the expression (15) is made to fit known experimental data. Such a program would be of questionable value, since most available thermoelectric data on alloys is subject to fairly large errors and since the alloys themselves have contained varying amounts of unspecified impurities. It will always be possible of course to fit a given S *vs* p curve if one is willing to use additional terms in the cross section expansion (9). For these reasons we shall show how the scattering parameters Q_0, α_1, and α_2 determine the thermopower by giving curves for some hypothetical alloys, and we shall give only a few applications to actual binary alloys, namely Cu−Zn, Cu−Si, Cu−Sn, and Cu−Ni.

Following Linde and Mott we introduce the quantities q_0, q_1, and z,

$$Q_0=q_0+q_1z^2, \quad Q_0, q_0, q_1 \text{ in A}^2 \text{ units}, \tag{16}$$

in which z has the same meaning as before and q_0 and q_1 are generally taken to be approximately constant for a given solvent. Actually, it is known from resistivity data on noble-metal base alloys that q_0 and q_1 vary by as much as a factor of 2 from one solute atom to another.[14] At temperatures above 400°K the absolute

[18] In this respect it might be mentioned that the transition-metal base alloys require special consideration, in contrast to those alloys with Cu, Ag, or Au as solvent.

[19] J. Friedel, Phil. Mag. **43**, 153 (1952).

[20] H. Jones, Phil. Mag. **44**, 907 (1953).

[21] J. B. Haworth and W. Hume-Rothery, Phil. Mag. **43**, 613 (1952).

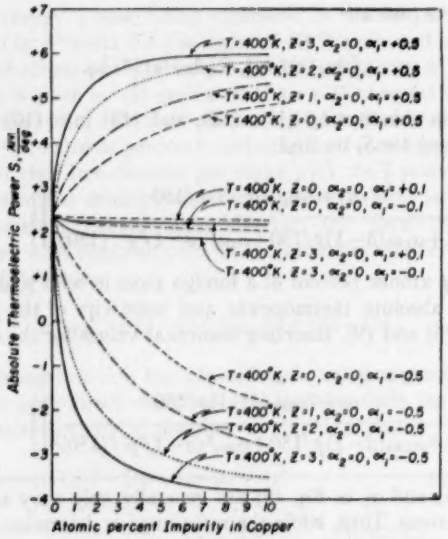
Absolute Thermoelectric Power S, μv/deg
Atomic percent Impurity in Copper
T=400°K, Z=3, α2=0, α1=+0.5
T=400°K, Z=2, α2=0, α1=+0.5
T=400°K, Z=1, α2=0, α1=+0.5
T=400°K, Z=0, α2=0, α1=+0.5
T=400°K, Z=0, α2=0, α1=+0.1
T=400°K, Z=0, α2=0, α1=−0.1
T=400°K, Z=3, α2=0, α1=+0.1
T=400°K, Z=3, α2=0, α1=−0.1
T=400°K, Z=0, α2=0, α1=−0.5
T=400°K, Z=1, α2=0, α1=−0.5
T=400°K, Z=2, α2=0, α1=−0.5
T=400°K, Z=3, α2=0, α1=−0.5

FIG. 1. Thermopower *vs* impurity concentration for hypothetical alloys.

thermopower S_0 and resistivity ρ_T of pure copper satisfy the relation $S_0\rho_T/T=3.46\times10^{-6}T$ sufficiently well for our purposes, with S_0 in μv/deg and ρ_T in $\mu\Omega$-cm. The resistivity is given by $6.00\times10^{-3}T$ $\mu\Omega$-cm. Using the abbreviation $y\equiv(\beta-1)p/150$ and restricting ourselves for the present to small values of α_1, α_2, β, and y, i.e., for

$$|\alpha_1|\leq0.2,\quad |\alpha_2|\leq0.4,\quad -1\leq\beta\leq+2,\quad |z|\leq5,$$

approximately, the formula (15) becomes

$$S\cong S_0\cdot\frac{1+(305/T)(q_0+q_1z^2)p[0.118+\alpha_1+8.5\alpha_2y]}{1+(72.3/T)(q_0+q_1z^2)p}. \quad (17)$$

This relation will serve to show the general behavior of the absolute thermopower as the several scattering parameters are varied; this behavior is illustrated in Fig. 1, in which are shown the values of S at 400°K for hypothetical alloys of copper as given by Eq. (17). The value of S_0 for pure copper at 400°K is +2.38 μv/deg, as given by Borelius *et al.*[22] and by Nyström.[23] We notice first that the general shape of the curves is that characteristic of most noble-metal alloys. Secondly, it is seen that the initial slope of the S *vs* p curve is positive only for values of α_1 greater than some critical value α_1^c. This critical value can most easily be found by taking the limiting form of Eq. (17) for very small p,

$$S/S_0\rightarrow1-(36.3Q_0p/T)(1-8.39\alpha_1),$$
$$[\partial(S/S_0)/\partial p]_{p=0}=-36.3T^{-1}(q_0+q_1z^2)(1-8.39\alpha_1); \quad (18)$$

we then find

$$\alpha_1^c=0.12. \quad (19)$$

[22] Borelius, Keesom, and Johansson, Leiden Comm. **196a** (1928) or Proc. Acad. Sci. Amsterdam **31**, 1046 (1928).
[23] J. Nyström, Arkiv. Mat. Astron. Fysik **A34**, No. 27 (1948).

Thus, a binary copper alloy will be thermoelectrically positive relative to pure copper if $\alpha_1>0.12$, negative to pure copper if $\alpha_1<0.12$, and this is so for all temperatures (above Θ_D). We conclude from the rule of Borelius and Kohler mentioned in the Introduction that most atoms dissolved in Cu have values of α_1 less than about +0.12, whereas Mn and possibly Ti and Cr have α_1 values larger than 0.12 when dissolved in Cu. The solvents Ag and Au would have values of α_1^c which are slightly different from 0.12, since α_1^c will be seen [Eq. (23)] to depend on μ_0 and on the thermopower S_0 for the pure solvent metal. Finally, it is seen from Fig. 1 and from Eq. (18) that for fixed values of α_1, q_0, and q_1, the initial slopes of the S/S_0 curves increase with increasing z, in agreement with the "rule" of Norbury mentioned in the Introduction. However, if one dissolves in succession the Row-4*b* atoms Zn, Ga, Ge, and As in Cu, according to Eq. (18) the initial S/S_0 *vs* p slopes will not necessarily increase with z^2 *alone*, since these slopes depend also on q_0, q_1, and α_1. This dependence on q_0, q_1, and α_1 should be particularly noticeable when one compares the thermopowers of such alloy series as Cu−Zn, Cu−Cd in Column II-B, or Cu−Si, Cu−Ge, Cu−Sn, and Cu−Pb in Column IV-B, since the parameter z certainly cannot be expected to be the only determining factor for the scattering. It turns out that the S *vs* p curves for this latter series at first dip down and then turn upwards again, the minimum lying around 2 or 3 atomic percent. The curves for Cu−Si and Cu−Sn at several temperatures are shown in Fig. 2. Data for Cu−Sn at 400°K do not seem to be available above about 2 atomic percent; however, since the S *vs* p curves generally have the same shape at the higher temperatures, we have used the data of

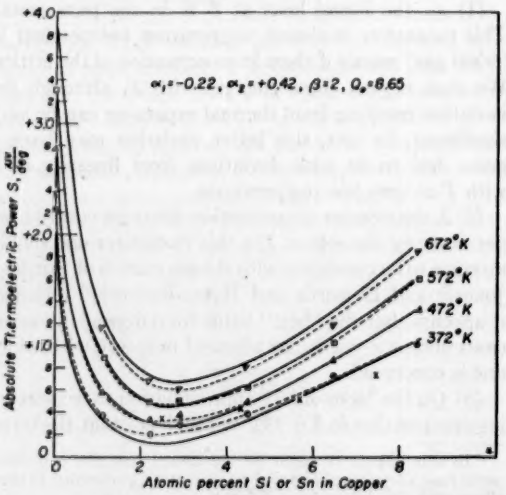

FIG. 2. Thermopower *vs* silicon content at various temperatures. The solid curves are theoretical, the dotted curves experimental. For comparison, experimental data on Cu−Sn alloys at 400°K are included (crosses).

Andrewartha and Evans,[24] who give mean relative thermopowers against copper between 283°K and 373°K, and after conversion to absolute thermopower we have then shifted the curve upward to coincide with $S_0=2.38$ μv/C° at 400°K for $p=0$. These data are shown by the crosses in Fig. 2. There are no thermopower data available for Cu–Ge, and Pb has only a very small solubility in Cu. Thus two of the four IV-B atoms Si, Ge, Sn, and Pb when dissolved in Cu show the behavior illustrated in Fig. 2. This behavior requires the use of the $\alpha_2(\epsilon-\mu_0)^2$ term in $Q_i(\epsilon)$, Eq. (9), and the values of the scattering coefficients α_1 and α_2 for Si in Cu are given in the figure. The data of Norbury[5] for Sn in Cu up to ~700°K give a somewhat steeper drop in S than is shown in Fig. 2, with increasing Sn content, but his alloys contained up to only 2 atomic percent Sn. We have therefore chosen to use instead the results of Andrewartha and Evans.

The actual experimental values for Cu–Zn alloys[5] are compared in Fig. 3 with the calculations using Eq. (17).

The metals Fe, Co, and Ni have unusually large effects on the thermopower of Cu, Ag, and Au, and their behavior is typified by the S *vs* p curves for Cu–Ni at 400°, 500°, 600°, and 700°K in Fig. 4. As before, the value of Q_0 used was determined from ζ values found experimentally. The initial slopes of the experimental S *vs* p curves can in principle be used to determine α_1; however, there seems to be little information on very dilute alloys at higher temperatures, so that it is better to use "hypothetical" curves such as those in Fig. 1 as a guide, and to adjust the scattering parameters slightly to get a good fit with experimental curves. The parameters necessary for describing the impurity scattering in Cu–Ni, Cu–Fe, and Cu–Co are too large to permit the use of Eq. (17), and one must return

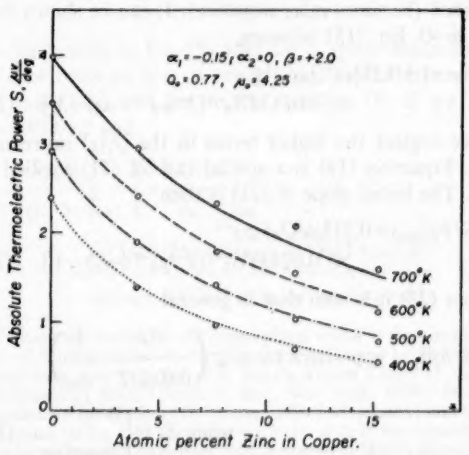

FIG. 3. Thermopower *vs* zinc content at various temperatures. All four curves are theoretical. Circles show experimental data.

[24] G. G. Andrewartha and E. J. Evans, Phil. Mag. **31**, 265 (1941).

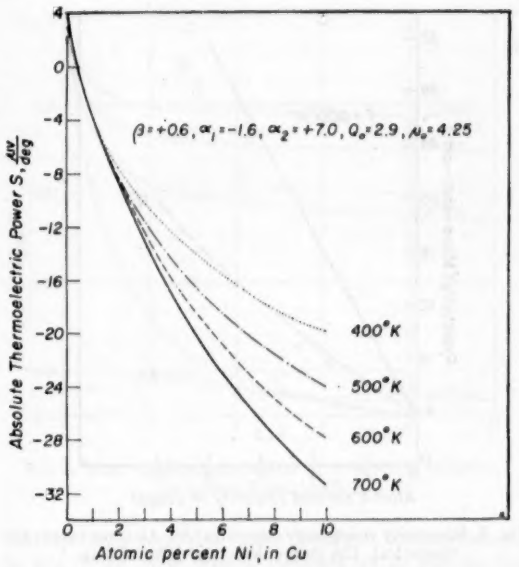

FIG. 4. Thermopower *vs* nickel content at various temperatures. All four curves are theoretical.

to the original expression (15). The theoretical curves in Fig. 4 were calculated to fit some very meager data on Cu–Ni obtained in our laboratory. The shapes of the curves are identical with those of Norbury,[5] but Norbury's thermopowers have larger negative values than ours.

Coles[25] has compared the electronic structures and physical properties of the systems Cu–Ni and Ag–Pd and has pointed out the striking difference between the S *vs* p curves for these two systems. Palladium reduces the absolute thermopower of Ag, but at a slow rate, of the order of 0.3 μv/deg per atom percent Pd; on the other hand, Ni reduces the thermopower of Cu at a rate of roughly 3 μv/deg per atom percent Ni. This means that the α_1 for Pd in Ag is much smaller than the α_1 for Ni in Cu.

C. RESISTIVITY

We come now to the question of how the scattering parameters α_1 and α_2 affect the resistivity ρ_i. From Eqs. (6), (9), and (5) it is seen that for Cu-, Ag-, and Au-base alloys

$$\rho_i=0.211\mu_0{}^{\frac{1}{2}}Q_0p\left[1-\left(\frac{\beta-1}{150}\right)p\right]\times\left[1+\alpha_1\mu_0\left(\frac{\beta-1}{150}\right)p+\alpha_2\mu_0{}^2\left(\frac{\beta-1}{150}\right)^2p^2\right]. \quad (20)$$

It is found for many dilute, noble-metal base alloys, that the ρ_i *vs* p curves increase approximately linearly with

[25] B. R. Coles, Proc. Phys. Soc. (London) **B65**, 221 (1952).

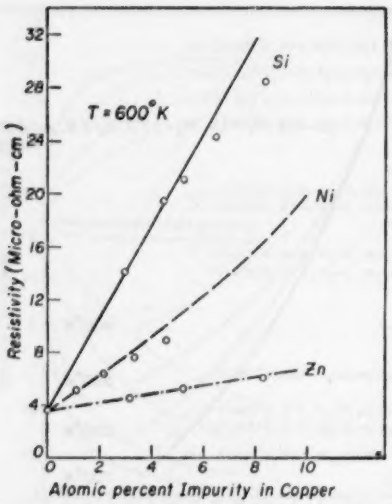

FIG. 5. Resistivity *vs* impurity concentration. All three curves are theoretical. The points show experimental data.

p. From Eq. (20) it is seen that the deviation of ρ_i from linearity with p is very sensitive to the values of the parameter β, the number of electrons contributed per atom of the solute. In cases where the thermopower varies slowly with p and for which therefore small values of α_1 and α_2 are required, the bracketed terms in (20) remain so near unity that comparison with experiment is difficult. It is no easy matter to determine accurately the impurity content of alloys. Nevertheless, in the cases of Cu−Zn and Cu−Si alloys, agreement with the theory is satisfactory as seen from Fig. 5. On the other hand, in the case of Cu−Ni, for example, large values of α_1 and α_2 are required to fit the thermopower curves. Now it has been customary to assign the value zero to the "valency" β of transition metals dissolved in Cu, Ag, and Au. If we use $\beta=0$ in Eq. (15) for thermopower, we require such large values of α_1 and α_2 (in the Cu−Ni case, for example) that at $p=10$ atomic percent the bracketed term in ρ_i from Eq. (20) attains values of about 2, which of course represents an enormous deviation from linearity. Experiment shows that ρ_i *vs* p for dilute Cu−Ni alloys is practically a straight line. (See Fig. 5.) But it has been shown by Jones[20] and by Haworth and Hume-Rothery[21] that in Cu alloys with Fe, Ni, Co, and Mn, both binary and ternary (with Zn or with Al), the valency of these transition metals is not only nonzero but actually varies with composition. They find, for example, that Ni, Co, Fe, and Mn behave as though they possessed valencies of about 0.6, 0.8, 1.0, and 1.9, respectively, in the systems Cu−Zn−Ni, Cu−Zn−Co, Cu−Zn−Fe, Cu−Zn−Mn, Cu−Al−Co, Cu−Al−Fe, and Cu−Al−Mn. In fact, Haworth and Hume-Rothery hold that the effective valence of Ni in Cu is radically different at the Cu-rich side of the phase diagram from what it is at the Ni-rich side. If, therefore, we use values of the order of $\beta\approx 0.6$ electron/Ni atom in Eqs. (15) and (20) we arrive at much more satisfactory agreement with experiments on the impurity resistivity of this alloy system. This situation we consider to be support for the metallurgical properties discussed by Jones, Haworth, and Hume-Rothery, although from Fig. 5 it is seen that the ρ_i *vs* p curves for Cu−Ni bend the wrong way.

D. APPLICATIONS TO OTHER ALLOY SYSTEMS

We attempt first to apply the theory to the alloys of aluminum. Crussard[26] has made a rather extensive study of dilute aluminum alloys and his results have been explained qualitatively by Galt[27] on the basis of Mott's equation (1). However, Galt does not consider scattering from the impurities themselves, and assumes as does Mott[10] that the effect of these impurities is simply to vary the Fermi level in the metal. According to our picture this assumption is not allowable.

Because of the difference in number of conduction electrons per atom between Cu and Al, our formula (15) for absolute thermopower must be altered slightly. Instead of using the factor $(\beta-1)p/150$ we should write $(\beta-3)p/150$, where we have assumed that Al has three valence electrons per atom. We mention this detail only to emphasize the fact that Eq. (15) applies as it stands only to Cu, Ag, Au, Li, Na, K, ···, etc., and the factor $(\beta-3)$ will not enter into the formulas we wish to discuss in connection with aluminum alloys.

We concern ourselves only with the following "rule" laid down by Crussard: The absolute thermopower of Al ($\Theta_D=390°$K) is negative (at ordinary temperatures); when small amounts of a metal preceding Al in the column-of-eight periodic table are dissolved in Al, the absolute thermopower is algebraically increased (becomes less negative); when the dissolved metal follows Al in this table the thermopower is algebraically decreased (becomes more negative). It can be shown that for $p\to 0$, Eq. (15) becomes

$$S/S_0\to 1+0.211\mu_0^{\frac{1}{3}}Q_0\rho_T^{-1}p \times[0.0243TS_0^{-1}(2^{-1}\mu_0^{-1}+\alpha_1)-1], \quad (21)$$

if we neglect the higher terms in the $Q_i(\epsilon)$ expression (9). Equation (18) is a special case of (21) applied to Cu. The initial slope of (21) is then

$$(\partial S/\partial p)_{p=0}=0.211\mu_0^{\frac{1}{3}}Q_0S_0\rho_T^{-1} \times[0.0243TS_0^{-1}(2^{-1}\mu_0^{-1}+\alpha_1)-1]. \quad (22)$$

From (22) it is seen that in general

$$(\partial S/\partial p)_{p=0} \text{ is positive for } \alpha_1 \gtrless \left(\frac{S_0}{0.0243T}-\frac{1}{2\mu_0}\right) \text{ when } S_0 \text{ is } \begin{cases}\text{positive}\\ \text{negative}\end{cases}. \quad (23)$$

[26] C. Crussard in Report of Conference on Strength of Solids, H. H. Wills Laboratory, Bristol (Physical Society, London, 1948), p. 119; Compt. rend. 226, 1003 (1948).
[27] J. K. Galt, Phil. Mag. 40, 309 (1949).

Taking $S_0=-0.00563T°\text{K}$ for Al and $\mu_0^{\text{Al}}=4$ ev, we find $(\alpha_1^e)^{\text{Al}}=-0.356(\text{ev})^{-1}$.

The application of Eq. (15) to Ni-, Fe-, and Co-base alloys is more difficult than in the alloys already considered. However, it should be possible to apply the basic arguments given here even in the cases of these alloys.

E. CORRELATION WITH THEORETICAL FORMULAS FOR SCATTERING CROSS SECTION

In order to arrive at a connection between our empirically determined scattering parameters Q_0, α_1, α_2, etc., and the atomic structure of the impurity scattering centers we have chosen a formula of Mott[17] which relates the impurity resistivity of binary alloys of Cu, Ag, Au, Li, Na, K, etc., to the velocity of the current-carrying electrons in the metal. Mott uses a one-electron approximation, of course, and takes the electron to be free ($\mathbf{v}=\hbar\mathbf{k}/m$). The foreign atom is shown to introduce a perturbing potential of the form $V=(1/r)\exp(-r/r_0)$, the so-called screening potential. Mott's final formula for the scattering cross section of a foreign atom is[28]

$$Q_i(\epsilon)=2\pi(ze^2/mv^2)^2 f(y), \tag{24}$$

where z has the same meaning as our z, $e=4.80\times10^{-10}$ esu, $m=9.1\times10^{-28}$ g, v is the velocity of the scattered electron in cm/sec, $Q_i(\epsilon)$ is in cm^2, and $f(y)$ is

$$f(y)=\ln\left(1+\frac{1}{y}\right)-\frac{1}{1+y}, \tag{25}$$

with the abbreviation $y=\hbar^2/(4m^2v^2r_0^2)$. Here r_0 is the "screening radius" in the scattering potential and is the reciprocal of the usual screening constant q_0. If the cross section is expressed in A^2 and the energy in electron-volts, Eq. (24) becomes

$$Q_i(\epsilon)=326(z^2/\epsilon^2)f(y). \tag{26}$$

We have seen in Eq. (9) that for a given dependence $Q_i(\epsilon)$ of cross section on energy, the Taylor expansion for this $Q_i(\epsilon)$ will be in the form of (9) if we set $\Delta\equiv0.953/r_0^2$ and

$$\alpha_1\equiv\left[\frac{1}{Q_i}\frac{\partial Q_i}{\partial\epsilon}\right]_{\mu_0}=\left[\frac{\partial\ln Q_i(\epsilon)}{\partial\epsilon}\right]_{\mu_0}$$
$$=\frac{\mu_0(3\mu_0+2\Delta)-2(\mu_0+\Delta)^2\ln(1+\mu_0/\Delta)}{\mu_0(\mu_0+\Delta)^2\ln(1+\mu_0/\Delta)-\mu_0^2(\mu_0+\Delta)}, \tag{27}$$

[28] There is a succession of typographical errors in the transcription of Mott's resistivity formula from his paper to Mott and Jones' book, and to p. 545 of F. Seitz's *Modern Theory of Solids* (McGraw-Hill Book Company, Inc., New York, 1939). Mott's formulas for $\Delta\rho$, his Eq. (17) on page 290 of reference 17 and that just above his Eq. (17), should have a factor of 2π in the numerator. This factor seems to have been used, however, in Mott's numerical calculations. On p. 294 of Mott and Jones (reference 10) and on p. 545 of Seitz, the resistivity formula should have e^2 in the denominator, not e^4. On the same page of Seitz's book, the expression for Mott's abbreviation y should have m^2 in the denominator, not m.

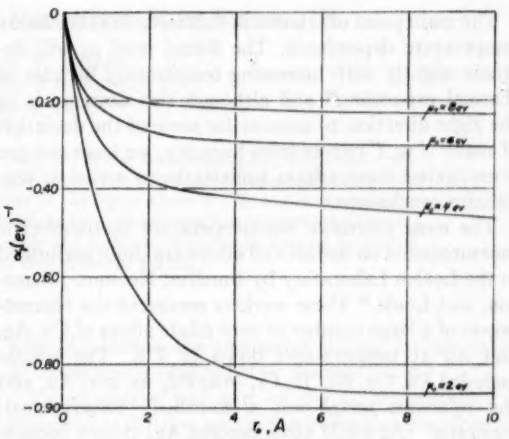

FIG. 6. First scattering parameter α_1 *vs* effective radius r_0, for various Fermi levels μ_0.

the last step requiring some algebraic manipulation. In Fig. 6 we show how α_1 depends on μ_0 and on the screening radius r_0. We have not attempted to calculate the second-order coefficient α_2. Mott has found that resistivity data call for screening constants of the order of $1/q_0\sim0.3\text{A}=r_0$, whereas calculations made on the basis of the Thomas-Fermi method give larger values of r_0. The values of α_1 for $r_0\sim0.3$A from Fig. 6 are of the order of $\alpha_1\sim-0.1$, being negatively larger the smaller the Fermi energy μ_0. Thus we see that Mott's cross section formula leads to just the right range of α_1 values for the thermopower *vs* composition curves discussed above. On the other hand, we see that formula (26) for Q_i does not permit *positive* values of α_1. According to Eq. (19) the thermopower of a binary alloy with copper base cannot be thermoelectrically positive relative to pure copper unless $\alpha_1>+0.12$, and we have mentioned that Mn and possibly Ti and Cr form dilute solutions in Cu which are positive against copper.[8]

F. FORMULAS FOR LOW TEMPERATURES

Mott's formula (1) is valid at lower temperatures than Θ_D provided $\rho_i\gg\rho_T$, so that the scattering is predominantly by impurities, or more generally, "lattice imperfection scattering." The formula for S at low temperatures can be obtained from Eq. (15) simply by letting $\rho_T\to0$. Thus

$$S=0.0243T\left[\frac{1}{2\mu_0[1+(\beta-1)p/150]}\right.$$
$$\left.+\frac{\alpha_1+2\alpha_2\mu_0(\beta-1)p/150}{1+\alpha_1\mu_0(\beta-1)p/150+\alpha_2\mu_0^2(\beta-1)^2p^2/(150)^2}\right], \tag{28}$$

where again S is in μv/deg, μ_0 in ev, α_1 in (ev)$^{-1}$, α_2 in (ev)$^{-2}$, and p is atomic percentage of the foreign atom (or vacancies, etc.).

The main point of interest in this formula is the linear temperature dependence. The Fermi level μ_0 will decrease slightly with increasing temperature because of thermal expansion,[29] and although this decrease is in the right direction to account for some of the deviation of many S *vs* T curves from linearity, we have not yet investigated these effects sufficiently to arrive at any definite conclusions.

The most extensive low-temperature thermoelectric measurements on metals and alloys are those performed in the Leiden Laboratory by Borelius, Keesom, Johansson, and Linde.[30] These workers measured the thermopower of a large number of very dilute alloys of Cu, Ag, and Au at temperatures down to 4°K. The solutes included Fe, Co, Ni, Ti, Cr, Mn, Pd, As, and Au, and the reference metal was a so-called "Silbernormallegierung" (Ag+0.37 atom percent Au) chosen because of its suitability for Thomson-coefficient measurements. Now the absolute thermoelectric powers of these alloys, according to the measurements of Borelius *et al.*, do not vary linearly with temperature even at temperatures so low that the impurity resistivity should exceed the thermal contribution by factors of tens or even hundreds. It is very unlikely that the scattering parameters α_1 and α_2 are temperature dependent. It is conceivable, although unlikely, that the effective valence of some elements may be sufficiently sensitive to interatomic distances to make β temperature sensitive. The experiments of Borelius *et al.* show that the thermopowers of the dilute Cu−Fe, Au−Fe, and Cu−Co alloys are not greatly sensitive to the amount of foreign atom dissolved, and this fact would indicate that even the variation of β with temperature is unlikely, as one can deduce from Eq. (28); for if β were mainly responsible for the large negative values of the bracket in (28), which would be required to give large negative S in these alloys, then changes in solute content should give rise to large variations in S. In the case of Cu−Ni, the α_1 required to give the experimental order-of-magnitude thermopower at 10°K is about -4 (even with $\alpha_2=+7$, the value used for a good fit at high temperatures), and this value is several times larger than the high-temperature value (-1.2).

The recent findings of Pullan[31] on silver and tin at liquid helium temperatures are more encouraging. Pullan shows that the thermopower of tin becomes more nearly linear with temperature as the impurity content increases; and that while $S\sim T^{1.79}$ for high purity, well annealed silver with very low residual resistivity, the thermopower of the same silver in the cold-drawn state satisfies the relation $S=+0.011T$ μv/deg. According to Eq. (28), the coefficient $+0.011$ calls for an α_1 of approximately $+0.35$ (for $\mu_0^{Ag}=3.3$ ev). The lattice imperfections caused by cold drawing of silver would thus have a *positive* scattering coefficient $\alpha_1=+0.35$

It is obvious that a great deal more experimental work needs to be done on the thermoelectric properties and on the resistivity of dilute noble metal alloys, and it would be most helpful to have both S and ρ for the same specimens.

G. CONCLUSIONS

We have shown that the theory of thermoelectric power as developed by Mott and others[32] can be used to explain many intricacies of thermoelectricity in metal alloys. The theory can also be used in reverse to derive information about electron scattering in metals. Furthermore, if a systematic study were made of the thermoelectric properties of quenched, cold-worked, and otherwise imperfect lattices, it should be possible to learn much about the nature of such imperfections. Finally, our specifications of the values which the scattering parameters must have, in order to explain the thermoelectric properties of imperfect metallic lattices, more precisely define one of the problems to be solved by the quantum theory, namely, the calculation of scattering cross sections of scattering centers in solids.[33]

The authors wish to express their appreciation to Dr. F. C. Nix for his valuable encouragement in this work, and to the Squier Signal Laboratories for their continued support.

[29] The temperature variation of μ_0 at *constant volume*, involving a factor $[1\text{-const }(T/T_0)^2]$, is completely negligible for our purposes.

[30] Borelius, Keesom, Johansson, and Linde, Leiden Comm. **206a** (1930); **206b** (1930); **217d** (1932); **217e** (1932). Most if not all of these communications also appear in the Proc. Acad. Sci. Amsterdam (Koninkl. Ned. Akad. Wetenschap. Proc.).

[31] G. T. Pullan, Proc. Roy. Soc. **A217**, 280 (1953).

[32] A formula identical with Mott's equation (1) is also a consequence of the recent theoretical work of A. W. Sáenz, Phys. Rev. **91**, 1142 (1953). See, e.g., his Eqs. (4.13).

[33] One might ask, for example, whether or not there exists an "internal or crystalline Ramsauer effect."

Measurements on Chromium Potassium Alum below 1°K

E. AMBLER AND R. P. HUDSON
National Bureau of Standards, Washington 25, D. C.

(Received May 18, 1954)

Measurements of the real part, χ', and imaginary part, χ'', of the ac susceptibility, the ballistic susceptibility, and the remanence were made on chromic potassium alum in the range of temperature below 1°K. The results provide confirmation of earlier measurements in the region above 0.1°K, but show some discrepancies at lower temperatures, particularly in the behavior of χ''. Some absolute temperature determinations, in the region of the "Curie point," were also made and these are of particular interest in view of wide discrepancies between such measurements made at Oxford and at Leiden.

INTRODUCTION

IN a recent series of investigations on the magnetic behavior of chromic methylamine alum at very low temperatures,[1] marked differences were found from that of chromic potassium alum, as reported by de Klerk, Steenland, and Gorter.[2] Specifically, the entropy *versus* susceptibility curve showed a tendency to flatten out at the expected value of $S=R\log_e 2$; the out-of-phase component of the ac susceptibility, χ'', attained measurable values only in an extremely small range of entropy and exhibited a very sharp maximum. Finally, when ballistic measurements were made of the susceptibility with a 5.6-sec period galvanometer very marked time effects were observed, and the remanence plotted as a function of entropy showed a maximum.

It was therefore thought of interest to investigate a specimen of the potassium alum with the same apparatus, and the results are reported here, inasmuch as they provide confirmation of earlier measurements in the region above 0.1°K,[2,3] show some discrepancies at lower temperatures, particularly in the behavior of χ'', and include some independent determinations of absolute temperatures in the region of the "Curie point" which are of particular interest in the light of wide discrepancies between such measurements made at Oxford[4] and at Leiden.[2]

RESULTS

The specimen used was a spherical single crystal, radius 25.4 mm, mass 15.61 g, and its susceptibility was determined along the direction of a cubic axis.

In the first series of experiments the crystal had been ground immediately before mounting it in the apparatus and was cooled from room temperature to 77°K at a fairly uniform rate in 12 hr. The same crystal was used in the second series of experiments, the only difference being that it had been reheated to room temperature in the meantime. (It was felt worth while to point out this fact, in view of some differences which were obtained in the two series of runs for the values of the ac susceptibility below the maximum.)

Values of the real part of the ac susceptibility χ' measured at 210 cps, and of the ballistic susceptibility χ obtained by reversing a field of 3.44 oersteds, are shown in Fig. 1. Agreement with the theory of Hebb and Purcell using the Onsager approximation for the internal field is obtained for temperatures down to 0.2°K, if the splitting between the electronic doublets is taken as 0.25_0 deg. This is in good agreement with the splittings obtained by de Klerk *et al.* (0.251 deg) and by Bleaney (0.245 deg) which, however, do not fit the data obtained from paramagnetic resonance.[5] There is a sharp maximum of χ' corresponding to a minimum in T^* of 0.029_7 at an entropy $S/R=0.40_6$. In contrast, the ballistic susceptibility shows a very flat maximum at somewhat lower entropy; we obtain for the minimum in T^* measured ballistically, 0.028_3 at $S/R=0.31_0$. These results are in satisfactory agreement with the results of de Klerk *et al.*, and in fairly good agreement with those of Daniels and Kurti. (The latter authors, using the ballistic method, obtained $T^*_{\min}=0.035$ deg at $S/R=0.35$.)

In Fig. 2 are plotted the values of the out-of-phase part of the ac susceptibility which does not show the maximum reported by de Klerk *et al.* down to an en-

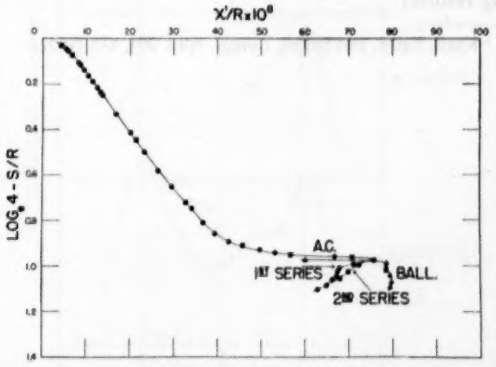

FIG. 1. Susceptibility as a function of entropy: ● and ■ ac susceptibility, first and second series respectively; ▲ ballistic susceptibility.

[1] R. P. Hudson and C. K. McLane, Phys. Rev. **95**, 932 (1954).
[2] de Klerk, Steenland, and Gorter, Physica **15**, 649 (1949).
[3] B. Bleaney, Proc. Roy. Soc. (London) **A204**, 216 (1950).
[4] J. M. Daniels and N. Kurti, Proc. Roy. Soc. (London) **221**, 243 (1954).
[5] B. Bleaney, Proc. Roy. Soc. (London) **A204**, 203 (1950).

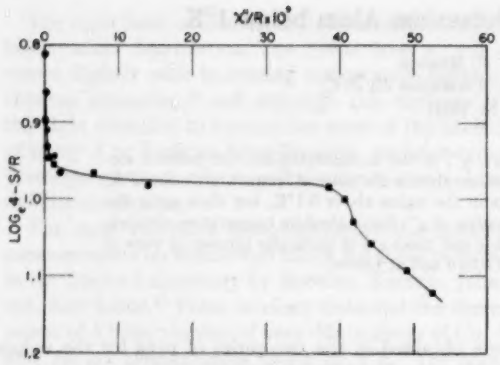

FIG. 2. Imaginary part of ac susceptibility, χ'', as a function of entropy.

tropy $S/R=0.26$; instead, there is a point of inflection at about the same entropy as that for which these authors report their maximum.

The values of the remanence obtained by reversing a field of 3.44 oersteds are plotted in Fig. 3. It was found that remanence sets in at an entropy $S/R=0.42$ (which lies between the figures quoted by Kurti, Lainé, and Simon[6] and by de Klerk *et al.*) then increases steadily with falling entropy to $\Sigma/R=4.6\times10^{-5}$ degree oersted^{-1} at $S/R=0.28$. Time effects, indicative of a sluggishness of the magnetic moment in following reversals of the external field, were not observed with this salt.

Absolute temperature determinations were made using the χ'' heating method, with χ' as a thermometric parameter. This method is naturally confined to the range where χ'' is usefully large and where χ' varies fairly rapidly with entropy, i.e., for $S/R<0.44$. In addition, we confined our measurements to the range above the χ' maximum in order to minimize uncertainties which arise because of inhomogeneous heating due to extraneous heat influxes. We obtained the following results:

[6] Kurti, Lainé, and Simon, Compt. rend. **204**, 675 (1937).

$(\ln 4-S/R)$	T^* ac	$T°K$
0.945	0.0435	0.02_0
0.962	0.0364	0.01_9
0.970	0.0317	0.01_7

These absolute temperatures are very much greater than those quoted by de Klerk *et al.* for the same entropies, and somewhat greater than the corresponding values of Daniels and Kurti.[7]

It is obvious that serious discrepancies exist in the absolute temperature determinations of various workers, although the reasons for these are not too clear. Undoubtedly the problem of allowing for the effect of the extraneous heat influx plays an important part, and therefore there is great need for developing apparatus where this heat influx is always kept to a very small value—say less than 5 ergs per minute. At the same time it is desirable for the same workers to carry out absolute temperature determinations using both methods

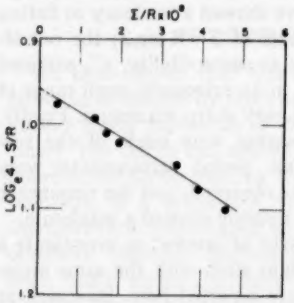

FIG. 3. Remanence as a function of entropy; measuring field 3.44 oersteds.

(i.e., by χ'' heating and by γ-ray heating) on the same specimen. The authors hope to carry out such experiments in the near future.

[7] The discrepancy between these results and those of Daniels and Kurti is undoubtedly due in part to the deviation of the former by assessing the "drift heating" on the assumption of uniform heating. In this connection it is of some interest to note that the actual experimental values of specific heat obtained by Daniels and Kurti in this region of entropy [Fig. 5, reference 4] deviate from their own drawn curve in such a direction that they would yield higher derived values of T.

Color Centers in Alkali Silicate and Borate Glasses

RYOSUKE YOKOTA
Matsuda Research Laboratory, Tokyo-Shibaura Electric Company, Kawasaki-shi, Japan
(Received April 2, 1954)

The color centers induced by x-ray irradiation in the alkali silicate and borate glasses and the mixed alkali glasses are studied. By preparing samples of various compositions in the reducing and in the oxidizing condition, and by optical and thermal bleaching, it is concluded that the visible band is due to electrons trapped by oxygen vacancies neighboring alkali ions and that the ultraviolet band is due to positive holes trapped by alkali ion vacancies neighboring oxygen ions.

I. INTRODUCTION

THE study of color centers in quartz and fused quartz was reported by the author.[1] It was established that in fused quartz, prepared in the reducing condition, there is an oxygen vacancy which can trap one or two electrons.

Most commercial glasses are silicate and borosilicate glasses which contain alkali and alkali-earth ions.

Prizbram[2] reported very briefly the position of the peak of the visible part of the induced absorption bands in alkali borate glasses by the β and γ irradiation of radium.

II. PREPARATION OF SAMPLES AND EXPERIMENTAL METHODS

We prepared the samples by melting the raw materials in a platinum crucible in air with an electric furnace whose heater was a platinum ribbon.

As raw materials, we used lithium, sodium, potassium, and rubidium[3] carbonates, and boric acid, all of which were Merck guaranteed reagent grade. The quartz powder was made from pure quartz which had no absorption up to 210 mμ. We used also the purest SiO_2 made from distilled pure tetraethylsilicate; however, the results obtained were the same as those derived using pure quartz powder.

In this method of preparation, the samples are made in nearly neutral condition, that is, in neither an oxidizing nor a reducing condition. The glass specimens were annealed and polished.

We measured the absorption with a Beckman DU spectrophotometer at room temperature.

Some of the samples were hygroscopic. Therefore every sample was inserted into a moisture-tightened vessel containing silica gels during the x-irradiation and absorption measurements.

III. COLOR CENTERS IN ALKALI DISILICATE AND DIBORATE GLASSES

We have studied the alkali disilicate and diborate glasses, because crystals of the same composition are known to exist and the glass is considered[4] to have a local order of arrangement similar to that of the crystal of the same composition. A comparative study of crystal and glass may be possible in future.

The increase of absorption resulting from x-irradiation (45-kv, 10-ma tungsten target) for two hours at room temperature is given in Fig. 1 for silicate glasses and in Fig. 2 for borate glasses. The ordinates of these curves are the reduced absorption coefficient, i.e., the ratio of the absorption coefficient to the value at maximum.

Figure 3 gives the induced absorption bands of alkali

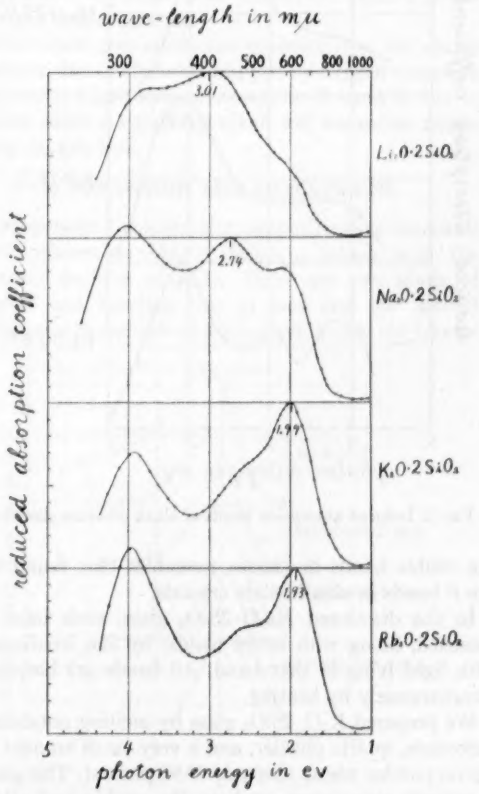

FIG. 1. Induced absorption bands of alkali disilicate glasses.

[1] R. Yokota, J. Phys. Soc. Japan **7**, 222, 316 (1952); Phys. Rev. **91**, 1013 (1953).
[2] K. Prizbram, Z. Physik **130**, 269 (1951).
[3] The rubidium carbonate is cp grade made in the Fisher Scientific Company (U. S. A.).
[4] R. Yokota, J. Phys. Soc. Japan **5**, 295 (1950); **6**, 489 (1951).

diborate glasses which are colored under different conditions of x-irradiation (100-kv, 3-ma tungsten target, at 45°C). The peak of the ultraviolet band is clearly observed.

We denote each band in the silicate glasses, measured from the long wavelength side, by A_1, A_2, and B. The corresponding bands in borate glasses are designated A and B, respectively.

The comparison of the peaks in Figs. 1 and 2 with the well-known F bands in the crystals of LiCl, NaCl, KCl, and RbCl obtained by Pohl[5] shows that the relation between the position of peak and the half-width in

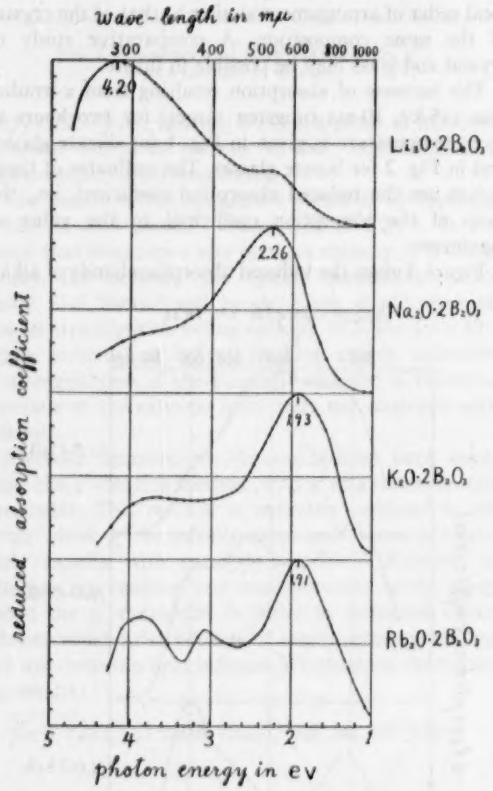

FIG. 2. Induced absorption bands of alkali diborate glasses.

the visible bands in glasses resembles that found for the F bands in alkali halide crystals.

In the discolored $Na_2O \cdot 2SiO_2$ glass, each band is bleached, along with other bands, by the irradiation with light lying in that band. All bands are bleached simultaneously by heating.

We prepared $K_2O \cdot 2SiO_2$ glass by melting potassium carbonate, quartz powder, and a very small amount of silicon powder whose purity is 99.98 percent. This glass is entirely transparent in both the visible and ultra-

[5] R. W. Pohl, Proc. Phys. Soc. (London) **49** (extra part), 3 (1937); Physik. Z. **39**, 36 (1938).

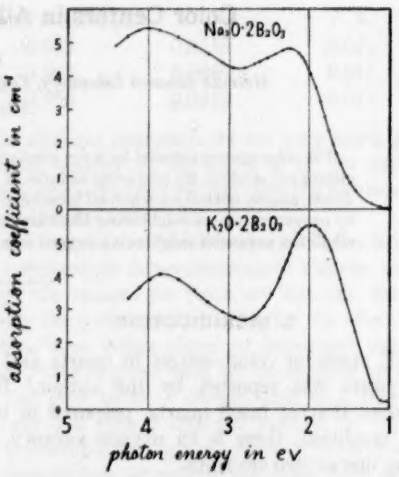

FIG. 3. Induced absorption bands of $Na_2O \cdot 2B_2O_3$ and $K_2O \cdot 2B_2O_3$ glasses (100-kv, 3-ma tungsten target, at 45°C).

violet regions; that is, the silicon does not act as a decolorizer, but acts as a reducing agent.

Furthermore, we prepared $K_2O \cdot 2SiO_2$ glass by melting potassium nitrate (Merck guaranteed reagent grade) and quartz powder in a sintered pure alumina crucible. It is well known that nitrate is more oxidizing than carbonate when the raw materials react at high temperature.

The induced absorption bands in these glasses, under the same condition of x-irradiation, are given in Fig. 4 together with those of the glass prepared in the nearly neutral condition.

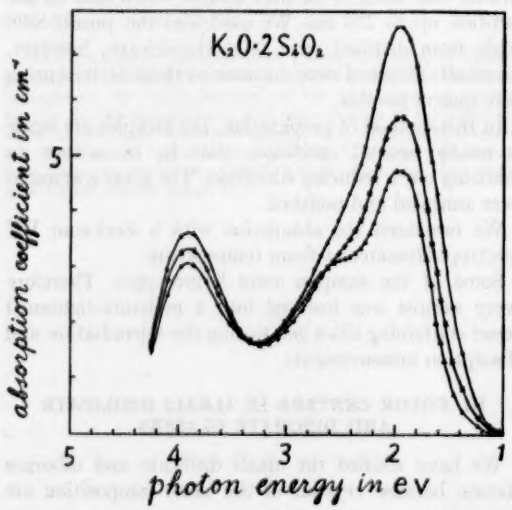

FIG. 4. Induced absorption bands of $K_2O \cdot 2SiO_2$ glass prepared in different conditions. The circular dots represent the glass prepared in reducing condition; the crosses represent the glass prepared in nearly neutral condition; and the triangles represent the glass prepared in oxidizing condition.

The oxidized glass has the smallest A_1 and A_2 bands and the largest B band. The reduced one has the reverse, and the neutral one has intermediate ratio of sizes.

IV. COLOR CENTERS IN Na_2O-SiO_2 GLASSES AND MIXED ALKALI GLASSES

We prepared Na_2O-SiO_2 glasses by melting sodium carbonate and quartz powder. The increase of the induced absorption as a result of x-irradiation is given in Fig. 5. For reference, in some cases the ordinates are given by the measured absorption coefficient. Figure 5 shows that the intensity and position of the

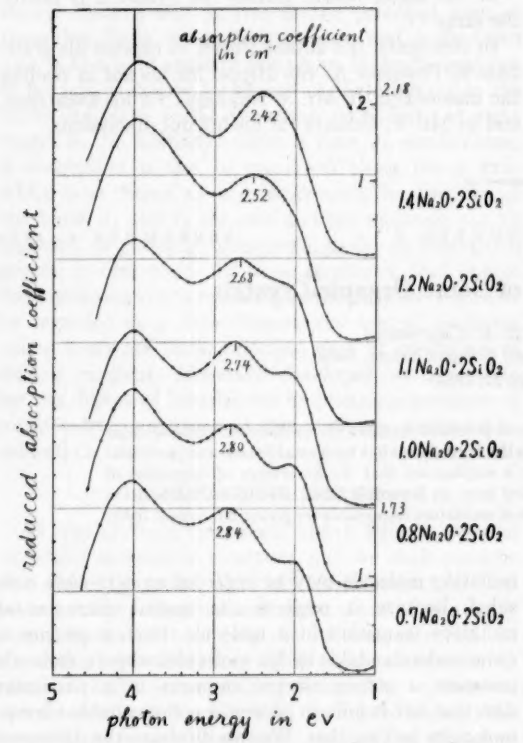

FIG. 5. Induced absorption bands in Na_2O-SiO_2 glasses.

peaks of the A_1 and A_2 bands change regularly with the Na_2O content, but those of the B band hardly change.

The situation is the same in K_2O-SiO_2 glasses.

We prepared the mixed alkali glasses of the molecular compositions represented as $xNa_2O\cdot(1-x)K_2O\cdot 2SiO_2$ and $xNa_2O\cdot(1-x)K_2O\cdot 2B_2O_3$, where x is 0, 0.25, 0.5, 0.75, and 1. The induced absorption bands in these glasses are given in Figs. 6 and 7. The figures show two facts: (A) the relative intensity and the peaks of the two visible bands in silicate glasses and the peak of the A band in borate glasses change approximately with the molecular fraction of Na_2O in K_2O. (B) The peak

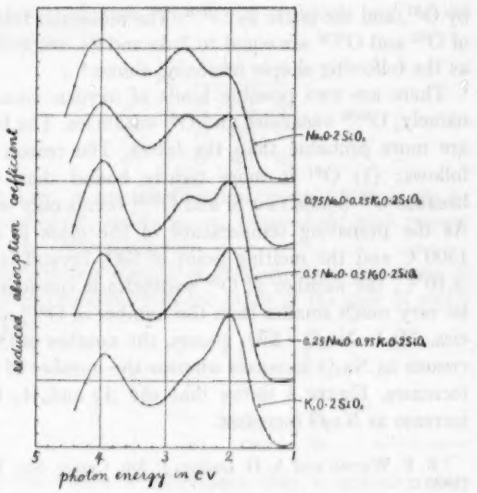

FIG. 6. Induced absorption bands in $xNa_2O\cdot(1-x)K_2O\cdot 2SiO_2$ glasses.

of the B band is nearly indifferent to the molecular composition, although some differences exist in potassium and sodium glasses.

These facts give additional evidence that the visible bands are due to electrons trapped by oxygen vacancies neighboring alkali ions, whereas the B band is due to positive holes trapped by alkali ion vacancies neighboring oxygen ions.

V. DISCUSSION AND CONCLUSIONS

We represent the molecular compositions of the alkali silicate glasses as $(M_2O)_x(SiO_2)_{1-x}$, where x is the molecular fraction of M_2O. There are two kinds of oxygens, one bonding two Si ions and the second bonding one Si and one alkali ion. We denote the former

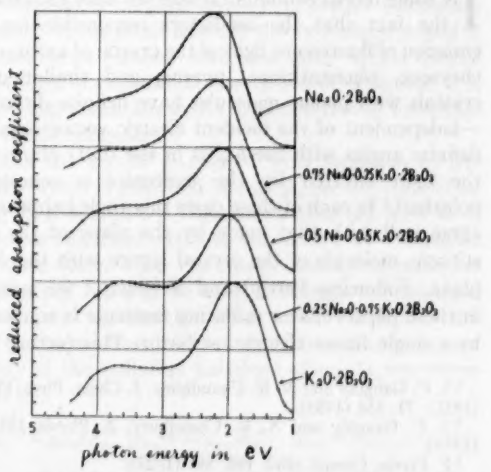

FIG. 7. Induced absorption bands in $xNa_2O\cdot(1-x)K_2O\cdot 2B_2O_3$ glasses.

by O^{Si}, and the latter by O^{SiM}. The molecular fractions of O^{Si} and O^{SiM} are equal to $2-3x$ and $2x$, respectively, as the following simple reasoning shows.[6]

There are two possible kinds of oxygen vacancies, namely, O^{SiM} vacancies and O^{Si} vacancies. The former are more probable than the latter. The reason is as follows: (1) O^{Si} is more tightly bound than O^{SiM}, because O^{Si} bonds two Si and O^{SiM} bonds only one Si. As the preparing temperature of the glass is about 1300°C and the melting point of SiO_2 crystal is 1713 ±10°C, the number of O^{Si} vacancies is considered to be very much smaller than the number of O^{SiM} vacancies. (2) In Na_2O-SiO_2 glasses, the number of O^{Si} decreases as Na_2O increases whereas the number of O^{SiNa} increases. Figure 5 shows that the A_1 and A_2 bands increase as Na_2O increases.

[6] B. E. Warren and A. D. Loring, J. Am. Ceram. Soc. **18**, 269 (1935).

There are two possible kinds of positive ion vacancies, namely, the alkali ion vacancies and Si ion vacancies. The former are more probable than the latter. The reasoning is as follows: (1) The Si ions are very tightly bound by four oxygens arranged at the corners of a tetrahedron. Since the preparing temperature of the glass is about 1300°C, the number of Si ion vacancies is considered to be very much smaller than that of the alkali ion vacancies. (2) In Na_2O-SiO_2 glasses, the number of Si ions decreases as Na_2O increases whereas that of Na ions increases. Figure 5 shows that the relative intensity of the B band and the A_1 and A_2 bands is nearly independent of the Na_2O content.

In the alkali borate glasses the situation is nearly the same.

In conclusion the author wishes to express his gratitude to Professor A. von Hippel for his aid in reading the manuscript, to Mr. S. Nakajima for his assistance, and to Mr. Y. Uemura for his helpful discussions.

PHYSICAL REVIEW VOLUME 95, NUMBER 5 SEPTEMBER 1, 1954

Anisotropy of Fluorescence of Some Organic Crystals

S. C. Ganguly and N. K. Chaudhury
Research Laboratory, Bangabasi College, Calcutta, India

(Received April 22, 1954)

A mathematical relationship between the intensities of polarized fluorescence in different perpendicular directions and the molecular orientations with respect to the crystal axes has been established, and particular reference is made to the plane aromatic molecules. It is emphasized that the knowledge of intensities of polarized fluorescence in different directions of a crystal may, in favorable cases, give direct information regarding the orientation of the molecule and the nature of oscillators responsible for giving fluorescent light.

1. INTRODUCTION

In some recent communications[1] we have emphasized the fact that the oscillators responsible for the emission of fluorescent light of the crystal of anthracene, chrysene, phenanthrene, pyrene, and similar other crystals with planar molecules have definite directions —independent of the incident electric vector—making definite angles with the b axis in the (001) plane, and the light emitted by the molecules is completely polarized.[2] In each of these cases this angle happened to agree well with that made by the plane of the constituent molecule of the crystal lattice with the (001) plane. Following Perrin[3] and Krishnan,[4] we assumed in these papers that a radiating molecule is equivalent to a single linear electric oscillator. This picture of a radiating molecule may be regarded as extremely one-sided, because it neglects the spatial character of radiative transition in a molecule. Such a picture is quite understandable in dye molecules where a molecule possesses a strong electric moment in a particular direction but it fails to present a commendable view in molecules lacking that. We can illustrate the difference between the two cases with the help of an azo-benzene molecule and a benzene molecule. A molecule of azo-benzene possesses a strong electric moment along the bond length in the molecule and absorption of light is the greatest when the incident light is polarized in the direction of the bond.[5] A molecule of benzene is planar and, because the π electrons are constrained to move in the plane of the molecule,[6] the virtual oscillators

[1] S. C. Ganguly and N. K. Chaudhury, J. Chem. Phys. **19**, 617 (1951); **21**, 554 (1953).
[2] S. C. Ganguly and N. K. Chaudhury, Z. Physik **135**, 255 (1953).
[3] F. Perrin, Compt. rend. **180**, 581 (1925).
[4] K. S. Krishnan and P. K. Seshan, Indian Acad. Science **8A**, 487 (1934); Current Sci. (India) **3**, 26 (1934); Z. Crystallogr. **A89**, 538 (1934).
[5] E. J. Bowen, *Chemical Aspects of Light* (Clarendon Press, Oxford, 1942), p. 11.
[6] C. V. Raman and K. S. Krishnan, Compt. rend. **184**, 449 (1927); Proc. Roy. Soc. (London) **A113**, 511 (1927); K. S. Krishnan *et al.*, Proc. Roy. Soc. (London) **A113**, 511 (1927); Trans. Roy. Soc. (London) **A231**, 235 (1933). K. S. Krishnan, Presidential Address, Section of Physics, Proceedings of the 27th Indian Science Congress, Part II (1940).

corresponding to radiative transitions are likely to lie in the molecular plane.[7] The oscillator strength f_{pq} corresponding to transition of a molecule from the state ψ_p to the state ψ_q, is given by $f_{pq}=(8\pi^2m/3he^2)\nu_{pq}|R_{pq}|^2$, where $R_{pq}=\int\psi_p^*(\sum e\mathbf{r}_i)\psi_q d\tau$ is the matrix component of the corresponding electric dipole moment, $\mathbf{r}_i$ being the position vector of the ith electron, and τ the volume. f_{pq} is a tensor quantity and as a result it is expected to have a spatial character of distribution the principal direction of transition being determined with reference to the symmetry of the molecule. To take an example, let us consider the benzene molecule which possesses a sixfold axis of symmetry passing perpendicularly to the plane of the molecule through the center of symmetry. Here x and y, two of the principal axes of transition, lie in the molecular plane, and z, the third axis, is at a right angle to this plane. If the fluorescence of benzene is caused by virtual oscillators lying in the molecular plane I_3 the transition probability at right angles to the molecular plane is zero. In azo-benzene, if absorption is due to transition along the x axis, which is so chosen as to coincide with the direction of the bond, I_2 and I_3 are zero and the molecule can be regarded as perfectly anisotropic as far as absorption process is concerned. All these combined, lead one to the conclusion that a radiating molecule must in general be regarded as a three-dimensional virtual oscillator where there are three principal axes of oscillation of electric moment. Jablonski[8] developed his expression for the degree of polarization of photoluminescence of rotation-free molecules of dye stuffs on similar considerations.

2. MONOCLINIC SYSTEM

All the crystals mentioned above have a type of molecular monoclinic structure, and we shall consider this class of crystals. They are characterized by possessing either a diagonal axis and a plane of symmetry perpendicular to it, or only one of these elements. In the following calculations it is most convenient to consider only orthogonal systems. The system of coordinates (a,b,c') consists of the crystal axis a, the rotation axis b, and the normal c' to these two directions [i.e., the perpendicular to the (001) plane]. The coordinates of equivalent points are $\pm(xyz;x\bar{y}z)$.

Let Ox, Oy, and Oz be the three principal directions of transition for absorption in a molecule and Ox', Oy', Oz' be the three principal directions of transition for emission in the molecule; Ox, Oy and Ox', Oy' are the plane of the molecule and Oz is at right angle to it. The orientation of axes of different oscillators with respect to the (a,b,c') axes is, in general, different. There is no fixed phase relation between the absorbed and the emitted light. Relative to the axes a, b, c', the direction cosines of the principal directions of transition probability of any one of the molecule and of its inversion will be

	x	y	z
a	l_1	m_1	n_1
b	l_2	m_2	n_2
c'	l_3	m_3	n_3

where l_1, m_1, n_1 are the direction cosines of Oa, l_2, m_2, n_2 are those of Ob, and l_3, m_3, n_3, those of Oc' with respect to Ox, Oy, Oz, respectively.

The direction cosines of the principal directions of transition probability of the other of the pair of molecules are

	x	y	z
a	l_1	m_1	n_1
b	$-l_2$	$-m_2$	$-n_2$
c'	l_3	m_3	n_3

From the above it is evident that a quantity that depends upon the squares of the direction cosines for a molecule, attains the same value for both pairs of molecules which go to build up the symmetry of the unit cell.

The molecule is regarded as a three-dimensional oscillator and the principal directions of the transition probability responsible for the emission of light may not agree with those responsible for the absorption of light.

It is well known that the intensity of an electronic transition from the upper state p to the lower state q is determined by the transition probability A_{pq} in emission, or B_{qp} in absorption. The transition probabilities A_{pq} and B_{qp} in turn are determined by the matrix element R_{pq} of the dipole moment following

$$A_{pq}\propto|R_{pq}|^2,\quad B_{qp}\propto|R_{pq}|^2$$

for nondegenerate electronic states.

If the matrix element $R_{pq}=\int\psi_p^*M\psi_q d\tau$ (transition moment) differs from zero for the two states p and q, the two states combine with each other with a certain probability of emission or absorption of radiation; if it is zero the transition under consideration is forbidden as a dipole transition.

When the crystal is excited with radiation of frequency which is polarized along Oa, the electric vector being E, a molecule is transferred from the level m of the lower electronic state to the level n of the higher electronic state. Then the energy density of radiation of frequency ν_{nm} is given by ρ_{nm}. Because the principal directions of upward transition of the molecules are Ox, Oy, Oz, we must take into consideration the energy density of the radiation polarized along Ox, Oy, Oz as given by

$$\rho_{nm}{}^{(x)}=\rho_{nm}l_1^2;\quad \rho_{nm}{}^{(y)}=\rho_{nm}m_1^2;\quad \rho_{nm}{}^{(z)}=\rho_{nm}n_1^2. \quad (1)$$

The probability of molecular transition along x from level m of the lower electronic state to the level n of the

[7] H. Sponer and E. Teller, Revs. Modern Phys. **13**, 76–114 (1941).

[8] A. Jablonski, Acta. Phys. Polonica **10**, 38 (1950).

higher electronic state (absorption) under energy density of radiation of frequency ν_{nm} is given by $\beta_{mn}^{(x)}\rho_{nm}^{(x)}$, where $\beta_{mn}^{(x)}$ is the transition probability along x. Similarly, those along y and z are $\beta_{mn}^{(y)}\rho_{nm}^{(y)}$ and $\beta_{mn}^{(z)}\rho_{nm}^{(z)}$ respectively, where $\beta_{mn}^{(y)}$ and $\beta_{mn}^{(z)}$ are the transition probabilities from the level m to the level n along y and z, respectively.

It is well known that when we are not considering resonance fluorescence, which is a special case, the molecules after being raised to the level n of the upper electronic state make radiative jumps to the level s of the lower electronic state, not from the level n but from some other level such as r, one of the lower vibrational levels of the upper electronic states. We have already discussed the transition probabilities from m to n (Fig. 1). Now we shall take into consideration the probabilities of nonradiative transfer that takes place in the passage from n to r, along x, y, and z. Since it is a nonradiative transfer, the energy of which may be lost by various processes such as heat, etc., they can be represented simply by $P(x)$, $P(y)$, and $P(z)$.

As we are considering a general case where the oscillator of absorption (let us call it D) is not same as the oscillator of fluorescence emission, denoted by F, suppose that D has principal transition probabilities along x, y, z fixed within the molecule and F has different transition probabilities along x', y', z' which are rotated to x, y, z by angles, the direction cosines of which are given by the following table:

	x'	y'	z'
x	α_1	α_2	α_3
y	β_1	β_2	β_3
z	γ_1	γ_2	γ_3

If the angles of rotation between the two systems are zero, i.e., F and D coincide, it means that the emission and absorption processes correspond to the same electronic transition and what is called resonance fluorescence takes place.

If the probabilities of spontaneous transition from the level r of the upper electronic state to the level s of the lower electronic state along x, y, z are represented by $A_{rs}^{(x)}$, $A_{rs}^{(y)}$, $A_{rs}^{(z)}$, respectively, where $A_{rs}^{(x)}$, $A_{rs}^{(y)}$, and $A_{rs}^{(z)}$ are the tensor components of the principal transition probabilities of the emission oscillator, along the principal axes of the absorption oscillator then the probability that a molecule will be raised from the level m of the lower electronic state to the level n of the upper electronic state, degraded from the level n to the level r of the same electronic state, and then fall from the level r to the level s of the lower electronic state (Fig. 1) with emission of radiation of frequency ν_{rs} is

$$\begin{aligned} &B_{mn}^{(x)}P^{(x)}A_{rs}^{(x)}\rho_{nm}^{(x)}\cdots\text{along } Ox,\\ &B_{mn}^{(y)}P^{(y)}A_{rs}^{(y)}\rho_{nm}^{(y)}\cdots\text{along } Oy,\\ &B_{mn}^{(z)}P^{(z)}A_{rs}^{(z)}\rho_{nm}^{(z)}\cdots\text{along } Oz, \end{aligned} \tag{2}$$

where $A_{rs}^{x}=I_1\alpha_1^2+I_2\alpha_2^2+I_3\alpha_3^2$, $A_{rs}^{(y)}=I_1\beta_1^2+I_2\beta_2^2+I_3\beta_3^2$, $A_{rs}^{(z)}=I_1\gamma_1^2+I_2\gamma_2^2+I_3\gamma_3^2$, and I_1, I_2, and I_3 are the principal transition probabilities of the emission oscillator.

Then the intensity I_{Oa} of the emitted light polarized along Oa is

$$I_{Oa}=N\rho_{nm}h\nu_{rs}(\beta_{mn}^{(x)}P^xA_{rs}^{(x)}l_1^4+\beta_{mn}^{(y)}P^yA_{rs}^{(y)}m_1^4+\beta_{mn}^{(z)}P^zA_{rs}^{(z)}n_1^4); \tag{3}$$

and the intensity I_{Ob} of the emitted light polarized along Ob is

$$I_{Ob}=N\rho_{nm}h\nu_{rs}(\beta_{mn}^{(x)}P^xA_{rs}^{(x)}l_1^2l_2^2+\beta_{mn}^{(y)}P^{(y)}A_{rs}^{(y)}m_1^2m_2^2+\beta_{mn}^{(z)}\rho^zA_{rs}^{(z)}n_1^2n_2^2), \tag{4}$$

where N is the number of molecules per unit cell. Consequently,

$$r=\frac{I_{Ob}}{I_{Oa}}=\frac{\beta_{mn}^{(x)}P^{(x)}A_{rs}^{(x)}l_1^2l_2^2+\beta_{mn}^{(y)}P^{(y)}A_{rs}^{(y)}m_1^2m_2^2+\beta_{mn}^{(z)}P^{(z)}A_{rs}^{(z)}n_1^2n_2^2}{\beta_{mn}^{(x)}P^{(x)}A_{rs}^{(x)}l_1^4+\beta_{mn}^{(y)}P^{(y)}A_{rs}^{(y)}m_1^4+\beta_{mn}^{(z)}P^{(z)}A_{rs}^{(z)}n_1^4}=\frac{K^{(x)}l_1^2l_2^2+K^{(y)}m_1^2m_2^2+K^{(z)}n_1^2n_2^2}{K^{(x)}l_1^4+K^{(y)}m_1^4+K^{(z)}n_1^4}, \tag{5}$$

where

$$K^{(x)}=\beta_{mn}^{(x)}P^{(x)}A_{rs}^{(x)},$$
$$K^{(y)}=\beta_{mn}^{(y)}P^{(y)}A_{rs}^{(y)},$$
$$K^{(z)}=\beta_{mn}^{(z)}P^{(z)}A_{rs}^{(z)}.$$

If we consider the case of crystals like anthracene, phenanthrene, pyrene, and chrysene in which the plane of the molecular constituent of the lattice cuts the $c(001)$ face about at a right angle or at a right angle, the above expression becomes simplified. Later on we shall discuss the experimental evidence in support of this and shall show that even without x-ray study it is quite possible to establish whether the molecular plane is normal to the c face or not. However, in any case we shall take the molecular plane normal to the c face.

Let the projection OD of the molecular plane ODx on the c face make an angle θ with Ob, and the angle between Ox and OD be ϕ. Then because Oz is perpendicular to the molecular plane ODx, Oz must lie in the c plane, and be at right angles to OD. From Fig. 2 it follows that

$$\begin{aligned} l_1&=\cos\phi\sin\theta, & l_2&=\cos\phi\cos\theta,\\ m_1&=\sin\phi\sin\theta, & m_2&=\sin\phi\cos\theta,\\ n_1&=-\cos\theta, & n_2&=\sin\theta, \end{aligned}$$

and thus, substituting the above values in expression (5), we get

$$r=\frac{\cot^2\theta[K^{(x)}\cos^4\phi+K^{(y)}\sin^4\phi+K^{(z)}]}{K^{(x)}\cos^4\phi+K^{(y)}\sin^4\phi+K^{(z)}\cot^4\theta}. \tag{6}$$

If we now suppose, which we must, that the transition probability perpendicular to the plane of the hexagonal benzene is zero, we can reasonably take the transition probability along the normal to the plane of homologous planar molecules to be zero.[7] Magnetic studies by Krishnan and his co-workers support the above view.

So finally we get

$$r=\cot^2\theta. \tag{7}$$

Since θ can be determined from x-ray work, r can be calculated, or conversely, if r is determined experimentally, θ can be calculated. The values of θ obtained from experimental determinations of r and the values obtained from x-ray studies are given in Table I.

3. SIGNIFICANCE OF THE CONSTANT VALUE OF r

It has been stated in previous communications[1,2,4] that the ratio of the intensities of fluorescent light along b and a is independent of the direction of the incident light vector, and so with unpolarized incident light the ratio of the two intensities remains the same. This result, as we have stated before, is very significant. We shall now show that in those crystals where the plane of the molecule is normal to the c face and light is normally incident on this face, this must be so.

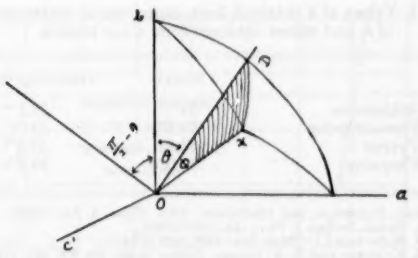

FIG. 2. The projection of the molecular plane on the c face of the crystal; Oa, Ob are crystallographic axes.

Suppose now that the incident light vector is polarized along Ob. Then, using the same notation as before, we get

$$\rho_{nm}{}^{(x)}=\rho_{nm}l_2{}^2;\quad \rho_{nm}{}^{(y)}=\rho_{nm}m_2{}^2;\quad \rho_{nm}{}^{(z)}=\rho_{nm}n_2{}^2.$$

The ratio of intensities is given by

$$r=\frac{I_b}{I_a}=\frac{K^{(x)}l_2{}^4+K^{(y)}m_2{}^4+K^{(z)}n_2{}^4}{K^{(x)}l_1{}^2l_2{}^2+K^{(y)}m_1{}^2m_2{}^2+K^{(z)}n_1{}^2n_2{}^2}.$$

Substituting the values of l_1, l_2, m_1, m_2, n_1, and n_2, we get

$$\frac{I_b}{I_a}=\frac{K^{(x)}\cos^4\phi\cos^4\theta+K^{(y)}\sin^4\phi\cos^4\theta+K^{(z)}\sin^4\theta}{K^{(x)}\cos^4\phi\sin^2\theta\cos^2\theta+K^{(y)}\sin^4\phi\sin^2\theta\cdot\cos^2\theta+K^{(z)}\cos^2\theta\cdot\sin^2\theta}=\frac{\cos^4\theta[K^{(x)}\cos^4\phi+K^{(y)}\sin^4\phi+K^{(z)}\tan^4\theta]}{\cos^2\theta\cdot\sin^2\theta[K^{(x)}\cos^4\phi+K^{(y)}\sin^4\phi+K^{(z)}]}=\cot^2\theta.$$

This shows, along with Eq. (7), that whether incident light is polarized along Oa or Ob, the ratio r of intensities along b and a remains the same, and it can be inferred that if the incident light is polarized in any direction, the value of this ratio remains the same.

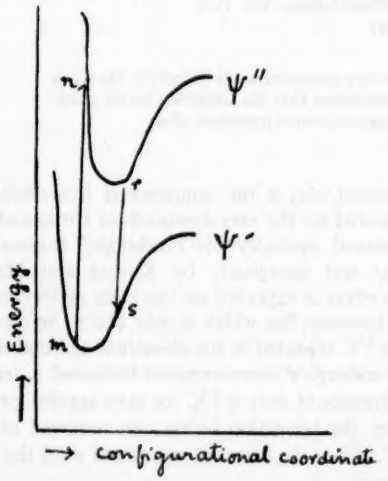

FIG. 1. mn represents the absorption energy and rs represents the energy of emission of radiation. ψ' and ψ'' are the two energy states.

4. DISCUSSION

Because of the brilliant work of Sponer and Teller,[7] Skalar,[9] and others, it can be inferred that in the benzene molecule the transition moment parallel to the plane of the molecule is responsible for emission of fluorescent light. It is equivalent to a plane symmetrical electronic oscillator with two of its principal transition probabilities equal, the third being zero. So, consideration of a linear virtual oscillator is representative. But this picture may appear to be too simple for crystals like anthracene, chrysene, phenanthrene, etc., though in these crystals the individual molecules retain their properties unaltered and the molecules are all planar.

In these organic molecules, which are characterized by the existence of so-called conjugated system of bonds, the σ electrons form bonds which maintain the molecular frame and the π electrons move in the potential of this frame. Such a carbon atom contributes one mobile π electron and two σ electrons for the chemical binding of the conjugated structure. The remaining one π electron for each carbon atom is practically free to migrate through the whole layer. The directional variation of some optical properties of these molecules in the crystalline state,[4,1,2] and the diamagnetic anisotropy of these molecules in the same

[9] A. L. Skalar, J. Chem. Phys. **5**, 671 (1937).

TABLE I. Values of θ obtained from experimental determinations of r, and values obtained from x-ray studies.

	From r	From x-ray studies
Anthracene	33°	28.1°[a]
Phenanthrene	33.5°	35°[b]
Pyrene	38.5°	38.5°[c]
Chrysene	32.0°[d]	29.5°[e]

[a] Sinclair, Robertson, and Mathieson, Acta. Cryst. **3**, 251 (1950).
[b] B. S. Basak, Indian J. Phys. **24**, 309 (1950).
[c] J. M. Robertson, J. Chem. Soc. **68A**, 358 (1947).
[d] K. S. Krishnan and P. K. Seshan, Indian Acad. Sci. **8A**, 487 (1938).
[e] J. Iball, Proc. Roy. Soc. (London) **A146**, 140 (1934).

state, prove that the π electrons—which are alone responsible for the phenomena mentioned above—migrate in the plane of the molecule. Recent publications[10] on conjugated hydrocarbons based on LCAO molecular orbital theory yield results regarding energy levels, free valence, and reactivities, etc., which are in agreement with experimental results. Our published results[1,2] derived with the assumption of a linear oscillator are in agreement with values derived from present considerations. From all these, it appears to be reasonable to assume the oscillators of these molecules of anthracene, phenanthrene, pyrene, chrysene, etc., to be equivalent to linear oscillators. Since the molecular planes of these crystals are not exactly at 90°, we find, quite reasonably, a little difference between the θ obtained from the x-ray result and the θ obtained from r, the ratio of intensities of fluorescence along b and along a. If the angle of the molecular plane with the b axis in the c face is other than 90°, it is not at all difficult to calculate the ratio of intensity along b and a.

In crystals where the plane of the molecule is normal to the c face on which light is incident normally, r (I_b/I_a) remains the same, whatever may be the direction of incident light vector. So, conversely, from the constant value of ratio of intensities along b and a, one can easily find the angle subtended by the plane of the molecule in the c face. It should be stated here that other conditions may also give similar results but they can be very easily eliminated, and so without any x-ray results, from a careful study of intensity of fluorescence along different perpendicular directions it is possible to find out the orientation of the molecules in a crystal and the nature of the oscillators responsible for such emission.

ACKNOWLEDGMENT

The authors wish to express their grateful thanks to the Government of West Bengal for the kind grant for research which it has made to one of us (S. C. Ganguly).

[10] C. W. Scherr, J. Chem. Phys. **9**, 1582 (1953); K. Raedenberg and C. W. Scherr, J. Chem. Phys. **9**, 1565 (1953).

PHYSICAL REVIEW VOLUME 95, NUMBER 5 SEPTEMBER 1, 1954

Dielectric Constant Behavior of Single-Domain, Single Crystals of Barium Titanate in the Vicinity of the Curie Point

M. E. DROUGARD AND D. R. YOUNG
International Business Machines Corporation, Poughkeepsie, New York

(Received April 28, 1954)

The dielectric constant of single crystals of barium titanate has been measured in the vicinity of the Curie point. An abrupt transition is observed substantiating earlier conclusions that the transition is first order. The Curie constant was found to be 1.73×10^{5}°C. The data indicate a thermal hysteresis effect.

CROSS[1] has indicated that the dielectric constant of barium titanate should increase discontinuously at the Curie point whereas published experimental data does not bear this out.[1,2]

We have made similar measurements using our equipment which automatically plots the dielectric constant as a function of temperature on a Leeds and Northrup X-Y recorder. The results are shown in Fig. 1. It can be seen that the dielectric constant does indeed rise abruptly at the Curie point. This is additional evidence indicating that the Curie transition in barium titanate is first order.

Of interest also is the temperature hysteresis effect not indicated by the measurements of Cross and Merz but observed optically by Forsbergh,[3] thermally by Roberts,[4] and electrically by Kanzig and Maikoff.[5] Such an effect is expected on the basis of Devonshire's theory, however, the width is only 2°C to be compared with the 7°C expected in the absence of thermal fluctuations. Forsbergh's[3] measurements indicated a temperature difference of only 0.7°C for zero applied pressure. However, the transition in his case occurred at about 107.5°C. When the pressure was raised until the transi-

[1] L. E. Cross, Phil. Mag. **44**, 1161 (1953).
[2] W. J. Merz, Phys. Rev. **91**, 513 (1953).
[3] P. W. Forsbergh, Phys. Rev. **93**, 686 (1954).
[4] S. Roberts, Phys. Rev. **85**, 925 (1952).
[5] W. Kanzig and N. Maikoff, Helv. Phys. Acta. **24**, 343 (1951).

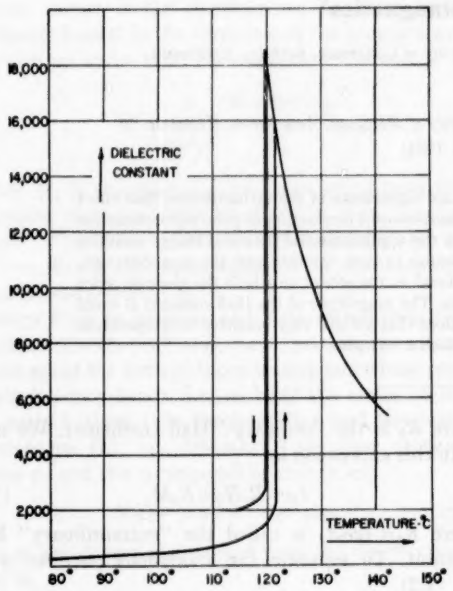

FIG. 1. Dielectric constant as a function of temperature.

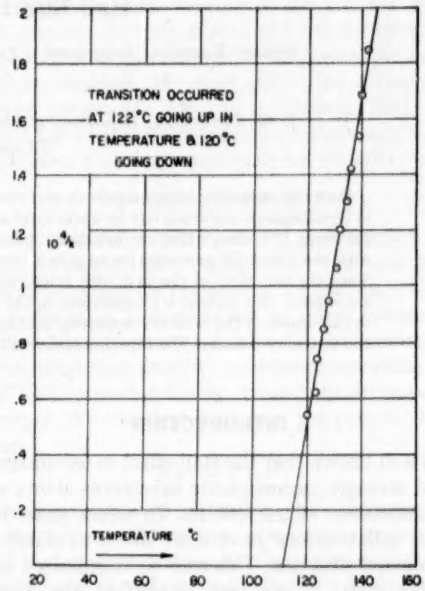

FIG. 2. Reciprocal dielectric constant *vs* temperature.

tion temperature became equal to ours (about 120°C), the temperature difference became equal to that observed by us. It is believed that the lower temperature difference was due to addition agents not present in our crystals.

The Curie-Weiss plot is shown in Fig. 2, and it is seen that the Curie-Weiss law is followed completely. The Curie constant is 1.73×10^5°C. This is to be compared with 1.56×10^5 as observed by Merz.[2]

After going through the temperature cycle it is noted that the dielectric constant is higher than before. This is due to the fact that the polarization is no longer uniformly perpendicular to the surface of the crystal. Consequently, there are contributions from the high dielectric constant in the "*a*" direction from regions where the polarization is parallel to the surface.

The authors are indebted to C. Karan, B. Skinner, H. Dunn, and E. Davin for growing the crystals and preparing them for our use. The temperature hysteresis effect has been discussed with R. Landauer.

Hall Effect in Ferromagnetics*

ROBERT KARPLUS,† *Department of Physics, University of California, Berkeley, California*

AND

J. M. LUTTINGER, *Department of Physics, University of Michigan, Ann Arbor, Michigan*

(Received May 21, 1954)

Both the unusually large magnitude and strong temperature dependence of the extraordinary Hall effect in ferromagnetic materials can be understood as effects of the spin-orbit interaction of polarized conduction electrons. It is shown that the interband matrix elements of the applied electric potential energy combine with the spin-orbit perturbation to give a current perpendicular to both the field and the magnetization. Since the net effect of the spin-orbit interaction is proportional to the extent to which the electron spins are aligned, this current is proportional to the magnetization. The magnitude of the Hall constant is equal to the square of the ordinary resistivity multiplied by functions that are not very sensitive to temperature and impurity content. The experimental results behave in such a way also.

I. INTRODUCTION

IT is well known that the Hall effect in ferromagnetic and strongly paramagnetic substances shows some quite anomalous characteristics. In recent years Pugh and his collaborators[1] have done much to clarify the experimental situation. This may be summarized in the following way: if one uses instead of the external magnetic field H_0 an "effective" field H_e, then the Hall effect in ferromagnetics behaves very much like the Hall effect in other metals as far as order of magnitude goes. The effective field is given by

$$H_e = H_0 + 4\pi M\alpha,$$

where M is the macroscopic magnetization of the sample and α is a parameter. The entire anomalous behavior is buried in α. Wannier[2] has shown that one may expect an effective internal field due to the magnetization of $2\pi(1+p)M$, where p measures the relative probability of a conduction electron penetrating into the interior of a polarized electron. Thus $p \gtrsim 1$ at most and one would expect a constant α of the order of unity. Experimentally α is extremely temperature dependent and can be considerably larger than unity. In very pure nickel, for example, α varies from 1 at very low temperatures[3] to about 100 at the Curie temperature. It is this huge magnitude and strong temperature dependence which has remained a puzzle until now.

It is convenient to express the experimental results a little differently. From the foregoing, the Hall field e_H per unit current density is

$$e_H = R_0 H_e = R_0(H_0 + 4\pi M\alpha), \tag{1.1}$$

where R_0 is the "ordinary" Hall coefficient. We may write this expression as

$$e_H = R_0 H_0 + R_1 M, \tag{1.2}$$

where $R_1 = 4\pi\alpha R_0$ is called the "extraordinary" Hall constant. To separate the anomalous part we write Eq. (1.2),

$$e_H = R_0[H_0 + 2\pi(1+p)M] + R_1' M, \tag{1.3}$$

$R_1' = R_1 - R_0 2\pi(1+p)$. R_1' describes only the anomalous effects. We shall be concerned with the calculation of R_1', which differs only insignificantly from R_1 at all but the very lowest temperatures.

In this paper we shall show that it is possible to understand all the unusual properties of R_1' (or α) as a consequence of the spin-orbit interaction of the magnetic electrons. The principle of the method is very simple. As a result of the spin-orbit interaction the stationary states of the system acquire a left-right asymmetry. When an external electric field is applied there results a current perpendicular both to the field and to the mean direction of spin of the particles. This current will therefore be proportional to the magnetization and its coefficient will yield R_1' or α. The result will depend in an intricate way on the Bloch functions of the electrons in a ferromagnetic. It is therefore only possible to make rough estimates of the final answer. Reasonable estimates, however, give results in excellent qualitative agreement with experiment.

II. METHOD OF CALCULATION

We now must develop a formalism capable of dealing with the consequences of spin-orbit interaction. The Hamiltonian $\mathcal{H}_T$ of an electron is a sum of three terms

$$\mathcal{H}_T = \mathcal{H}_0 + \mathcal{H}' + \mathcal{H}''; \tag{2.1}$$

$\mathcal{H}_0 = p^2/2m + V(\mathbf{r})$ is the Hamiltonian of an electron in the crystal potential energy $V(\mathbf{r})$; $\mathcal{H}' = [\boldsymbol{\sigma} \times \nabla V(\mathbf{r})] \cdot \mathbf{p}/4m^2c^2$ is the spin-orbit interaction,[4,5] $\boldsymbol{\sigma}$ being the Pauli

* This work was assisted in part by the U. S. Office of Naval Research and the U. S. Signal Corps.

† On leave of absence from Harvard University, Cambridge, Massachusetts.

[1] An excellent recent summary on the ferromagnetics may be found in E. M. Pugh and N. Rostoker, Revs. Modern Phys. **25**, 151 (1953). The strongly paramagnetic rare earths have been investigated by Kevane, Legvold, and Spedding, Phys. Rev. **91**, 1372 (1953).

[2] G. Wannier, Phys. Rev. **72**, 304 (1947).

[3] E. M. Pugh (private communication).

[4] Units have been chosen such that $\hbar = 1$.

[5] See for example D. Bohm, *Quantum Theory* (Prentice-Hall, Inc., New York, 1951), p. 405. Spin-orbit interaction has been

matrix vector. If the electrons are polarized (say by exchange forces) in the direction of the magnetization, the average value of $\mathcal{H}'$ for a magnetic electron is

$$\mathcal{H}'=\frac{1}{4m^2c^2}\frac{(\mathbf{M}\times\nabla V)\cdot\mathbf{p}}{M_s}, \tag{2.2}$$

where M_s is the magnetization one would have if the magnetic electrons were lined up to their maximum extent. For other electrons $\mathcal{H}'$ averages to zero. $\mathcal{H}''=-e\mathbf{E}\cdot\mathbf{r}$ is the Hamiltonian of the electrons in the external electric field E.

Since $V(\mathbf{r})$ is periodic and $\mathbf{p}$ is translationally invariant, $\mathcal{H}\equiv\mathcal{H}_0+\mathcal{H}'$ will have stationary solutions which are of the form of Bloch waves, and whose energy levels fall into bands. Let us label the states of $\mathcal{H}$ by an index l which tells the band (n) and the pseudomomentum $(\mathbf{k})$, i.e., $l\equiv(n,\mathbf{k})$. Call these stationary states ϕ_l and the corresponding energy ϵ_l;

$$\mathcal{H}\phi_l=(\mathcal{H}_0+\mathcal{H}')\phi_l=\epsilon_l\phi_l. \tag{2.3}$$

The ϕ_l are chosen normalized over the entire crystal; that is,

$$(\phi_l,\phi_{l'})=\int_\Omega\phi_l^*(\mathbf{r})\phi_{l'}(\mathbf{r})d^3x=\delta_{ll'}, \tag{2.4}$$

Ω being the volume of the crystal.

It is now necessary to compute the effect of the spin-orbit coupling on the transverse conductivity of the substance. The usual theory of conductivity based on the Boltzmann transport equation[6] proves to be insufficient for our purposes, yielding in fact a vanishing result (Appendix A). To see the necessary extension let us consider the interaction $\mathcal{H}''$ with the electric field in detail. In the representation based on the wave functions ϕ_l, the matrix elements of $\mathcal{H}''$ may be written

$$\begin{aligned}(n\mathbf{k}|\mathcal{H}''|n'\mathbf{k}')&=-eE_b(n\mathbf{k}|x_b|n'\mathbf{k}')\\&=-eE_b\left\{i\delta_{nn'}\frac{\partial}{\partial k_b}\delta_{\mathbf{k}\mathbf{k}'}+i\delta_{\mathbf{k}\mathbf{k}'}J_b^{nn'}(\mathbf{k})\right\},\end{aligned} \tag{2.5}$$

where

$$\begin{aligned}J_b^{nn'}(\mathbf{k})&=\int_\Omega w_{n\mathbf{k}}^*(\mathbf{r})\frac{\partial}{\partial k_b}w_{n'\mathbf{k}}(\mathbf{r})d^3x,\\J_b^{nn}(\mathbf{k})&=J_b(l)\neq0,\end{aligned} \tag{2.6}$$

with $\phi_l=e^{i\mathbf{k}\cdot\mathbf{r}}w_{n\mathbf{k}}(\mathbf{r})$ (see Appendix B). This second term in the expression for $\mathcal{H}''$ is completely regular. It is usually ignored because in the absence of spin-orbit coupling the only effects of it are second order in the electric field E_b and thus of no interest for the conductivity problem. We shall show that actually it is entirely responsible for the anomalous Hall effect. Since it has nonvanishing matrix elements only if $\mathbf{k}=\mathbf{k}'$, it represents a periodic potential. Let us write

$$\mathcal{H}''=\mathcal{H}_1''+\mathcal{H}_i'', \tag{2.7}$$

where $\mathcal{H}_1''$ is the regular periodic perturbation whose matrix elements are $-ie\delta_{\mathbf{k}\mathbf{k}'}E_bJ_b^{nn'}(\mathbf{k})$ and $\mathcal{H}_i''$ is the singular operator responsible for the usual conductivity effects. It is easy to see by direct computation that in any representation with Bloch functions H_i'' has the same form and H_1'' transforms according to the usual transformation theory. Hence the decomposition is unique. We therefore introduce the periodic Hamiltonian,

$$\mathcal{H}_p=\mathcal{H}+\mathcal{H}_1'', \tag{2.8}$$

whose eigenfunctions comprise the stationary one-electron states. H_i'' causes transitions among these states and must be treated by time-dependent methods together with the effects of the lattice vibrations.

The electron distribution is described by the density matrix[7] ρ which consists of two parts,

$$\rho=\rho_0(\mathcal{H}_p)+\rho_1, \tag{2.9}$$

where $\rho_0(\mathcal{H}_p)$ is the Fermi distribution at the lattice temperature T,

$$\rho_0(\mathcal{H}_p)=\{\exp[(\mathcal{H}_p-E_F)/kT]+1\}^{-1},\ \mathrm{Tr}\{\rho_0\}=1, \tag{2.10}$$

and ρ_1 contains the deviation from thermal equilibrium caused by the combined effect of $\mathcal{H}_i''$ and collisions with the lattice. It leads only to the ordinary conductivity formula discussed in Appendix A. The Hall effect must therefore be contained in the average velocity

$$\bar{v}_a=\mathrm{Tr}\{\rho_0v_a\}, \tag{2.11}$$

where v_a is the velocity operator,

$$v_a=i[\mathcal{H}_T,x_a]=i[\mathcal{H},x_a]=i[\mathcal{H}_p,x_a]-i[\mathcal{H}_1'',x_a]. \tag{2.12}$$

The first term in v_a averages to zero because

$$\mathrm{Tr}\{\rho_0(\mathcal{H}_p)[\mathcal{H}_p,x_a]\}=\mathrm{Tr}\{[\rho_0(\mathcal{H}_p),\mathcal{H}_p]x_a\}\equiv0. \tag{2.13}$$

In the calculation of the second term, which is already linear in the electric field, one may use the distribution function $\rho_0(\mathcal{H})$ and the wave functions ϕ_l in the absence of the field to calculate the average velocity,

$$\begin{aligned}\bar{v}_a&=-i\,\mathrm{Tr}\{\rho_0(\mathcal{H})[\mathcal{H}_1'',x_a]\}=-i\,\mathrm{Tr}\{[x_a,\rho_0(\mathcal{H})]\mathcal{H}_1''\}\\&=-i\sum_{n\mathbf{k}}(n\mathbf{k}|[x_a,\rho_0(\mathcal{H})]|n\mathbf{k})(n\mathbf{k}|\mathcal{H}_1''|n\mathbf{k})\\&\quad-i\sum_{n\mathbf{k}}\sum_{n'\neq n}(n\mathbf{k}|[x_a,\rho_0(\mathcal{H})]|n'\mathbf{k})\\&\qquad\times(n'\mathbf{k}|\mathcal{H}_1''|n\mathbf{k}).\end{aligned} \tag{2.14}$$

proposed previously for this problem by A. Samoilovich and U. Kon'Kov, J. Exptl. Theoret. Phys. (U.S.S.R.) **20**, 782 (1950). However, their treatment of the spin-orbit interaction which neglects the fact that it has the lattice periodicity is quite incorrect and consequently leads to a temperature-independent α, in conflict with experiment.

[6] N. F. Mott and H. Jones, *Theory of the Properties of Metals and Alloys* (The Clarendon Press, Oxford, 1936), pp. 189 ff.

[7] See R. C. Tolman, *Principles of Statistical Mechanics* (Oxford University Press, New York, 1930), Chap. IX.

The sum over the diagonal matrix elements in Eq. (2.14) can be simplified with the help of the formula in Appendix C and the definition of $\mathcal{H}_1''$ to yield ($\rho' = \partial\rho/\partial\epsilon$)

$$-ieE_b\sum_l \rho_0'(\epsilon_l)v_a(l)J_b(l). \quad (2.15)$$

The sum over the off-diagonal elements, on the other hand, does not involve any singular matrix elements at all. If the $J^{nn'}(k)$ are used to express the matrix elements of x_a and $\mathcal{H}_1''$, this sum becomes equal to

$$ieE_b\sum_l \rho_0(\epsilon_l)\sum_{n'}\{J_a^{nn'}(\mathbf{k})J_b^{n'n}(\mathbf{k}) - J_b^{nn'}(\mathbf{k})J_a^{n'n}(\mathbf{k})\}. \quad (2.16)$$

The sum has now been extended to include the term $n'=n$ which vanishes because J^{nn} is finite. The completeness of the functions $w_{n\mathbf{k}}(\mathbf{r})$ implies that

$$\begin{aligned}\sum_{n'} J_b^{nn'}(\mathbf{k})J_a^{n'n}(\mathbf{k}) &= -\int_\Omega \frac{\partial w_{n\mathbf{k}}^*(\mathbf{r})}{\partial k_b}\Big(\sum_{n'} w_{n'\mathbf{k}}(\mathbf{r})w_{n'\mathbf{k}}^*(\mathbf{r}')\Big)\frac{\partial w_{n\mathbf{k}}(\mathbf{r}')}{\partial k_a}d^3x\,d^3x' \\ &= -\int_\Omega \frac{\partial w_{n\mathbf{k}}^*(\mathbf{r})}{\partial k_b}\frac{\partial w_{n\mathbf{k}}(\mathbf{r})}{\partial k_a}d^3x \\ &= -\frac{\partial}{\partial k_b}J_a(l) + \int_\Omega w_{n\mathbf{k}}^*(\mathbf{r})\frac{\partial^2}{\partial k_a\partial k_b}w_{n\mathbf{k}}(\mathbf{r})d^3x. \quad (2.17)\end{aligned}$$

Since only the antisymmetric part of the product enters in Eq. (2.16), the second term cancels and leaves us with

$$-ieE_b\sum_l \rho_0'(\epsilon_l)[v_b(l)J_a(l) - v_a(l)J_b(l)], \quad (2.18)$$

after an integration by parts with respect to k. If we add this result to Eq. (2.15), we obtain the average velocity

$$\bar{v}_a = -ieE_b\sum_l \rho_0'(\epsilon_l)v_b(l)J_a(l). \quad (2.19)$$

Formally speaking, we may say that our effect arises from the consideration of the interband matrix elements of the electric interaction and of the velocity operator, whereas the usual theory only treats the intraband matrix elements.

In the next section we shall show that the transverse current contained in Eq. (2.19) is perpendicular to both the magnetization and the electric field and that it vanishes in the absence of the spin orbit coupling. We can therefore write

$$J_y = rM_zE_x, \quad (2.20)$$

where r is obtained by carrying out the summation over matrix elements in Eq. (2.14). From its structure we can see that r depends on temperature only weakly through the distribution function $\rho_0(\epsilon_l)$. If we therefore express the Hall voltage which prevents a current from flowing in the y direction,

$$E_y = -\rho J_y (\rho = \text{resistivity}), \quad (2.21)$$

as a voltage per unit current density,

$$e_H = E_y/J_x = -\rho rM_zE_x/J_x = -\rho^2 rM_z, \quad (2.22)$$

we see that the Hall constant $R_1' = -\rho^2 r$ should depend strongly on temperature like the square of the resistivity. Such a temperature dependence is actually the most striking feature of the experimentally determined Hall constants R_1. It follows in our theory from the approximate constancy of r. We now turn to an estimate of the magnitude of the extraordinary Hall effect.

III. THE HALL EFFECT FORMULA

The first step is to express the $J_a(l)$ in terms of the eigenfunctions $\psi_l = e^{i\mathbf{k}\cdot\mathbf{r}}u_{n\mathbf{k}}(\mathbf{r})$ and eigenvalues ϵ_l^0 of the electrons unperturbed by spin-orbit coupling. The matrix element in this representation will be denoted by a subscript zero. First-order perturbation theory on the energy gives $\epsilon_l = \epsilon_l^0$ (Appendix D), while the wave function is

$$w_{n\mathbf{k}}(\mathbf{r}) = u_{n\mathbf{k}}(\mathbf{r}) + \sum_{n'\neq n} u_{n'\mathbf{k}}(\mathbf{r})(n'\mathbf{k}|\mathcal{H}'|n\mathbf{k})_0/\epsilon_{n\mathbf{k}} - \epsilon_{n'\mathbf{k}}, \quad (3.1)$$

since the periodic character of $\mathcal{H}'$ gives matrix elements only between states with the wave vector $\mathbf{k}$. From now on all equations will have a common index $\mathbf{k}$ which we shall suppress, writing Eq. (3.1), for example,

$$w_n = u_n + \textstyle\sum_{n'} u_{n'}(n'|\mathcal{H}'|n)_0/\epsilon_n - \epsilon_{n'}. \quad (3.2)$$

Substitution in the definition of $J_a(l)$ gives

$$J_a(l) = 2\sum_{n'\neq n} I_a^{nn'}(n'|\mathcal{H}'|n)_0/\omega_{nn'}, \quad (3.3)$$

where

$$\begin{aligned} &I_a^{nn} = 0, \quad \omega_{nn'} = \epsilon_n - \epsilon_{n'}, \\ &I_a^{nn'} = \int_\Omega u_n^*\frac{\partial u_{n'}}{\partial k_a}d^3x \\ &\qquad = -(n|p_a|n')_0/m\omega_{nn'}(n\neq n'). \quad (3.4)\end{aligned}$$

$I_a^{nn'}$ is the same as $J_a^{nn'}$ except that it is evaluated with the functions u_n in the absence of spin-orbit coupling. It is discussed in Appendix D.

These expressions used in Eq. (3.3) finally yield the formula,

$$\bar{v}_a = -2ieE_b\sum_l \rho_0'(\epsilon_l)\sum_{n'\neq n} v_a(l)(n|p_b|n')_0 \times (n'|\mathcal{H}'|n)_0\omega_{nn'}^{-2}, \quad (3.5)$$

in which no approximations have been made other than the use of perturbation theory.

To proceed further with Eq. (3.5) one has to make additional and cruder approximations. The magnetic electrons belong to different "d bands" made up of the fivefold degenerate d state of the free atom. Let n be in one of these d bands. Then we would expect that

those n' ($\neq n$) which are also in d bands contribute most to Eq. (3.5). If n' represents a higher band (say the "s band") where the electrons are almost free, $(n'|p_b|n)_0$ is almost zero, since it is exactly zero for n' representing a band where the electrons are free. On the other hand for n' in a lower band the matrix elements are approximately just those for transitions of the isolated atoms, and therefore independent of k. For these though the sum over k vanishes, since $\sum_l \rho_0'(l)v_a(l)=0$. We shall then assume that the main contribution to the n' sum in Eq. (3.5) comes from transitions between the "d bands." Assuming this, we may replace $\omega_{nn'}{}^2$ by Δ^2, where Δ^2 is some mean square energy separation between different d bands for the same $\mathbf{k}$ at the top of their Fermi surfaces. Thus Eq. (3.5) becomes

$$\bar{v}_a=-\frac{2ieE_b}{m\Delta^2}\sum_{l(d)}\rho_0'(l)\sum_{n'\neq n}v_a(l)(n|p_b|n')_0 \times(n'|\mathcal{H}'|n)_0, \quad (3.6)$$

where the sum over l only covers the polarized d bands. Using

$$(n|p_a|n')_0=(n'|p_a|n)_0$$

and

$$(n|\mathcal{H}'|n')_0=-(n'|\mathcal{H}'|n)_0,$$

we can rewrite Eq. (3.6),

$$\bar{v}_a=-\frac{eE_b}{\Delta^2 m}\sum_{l(d)}\rho_0'(l)(n|i[\mathcal{H}',p_a]|n)_0v_b(l). \quad (3.7)$$

Equation (3.7) may be put into a much more transparent form, since the quantity $(n|i[\mathcal{H}',p_a]|n)_0$ is just the expectation value of the force due to spin-orbit interaction on an electron in an unperturbed state l. To see this we write the a component of the force F_a as

$$F_a=i[\mathcal{H},mv_a]=i[\mathcal{H}_0,mv_a]+i[\mathcal{H}',p_a],$$

to the first order in $\mathcal{H}'$. Then

$$(n|F_a|n)_0=(n|i[\mathcal{H}_0,mv_a]|n_0+(n|i[\mathcal{H}',p_a]|n)_0 =(n|i[\mathcal{H}',p_a]|n)_0\equiv F_a(l), \quad (3.8)$$

since the diagonal matrix elements in the $\mathcal{H}_0$ representation of the commutator of $\mathcal{H}_0$ with a regular operator vanish. Therefore substitution of Eq. (3.8) into Eq. (3.7) gives

$$\bar{v}_a'=-\frac{eE_b}{\Delta^2 m}\sum_{l(d)}\rho_0'(l)F_a(l)v_b(l), \quad (3.9)$$

the entire result being expressed by averages within a band. Equation (3.9) may also be written as the vector equation,

$$\bar{\mathbf{v}}=-\frac{e}{m\Delta^2}\sum_{l(d)}\rho_0'(\epsilon_l)[\mathbf{E}\cdot\mathbf{v}(l)]\mathbf{F}(l), \quad (3.10)$$

which shows that the additional current is in the direction of the spin-orbit force.

IV. CONCLUSIONS

For the final evaluation of the spin-orbit contribution to the Hall effect one must estimate Eq. (3.10). The chief difficulty is that the wave functions are so poorly known that it is impossible to find a really reliable estimate for $F(l)$. A very rough estimate however can be obtained by setting

$$\mathbf{F}(l)=+(e/c)[\mathbf{v}(l)\times\mathbf{H}], \quad (4.1)$$

where H is of the order of the mean value of the magnetic field giving rise to the spin-orbit interaction[8] times the ratio of the magnetization to saturation magnetization [see Eq. (2.2)],

$$\mathbf{H}=H_{s.o.}\mathbf{M}/M_s. \quad (4.2)$$

We obtain

$$\bar{\mathbf{v}}=-\frac{e^2}{\Delta^2 mc}H_{s.o.}\mathbf{E}\cdot[\sum_{l(d)}\mathbf{v}(l)\rho_0'(\epsilon_l)\mathbf{v}(l)]\times\mathbf{M}/M_s. \quad (4.3)$$

Comparison with Appendix A reveals that the sum in Eq. (4.3) is just the same one as that which occurs in the ordinary conductivity tensor. In a cubic crystal it is diagonal and

$$\bar{\mathbf{v}}=\frac{e^2}{\Delta^2 mc}H_{s.o.}\frac{\mathbf{M}\times\mathbf{E}}{M_s}\sum_{l(d)}\rho_0'(\epsilon_0)v_x{}^2(l). \quad (4.4)$$

The velocity is perpendicular to both the electric and magnetic fields. It therefore represents a Hall effect. With the electric and magnetic fields in the x and z directions, respectively, the velocity has only a y component. Hence the resultant transverse current is

$$J_y=N_d e\bar{v}_y=rM_sE_z, \quad (4.5)$$

where N_d is the total number of magnetic electrons contributing to the current; the constant of proportionality r defined in Eq. (2.20) is

$$r=-\frac{e^3}{mc\Delta^2}H_{s.o.}\frac{N^d}{M_s}\sum_{l(d)}\rho_0'(\epsilon l)v_x{}^2(l). \quad (4.6)$$

The sum can be simplified by the usual methods employed in discussions of the conductivity. It yields

$$-\sum_{l(d)}\rho_0'(l)v_x{}^2(l)=\delta\left\langle\frac{1}{m^*}\right\rangle_{d\,\text{av}}, \quad (4.7)$$

where m^* is the effective mass and δ is the number of incompletely filled d bands.[9] The maximum possible

[8] This field can be estimated by the condition that it should produce the correct separation for the spin-orbit doublets. Since for Fe or Ni these separations are of the order of 500 cm^{-1} or 10^{-12} erg, we have $H_{s.o.}\mu_B\sim10^{-12}$, $H_{s.o.}\sim10^7$ gauss.

[9] The effective mass has been discussed in connection with the large electronic heat capacity of transition metals [F. Seitz, *Modern Theory of Solids* (McGraw-Hill Book Company, Inc., New York, 1940), pp. 153 ff.] In our notation, the effective mass m_t of the electrons near the top of the Fermi distribution can be written $m_t=\delta\langle m^*\rangle_{d\,\text{av}}$ or $\langle 1/m^*\rangle_{d\,\text{av}}\sim\delta/m_t$ if only a narrow band of levels is either occupied or unoccupied.

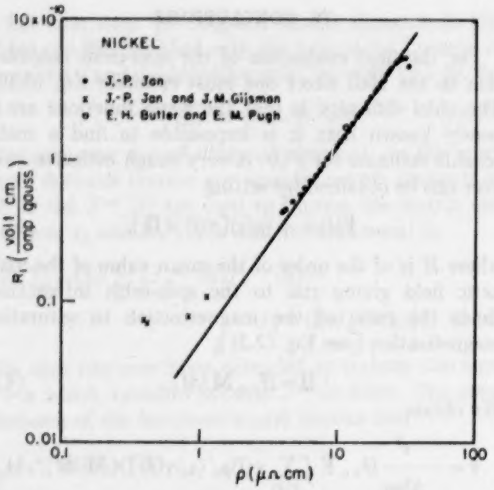

FIG. 1. Experimental results for iron. The equation of the straight line is $R'=0.7\times10^{-10}(\rho/\rho_0)^{1.94}$, with $\rho_0=10$ micro-ohm cm.

magnetization M_s is equal to

$$M_s=eN_d/2mc\Omega. \tag{4.8}$$

As a result Eq. (4.6) yields the extraordinary Hall constant

$$R_1'=\frac{2e^2H_{s.o.}}{m\Delta^2}\delta\left\langle\frac{m}{m^*}\right\rangle_{d\,k_H}\rho^2. \tag{4.9}$$

If we know the ordinary Hall constant R_0, we may compute the field paramerer $\alpha(\alpha\gg1)$ from

$$\alpha=\frac{R_1'}{4\pi R_0}=\delta\left\langle\frac{m}{m^*}\right\rangle_{d\,k_H}\frac{e^2H_{s.o.}}{\pi m\Delta^2R_0}\rho^2$$

$$\cong0.7\times10^{-7}\left\langle\frac{m}{m^*}\right\rangle_{d\,k_H}\frac{H_{s.o.}}{\Delta^2R_0}\rho^2\delta, \tag{4.10}$$

where $H_{s.o.}$, Δ, R_0, and ρ are expressed in the usual units: gauss, electron volts, volt cm/amp gauss, and ohm cm, respectively. To get an idea of the magnitude of α, we insert the measured values $H_{s.o.}\sim10^7$ gauss,[8] $\Delta\sim2$ ev,[10] $R_0\sim\frac{1}{2}\times10^{-12}$ volt cm/amp gauss, $\rho(0°)\sim10^{-5}$ ohm cm$=\rho_0$, $\delta\sim3$ and $\langle m/m^*\rangle_{d\,k_H}\sim1/10$:

$$\alpha(0°\text{C})\sim10, \tag{4.11}$$

at room temperature, which agrees quite well with the observed values for Fe and Ni.

Actually from the entire calculation we see that the quantity $4\pi M\alpha$ is not really an effective field at all, and the anomalous temperature dependence arises solely out of our desire to write the effect as we would an ordinary Hall effect. It is therefore more natural perhaps to compare R_1' with experiment, since that is what one actually measures. Then Eq. (4.9) becomes

$$R_1'\approx0.7\times10^{-10}(\rho/\rho_0)^2 \text{ volt cm/amp gauss.} \tag{4.12}$$

The most striking prediction of our theory is the fact that the extraordinary Hall coefficient should be proportional to the square of the resistivity. If one takes the measurements of Jan,[11] Jan and Gijsman,[12] and Butler and Pugh,[13] Figs. 1 and 2, one finds

$$R_1'=0.7\times10^{-10}(\rho_T/\rho_0)^{1.94} \text{ for Fe,}$$

and

$$R_1'=1.3\times10^{-10}(\rho_T/\rho_0)^{1.42} \text{ for Ni.}$$

For iron especially the agreement is excellent, though for nickel it is only qualitatively right. The agreement is good enough however to convince us that we have found the proper mechanism of the extraordinary Hall effect. The deviations from straight lines to low Hall constant values have to do with the fact that R_1 and R_1' differ significantly in this region. R_1', of course, will be less than R_1, and may be no more than one-half as big.

We should like to thank C. Kittel, who called this problem to our attention, for many stimulating discussions. One of us (J. M. Luttinger) would also like to thank the staff of the Physics Department of the University of California for their hospitality during the summer of 1953, where this work was begun.

APPENDIX A

The transport theory result[6] for the average velocity of an electron in a crystal subject to an electric field E is

$$\bar{v}_a=-eE_b\tau\sum_l\rho_0'(\epsilon_l)\frac{\partial\epsilon_l}{\partial k_b}v_a(l), \tag{A.1}$$

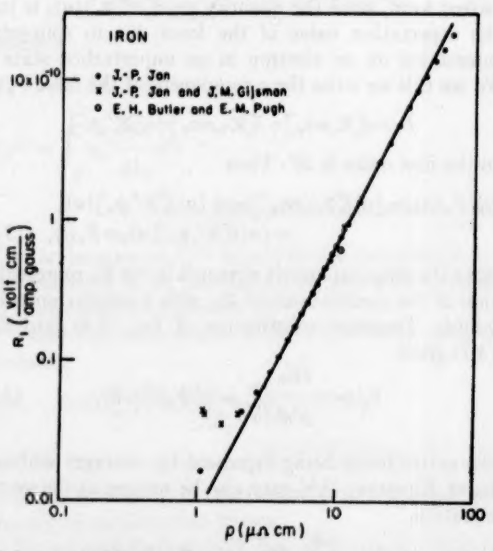

FIG. 2. Experimental results for nickel. The equation of the straight line is $R'=1.3\times10^{-10}(\rho/\rho_0)^{1.42}$, with $\rho_0=10$ micro-ohm cm.

[10] G. C. Fletcher, Proc. Phys. Soc. (London) **A65**, 192 (1952).

[11] J.-P. Jan, Helv. Phys. Acta. **25**, 677 (1952).

[12] J.-P. Jan and J. M. Gijsman, Physica **18**, 339 (1952).

[13] E. H. Butler and E. M. Pugh, Phys. Rev. **57**, 916 (1940).

where $v(l)$ and ϵ_l are the diagonal elements of the velocity and Hamiltonian operators including spin-orbit coupling in the state l; $\rho_0(\epsilon_l)$ is the Fermi distribution function at the lattice temperature. It is shown in Appendix C that

$$v_a(l)=\partial\epsilon_l/\partial k_a \tag{A.2}$$

in the general case of an electron subject to a periodic Hamiltonian. This applies in our case because the spin-orbit interaction is periodic. Any spin-orbit effects on the current through the velocity in Eq. (A.1) therefore depend on the energy shifts caused by this perturbation. Since the first-order effect of the spin-orbit coupling on the energy vanishes (Appendix D), there is no linear dependence on the magnetization in Eq. (A.1), and this expression can never contain a Hall effect.

APPENDIX B. PROPERTIES OF THE VELOCITY AND COORDINATE MATRICES

The velocity operator is given by the rate of change of the corresponding coordinate

$$v_a=i[\mathcal{H},x_a]. \tag{B.1}$$

When $\mathcal{H}$ is given by Eq. (4), then

$$v_a=\frac{p_a}{m}+\frac{1}{4m^2c^2}\frac{(\mathbf{M}\times\boldsymbol{\nabla}V)_a}{M_s}. \tag{B.2}$$

Since p_a and V both have the lattice periodicity, v_a will only connect states with the same k. Further, all the operators in Eq. (B.2) are regular in the sense that they have diagonal matrix elements for Bloch functions. If we express the velocity matrix in terms of the coordinate matrix, we get

$$(l|v_a|l')=i\omega_{ll'}(l|x_a|l'), \tag{B.3}$$

from Eq. (B.1). This equation is not very convenient for the diagonal elements, since those of x_a do not exist, strictly speaking. However, for off-diagonal elements (that is, interband matrix elements) it is useful since in this case $(l|x_a|l')$ may be expressed simply.

In general we may write:

$$\begin{aligned}
&(n\mathbf{k}|x_a|n'\mathbf{k}')\\
&=\int_\Omega e^{-i\mathbf{k}\cdot\mathbf{r}}w_{n\mathbf{k}}{}^*x_ae^{i\mathbf{k}'\cdot\mathbf{r}}w_{n'\mathbf{k}'}d^3x\\
&=\int_\Omega e^{-i\mathbf{k}\cdot\mathbf{r}}w_{n\mathbf{k}}{}^*\frac{1}{i}\frac{\partial e^{i\mathbf{k}'\cdot\mathbf{r}}}{\partial k_a'}w_{n'\mathbf{k}'}d^3x\\
&=\int_\Omega e^{i\mathbf{k}\cdot\mathbf{r}}w_{n\mathbf{k}}{}^*\frac{1}{i}\left[\frac{\partial}{\partial k_a'}(e^{i\mathbf{k}'\cdot\mathbf{r}}w_{n'\mathbf{k}'})-e^{i\mathbf{k}'\cdot\mathbf{r}}\frac{\partial w_{n'\mathbf{k}'}}{\partial k_a'}\right]d^3x\\
&=\frac{1}{i}\frac{\partial}{\partial k_a'}\int_\Omega\phi_{n\mathbf{k}}{}^*\phi_{n'\mathbf{k}'}d^3x\\
&\qquad+i\int_\Omega e^{i(\mathbf{k}'-\mathbf{k})\cdot\mathbf{r}}w_{n\mathbf{k}}{}^*\frac{\partial w_{n'\mathbf{k}'}}{\partial k_a'}d^3x\\
&=-i\frac{\partial}{\partial k_a'}(\delta_{nn'}\delta_{\mathbf{k}\mathbf{k}'})\\
&\qquad+i\int_\Omega e^{i(\mathbf{k}'-\mathbf{k})\cdot\mathbf{r}}w_{n\mathbf{k}}{}^*\frac{\partial w_{n'\mathbf{k}'}}{\partial k_a'}d^3x,
\end{aligned} \tag{B.4}$$

since the $w_{n\mathbf{k}}$ are orthonormal. However, the fact that the $w_{n\mathbf{k}}(\mathbf{r})$ are periodic means that the exponential factor will cause the remaining integral to vanish unless $\mathbf{k}=\mathbf{k}'$. Thus

$$(n\mathbf{k}|x_a|n'\mathbf{k}')=i\delta_{nn'}\frac{\partial}{\partial k_a}\delta_{\mathbf{k}\mathbf{k}'}+iJ_a{}^{nn'}(\mathbf{k}), \tag{B.5}$$

where J is defined in Eq. (2.6).

APPENDIX C

We shall prove that no matter what the nature of the interaction of the electrons and another system, so long as Bloch-like solutions,

$$\phi_{n\mathbf{k}}=e^{i\mathbf{k}\cdot\mathbf{r}}u_{n\mathbf{k}}, \tag{C.1}$$

exist with energy $\epsilon_n(\mathbf{k})$, then the expectation value of the commutator of a function $f(\mathcal{H})$ of the electronic Hamiltonian with the coordinate vector x_a is given by the derivative with respect to k_a,

$$\partial f(\epsilon_n(\mathbf{k}))/\partial k_a=+i\langle[f(\mathcal{H}),x_a]\rangle_{n,\mathbf{k}}. \tag{C.2}$$

To show this identity, we recognize that Eq. (C.1) and

$$\mathcal{H}(\mathbf{p},\mathbf{r})\phi_{n\mathbf{k}}=\epsilon_n(\mathbf{k})\phi_{n\mathbf{k}} \tag{C.3}$$

imply that

$$\mathcal{H}(\mathbf{p}+\mathbf{k})u_{n\mathbf{k}}=\epsilon_n(\mathbf{k})u_{n\mathbf{k}}. \tag{C.4}$$

Consequently the matrix element in Eq. (C.2) becomes

$$\begin{aligned}
&\langle[f(\mathcal{H}),x_a]\rangle_{n\mathbf{k}}\\
&=\int d^3xu_{n\mathbf{k}}{}^*e^{-i\mathbf{k}\cdot\mathbf{r}}[f(\mathcal{H}(\mathbf{p},\mathbf{r}))x_a\\
&\qquad-x_af(\mathcal{H}(\mathbf{p},\mathbf{r}))]e^{i\mathbf{k}\cdot\mathbf{r}}u_{n\mathbf{k}}\\
&=-i\int d^3xu_{n\mathbf{k}}{}^*\frac{\partial}{\partial k_a}[e^{-i\mathbf{k}\cdot\mathbf{r}}f(\mathcal{H}(\mathbf{p},\mathbf{r}))e^{i\mathbf{k}\cdot\mathbf{r}}]u_{n\mathbf{k}}\\
&=-i\int d^3xu_{n\mathbf{k}}{}^*\frac{\partial}{\partial k_a}[f(\mathcal{H}(\mathbf{p}+\mathbf{k},\mathbf{r}))]u_{n\mathbf{k}}.
\end{aligned} \tag{C.5}$$

Because the normalization integral $\int d^3xu_{n\mathbf{k}}{}^*u_{n\mathbf{k}}=1$ is independent of k_a, and $u_{n\mathbf{k}}$ is an eigenfunction of the differentiated operator by Eq. (C.4), the derivative may be taken outside the integral. The matrix element then immediately yields Eq. (C.2).

We obtain a well-known special case of the relationship if we choose

$$f(\mathcal{H})=\mathcal{H}, \quad f(\epsilon_n(\mathbf{k}))=\epsilon_n(\mathbf{k}). \tag{C.6}$$

Then Eq. (C.2) states

$$\langle +i[\mathcal{H},x_a]\rangle_{n\mathbf{k}}=\langle \dot{x}_a\rangle_{n\mathbf{k}}=\langle v_a\rangle_{n\mathbf{k}}=\partial\epsilon_n(\mathbf{k})/\partial k_a. \tag{C.7}$$

In the general case we can then express the derivative in a simpler way,

$$\frac{\partial f(\epsilon_n(\mathbf{k}))}{\partial k_a}=\frac{\partial f(\epsilon_n(\mathbf{k}))}{\partial \epsilon_n(\mathbf{k})}\langle v_a\rangle_{n\mathbf{k}}. \tag{C.8}$$

APPENDIX D. SYMMETRY PROPERTIES

We consider here the symmetry properties of various matrix elements with respect to the eigenfunctions $\psi_{n\mathbf{k}}$ of $\mathcal{H}_0$. It follows at once from the reality of $\mathcal{H}_0$ that one may always choose

$$\chi_{n,-\mathbf{k}}{}^*=\chi_{n,\mathbf{k}}, \tag{D.1}$$

which is equivalent to time-reversal invariance. Further, if the crystal has a center of symmetry—which is true for all cases that we consider—then we also may choose

$$\chi_{n,-\mathbf{k}}(-\mathbf{r})=\chi_{n,\mathbf{k}}(\mathbf{r}). \tag{D.2}$$

Since H' (see Eq. (2.2)) is pure imaginary and reflection invariant, we have

$$\mathcal{H}'^*=-\mathcal{H}', \tag{D.3}$$

$$\mathcal{H}'(-\mathbf{r})=\mathcal{H}'(\mathbf{r}). \tag{D.4}$$

From Eqs. (D.1) and (D.3) we obtain at once

$$(n'\mathbf{k}|\mathcal{H}'|n\mathbf{k})_0=\int\chi_{n'\mathbf{k}}{}^*\mathcal{H}'\chi_{n\mathbf{k}}d^3x=\int(\mathcal{H}'\chi_{n'\mathbf{k}})^*\chi_{n\mathbf{k}}d^3x$$

$$=\int(\mathcal{H}'^*\chi_{n'\mathbf{k}}{}^*)\chi_{n\mathbf{k}}d^3x$$

$$=-\int(\mathcal{H}'\chi_{n',-\mathbf{k}})\chi_{n,-\mathbf{k}}{}^*d^3x$$

$$=-\int\chi_{n,-\mathbf{k}}{}^*\mathcal{H}'\chi_{n',-\mathbf{k}}d^3x.$$

Thus

$$(n'\mathbf{k}|\mathcal{H}'|n\mathbf{k})_0=-(n,-\mathbf{k}|\mathcal{H}'|n',-\mathbf{k})_0$$

$$=(n',-\mathbf{k}|\mathcal{H}'|n,-\mathbf{k})_0. \tag{D.5}$$

From Eqs. (D.2) and (D.4), on the other hand, we have

$$(n'\mathbf{k}|\mathcal{H}'|n\mathbf{k})_0=\int\chi_{n'\mathbf{k}}{}^*\mathcal{H}'\chi_{n'\mathbf{k}}d^3x$$

$$=\int\chi_{n',+\mathbf{k}}{}^*(-\mathbf{r})\mathcal{H}'(-\mathbf{r})\chi_{n,+\mathbf{k}}(-\mathbf{r})d^3x$$

$$=\int\chi_{n',-\mathbf{k}}{}^*(\mathbf{r})\mathcal{H}'(\mathbf{r})\chi_{n,-\mathbf{k}}(\mathbf{r})d^3x,$$

or,

$$(n'\mathbf{k}|\mathcal{H}'|n\mathbf{k})_0=(n',-\mathbf{k}|\mathcal{H}'|n,-\mathbf{k})_0. \tag{D.6}$$

Combining (D.5) with (D.6) we have

$$(n'\mathbf{k}|\mathcal{H}'|n\mathbf{k})_0=-(n\mathbf{k}|\mathcal{H}'|n'\mathbf{k})_0. \tag{D.7}$$

From this we see at once that the diagonal elements of $\mathcal{H}'$ vanish, and therefore there is no first-order correction to the energy due to the perturbation $\mathcal{H}'$.

We may also use Eq. (D.1) and Eq. (D.2) to obtain some properties of the $I_a{}^{nn'}(\mathbf{k})$. By writing $\psi_{n\mathbf{k}}=e^{i\mathbf{k}\cdot\mathbf{r}}u_{n\mathbf{k}}$, Eqs. (D.1) and (D.2) become

$$u_{n,-\mathbf{k}}{}^*=u_{n\mathbf{k}}, \tag{D.8}$$

$$u_{n,-\mathbf{k}}(-\mathbf{r})=u_{n,\mathbf{k}}(\mathbf{r}). \tag{D.9}$$

From Eq. (D.8) we have

$$I_a{}^{nn'}(\mathbf{k})=\int u_{n\mathbf{k}}{}^*\frac{\partial u_{n'\mathbf{k}}}{\partial k_a}d^3x=\int u_{n,-\mathbf{k}}\frac{\partial u_{n',-\mathbf{k}}{}^*}{\partial k_a}d^3x$$

$$=-\int u_{n,-\mathbf{k}}\frac{\partial u_{n',-\mathbf{k}}{}^*}{\partial(-k_a)}d^3x=-(I_a{}^{nn'}(-\mathbf{k}))^*,$$

$$I_a{}^{nn'}(\mathbf{k})=I_a{}^{n'n}(-\mathbf{k}). \tag{D.10}$$

Similarly from Eq. (D.9),

$$I_a{}^{nn'}(\mathbf{k})=\int u_{n\mathbf{k}}{}^*(\mathbf{r})\frac{\partial u_{n'\mathbf{k}}(\mathbf{r})}{\partial k_a}d^3x$$

$$=\int u_{n\mathbf{k}}{}^*(-\mathbf{r})\frac{\partial u_{n'\mathbf{k}}(-\mathbf{r})}{\partial k_a}d^3x$$

$$=\int u_{n,-\mathbf{k}}{}^*(\mathbf{r})\frac{\partial u_{n',-\mathbf{k}}(\mathbf{r})}{\partial k_a}d^3x$$

$$=-\int u_{n,-\mathbf{k}}{}^*\frac{\partial u_{n',-\mathbf{k}}}{(-k_a)}d^3x,$$

$$I_a{}^{nn'}(\mathbf{k})=-I_a{}^{n'n}(\mathbf{k}). \tag{D.11}$$

Thus the diagonal elements $I_a{}^{nn}(\mathbf{k})$ vanish identically.

Magnetic Neutron Diffraction from Fe_3O_4

A. W. McReynolds* and T. Riste
Joint Establishment for Nuclear Energy Research, Kjeller, Norway

(Received May 21, 1954)

By neutron diffraction intensity measurements, the spin alignment structure has been studied from the room temperature to above the Curie point in an unmagnetized (random domain orientation) crystal of Fe_3O_4. Intrinsic magnetization is found to follow approximately the Weiss theory and to go to zero at a sharply defined Curie point, where domain structure disappears. An additional diffuse component of the magnetic Bragg peaks is observed to be independent of external fields and indicates transient short-range ordering of spins, which reaches a sharp maximum at the Curie point but exists at both higher and lower temperatures.

I. INTRODUCTION

DIFFRACTION of neutrons in magnetic crystals consists of two components, one nuclear scattering and the other magnetic. The nuclear component arises from diffraction from the lattice arrangement of nuclei, and the magnetic component from interaction of the neutron moment with a magnetic lattice consisting in an ordered arrangement of spin directions of unpaired electrons at atom sites. A number of studies have been made at room temperatures and below to determine the arrangement of the magnetic lattice.[1–3] We have studied the variation of the intensity of magnetic diffraction peaks with temperature to investigate the process by which it transforms from a perfectly ordered array of spins at zero temperature to a random distribution above the Curie temperature. An unmagnetized ferro or antiferromagnetic crystal at low temperatures is divided into domains of many atoms, in each of which all atomic spins are perfectly aligned. With increasing temperatures thermal agitation causes increasingly greater deviation from perfect alignment, with corresponding decrease of the average moment along the direction of domain magnetization. This decrease in domain magnetization follows approximately the Weiss formula, going abruptly to zero at the Curie temperature. At higher temperatures a paramagnetic state, without long-range ordering exists. It is of interest to determine further details of the structural and substructural changes in domains during this transition, in particular whether the domains remain of the same size as their moment goes to zero and to what extent coupling between neighboring atoms produces local ordering within the domains. These questions may be partly answered from neutron diffractions data. As derived by Halpern and Johnson,[4] the diffracted intensity in an elastic Bragg peak from a small crystallite is proportional to the structure factor squared. For a simple cubic lattice this equals the differential scattering cross section of a single ion,

$$F^2=C^2+\mathbf{q}\cdot\boldsymbol{\lambda}CD+q^2D^2, \tag{1}$$

where C, D = nuclear and magnetic scattering amplitudes, respectively; $\mathbf{q}=\mathbf{e}(\mathbf{e}\cdot\mathbf{K})-\mathbf{K}$, and $\mathbf{e}$, $\mathbf{K}$, and $\boldsymbol{\lambda}$ are the unit vectors; $\mathbf{e}$ = scattering vector (see Fig. 1a); $\mathbf{K}$ = direction of magnetization; and $\boldsymbol{\lambda}$ = polarization of neutron, parallel or antiparallel to $\mathbf{K}$. In the case of an unpolarized beam $\mathbf{q}\cdot\boldsymbol{\lambda}$ has average value 0 so (1) reduced to

$$F^2=C^2+q^2D^2. \tag{2}$$

It further simplifies for special cases of direction of magnetization to

$$\begin{aligned} &F^2=C^2, && \mathbf{e}\parallel\mathbf{K},\\ &F^2=C^2+D^2, && \mathbf{e}\perp\mathbf{K},\\ &F^2=C^2+\tfrac{2}{3}D^2, && \text{random orientation (unmagnetized).}\end{aligned} \tag{3}$$

F^2 is a similar sum of independent nuclear and magnetic component for each plane of the magnetic lattice. Thus by application of a magnetic field parallel to the scattering vector, the magnetic component is reduced to zero to determine the residual nuclear component

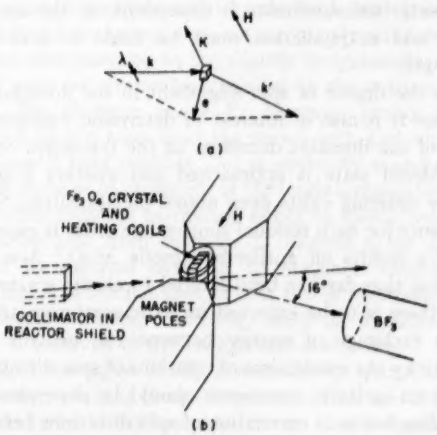

FIG. 1. (a) Illustration of the vectors of propagation $\mathbf{k}$, magnetization $\mathbf{K}$, scattering $\mathbf{e}$, and polarization $\boldsymbol{\lambda}$ determining diffraction from the crystal. (b) Arrangement of apparatus for observation of neutron magnetic diffraction from Fe_3O_4 single crystal.

* On leave from Brookhaven National Laboratory; now returned there.

[1] Shull, Strauser, and Wollan, Phys. Rev. **83**, 333–345 (1951).
[2] Shull, Wollan, and Strauser, Phys. Rev. **81**, 483–4 (1951).
[3] Shull, Wollan, and Koehler, Phys. Rev. **84**, 912–21 (1951).
[4] O. Halpern and M. H. Johnson, Phys. Rev. **55**, 898 (1939).

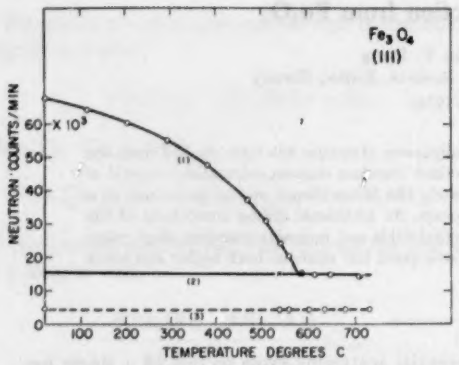

FIG. 2. Total intensity in neutron beam diffracted from the (111) planes of Fe_3O_4. Curves: (1) unmagnetized crystal, (2) magnetized parallel to scattering vector, (3) background, crystal turned.

independently. Proportionality of diffracted intensity to F^2 requires that the crystal be sufficiently thin (a few millimeters) to avoid extinction effects.[5]

Since the magnetic scattering amplitude is given by $D=(e^2/mc^2)\gamma Sf$, where γ = neutron magnetic moment, S = average magnetic moment/atom, and f = form factor depending on space distribution of magnetic electrons, the variation of diffracted intensity is a direct measure of the average atomic magnetic moment. Further, as seen in the third case of Eqs. (3), this applies equally well to an unmagnetized sample, with random domain orientations. It is thus possible to determine the shape of the intrinsic magnetization *vs* temperature, for comparison with both theory and direct magnetic measurements, which require alignment of the domains by an external field. This property is of particular interest for measurements in the vicinity of the Curie point, where the shape of the curve from magnetic measurements is dependent on the applied field and extrapolation must be made to zero field strength.[6]

As the degree of spin alignment in the domains decreases it is also of interest to determine whether the size of the domains decreases as the transition to the disordered state is approached and whether a short-range ordering exists even above the transition. Some evidence for such residual short-range order is given by Shull's results on antiferromagnetic MnO.[2] Also discussion thus far has been limited to elastic scattering, but there is to be expected inelastic scattering arising from exchange of energy between the neutron and lattice by the mechanism of rotations of spin directions. Such an inelastic component should be dependent on coupling forces or correlation of spin directions between neighboring atoms.

[5] G. E. Bacon, Proc. Roy. Soc. (London) **A209**, 1097 (1951).
[6] P. Weiss and R. Forrer, Compt. rend. **178**, 1670–3 (1924).

II. EXPERIMENTAL METHODS

It is convenient to choose a substance and crystal plane for which the magnetic amplitude is large compared to the nuclear, as has been found to be the case for the Fe_3O_4 (111) plane.[2] The samples used were cut from large natural crystal geological specimens. They were cut in two sizes, 2×6×10 mm and 6×12×25 mm. Previous neutron measurements of rocking curves[7] had shown the mosiac spread to be very large, about 1.3 degrees half-width. In addition, diffraction was in transmission through the thinnest dimension, to avoid extinction. The experimental arrangement is shown schematically in Fig. 1b. The neutron beam from a graphite scatterer in the center of the reactor at Instituttet for Atomenergi, Kjeller, Norway,[8] was defined to about 12 minutes half-width by a graphite and Cd collimator. The sample crystal, in a miniature quartz furnace with electrical heating windings, was mounted on the neutron crystal spectrometer table. The direct heterogeneous neutron beam was incident at 8 degrees angle to the (111) plane, and the 2-inch diameter BF_3 counter set at 16 degrees was large enough to receive the entire diffracted beam. This incident angle was chosen such that the diffracted neutrons, 1.3 angstroms wavelength, lie near the maximum of the reactor spectrum, but the higher orders, 0.65 angstrom from the (222) planes, and 0.33 angstrom from the (444) planes, are negligible in abundance. This was necessary since the higher-order reflections are mostly nuclear, although small higher-order components should not affect the relative curve shape. Temperatures were measured by a thermocouple and potentiometer and controlled by manual adjustment to better than 1 degree C. The crystal and electric furnace were in the 20-mm wide gap between pole faces of an electromagnet, with field direction parallel to the scattering vector and

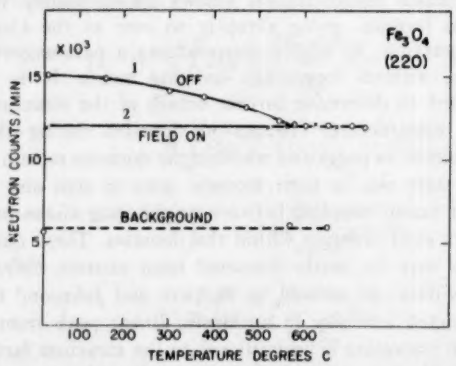

FIG. 3. Diffracted intensity from the (220) planes of Fe_3O_4 for crystal (1) unmagnetized, (2) magnetized parallel to scattering vector.

[7] A. W. McReynolds, Phys. Rev. **88**, 958–9 (1952).
[8] Additional measurements at Brookhaven National Laboratory under auspices of the U. S. Atomic Energy Commission are also included.

strength about 2000 gauss. Tests indicated this was sufficient to saturate the crystal in that further increase to 3500 gauss did not decrease diffracted intensity. Measurements were then made both with and without magnetic field, corresponding to the first and third cases of Eq. (3).

In those measurements made with a monochromatic incident beam, the reactor beam, defined by a soller slit system was incident at 12.5 degrees on the (200) planes of a Pb monochromator crystal. The diffracted beam incident on the Fe_3O_4 crystal thus had a wavelength of 1.08 angstroms and a geometrical spread of about one degree half-width. Where width of the diffracted peak from the Fe_3O_4 was measured, collimating slits of equal divergence were introduced between crystal and counter.

III. RESULTS AND DISCUSSION

Because of the high intensity of magnetic scattering, compared to nuclear, for the Fe_3O_4 (111) plane, most measurements were made for that plane, with some additional data on the (220) and (113) planes. Figures 2 and 3 show the total diffracted intensity as a function of temperature for the Fe_3O_4 (111), under various conditions. Curve 1 with magnetic field off contains all components of diffraction. In curve 2 application of the magnetic field eliminates the magnetic component leaving only background plus nuclear scattering, and in curve 3, with the crystal slightly rotated, only the background, primarily scattering from the furnace and multiple scattering in the crystal, reaches the counter. The difference between curves 1 and 2 should represent the magnetic component, $\frac{2}{3}D^2$, and it is seen that it follows approximately the shape of the Weiss equation.

In Fig. 4, the diffracted intensity with magnetic field on is shown on larger scale, showing a decrease at low temperatures and a second sharper decrease in the range just above the Curie temperature. For purely nuclear diffraction the intensity would be expected to decrease slightly and approximately linearly as a result of increasing thermal diffuse scattering, with no

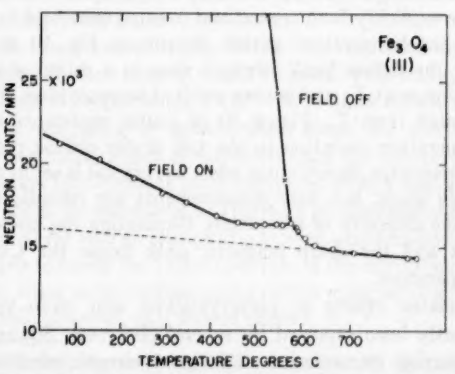

FIG. 4. Diffracted intensity from (111) planes of Fe_3O_4. Same curves as (1) and (2) of Fig. 2.

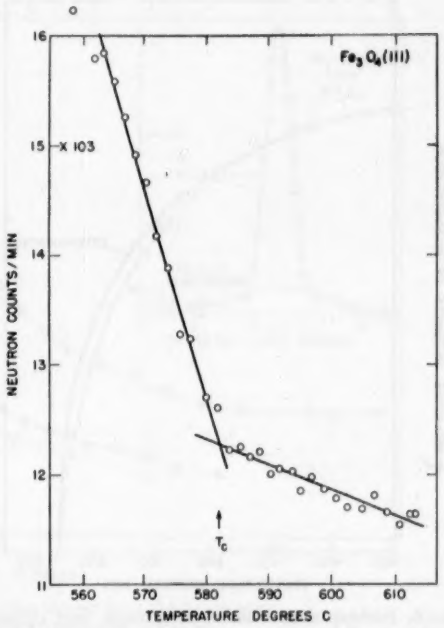

FIG. 5. Diffracted intensity *vs* temperature in the region near Curie temperature. Magnetic elastic component of intensity goes sharply to zero at T_c and increases linearly below, in accordance with Weiss equation.

anomaly at the Curie point. This slight temperature dependence of the nuclear component was measured on the (113) peak, where the magnetic contribution is very small. The dotted line in Fig. 3 shows the nuclear intensity for the (111) reflection, as derived from the (113) data. Deviation of curve 2 from this line amounts to a few percent of the magnetic peak intensity and probably is to be attributed to slight residual magnetic elastic scattering not canceled by the field. Such would be expected if the crystal were not completely saturated, or if the field direction in the slightly irregular shaped crystal were not everywhere parallel to the scattering vector. The decrease above T_c, however, cannot be explained on this basis since the curves with and without magnetic field coincide, but is obviously magnetic in origin because of proximity of the Curie temperature. It therefore must be attributed either to elastic magnetic diffraction from domains of aligned spins unaffected by external fields or to magnetic inelastic scattering. It is evident though that the decrease is not an isotropic inelastic scattering, since no significant change is observed in the background scattering.

In Fig. 5 the region of Fig. 2 immediately around the Curie temperature is shown in greater detail and indicates that the Curie temperature as thus measured without applied magnetic field is quite sharp. According to theory the neutron intensity, being proportional to (intensity of magnetization),[2] should vary linearly with temperature near T_c as is the case. The solid curve

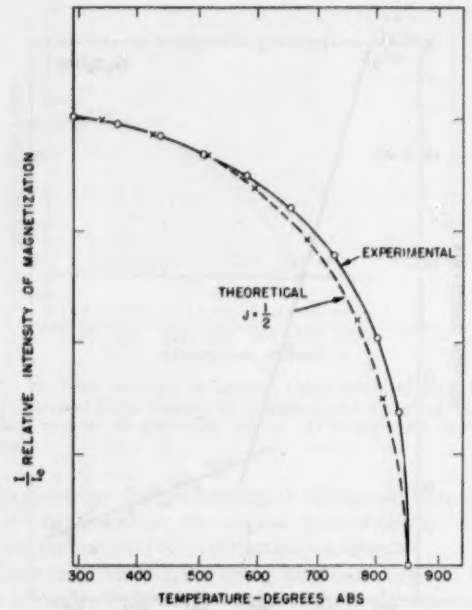

FIG. 6. Intrinsic magnetization as deduced from diffraction measurements. Points represent experimental data, curves theoretical Brillouin function for indicated J value.

drawn below T_c is for the theoretical relation,

$$\frac{I_s}{I_0}=\tanh\left(\frac{I_s/I_0}{T/\theta}\right).$$

In Fig. 6, the complete curve of (diffracted intensity)$^{\frac{1}{2}}$ *vs* temperature is shown, the points representing experimental data and the curves theoretical relations on the basis of the Brillouin function for $J=\frac{1}{2}$. Deviation from theoretical relations is qualitatively similar to the results of measurements by magnetic methods.

Further to investigate phenomena immediately around the Curie point additional measurements were made with a monochromatic incident beam on the crystal and soller slits between crystal and counter. In Fig. 7 is shown the diffraction peak as measured at different temperatures with crystal fixed at the Bragg angle. Under these conditions the peak width is determined by geometrical and wavelength resolution of the incident beam, but would be broadened if the coherent scattering regions, that is the domains, became small. Since the width of the nuclear peak immediately above T_c is very close to the width of nuclear plus magnetic peak about 10° below T_c, it can be concluded that the size of the domains does not become small enough (<about 100 angstroms) to result in peak broadening as T_c is approached. Examination of the peaks thus measured shows that although peak height has only a slight decrease in the region just above T_c, the integrated intensity follows the form of Fig. 3. The intensity decrease in Fig. 3 is thus indicated to arise from changes in a broad diffuse peak surrounding the main diffraction peak. This is seen more directly in Fig. 8, where the Fe_3O_4 crystal was rotated a few degrees from the Bragg angle such that the normal elastic peak no longer occurs. It is seen however that in spite of the rotation of the crystal planes and lack of satisfaction of the Bragg conditions, there persists a diffuse peak centered around the direction in which a (111) peak would occur at the wavelength used. Reference to Fig. 9 shows that such would be expected if the diffuse peak is attributed to inelastic scattering. Here, $\mathbf{k}$ and $\mathbf{k}'$ are representations in reciprocal space of the propagation vectors of the incident and scattered neutrons. The Bragg condition is satisfied when the crystal is so oriented that one of the reciprocal lattice points lies on the sphere of reflection. Although rotation of the crystal moves the (111) reciprocal lattice point off the sphere of reflection, inelastic scattering is still centered about the lattice point so that the direction of the $\mathbf{k}'$ propagation vector is approximately the same as for elastic scattering. In agreement with Fig. 3 the application of a magnetic field caused no change in the diffuse peak. Figure 8 shows further that although a diffuse peak exists even at room temperature it is much stronger near T_c. To study temperature variation more explicitly both crystal and counter were held fixed and the temperature varied. Results in Fig. 10 show that the diffuse peak strength rises to a rather sharp maximum at T_c, and is very small at temperatures 100° or more from T_c. Figure 10 of course represents the temperature variation in the tail of the diffuse peak. Its maximum should come when the crystal is set at the Bragg angle, but here measurements are complicated by the difficulty of completely eliminating the nuclear peak and the sharp magnetic peak below the Curie temperature.

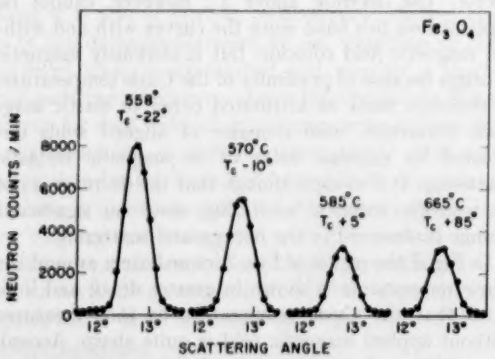

FIG. 7. Shape of the diffracted peak from Fe_3O_4 (111) planes for various temperatures. Nuclear plus magnetic peak just below T_c has same shape as purely nuclear peak above T_c.

Related effects in polycrystalline iron have very recently been reported by several observers. Squires,[9] measuring transmission of long-wavelength neutrons,

[9] G. L. Squires (private communication).

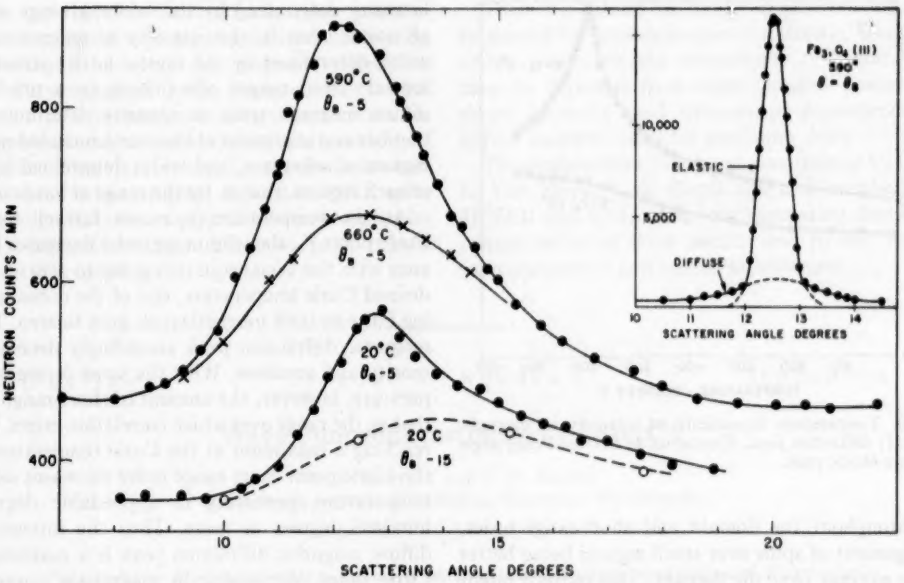

FIG. 8. Diffraction pattern with crystal fixed a few degrees from the Bragg angle. Diffuse peak appears at same angle where elastic peak would be.

found the total scattering cross section to have a maximum at T_c. Palevsky and Hughes[10] also using long-wavelength neutrons, measured total cross section *vs* λ at a number of temperatures and found the magnetic inelastic component to be maximum at T_c. Van Hove[11] has recently interpreted these latter results in terms of a time- and temperature-dependent correlation between spins of nearby atoms. For more energetic neutrons of 0.9-angstrom wavelength, Shull and Wilkinson[12] found around the direct beam a broader beam, a few degrees wide, deriving from magnetic small-angle scattering. Increased intensity near T_c and variations of angular spread could be interpreted in terms of the change in size of coherent scattering regions. A more extensive theoretical consideration by Van Hove[13] is in good qualitative agreement with these observations and those of the present paper.

It can be seen in Fig. 9 that the expected energy change in the neutrons would be small. This energy difference is proportional to $(k)^2-(k')^2$. Since diffuse magnetic scattering is concentrated about the reciprocal lattice point, which is displaced from the sphere of reflection by a distance small compared to k, $\mathbf{k}$ and $\mathbf{k}'$ are of about the same length. Therefore no direct determination of the energy change in scattered neutrons has been made to verify the inelastic nature of the diffuse scattering. Data on the diffuse peaks will be reported in greater detail, however, in a second paper.

IV. CONCLUSIONS

From the results of the previous section one can deduce the nature of the magnetic lattice and the sequence of changes in it with temperature. On the basis of a semiclassical picture: At low temperatures each domain is virtually perfect, all spins being parallel (see Fig. 11). As temperature increases spins are partly disoriented by thermal agitation. The arrangement is transient but there exists both a long-range and a short-range correlation, such that at any instant there is long-range

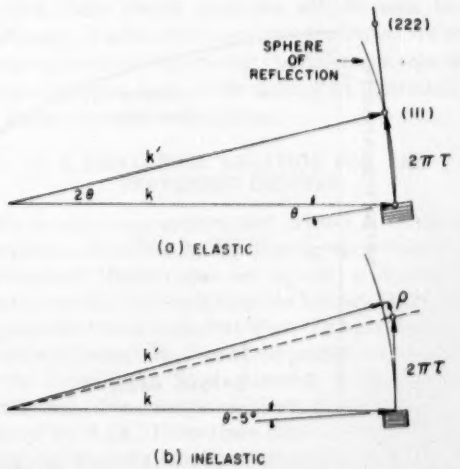

FIG. 9. Reciprocal space plots of propagation vectors $\mathbf{k}$, $\mathbf{k}'$ of incident and scattered neutrons with (a) $\theta=\theta_{Bragg}$; (b) $\theta=\theta_B-5°$. In case (b), ρ represents momentum exchanged with magnetic lattice.

[10] H. Palevsky and D. J. Hughes, Phys. Rev. **92**, 202 (1953).
[11] Leon Van Hove, Phys. Rev. **93**, 268 (1954).
[12] C. G. Shull and M. K. Wilkinson, Phys. Rev. **94**, 1439 (1954).
[13] Leon Van Hove (private communication).

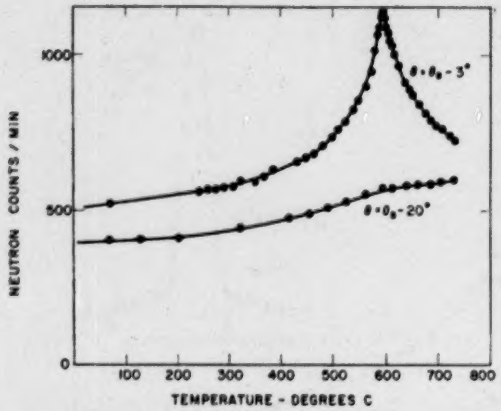

FIG. 10. Temperature dependence of intensity in magnetic diffuse (111) diffraction peak. Crystal set at 5° from Bragg angle to eliminate elastic peak.

order throughout the domain and short-range order, local alignment of spins over small regions being better than the average over the domain. This pattern might also be viewed as a uniform intensity of magnetization with a transient domain substructure of regions of fluctuation about the mean. The first (long-range) effect leads to a narrow magnetic diffraction peak of intensity determined by the vector average of spins of all atoms, that is, the intensity of magnetization and width determined by the crystal lattice structure. The second (short-range) effect leads to a much weaker diffuse magnetic peak of intensity determined by the number and alignment of the atoms included in the local regions of coherence, and width determined by the size of such regions, that is, by the range of local correlation.

As the temperature increases further toward the Curie point T_c, the long-range order decreases in accordance with the Weiss equation going to zero at a sharply defined Curie temperature, size of the domains remaining finite as their magnetization goes to zero. The sharp magnetic diffraction peak accordingly decreases in intensity and vanishes. With the same increases of temperature, however, the amount of short-range ordering, that is, the range over which correlation exists, increases, reaching a maximum at the Curie temperature. Above the Curie point short-range order decreases slowly with temperature, persisting in appreciable degree for a hundred degrees or more. Thus the intensity of the diffuse magnetic diffraction peak is a maximum at the Curie point, decreasing in magnitude approximately symmetrically above and below. The long-range ordering depends in direction on longer-range dipole interactions between atoms and is affected by external fields. The constant average moment per atom, which it

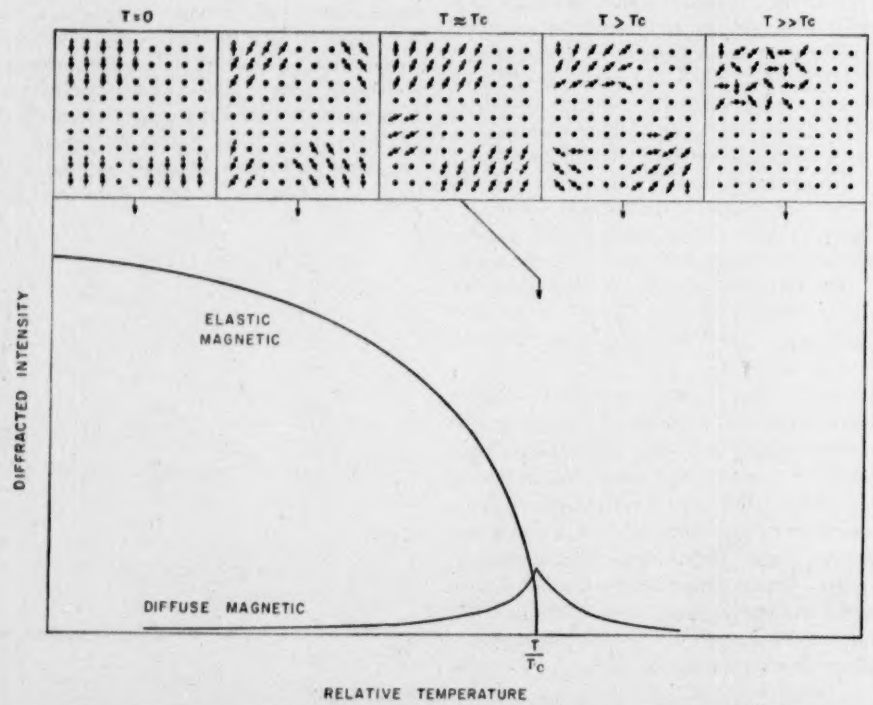

FIG. 11. Simple two-dimensional representation of instantaneous spin arrangements in a magnetic lattice at different temperatures. Intermediate stages between perfect order and disorder show short-range ordering varying approximately with diffuse curve while long-range order goes to zero with elastic diffraction curve.

represents, can therefore be rotated by these fields, in particular to a direction perpendicular to the scattering plane considered, so that the magnetic diffraction vanishes. Short-range ordering, being transient and dependent on shorter-range exchange interactions between nearby atoms, is substantially independent of applied fields. Thus just above T_c, the instantaneous pattern of spins is one of small regions in which spins are partly aligned, but not subject to re-orientation by a magnetic field. The diffuse diffraction peak is then independent of applied fields.

These conclusions are largely qualitative and likely to be general for various magnetic materials. More quantitative results on the interatomic magnetic coupling may be expected from more detailed studies of the shape, intensity, and temperature dependence of the diffuse magnetic peak for particular cases.

The authors wish to express gratitude to C. G. Shull, L. Van Hove, J. A. Goedkoop, and members of the JENER and BNL staffs for illuminating discussions in interpretation of these results, and to Mr. Aabakken for assistance in performing experiments.

PHYSICAL REVIEW VOLUME 95, NUMBER 5 SEPTEMBER 1, 1954

Wave Functions for Impurity Levels*†

G. F. KOSTER‡ AND J. C. SLATER
Massachusetts Institute of Technology, Cambridge, Massachusetts

(Received April 22, 1954)

The calculation of impurity levels in crystals is set up in terms of a linear combination of Wannier functions. The coefficients of this linear combination are shown to satisfy a set of difference equations. These difference equations are solved for two simple linear chain impurity problems. The difficulties encountered in solving the difference equations are explored on the basis of these examples and a general method of solving difference equations arising from impurity calculations is presented. This method seems to have advantages over previous methods of solving the impurity problem in crystals.

I. INTRODUCTION

THE customary approach to treating the effect of a perturbation on a perfect periodic lattice consists of expanding the perturbed wave function in terms of the wave functions of the unperturbed crystal. In almost all cases a one-electron approximation is used and instead of expanding the wave function in terms of the Bloch functions of the crystal, the complete set of Wannier functions[1] is used. These functions have the desirable property of being localized. This makes them most convenient for discussing a localized perturbation and the localized states arising from this perturbation. If the matrix of the total perturbed Hamiltonian is set up using the Wannier functions as a basis, it will be shown that coefficients of the Wannier functions in the expansion of the perturbed wave function satisfy a set of difference equations. One common way of treating these difference equations is to convert them to an approximate differential equation.[1,2] In this paper, we shall attempt to deal with the difference equations directly and shall present a general procedure for solving them in the hope of avoiding the assumptions and approximations involved in using the differential equation approximation. We shall first set up the difference equations involved in the impurity calculation and discuss some simplified cases. These simple examples illustrate with little calculation points which are typical of more realistic impurity calculations. The methods used to solve these simple problems will be seen to be inadequate to solve more complex problems. We shall then give a method for solving the difference equations which overcomes some of the difficulties illustrated by our simple impurity calculations.

II. A DIFFERENCE EQUATION FOR THE PERTURBED CRYSTAL

We describe our unperturbed crystal in terms of a one-electron Hamiltonian H_0. The eigenfunctions of this unperturbed Hamiltonian are $u_{n,\mathbf{k}}(\mathbf{r})$. n denotes the band to which this Bloch function belongs and $\mathbf{k}$ is the propagation vector such that when the wave function is translated through $\mathbf{R}_n$ (one of the primitive translations of the crystal) the Bloch function is multiplied by $\exp(i\mathbf{k}\cdot\mathbf{R}_n)$. The energy of these Bloch functions is denoted by $E_n(\mathbf{k})$. From these Bloch functions one can define the Wannier functions for a given band:

$$a_n(\mathbf{r}-\mathbf{R}_n)=N^{-\frac{1}{2}}\sum(\mathbf{k})u_{n,\mathbf{k}}(\mathbf{r})\exp(-i\mathbf{k}\cdot\mathbf{R}_n). \quad (1)$$

(N is the number of primitive translations in the

* Supported in part by the U. S. Office of Naval Research, in part by the Army, Navy, and Air Force.

† G. F. Koster and J. C. Slater, Letter to the Editor under same title in Phys. Rev. **94**, 1392 (1954). M. Lax, this issue [Phys. Rev. **94**, 1391 (1954)].

‡ Staff member, Lincoln Laboratory, Massachusetts Institute of Technology, Cambridge, Massachusetts.

[1] G. H. Wannier, Phys. Rev. **52**, 191 (1937).

[2] J. C. Slater, Phys. Rev. **76**, 1592 (1949), and various other papers. See however, for instance, P. Feuer, Phys. Rev. **88**, 92 (1952), in which the difference equations are treated directly.

macrocrystal over which periodic boundary conditions are defined.) It has been shown that the Wannier functions associated with a given band satisfy a set of simultaneous differential equations,[3]

$$H_0 a_n(\mathbf{r}-\mathbf{R}_j)=\sum(\mathbf{R}_i)\mathcal{E}_n(\mathbf{R}_i-\mathbf{R}_j)a_n(\mathbf{r}-\mathbf{R}_i), \quad (2)$$

where the $\mathcal{E}_n(\mathbf{R}_l)$ are the coefficients of the energy of the Bloch waves in its Fourier decomposition, and

$$E_n(\mathbf{k})=\sum(\mathbf{R}_l)\mathcal{E}_n(\mathbf{R}_l)\exp(-i\mathbf{k}\cdot\mathbf{R}_l). \quad (3)$$

These Fourier components of energy are also given by

$$\mathcal{E}_n(\mathbf{R}_l)=\int a_n^*(\mathbf{r})H_0 a_n(\mathbf{r}-\mathbf{R}_l)d\tau. \quad (4)$$

This can most easily be seen by multiplying Eq. (2) by $a_n^*(\mathbf{r})$ and integrating over all space using the orthogonality properties of the Wannier functions,

$$\int a_n^*(\mathbf{r}-\mathbf{R}_j)a_m(\mathbf{r}-\mathbf{R}_l)d\tau=\delta_{nm}\delta_{jl}. \quad (5)$$

We now have defined sufficient notation to describe our impurity problem in terms of Wannier functions. We wish to find the eigenfunctions associated with the Hamiltonian H_0+H_1. H_1 is the perturbation to our unperturbed Hamiltonian H_0. The perturbed wave function is described in terms of the complete set of Wannier functions

$$\psi(\mathbf{r})=\sum(n)\sum(\mathbf{R}_j)U_n(\mathbf{R}_j)a_n(\mathbf{r}-\mathbf{R}_j). \quad (6)$$

The unknown coefficients $U_n(\mathbf{R}_j)$ and the energy of the perturbed state are determined by the condition that

$$(H_0+H_1)\psi=E\psi. \quad (7)$$

Multiplying both sides of this equation by $a_m^*(\mathbf{r}-\mathbf{R}_i)$ and using the properties of the Wannier function given above, we are led to the simultaneous equations:

$$\sum(m,\mathbf{R}_j)[\mathcal{E}_n(\mathbf{R}_i-\mathbf{R}_j)\delta_{nm}+V_{nm}(\mathbf{R}_i,\mathbf{R}_j)]U_m(\mathbf{R}_j) =EU_n(\mathbf{R}_i). \quad (8)$$

Here

$$V_{nm}(\mathbf{R}_i,\mathbf{R}_j)=\int a_n^*(\mathbf{r}-\mathbf{R}_i)H_1 a_m(\mathbf{r}-\mathbf{R}_j)d\tau. \quad (9)$$

The solution of these difference equations gives us the solution to our perturbed periodic potential problem. We notice that if we let our perturbation go to zero we are left with the equation

$$\sum(\mathbf{R}_j)[\mathcal{E}_n(\mathbf{R}_i-\mathbf{R}_j)]U_n(\mathbf{R}_j)=EU_n(\mathbf{R}_i),$$

which can be solved by letting $U_n(\mathbf{R}_j)=\exp(i\mathbf{k}\cdot\mathbf{R}_j)$. This gives as the energy

$$E_n(\mathbf{k})=\sum(\mathbf{R}_s)\exp(-i\mathbf{k}\cdot\mathbf{R}_s)\mathcal{E}_n(\mathbf{R}_s), \quad (10)$$

which is correct.

[3] G. F. Koster, Phys. Rev. 89, 67 (1953).

The differential equation approach to this set of difference equations arises from considering the coefficients $U_n(\mathbf{R}_i)$ as a continuous function of some variable $\mathbf{r}$. It is then noted that if $\mathbf{k}$ is replaced by $\mathbf{p}/\hbar$ where $\mathbf{p}$ is a pseudo-momentum, and if $\mathbf{p}$ is then replaced by $-i\hbar\nabla$ (where ∇ acts on $\mathbf{r}$) in the usual quantum-mechanical manner, that

$$E_n(\mathbf{p}/\hbar)f(\mathbf{r})=\sum(\mathbf{R}_m)\mathcal{E}_n(\mathbf{R}_m)f(\mathbf{r}-\mathbf{R}_m),$$

where f is any function. If we in addition restrict ourselves to one band and make the additional assumption that $V(\mathbf{R}_i,\mathbf{R}_j)=\delta_{ij}V(\mathbf{r})$ where $\mathbf{R}_i$ is replaced by the continuous variable $\mathbf{r}$, we can rewrite Eq. (8) to be

$$E(-i\nabla)U(\mathbf{r})+V(\mathbf{r})U(\mathbf{r})=EU(\mathbf{r}), \quad (11)$$

which is like an ordinary Schrödinger equation. We notice that if $V(\mathbf{r})$ vanishes, $U(\mathbf{r})=\exp(i\mathbf{k}\cdot\mathbf{r})$ is a solution to this equation giving the energy (10). In the event that $V(\mathbf{r})$ does not vanish, $E(\mathbf{k})$ is usually expanded about its minimum up to terms of the second order in k which converts Eq. (11) into a second-order differential equation. If we call $\mathbf{k}_0$ the point where the minimum of $E(\mathbf{k})$ lies, it is convenient to rewrite $U(\mathbf{r})$ as $W(\mathbf{r})\exp(i\mathbf{k}_0\cdot\mathbf{r})$. The exponential function takes out the rapidly varying part of $U(\mathbf{r})$ leaving $W(\mathbf{r})$ to be smoothly varying. If this is done and a rotation of the axes in ordinary space is performed to remove the cross second derivatives in the expansion of $E(\mathbf{k})$, Eq. (11) can be written, up to terms of the second order, as

$$-\frac{\hbar^2}{8\pi^2}\left(\frac{1}{m_x}\frac{\partial^2 W}{\partial x^2}+\frac{1}{m_y}\frac{\partial^2 W}{\partial y^2}+\frac{1}{m_z}\frac{\partial^2 W}{\partial z^2}\right) +[E_0+V(\mathbf{r})]W=EW, \quad (12)$$

where

$$m_x=\hbar^2\Big/\frac{\partial^2 E}{\partial k_x^2}, \text{ etc., } E_0=E(\mathbf{k}_0).$$

This is the form which the impurity problem takes in most treatments of impurities in semiconductors. Additional assumptions are also made in this case, namely: that $m_x=m_y=m_z$ and that $V(\mathbf{r})$ is a Coulomb potentiar in a dielectric medium. In the case of germanium, for instance, with a dielectric constant in the neighborhood of 16 and effective masses of the order of half the electron mass, this leads to wave functions extended over a good many angstroms, with energies which are a very small fraction of a volt.

These widely extended wave functions, which can be formed by solution of (12), allow us to examine the justification of the assumption that third and higher derivatives can be neglected in the expansion of $E(\mathbf{k})$ in Eq. (11). The energy, as we know, can be expanded in a Fourier series and ordinarily the first few terms of this series are the important ones. Thus we see that the successive derivatives of $E(\mathbf{k})$ with respect to k will be in the ratio of the powers of $\mathbf{R}_j$, the lattice spacing. If the function W is falling off like an exponential $\exp(-ar)$, as

we should have for a hydrogen-like case, the successive derivatives will be in the ratio of powers of a, inversely proportional to the linear dimensions of the wave function. In other words, we may expect the terms in (11) in successively higher derivatives of W to fall off in the ratio of the lattice spacing to the linear dimensions of the wave function. If the wave function extends over many lattice spacings, as in the case of germanium, we may expect successive terms to get rapidly smaller, so that the reduction of the equation to the Schrödinger form is legitimate. On the other hand, if it does not extend out very far, as is the more usual case in a material of smaller dielectric constant, it is not legitimate to neglect higher derivatives. In such a case, we can try to retain additional terms in (11), but it is much better and more straightforward to return to the difference equation and try to solve this directly. The writers suspect that the number of actual cases where the approach by means of the differential equation is justified is very limited, and that in most cases we are on much firmer ground to use the difference equation. The differential equation may, however, be useful in pointing out the general form of the solution to be expected.

In order to familiarize ourselves with the methods of treating the difference equations directly, we shall in the next section solve the difference equations in a one-dimensional case. Even though these one-dimensional crystals are not met with in nature, the mathematics involved gives us insight into the more complex three-dimensional cases.

III. A ONE-DIMENSIONAL IMPURITY CALCULATION

In this section, we treat the effects of a perturbation on a one-dimensional crystal of equally spaced atoms. We further restrict ourselves to a single band describable in terms of a Wannier function which has reflection symmetry with respect to a plane passing through the atom about which the Wannier function is located. In this case, the difference equation (8) can be written in the form

$$\sum(q)[\mathcal{E}(p-q)+V(p,q)]U(q)=EU(q). \tag{13}$$

The index p denotes the pth atom in the chain. The simplest case of an impurity in a linear chain is the case where the Wannier functions only have nearest-neighbor interactions and the impurity only extends over one lattice site. The first of these restrictions means that $\mathcal{E}(p)=0$ for $p>1$. The second of these assumptions means that $V(p,q)$ is zero unless both p and q are equal to zero. In this case, our difference equations (13) can be rewritten

$$\begin{aligned}&\mathcal{E}(0)U(p)+\mathcal{E}(1)[U(p+1)+U(p-1)]\\&\qquad=EU(p);\quad p\gtrless 1,\\&\mathcal{E}(0)U(0)+\mathcal{E}(1)[U(1)+U(-1)]\\&\qquad=[E-V(0)]U(0);\quad p=0.\end{aligned} \tag{14}$$

The usual way to solve the general equations in (14) (the first set) is to make the assumption that $U(q)=b^{\pm q}$. If we substitute this into the first of Eqs. (14) we see that this is indeed a solution provided that

$$\mathcal{E}(0)+\mathcal{E}(1)[b+1/b]=E. \tag{15}$$

If we let $b=\exp(ikR)$, where R is the lattice spacing the condition (15) becomes

$$\mathcal{E}(0)+2\mathcal{E}(1)\cos kR=E. \tag{16}$$

We note that in this relation k may be either real or complex. In fact, we can at once say that if E is such that $|[E-\mathcal{E}(0)]/2\mathcal{E}(1)|>1$ then k must be pure imaginary. If the inequality is in the other direction, then k is pure real. We recognize the latter case as the states lying in the band. These are of course the states for which the coefficients of the Wannier function are all of unit absolute value, or the propagating states. The states where k is pure imaginary are those for which the coefficients of the Wannier function increase exponentially for either large positive or negative values of p.

We are now left with the necessity of solving the second of Eqs. (14). Let us set up periodic boundary conditions such that $U(p+2N)=U(p)$, and start by discussing the case where our energy falls in the band (k pure real). We notice at once because of the symmetry of the problem that our solutions must be either symmetric or antisymmetric about the central atom. In the first case $U(p)=U(-p)$; in the second $U(p)=-U(-p)$. For the antisymmetric state, the wave function has a node at the origin and therefore our perturbed problem just reduces to the unperturbed problem. This can most easily be seen by putting the condition of antisymmetry into the difference equations and noticing that the effect of the perturbation disappears completely from the equation. For this case we take as the solution $U(p)=\sin(kRp)$, which satisfies the boundary conditions provided that $kRN=n\pi$. [$\mathrm{Sin}(kRp)$ is of course a linear combination of our two solutions b^{+p} and b^{-p}.] We see that there are $N-1$ antisymmetric solutions.

The most convenient form in which to take the solution of the symmetric states is in the form $\cos[kR(p-N)]$. This form of the solution automatically satisfies the boundary condition at $p=N$. The energy is given at once by Eq. (16). Substituting this form of the solution in Eq. (14) for $p=0$ we arrive at the condition

$$-\tan(kRN)\sin(kR)=V(0)/2\mathcal{E}(1). \tag{17}$$

In arriving at this condition, we have made use of the fact that E is given by Eq. (16). There are N solutions of this symmetric type. We can solve Eq. (17) graphically by plotting the left side as a function of k, and finding the k's for which this equals $V(0)/2\mathcal{E}(1)$. A plot of this function for $N=6$ as a function of kR, is given in Fig. 1. We see that the axis of abscissas cuts this curve in seven places. For the other horizontal lines, where there are only six intersections the missing state is a state for an imaginary value of k. This state gives a total of $N+1$ symmetric states and $N-1$ antisymmetric states giving

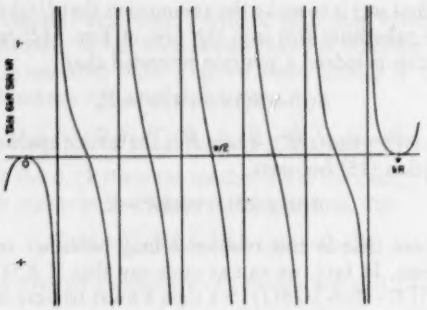

FIG. 1. Function $-\tan(kRN)\sin(kR)$, for $N=6$.

in total the required $2N$ states. We shall now go on and study in detail the state corresponding to the imaginary value of k.

If k is imaginary, then let us denote ik by γ. This is the case where E is such that it lies outside of the band. In this case, our solution to the difference equation is given by $\exp(\pm\gamma pR)$. The coefficients of our Wannier functions are thus seen to increase exponentially in one direction. We could proceed as before setting up a bound state which satisfies our periodic boundary conditions, but for large N it can be easily shown that proceeding in this manner gives the same result as demanding that our wave function go to zero for p infinite. If this is the case then the solution to the first of Eqs. (14) is taken as $U(p)=U(-p)=\exp(-\gamma Rp)$. We have of course the condition from the first of Eqs. (14) that

$$E=\mathcal{E}(0)+2\mathcal{E}(1)\cosh(\gamma R). \tag{18}$$

In order to satisfy the second of Eqs. (14), we must satisfy $\sinh(\gamma R)=V(0)/2\mathcal{E}(1)$. This determines a value of γ corresponding to a given value of $V(0)$. With this value of γ, the energy is given by Eq. (18). We can, of course, substitute for the cosh in terms of the sinh and get the relation that

$$E=\mathcal{E}(0)+2\mathcal{E}(1)\{1+[V(0)/2\mathcal{E}(1)]^2\}^{\frac{1}{2}}. \tag{19}$$

This shows that for small values of the perturbing potential the bound state leaves the band quadratically in $V(0)$.

In all the preceding discussion, we have tacitly assumed that the sign of the perturbation is the same as the sign of the nearest-neighbor interaction. This means that the bound state pushes out of the band at the point where $E=\mathcal{E}(0)+2\mathcal{E}(1)$. If the signs of the perturbing potential and the nearest-neighbor interaction are different then the bound state will push out of the band at the point where $E=\mathcal{E}(0)-2\mathcal{E}(1)$. In this case, it can easily be seen that the solution to the difference equation is given by $(-1)^p\exp(-\gamma Rp)$. The energy of the bound state is then given by Eq. (19) where the plus sign outside of the square root is replaced by a minus sign.

We have now accounted for our $2N$ states. We have one bound state, $N-1$ antisymmetric states in the band, and N symmetric states in the band. In Fig. 2 we plot the energies of these states for the case $N=6$ as a function of the perturbing potential. We have also included for comparison the energies of the antisymmetric states which are not affected by the perturbation. The interesting thing to notice is the way in which each of the energy levels within the band is displaced by the perturbation, only far enough to approach the mid-point between neighboring antisymmetric states, with the exception of the limiting state which becomes detached from the band, and forms the separate impurity state which we have discussed earlier. The case which we have shown is that of positive $\mathcal{E}(1)$, in which case it is the top of the band where the separate level appears for positive $V(0)$. We have shown the case for a small N value; but if N is very large, it is clear that the displacements of all levels but the one which becomes detached from the band will be negligible.

We have seen that a single energy level pushes away from the energy band under the action of the perturbation $V(0)$, and that its wave function falls off exponentially as we go away from the perturbing atom. As $V(0)$ becomes very large compared to the band width, the exponential fall off becomes very rapid, though it is small for small $V(0)$. At this point we can give an elementary check of the procedure of the preceding section, in which the difference equation was replaced by a differential equation. We start with the energy expression (16) and replace k in it by the operator $-id/dx$. We then use this operator to set up a differential equation. In this case, this leads to

$$\mathcal{E}(0)W(x)+2\mathcal{E}(1)\left[W+\frac{1}{2!}R^2\frac{d^2W}{dx^2}+\frac{1}{4!}R^4\frac{d^4W}{dx^4}+\cdots\right]+V(x)W(x)=EW(x), \tag{20}$$

where $V(x)$ is the perturbative potential, which is zero except when x is zero, so that except when x is zero we can omit the term in V. The simplified Schrödinger equation corresponding to (12) is obtained by omitting

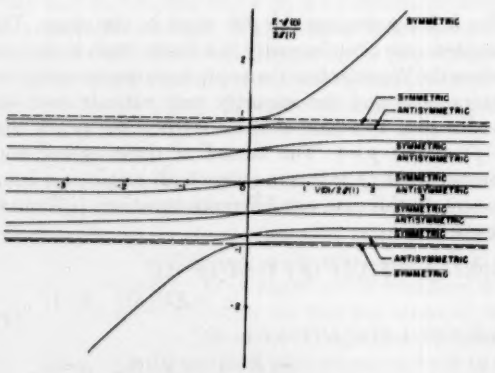

FIG. 2. Energy of perturbed energy levels, as a function of perturbative energy.

everything beyond the second derivative in (20). Now we can, in this simple case, solve either the approximate or the exact problem by assuming $W=\exp(-\gamma x)$, the only difference being in the relation which we find between γ and E. If we substitute this expression in (20), we find a solution of the exact equation if

$$E=\mathcal{E}(0)+2\mathcal{E}(1)[1+(\gamma R)^2/2!+(\gamma R)^4/4!+\cdots] =\mathcal{E}(0)+2\mathcal{E}(1)\cosh\gamma R,$$

in agreement with (18). If on the contrary we neglect fourth and higher derivatives, we have $E=\mathcal{E}(0)+2\mathcal{E}(1)[1+(\gamma R)^2/2!]$ which is a satisfactory approximation only if $(\gamma R)^2$ is small in comparison to unity. This is the case in which the wave function $\exp(-\gamma x)$ falls off by only a small amount in the distance R, which agrees with the condition for the applicability of the second-order differential equation in the last section. If the perturbation is greater, so that the wave function falls off more rapidly, and the extra level is further from the band, the second-order differential equation is inapplicable, and we must use the difference equation, or the differential equation of infinite order, which is of course rigorously equivalent to it.

Before leaving this simple example it is informing to look at the states within the band in a somewhat different manner. For the symmetric states in the band, we can take a solution of the form $U(p)=U(-p)=\cos(kRp-\alpha)$. (We are no longer using periodic boundary conditions here.) If we do this, once again the energy is given by (16) and Eq. (14) gives a condition on α,

$$\tan\alpha=-V(0)/[2\mathcal{E}(1)\sin kR]. \tag{21}$$

This is instructive because it shows us that in the band there is a perturbed state corresponding to every energy in the band. The perturbation only has the effect of determining the phase factor α. We could of course do scattering theory in the band which would be closely related to this phase angle α. We can also notice that as $V(0)$ becomes infinite the phase angle approaches $\pi/2$. In this case, the symmetric state in the band approaches zero at the perturbed site. This means that whereas the perturbed states in the band avoid the impurity site the bound state which pulls out of the band becomes concentrated about the impurity site. We can see that this must be so in a very fundamental manner.

Let us consider the case of periodic boundary conditions. We are building up wave functions as linear combinations of the $2N$ Wannier functions on the atoms of the fundamental period. These Wannier functions are an orthonormal set of functions, as are the final linear combinations, so that the $U(p)$'s, which are the transformation coefficients from one set of functions to the other, form a unitary matrix. This is a matrix with $2N$ rows and columns: we have $2N$ energy levels, and $2N$ p's. If we now form the sum of the quantities $U^*(p)U(p)$, for a given p value, summed over the $2N$ energy levels, we know on account of the unitary property that this sum must be unity. Let us carry out this sum for $p=0$ corresponding to the impurity atom. For the separated state, with large perturbative potential $V(0)$, we know that the wave function will fall off as $\exp(-\gamma Rp)$ where γ is very large, so that the coefficients $U(p)$ will be very small for $p\neq 0$. Since the wave function must be normalized, we must have the sum of $U^*(p)U(p)$ over p, for a given energy level, equal to unity, which means that the contributions to the sum for $p\neq 0$ are very small, the term for $p=0$ must be very nearly equal to unity. We now return to our statement that the sum of $U^*(p)U(p)$ over all levels, for a fixed p must equal unity. For $p=0$, we have just seen that the contributions from all other levels must be very small, showing that with a large perturbation, the wave functions of the states in the band avoid the perturbing atom almost completely. This general type of proof is important, for it can be used in more complicated cases, where we cannot get explicit solutions.

We can introduce further complications into this one-dimensional impurity problem. It is possible to introduce next nearest neighbor interactions into the problem and still find solutions. We shall do this and introduce a perturbation which, once again, only extends over one lattice site. For this case the difference equations become

$$[\mathcal{E}(0)-E]U(p)+\mathcal{E}(1)[U(p+1)+U(p-1)] +\mathcal{E}(2)[U(p+2)+U(p-2)]=0, \tag{22}$$

for p greater than zero and

$$[\mathcal{E}(0)+V(0)-E]U(0)+\mathcal{E}(1)[U(1)+U(-1)] +\mathcal{E}(2)[U(2)+U(-2)]=0, \tag{23}$$

for p equals zero. By substitution of a propagating solution we find that the energy band is given by

$$E(k)=\mathcal{E}(0)+2\mathcal{E}(1)\cos(kR)+2\mathcal{E}(2)\cos(2kR). \tag{24}$$

It is informing to choose the parameters in this energy expression so that the minimum of the energy falls away from $k=0$. In order to do this, it is necessary that $|\mathcal{E}(2)|>|\mathcal{E}(1)|/4$. Figure 3 shows a plot of the energy as a function of k in this case. It should be emphasized that this is an imaginary problem since it is well known that the minimum of the energy for a one-dimensional crystal cannot fall away from either the center or the edges of the first Brillouin zone.[4] However, it is possible for the minimum of the band to come at an arbitrary point in the Brillouin zone for three-dimensional crystals. Because of the importance of this case in the theory of semiconductors, we thought it profitable to follow through this imaginary one-dimensional case in order to study the mathematics involved.

We follow the same method that we used in the nearest-neighbor example to solve this difference equation. We make the substitution $U(p)=b^p$. When this is

[4] W. Shockley, *Electrons and Holes in Semiconductors* (D. Van Nostrand Company, Inc., New York, 1950), p. 406.

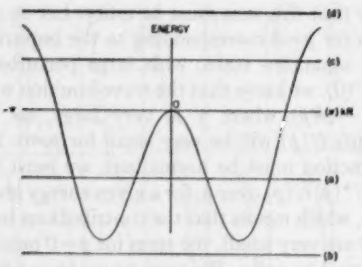

FIG. 3. Energy *vs* kR, for second-nearest neighbor interaction.

substituted into Eq. (22) we obtain an equation for b

$$[\mathcal{E}(0)-E]+\mathcal{E}(1)[b+b^{-1}]+\mathcal{E}(2)[b^2+b^{-2}]=0. \quad (25)$$

This is an equation of the fourth order in b. From its form we notice that if b is a solution to this equation so is b^{-1}. Since all complex roots of this equation must occur with their complex conjugates, b^* must also be a solution. This means of course that if b is taken in the form $\exp(ikR)$ then if k is complex all four roots are related by being all possible combinations of the complex conjugate and the inverse. By making the substitution $c=b+b^{-1}$, Eq. (25) can be reduced to an equation of the second order:

$$\mathcal{E}(2)(c^2-2)+\mathcal{E}(1)c+\mathcal{E}(0)-E=0. \quad (26)$$

By studying the solution of this equation as a function of the energy E, it is possible to determine whether k in $b=\exp(ikR)$ is real, complex, or pure imaginary. For the energy (d) in Fig. 3, k has two values both of which are pure imaginary. For the energy (c) k has two values, one pure real and the other pure imaginary. The energy (b) gives k two values both real. Finally for the energy (a) there is a complex value of the propagation constant. We will not discuss all of these cases in detail, but shall focus our attention on the case (a), since this is the case that corresponds to a bound state coming out of the bottom of the energy band.

Our solution to the difference equations will be some linear combination of the four solutions to Eq. (25). The constants in this linear combination are to be determined by the special Eq. (23). [The solution of (25) insures the solution of (22).] We can as before make use of the symmetry or antisymmetry of the solution to the difference equation to simplify our work. This will once again tell us that for the antisymmetric solution the effect of the perturbation vanishes. This means that the antisymmetric states in the band are unperturbed. For the bound state [case (a)], we need only study the symmetric solution. If we make the assumption of symmetry in Eqs. (22) and (23), we find that these two special equations are to be satisfied

$$[\mathcal{E}(0)+V(0)-E]U(0)+2\mathcal{E}(1)U(1)+2\mathcal{E}(2)U(2)=0, \quad (27)$$

$$[\mathcal{E}(0)-E]U(1)+\mathcal{E}(1)[U(2)+U(0)]+\mathcal{E}(2)[U(3)+U(1)]=0. \quad (28)$$

For the case (a), we therefore take the solution of our difference equation in the form

$$U(-p)=U(p)=e^{-\gamma p}(Ae^{i\kappa p}+A^*e^{-i\kappa p}), \quad (29)$$

where A and A^* are the unknown constants to be determined and $k=\kappa+i\gamma$. The energy is of course given by (25) and takes the form

$$E=2\mathcal{E}(1)\cos\kappa\cosh\gamma+2\mathcal{E}(2)\cos 2\kappa\cosh 2\gamma. \quad (30)$$

We are in the position where we have just enough constants to solve the pair of Eqs. (27) and (28). (The boundary conditions which are assumed here are that the wave function go to zero at infinity.) The mathematics of finding the energy as a function of the perturbation $V(0)$ is rather tedious and the results will be described instead of worked out in detail. For small perturbations, the bound state pulls out of the bottom of the band quadratically with the perturbation. As the perturbation increases the energy finally becomes linear with the perturbation. This is of course similar to the nearest-neighbor case worked out above. For small values of the perturbation the imaginary part of k is nearly zero and the real part is very nearly equal to k_0, the value of the propagation constant at the minimum of the band. As the strength of the perturbation increases the magnitude of the imaginary part increases, which means that the solution to the difference equation falls off more rapidly with distance from the central atom. We have the case where the wave function of the bound state becomes more localized. This means, in turn that the remaining states in the band avoid the impurity.

For a perturbation of the opposite sign to that which pulls a state out of the bottom of the band, a bound state will appear at the top of the band. This is the case (d). In this case, there are solutions to the difference equations with propagation constants which are pure imaginary. The solution of the difference equation which satisfies the special equation at the origin will consist of a linear combination of two terms both of which fall off exponentially with the distance from the origin. The two coefficients in this linear combination are determined by the two Eqs. (27) and (28). This state pulls out of the top of the band quadratically with the perturbation. The remaining two cases (b) and (c) are unbound impurity states in the band. The case (b) is the case of two real propagation constants and could be treated by the method of phase shifts introduced in the case of nearest-neighbor interactions. In this case there would be two phase shifts, one for each propagation constant. The case (c) is the case where there are two propagation constants; one pure real and the other pure imaginary. This means that the solution to our difference equation would consist of two terms one of which is a propagating term extending out to infinity coming from the ordinary band state. The other term is an exponentially damped term which dies out at infinity. Once again the special Eqs. (27) and (28) can be used to

determine the unknown coefficients in this linear combination.

It is important to note, for this case, that even though we are in the band it is not legitimate to throw away the exponentially damped part of the solution to the difference equation and only consider the ordinary energy band state. The additional root to the Eq. (25) must be taken into account in addition to the propagating solution which makes up the ordinary Bloch state. This is an additional feature of the case of next-nearest neighbor interactions which was missing in the simple case of nearest-neighbor interactions. In the case of nearest-neighbor interactions, the only solutions to the analogous equation to (25) were the ordinary energy band solutions. Whereas this additional complication can be taken into account in the case of next-nearest neighbor interactions, we may imagine cases where it is necessary to take into account interactions with more distant neighbors. If we must do this the equation we get analogous to (25) will be of order twice the order of neighbors taken into account. It can readily be seen that the solution of this equation will become very difficult because of its high order. This factor is what makes the method we have been using to solve our difference equations in these simple cases inapplicable when it comes to more complex cases. In the next section, we shall try to formulate a method which does not have this drawback.

IV. A GENERAL METHOD OF TREATING DIFFERENCE EQUATIONS

In treating the impurity problem for more dimensions we might try to proceed as we did in the last paragraph. If we were to do this we would again have general and special equations arising from Eq. (8). The general equations would consist of the unperturbed equations which would be valid outside of the region where the perturbation acts. We would try to find solutions to these general equations of the form $\exp(i\mathbf{k}\cdot\mathbf{R}_n)$. Upon substituting this into the general equation we would get Eq. (9). Now however E is not restricted to be in the band nor is $\mathbf{k}$ restricted to be real. We must find all possible solutions to this equation solving for $\mathbf{k}$ as a function of E. This includes the exponentially damped solutions we ordinarily throw away while searching for the energy bands. After having found these general solutions to our unperturbed difference equations we must form linear combinations of solutions of a given energy so as to satisfy the special difference equations which involve the perturbation. We put in enough adjustable linear coefficients to be able to satisfy these special equations. This would lead to a set of simultaneous equations in the unknown coefficients. The number of equations would be of the order of the number of lattice sites over which the perturbing potential acts. As was mentioned in the last section we can see at once the great drawback of this method. It is in the finding of all the propagation constants which give rise to the energy E when substituted in Eq. (9) which forms the stumbling block. We saw that even in the case of higher-order interactions in the linear chain this could be a difficult task. In the case of a three-dimensional crystal where our propagation constant will have three components it seems hopeless.

If we reject this approach, we might think that we could treat our difference equations (8) simply as a set of linear equations, the determinant of the unknown coefficients $U(\mathbf{R}_n)$ being set equal to zero in order to determine the eigenvalues. The order of this secular equation in this case would be of the order of the number of lattice sites we choose to include in our crystal. This would in general far exceed the region over which the perturbation acts, since we know that the solution to the difference equations extends beyond the region of the perturbation. This approach might be quite hopeful in the case where we were looking for a highly localized bound state which falls off near the perturbed region. In the case where we have no reason to believe that our perturbed wave function is so localized, this approach would give rise to a prohibitively large secular equation. What would be desirable would be to deal only with the states which are the propagating energy-band states and still only be forced to solve a set of simultaneous equations no larger than the number of sites over which the impurity acts. We shall now show that this can be done by expanding our perturbed wave function in terms of the known Bloch functions.

We try to solve our perturbed problem by a linear combination of Bloch functions from various bands,

$$\psi(\mathbf{r})=\sum(n,\mathbf{k}')f_n(\mathbf{k}')u_{n,\mathbf{k}'}(\mathbf{r}), \tag{31}$$

where the Bloch functions are the eigenfunctions corresponding to our unperturbed Hamiltonian,

$$H_0u_{n,\mathbf{k}}(\mathbf{r})=E_n(\mathbf{k})u_{n,\mathbf{k}}(\mathbf{r}). \tag{32}$$

We wish to solve the problem

$$(H_0+H_1)\psi=E\psi. \tag{33}$$

Substituting (31) into (33), multiplying by $u_{m,\mathbf{k}}(\mathbf{r})$, integrating, and using the properties of the Bloch functions we arrive at the result that

$$f_m(\mathbf{k})[E_m(\mathbf{k})-E]+\sum(n,\mathbf{k}')V_{n,m}(\mathbf{k},\mathbf{k}')f_n(\mathbf{k}')=0, \tag{34}$$

where

$$V_{n,m}(\mathbf{k},\mathbf{k}')=\int u_{n,\mathbf{k}}^*(\mathbf{r})H_1u_{m,\mathbf{k}'}(\mathbf{r})d\tau. \tag{35}$$

It can easily be seen using the definition of $V_{n,m}(\mathbf{R}_i,\mathbf{R}_j)$ that (35) can be rewritten as

$$V_{n,m}(\mathbf{k},\mathbf{k}')=(1/N)\sum(\mathbf{R}_i,\mathbf{R}_j)V_{n,m}(\mathbf{R}_i,\mathbf{R}_j)e^{-i\mathbf{k}\cdot\mathbf{R}_i}e^{i\mathbf{k}'\cdot\mathbf{R}_j}. \tag{36}$$

Substituting (36) into (34) we arrive at the equation

$$f_m(\mathbf{k})+\frac{1}{N}\sum(n,\mathbf{R}_i,\mathbf{R}_j)\frac{e^{-i\mathbf{k}\cdot\mathbf{R}_i}V_{m,n}(\mathbf{R}_i,\mathbf{R}_j)}{E_m(\mathbf{k})-E}\times\sum(\mathbf{k}')e^{i\mathbf{k}'\cdot\mathbf{R}_j}f_n(\mathbf{k}')=0, \quad (37)$$

where we have divided by $E_m(\mathbf{k})-E$. We now multiply both sides of this equation by $\exp(i\mathbf{k}\cdot\mathbf{R}_p)$ and sum over the values of $\mathbf{k}$ in the first Brillouin zone,

$$U_m(\mathbf{R}_p)+\frac{1}{N}\sum(n,\mathbf{R}_i,\mathbf{R}_j,\mathbf{k})\times\frac{e^{i\mathbf{k}\cdot(\mathbf{R}_p-\mathbf{R}_i)}}{E_m(\mathbf{k})-E}V_{mn}(\mathbf{R}_i,\mathbf{R}_j)U_n(\mathbf{R}_j)=0. \quad (38)$$

We have, in this equation, made use of the fact that the transformation between the coefficients of the Wannier function and those of the Bloch functions are given by

$$U_m(\mathbf{R}_p)=N^{-\frac{1}{2}}\sum(\mathbf{k})e^{i\mathbf{k}\cdot\mathbf{R}_p}f_m(\mathbf{k}). \quad (39)$$

This constitutes a set of simultaneous equations between the coefficients of the Wannier functions. We notice that there are as many equations as the number of lattice sites in the crystal times the number of bands under consideration. In order to satisfy this set of simultaneous linear homogeneous equations, the determinant of the coefficients must vanish. There is a simplifying feature to this determinant. Let us put those U's for which the perturbation has nonvanishing matrix elements in the earliest part of the determinant. If this is done, the determinant has the form in Fig. 4 where the shaded region is a region of nonvanishing elements and the unshaded region is the region which has vanishing elements except for the indicated 1's. We can see at once that all that is necessary for the vanishing of the determinant is the vanishing of the upper left-hand corner which is enclosed by the heavy lines. This is a determinant of size equal to the number of lattice sites over which the perturbation extends multiplied by the number of bands between which it has matrix elements. This is the form in which we propose to do the impurity calculations. We see that all that is necessary is a knowledge of the energy as a function of k for the energy-band solutions. The size of the determinant to be solved is limited to the size of region over which the effect of the impurity is felt.

FIG. 4. Schematic diagram of secular equation used to solve the impurity problem.

We can now state in words what is involved if this formalism is used in an impurity calculation. We must first find the quantities

$$\sum(\mathbf{k})\frac{e^{i\mathbf{k}\cdot\mathbf{R}_l}}{E_m(\mathbf{k})-E} \quad (40)$$

as a function of the energy. This summation may be replaced by an integration over the first Brillouin zone if the allowed $\mathbf{k}$ values are dense. We must then solve the set of simultaneous equations (38) for those U's for which there are corresponding nonvanishing matrix components of the perturbation. This involves the vanishing of the determinant

$$\left|\delta_{m,n}\delta_{p,j}+\frac{1}{N}\sum(\mathbf{R}_i,\mathbf{k})\frac{e^{i\mathbf{k}\cdot(\mathbf{R}_p-\mathbf{R}_i)}}{E_m(\mathbf{k})-E}V_{m,n}(\mathbf{R}_i,\mathbf{R}_j)\right|=0. \quad (41)$$

If we are looking for a bound state, the values of E for which this determinant vanishes are the energies of the bound states. For an energy for which this determinant vanishes we solve the set of simultaneous equations for the U's for which there are nonvanishing matrix elements of the perturbation. Having found these values of the U's the remaining values, outside of the region of the impurity, are given in terms of those within the region by (38). It is clear from the formalism that this method is very similar to a Green's function method of solving differential equations. Here we have a Green's function solution to the difference equation, the quantity (40) acting as the Green's function. This can be arrived at by considering the Green's function solution to the differential equation, as is shown in Appendix (1).

It is instructive to solve as an example the case in which we consider only one band and limit the effect of the impurity to one site. $[V(\mathbf{R}_i,\mathbf{R}_j)=\delta_{i,0}\delta_{j,0}\times V(0)]$. Equation (38) becomes

$$U(\mathbf{R}_p)=\frac{1}{N}V(0)\left[\sum(\mathbf{k})\frac{e^{i\mathbf{k}\cdot\mathbf{R}_p}}{E-E(\mathbf{k})}\right]U(0). \quad (42)$$

The determinant (41) in this case has only one row and one column and gives directly the energy as a function of the perturbation,

$$(V(0)/N)\sum(\mathbf{k})\frac{1}{E-E(\mathbf{k})}=1. \quad (43)$$

To show the power of this method, we shall use it to discuss the one-dimensional chain with nearest-neighbor interaction. For the one-dimensional case, we know that

$E(k)=\mathcal{E}(0)+2\mathcal{E}(1)\cos kR$. We must then evaluate the sum $\sum(k)1/[E-E(k)]$ in (43). In the case we are dealing with the discrete state, so that E lies outside the unperturbed band, we can convert this sum into an integral without trouble. We find that kR goes by equal steps from $-\pi$ to π or from 0 to 2π, there being N intervals. That is, we can replace $\sum(k)$ by $N/2\pi\int_0^{2\pi}d(kR)$. Thus (43) reduces to

$$[V(0)/N][N/2\pi]\times\int_0^{2\pi}[E-\mathcal{E}(0)-2\mathcal{E}(1)\cos\alpha]^{-1}d\alpha=1. \quad (44)$$

This can be integrated by elementary means, and gives

$$V(0)/\{[E-\mathcal{E}(0)]^2-[2\mathcal{E}(1)]^2\}^{\frac{1}{2}}=1. \quad (45)$$

When we solve (45) for the energy E, the result is identical with (19) which we obtained by straightforward solution of the difference equations. The integral in (42) can also be evaluated simply and gives the proper exponential falling off of the solution.

This solution of the problem of the single lattice site impurity which is embodied in Eqs. (42) and (43) also gives us additional insight into the solution of the problem with a more general impurity. In the case of a more general impurity, Eq. (38) instructs us to sum up the effects of single lattice site impurities at the various lattice sites over which the perturbation extends in order to get the total effect of the impurity. This most clearly illustrates the Green's function nature of our solution.

In simple cases, we can use (42) to obtain results about the wave function in an analytic way. Thus, let us consider the problem of a three-dimensional lattice, in which the energy $E(\mathbf{k})$ can be expanded about a minimum or maximum energy which we take to come at $k=0$, in a power series starting with the terms $a(k_x^2+k_y^2+k_z^2)$, where $a=h^2/8\pi^2m$, m being the effective mass. Let us have a perturbation at the atom at the origin, such that the discrete level lies at an energy E, below the bottom of the band (and hence negative if the bottom of the band is at zero energy). Then $E-E(k)$ can be approximated by $E-a(k_x^2+k_y^2+k_z^2)$, which is numerically small near $k=0$, but increases rapidly as we go away from this point. The significant contributions to the sum or the integral in (42) will then come from small values of k, and we shall not make serious errors if we integrate, not merely over the unit cell in k space, but out to infinity. The quantity $1/[E-E(k)]$ will depend only on the magnitude of k, to the approximation we are using, so that in carrying out the integration over k we may first average over angles, in which case the exponential $e^{i\mathbf{k}\cdot\mathbf{R}_p}$ can be replaced by the spherical Bessel function $\sin(kR_p)/(kR_p)$, where k and R_p stand for the magnitudes of the vectors. Thus the sum in (42) becomes proportional to

$$\int_0^\infty\frac{2\pi k^2\sin(kR_p)}{(E-ak^2)kR_p}dk=\frac{\pi^2}{aR_p}e^{-\gamma R_p}, \quad (46)$$

where $\gamma=(-E/a)^{\frac{1}{2}}=(2\pi/h)(-2mE)^{\frac{1}{2}}$. But this simply tells us that the quantity $U(R_p)$ is proportional to $e^{-\gamma R_p}/R_p$. This turns out to be the same result which would be obtained from the differential equation approach to the difference equations even down to the value of γ we have obtained.

We can, in other words, reproduce the results of the free electron approximation for the wave function very easily; but at the same time we have the machinery for easily improving the approximation. We merely have to investigate the change in the sum or the integral in (42) or (38) when we take a better approximation to the energy $E(\mathbf{k})$. In the limit, as we have very large perturbation, so that the energy E departs widely from the energy band, the constant term in the Fourier representation will outweigh any of the other terms; this means that $U(\mathbf{R}_p)$ is much larger for $\mathbf{R}_p=0$, or on the perturbing atom, than on any other lattice site, as we know should be the case from our earlier qualitative discussion. But it would be an easy thing, with any given function $E(\mathbf{k})$, to obtain numerical values for the other components, of the other $U(\mathbf{R}_p)$'s, to any desired degree of approximation. By (42) or (38), we have reduced the problem of any lattice with a single perturbing or many perturbing atoms to quadratures, and as more examples are worked out, the wave functions and energy levels of the discrete states in such problems can be completely investigated.

In all of the treatment above, we have assumed that we have the exact energy bands and Bloch functions. That is, we have assumed that we have already found the eigenfunctions of our unperturbed Hamiltonian. The finding of the exact eigenfunctions for the periodic potential problem is a task in itself. In many cases the exact eigenfunctions of the periodic potential problem are approximated by a linear combination of Bloch functions made up of linear combinations of atomic orbitals.[5] If this is the case, the unperturbed part of the Hamiltonian has matrix elements between the Bloch combinations of the atomic orbitals. Sometimes the perturbing part of the Hamiltonian has matrix elements which are better known between the original set of atomic orbitals rather than in terms of the Wannier functions. For these reasons it is profitable to find a formulation of the impurity problem which does not make the assumption that the eigenfunctions of the unperturbed Hamiltonian have been found.

We imagine that we have some set of mutually orthogonal atomic orbitals $\phi_n(\mathbf{r}-\mathbf{R}_i)$. From these we define Bloch functions

$$u_{n,\mathbf{k}}(\mathbf{r})=N^{-\frac{1}{2}}\sum(\mathbf{R}_i)e^{i\mathbf{k}\cdot\mathbf{R}_i}\phi_n(\mathbf{r}-\mathbf{R}_i). \quad (47)$$

[5] J. C. Slater and G. F. Koster, Phys. Rev. 94, 1498 (1954).

With respect to these, we assume that our unperturbed Hamiltonian has matrix elements given by

$$H_{n,m}(\mathbf{k})=\int u_{n,\mathbf{k}}^*(\mathbf{r})H_0u_{m,\mathbf{k}}(\mathbf{r})d\tau. \quad (48)$$

We now proceed as we did in Eqs. (31) through (36). Every definition involving the Wannier functions is replaced by a corresponding one involving the ϕ's. Instead of Eq. (37) we arrive at the result that

$$\sum(m)f_m(\mathbf{k})[H_{m,n}(\mathbf{k})-E]+\frac{1}{N}\sum(s,\mathbf{R}_i,\mathbf{R}_j)e^{-i\mathbf{k}\cdot\mathbf{R}_i}V_{n,s}(\mathbf{R}_i,\mathbf{R}_j)\times\sum(\mathbf{k}')e^{i\mathbf{k}'\cdot\mathbf{R}_j}f_s(\mathbf{k}')=0. \quad (49)$$

If E is outside of the bands, it is possible to define an inverse to the matrix $H_{n,m}(\mathbf{k})-E$. Let us call this inverse $A_{p,n}(\mathbf{k})$. If we multiply Eq. (49) by $A_{p,n}(\mathbf{k})$, sum over n, and make use of the properties of the inverse of a matrix, we arrive at the result that

$$f_p(\mathbf{k})+\frac{1}{N}\sum(n,s,\mathbf{R}_i,\mathbf{R}_j)e^{-i\mathbf{k}\cdot\mathbf{R}_i}A_{p,n}(\mathbf{k})V_{n,s}(\mathbf{R}_i,\mathbf{R}_j)\times\sum(\mathbf{k}')e^{i\mathbf{k}'\cdot\mathbf{R}_j}f_s(\mathbf{k}')=0. \quad (50)$$

We can as before multiply by $e^{i\mathbf{k}\cdot\mathbf{R}_l}$ and sum over $\mathbf{k}$:

$$U_p(\mathbf{R}_l)+\frac{1}{N}\sum(n,s,\mathbf{R}_i,\mathbf{R}_j)V_{n,s}(\mathbf{R}_i,\mathbf{R}_j)\times[\sum(\mathbf{k})e^{i\mathbf{k}\cdot(\mathbf{R}_l-\mathbf{R}_i)}A_{p,n}(\mathbf{k})]U_s(\mathbf{R}_j). \quad (51)$$

Here of course the U's are the coefficients of the ϕ's. In order to satisfy this set of equations, by the same argument as in the case of the Wannier functions, we must have the determinant of the coefficients vanish. This can once again be reduced to a determinant where the indices only go over those lattice sites and atomic orbitals which have nonvanishing matrix elements of the perturbation. In this case the determinant which vanishes is the following:

$$\left|\delta_{p,s}\delta_{l,j}+\frac{1}{N}\sum(n,\mathbf{R}_i)V_{n,s}(\mathbf{R}_i,\mathbf{R}_j)\times[\sum(\mathbf{k})e^{i\mathbf{k}\cdot(\mathbf{R}_l-\mathbf{R}_i)}A_{p,n}(\mathbf{k})]\right|=0. \quad (52)$$

We notice that in this formulation it is the inverse of the matrix $H_{n,m}(\mathbf{k})-E$ which has the same role as $1/[E_n(\mathbf{k})-E]$. It might be mentioned in passing that both Eqs. (52) and (41) will be considerably reduced in size by considering the symmetry of the perturbed state which is desired.

APPENDIX

We could also solve for the impurity levels by a Green's function applied to the differential equation. In order to find the Green's function $G(\mathbf{r},\mathbf{r}')$ for the unperturbed Hamiltonian, we must solve the equation

$$(H_0-E)G(\mathbf{r},\mathbf{r}')=-\delta(\mathbf{r}-\mathbf{r}'). \quad (A1)$$

It is well known that the solution to this inhomogeneous differential equation is given in terms of the eigenstates of the unperturbed Hamiltonian by

$$G(\mathbf{r},\mathbf{r}')=\sum(n,\mathbf{k})\frac{u_{n,\mathbf{k}}^*(\mathbf{r}')u_{n,\mathbf{k}}(\mathbf{r})}{E_n(\mathbf{k})-E}. \quad (A2)$$

We can then express the solution to the perturbed Hamiltonian with energy E,

$$(H_0+H_1)\psi=E\psi, \quad (A3)$$

in the form of an integral equation:

$$\psi(\mathbf{r}')=\int\psi(\mathbf{r})H_1G(\mathbf{r},\mathbf{r}')d\tau=\int\psi(\mathbf{r})H_1\sum(n,\mathbf{k})\frac{u_{n,\mathbf{k}}^*(\mathbf{r}')u_{n,\mathbf{k}}(\mathbf{r})}{E_n(\mathbf{k})-E}. \quad (A4)$$

If we let $\psi(\mathbf{r})=\sum(l,\mathbf{R}_i)U_l(\mathbf{R}_i)a_l(\mathbf{r}-\mathbf{R}_i)$ and let $u_{n,\mathbf{k}}(\mathbf{r})=N^{-\frac{1}{2}}\sum e^{i\mathbf{k}\cdot\mathbf{R}_j}a_n(\mathbf{r}-\mathbf{R}_j)$ we can substitute these expressions in (A4) and multiply by $a_m^*(\mathbf{r}'-\mathbf{R}_p)$ and integrate over all space to give the result that

$$U_m(\mathbf{R}_p)+\frac{1}{N}\sum(n,\mathbf{R}_i,\mathbf{R}_j,\mathbf{k})\times\frac{e^{i\mathbf{k}\cdot(\mathbf{R}_p-\mathbf{R}_i)}}{E_m(\mathbf{k})-E}V_{m,n}(\mathbf{R}_i,\mathbf{R}_j)U_n(\mathbf{R}_j)=0. \quad (A5)$$

This is of course identical with the result in Eq. (38).

Neutron Irradiation of Indium Antimonide

J. W. CLELAND AND J. H. CRAWFORD, JR.
Oak Ridge National Laboratory, Oak Ridge, Tennessee

(Received May 3, 1954)

Hall coefficient and resistivity measurements as a function of temperature have been made on both *n*- and *p*-type single crystalline samples of InSb after successive periods of exposure in the Oak Ridge graphite reactor. Effects due to the introduction of Sn, a donor impurity, were minimized by shielding the specimens from those neutrons leading to In transmutation with cadmium and indium foil. The results of these measurements indicate conclusively that lattice defects produced by fast-neutron bombardment convert *p*-type InSb to *n* type. In addition they appear to act as shallow electron traps in *n*-type material. The mobility of carriers is markedly decreased by the bombardment-produced defects, but this decrease in mobility, as well as changes in carrier concentration resulting from bombardment-produced energy states can be essentially completely removed by appropriate heat treatment. An attempt has been made to correlate the various possible simple defects expected in the InSb structure with the nature of energy levels introduced by fast-neutron bombardment.

I. INTRODUCTION

THE electrical properties of certain semiconductors are markedly altered by nucleon bombardment at or near room temperature. Studies of Ge[1–5] and Si[1] reveal that lattice defects resulting from collisions of nucleons with lattice atoms introduce localized energy states in the forbidden energy band which may act as electron traps or hole traps. In Si these two types of traps appear to be equally effective in removing charge carriers, and essentially intrinsic behavior is produced after prolonged bombardment.[6] In Ge, however, the hole traps appear to be quite shallow,[3] and some of the electron traps lie sufficiently deep in the forbidden energy band to act as acceptors in *p*-type material, causing conversion from *n* type to *p* type after adequate irradiation. Investigations of radiation effects have been extended to include the intermetallic compound InSb. Both poly- and single-crystalline specimens have been irradiated in the Oak Ridge graphite reactor and changes in both carrier concentration and mobility have been determined.

The electrical properties of InSb have been extensively studied.[7–9] In many respects its properties are quite similar to those of Si and Ge. It is distinguished, however, by a narrow forbidden energy gap E_g and an extremely large electron mobility. Recent studies of Tannenbaum and Maita[9] on single-crystalline, high purity InSb indicate that E_g is temperature dependent, being ~0.18 ev at 300°K, and the room temperature electron mobility is as large as 4×10^4 cm^2 volt^{-1} sec^{-1}. Because of the large electron to hole mobility ratio (~85 at 300°K),[9] *p*-type material for even moderate carrier concentration (~10^{16}) is in the intrinsic range well below room temperature.

InSb is one of a series of semiconducting intermetallic compounds formed between elements of the third and fifth groups of the periodic system. It crystallizes in the zincblende lattice, one which would reduce to the diamond lattice if only one type of atom were involved. Because of its binary nature, this compound offers the possibility of a greater variety of simple defects than do the elemental semiconductors. A vacancy may be either an In or an Sb vacant lattice site and an interstitial atom may possess either three or five outer electrons. In addition, the ordered arrangement of In and Sb atoms in the lattice admits the possibility of an additional type of lattice damage not present in elemental structures. As a high-energy recoil from the collision of a neutron nears the end of its range, the rate of energy loss to the lattice becomes so large that a region variously estimated to contain between 1000 and 10 000 atoms is heated to very high temperatures (~10^4°K) and rapidly quenched (~10^{-11} sec). This so-called thermal spike[10] permits the rearrangement or interchange of atoms which may then be quenched into their new positions. Disordering of an ordered Cu_3Au alloy has been explained by this mechanism.[11] Similar effects are a distinct possibility in InSb but their observability would depend on a number of factors including (1) the extent of their influence on measurable properties, (2) the mobility of the con-

[1] For a review of early work see K. Lark-Horovitz, *Semi-Conducting Materials*, edited by H. K. Henisch (Academic Press, Inc., New York, 1951), p. 47 ff.
[2] Cleland, Crawford, Lark-Horovitz, Pigg, and Young, Phys. Rev. **83**, 312 (1951).
[3] Cleland, Crawford, Lark-Horovitz, Pigg, and Young, Phys. Rev. **84**, 861 (1951).
[4] E. E. Klontz and K. Lark-Horovitz, Phys. Rev. **86**, 643 (1952). See also E. E. Klontz, thesis, Purdue University (unpublished).
[5] Brown, Fletcher, and Wright, Phys. Rev. **92**, 591 (1953).
[6] Cleland, Crawford, and Pigg (unpublished).
[7] H. Welker, Z. Naturforsch. **7a**, 744 (1952); **8a**, 248 (1953).
[8] Breckenridge, Hosler, and Oshinsky, Phys. Rev. **91**, 243 (1953).
[9] M. Tannenbaum and J. P. Maita, Phys. Rev. **91**, 1009 (1953).
[10] F. Seitz, Discussions Faraday Soc. No. 5, 271 (1949); see also J. C. Slater, J. Appl. Phys. **22**, 237 (1951). Recent studies by J. A. Brinkman [NAA-SR-198, North American Aviation, Downey, California (unpublished)] indicate that the atomistic (displaced atom) approach and the thermodynamic (thermal spike) approach are not necessarily mutually exclusive but should be applied to the initial and final portions of the range of the high-energy ion, respectively.
[11] S. Siegel, Phys. Rev. **75**, 1823 (1949).

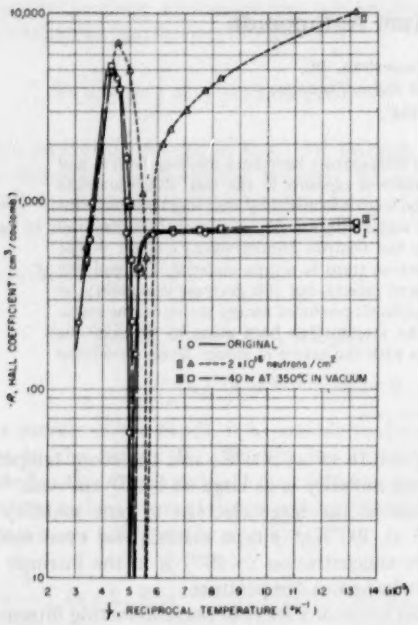
10,000
1,000
100
10
2 3 4 5 6 7 8 9 10 11 12 13 14 (x10³)
1/T, RECIPROCAL TEMPERATURE (°K⁻¹)
I ○ —— ORIGINAL
II △ ---- 2 x10¹⁶ neutrons/cm²
III □ —— 40 hr AT 350°C IN VACUUM

FIG. 1. Hall coefficient of p-type InSb as a function of temperature. (1) Prior to irradiation, (2) after reactor irradiation, (3) after a 40-hr 350° vacuum anneal.

stituent atoms at the temperature of irradiation, and (3) the magnitude of the excess free energy of the disordered region. In view of these considerations, one might expect radiation effects in this material to be more complex than in Ge or Si.

A preliminary report of this work,[12] based on results obtained on polycrystalline InSb, indicates that the influence of impurities introduced by transmutations on carrier concentration is comparable to, if not greater than, that due to lattice defects produced by fast neutrons. This behavior results from the extremely large capture cross section of In for the neutron spectrum encountered in the reactor, and the fact that the decay product, Sn, is a donor impurity when substituted for an In atom in the InSb lattice. Although its cross section is considerably smaller, Sb also transmutes to the donor impurity Te. Therefore, in order to study separately the effects resulting from fast neutron induced lattice defects, it is necessary to minimize the introduction of chemical donors by shielding the specimen from those neutrons for which the In cross section is large. After accounting for the effects due to transmutations, these early results indicate conclusively that certain of the bombardment-produced lattice defects act as electron traps in low resistivity n-type InSb.

In the present paper, we wish to present the results of more extensive studies, particularly those on single-crystalline material. The experimental data will be interpreted in the light of ideas concerning the nature of radiation effects in Ge and Si. The different types of defects expected as a result of bombardment will be discussed and, to the extent possible, inferences will be drawn concerning the nature of the defects giving rise to those localized states whose existence is indicated by experimental data.

[12] J. W. Cleland and J. H. Crawford, Phys. Rev. **93**, 894 (1954).

II. EXPERIMENTAL RESULTS

High-purity single-crystal specimens of both p- and n-type InSb were given successive exposures in the reactor at a temperature of about 25°C. The samples were wrapped with Cd and In foil of sufficient thickness to reduce greatly the incident flux of thermal and resonance neutrons responsible for transmutations. Conductivity measurements during irradiation at the temperature of bombardment are of little value in following the progress of the irradiation since the samples employed are already in the intrinsic range at 25°C. Consequently, Hall coefficient and resistivity measurements were made as a function of temperature in the range from 77°K to 300°K after each exposure.

In order to investigate the effect of short exposures on p-type InSb and to examine the shielding efficiency of the Cd and In foil, a p-type sample with an initial hole concentration of $n_h^0 = 1.1 \times 10^{16}$ cm^{-3} at 77°K was given a relatively short exposure [integrated fast flux[13]

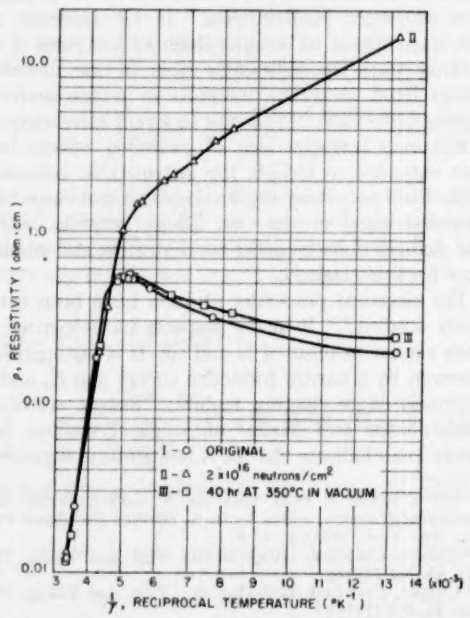
10.0
1.0
0.10
0.01
ρ, RESISTIVITY (ohm-cm)
3 4 5 6 7 8 9 10 11 12 13 14 (x10⁻³)
1/T, RECIPROCAL TEMPERATURE (°K⁻¹)
I - ○ ORIGINAL
II - △ 2 x10¹⁶ neutrons/cm²
III - □ 40 hr AT 350°C IN VACUUM

FIG. 2. Resistivity of p-type InSb as a function of temperature. (1) Prior to irradiation, (2) after reactor irradiation, (3) after a 40-hr 350° vacuum anneal.

[13] The fast flux as employed here is that flux of neutrons whose energy is greater than 0.1 Mev. The absolute value of this flux may be in error by as much as a factor of two. Relatively, however, this scale of integrated flux is consistent with that used in references 1, 2, 3, and 12.

$(nvt)_f \cong 2\times10^{16}$ cm^{-2}], followed by a vacuum anneal at 350°C for 40 hours. Semilog plots of the Hall coefficient R and resistivity ρ *vs* reciprocal temperature of the specimen for each condition are shown in Figs. 1 and 2, respectively. The large decrease in hole concentration in the extrinsic range which is almost completely removed by the heat treatment indicates that fast neutron-produced lattice defects serve as hole traps in p-type InSb. The slope and curvature of the R and ρ curves after the exposure (Curve II) seem to indicate the existence of one group of relatively shallow hole traps which are distributed in energy. The slope of the log ρ *vs* $1/T$ curve in the initial portion of the extrinsic range, where the slope is relatively constant, corresponds to an energy of ~0.02 ev. If this value, or twice this value,[14] is a representative depth of the more numerous traps in this group, the bending down of the curve toward lower temperature indicates an appreciable concentration of more shallow hole traps.

Comparison of the values of R at 77°K before irradiation and after heat treatment subsequent to irradiation indicates that the final hole concentration was decreased by $\sim1\times10^{15}$ cm^{-3}, presumably through the introduction of an equivalent number of donor impurities by transmutations. Actually, because of the shielding geometry of the sample holder employed, the shielding was not completely effective. Consequently, a leakage of thermal and resonance neutrons amounting to ~6 percent of the integrated fast flux, an amount which would account for the observed decrease of n_h, is not unreasonable.

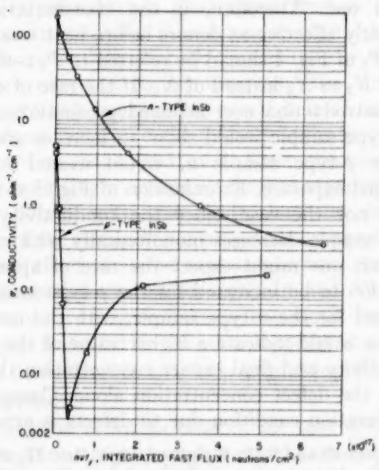

FIG. 3. Conductivity of InSb at −196°C after successive reactor irradiations.

[14] Whether the value yielded by the slope, or twice that value, corresponds to the ionization energy of a discrete level depends on the statistical situation. See N. F. Mott and R. W. Gurney, *Electric Processes in Ionic Crystals* (Oxford University Press, London, 1948), pp. 157–160.

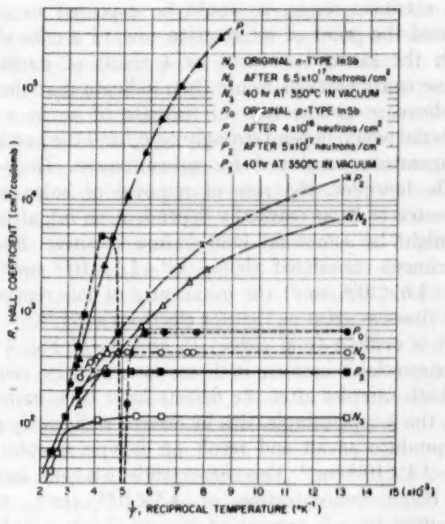
ORIGINAL n-TYPE InSb
AFTER 6.5x10¹⁷ neutrons/cm²
40 hr AT 350°C IN VACUUM
ORIGINAL p-TYPE InSb
AFTER 4x10¹⁶ neutrons/cm²
AFTER 5x10¹⁷ neutrons/cm²
40 hr AT 350°C IN VACUUM
R, HALL COEFFICIENT (cm³/coulomb)
2 3 4 5 6 7 8 9 10 11 12 13 14 15 (x10³)
1/T, RECIPROCAL TEMPERATURE (°K⁻¹)

FIG. 4. Hall coefficient of InSb as a function of temperature after various reactor irradiations.

The conductivity of both n- and p-type samples measured at 77°K after successive irradiations is plotted as a function of $(nvt)_f$ in Fig. 3. The n-type sample decreases in conductivity monotonically toward a saturation value, whereas the conductivity of the p-type sample first decreases rapidly, passes through a minimum value, and then increases toward the same saturation value approached by the n-type sample. This behavior suggests that p-type InSb is converted to n-type by the action of bombardment produced defects alone. Hall coefficient measurements taken concurrently with the above conductivity data confirm this view and further indicate that both the originally p-type and the n-type sample tend to approach the same saturation value of electron concentration n_e^*, which is $\sim7\times10^{14}$ cm^{-3} at 77°K. Representative log R *vs* $1/T$ curves for these two specimens are shown in Fig. 4. The curves of the originally p-type sample are labeled P and those of the n-type sample are labeled N. P_0 and N_0 represent the original values. P_1, taken after a moderate exposure, is the curve for the p-type sample shortly after its conversion to n-type. P_2 and N_2 indicate the approach to a common saturation after a relatively long exposure and P_3 and N_3 were obtained after a vacuum anneal at 350°C for 40 hours.

The log R *vs* $1/T$ curve for a sample in the condition of complete saturation would presumably lie somewhere between P_2 and N_2 of Fig. 4. If this saturation condition is due only to defects and is unaffected by the introduction of donors by transmutations and room temperature annealing of defects (see below), an n-type sample with $n_e^0 < n_e^*$ at a given temperature would be expected to show an increase in n_e on bombardment. Therefore, should the Hall coefficient curve of such a specimen intersect that representing the saturation condition in

the extrinsic range, it would be expected to rotate around the point of intersection toward a coincidence with the saturation curve as a result of irradiation. These considerations would then indicate that the rate of decrease or the rate of increase of n_e in n-type material would depend strongly on n_e^0 and the particular temperature employed for measurement. In p-type InSb, however, the rate of removal of holes is not expected to be as markedly dependent on n_h^0, although it might be somewhat temperature sensitive. For the specimens considered above ($n_h^0 = 1.1\times10^{16}$ cm^{-3} and $n_e^0 = 1.6\times10^{16}$ cm^{-3}) the initial rate of hole removal is $\sim$4 times as great as that for electrons at 77°K.

It is evident from curves P_3 and N_3 of Fig. 4 that an appreciable increase in donor concentration remains in both samples after the defects have been annealed. For the p-type sample, this increase is sufficiently great to produce as an end result an n-type sample with $n_e = 2.4\times10^{16}$ cm^{-3}. This corresponds to a total increase in donor concentration of 3.5×10^{16} cm^{-3}, which amounts to $\sim$7 percent of the total integrated fast flux, $(nvt)_f = 5\times10^{17}$ cm^{-2}, in reasonable agreement with the magnitude of shield leakage estimated above. Similar considerations for the n-type sample indicate that the donor concentration increase of 4.5×10^{16} cm^{-3} is again $\sim$7 percent of the 6.5×10^{17} $(nvt)_f$ received.

The introduction of donors by transmutations in no way invalidates the statement made above that p-type InSb is converted to n type by the action of fast neutron produced lattice defects alone. Since the half-lives of the more important activities of In are short compared to the time interval between irradiation and subsequent measurement, the donor concentration due to leakage would be a linear function of the integrated flux. Examination of Fig. 3 reveals that conversion is indicated at an $(nvt)_f$ less than 4×10^{16} cm^{-2}, a fact also borne out by curve P_1 of Fig. 4. Since this exposure corresponds to the introduction of only $\sim2.8\times10^{15}$ chemical donors (less than one-third of the original acceptor concentration), conversion must result from defect hole traps which lie above the middle of the forbidden band and, therefore, may act as donors in n-type InSb. It is possible, however, that the introduction of chemical donors may affect to some extent the actual position of the saturation condition mentioned above. This point will be considered below in more detail.

Both electron and hole mobilities in single crystals are decreased as a result of irradiation. This is in agreement with previous observations on polycrystalline material.[12] The electron mobility at 77°K for the n-type sample of Fig. 4 before irradiation is 6.6×10^4 cm^2 volt^{-1} sec^{-1}. It is decreased to 2.2×10^3 cm^2 volt^{-1} sec^{-1} after an exposure of $(nvt)_f = 6.5\times10^{17}$ cm^{-2}. That the major portion of this decrease is produced by additional scattering from bombardment-induced lattice defects is indicated by the effect of vacuum annealing, which restores the mobility to 1.5×10^4 cm^2 volt^{-1} sec^{-1}. The residual additional scattering after the anneal may be due to both an increase in impurity scattering associated with the additional chemical donors and to scattering from any defects not removed by heat treatment. The mobility that would result from lattice scattering alone at 77°K can be estimated by extrapolating the results of Tannenbaum and Maita.[9] Since this appears to be $\sim10^6$ cm^2 volt^{-1} sec^{-1}, the observed mobilities quoted above are due almost entirely to impurity scattering. According to the Conwell-Weisskopf theory of impurity scattering,[15] the mobility, when limited by impurity scattering alone, is approximately inversely proportional to the concentration of ionized impurities. For the sample in question, the chemical donor concentration after irradiation is 3.8 times the original value, whereas the mobility has been decreased by a factor of 4.4. We may therefore conclude that the increase in scattering that remains after vacuum anneal is due principally to the increase in donor concentration as a result of transmutations.

III. DISCUSSION OF RESULTS

Before considering the nature of the defects which are the principal cause of the behavior described above, it is desirable to examine the saturation condition approached by both types of specimens. If the defect levels alone were responsible for this saturation, the limiting value would be of aid in determining the positions of such levels. Since chemical donors are introduced simultaneously with defects, each measurement after a certain period of irradiation reflects the effects due to defect introduction into a material whose chemical impurity concentration is no longer the original one. Therefore, if the transmutations are completely effective as donors before heat treatment,[16] curve P_2 of Fig. 4 should be referred to P_3 rather than P_0 and N_2 to N_3 instead of N_0. If the rate of chemical donor introduction ever attained predominance, n_e of the n-type sample would show an increase and in the initially p-type sample n_e would exceed n_e^* after prolonged exposure. Examination of Fig. 3 shows that this is not the case, since the conductivity of the n-type sample decreases monotonically with exposure. However, one might expect the rate of approach to saturation to be increased for the p-type sample, and decreased for the n-type sample, with the result that the data would indicate a higher value of the limiting conductivity and final carrier concentration than that due to the defect concentration alone. Consequently, the saturation condition due to defects is expected to

[15] E. Conwell and V. F. Weisskopf, Phys. Rev. 77, 388 (1950).

[16] If the decay product is displaced from its position to an interstitial position by some agency, its action will be essentially the same as that of a displaced atom. This point was mentioned in reference 1, where the possibility of displacement as a result of recoil from the radiation emitted during decay was considered. It has been pointed out to the authors by H. P. Yockey that recoil from the γ ray emitted on neutron capture is amply great to displace the activated atom before decay, a process quite similar to the Szilard-Chalmers reaction.

lie nearer P_2 than N_2. This expectation is supported by the conductivity curve of the p-type sample in Fig. 3, which shows little change after an exposure of $(nvt)_f \sim 2\times10^{17}$ cm^{-2}. Thus we expect 4.5×10^{14} cm$^{-3} < n_e^* < 7\times10^{14}$ cm^{-3} at 77°K.

Any attempt to explain the observed electrical behavior in terms of specific properties of various defects must account for the following groups of localized states whose existence is inferred from experiment: (1) a shallow group of electron traps below the conduction band which cause a decrease in n_e in n-type material with $n_e^0 > n_e^*$; (2) a wide distribution of shallow hole traps above the valence band whose presence is indicated by Fig. 1; and (3) a second group of hole traps which, in order to explain conversion, must lie above the middle of the forbidden band and may, therefore, act as donors in n-type material. The last group of states may be a continuation of the distribution mentioned in (2). In the following it will be assumed that the major result of fast neutron collisions with lattice atoms is the generation of Frenkel defects and that as many In atoms are displaced as Sb atoms.

Four possible single defects can be expected for a binary compound since there are two possible interstitial atoms and two possible vacant lattice sites. We shall first examine the two types of interstitials, In and Sb. Since these may release electrons on ionization, they are expected to give rise to donor levels or hole traps. James and Lark-Horovitz[17] have considered in detail the ionization of interstitial atoms in diamond-lattice semiconductors, and they find that if the dielectric constant is large, the first ionization potential may be calculated to a good approximation from a hydrogenic model. To this approximation, the first ionization potentials of both interstitial In and Sb atoms are expected to be identical. The dielectric constant of InSb is unknown, but if it is of the same magnitude as that in Ge, the primary ionization energy is expected to be $\sim$0.05 ev.[18] Since the remaining electrons on a singly ionized interstitial atom are more strongly bound, with the result that the dielectric constant of the lattice is not expected to have as large a shielding effect as in the case of a neutral atom, the second ionization energy for both In and Sb might be expected to be greater than the small forbidden energy gap in InSb.[9] It therefore appears likely that only one donor level or hole trap is introduced for each interstitial atom.

The situation is not as clear in the case of the two types of vacant lattice sites. James and Lark-Horovitz[17] have also examined the localized states associated with vacancies in Ge and Si, but complications arising from the complex nature of the wave functions in the diamond lattice and the large perturbations introduced by vacant lattice sites prevent a quantitative estimation of the positions of these energy levels. Consequently, these authors found it necessary to use experimental indications in order to place these levels in their model of the band scheme. With respect to vacancies in InSb, we shall, therefore, attempt only to indicate differences that might be expected between vacant In and Sb sites. An In vacancy has associated with it five extra electrons from the neighboring Sb atoms. From an atomistic point of view, if the perturbation is not so great as to destroy the tendency for covalent bond formation, there exist three half-filled orbitals and one complete orbital in the region of the vacancy. An Sb vacancy, on the other hand, contains three extra electrons from the neighboring In atoms. Hence, there exist three half-filled orbitals and one that is completely empty. It therefore seems reasonable to assume that the energy required to place an additional electron into a vacancy (to ionize a vacancy) might be quite different in the two cases.[19] Because of the complexity of the electronic structure and the large perturbations mentioned above, it is difficult to estimate with any certainty how the differences between these vacancies affect their energies of ionization.

For the want of a better approach, a vacancy will be considered analogous to a free atom with the same numbers of valence electrons as there are extra electrons in the region of the vacancy. The addition of an electron to an Sb vacancy would, therefore, result in four half-filled orbitals, in contrast to two half-filled and two completely filled orbitals for an In vacancy plus an electron. Since half-filled subshells in atoms or ions are known to be more stable than other partially filled subshells, this analogy suggests that the stabilization of the Sb vacancy, resulting from the addition of an electron, would tend to reduce the energy required to introduce the excess electron below that required for the In vacancy, for which such a stabilization is not expected. In this view, therefore, an Sb vacancy would correspond to an acceptor with a smaller ionization energy than that of the acceptor created by the In vacancy. Since, because of Coulombic repulsion, the energy required to introduce a second electron would be expected to be considerably greater in either case, this energy might reasonably be expected to correspond to an acceptor state in the conduction band for the small value of E_g in InSb. Hence, higher levels will not be considered.

The above remarks are concerned only with the

[17] H. M. James and K. Lark-Horovitz, Z. physik. Chem. **198**, 107 (1951).

[18] In this treatment the ionization energy is inversely proportional to the effective mass and the square of the dielectric constant. From indications of reference 9, it appears that m_e^*/m is considerably less than unity. Hence, for a dielectric constant the same as in Ge, the ionization energy is decreased below this value.

[19] Use of the band theoretical approach of reference 17 also indicates marked differences since the perturbing effect of the missing ion core, which causes localized states to split out of the valence band, is due to an absence of three charges in the case of In and an absence of five in the case of Sb.

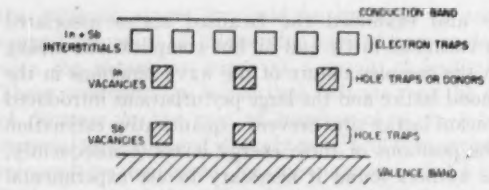

FIG. 5. A possible defect energy-level scheme for irradiated InSb.

localized states arising from separate defects. Since equal quantities of each type of defect are expected to be produced by irradiation, the resultant nature of each defect state is determined by the redistribution of the electrons arising from the interstitial atoms to positions of lowest energy. The situation resulting from the tentative model postulated above is shown schematically in Fig. 5. It is expected that the shallow donors associated with the interstitial atoms will lose their electrons to the lower-lying acceptors created by the lattice vacancies and may, therefore, behave as electron traps. The states corresponding to the vacancies have been labeled according to the atomistic picture described above, and those states corresponding to the In vacancies have been arbitrarily placed above the center of the forbidden band in order to account for the experimental observation that donors are introduced. Since these are now occupied, the Sb vacancy acts as a hole trap, whereas the In vacancy plays a dual role, being a hole trap in *p*-type material and a donor in *n*-type material. It should be noted that there are twice as many electron traps as there are states in the two lower levels. Because of the inhomogeneous distribution of defects resulting from bombardment, the associated energy levels are expected to be broadened as a result of perturbations arising from interactions between defects. This broadening is indicated roughly in Fig. 5 by the width of the levels.

It should be emphasized that this model involves a number of assumptions, the principal ones being (1) the hydrogenic model is applicable to interstitial atoms and the atomistic analogy accounts for differences in ionization energy of the states created by lattice vacancies; (2) there is no difference in annealing rate at room temperature for the various defects under consideration; and (3) essentially all of the bombardment produced defects can be treated in terms of Frenkel defects. Implications of the first assumption have been indicated above. As to the second assumption, because of the method of measurement, it is impossible without further experimental study to say anything about either the extent of annealing or the amount of differential annealing that takes place during irradiation and prior to the time of measurement. It is known in the case of Ge that an extensive rearrangement of disorder of some sort occurs as low as 110°K, but that such activity is essentially complete at 220°K with little further rearrangement taking place in the room temperature range.[20,21] If appreciable differential annealing does take place in InSb at room temperature, extensive modification of the proposed model would be required. The third assumption does not include effects associated with the formation of defect clusters and thermal spikes. In this connection, it should be pointed out that although disorder of the ordered arrangement of In and Sb atoms resulting from thermal spikes is a distinct possibility, there are no experimental observations which, according to past experience with Ge and Si, explicitly require the postulation of effects associated with thermal spikes for their explanation. It appears that more extensive studies of electrical properties and studies of structure as well are necessary to determine whether such disordered regions are actually introduced into this material by fast neutron bombardment.

There is little doubt but that alternative models of defect energy levels might be constructed which would also account satisfactorily for the experimental observations considered here.

IV. ACKNOWLEDGMENTS

The authors are deeply indebted to Dr. M. Tannenbaum of the Bell Telephone Laboratories who furnished the high-purity single crystals upon which these experiments were performed. The helpful criticism of D. K. Holmes is also gratefully acknowledged.

[20] Crawford, Cleland, Holmes, and Pigg, Phys. Rev. **91**, 243 (1953).

[21] Forster, Fan, and Lark-Horovitz, Phys. Rev. **91**, 229 (1953).

Spectral Dependence of Thermionic Emission with Activation from (Ba−Sr)O Cathodes Over 0.6-3.5 ev Region

TADATOSI HIBI AND KAZUO ISHIKAWA
Research Institute for Scientific Measurements, Tôhoku University, Sendai, Japan
(Received January 22, 1954; revised manuscript received June 1, 1954)

The spectral dependence of thermionic emission with activation from (Ba−Sr)O cathodes was observed in the region 0.6–3.5 ev by using a monochromator. At 775°K in the early stage of activation, an intense peak appeared at about 3.2 ev and, with further activation, it gradually increased. In addition several other peaks appeared in the visible and infrared regions. A remarkable temperature dependence of the 3.2-ev peak intensity was also observed during activation. Also, on cathodes which were difficult to activate, a peak at about 2.3 ev first appeared in the earliest stages of activation and then the total thermionic emission decreased with light illumination in the ultraviolet region.

AS already reported,[1] the spectral dependence of thermionic emission from (Ba−Sr)O cathodes over the visible region changes with activation. To further confirm this, the spectral dependence was observed more precisely in the region 0.6–3.5 ev by using a monochromator.

This observation differs from the previous one[1] in the following points: (1) (Ba−Sr)O cathodes were prepared on a flat nickel sleeve coating an area of 4×5 mm. (2) An Adam-Hilger spectrometer was used as a monochromator in place of the glass filters. The resolving power of the monochromator providing the illuminating light is 20 mμ and 50 mμ at 2.5–3.5 ev and 0.6–2.5 ev, respectively. (3) To obtain the spectral distribution curves, values of ΔI_{th} (change of thermionic emission due to illumination) were taken after illumination for 30 seconds.

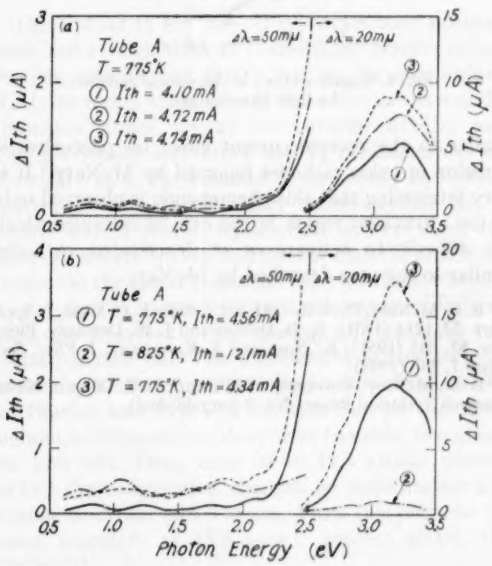

FIG. 1. Spectral dependence of thermionic emission from oxide cathode (a) with activation measured at 775°K and (b) when the temperature is raised to 825°K. ①, ②, and ③ show the order of the observations. The ordinates of the curves over the region 0.6–2.5 ev are magnified five times compared with those of the region 2.5–3.5 ev.

In the case of observation at 775°K in the early stage of activation, an intense peak appeared at about 3.2 ev and the responses in the visible and infrared regions were very poor as shown in Fig. 1(a). With activation, repeating a large increase and a small decrease alternately, the peak intensity at 3.2 ev gradually increased. Also, several peaks appeared over the visible and infrared regions though they were not so pronounced. When the value of the total emission ceased to increase by activation treatment, the characteristic curve only changed slightly. At this stage, the temperature of the cathode was elevated to 825°K. As shown in Fig. 1(b), the peak intensity at 3.2 ev decreased pronouncedly, while ΔI_{th} over the visible and infrared regions increased considerably compared with the case of 775°K, showing a remarkable temperature dependence. After returning to 775°K again, ΔI_{th} over the whole observed region increased compared with that at the previous 775°K observation, notwithstanding a slight decrease of total emission. After repeated observations at 775°K and 825°K alternately, the total emission gradually decreased, while ΔI_{th} at 775°K over the whole observed region reached a maximum and

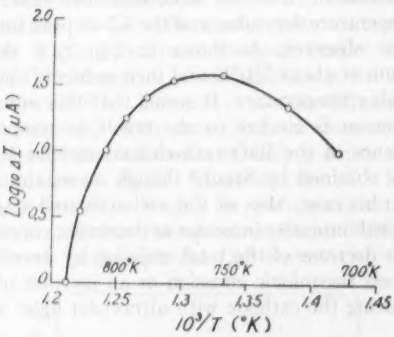

FIG. 2. Temperature dependence of the intensity of the 3.2-ev peak.

[1] T. Hibi and K. Ishikawa, Phys. Rev. 87, 673 (1952).

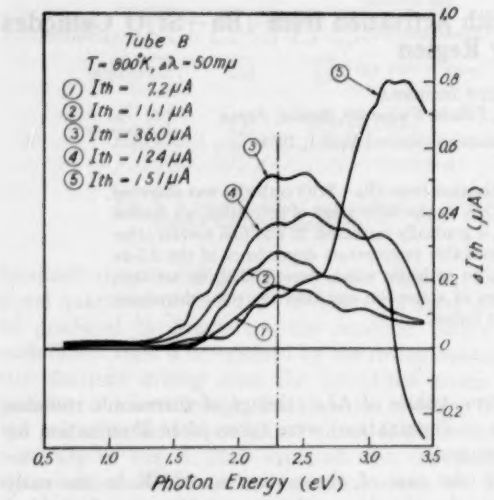

FIG. 3. Spectral dependence of thermionic emission with activation of oxide cathodes which are difficult to activate.

then decreased. After the aforementioned observation the temperature dependence of the 3.2-ev peak intensity was also observed. As shown in Fig. 2, it shows a maximum at about 750°K and then suddenly decreases with rising temperature. It seems that this interesting phenomenon is similar to the result in temperature dependence of the BaO cathodoluminescence band of 345 mμ obtained by Stout,[2] though no maximum appears in his case. Also, at the well-activated stage, the 3.2-ev peak intensity increases or decreases, corresponding to a decrease of the total emission by drawing out the excess thermionic emission or an increase of it by illuminating the cathode with ultraviolet light, respectively.

The spectral distribution was also observed at the earliest stages of activation. As shown in Fig. 3, a peak at about 2.3 ev grew first and then the intensity near the ultraviolet region began to increase with activation. However, it ceased to grow and showed an abrupt negative change. With further activation, the 2.3-ev peak intensity reached a maximum and then decreased, while the 3.2-ev peak continued to grow towards the case of Fig. 1(a). However, the appearance of a distinct peak at 2.3 ev was seen only on the cathodes which were difficult to activate. It seems that a pronounced peak at 2.3 ev in the case of ordinary cathodes may appear and disappear at such an early stage of the activation that the observation of the spectral dependence of the thermionic emission may be impossible. This 2.3-ev peak is in good agreement with that appearing at 500 mμ in previous observations[1] and also with a peak at 2.4 ev observed by many workers[3] on photoelectric emission or optical absorption of active oxide cathodes. Thus this peak may perhaps be an *F* band.

There are cases where total emission decreases with light illumination as mentioned above. Several examples of this phenomenon are shown in Fig. 4. This is

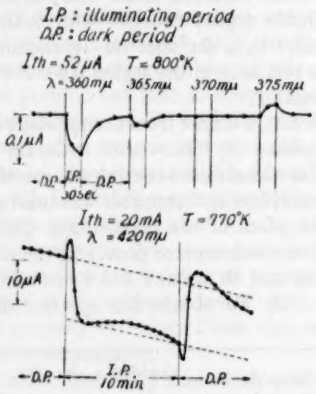

FIG. 4. Negative effect of thermionic emission by light illumination.

similar to the reverse current effect on photoelectric emission of oxide cathodes reported by McNary.[4] It is very interesting that this phenomenon is observed only in the ultraviolet region in the case of cathodes which are difficult to activate or of deactivated cathodes similar to the case described by McNary.

[2] V. L. Stout, University of Missouri, U. S. Office of Naval Research Technical Report No. 12 (unpublished).

[3] B. D. McNary, Phys. Rev. **81**, 631 (1951); E. O. Kane, J. Appl. Phys. **22**, 1214 (1951); H. B. DeVore and J. W. Dewdney, Phys. Rev. **83**, 805 (1951); K. Noga and S. Kawamura, J. Phys. Soc. Japan **7**, 287 (1952).

[4] B. D. McNary, University of Missouri, U. S. Office of Naval Research Technical Report No. 8 (unpublished).

Diffusion of Co^{60} in Some Ni-Al Alloys Containing Excess Vacancies*

A. E. Berkowitz,† F. E. Jaumot, Jr., and F. C. Nix
Randal Morgan Laboratory of Physics, University of Pennsylvania, Philadelphia, Pennsylvania
(Received May 20, 1954)

The aluminum-rich compositions in the δ phase of Ni−Al exhibit vacancy densities considerably greater than the normal equilibrium concentrations. Measurements were made of the diffusion of Co^{60} in six compositions in the δ phase of Ni−Al at 1050°C, 1150°C, 1250°C, and 1350°C. The diffusion coefficient had a minimum value at the stoichiometric composition. The activation energies had a maximum value at this composition and remained essentially constant at a lower value for the aluminum-rich alloys. An interpretation of this behavior in terms of a vacancy mechanism is discussed.

INTRODUCTION

In most cases, experimental studies of diffusion in metals are difficult to interpret uniquely in terms of one or another of the commonly proposed diffusion mechanisms; namely, the interstitial, vacancy, and Ring mechanisms. This is due, in part, to the limited accuracy of many diffusion experiments, but other factors also contribute to this problem. For example, when a vacancy mechanism is considered, there is usually little information available concerning the distribution of vacancies in the lattice. Therefore, diffusion measurements in those systems in which the concentration of excess vacancies is known may be described more precisely in terms of a particular mechanism. The present investigation was concerned with such a system.

THE δ PHASE OF Ni−Al

The δ phase of the Ni−Al system is body-centered cubic and extends from 45 to 60 atomic percent nickel. Bradley and Taylor[1] found that at the composition NiAl, the nickel atoms occupy the cube centers and the aluminum atoms are at the corners. Bradley and Taylor's density and lattice spacing measurements are shown in Fig. 1. The behavior of the density and lattice spacing for the excess nickel concentrations are in accord with a simple replacement process since the nickel atoms are heavier and smaller than the aluminum atoms. On the excess aluminum side, the dashed branch of the density curve indicates the values calculated using the measured lattice spacings and assuming two atoms per unit cell. The considerable discrepancy between the calculated and measured values of the density led Bradley and Taylor to conclude that for the excess aluminum compositions there were less than two atoms per unit cell. Thus, from 60 to 49.5 atomic percent nickel, the composition changes by substituting aluminum atoms for nickel atoms. From this point to the phase boundary at 45.3 atomic percent nickel, the change in composition takes place by dropping nickel atoms out of their lattice positions and leaving these sites vacant. Bradley and Taylor confirmed these conclusions by careful measurements on the degree of order of the alloys. A similar defect structure is found in the ε phase of Co−Al.[2]

PREVIOUS DIFFUSION STUDIES ON Ni−Al AND Co−Al

The considerable ranges of vacancy concentrations in these defect alloys have resulted in two previous investigations of the influence of these vacancies on diffusion. Smoluchowski and Burgess[3] studied the diffusion of Co^{60} in a series of compositions in the δ phase of Ni−Al at 1150°C. They found that the diffusion coefficients increased with increasing concentrations of excess nickel but remained essentially constant for the excess aluminum alloys. Smoluchowski and Burgess suggested that their results for the excess aluminum alloys indicated that the nickel vacancies $V(\mathrm{Ni})$ were unable to exchange with the Co^{60} atoms since such an

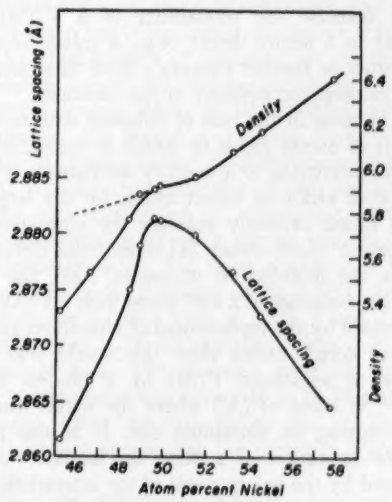

FIG. 1. The density and lattice spacing as a function of composition for the δ phase of Ni−Al. (After Bradley and Taylor.)

* Supported by the U. S. Office of Naval Research. This work is part of a dissertation by A. E. Berkowitz presented in candidacy for the degree of Doctor of Philosophy at the University of Pennsylvania.

† Now at The Franklin Institute Laboratories for Research and Development, Philadelphia 3, Pennsylvania.

[1] A. J. Bradley and A. Taylor, Proc. Roy. Soc. (London) **A159**, 56 (1937).

[2] A. J. Bradley and G. C. Seager, J. Inst. Metals **64**, 81 (1939).

[3] R. Smoluchowski and H. Burgess, Phys. Rev. **76**, 309 (1949).

TABLE I. Values of the diffusion coefficients as a function of temperature for various compositions in the δ phase of Ni—Al.

Atom percent nickel	D (cm² sec⁻¹) 1050°C	1150°C	1250°C	1350°C
47.3	2.5×10^{-11}	8.85×10^{-11}	3.68×10^{-10}	1.05×10^{-9}
48.5	1.66×10^{-11}	6.00×10^{-11}	2.30×10^{-10}	8.32×10^{-10}
49.4		3.96×10^{-11}	1.14×10^{-10}	3.96×10^{-10}
50.7		2.46×10^{-11}	1.52×10^{-10}	8.36×10^{-10}
53.1	2.44×10^{-11}	1.03×10^{-10}	5.66×10^{-10}	1.97×10^{-9}
55.5	7.84×10^{-11}	4.00×10^{-10}	1.38×10^{-9}	3.11×10^{-9}

exchange would necessitate the intermediate step of the V(Ni) exchanging with a nearest-neighbor aluminum atom. It was assumed that this latter exchange was precluded by the fact that a V(Ni) is considerably smaller than an Al atom.

Significantly different results were reported by Nix and Jaumot[4] who investigated the diffusion of Co^{60} in five compositions in the ϵ phase of Co—Al. Their measurements were made for diffusion temperatures of 1050°C, 1150°C, and 1250°C. For each of these temperatures, they found that the diffusion coefficient had a minimum value in the vicinity of the 50 atomic percent cobalt composition. Furthermore, the activation energies calculated from these data had a maximum value at the same composition. Nix and Jaumot concluded that their data showed that the excess vacancies V(Co) in the aluminum-rich alloys did increase the diffusion rate. They argued that at the relatively high temperatures of the diffusion anneals there must exist an appreciable degree of disorder which would permit some of the excess V(Co) to be distributed over the lattice sites in a random fashion. They further suggested that the large numbers of excess V(Co) would greatly increase the probability of a V(Co) being adjacent to a lattice defect (e.g., a cobalt atom in a cube corner or another vacancy). Both these situations would increase the mobility of the vacancies.

The increase in the rate of diffusion with increasing amounts of excess nickel or cobalt is compatible with either an interstitial or a vacancy mechanism. The substitution of nickel or cobalt atoms for the larger aluminum atoms certainly enlarges the interstices. This enlargement could either aid interstitial diffusion or increase the mobility of vacancies. Also, the opportunity for exchange of a Co^{60} atom with a V(Al) would be increased by the replacement of aluminum atoms by nickel or cobalt atoms since this would lead to the creation of additional V(Al) by a process such as V(Ni)+Ni atom$\rightarrow V$(Al) where the nickel atom was one occupying an aluminum site. It is also possible that the operation of a Ring mechanism would be facilitated by the enlargement of the interstices.

For the aluminum-rich alloys, both the replacement of nickel or cobalt by the larger aluminum atoms and the decrease in lattice spacing with increasing aluminum would decrease the interstices. This would be unfavorable to the operation of either an interstitial or a Ring mechanism. However, it might be argued that the presence of the excess vacancies would relax the lattice to a degree sufficient to offset the influence of the decreased interstices on Ring or interstitial diffusion. Such an interpretation would probably suffice to explain the results obtained by Smoluchowski and Burgess for the Ni—Al alloys, where the diffusion coefficients remained essentially constant for the excess nickel compositions. It is considerably more difficult to interpret the data of Nix and Jaumot on this basis, since these authors found that the diffusion coefficients increased with increasing amounts of excess aluminum in the ϵ phase of Co—Al. It seems more reasonable to consider a vacancy mechanism to be responsible for this type of behavior. This involves assuming a sufficient mobility of the defect V(Co) in the manner discussed in the foregoing. In addition, the sharp drop in activation energy for the aluminum-rich alloys is more readily explained by a vacancy mechanism.

Thus, the interpretation of the behavior of the diffusion coefficients for the aluminum-rich defect alloys is critically dependent on the details of the data. In view of the decided lack of agreement between the previous investigations as to the trend of the diffusion coefficients for the defect alloys, it was decided to investigate in more detail the diffusion of Co^{60} in the δ phase of Ni—Al.

THE EXPERIMENT

We studied the diffusion of Co^{60} in six compositions in the δ phase of Ni—Al. Three of these compositions were nickel-rich and three had excess aluminum. The alloys were prepared by melting under vacuum in an induction furnace. The resulting ingots, which were extensively annealed, were cut into samples $\frac{1}{2}$ in.$\times\frac{1}{2}$ in. $\times\frac{1}{8}$ in. The samples used were uniformly free from visible porosity and their grain sizes ranged from one to three mm. The composition was determined by chemical analysis and by x-ray lattice spacing measurements, using the data of Bradley and Taylor in Fig. 1.

Since the alloys were extremely hard and often very brittle, sectioning techniques, using available equipment, were precluded. We used the standard method of surface counting. The use of this method requires knowledge of the absorption of the β rays from Co^{60} by the Ni—Al alloys. Since we were unable to fabricate foils of the alloys sufficiently thin to make useful absorption measurements, we obtained the absorption in

TABLE II. Values of the activation energies Q and diffusion constants D_0 in the equation $D_0e^{-Q/RT}$, for various compositions in the δ phase of Ni—Al.

Atom percent nickel	47.3	48.5	49.4	50.7	53.1	55.5
Q (kcal/mol)	56.6	59.9	52.5	80.6	67.6	47.1
D_0 (cm²/sec)	4.7×10^{-3}	9.3×10^{-3}	4.4×10^{-3}	57.7	2.6	7.2×10^{-3}

[4] F. C. Nix and F. E. Jaumot, Jr., Phys. Rev. 83, 1275 (1951).

nickel and aluminum foils and combined these data to give the absorption in the alloys. These data revealed a considerable departure from exponential absorption; this phenomenon is discussed more fully in another paper.[5]

Co^{60} was evaporated onto the polished faces of the samples. Pairs of samples of the same composition and similar surface activities were annealed with active faces together. Six compositions were given diffusion anneals in vacuum at 1150°C, 1250°C, and 1350°C, for 24, 18, and 12 hours, respectively. Four compositions were annealed at 1050°C for 18 hours. A minimum of three pairs of samples of each composition were used at each temperature investigated. The summed activity of a pair was used to calculate the diffusion coefficients.

RESULTS

The results of the diffusion measurements are presented in Tables I and II. Figures 2 and 3 are semilog plots of the diffusion coefficient *versus* reciprocal temperature for the excess aluminum alloys and the excess nickel alloys, respectively. The data spreads in Figs. 2 and 3 indicate the extreme values of the diffusion coefficients measured at the given temperature and composition. The straight lines were drawn according to a least squares fit of the data for the three highest temperatures. The data at 1050°C are much less reliable

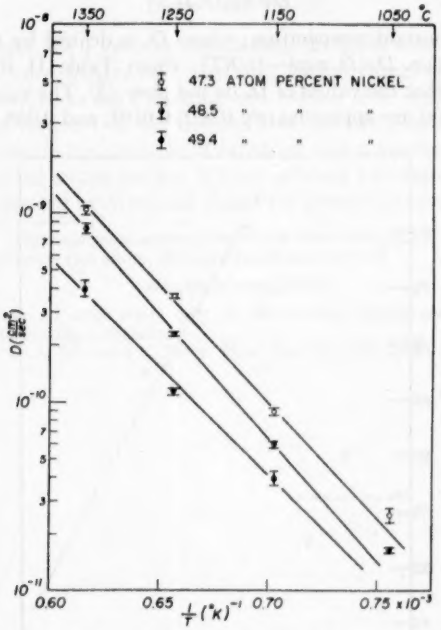

FIG. 2. Values of the diffusion coefficients for excess aluminum alloys in the δ phase of Ni—Al.

[5] Submitted to the *Journal of Applied Physics*. A brief report of this behavior was presented at the 1954 Michigan Meeting of the American Physical Society, see A. E. Berkowitz, Phys. Rev. 94, 1407 (1954).

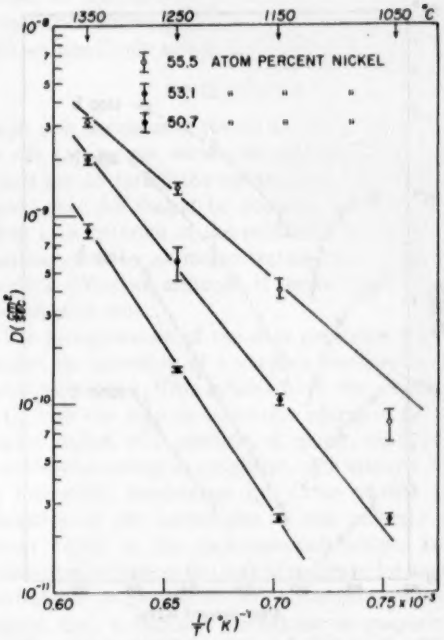

FIG. 3. Values of the diffusion coefficients for the excess nickel alloys in the δ phase of Ni—Al.

than those for the higher temperatures. The reasons for this relative unreliability are the following: First, the diffusion anneals at 1050°C were rather short (18 hours) so that the mean diffusion distance was within the anomolous β-absorption region[5] which resulted in the surface activities after diffusion being greater than those before diffusion. Not only did this involve a larger probable error, but it also indicated that an appreciable amount of undiffused Co^{60} remained on the surface of the samples. Second, we used Lavite sample holders for the 1050°C anneals. Although these holders were carefully cleaned and baked in vacuum, there was considerable outgassing during the diffusion anneals which resulted in some contamination of the samples. This difficulty was eliminated in subsequent anneals at higher temperatures by using sample holders made of pure aluminum oxide. For these reasons and because of the scatter in the positions of the 1050°C data with respect to the straight lines in Figs. 2 and 3, we do not feel justified in basing any conclusions on the lower temperature data. The probable error for the three higher temperatures was estimated to be 15 percent for each point. From the data spread and the fit to the straight lines, it seems that this estimate is somewhat too high.

In Fig. 4, the diffusion coefficients are plotted against composition for the four annealing temperatures. The composition spreads indicate the difference between the chemical analyses and the x-ray measurements. Figure 4 shows very clearly that for each of the annealing

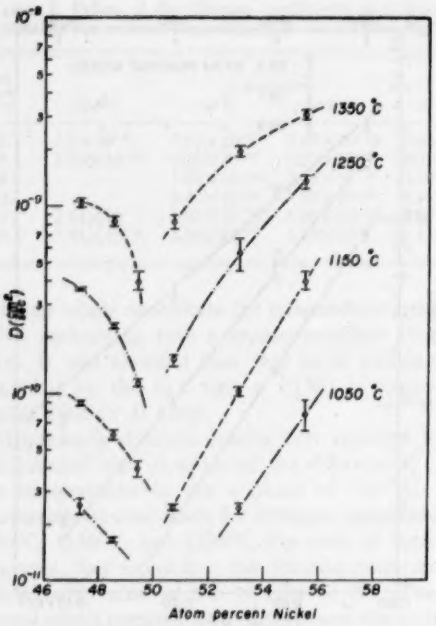

FIG. 4. The composition dependence of D in the δ phase of Ni–Al.

temperatures, the diffusion coefficients have a minimum value in the vicinity of 50 atomic percent nickel. The absence of any overlap in the data spreads for adjacent compositions indicates that the general trend of the diffusion coefficients is as shown in Fig. 4.

In Fig. 5, the activation energy is plotted as a function of composition. The activation energy was obtained from the slopes of the straight lines in Figs. 2 and 3. On the basis of the extreme values of the slopes of the straight lines that can be drawn through the data spreads in Figs. 2 and 3, we can assign a probable error of less than 10 percent to the values of the activation energies. The dashed curve in Fig. 5 serves only to indicate the general trend of the activation energies. Considerably more data would be necessary to define the structure of the curve accurately. However, we have no reason to doubt that the dashed curve represents the general behavior of the activation energies.

DISCUSSION

A fairly simple interpretation of the behavior of the activation energies can be made in terms of a vacancy model. In general, the vacancy mechanism predicts that[6]

$$D \propto Ae^{-Q_f/RT}e^{-Q_e/RT};$$

where $Ae^{-Q_f/RT}$ = fractional concentration of vacancies at thermal equilibrium (Q_f being the energy required for formation of a vacancy), and Q_e = energy required for exchange of a vacancy with a neighbor. When the vacancies are present only in the normal equilibrium concentration the activation energy measured is

$$Q = Q_f + Q_e.$$

If $n(v)$ = fractional concentration of excess defect vacancies, we have $n(v) \gg Ae^{-Q_f/RT}$. In addition, if we assume that the excess vacancies in the aluminum-rich alloys are sufficiently mobile,

$$D \propto n(v)e^{-Q_e/RT}. \quad (1)$$

On this model the activation energy measured for the excess aluminum alloys is only Q_e. The fact that Fig. 5 indicates that Q_e is essentially constant for the aluminum-rich alloys is reasonable if one considers that the excess V(Ni) must exchange with a nearest neighbor. Bradley and Taylor have shown that the nearest neighbors to nickel sites are all aluminum atoms, irrespective of the composition of the excess aluminum alloys. Furthermore, if this model is correct, then the difference between the maximum activation energy measured for the nickel-rich alloys, and Q_e should correspond to Q_f. Assuming that Q_e is the approximately constant value of the activation energy for the aluminum-rich alloys, Q_f is calculated to be about 23 kcal/mole, which is a very reasonable value. From (1) and the constant value of Q_e for the aluminum-rich alloys it follows that for these defect alloys,

$$D \propto n(v) \propto D_0 \quad (2)$$

for constant temperature; where D_0 is defined by the equation $D = D_0 \exp(-Q/RT)$. From Table II it is seen that the values of D_0 do not obey (2). The values for $n(v)$ are approximately 0.002, 0.0195, and 0.038 for

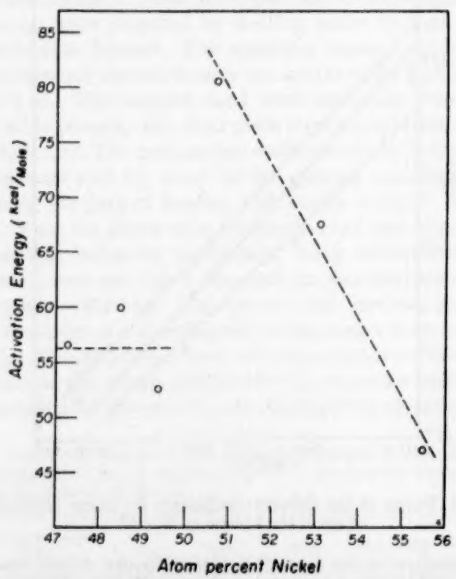

FIG. 5. Values of the activation energies for various compositions in the δ phase of Ni–Al.

[6] A. D. Le Claire, *Progress in Metal Physics* (Interscience Publishers, Inc., New York, 1953), Vol. 4.

49.4, 48.5, and 47.3 atomic percent nickel, respectively. However, since D_0 is so very sensitive to small errors in Q, the estimated probable error for Q includes values of D_0 which are in line with (2). Furthermore, we can test the validity of the left-hand side of (2), i.e., $D \propto n(v)$, using the data for the aluminum-rich alloys. We normalize the values for D, for each temperature, to the value of D at 47.3 atomic percent nickel. If we average these normalized D values for the three highest temperatures and plot these averages against $n(v)$ we find an almost linear dependence. That is, if

$$A_j=\tfrac{1}{3}\sum_i \frac{D_j^i}{D_{47.3}^i}, \quad \begin{matrix} i=1150°C,\ 1250°C,\ 1350°C, \\ j=47.3,\ 48.5,\ 49.4 \text{ atomic percent nickel,} \end{matrix}$$

then $A_j \propto n(v)_j$. That this linear dependence is present may, of course, be entirely fortuitous. However, it is interesting to note that the spread in the A_j values is much smaller than would be expected from the estimated probable error of 15 percent for the individual D values. A significant implication of the relation $A_j \alpha n(v)$ is that $D_0 \alpha n(v)$. This follows from the fact that if $Q=Q_e$ for the aluminum-rich alloys, then

$$A_j=\left\langle \frac{(D_0)_j}{(D_0)_{47.3}} \right\rangle_{Av}.$$

A commonly accepted interpretation[6] of D_0 is[7]

$$D_0=a^2\nu \exp(\Delta S/R), \tag{3}$$

where, for a vacancy mechanism, ΔS is the sum of the entropy changes associated with the free energy changes involved in the formation and motion of a vacancy in the lattice, ν is the frequency of the vibration of the atoms in the direction of exchange with a vacancy, and a is the lattice spacing. We can estimate ν in the manner suggested by Wert and Zener[8] for interstitial motion of atoms, by assuming that the potential energy of an atom varies sinusoidally as it exchanges with a vacancy with an amplitude equal to Q_e. This assumption gives

$$\nu=(Q_e/2ma^2)^{\frac{1}{2}},$$

where m is the mass of the atom. Using this expression for ν in (3), we get, within the probable error, positive values for ΔS for all the compositions. Since it can be shown that ΔS should be positive, this is sometimes taken as a criterion of the reliability of the D_0 value. However, it is by no means certain that (3) applies to chemical diffusion, although it seems to hold for most self-diffusion data.

The interpretation of the data presented above also implies the operation of a vacancy mechanism for the nickel-rich alloys. This follows from the identification of Q_f with the drop in activation energy at 50 atomic percent nickel. It is possible, of course, that this drop in activation energy is consistent with either a Ring or an interstitial mechanism by virtue of the general relaxation in the lattice due to the presence of the excess V(Ni) in the aluminum-rich alloys. For this reason and because of the lack of evidence for a vacancy mechanism in body-centered structures, we cannot suggest that a vacancy mechanism is uniquely compatible with our data for the nickel-rich alloys.

In summary, we feel that the data shows that the excess vacancies in the defect alloys markedly influence the rate of diffusion. Although several interpretations of the data can be offered with respect to the mechanism of diffusion, we feel that a vacancy mechanism is most strongly indicated, especially for the defect alloys. The abruptness and magnitude of the changes in the diffusion coefficients and activation energies at the stoichiometric composition suggest a vacancy mechanism. Also, a simple interpretation of the general trends of the diffusion coefficients and activation energies can be made in terms of a vacancy model. In particular, a reasonable value for the energy for formation of a vacancy can be identified. In addition, the variation of the diffusion coefficients with defect vacancy concentration can be satisfactorily explained.

[7] This expression applies only to the nickel-rich alloys. For the aluminum-rich alloys, the appropriate expression is

$$D_0=n(v)a^2\nu \exp(\Delta S/R),$$

where ΔS now refers only to the entropy change associated with moving a vacancy.

[8] C. A. Wert and C. Zener, Phys. Rev. **76**, 1169 (1949).

Scattering of Ions by Polarization Forces

ERICH VOGT* AND GREGORY H. WANNIER
Bell Telephone Laboratories, Murray Hill, New Jersey

(Received May 19, 1954)

The interaction potential of a charge carrier and a gaseous atom is attractive at large distances, varying as r^{-4}. This potential has simple classical properties since it has a cross section which varies inversely as the speed. For most ions the mechanism which removes the singularity of the potential is irrelevant classically—we find that this is also the case in quantum theory: the well-known indeterminacy of the wave function for singular potentials can be removed in an obvious way and a cross section of the capture type can be computed. This cross section oscillates sinusoidally about its classical value but has apparently no average deviation over one cycle, even when the de Broglie wavelength is long. In the limit of low velocities, the quantum-mechanical cross section has twice the classical value. These two facts combine to make the classical law of variation of the cross section approximately valid even in the quantum range.

I. INTRODUCTION

WHEN gaseous ions or electrons move through a gas whose molecules are not too large, then the two interact according to the law

$$V=-\tfrac{1}{2}e^2\alpha/r^4, \tag{1}$$

where e is the ionic charge, α the molecular polarizability, and r the distance between the ion and the molecule. The classical theory of the motion under this force is simple because the cross sections derived from this force are proportional to $1/v$, where v is the relative velocity. This feature of the classical theory can be derived from a dimensional argument. The cross sections must be constructed from the quantities $e^2\alpha$, v, and m, where m is the reduced mass. This construction can be made only in a single way, namely,

$$\sigma=\text{const}(e^2\alpha/mv^2)^{\frac{1}{2}}, \tag{2}$$

where the constant is a pure number. However, this simple result of classical mechanics will be modified if the relative velocity is so small that the square of the de Broglie wavelength,

$$\lambda^2=\hbar^2/m^2v^2, \tag{3}$$

becomes comparable with the cross section (2). This can easily occur in practical situations. The question of interest is: what modifications does quantum theory introduce into the classical description of the motion of ions in gases?

It is a common experience in modern physics to find an analogy between classical and quantum results which goes beyond the limiting law of quantum mechanics. This is particularly true for simple classical results such as Rutherford's law or the resonance frequency of a harmonic oscillator. Since we are dealing here with another simple classical answer, it is of interest to see how this becomes modified in quantum theory. This is a second point of interest in the problem.

A third point of interest is provided by the fact that we have here a simple case of a singular potential, that is, a case in which the negative energy states cannot be quantized. Such states have been considered in the study of Case.[1] Case points out that the attractive potential is always terminated in reality by a repulsive wall and that this wall will determine the choice of the phase of the rapidly oscillating wave function. While this observation is undoubtedly true, in a great number of physical situations the choice of phase at the repulsive wall is very complicated. Further, this manner of pointing out that the singular potentials are "really" not singular is actually side-stepping the issue; there are many classical situations, generally in the positive energy spectrum, where the presence of a repulsive term in addition to (1) has no importance; furthermore, when it is important the simple classical properties just described are destroyed. Extremely complicated treatments are then required as, for instance, those of Langevin,[2] Hassé and Cook,[3] and others. Hence, to follow up the suggestion of Case of introducing the repulsive wall explicitly into the theory would simply mean making a difficult problem needlessly more complicated. Analogy with classical physics suggests that there must be a way of removing the ambiguity of the wave function by physical reasoning, without appeal to an irrelevant repulsive force. Indeed, the ambiguity is present in classical physics also: there exist separate ingoing and outgoing spiralling orbits rather than a single hyperbolic type orbit which combines the ingoing and the outgoing features in a fixed way. Hence, whatever argument is used to remove the ambiguity in the latter case should also be applicable in some form to the former.

II. CLASSICAL AND ELEMENTARY QUANTUM DESCRIPTION OF THE $-1/r^4$ POTENTIAL

The wave equation for a particle moving in the potential (1) is

$$\nabla^2\psi+\frac{A^2}{r^4}\psi+\frac{q^2}{A^2}\psi=0, \tag{4a}$$

* Now at Palmer Physical Laboratory, Princeton, New Jersey.

[1] K. M. Case, Phys. Rev. **80**, 797 (1950).
[2] P. Langevin, Ann. chim. et phys. **5**, 245 (1905).
[3] H. R. Hassé and W. R. Cook, Phil. Mag. **12**, 554 (1931).

where

$$A=(e^2\alpha m/\hbar^2)^{\frac{1}{4}}, \tag{5}$$

$$q=A(mv/\hbar)=(2e^2\alpha m^2E/\hbar^4)^{\frac{1}{4}}. \tag{6}$$

A has the dimensions of a length; q is a dimensionless quantity giving the De Broglie wave vector in terms of this length. The Hamilton-Jacobi equation for the particle moving in the potential (1) is

$$(\nabla S)^2=\frac{A^2}{r^4}+\frac{q^2}{A^2}. \tag{4b}$$

For zero q we may apply to (4a) and (4b) the substitution

$$u=1/r, \tag{7}$$

yielding, respectively,

$$\nabla_u^2\left(\frac{1}{u}\psi\right)+A^2\left(\frac{1}{u}\psi\right)=0, \tag{8a}$$

$$(\nabla_u S)^2=A^2, \tag{8b}$$

while for finite q the substitution

$$\rho=A^2/qr \tag{9}$$

yields

$$\nabla_\rho^2\left(\frac{1}{\rho}\psi\right)+\frac{A^2}{\rho^4}\left(\frac{1}{\rho}\psi\right)+\frac{q^2}{A^2}\left(\frac{1}{\rho}\psi\right)=0, \tag{10a}$$

$$(\nabla_\rho S)^2=\frac{A^2}{\rho^4}+\frac{q^2}{A^2}. \tag{10b}$$

Equations (8a) and (8b) show that, in both classical and quantum theory, the zero-energy case is equivalent to the free particle problem for finite energy. The case of finite energy, on the other hand, is mapped upon itself by inversion since the Eqs. (10) are identical in form to (4). The radius r_0 of the circle of symmetry is obtained from (9) as

$$r_0=A/q^{\frac{1}{4}}. \tag{11}$$

It follows from the above that the classical orbits at zero energy are straight lines through the origin if the angular momentum is zero and circles through the origin if it is finite. In the former case the sense of motion can be either away from or toward the scattering center; in the latter case the two types are linked in a fixed way because the orbit is bound. In the same way Eq. (15) has two solutions of zero angular momentum,

$$\psi_{0,+}=e^{iA/r}, \tag{12}$$

$$\psi_{0,-}=e^{-iA/r}, \tag{13}$$

which are distinguished by their sense of motion. For finite angular momentum, on the other hand, only the function

$$\psi_l=\frac{1}{r^{\frac{1}{4}}}J_{l+\frac{1}{2}}\left(\frac{A}{r}\right)Y_{l,m}(\theta,\varphi) \tag{14}$$

is possible. In analogy to the classical case this wave function links ingoing and outgoing waves in a fixed way and vanishes at large distance.

When we now pass from zero to positive energy the classical picture changes as follows. For small angular momentum the orbits are similar to the straight lines discussed previously: they are spirals passing through the center of force and reaching to infinity. For large angular momentum there is no qualitative change; the bound orbits remain bound; however, because of the internal symmetry just discussed there is a second orbit which results from a bound one by inversion at the circle of symmetry. This second orbit is a dibrachoid similar to the hyperbola familiar from the case of $1/r^2$ forces. The two types of orbits are separated from each other by limiting orbits such as

$$r=\frac{A}{q^{\frac{1}{4}}}\coth\frac{\varphi}{\sqrt{2}}, \tag{15}$$

in which the particle cannot make up its mind where to go and thus ends up, asymptotically, on the circle of symmetry. The impact parameter b_0 for this orbit is

$$b_0=\sqrt{2}A/q^{\frac{1}{4}}=\sqrt{2}r_0. \tag{16}$$

It defines a simple intrinsic cross section for this potential, that is, the cross section for spiralling orbits or capture cross section σ_0,

$$\sigma_0=\pi b_0^2=2\pi A^2/q=2\pi(e^2\alpha/mv)^{\frac{1}{2}}. \tag{17}$$

The form of it is, of course, in agreement with (2). Figure 1 shows the classical pattern of orbits resulting from a uniform ion stream. The critical impact parameter b_0 is clearly discernible.

It has been pointed out elsewhere[4] that the capture

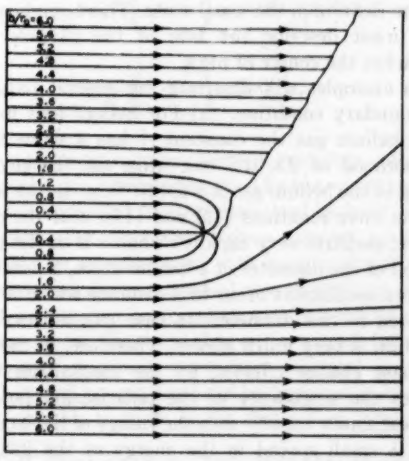

FIG. 1. The pattern of classical orbits for the $-1/r^4$ potential. The same pattern applies in quantum theory for large energy except for local corrections behind the scattering center.

[4] G. H. Wannier, Bell System Tech. J. 32, 70 (1953), Sec. IIIB.

cross section σ_0, defined by (17), is a good approximation to the usual kinetic type of cross section,

$$\sigma_k=\int(1-\cos\theta)d\sigma. \tag{18}$$

The reason for this fact is that the final directions of the spiralling orbits are very nearly random—$\langle\cos\theta\rangle=0$—, whereas the deflections in the dibrachoids are so small that the latter type of scattering events make a small contribution to an integral of the above type. Because of this the capture cross section is a generally useful expression. The development which follows will discuss principally the quantum-mechanical analog of this classical capture cross section.

Without calculation the behavior of the wave functions, for finite energy, can be understood in analogy to the classical picture. There will now be two wave functions for finite as well as zero angular momentum, in analogy to the independent existence of ingoing and outgoing spirals. Furthermore, in contradistinction to the classical case, there will be no finite angular momentum where this behavior ceases, since the classical decomposition of the orbit into two independent pieces arises because there is a belt in which the potential of the centrifugal force is stronger than the total kinetic energy available. This type of separation is not complete in quantum mechanics because of the tunnel effect. Hence, there will be two permissible radial wave functions at all angular momenta. These two wave functions can be distinguished either by their behavior near the origin, where they can behave like (12) or (13), or else by their behavior at large distances, where they behave as $(1/r)e^{iqr/A}$ or $(1/r)e^{-iqr/A}$. Connection formulas will link any three of these asymptotic forms. An extra boundary condition must be imposed to make the problem definite in the usual sense. This boundary condition must describe the fate of the particle as it approaches the center of force.

Two examples will illustrate the general nature of this boundary condition. (a) For helium ions moving in the helium gas the constant A has a value in the neighborhood of 2×10^{-7} cm, while for (b) electrons moving in the helium gas $A\approx6\times10^{-9}$ cm. In the former case the wave functions (12) and (13), near the center of force, oscillate very rapidly: when r is in the neighborhood of the diameter of a helium atom, a number of complete oscillations occur in a distance which is small compared to this diameter. In case (b), however, the oscillation is very much slower. Therefore, in case (a), the phase change effected by the mechanism which removes the singularity of the polarization potential varies extremely rapidly with the energy of the incoming wave. A small spread in the energy of the incoming wave will make the outgoing wave incoherent. Thus, the proper boundary condition is obtained by treating the origin of co-ordinates as a sink. In case (b) the total change of phase is always comparatively small. Only the s-wave phase shift η_0 is large[5] and it is never larger than 3π. The detailed properties of the "repulsion" mechanism are therefore important here—the coherently scattered waves yield the familiar Ramsauer-Townsend effect.

For most ions other than electrons the physical situation is similar to the example (a), above. The detailed properties of the "repulsion" mechanism are irrelevant just as in the classical description of this motion. On the other hand, when the properties of the "repulsion" mechanism are important, as in case (b) above, then the classical description becomes very complicated and in quantum theory the involved prescription of Case[1] is necessary. Our discussion will be limited to those cases in which the origin of coordinates may be considered as a sink.

With the definition of the origin as a sink the wave function near the origin consists entirely of ingoing waves and hence behaves as

$$[\psi]_{r\to0}\sim e^{iA/r}g(\theta). \tag{19}$$

This, together with the usual specification that the wave function at large distance behave as

$$[\psi]_{r\to\infty}\sim e^{iqz/A}+f(\theta)(1/r)e^{iqr/A}, \tag{20}$$

completely determines the wave function. The capture cross section σ_c is then obtained by computing the flux entering the sink at the origin divided by the flux density in the plane wave, that is

$$\sigma_c=\frac{A^2}{q}\int|g(\theta)|^2d\Omega. \tag{21}$$

For small energy the program just outlined can be implemented immediately. If the energy is so small that $e^{iA/r}$ has reached unity before $e^{iqz/A}$ differs materially from this value, that is, if $q\ll1$, then the two limiting functions may simply be patched together by multiplication, yielding the wave function

$$\psi\approx e^{i(A/r+qz/A)}. \tag{22}$$

Figure 2 shows the streamlines resulting from this procedure. The resemblance of these streamlines to the classical orbits of Fig. 1 is marked. There exists even in this extreme quantum limit an impact parameter b_{lim} separating capture and escape; its shift in location from Fig. 1 is small. From (21) and (22) the cross section is found to be[6]

$$\sigma_c=4\pi A^2/q=4\pi(e^2\alpha/mv^2)^{\frac{1}{2}}. \tag{23}$$

This is exactly twice the classical capture cross section

[5] H. S. W. Massey and E. H. S. Burhop, *Electronic and Ionic Impact Phenomena* (The Clarendon Press, Oxford, 1952), p. 118.

[6] There are rigorous methods of deriving (23) which will not be discussed here. We hope to extend them so as to gain a procedure valid at small as well as zero velocity.

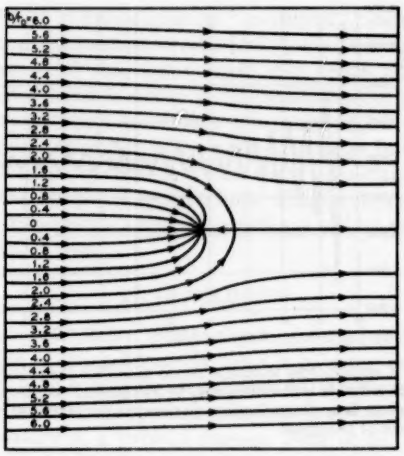

FIG. 2. Streamlines for the extreme quantum case (small energy). Comparison with Fig. 1 shows a strong resemblance of these two extreme situations.

(17). It appears surprising at first sight that this extreme quantum case does not contain h at all. Upon reflection, we can understand the answer on dimensional grounds, as follows. If the energy is made small enough the capture process becomes independent of energy because the wave function (22) becomes identical to (12). Anything derived from this wave function must then be proportional to the particle density D outside the scattering center; hence the inward flux I must also be proportional to this density:

$$I=\text{const}\,D.$$

Now the cross section is defined as

$$\sigma=I/Dv.$$

Combining the two predictions, we find that σ must vary as $1/v$. Now there is only one way in which an area can be made up out of (2) and (3) in such a way that it varies as $1/v$, namely by using only (2). Hence the result (23) follows.

For finite energies the wave function is not as easily written down. To obtain it requires a study of the Mathieu differential equation of imaginary argument.

III. THE QUANTUM-MECHANICAL CAPTURE CROSS SECTION

The radial equation obtained from the Schrödinger Eq. (4) is

$$\frac{\partial^2\psi}{\partial r^2}+\frac{2}{r}\frac{\partial\psi}{\partial r}-\frac{l(l+1)}{r^2}\psi+\frac{A^2}{r^4}\psi+\frac{\alpha^2}{A^2}\psi=0. \tag{24}$$

If we substitute

$$\psi=\varphi/r^{\frac{1}{2}}, \tag{25a}$$

$$r=r_0e^z, \tag{25b}$$

where r_0 is given by (11), then the radial equation becomes

$$\frac{d^2\varphi}{dz^2}-[(l+\tfrac{1}{2})^2-2q\cosh 2z]\varphi=0, \tag{26}$$

which is Mathieu's equation of imaginary argument.[7] The transformation (25) has mapped the radius of symmetry r_0 on the origin; small values of $r(1/r\gg 1/r_0)$ have become large negative values of z and large values of r ($r\ll r_0$) have become large positive values of z.

The asymptotic behavior of the solutions of (24) at large distance is

$$\varphi(r)\sim\frac{1}{r^{\frac{1}{2}}}e^{\pm iqr/A}. \tag{27}$$

They are the Mathieu analogs of the Hankel functions, that is, the functions $he^{(1)}$ and $he^{(2)}$, defined in (29) and (30) of reference 7. Near the sink at the origin we find the behavior

$$\varphi(r)\sim(r)^{\frac{1}{2}}e^{\pm iA/r}. \tag{28}$$

The solutions with this behavior are the two remaining Hankel-type functions $he^{(3)}$ and $he^{(4)}$. More exactly, we have, for large r,

$$\frac{1}{r^{\frac{1}{2}}}he_l^{(1)}\left(i\ln\frac{r}{r_0}\right)\sim e^{-i\pi/4}\left(\frac{A}{q}\right)^{\frac{1}{2}}\frac{1}{r}e^{-iqr/A}, \tag{29}$$

$$\frac{1}{r^{\frac{1}{2}}}he_l^{(2)}\left(i\ln\frac{r}{r_0}\right)\sim e^{i\pi/4}\left(\frac{A}{q}\right)^{\frac{1}{2}}\frac{1}{r}e^{iqr/A}, \tag{30}$$

and for small r,

$$\frac{1}{r^{\frac{1}{2}}}he_l^{(3)}\left(i\ln\frac{r}{r_0}\right)\sim e^{-i\pi/4}\frac{1}{A^{\frac{1}{2}}}e^{-iA/r}, \tag{31}$$

$$\frac{1}{r^{\frac{1}{2}}}he_l^{(4)}\left(i\ln\frac{r}{r_0}\right)\sim e^{i\pi/4}\frac{1}{A^{\frac{1}{2}}}e^{iA/r}. \tag{32}$$

$he_l^{(1)}$ and $he_l^{(2)}$ together form a complete solution of (26) and so do $he_l^{(3)}$ and $he_l^{(4)}$. The boundary condition (19) demands that the solutions used be $he_l^{(4)}$, and the condition (20) that the various angular momentum solutions be superimposed with such multipliers as to make the incoming spherical waves at large distance [that is the types $he_l^{(1)}$] agree with the contribution of a plane wave. To carry this out we need the decomposition of a plane wave into spherical harmonics, which is well known,[8] and the behavior of $he_l^{(4)}$ at large distance; this is given in the connection formula (64)

[7] G. H. Wannier, Quart. Appl. Math. **11**, 33 (1952). Our equation is equivalent to Eq. (3) of this reference. Most of the properties of the Mathieu equation required for our development are to be found there.

[8] N. F. Mott and H. S. W. Massey, *The Theory of Atomic Collisions* (Clarendon Press, Oxford, 1949), Sec. II, p. 1.

of reference 7.

$$he_l^{(4)} = -ie^{\Phi} he_l^{(2)} + (ie^{\Phi}\cos\pi\beta - \cos\pi\gamma) he_l^{(1)}. \quad (33)$$

Here Φ is a real function of the equation parameters which is discussed in Sec. (2) of reference 7; β and γ are also functions of the equation parameters, the only property of which this discussion requires is that

$$i\sin\pi\gamma/\sin\pi\beta = e^{\Phi}, \quad (34)$$

and that $\cos\pi\beta$ and $\cos\pi\gamma$ are always real. Carrying out these operations, we find for the wave function

$$\psi = \tfrac{1}{2}\left(\frac{A}{rq}\right)^{\frac{1}{2}} e^{3i\pi/4} \times \sum_{l=0}^{\infty} \frac{(-)^l(2l+1)P_l(\cos\theta) he_l^{(4)}(i\ln r/r_0)}{ie^{\Phi}\cos\pi\beta - \cos\pi\gamma}. \quad (35)$$

The radial current flowing toward the origin can be found anywhere in principle. We shall do it here by the method indicated in (19) and (21). We find

$$g(\theta) = -\frac{1}{2q^{\frac{1}{2}}} \sum_{l=0}^{\infty} \frac{(-)^l(2l+1)P_l(\cos\theta)}{ie^{\Phi}\cos\pi\beta - \cos\pi\gamma}, \quad (36)$$

and hence, with the help of (34),

$$\sigma_c = \frac{A^2}{\pi q^2} \sum_{l=0}^{\infty} \frac{2l+1}{1+e^{2\Phi}}. \quad (37)$$

Comparison with Eq. (17) yields

$$\sigma_c/\sigma_0 = \frac{1}{2q} \sum_{l=0}^{\infty} \frac{2l+1}{1+e^{2\Phi(l+\frac{1}{2},q)}}, \quad (38)$$

as the ratio of the quantum-mechanical capture cross section to its classical analog.

The result of the above development, although exact, imparts only an imperfect knowledge of the capture cross section σ_c. The reason for this is the appearance of the function $\Phi(l+\frac{1}{2}, q)$ which is exactly defined, but only approximately known. In reference 7, Sec. 2, a lower limit Φ_0 and two upper limits Φ_1 and Φ_2 are derived [Eqs. (16), (24), and (27)], which bracket it quite closely for large l and q. Asymptotic expansions of the cross section σ_c for large velocity are derived in the Appendix. If $\frac{1}{2}(\Phi_0+\Phi_1)$ is used for Φ, the result is formula (y) for σ_c, or (z) for the ratio σ_c/σ_0. The curve in Fig. 3 illustrates the result (z). This curve must be qualified by a statement about the accuracy of the asymptotic expansion (z) and about the intrinsic error caused by the lack of knowledge of Φ.

Calculations of individual points on the plot of Fig. 3 can be made without reliance on an asymptotic expansion, namely, by summing (38) directly by numerical methods. Such calculations are indicated by rings in Fig. 3. [Near $2q=100$ the numerical points are actually more dense than shown; they prove that the asymptotic expansion is accurate to less than 0.02 percent, in this neighborhood; this justifies its use also for values of q, which are larger.]

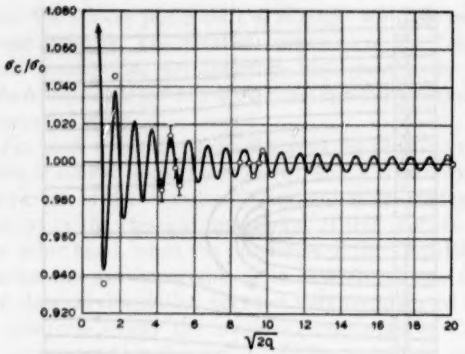

FIG. 3. Capture cross section σ_c *versus* speed for the polarization force. The ordinate is the ratio of σ_c to its classical counterpart σ_0. The abscissa is a dimensionless parameter proportional to the spuare root of the speed.

The error caused by the lack of knowledge of Φ is indicated by the vertical bars attached to some of the rings in Fig. 3. This error becomes larger as the energy becomes smaller; this, in fact, makes it very hard to connect the curve to the point $\sigma_c/\sigma_0=2$, for $q=0$, which we can substantiate by other means. We believe that the arithmetic mean of the two limits, $\frac{1}{2}(\Phi_0+\Phi_1)$, which was used to obtain the curve in Fig. 3, is very close to the correct value of Φ over most of the range shown, because it results from a first-order perturbation applied to Φ_0.

The most striking feature in Fig. 3 is the oscillation which the cross section exhibits when plotted against velocity. This can be understood qualitatively from the Bohr theory. If we treat the problem classically but postulate that the impact parameters assume only the discrete values allowed by the quantum condition for the angular momentum, then the capture cross section jumps suddenly each time that b_0 has increased sufficiently to include one more such impact parameter. The result would be a sawtooth oscillation of the cross section about the classical value. In the wave mechanical result the term $1/(1+e^{2\Phi})$ is a smoothed out step function reminiscent of the simple picture. As expected, the sawtooth oscillations of the Bohr theory capture cross section have an amplitude ($\sim 0.5/q^{\frac{1}{2}}$) which is an order of magnitude larger than the amplitude of the sinusoidal oscillation of the quantum-mechanical cross section, but the oscillation period deduced from this picture, coincides exactly with the one exhibited in Fig. 3.

A surprising feature of Fig. 3 is the fact that there is no indication of a steady deviation of the capture cross section from its classical value. This was first noticed in the numerical evaluation of the cross section. This same feature reappears in the asymptotic expan-

sion, where it shows up as an "accidental" cancellation of terms representing steady deviations; thus the final expression (y) does not contain such terms although they are present in earlier partial results such as (u). It appears plausible to us that this maintenance of the classical cross section in the mean is an exact feature of the quantum mechanics of the $-1/r^4$ potential. However, the method employed here, with its dependence on an imperfectly known Φ, could not yield a proof of this fact, if true.

IV. CONCLUSION

It has been shown that the quantum-mechanical description of the polarization force is in many respects similar to the classical description of this force. The development of the preceding sections have brought out this analogy in a twofold manner. First of all, it was shown that when the method of removing the singularity of such a potential is irrelevant in classical theory then it is also irrelevant in quantum theory. Within this range of validity the reasoning employed is clearly applicable to all singular potentials, thus offering a simple alternative to the procedure of Case.[1] Secondly, a detailed comparison of the quantum-mechanical capture cross section to its classical analog has been made. The result is summed up in Fig. 3 and Eq. (23). It means that the $1/v$ law for the cross section is correct, within certain limits of error and with specifically known deviations, for all values of the velocity.

The theory of the capture cross section developed above, is valid when the "repulsion mechanism" is unimportant. Expressions for other types of cross sections are obtainable from the wave function (35), but their evaluation is encumbered by the lack of knowledge of the parameter β which occurs in the wave function. A numerical calculation of these cross sections at a few values of q indicated that in quantum theory also the capture cross section makes much the largest contribution to the kinetic cross sections.

APPENDIX

Asymptotic Evaluation of the Capture Cross Section

In evaluating the sum entering into the capture cross section (38), namely

$$S=\sum_{l=0}^{\infty}\frac{2l+1}{1+e^{2\Phi(l+\frac{1}{2},q)}}, \tag{a}$$

we may observe first that it converges rapidly for small values of q. The case of q large is, however, more important. For this case we shall follow the basic procedure of Mulholland[9] of comparing S with the corresponding integral by means of contour integration. The

[9] H. P. Mulholland, Proc. Cambridge Phil. Soc. (London) **24**, 280 (1928).

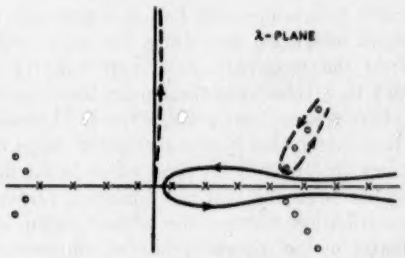

FIG. 4. Path of the contour integrals arising in the evaluation of S. ×—poles of $\tan\pi\lambda$; ○—poles of $1/(1+e^{2\Phi})$; —— Path of integration, Eq. (b); ---- Path of integration, Eq. (c).

function

$$-\pi\tan\pi\lambda$$

has poles of unit strength at the positions $\lambda=\frac{1}{2}, \frac{3}{2}, 5/2, 7/2, \cdots$. Hence, S may be written in the form

$$S=-\frac{1}{i}\int\frac{\lambda\tan\pi\lambda}{1+e^{2\Phi(\lambda,q)}}d\lambda. \tag{b}$$

Here, the contour proceeds in the complex λ plane as shown by the solid curve of Fig. 4, *including* all positive poles of $\tan\pi\lambda$, and *excluding* all negative poles of $\tan\pi\lambda$ and all poles of $1/(1+e^{2\Phi})$. We observe that the two parts of the path of integration on either side of the real axis give conjugate complex contributions. Hence, we may drop one of these parts and write S in the form

$$S=\Re\left[\frac{2}{i}\int_0^{\infty+\epsilon i}\frac{\lambda\tan\pi\lambda}{1+e^{2\Phi}}d\lambda\right],$$

where $\Re[\ ]$ denotes the real part of the bracketed quantity. The path of integration goes through the first quadrant, leaving all poles of $\tan\pi\lambda$ on the right and all poles of $1/(1+e^{2\Phi})$ on the left. Now follows the transformation which Mulholland ascribes to Lindelöf:

$$\tan\pi\lambda=i-\frac{2i}{e^{-2\pi i\lambda}+1},$$

which yields

$$S=\int_0^{\infty}\frac{2\lambda d\lambda}{1+e^{2\Phi}}-\Re\left[\int_0^{\infty+\epsilon i}\frac{4\lambda d\lambda}{(1+e^{2\Phi})(e^{-2\pi i\lambda}+1)}\right].$$

The next step is made possible by the fact that, for large λ, the limits bracketing Φ approach each other. Using the analytic expressions for any of these limits one obtains, for large λ,

$$\Phi\sim 2\lambda\ln(2\lambda/ek), \tag{c}$$

where we have set

$$q=k^2, \tag{d}$$

in accordance with the usual nomenclature for the Mathieu equation. Formula (c) shows that $1/(1+e^{2\Phi})$ decreases exponentially when λ gets large along the

positive real axis, approaches 1 when λ gets large along the positive imaginary axis. On a line asymptotically parallel to the imaginary axis there are the poles $\Phi=\frac{1}{2}(2m+1)\pi i$. Inbetween these poles there are saddle points where $\Phi=m\pi i$ and $1/(1+e^{2\Phi})=\frac{1}{2}$. Therefore, as the path of integration is extended out to large imaginary values, that part of the path which in the limit is infinitely far from the real axis makes a vanishingly small contribution because the second factor in the denominator of the integral produces convergence. It follows that the path of integration in the first quadrant can be broken as shown by the dashed curve of Fig. 4. One integral runs from 0 to $i\infty$, the other is shrunk onto the poles of $1/(1+e^{2\Phi})$. This converts part of the integral back into a sum but of a different type, namely

$$S=\int_0^\infty \frac{2\lambda d\lambda}{1+e^{2\Phi}}-\Re\left[\int_0^{i\infty}\frac{4\lambda d\lambda}{(e^{2\Phi}+1)(e^{-2\pi i\lambda}+1)}\right]$$
$$-\Re\left[\sum_m \oint_{\lambda_1+m}\frac{4\lambda d\lambda}{(e^{2\Phi}+1)(e^{-2\pi i\lambda}+1)}\right]. \quad \text{(e)}$$

Here, $\lambda_1, \lambda_2, \cdots$ are the poles of $1/(1+e^{2\Phi})$ in the first quadrant and the integrals under the summation sign are residue integrals proceeding in the positive sense around these poles.

It is remarkable that we have in (e) a rigorously correct decomposition of the sum S into

1. the corresponding integral;
2. a smoothly varying deviation term;
3. a sum of residues oscillating rapidly with q.

In order to evaluate the quantities in (e) explicitly, Φ should be known as a function of λ. Since only upper and lower limits on Φ are known we shall determine S first using the lower limit Φ_0, and then using the next order approximation, $\frac{1}{2}(\Phi_0+\Phi_1)$. The evaluation will be carried out assuming that q is moderately large. (See Fig. 3.)

Utilizing Φ_0, we consider, first of all, the second term. For k large and λ zero, $2\Phi_0$ equals $-3.4k$, and hence the exponential will be small. This is true, *a fortiori*, along the imaginary axis. Hence we may write

$$\text{second term}=-\int_0^{i\infty}\frac{4\lambda d\lambda}{e^{-2\pi i\lambda}+1}+O(e^{-3.4k}),$$

or

$$\text{second term}=(1/12)+O(e^{-3.4k}). \quad \text{(f)}$$

The procedure for evaluating the two other terms in (e) is based on the fact that they both depend critically only on the variations of Φ near the crossing of the two sets of poles (Fig. 4). Hence an expansion about this crossing point can be substituted for the analytic expressions for Φ which involve elliptic integrals. As a first approximation we set

$$2\Phi=\sigma\lambda^2-\tau, \quad \text{(g)}$$

in which σ and τ are constants. This yields

$$(\text{first term})_1=\frac{1}{\sigma}\ln(e^\tau+1)=\frac{\tau}{\sigma}+O(e^{-\tau k}). \quad \text{(h)}$$

In the case $\Phi=\Phi_0$, we have $\sigma=\pi/2k$, $\tau=\pi k$, and hence

$$(\text{first term})_1=2k^2+O(e^{-\tau k}). \quad \text{(i)}$$

Obviously, this approximation must be improved. We do this by observing that Φ_0 is of the form

$$\Phi_0(\lambda,k)=k\varphi(\lambda/k), \quad \text{(j)}$$

and hence, for $\Phi=\Phi_0$,

$$(\text{first term})=k^2\int_0^\infty\frac{2\xi d\xi}{e^{2k\varphi(\xi)}+1}.$$

Differentiation will remove the leading term just found:

$$\frac{d}{dk}\left(\frac{\text{first term}}{k^2}\right)=-\frac{1}{k^3}\int_0^\infty\frac{\lambda\Phi_0(\lambda,k)d\lambda}{\cosh^2\Phi_0(\lambda,k)}$$
$$=-\frac{1}{k^3}\int_{-\infty}^\infty\frac{\lambda(d\lambda/d\Phi_0)\Phi_0 d\Phi_0}{\cosh^2\Phi_0}+O(e^{-3.4k}). \quad \text{(k)}$$

The error arises here from extending the lower limit of integration beyond $\lambda=0$. The term $\lambda(d\lambda/d\Phi)$ must now be expanded in powers of Φ_0. From the structural relation (j),

$$\lambda\frac{d\lambda}{d\Phi_0}=k\cdot(\text{a function of }\Phi_0/k),$$

or in detail, from reference 7, Eq. (16),

$$\lambda\frac{d\lambda}{d\Phi_0}=\frac{2k}{\pi}+\frac{1}{2\pi^2}\Phi_0+O\left(\frac{\Phi_0^2}{k}\right)+O\left(\frac{\Phi_0^3}{k^2}\right). \quad \text{(l)}$$

Substitution into (k) and subsequent integration yields

$$(\text{first term})_{\Phi=\Phi_0}=2k^2+\frac{1}{25}+O\left(\frac{1}{k^2}\right)+O(e^{-3.4k}). \quad \text{(m)}$$

For the third term in (e) we also start out with a first approximation based on (g), then follow up with a better technique, applicable to Φ_0 only, using (j). In first approximation the poles λ_m are given by

$$\sigma\lambda_m^2-\tau=(2m+1)\pi i, \quad m=0, 1, 2, 3, \cdots. \quad \text{(n)}$$

The third term then takes on the form

$$(\text{third term})_1=-\frac{2\pi}{\sigma}\sum_{m=0}^\infty\frac{\sin 2\pi u_m}{\cosh 2\pi v_m+\cos 2\pi u_m}, \quad \text{(o)}$$

where

$$\lambda_m=u_m+iv_m, \quad \text{(p)}$$

and u_m and v_m are positive. For large k, they are ap-

proximately given by

$$u_m \approx \sqrt{2}k, \quad v_m \approx \sqrt{2}(m+\tfrac{1}{2}).$$

Upon substitution of these quantities into (o), the oscillatory character of the third term becomes evident. Another feature also comes out, namely that all terms in the sum are negligible compared to the first because they are of the order $e^{-3\pi\sqrt{2}} \sim 10^{-5}$. Thus dropping all but the first term in (o), and using (n) and (p), we get

$$\text{(third term)}_1$$
$$-\frac{4\pi}{\sigma}\left\{\exp\left(-\frac{\pi^2}{(\sigma\tau)^{\frac{1}{2}}}\right)\sin\left[2\pi\left(\frac{\tau}{\sigma}\right)^{\frac{1}{2}}+O\left(\frac{1}{k}\right)\right]\right.$$
$$\left.-\exp\left(-\frac{2\pi^2}{(\sigma\tau)^{\frac{1}{2}}}\right)\sin\left[4\pi\left(\frac{\tau}{\sigma}\right)^{\frac{1}{2}}\right]\right\}+O(ke^{-3\pi\sqrt{2}})$$
$$+O\left(\frac{1}{k}e^{-\sqrt{2}\pi}\right)\sin\left[2\pi\left(\frac{\tau}{\sigma}\right)^{\frac{1}{2}}\right]+O\left(\frac{1}{k^2}e^{-\sqrt{2}\pi}\right). \quad \text{(q)}$$

To improve this approximation for $\Phi=\Phi_0$ we still need only the residue at the first pole. Let λ_0 be the value attained by λ when Φ_0 equals $\frac{1}{2}\pi i$. Then we may write

$$\text{(third term)} = -\Re\left[\frac{4\lambda_0\left(\frac{d\lambda}{d\Phi_0}\right)_{\lambda=\lambda_0}}{e^{-2\pi i\lambda_0}+1}\right.$$
$$\left.\times\oint^{(\frac{1}{2}\pi i)}\frac{d\Phi_0}{e^{2\Phi_0}+1}\right]+O(ke^{-3\sqrt{2}\pi})$$
$$=\Re\left[\frac{4\pi i\lambda_0\left(\frac{d\lambda}{d\Phi_0}\right)_{\lambda=\lambda_0}}{e^{-2\pi i\lambda_0}+1}\right]+O(ke^{-3\sqrt{2}\pi});$$

or, substituting (p) and dropping superfluous indices,

$$\text{(third term)} = -\frac{4\pi\Re\left[\lambda\frac{d\lambda}{d\Phi_0}\right]_{\lambda=\lambda_0}\sin 2\pi u}{e^{2\pi v}+2\cos 2\pi u}$$
$$-\frac{4\pi\Im\left[\lambda\frac{d\lambda}{d\Phi_0}\right]_{\lambda=\lambda_0}(\cos 2\pi u+e^{-2\pi v})}{e^{2\pi v}+2\cos 2\pi u}. \quad \text{(r)}$$

u and v can be found from the power series (*l*), with $\Phi_0=\pi i/2$. This yields

$$u=\sqrt{2}k\left[1+\frac{3}{32k^2}+O\left(\frac{1}{k^4}\right)\right], \quad \text{(s}_1\text{)}$$

$$v=\frac{1}{\sqrt{2}}+O\left(\frac{1}{k^2}\right). \quad \text{(s}_2\text{)}$$

We can now write the third term in its final form, adding cosine terms as phase shifts to the sine terms.

$$\text{(third term)}_{\Phi=\Phi_0} = -8ke^{-\sqrt{2}\pi}\sin\left(2\pi\sqrt{2}k+\frac{3\pi\sqrt{2}}{16k}+\frac{1}{8k}\right)$$
$$+8ke^{-2\pi\sqrt{2}}\sin\left(4\pi\sqrt{2}k+\frac{3\pi\sqrt{2}}{8k}+\frac{1}{8k}\right)$$
$$+O\left(\frac{1}{k}e^{-\sqrt{2}\pi}\right)\sin(2\pi\sqrt{2}k)$$
$$+O\left(\frac{1}{k^2}e^{-\sqrt{2}\pi}\right)+O(ke^{-3\pi\sqrt{2}}). \quad \text{(t)}$$

We now combine (f), (m), and (t) to yield (e) for the case $\Phi=\Phi_0$. Calling this result S_0, we get

$$S_0 = 2k^2+\tfrac{1}{8}+O(1/k^2)+O(e^{-3.4k})$$
$$-8ke^{-\sqrt{2}\pi}\sin\left(2\pi\sqrt{2}k+\frac{3\pi\sqrt{2}}{16k}+\frac{1}{8k}\right)$$
$$+8ke^{-2\pi\sqrt{2}}\sin\left(4\pi\sqrt{2}k+\frac{3\pi\sqrt{2}}{8k}+\frac{1}{8k}\right)$$
$$+O\left(\frac{1}{k}e^{-\sqrt{2}\pi}\right)\sin(2\pi\sqrt{2}k)+O(ke^{-3\pi\sqrt{2}}). \quad \text{(u)}$$

We must now consider the modifications imposed upon S if Φ_0 is replaced by $\frac{1}{2}(\Phi_0+\Phi_1)$. Obviously the second term is not modified since Φ terms enter only in the estimation of the error. For the other two terms the change is also a small correction of higher order; it is therefore sufficient to look at the modification in the first order results (i) and (g) when the more accurate values for σ and τ in (g) are employed. The new values are

$$\sigma=\frac{\pi}{2k}-\frac{5\pi}{256k^3}+O\left(\frac{1}{k^5}\right), \quad \text{(v}_1\text{)}$$

$$\tau=\pi k-\frac{13\pi}{128k}+O\left(\frac{1}{k^3}\right). \quad \text{(v}_2\text{)}$$

They yield

correction to the first term

$$=(\tau/\sigma)_{\Phi=\frac{1}{2}(\Phi_0+\Phi_1)}-(\tau/\sigma)_{\Phi=\Phi_0}$$
$$=-\tfrac{1}{8}+O(1/k^2). \quad \text{(w)}$$

In the third term most of the modifications produced are comparable with terms already neglected. The most important exception is a phase shift in the first sine

term which is

phase correction

$$=2\pi\{[(\tau/\sigma)_{\Phi=\frac{1}{2}(\Phi_0+\Phi_1)}]^{\frac{1}{2}}-[(\tau/\sigma)_{\Phi=\Phi_0}]^{\frac{1}{2}}\}$$
$$=-\pi\sqrt{2}/16k. \quad \text{(x)}$$

A similar phase correction in the second sine term will be neglected. Combination of (u), (w), and (x) yields then, for $\Phi=\frac{1}{2}(\Phi_0+\Phi_1)$ and $k^2=q$,

$$S=2k^2-8ke^{-\sqrt{2}\pi}\sin[2\pi\sqrt{2}k+(\sqrt{2}\pi+1)/8k]$$
$$+8ke^{-2\pi\sqrt{2}}\sin[4\pi\sqrt{2}k+O(1/k)]$$
$$+O(1/k^2)+O(e^{-\sqrt{2}\pi}/k)\sin(2\pi\sqrt{2}k)$$
$$+O(ke^{-3\pi\sqrt{2}})+O(e^{-3.4k}). \quad \text{(y)}$$

Inserting this value into Eq. (38) of Sec. III, we end up with the following value for the ratio of the quantum to the classical capture cross section:

$$\frac{\sigma_e}{\sigma_0}=1-\frac{4}{k}e^{-\sqrt{2}\pi}\sin[2\pi\sqrt{2}k+(\sqrt{2}\pi+1)/8k]$$
$$+\frac{4}{k}e^{-2\pi\sqrt{2}}\sin[4\pi\sqrt{2}k+O(1/k)]$$
$$+O\left(\frac{1}{k^4}\right)+O\left(\frac{1}{k^3}e^{-\pi\sqrt{2}}\right)\sin(2\pi\sqrt{2}k)$$
$$+O\left(\frac{1}{k}e^{-3\pi\sqrt{2}}\right)+O\left(\frac{1}{k^2}e^{-3.4k}\right). \quad \text{(z)}$$

PHYSICAL REVIEW VOLUME 95, NUMBER 5 SEPTEMBER 1, 1954

Ionizing Collisions of Very Fast Particles and the Dipole Strength of Optical Transitions

U. FANO
National Bureau of Standards, Washington, D. C.
(Received May 21, 1954)

This note discusses how the Bethe theory of ionizing collisions should be adapted to gases other than atomic hydrogen. Experimental data on primary ionization, analyzed by the method of McClure, yield the value of the total dipole strength for ionization, $\int_I^\infty |x_W|^2 dW$, an atomic property which is otherwise poorly known and whose relationship to the diamagnetic susceptibility should be of interest.

THE primary specific ionization of fast charged particles in gases has been calculated long ago by Bethe.[1,2] His calculation applies specifically to atomic hydrogen, and its application to other gases does not seem to have been developed adequately.[3,4] McClure[4] utilized the general structure of the Bethe theory to express his experimental results—specific ionization *vs* energy of incident electrons—in terms of two empirical constants for each gas. It is proposed, in the present note, to review briefly the pertinent elements of the Bethe theory, to specify the theoretical definition of McClure's constants, and to point out that one of these constants represents an atomic property of considerable interest and is a worthwhile target for systematic experimental study.

The majority of the ionizing collisions of fast particles are of the "glancing" (or "optical") type, with large impact parameters. These collisions affect gas molecules through a short electromagnetic pulse whose spectrum has a practically uniform intensity over the frequency range of interest. The portion of this spectrum most effective in producing ionizations lies in the very far ultraviolet, where the optical properties of different substances have not yet been studied systematically. Therefore, data on ionizing collisions may complement conventional optical studies.

This connection with optical properties takes a precise form through an analysis of the *dependence of ionizing collisions on the energy* of the incident particles. When the collisions are classified according to impact parameter—more precisely, according to momentum transfer—the majority of them have a probability inversely proportional to the particle velocity squared. In addition, the maximum impact parameter depends on the velocity. This particular dependence affects only "optical" collisions and thus provides an opportunity to disentangle optical properties of gas molecules from other properties which influence the occurrence of close collisions.

A particle of charge ze and velocity $v=\beta c$ produces per cm path in a gas an average number of ionizations ("primary specific ionization") represented by the formula

$$S=(2\pi z^2e^4N/mc^2)\beta^{-2}\int_I^\infty dW\int_{Q_{\min}}^{Q_{\max}} dQ\,Q^{-2}|\eta_W(Q)|^2, \quad (1)$$

which is an integral of (B50.8).[2,5] Here e and m are the

[1] H. A. Bethe, Ann. Physik **5**, 325 (1930).
[2] Geiger-Scheel, *Handbuch der Physik* (J. Springer, Berlin, 1933), Vol. 24/1, p. 491 ff., which will be referred to as "B".
[3] See, e.g., B. Rossi, *High Energy Particles* (Prentice Hall, Inc., New York, 1952), p. 45.
[4] G. W. McClure, Phys. Rev. **90**, 796 (1953).

[5] A factor $E'/E=1-W/E$ has been dropped from (B50.8) because it practically equals 1 in most collisions as pointed out in reference 2.

charge and mass of the atomic electrons, N is the number of gas molecules per cm³, W the energy absorbed by the electron ejected in a collision (which must exceed the ionization threshold I); Q is a function of the momentum Δp transferred in a collision and equals the recoil energy $\Delta p^2/2m$ of an electron assumed initially free and at rest, and $\eta_W(Q)$ is the relativistic form factor (B50.2).[2] ($|\eta_W(Q)|^2$ represents the probability that the atomic electrons absorb the energy W as a consequence of receiving the momentum transfer indicated by Q.)

The form factor η_W is not known in detail for gases other than atomic hydrogen. Therefore this discussion aims at analyzing the dependence of S on the incident particle's velocity by taking advantage of available general information about η_W. As discussed in reference 2 below Eq. (56.13), no appreciable error is incurred for our purpose by taking

$$|\eta_W(Q)|^2=|F_W(Q)|^2-|x_W|^2 2m\hbar^{-2}W^2(1-\beta^2)/2mc^2, \quad (2)$$

where F_W is the nonrelativistic form factor, and x_W is an optical constant, namely the dipole matrix element corresponding to the transition of the ejected electron. Both F_W and x_W are independent of the energy of the incident particle.

The integration limits $Q_{\min}$ and $Q_{\max}$ depend on the incident energy. However, $Q_{\max}$ can be effectively replaced by ∞ in calculations of the *number* of collisions, because large-Q collisions are exceedingly rare (though their energetic import is essential in stopping power calculations). The lower limit of integration $Q_{\min}$ is given by (B50.9),[2]

$$Q_{\min}=W^2(1-\beta^2)/2mc^2\beta^2. \quad (3)$$

The second term of (2), multiplied by Q^{-2} and integrated over Q from the limit (3) to ∞, yields

$$|x_W|^2 2m\hbar^{-2}\beta^2. \quad (4)$$

The first term of (2), $|F_W(Q)|^2$, is not known for most gas molecules. However, for the "optical" collisions, which are characterized by $Q\ll W$, it has the form

$$|F_W(Q)|^2=Q|x_W|^2 2m\hbar^{-2}. \quad (5)$$

To take advantage of this simpler form, we split the integral over Q of $|F_W|^2 dQ\,Q^{-2}$ into two sections. One section is confined to optical collisions and its value depends on the incident particle's velocity through the lower limit $Q_{\min}$. The remaining section is more difficult to calculate but is independent of the incident particle's energy. It is convenient to separate the two sections at $Q=W^2/2mc^2\ll W$, and we write, utilizing (5) and (3),

$$\begin{aligned}\int_{Q_{\min}}^{\infty}|F_W(Q)|^2 dQQ^{-2}&=|x_W|^2 2m\hbar^{-2}\int_{Q_{\min}}^{W^2/2mc^2}dQ\,Q^{-1}+\int_{W^2/2mc^2}^{\infty}|F_W(Q)|^2 dQ\,Q^{-2}\\&=|x_W|^2 2m\hbar^{-2}\ln[\beta^2/(1-\beta^2)]+G(W), \quad (6)\end{aligned}$$

where

$$G(W)=\int_{W^2/2mc^2}^{\infty}|F_W(Q)|^2 dQ/Q^2. \quad (7)$$

Equations (6), (4), and (2) together yield

$$\int_{Q_{\min}}^{\infty}dQ\,Q^{-2}|\eta_W(Q)|^2=|x_W|^2 2m\hbar^{-2}\times\{\ln[\beta^2/(1-\beta^2)]-\beta^2\}+G(W). \quad (8)$$

It is convenient to express $2m/\hbar^2$ in (8) in terms of the Bohr radius $a_0=0.53\times10^{-8}$ cm and of the ionization potential of atomic hydrogen, $Ry=\hbar^2/2ma_0^2$. Accordingly we write

$$|x_W|^2 2m\hbar^{-2}=(|x_W|^2/a_0^2)Ry^{-1}, \quad (9)$$

so that the "dipole strength" $|x_W|^2$ is expressed in atomic units. Similarly, Ry plays the role of an atomic unit and should *not* be regarded as the ionization potential of the gas molecules, contrary to previous surmises,[3,4] The factor Ry^{-1} in (9) combines with the factor in parentheses in (1) to yield

$$z^2 2\pi e^4 N/mc^2 Ry=0.50\,z^2\ \text{cm}^{-1}, \quad \text{at NTP.} \quad (10)$$

Substitution of (8) into (1), taking into account (9) and (10), yields the simplified expression of the specific ionization:

$$S=0.50z^2\beta^{-2}\{\bar{A}[\ln(\beta^2/(1-\beta^2))-\beta^2]+\bar{C}\}\ \text{cm}^{-1}, \quad \text{at NTP,} \quad (11)$$

where

$$\bar{A}=\int_I^{\infty}dW(|x_W|^2/a_0^2) \quad (12)$$

is the total dipole strength of ionizing transitions in the gas molecules (expressed in atomic units) and

$$\bar{C}=Ry\int_I^{\infty}dW\,G(W) \quad (13)$$

is another molecular constant.[6,7]

The constants $\bar{A}$ and $\bar{C}$ ought to be determined conveniently from the experimental values of S at different velocities of the incident particle by plotting $2.0\beta^2 z^{-2}S$ against $\{\ln[\beta^2/(1-\beta^2)]-\beta^2\}$. The plot should be a straight line with slope $\bar{A}$ and intercept $\bar{C}$.

As indicated above, $\bar{A}$ represents a property of each atom or molecule which is of considerable general interest and whose value is hardly known, experimentally or theoretically, except for atomic hydrogen.

[6] The bar over the symbols $\bar{A}$ and $\bar{C}$ distinguishes them from the corresponding symbols of reference 4 which equal, respectively, 0.50 $\bar{A}$ cm^{-1} and 0.50 $\bar{C}$ cm^{-1}.

[7] The constant $\bar{A}$ corresponds to the quantity indicated by Za in reference 4. Factoring out the atomic number might be suggested by the related theory of stopping power but, in fact, is not suited to the theory of collision probability, because this probability should tend to increase, on the whole, in proportion to Z^1, rather than in proportion to Z.

TABLE I. Values of the parameters $\bar{A}$, $\bar{A}_{tot}$, $\bar{C}$, and $\bar{C}/\bar{A}$.

	H (theory)	H_2	He	Ne	A
$\bar{A}$	0.285	0.71±0.06	0.84±0.08	2.3±0.2	4.7±0.5
$\bar{A}_{tot}$	1	1.65	0.79	2.8	7.6
$\bar{C}$	4.07	8.70±0.04	7.96±0.04	19.3±0.2	43.6±0.4
$\bar{C}/\bar{A}$	14.3	12.2	9.45	8.53	9.20

Of considerable interest is also the comparison of $\bar{A}$ with the total dipole strength for all transitions,[8]

$$\bar{A}_{tot}=\bar{A}+\sum_n|x_n|^2/a_0^2=\langle x^2\rangle/a_0^2 =0.42\times10^{-6}(-\chi_{dia})M. \quad (14)$$

Here x_n is the dipole matrix element for transitions from the ground state to the nth level of the discrete spectrum, the $\sum_n$ extends over the discrete spectrum, $\langle x^2\rangle$ is the mean square value for the ground state of the sum of the x coordinates of all electrons in a molecule, χ_{dia} is the diamagnetic susceptibility per unit mass of the gas, and M is the molecular weight.

The ratio $\bar{A}/\bar{A}_{tot}$ should be of the order of $\frac{1}{2}$, larger for substances with high ionization potentials and lower for substances with loosely bound electrons,[9] but there is little real information on this subject. Table I compares the values of $\bar{A}$ measured by McClure[4] with the values of $\bar{A}_{tot}$ derived from a table of susceptibilities;[10] the values of $\bar{C}$ are also listed, as well as those of $\bar{C}/\bar{A}$ which may vary less sharply from one substance to another, as pointed out by Rossi.[3] (For atomic hydrogen $\bar{C}/\bar{A}$ equals the Bethe constant 3.04 plus 2ln274.)

The values of $\bar{A}$ and $\bar{A}_{tot}$ for He coincide within the experimental error, whereas (14) implies that $\bar{A}_{tot}>\bar{A}$. However, the addition of some H_2 to He in McClure's experiment has probably caused *the excitations* produced in He to be *converted into ionizations* of H_2 and thus to be scored as ionizations. Accordingly, the experiment would yield a measurement of $\bar{A}_{tot}$ itself, rather than of $\bar{A}$. This interpretation stems from the observation of Jesse and Sadauskis[11] that the ionization yield in He (and in other gases with high excitation potentials) increases sharply in the presence even of traces of other gases. The same mechanism should presumably operate in Ne as well as in He, but here McClure's value of $\bar{A}$ amounts to only about 80 percent of $\bar{A}_{tot}$ and the interpretation of this value of $\bar{A}$ remains unclear. Argon has a lower ionization potential than He or Ne, comparable to that of H_2, but still rather high, so that the measured ratio $\bar{A}/\bar{A}_{tot}\sim0.6$ does not appear surprising on first inspection. Similarly, the ratio $\bar{A}/\bar{A}_{tot}$ for H_2 being higher than for H seems to conform to qualitative expectation since electrons are more tightly bound in H_2 than in H.

In conclusion, however, the present brief discussion of values of $\bar{A}$ and $\bar{A}_{tot}$ should only indicate the existence of an area for further experimental and theoretical study.

[8] See, e.g., J. H. Van Vleck, *Electric and Magnetic Susceptibilities* (Oxford University Press, London, 1932), p. 90.
[9] See, e.g., U. Fano, Phys. Rev. **70**, 44 (1946).
[10] *Handbook of Chemistry and Physics* (Chemical Rubber Publishing Company, Cleveland, 1947), thirtieth edition.
[11] W. P. Jesse and J. Sadauskis, Phys. Rev. **88**, 417 (1952). I wish to thank Professor R. L. Platzman for a discussion of his unpublished analysis of the Jesse-Sadauskis results and of its implications regarding the McClure experiments.

Direct *l*-Doublet Transition of HCN in the 10-Centimeter Wavelength Region*

ROBERT J. COLLIER†
Sloane Physics Laboratory, Yale University, New Haven, Connecticut
(Received May 27, 1954)

A variable-frequency, Stark modulation, resonant cavity spectrometer was developed for spectroscopy in the 10-cm spectral region. The direct *l*-doublet transition of HCN for $J=3$ and $v_2=1$ was measured to be $\nu_0=2693.21\pm0.08$ Mc/sec, with an absorption coefficient determined to be $\alpha=3\times10^{-8}$ cm^{-1}.

INTRODUCTION

COMPARATIVELY little work in molecular spectroscopy at 10-centimeter wavelengths has been reported in the literature.[1-3] There are two major reasons for this: the number of transitions having frequencies in this region is small and their intensity is low. In certain cases, the absorption coefficient for the direct *l*-doublet transition of a linear polyatomic molecule or for the direct Λ-doublet transition of a diatomic molecule is sufficiently large as to allow their investigation in the 10-centimeter region. In this paper we report the observation of the direct *l*-doublet transition for HCN in the $J=3$ rotational state and $v_2=1$ vibrational state. The *l*-doubling of rotational levels in linear molecules is due to the interaction of rotation with bending vibration. A quantitative theory of the effect has been presented by Nielsen,[4] who gives for the doublet splitting

$$\nu_0=qJ(J+1).$$

Prior to the present work, two investigations of *l*-doublet transitions in HCN had been made for $J>6$: the first by Shulman and Townes[5] and the second by Weatherly and Williams.[6] The quantity q was found to increase with increasing J by the first investigators and to decrease with increasing J by the second. Extrapolation of the data of Shulman and Townes to $J=3$ gave $\nu_0\sim2684$ Mc/sec, while extrapolation of the data of Weatherly and Williams gave $\nu_0\sim2695$ Mc/sec.

APPARATUS

A 10-cm variable-frequency spectrometer making full use of a single resonant cavity was developed. All components, including the cavity, were coaxial. The single cavity served as the Stark-modulated absorption cell and as the frequency tuning and stabilizing mechanism. Noncontacting cavity end plungers were designed so as to simulate good microwave short circuits and maintain the Q over a broad band of frequencies corresponding to various cavity lengths. The inner conductor of the coaxial cavity was insulated to withstand the 30-cps Stark voltage. Variation and stabilization of the klystron frequency were accomplished by making the cavity the reference in a dc Pound stabilization system.[7] The rf power transmitted through the cavity was detected by a broad-band, coaxially mounted bolometer. The signal component at the fundamental modulation frequency was amplified in a tuned receiver, the output passing to a phase-sensitive detector. A complete description of the spectrometer will be presented in an article to be published elsewhere.

MODULATION

According to the theory of Penney,[8] application on an electric field to the molecule HCN produces a second-order Stark splitting. If the *l*-doublet energies in the absence of an external field are $W_1(0)$ and $W_2(0)$, they become, in the presence of a small electric field E,

$$W_1\sim W_1(0)+\frac{\mu^2E^2l^2M^2}{[W_1(0)-W_2(0)][J(J+1)]^2},$$

$$W_2\sim W_2(0)-\frac{\mu^2E^2l^2M^2}{[W_1(0)-W_2(0)][J(J+1)]^2},$$

where μ is the electric dipole moment and $M=J, J-1, \cdots, -J$. For best modulation efficiency, it is desired that, at a given applied field, the Stark component of largest intensity be split furthest from the zero-field *l*-doublet transition frequency. Consideration of the splitting and relative intensities of the Stark components shows that observation of the $\Delta M=0$ transitions provides the largest signal amplitude. To observe these $\Delta M=0$ transitions the applied electric field direction must be parallel to the microwave electric field direction. For this purpose the cavity was made coaxial and operated in the *TEM* mode, where both the modulating and microwave electric fields are radial. The troughs of the modulating sine wave were biased to zero so that the signal component at the fundamental

* Assisted by the U. S. Office of Naval Research.
† This paper is part of a dissertation submitted to the Graduate School of Yale University for the Ph.D. degree. Now at Bell Telephone Laboratories, Murray Hill, New Jersey.
[1] Lyons, Rueger, Nuckolls, and Kessler, Phys. Rev. **81**, 630 (1951).
[2] Kojima, Tsudaka, Hagiwara, Mizushima, and Ito, J. Chem. Phys. **20**, 804 (1952).
[3] Beers, Weisbaum, and Herrmann, Low Frequency Microwave Project Report No. 195.1, New York University College of Engineering (unpublished).
[4] H. H. Nielsen, Phys. Rev. **77**, 130 (1950); Phys. Rev. **78**, 296 (1950).
[5] R. G. Shulman and C. H. Townes, Phys. Rev. **77**, 421 (1950).
[6] T. L. Weatherly and D. Williams, Phys. Rev. **87**, 517 (1952).
[7] R. V. Pound, Rev. Sci. Instr. **17**, 490 (1946).
[8] W. G. Penney, Phil. Mag. **11**, 602 (1931).

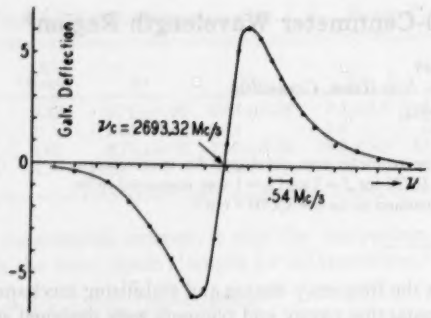

FIG. 1. First harmonic signal due to the $J=3$ l-doublet transition of HCN. Gas pressure was 0.030 mm Hg and modulation voltage amplitude was 165 v.

modulation frequency could be observed. The shape of this signal component is shown in Fig. 1. An approximately linear extrapolation of the graph of crossover frequency, ν_c, *vs* the square of the modulation voltage, V_0, to zero applied voltage gave the direct l-doublet transition frequency ν_0.

RESULTS AND CONCLUSIONS

Interaction of the quadrupole moment of the N^{14} nucleus with the electric field gradient at that nucleus causes each l-doublet level to be split into three hyperfine levels. Although, under the selection rules $\Delta F=0, \pm 1$, there are seven possible transitions from the lower doublet component to the upper, only the $\Delta F=0$ transitions were observed. This is because 90 percent of the intensity goes into these transitions. Further the three possible $\Delta F=0$ transitions have frequencies which are coincident and equal to the frequency difference between the nonhyperfine split l-doublet levels. Hence observation of the $\Delta F=0$ transition gives directly the frequency

$$\nu_0=2693.21\pm 0.08 \text{ Mc/sec}$$

for the first excited bending vibration level $v_2=1$ and the rotational level $J=3$. From the theoretical formula for ν_0 we determined q to be

$$q=224.434\pm 0.007 \text{ Mc/sec.}$$

These values agree roughly with those extrapolated from the data of Weatherly and Williams and support the conclusion that q is a decreasing function of increasing J. After the completion of this experiment, the work of Westerkamp,[9] repeating the measurements of Shulman and Townes, was published. He gives, for the variation of q with J,

$$q=224.471-0.002614J(J+1).$$

The value of q for $J=3$ predicted by Westerkamp's formula and the value of q measured in this experiment agree within the experimental error.

From the amplitude of the signal observed, the total absorption coefficient for the $\Delta F=0$ transitions was determined to be $\alpha=3\times 10^{-8}$ cm^{-1}. This agreed with the predicted absorption coefficient to within a factor 2.

I wish to thank Professor Robert Beringer for his aid and advice throughout the course of this work.

[9] J. Westerkamp, Phys. Rev. **93**, 716 (1954).

Corrected Values of Tungsten *K*-Series X-Ray Wavelengths with the 2-Meter Curved Crystal Diffraction Spectrometer*

PHILIP SNELGROVE, JASSIM EL-HUSSAINI, AND JESSE W. M. DUMOND
California Institute of Technology, Pasadena, California

(Received May 17, 1954)

Certain minor mechanical errors occasioned by small flexures in some components of our 2-meter curved crystal γ-ray spectrometer were discovered recently through comparison of wavelength measurements in different orders of reflection. These errors and the means adopted for their correction have been described in published papers and a program of redeterminations of nuclear γ and x-ray wavelengths is underway. In this program, a by-product of the study of the radioisotope Ta^{182} has led to measurements of the tungsten *K*-series x-ray lines, since tungsten is the daughter product of β decay of Ta^{182}. In this way we have obtained the following results: W-$K\alpha_2$=213.387±0.010; W-$K\alpha_1$=208.575±0.008; W-$K\beta_3$=184.785±0.027; W-$K\beta_1$ =183.997±0.019 all expressed in x.u. (Siegbahn). The agreement with other measurements, particularly those given in E. Ingelstam's dissertation (1937), is now well within the estimated standard deviation of our measurements, and to avoid further confusion (because our earlier values disagreed slightly from Ingelstam's) we wish to announce that our earlier results [published in Phys. Rev. 75, 505 (1949)] are herewith superseded by these present ones.

IN 1949 a paper[1] was published entitled "A Precision Study of the Tungsten *K*-Spectrum Using the 2-Meter Focusing Curved Crystal Spectrometer." The primary purpose of this study was to calibrate the wavelength scale of the 2-meter curved crystal (diffraction) γ-ray spectrometer in terms of a well-established x-ray wavelength. With this in view a careful determination was first made of the wavelength ratio of the Mo-$K\alpha_1$ and W-$K\alpha_1$ lines using reflections from the (310) planes of two flat quartz lamina in a precision two-crystal spectrometer described in an earlier paper.[2] The Mo-$K\alpha_1$ line was chosen as a reference standard since its value on the Siegbahn scale (in x-units) is so well established.[3] The wavelengths of seven lines in the tungsten *K* spectrum α_2, α_1, β_3, β_1, β_2^{II}, β_2^{I}, δ, and the critical absorption edge, were then measured with the 2-meter curved crystal spectrometer on its nominal wavelength screw scale corrected for all the instrumental systematic errors which we were at that time aware of. The instrument design is such that ideally the wavelength screw readings should be strictly proportional to the sine of the Bragg angle and hence to the wavelength. On this assumption of a strictly linear wavelength scale, it was believed that all that was necessary was to establish a constant multiplying factor between nominal wavelengths after correction for screw errors and other small known instrumental errors on the one hand and true wavelengths in x-units (or angstrom units) on the other hand by a comparison of the nominal wavelength scale reading for the W-$K\alpha_1$ line with the true value established by the above-mentioned 2-crystal spectrometer determination.

Subsequent to publication of this 1949 paper,[1] however, we have discovered certain small departures from linearity in the relation between the nominal instrument scale of wavelengths and true wavelengths which we have found to be caused by slight mechanical flexures in certain components of the instrument.[4] As a result all the W-*K*-series wavelengths published in the 1949 paper, except of course the $K\alpha_1$ calibration line itself, are slightly in error. Relative to our quoted probable errors in that paper, these systematic departures are not very serious, and since our principal attention has been focused on gamma rays rather than on x-rays we have not until now attempted to correct these published values. We are indebted, however, to Erik Ingelstam of the Royal Institute of Technology, Stockholm, for (1) pointing out to us certain small discrepancies between these 1949 published wavelengths of ours and those he had obtained[5] by photographic methods, also with a curved crystal spectrometer, and (2) for suggesting that since the disagreement existed and physicists were using two discrepent sets of x-ray wavelength values indiscriminately, we should remeasure these *K*-series x-ray lines making use of the

* Assisted by contracts with the U. S. Atomic Energy Commission and the U. S. Office of Naval Research.

[1] Watson, West, Lind, and DuMond, Phys. Rev. **75**, 505 (1949).

[2] Jesse W. M. DuMond, Rev. Sci. Instr. **8**, 112 (1937).

[3] The ratio of wavelengths on the nominal Siegbahn x-unit scale to wavelengths as measured in milliangstroms is known by the work of four different workers (Bearden, Bäcklin, Söderman, and Tyrén) with x-ray diffraction at grazing incidence on ruled gratings previously calibrated with optical wavelengths. The relative uncertainty in our knowledge of this ratio is insignificant for the accuracy available with the 2-meter curved crystal γ-ray spectrometer over most of its scale.

[4] For a discussion of these small effects, which were discovered by a comparison of the nominal values of wavelengths reflected in different orders of reflection, and the means developed for their correction, the reader is referred to the following papers: Muller, Hoyt, Klein, and DuMond, Phys. Rev. **88**, 775 (1952); J. W. M. DuMond, Phys. Today **5**, 13 (1952); and "The Spectroscopy of Nuclear Gamma-Rays by Direct Crystal Diffraction Methods," J. W. M. DuMond, Special Technical Report No. 28 to the Office of Naval Research and No. 8 to the Atomic Energy Commission, March 1954 (unpublished). Optical means in the form of a well-corrected 6-inch concave mirror and a microscope have since been installed for measuring the flexural errors each time precision measurements are made, and a program of remeasuring our earlier wavelengths to take account of these so-called "mirror corrections" is now in progress.

[5] Erik Ingelstam, Inaugural dissertation, Uppsala, 1937 (unpublished).

TABLE I. Tungsten K-series wavelengths in x.u.

	W-$K\alpha_2$	W-$K\alpha_1$	W-$K\beta_3$	W-$K\beta_1$
Present corrected results	213.387±0.010	208.575±0.008	184.785±0.027	183.997±0.019
Ingelstam (1937)	213.382	208.571	184.795	183.991

new optical means we have installed for correcting for the flexures in the instrument and publish a set of corrected values. This we have recently done for the case of the Ta-$K\beta_1$ and β_3 lines using as the source of x-rays a strip of neutron activated tantalum (Ta^{182}) which after β decay becomes W^{182} and emits, in addition to a rich spectrum of nuclear γ rays, copious K-series x-ray lines of tungsten. In addition to corrections for all systematic instrumental errors, correction has also been made, in the case of the W-$K\beta_3$ line, for the presence of two weak Ta-K lines, β_2^{I} and β_2^{II}, also emitted by such a source which appear superposed on the W-$K\beta_3$ line in such a way as to distort and shift the total profile and increase the peak height, relative to W-$K\beta_1$, quite noticeably. This correction could be made with considerable certainty because the (much stronger) Ta-$K\alpha_1$ and α_2, β_1, and β_3 lines are also observed in this spectrum so that the Ta-K β_2^{I} and β_2^{II} line profiles can be inferred as to intensity and position from measurements by others on the Ta-K spectrum with amply sufficient accuracy for the purpose of this relatively small correction. The accompanying Fig. 1 shows the observed and corrected profiles, from which it can be seen that after subtracting the Ta-K β_2^{I} and β_2^{II} lines the W-$K\beta_3$ line takes on its normal shape, width and peak height relative to W-$K\beta_1$.

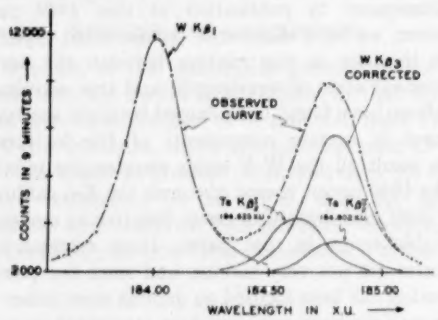

FIG. 1. Observed and corrected line profiles of W-K β_1 and β_3 x-ray lines emitted by a neutron activated source consisting of a strip of pure tantalum. The active Ta^{182} decays to W^{182} and emits copiously both nuclear gamma rays of tungsten and the x-ray lines of that element.

No correction is necessary, of course, for the standardizing wavelength, W-$K\alpha_1$, since its value depends only on the 2-crystal spectrometer measurements, but is independent of the calibration of the 2-meter curved crystal instrument. W-$K\alpha_2$ is so close to this that no significant instrumental correction is needed for this wavelength either. We show in Table I our present corrected results compared with the corresponding results of Ingelstam's (1937) work.

Our latest measurements with the "mirror" and other corrections[4] are seen to agree with Ingelstam's 1937 results well within our independently assigned probable errors. We have not troubled to measure the much weaker W-$K\beta_2^{II}$ and $K\beta_2^{I}$ lines,[6] but our agreement with Ingelstam for the closely adjacent W-$K\beta_1$ line is so satisfactory that it seems very safe to assume that our 2-meter instrument would have yielded values in good agreement with his for these two lines also.

[6] These are much attenuated because they fall on the high absorption side of the tantalum K edge.

Half-Life of Thallium-204†

D. L. HORROCKS AND A. F. VOIGT
Institute for Atomic Research and Department of Chemistry, Iowa State College, Ames, Iowa

(Received May 17, 1954)

A determination of the half-life of Tl^{204}, based on measurements over a 3-year period, gives a value of 4.1±0.1 years.

THERE appear to be two distinct groups of values for the half-life of Tl^{204} as reported in the literature, approximately 2.7 years[1–3] and approximately 4.0 years.[4,5] Since we had taken decay data on a sample of Tl^{204} over a period of three years, we felt it worth while in view of the discrepancy to calculate and report our results.

The sample was prepared from active $TlNO_3$ which was supplied by the Oak Ridge National Laboratory. The $TlNO_3$ was oxidized to $TlCl_3$ with aqua regia and the $TlCl_3$ extracted into ethyl ether. The thallium was re-extracted into an aqueous solution and reduced to $TlNO_3$. Finally, the active thallium was precipitated and mounted as TlI. The sample was held in place with thin onionskin paper (3.22 mg/cm²).

A Lauritsen electroscope was used to measure the activity of the sample. Before each reading the stability of the electroscope was checked with a uranium standard. Measurements were made both with no absorber (Curve 1) and also with 8.9 mg/cm² of aluminum absorber (Curve 2). The activity has been measured for 3.4 years over which time the electroscope has remained remarkably stable.

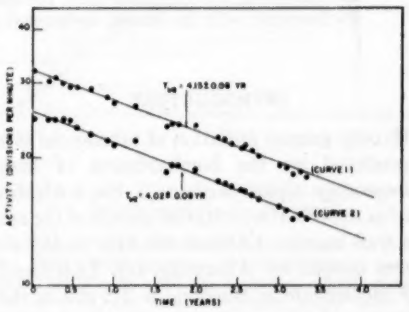

FIG. 1. Decay curve of Tl^{204}.

The method of least squares[6] was used to draw the best possible straight line through each set of data (Fig. 1). Curve 1 gave the half-life as 4.15±0.08 years while Curve 2 gave 4.02±0.08 years. A value of 4.1±0.1 years would appear to be the best representation of these two sets of data. This value supports the recent value of 4.02±0.12 years published by Harbottle.[5]

The authors wish to acknowledge the assistance of Owen E. Smith in preparing the sample and making the early measurements.

† Contribution No. 325 from the Institute for Atomic Research and Department of Chemistry, Iowa State College, Ames, Iowa. Work was performed in the Ames Laboratory of the U. S. Atomic Energy Commission.

[1] Seaborg, Hollander and Perlman, Revs. Modern Phys. **25**, 469–651 (1953); A. F. Voigt (private communication).

[2] E. E. Lockett and R. H. Thomas, Nucleonics **11**, 14 (1953).

[3] S. A. Reynolds and W. A. Brooksbank, Jr., Nucleonics **11**, 46 (1953).

[4] K. Fajans and A. F. Voigt, Phys. Rev. **60**, 619 (1941).

[5] G. Harbottle, Phys. Rev. **91**, 1234 (1953).

[6] A. G. Worthing and J. Geffner, *Treatment of Experimental Data* (John Wiley and Sons, Inc., New York, 1946), Chap. XI.

Observations on the 4.43-Mev Gamma Rays from C^{12}†

W. R. Mills, Jr., and R. J. Mackin, Jr.
Kellogg Radiation Laboratory, California Institute of Technology, Pasadena, California
(Received May 24, 1954)

A scintillation spectrometer has been used for "fore and aft" measurements to demonstrate that the 4.43-Mev gamma radiation from $Be^9(\alpha,n\gamma)C^{12}$ exhibits a Doppler shift as the result of motion of the emitting nucleus. This implies a lifetime for the C^{12} excited state less than 3×10^{-13} second. The Compton electron spectrum from a thin converter has been studied in a magnetic lens spectrometer to produce a value for the level excitation of 4.425 ± 0.020 Mev. The spectrum of internal pairs has been found to agree most closely (to 5 percent) with the (known) assignment of the radiation as electric quadrupole.

INTRODUCTION

THE only gamma radiation of substantial intensity produced by the bombardment of beryllium with low-energy alpha particles is the 4.43-Mev line from $Be^9(\alpha,n\gamma)C^{12}$. The excitation energy of the emitting level is well known: 4.432 ± 0.008 Mev is the average of figures quoted by Ajzenberg and Lauritsen.[1] The angular momentum of the level is 2^+: this is the only assignment which is consistent with all of 13 angular distribution and correlation measurements quoted by the above authors as well as the observed branching ratio of the B^{12} beta decay.[2] Such a well-investigated solitary gamma line constitutes a useful standard for the evaluation of techniques of gamma-ray spectroscopy. This paper presents evidence that the line exhibits a Doppler shift due to motion of the emitting nucleus. This is followed by an energy measurement based on the spectrum of Compton electrons from a thin converter, and a multipole-order determination from the internal pair spectrum. Only the first datum provides new information about the excited nuclear state; the others may be regarded primarily as demonstrations of method.

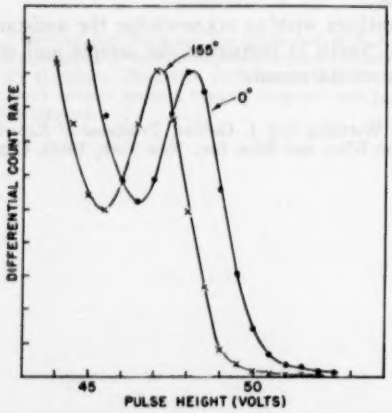

FIG. 1. Pulse-height spectrum in NaI(Tl) from $Be^9(\alpha,n\gamma)C^{12}$ in the region of the "full-energy" peak for the 4.43-Mev gamma radiation. Circles represent readings taken with counter in line with the beam; crosses correspond to 155 degrees. Peak heights have been drawn equal.

DOPPLER SHIFT

This experiment consisted of a measurement of the energy difference of gamma rays emitted at different directions with respect to a beam of He^+ ions from a 3-Mev electrostatic accelerator. Such a difference is expected to be caused by the net forward motion of the emitting nuclei (imparted by the bombarding particles) unless these are stopped before the emission. The beam energy was adjusted by electrostatic analysis to give maximum gamma-ray yield from an 0.09-mg/cm² Be target at a strong resonance[3] at 1.90 Mev. The gamma rays were studied with a scintillation spectrometer employing a cylindrical NaI(Tl) crystal (1.5 in. diam. ×1.5 in. long), a Dumont type-6292 photomultiplier, and a 10-channel pulse analyzer. The counter was placed 15 centimeters from the target, in turn at 0 degrees and at 155 degrees with respect to the beam. At each position, the "full-energy" peak produced by the 4.43-Mev line was studied. The stability of the system was checked frequently by measurements on the 2.62-Mev line from ThD.

One of three sets of spectra is shown in Fig. 1. The average distance between the peaks corresponds to an energy difference of 2.1 ± 0.3 percent of the line energy, or about 93 kev. The maximum shift expected to result from center-of-mass motion, given (to first order) by

$$(v/c)(\cos0°-\cos155°),$$

where v/c is the velocity of the center of mass relative to the velocity of light, is 1.88 percent. From this good agreement, it appears that the lifetime of the 4.43-Mev level is less than the stopping time for the recoiling C^{12*} in the tantalum backing, about 3×10^{-13} second. The single-particle model[4] suggests a lifetime of about 1.5×10^{-13} second.

† Assisted by the joint program of the U. S. Office of Naval Research and the U. S. Atomic Energy commission.

[1] F. Ajzenberg and T. Lauritsen, Revs. Modern Phys. **24**, 321 (1952).

[2] G. Vendryes, Compt. rend. **233**, 391 (1951).

[3] F. L. Talbott and N. P. Heydenburg, Phys. Rev. **90**, 186 (1953).

[4] J. M. Blatt and V. F. Weisskopf, *Theoretical Nuclear Physics* (John Wiley and Sons, Inc., New York, 1952).

GAMMA-RAY ENERGY

In the following measurements, a magnetic-lens spectrometer was used in a manner described in earlier communications.[5,6] The detector of focused particles was an Amperex type-200C Geiger counter with a 1.2-mg/cm² mica end window. The He^+ beam energy was set at 2.2 Mev.

Figure 2 shows the spectrum of Compton electrons produced in a 19-mg/cm² Be target-converter. The solid curve is a theoretical spectrum expected from gamma radiation of energy 4.465 Mev. It was computed by folding the Klein-Nishina momentum distribution [TL, Eq. (4a)][5] with functions representing the spectrometer window (a Gaussian of width 1.9 percent of electron momentum), energy losses in the converter, and Doppler shift distribution (computed from nuclear motion in the center-of-mass system). The calculations were simplified by approximating the last two functions by Gaussians (widths 0.5 percent and 1.1 percent of

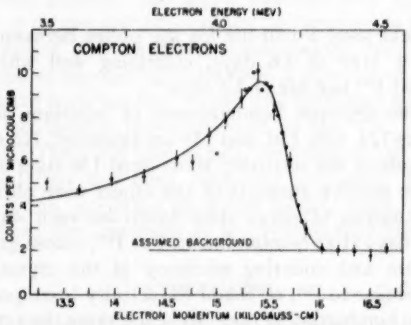

FIG. 2. Spectrum of Compton electrons produced by 4.43-Mev gamma radiation in a 19-mg/cm² Be converter. The solid curve represents a theoretical line shape. All points near peak correspond to same total bombardment.

electron momentum at 15.3 kilogauss-cm, respectively). The Doppler shift distribution is expected to be uniform, since the gamma emission follows the emission of *s*-wave neutrons (see reference 1), so the approximation is adequate. Account was taken of the variation of the spectrometer window with momentum setting and of the effect of the Compton recoil angle [TL, Eq. (7a)], though the latter correction amounted to less than 1.5 percent over the range covered. Multiple scattering corrections were estimated to be negligible.

The energy of gamma radiation emitted at 20° with respect to the beam (the spectrometer acceptance angle) is thus found to be 4.465±0.020 Mev. Correcting for the Doppler shift gives as a value for the level excitation 4.425±0.020 Mev, in good agreement with other data. An earlier measurement at this laboratory,[5] made by employing a thick converter, gave a level energy 4.443±0.020 Mev.

[5] R. G. Thomas and T. Lauritsen, Phys. Rev. **88**, 969 (1952); this paper will be referred to as TL.
[6] R. J. Mackin, Jr., Phys. Rev. **94**, 648 (1954).

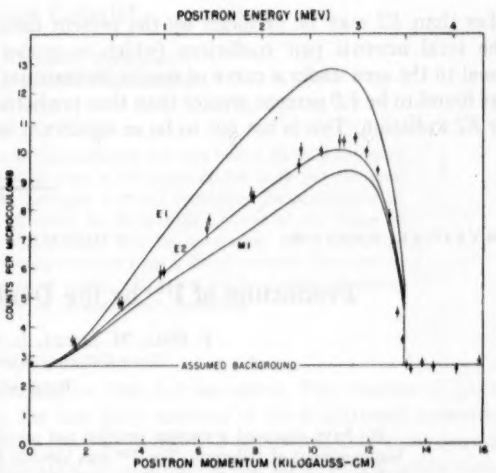

FIG. 3. Positron spectrum. Internal pairs from the 4.43-Mev transition. Solid curves represent theoretical spectra normalized on measured gamma-ray yield. *E*1 represents electric dipole; *E*2, electric quadrupole; etc. Circles represent points taken with a 19-mg/cm² target; crosses, those from an 0.25-mg/cm² target (arbitrarily normalized at 11 kilogauss-cm).

INTERNAL PAIRS

The same target was used to investigate the positron spectrum (shown in Fig. 3, solid circles). It was then backed with a thick (700-mg/cm²) Al converter to measure the gamma-ray yield, employing the method[5,6] of comparison of experimental points with a theoretical spectrum. This yield value (uncertain to about 8 percent) was then used to normalize the theoretical positron spectra corresponding to the various multipole orders shown in Fig. 3 (where *E*1 designates the electric dipole curve, etc.). The Born approximation spectra[7] have been corrected at the end point,[8] although the fold with the spectrometer window would largely offset this adjustment.

As a test of the effect of target thickness on the spectrum, the positron measurement was performed on an unbacked 0.25-mg/cm² Be target. The points, arbitrarily normalized to match the earlier ones at 11 kilogauss-cm, are shown as crosses in the figure. They show no discernible deviation from the others.

The ratios of the areas under the theoretical curves to the area under the experimental curve (between 2 and 13 kilogauss-cm) give a measure of agreement between data and theory. They are:

*E*1:	1.33±0.12,
*E*2:	0.95±0.09,
*M*1:	0.83±0.08,
Others:	$\leqslant$0.78±0.07,

where the assigned errors include the yield uncertainty. The comparison shows to what extent assignments

[7] M. E. Rose, Phys. Rev. **76**, 678 (1949); **78**, 184 (1950).
[8] M. E. Rose and G. Uhlenbeck, Phys. Rev. **48**, 211 (1935).

other than $E2$ may be excluded by the present data. The total internal pair coefficient (which is proportional to the area under a curve of counts/momentum) was found to be 4.0 percent greater than that predicted for $E2$ radiation. This is not felt to be as significant as the previous comparison because of the extra weight given the low-momentum points.

The authors are grateful to J. Thirion for considerable assistance with the first part of the experiment and to T. Lauritsen for valuable discussions.

PHYSICAL REVIEW VOLUME 95, NUMBER 5 SEPTEMBER 1, 1954

Production of I^{124} by the Deuteron Bombardment of Tellurium

T. HALL, M. SIEGEL, L. M. SHARPE, AND D. PRESSMAN
Sloan-Kettering Institute, New York, New York

(Received May 17, 1954)

We have observed a nuclear reaction not previously reported: the production of I^{124} by the deuteron bombardment of tellurium. The I^{124} was identified by decay and gamma-ray pulse height studies using a well-type scintillation counter. We report also some observations on the relative amounts of the different iodine isotopes produced by the bombardment.

FOR those who are interested in the use of radioactive iodine isotopes, we would like to call attention to a means of producing I^{124}, which apparently has not been reported previously in the literature.[1] We have observed that substantial amounts of I^{124} are produced when ordinary tellurium is bombarded with the deuteron beam of a cyclotron, the reactions presumably being $Te^{124}(d,2n)$ and $Te^{123}(d,n)$.

In our work the tellurium was exposed to a beam of 20-Mev deuterons for 50-microampere hours. The I^{124} was identified by the study of its gamma-ray spectrum with a well-type (2-in. × 1¾-in. diameter) NaI scintillation crystal and a single-channel pulse-height analyzer. After five days (during which time the I^{130} component in the product decayed to an insignificant amount) the bulk of the gamma radiation, apart from the contribution from I^{131}, was observed to count in the pulse-height range between 0.50 and 0.75 Mev, while the main I^{124} gamma lines have been reported to be 0.60 and 0.73 Mev.[2] Scintillation pulses were observed in much weaker intensity up to about 2 Mev but not higher, which is consistent with the reported weak gamma rays of 1.7 and 1.95 Mev from I^{124}. Also, decay data taken between eight and thirty days after bombardment gave a half-life for the pulses between 0.75 and 1.4 Mev of 4.6 days, coinciding well with the reported I^{124} half-life of 4.5 days.[3]

In the deuteron bombardment of tellurium, iodine isotopes 124, 126, 130, and 131 are produced. No study was made of the relatively short-lived 130 component, but the relative amounts of the others were obtained from analysis of decay data taken between six and thirty days after bombardment. For I^{126}, whose gamma spectrum and counting efficiency in the crystal are quite similar to I^{131}, we found the activity (extrapolated back to bombardment time) to be 0.4 times the activity of the 131 component. For I^{124}, the counting efficiency in the crystal is quite different, but we estimate the I^{124} activity to be approximately twice the I^{131} activity immediately after bombardment.

The iodine was separated from the tellurium prior to the measurements by chemical procedures which should have precluded the presence of tellurium or any other elements. The fact that all the activity was from iodine isotopes was confirmed by a chemical reaction: When the active material was coupled to antibody protein, its degree of combination was the same as that of I^{131} in the sample.

We wish to thank W. Harris of the Brookhaven National Laboratories for his collaboration in this work.

[1] The compilation of Hollander, Perlman, and Seaborg, Revs. Modern Phys. **25**, 469 (1953) lists three means of producing I^{124}: the spallation of tin, the alpha-particle bombardment of antimony, and the proton bombardment of tellurium.

[2] The values quoted for the radiations from I^{124} are taken from *Nuclear Data*, National Bureau of Standards Circular No. 499 (U. S. Government Printing Office, Washington, D. C., 1950).

[3] The decay data were taken in this pulse-height band, despite its exclusion of the main I^{124} lines, in order to avoid any counts from the 0.64-Mev gamma line of I^{131}. The observed pulses were from Compton scattering of the high-energy I^{124} gamma rays.

Photoprotons from Cobalt*

M. Elaine Toms† and William E. Stephens
University of Pennsylvania, Philadelphia, Pennsylvania
(Received May 26, 1954)

The charged particles ejected from a thin cobalt foil by the bremsstrahlung x-rays from a 24-Mev betatron have been observed in nuclear emulsions. Yields measured in units of 10^4 particles per mole per roentgen unit are: protons, 49 ± 10; deuterons, less than 1; alpha particles 1.6 ± 0.5 (corrected for absorption in cobalt foil). The angular distribution of the photoprotons could be fitted with a curve of the shape of $I(\theta)=71+8(\sin\theta+\sin\theta\cos\theta)^2$. The photoproton energy distribution can be accounted for mainly by evaporation from a compound nucleus, although 5 or 10 percent could be from a direct process. The relative absence of photodeuterons in cobalt, compared with the case of copper which has similar binding energies, suggests that the shell structure may be important in allowing photodeuteron emission.

INTRODUCTION

THE anomalous yield of photodeuterons from copper[1] has prompted further investigation to find additional information about photodeuteron emission. Cobalt has binding energies for deuterons, neutrons, protons, and alpha particles very close to those of copper and hence might be expected to photodisintegrate very similarly. Consequently, the photoemission of charged particles from a thin foil of cobalt irradiated with betatron x-rays was examined with the same technique as previously used on Mg,[2] Cu,[1] Ce, In, and Bi.[3] The yield[4] and angular distribution[5] of cobalt photoprotons has been measured previously with a scintillation detector. Our initial results, using nuclear emulsions were reported at the Washington meeting.[6]

EXPERIMENT

A collimated beam of bremsstrahlung x-rays from the University of Pennsylvania betatron operated at 24 Mev was used to irradiate a thin foil of cobalt of thickness 1.4 mil or 31.5 mg per cm^2. The foil was placed at an angle of 30° to the beam and 200-micron Ilford *E*-1 nuclear emulsion plates were placed at angles of 30°, 50°, 70°, and 90° to the beam on the left and 90°, 110°, 130°, and 150° on the right. The camera was evacuated and the foil was irradiated with 44 200-roentgen units of x-rays. The x-ray yield was calibrated against a Victoreen 100-r chamber in a 15-cm diameter Lucite cylinder. After development, about 0.44 cm^2 of each plate was scanned and the ranges of 4926 tracks in the correct direction were measured. About 150 tracks which left the emulsion were grain-counted to allow an estimation of the residual range. About sixty tracks below 150 microns in length were grain-counted to look for deuterons. The number of grains in the last forty microns of track scattered somewhat more than in faded *C*-2 emulsions, but there was no indication of a group of particles with a grain count distinctly above that of the recoil protons used as a check. 335 alpha particles were identified by their denser tracks. The observed proton ranges were increased by the equivalent half-foil thickness in the emulsion and the range-energy curve of Rotblat was used to convert to proton energy. Since the foil was thick enough to stop some of the alpha particles and since it seems likely that some of the low-energy alpha particles were missed in scanning, the observed alpha track distribution was not corrected for foil thickness, but the theoretical curve was corrected for absorption

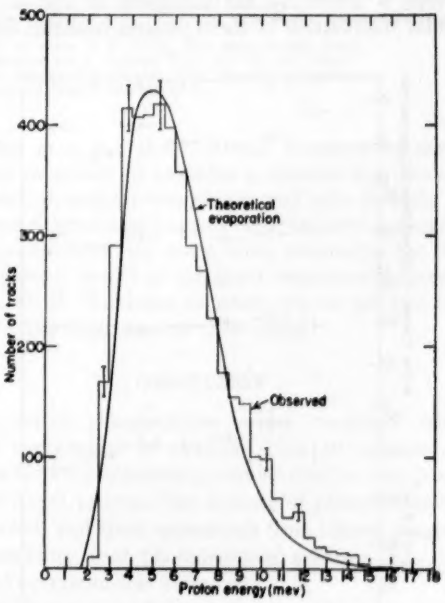

FIG. 1. The number of observed proton tracks from cobalt as a function of proton energy is shown in the histogram. The theoretical curve is calculated as proton evaporation from a statistical model nucleus and corrected for absorption in the cobalt foil.

* Supported in part by the joint program of the U. S. Office of Naval Research and the U. S. Atomic Energy Commission.
† Now at Naval Research Laboratory, Washington, D. C.
[1] P. R. Byerly, Jr., and W. E. Stephens, Phys. Rev. **83**, 54 (1951).
[2] M. E. Toms and W. E. Stephens Phys. Rev. **82**, 709 (1951).
[3] M. E. Toms and W. E. Stephens, Phys. Rev. **92**, 362 (1953).
[4] A. K. Mann and J. Halpern, Phys. Rev. **82**, 733 (1951).
[5] Mann, Halpern and Rothman, Phys. Rev. **87**, 146 (1952).
[6] Toms, Gerardo, and Stephens, Phys. Rev. **95**, 629(A) (1954).

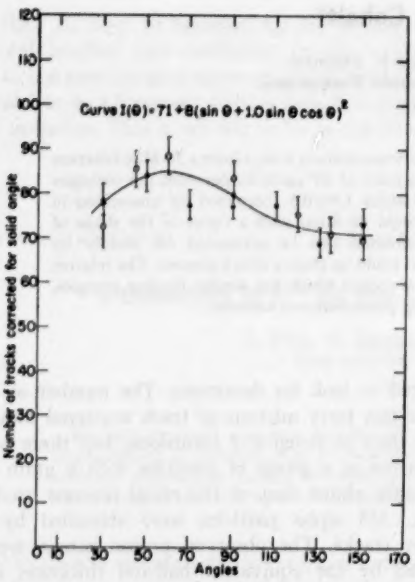

FIG. 2. The observed angular distribution of photoprotons from cobalt. The dots are the present work; the squares are from the scintillation detector work of Mann and Halpern. The curve is described by $I(\theta)=71+8(\sin\theta+\sin\theta\cos\theta)^2$.

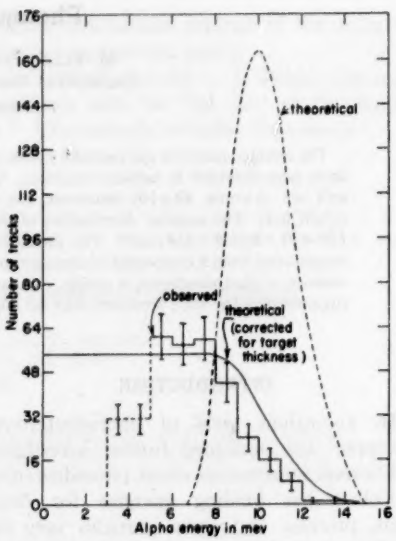

FIG. 4. Energy distribution of photo alpha particles from cobalt. The histogram shows the observed alpha tracks. The dotted curve is the evaporated calculation distribution. The solid curve is the evaporated distribution corrected for cobalt foil thickness.

in the foil. The background determined in a manner similar to previous work[3] is negligible.

The energy distribution of the observed photoprotons is shown by the histogram of Fig. 1. The angular distribution of these protons is shown for all energies in Fig. 2, and in Fig. 3 for various energy groups of protons. The alpha-particle energy and angular distributions are shown in Figs. 4 and 5. Figure 5 shows the number of alphas per unit solid angle of range greater than 20 microns as a function of angle with the beam.

The observed photoparticle yields corrected for angular distribution are given in Table I. The alpha yield is also corrected for absorption in the foil and for missed short-range tracks.

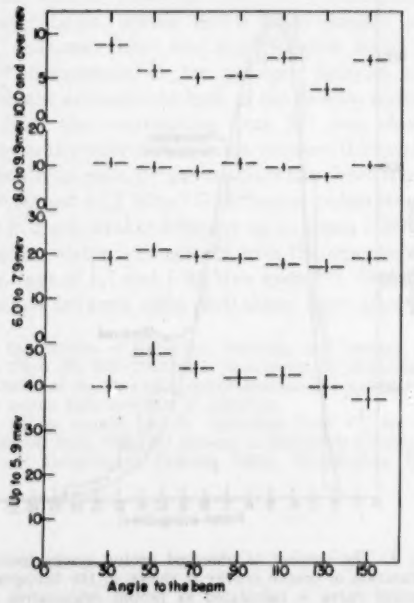

FIG. 3. Observed angular distribution of various energy photoprotons from cobalt.

DISCUSSION

The observed energy distribution of the protons in Fig. 1 can be compared with a curve calculated on the basis of evaporation from a statistical-model nucleus. This calculation is based on the (γ,n) cross-section

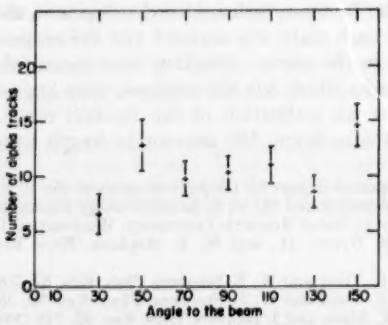

FIG. 5. Angular distribution of the cobalt photo alpha particles of range greater than 20 microns.

curve of Nathans and Halpern,[7] the bremsstrahlung photon distribution curve, Weisskopf's level density and penetrability values,[8] and the binding energies of Table I. This theoretical curve has been approximately corrected to take account of the broadening of the curve due to foil thickness. Most of the photoprotons have an energy distribution consistent with evaporation. However, about 5 percent of the protons have energies slightly higher than expected. This difference may be due either to the use of an incorrect level density or to the occurrence of a direct photoeffect. As much as 10 percent of a direct effect in addition to the evaporated protons would be consistent with the observed energy distribution.

The yield of 49×10^4 protons per mole-roentgen is in agreement with the 37×10^4 reported by Mann and Halpern[4] from their scintillation detector survey using 23-Mev bremsstrahlung. The agreement with the theoretical calculated value from evaporation, 75×10^4 protons per mole-roentgen, is also reasonable. The ratio of proton yield to neutron yield is observed to be 0.21 in good agreement with the value, 0.2, calculated from Weisskopf's[8] F ratios.

The numbers of alpha particles observed were increased by those estimated from the theoretical curve of Fig. 4 to have been absorbed in the foil or missed in the emulsion because of short length. The resultant yield, 1.6×10^4 α particles per mole-roentgen, is not much greater than that expected from evaporation, considering that there is some uncertainty in the alpha binding energy which is known only from the mass formula. The observed alpha energy distribution is most easily compared to a calculated curve approximately corrected for foil absorption. As shown in Fig. 4, a number of short alpha particles (below 20 microns) must have been missed in scanning. In order to be sure that none of the observed alpha particles was due to radioactive contamination in the cobalt, we exposed the foil directly on a nuclear emulsion but found no appreciable alpha activity.

The observed proton angular distribution is shown in Fig. 2 together with the scintillation detector measurements of Mann and Halpern. The agreement is reasonable despite the difference in the proton spectrum observed. (The foil thickness in the scintillation detector measurements was 113 mg/cm² plus 11 mg/cm² of additional absorption in the scattering chamber which favored the higher-energy protons.)

Figure 4 suggests that the anisotropic protons are primarily in the 3–7 Mev region. The proton energy distribution calculated for direct effect protons has its peak at 5 to 6 Mev proton energy. Consequently the anisotropy can still be ascribed to the presence of a few percent of direct effect protons.

[7] R. Nathans and J. Halpern, Phys. Rev. **93**, 437 (1954).
[8] J. M. Blatt and V. F. Weisskopf, *Theoretical Nuclear Physics* (John Wiley and Sons, Inc., New York, 1952), pp. 352 and 372.

The alpha-particle angular distribution (Fig. 5) does not depart from isotropy significantly in comparison with the statistical uncertainty although the 30° and 150° values are somewhat off.

The absence of photodeuterons was surprising in view of the fact that cobalt has binding energies for the last deuteron, proton, neutron, or alpha particle which are very close to those of copper where considerable photodeuterons were observed.

A possibly significant difference between cobalt and copper may be the shell structure associated with the ground state. In copper, the last proton is considered to be in a $p_{3/2}$ shell[10] while the last neutrons occupy $p_{3/2}$ and $f_{5/2}$ shells close together. Cobalt on the other hand has an almost closed shell of $f_{7/2}$ protons and four

TABLE I. Binding energies and photo yields for cobalt.

Particle	Binding energy (Mev)	Observed yield (10^4 particles per mole-roentgen)	Calculated evaporated yield[a]
neutron	10.25±0.2[a]	235,[d] 228[e]	...
proton	7.17±0.2[b]	49±10, 37±7[f]	75
deuteron	14.87[c]	<1	0.03
alpha	6.03[c]	1.6±0.5 (corrected for absorption)	0.6

yield ratios (γ_p/γ_n)	observed	calculated evaporation[f]
	0.21	0.2

[a] Sher, Halpern, and Mann, Phys. Rev. **84**, 387 (1951).
[b] Calculated from Co^{58} β^+ energy and reference a.
[c] N. Metropolis and G. G. Reitwiesner, U. S. Atomic Energy Commission Report NP-1980, 1950 (unpublished).
[d] G. A. Price and D. W. Kerst, Phys. Rev. **77**, 806 (1950).
[e] R. Nathans and J. Halpern, Phys. Rev. **93**, 437 (1954).
[f] A. K. Mann and J. Halpern, Phys. Rev. **82**, 733 (1951).
[g] Calculated using $r_0=1.5\times10^{-13}$ cm.

neutrons in a $p_{3/2}$ shell. It may therefore be more difficult in cobalt to assemble a neutron and proton with similar angular momentum and spin to make a deuteron either in a pickup process or in direct emission. These conjectures are made more reasonable by the single-particle model of the giant resonance proposed by Dr. D. H. Wilkinson to whom we are grateful for enlightening discussions of these ideas.

CONCLUSION

The cobalt photoemission seems consistent with simple evaporation of particles plus 10 percent of protons showing anisotropic angular distributions from a more direct process. The absence of photodeuterons from cobalt and their appearance from copper suggest the possibility that photodeuteron emission may be affected by the nuclear structure.

We wish to acknowledge the help of Henry Gerardo in scanning part of the nuclear emulsion plates.

[10] P. F. A. Klinkenberg, Revs. Modern Phys. **24**, 63 (1952).

Elastic Scattering of Intermediate-Energy Alpha Particles by Heavy Nuclei*

GEORGE W. FARWELL AND HARVEY E. WEGNER†
Department of Physics, University of Washington, Seattle, Washington
(Received May 24, 1954)

The deflected alpha-particle beam of the University of Washington 60-inch cyclotron has been used to study the elastic scattering of 13- to 42-Mev alpha particles by Ag, Ta, Pb, and Th at 60°. The alpha-particle energy was decreased in steps of approximately 1 Mev by placing remotely controlled absorbers in the cyclotron beam. Elastically scattered alpha particles were selected and counted by a differential-range coincidence proportional-counter telescope.

Up to a certain critical energy E_0, which increases with Z, the cross section for each element decreases with increasing alpha-particle energy in agreement with the Rutherford formula. At higher energies, the dependence is given by the empirical formula $\sigma(E)=\sigma(E_0)\exp\{-K(E-E_0)\}$. The slope parameter K is about 0.26 Mev^{-1} and decreases slightly as Z increases. Interpretation of results in terms of a semiclassical strong absorption model leads to values of the sum of nuclear radius and alpha-particle radius best fitted by the empirical formula $D=(1.50A^{\frac{1}{3}}+1.4)\times10^{-13}$ cm.

I. INTRODUCTION

THE first observation[1] of scattering of alpha particles through large angles led Rutherford[2] to suggest a nuclear structure for the atom. Subsequent experiments[3-5] verified the predictions of Rutherford's theory with regard to the dependence of the scattering probability upon thickness of scatterer, alpha-particle energy, and scattering angle, and established the correspondence between nuclear charge and atomic number. Assuming classical trajectories for the scattered alpha particles, Coulomb's law was found to hold for encounters between alpha particles and nuclei for which the distances of closest approach, or apsidal distances, were as small as 3.2×10^{-12} cm (Au), 2.0×10^{-12} cm (Ag), and 1.2×10^{-12} cm (Cu).

The first evidence of departures from Coulomb's law, other than those observed in alpha scattering by H and He, was obtained by Bieler,[6] who studied the angular distribution of Ra (B+C) alphas scattered by Mg and Al. For Al, the ratio of the observed scattering cross section to the Coulomb cross section, $\sigma/\sigma_{\text{Coul}}$, was found to decrease from 1.0 at small angles to about 0.6 at 110°. Rutherford and Chadwick,[5] measuring the dependence of cross section upon alpha-particle energy, found in the case of Al that $\sigma/\sigma_{\text{Coul}}$ at 135° dropped from about 1 at apsidal distances greater than 13×10^{-13} cm to less than 0.4 at $7\text{–}8\times10^{-13}$ cm, increasing again to about 0.7 at 6×10^{-13} cm. Similar results, but without the rise at very small apsidal distances, were observed for 90° scattering from Al. Extensive investigations in the non-Coulomb region were not feasible because of the limited range of alpha-particle energies available from natural alpha sources.

The 43-Mev alpha-particle beam of the University of Washington 60-inch cyclotron has been used in a recent series of experiments to measure cross section for elastic scattering by heavy nuclei as a function of alpha-particle energy, and considerable information has been obtained in the non-Coulomb region.

Results for 60° and 95° scattering by Au have been reported previously.[7] The observed scattering cross section for Au follows the Rutherford dependence closely at low energies, but drops sharply as the alpha-particle energy increases above a well-defined "critical energy" which depends upon the scattering angle. The classical apsidal distance corresponding to the critical energy is considerably larger ($\sim13\times10^{-13}$ cm) than the sum of the presently accepted values of the Au nuclear radius ($8\text{–}9\times10^{-13}$ cm) and the alpha-particle radius ($1\text{–}2\times10^{-13}$ cm). At energies above the critical energy E_0, the dependence of cross section upon energy is well represented by the simple empirical formula $\sigma(E)=\sigma(E_0)\exp\{-K(E-E_0)\}$, where the coefficient K depends upon the scattering angle.

The present paper reports results obtained for elastic alpha-particle scattering by Ag, Ta, Pb, and Th. The dependence of cross section upon energy is in all cases similar to that for Au, although the critical energy E_0 and (to a much lesser degree) the coefficient K depend upon the atomic number of the scattering element. The results are interpreted in terms of a semiclassical strong absorption model due to Blair,[8] and information obtained about nuclear and alpha-particle radii is presented.

II. APPARATUS AND EXPERIMENTAL METHOD

A schematic view of the apparatus used in the present experiments is shown in Fig. 1. The deflected alpha-particle beam of the 60-inch cyclotron enters the evacuated target box T. Part of the beam passes through a defining aperture A in plate B. Variable

* Partially supported by the U. S. Atomic Energy Commission.
† Now at Brookhaven National Laboratory, Upton, New York.
[1] H. Geiger and E. Marsden, Proc. Roy. Soc. (London) **A82**, 495 (1909).
[2] E. Rutherford, Phil. Mag. **21**, 669 (1911).
[3] H. Geiger and E. Marsden, Phil. Mag. **25**, 604 (1913).
[4] J. Chadwick, Phil. Mag. **40**, 734 (1920).
[5] E. Rutherford and J. Chadwick, Phil. Mag. **50**, 889 (1925).
[6] E. S. Bieler, Proc. Roy. Soc. (London) **A105**, 434 (1924).
[7] George W. Farwell and Harvey E. Wegner, Phys. Rev. **93**, 356 (1954).
[8] J. S. Blair, following paper, Phys. Rev. **95**, 1218 (1954).

absorbers C_1 and C_2 reduce the alpha-particle energy; energies from 43 Mev down to 13 Mev are available in intervals of about 1 Mev. The alpha particles enter the thin foil target D, most of them being transmitted to the Faraday cup E, the current to which is monitored by a beam current integrator. Alpha particles scattered through an angle of approximately 60° pass down tube F and out through a vacuum-tight thin foil exit window W. A system of variable aluminum absorbers J and a coincidence proportional-counter telescope K_1, K_2 serve as a differential range device, giving both the number and the range of the elastically scattered alpha particles. Studies of elastic scattering at angles other than 60° can be made by using tubes G and H, which are mounted at approximately 90° and 125°, respectively, to the incident beam.

At each value of the incident alpha-particle energy (i.e., for each configuration of absorbers C_1 and C_2) the number of alpha particles scattered elastically during a convenient time interval is observed with the counter telescope and normalized against the integrated beam current; at the same time, a mean range determination is made which yields the energy of the incident alpha particles. Thus relative elastic scattering cross section is obtained as a function of alpha-particle energy.

The water-cooled absorber C_1 is constructed of five layers of 0.35-mil copper foil arranged in a stepwise manner as shown in Fig. 1; each step is wider than the aperture A. Absorber C_2 is similar in construction, with individual copper foil thicknesses of 1.8 mils. The two absorbers may be moved across the aperture A by remote control, allowing the absorber thickness to be adjusted in steps of approximately 0.35 mil. Thus incident alpha-particle energies ranging from 43 Mev (no absorber) down to about 13 Mev (the minimum energy necessary for a range measurement in the detecting system) are available in steps of approximately 1 Mev.

The target foil D is preceded by a defining baffle (not shown) which prevents alpha particles scattered by absorbers C_1 and C_2 from registering on the Faraday cup E without traversing the target foil. The usual target thickness is about 0.3 mil.[9]

Since the entire target assembly is located within the fringing field of the cyclotron magnet, the trajectories of the scattered alpha particles are curved. The curvature depends upon alpha-particle energy, and it is difficult to determine the exact angle of scattering for each energy. Study of calculated trajectories indicates that for the "60°" case, the angle of scattering ranges from about 62° at 10 Mev to 59° at 40 Mev; 60° is the estimated value at the energies of primary interest (Sec. III).

[9] Very uniform thin foils of a number of elements were obtained from Baker and Company, Inc., 113 Astor Street, Newark 5, New Jersey. The Pb foil was rolled in our laboratory. The Th foil, made by electrolytic methods, was kindly furnished by Professor F. H. Schmidt.

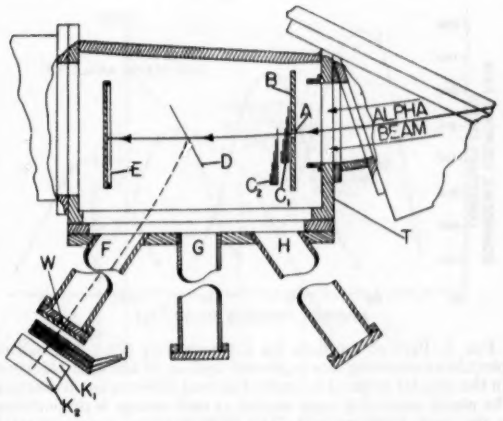

FIG. 1. Plan view (schematic) of scattering apparatus. A, aperture in plate B for defining the alpha-particle beam; C_1 and C_2, remotely controlled absorbers for reducing beam energy; D, thin foil target; E, Faraday cup; F, G, and H, observation ports; W, thin foil exit window; J, variable aluminum absorber for differential-range proportional-counter telescope K_1, K_2.

The variable aluminum absorber J consists of three remotely controlled foil wheels mounted on a common axis. Each foil wheel contains a series of Al foil stacks of increasing thickness mounted in equally spaced holes near its periphery. The position of each foil wheel can be controlled independently, so that total absorber thicknesses of from zero to 412 mg/cm² of Al, in steps of 1.2 mg/cm², can be interposed between scattering foil and counters.

The proportional counters K_1 and K_2 are contained in a common envelope filled with argon at a pressure of about $\frac{1}{4}$ atmosphere. Collecting electrodes are 2-mil wolfram wires maintained at a positive potential of 800 volts.

Pulses from each counter pass through a well-shielded battery-operated preamplifier, located in the cyclotron room, to a linear amplifier and discriminator located in the control room. Discriminator outputs are fed to a coincidence circuit and scaler. The coincidence circuit requires that an alpha particle pass through both counter K_1 and counter K_2 in order to be registered. Proton pulses are biased out. Energy selectivity is adjusted by means of discriminator bias on the K_2 channel; the higher the bias, the more strict the requirement that the particle just end its range in counter K_2, thus giving the maximum possible ionization in that counter.

Figure 2 shows a small part of the data for a typical run. Coincidence counting rate, normalized to the integrated beam current, is plotted against Al absorber thickness for each of several different beam energies. The elastic scattering cross section at each energy is proportional to the peak counting rate. The alpha-particle energy for a given peak is found by noting the Al absorber thickness at the peak and adding corrections for energy loss in the target foil, the exit window, the

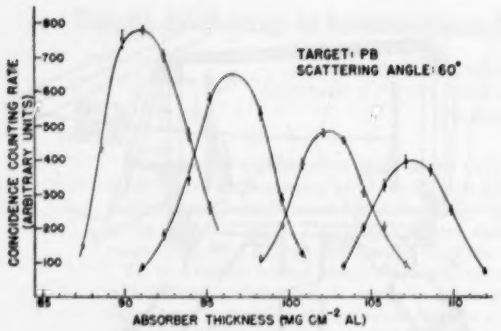

FIG. 2. Part of the data for a typical run (Pb). Normalized coincidence counting rate is plotted against Al absorber thickness (in the counter system) for each of several different beam energies. The elastic scattering cross section at each energy is proportional to the peak counting rate. The alpha-particle energy for each peak is found from the absorber thickness after addition of appropriate corrections (see text).

air path to the counter, and the counter itself. Total equivalent range in Al is then found and converted to energy by use of range-energy curves.[10]

The data plotted in Fig. 2 were taken with biases set for less-than-maximum energy selectivity. The average peak width (full width at half-maximum) is about 6 mg/cm²; at an alpha-particle energy of 30 Mev the corresponding energy width is about 1.0 Mev. Use of maximum selectivity was found to give peaks approximately two-thirds as broad, indicating an actual beam energy spread of perhaps 0.4 Mev, if range straggling in the absorbers is taken into account.

Despite the broadened energy window, the conditions of less-than-maximum energy selectivity were found to give more reliable data. Location of peak positions with an uncertainty of 1 mg/cm² Al or less was easy under these conditions. Under conditions of maximum selectivity, the Al absorber steps were large enough so that the true peak counting rate was often not achieved; further, very slight shifts in beam energy during traversal of a peak caused difficulties.

A possible question concerning the operating conditions actually used is whether alpha particles scattered inelastically with small energy losses were counted in significant numbers. The quite accurate Coulomb dependence of the cross sections at low energies (Sec. III) argues against this possibility. Further evidence is found in the fact that occasional checks made with maximum selectivity showed counting rates of not more than 5 percent of the peak counting rate for energies immediately below the elastic peak energy. Contributions from elastically scattered alphas from surface contaminants such as C and O were shown to be well out of the picture because of the relatively large amounts of energy lost to the light recoil nuclei.

The counters were checked at frequent intervals during each run by observing the 8.8-Mev Th C′ alpha particles from a Th B source mounted in one of the foil wheels. In this way it was established that the counter efficiency did not change during a run. The natural alpha source was also useful in measuring the Al equivalent of the counter, counter window, and air path, as well as in demonstrating that the cyclotron magnetic field and the intense gamma-ray and neutron fluxes present under operating conditions had no adverse effects upon the counter system.

Because of the directional sensitivity of the counter telescope, it was necessary to correct the data to take into account multiple small-angle scattering in the variable aluminum absorber J (Fig. 1). A correction factor varying by about 10 percent over the extreme energy range 43 to 13 Mev was applied to the data, the efficiency of the counter system being greatest for particles of lowest energy.

Further details of the apparatus and experimental procedures are given elsewhere.[11]

III. RESULTS AND DISCUSSION

Typical of the results[12] obtained are those for elastic scattering of alpha particles by Pb at 60° in the laboratory system. These results are shown in Fig. 3, in which cross section is plotted against alpha-particle

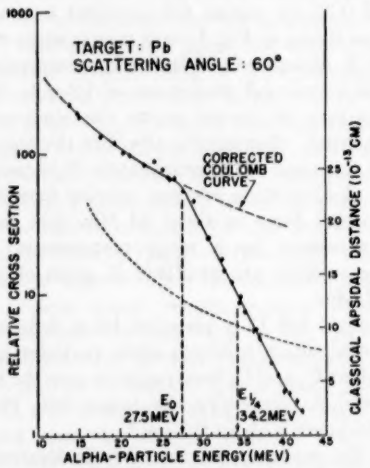

FIG. 3. Elastic scattering of alpha particles by lead at 60° (laboratory system). Cross section (relative) is plotted on a logarithmic scale against alpha-particle energy. The low-energy data are normalized to a corrected Coulomb curve (see text). The critical energy E_0 corresponds to the intercept of the straight-line portion of the experimental curve with the corrected Coulomb curve. At the energy $E_{1/4}$, the experimental cross section is one-quarter of the Coulomb cross section. The lower dashed curve and the scale on the right show the apsidal distance for the classical alpha-particle trajectory as a function of alpha-particle energy.

[10] Aron, Hoffman, and Williams, U. S. Atomic Energy Commission, Document AECU-663, 1949 (unpublished).

[11] Harvey E. Wegner, thesis, University of Washington, 1953 (unpublished).

[12] Most of these results were first presented at the 1954 Washington meeting of the American Physical Society; see G. W. Farwell and H. E. Wegner, Phys. Rev. **95**, 664(A) (1954).

energy. The alpha-particle energy is that measured by the counter system, and is about 2 percent less than the incident energy because of the energy lost to the recoil nucleus. A logarithmic scale is used for the cross section in order to avoid undue compression of the high-energy part of the curve and to bring out its simple nature.

The "corrected Coulomb curve" shown is normalized to the low-energy experimental data. This curve follows approximately the inverse square dependence of the Coulomb (Rutherford) cross section upon alpha-particle energy, but it is altered slightly to take into account the small variation of scattering angle with energy due to the fringing magnetic field of the cyclotron (Sec. II).

At low energies, the observed cross section follows the Coulomb dependence satisfactorily. At about 27 Mev, however, the cross section begins to drop very rapidly as the alpha-particle energy increases. As in the case of Au (Sec. I), the energy dependence of the cross section over a considerable range of energies is given by the simple empirical formula

$$\sigma(E)=\sigma(E_0)\exp\{-K(E-E_0)\}.$$

The critical energy E_0 corresponds to the intercept of the straight-line portion of the experimental curve with the corrected Coulomb curve. In this case it has the value 27.5 ± 0.3 Mev. The coefficient K is 0.266 ± 0.006 Mev^{-1}.

The lower dashed curve in Fig. 3 shows the classical apsidal distance as a function of alpha-particle energy. The critical energy E_0 is seen to correspond to an apsidal distance of about 13×10^{-13} cm, a distance much larger than the sum of the accepted values of the Pb nuclear radius (8–9×10^{-13} cm) and the alpha-particle radius (1–2×10^{-13} cm), and it is evident that nuclear effects are strongly felt at somewhat larger distances than might be expected intuitively.

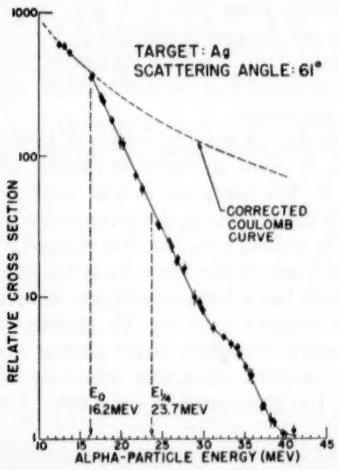

FIG. 4. Elastic scattering of alpha particles by silver at 61°.

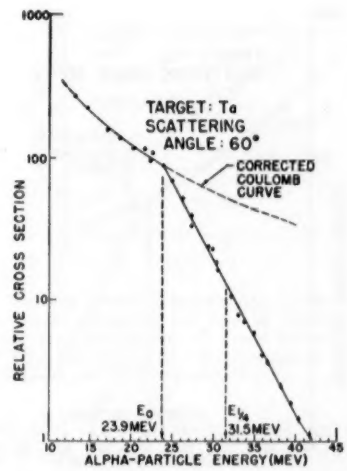

FIG. 5. Elastic scattering of alpha particles by tantalum at 60°.

The significance of the parameter $E_{1/4}$, the energy at which the observed cross section has fallen to one-quarter of the Coulomb cross section, is discussed below (Sec. IV). In the case of Pb, $E_{1/4}$ has the value 34.2 ± 0.4 Mev, corresponding to a classical apsidal distance of about 10.3×10^{-13} cm.

Figures 4, 5, and 6 show the experimental results for Ag, Ta, and Th, respectively.

In the case of Ag (Fig. 4), normalization to the Coulomb curve is less certain than for the other elements studied. Because of the low Coulomb barrier, nuclear effects leading to a rapidly decreasing cross section set in at much lower energies. Another feature which distinguishes the Ag curve is the abrupt shift of the straight-line portion of the curve which takes place between 31 and 35 Mev; this shift is as yet unexplained.

Table I summarizes the results for the parameters E_0, $E_{1/4}$, and K. For completeness, data[7] for Au are included, although the experimental curves are not presented in this paper. The probable errors given take into account uncertainties in determination of total range of the scattered particles at each energy and in fitting Coulomb and straight-line curves to the appropriate parts of the experimental data. Allowance for errors in the range-energy curves has not been made; however, such errors should be of the order of 1 percent or less and would affect all results similarly. The values given for K were obtained by means of least squares solutions of the data for the high-energy portions of the curves.

IV. INTERPRETATION

The parameters E_0, $E_{1/4}$, and K listed in Table I can be measured quite accurately. If a correlation can be made between these parameters and the alpha-particle and nuclear radii, the experiments offer a promising means of obtaining information about nuclear radii.

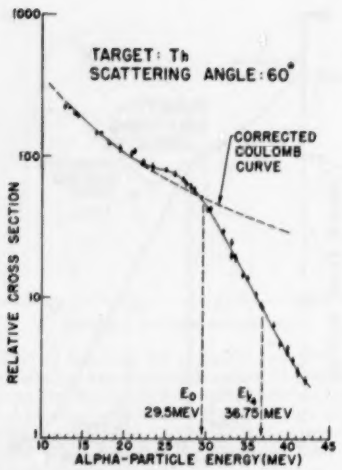

FIG. 6. Elastic scattering of alpha particles by thorium at 60°.

A semiclassical strong absorption model has been used by Blair[8] to interpret the present experiments. In this model the outgoing lth partial wave is assumed to vanish if the apsidal distance for the corresponding classical trajectory is less than the sum of the radius of the nucleus and the radius of the alpha particle; otherwise it has a phase characteristic of pure Coulomb scattering. The theory predicts that the sum of nuclear and alpha-particle radii is approximately equal to the classical apsidal distance evaluated at the energy for which the experimental cross section is one-quarter of the corresponding Coulomb cross section. It is this energy which is given in Table I as $E_{1/4}$.

Table II gives the classical apsidal distances D_0 and $D_{1/4}$ corresponding to the observed alpha-particle energies E_0 and $E_{1/4}$, respectively. Allowance for the motion of the recoil nucleus has been made in the calculations. The estimated probable errors are based upon the uncertainties in E_0 and $E_{1/4}$ and in the angle of scattering.

As a measure of the consistency of the results and the validity of the interpretation, Table II also lists the values of the quantity $D_{1/4}-R_n$. (The nuclear radii are calculated from $R_n=r_0A^{\frac{1}{3}}$, with $r_0=1.50\times10^{-13}$ cm.) According to Blair's interpretation, $R_\alpha=D_{1/4}-R_n$ represents the effective collision radius of the alpha particle and should be the same for all cases. The results for R_α agree within the experimental uncertainties except for the case of Au at 96°, which gives a value slightly larger than the others.

Other values of r_0 give reasonable agreement with the present results if one is willing to accept larger values for the alpha-particle radius. In Fig. 7, the experimental values of $D_{1/4}$ are plotted against $A^{\frac{1}{3}}$. Under the assumption that $D_{1/4}=r_0A^{\frac{1}{3}}+R_\alpha$, curves are shown for several values of r_0 and R_α. The best fit to the experimental points is given by $r_0=1.50$ and $R_\alpha=1.38$ (units of 10^{-13} cm). Taking $r_0=1.35$ and $R_\alpha=2.24$ also gives reasonable agreement although the Ag point is then low. For $r_0=1.20$, the Ag point is even farther off and the very large value $R_\alpha=3.10$ is indicated.

In estimating nuclear radii from lifetimes and energies in alpha decay, Blatt and Weisskopf[13] have assumed an effective alpha-particle radius of 1.2×10^{-13} cm. This gives satisfactory agreement with nuclear radii determined from total neutron cross-section measurements in cases (Pb and Bi) where both types of data are available. Although a radius of 2.24×10^{-13} cm, here corresponding to $r_0=1.35\times10^{-13}$ cm, would not be unreasonable,[14] it would be difficult to accept the very large values of R_α required by the choice of still smaller values of r_0.

It should be noted that the one-quarter point interpretation used here is defined most sharply for scattering angles near 90° (see following paper by J. S. Blair). For scattering at 60°, the best theoretical fit to the experimental data is obtained by using radii about 0.5×10^{-13} cm larger than those obtained from the one-quarter point recipe. A still larger increase is indicated for the best theoretical fit for silver; since the experimental result is both the lowest (with respect to the general trend) and the least precisely determined, this is not surprising.

The values for the slope parameter K for 60° scattering (Table I) show a slight downward trend with increasing Z. The exception to this trend is Ta. The exception is also visible in the abnormally large value of D_0 for Ta, although $D_{1/4}$ for this element follows the general trend accurately. Since Ta is the only element studied which has a large quadrupole moment, one is tempted to suggest that the Ta nucleus presents a slightly smaller or slightly larger nuclear "radius" to the alpha particle, depending upon its orientation relative to the alpha-particle trajectory. The average

TABLE I. Summary of experimental parameters. E_0 is the critical energy above which departures from Coulomb scattering occur. (See also the caption for Fig. 3.) $E_{1/4}$ is the energy at which the observed cross section is one-quarter of the Coulomb cross section. K is the slope parameter for the high-energy part of the curve. Above the critical energy, the cross section follows the energy dependence $\sigma(E)=\sigma(E_0)\exp\{-K(E-E_0)\}$.

Target element	Scattering angle[a]	Z	E_0 (Mev)	$E_{1/4}$ (Mev)	K (Mev^{-1})
Ag	61°	47	16.2±0.4	23.7 ±0.4	0.281±0.004
Ta	60°	73	23.9±0.3	31.5 ±0.4	0.251±0.004
Au	60°	79	27.0±0.3	33.6 ±0.4	0.271±0.004
Pb	60°	82	27.5±0.3	34.2 ±0.4	0.266±0.006
Th	60°	90	29.5±0.4	36.75±0.5	0.246±0.004
Au	96°	79	20.4±0.4	24.9 ±0.4	0.394±0.010

[a] Estimated for the energies near E_0 and $E_{1/4}$. The uncertainty is about ±1°.

[13] J. M. Blatt and V. F. Weisskopf, *Theoretical Nuclear Physics* (John Wiley and Sons, Inc., New York, 1952), p. 574.
[14] Reference 13, p. 357.

"radius" is not abnormal, but the steepness of the high-energy $\sigma(E)$ curve is lessened, and nuclear effects are felt at slightly larger distances than would be the case for a spherical nucleus. This possibility will be tested by looking at other elements with large quadrupole moments.

Blair's theoretical curves of cross section *versus* energy[8] show a slight increase over the Coulomb cross section just before the sudden drop at the critical energy. The experimental curve for Th exhibits such a rise, but it is considerably more spread out than that of the theoretical curve. The Pb and Ta data are not inconsistent with such a rise, but the evidence is considered inconclusive.

V. SUMMARY AND CONCLUSIONS

Cross sections for the elastic scattering of alpha particles by Ag, Ta, Au, Pb, and Th show the same general energy dependence. Up to a certain critical energy E_0, which increases with Z, the cross section for each element decreases with increasing alpha-particle energy in agreement with the Rutherford formula. At higher energies, the cross section drops sharply with increasing energy and can be represented over a considerable energy range by the simple empirical formula $\sigma(E)=\sigma(E_0)\exp\{-K(E-E_0)\}$. The slope parameter K appears to decrease slightly with increasing Z, although the value of K for Ta is out of line with this trend.

TABLE II. Classical apsidal distances. D_0 and $D_{1/4}$ are the classical apsidal distances corresponding to alpha-particle energies E_0 and $E_{1/4}$, respectively (see Table I). $D_{1/4}-R_n$ may be interpreted as the effective radius of the alpha particle (see text).

Target element	Scattering angle	A	D_0 (10^{-13} cm)	$D_{1/4}$ (10^{-13} cm)	R_n* (10^{-13} cm)	$D_{1/4}-R_n$ (10^{-13} cm)
Ag	61°	107.9	12.2 ±0.4	8.3 ±0.3	7.14	1.2 ±0.3
Ta	60°	180.9	13.05±0.21	9.90±0.16	8.48	1.42±0.16
Au	60°	197.2	12.50±0.20	10.05±0.16	8.73	1.32±0.16
Pb	60°	207.2	12.76±0.21	10.26±0.17	8.88	1.38±0.17
Th	60°	232.1	13.06±0.21	10.48±0.17	9.22	1.26±0.17
Au	96°	197.2	12.76±0.35	10.45±0.25	8.73	1.72±0.25

* Nuclear radius calculated from $R_n=r_0A^{1/3}$, with $r_0=1.50\times10^{-13}$ cm.

Analysis of the elastic scattering problem in terms of a semiclassical strong absorption model leads to the conclusion that the experimental cross section should be equal to one-quarter of the Coulomb (Rutherford) cross section at the alpha-particle energy for which the classical apsidal distance $D_{1/4}$ is equal to the sum of the nuclear and alpha-particle radii.

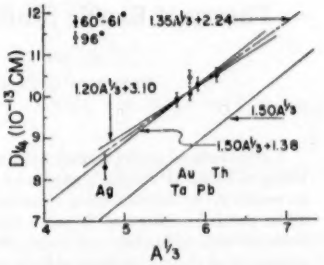

FIG. 7. Classical apsidal distance $D_{1/4}$, which in the strong absorption model represents the sum of nuclear and alpha-particle radii, is plotted against $A^{\frac{1}{3}}$. Under the assumption that $D_{1/4}=r_0A^{\frac{1}{3}}+R_\alpha$, the best fit to the experimental data is given by $r_0=1.50$ and $R_\alpha=1.38$ (units of 10^{-13} cm).

Assuming $D_{1/4}=r_0A^{\frac{1}{3}}+R_\alpha$, the best fit for the experimental data is given by $r_0=1.50\times10^{-13}$ cm, $R_\alpha=1.38\times10^{-13}$ cm. Values of r_0 less than 1.35×10^{-13} cm lead to poor fits to the experimental data and to unreasonably large values for the alpha-particle radius.

More data are needed at both higher and lower Z. Going to lower Z requires observation at smaller scattering angles in order to include a region of pure Coulomb scattering. It is also desirable to test the theoretical interpretation of the results by observations on the present target materials at angles other than 60°, since the indicated nuclear radii should be independent of the scattering angle. Preparations are being made for these experiments.

VI. ACKNOWLEDGMENT

We are indebted to Dr. J. S. Blair for many valuable discussions concerning the progress of the experimental work and the theoretical interpretation of the results. Thanks are also due Mr. T. J. Morgan and other members of the cyclotron group, particularly Mr. D. D. Kerlee, Mr. D. J. Farmer, and Mr. J. R. Penning, for their assistance in cyclotron operation and construction of experimental equipment.

Theory of Elastic Scattering of Alpha Particles by Heavy Nuclei*

J. S. BLAIR
Department of Physics, University of Washington, Seattle, Washington
(Received May 24, 1954)

A semiclassical model is used to interpret recent experiments of Farwell and Wegner on the elastic scattering of 13–42 Mev alpha particles by heavy nuclei. In this model the outgoing lth partial wave is assumed to vanish if the corresponding classical turning point is less than the radius of the nucleus plus that of the alpha particle; otherwise, it has a phase characteristic of pure Coulomb scattering. The theory predicts that the sum of nuclear and alpha-particle radii is approximately equal to the classical apsidal distance evaluated at the energy for which the experimental cross section is one-quarter of the corresponding Rutherford cross section.

FARWELL and Wegner have measured the differential cross section for the elastic scattering of 13–43 Mev alpha particles as a function of energy for several heavy nuclei at a scattering angle of 60° and for gold at 96°.[1,2] Below a certain "critical energy" E_0, the cross sections have the energy dependence characteristic of pure Coulomb scattering, i.e., they follow the Rutherford formula. Above this critical energy the observed cross sections markedly drop below the pure Coulomb scattering cross section; when the logarithm of the cross section is plotted *versus* the energy, in the region above E_0 the curves are approximately straight lines with slopes which depend chiefly on scattering angle. The energy E_0 is a function of both scattering nucleus and angle. In the present note an attempt is made to explain these experimental results by means of a phase shift analysis which incorporates a crude semiclassical boundary condition at the nuclear surface.

Before discussing this model, however, let us briefly consider the scattering using the hypothesis that the motion of the alpha particle can be described classically and that the alpha particle and nucleus can be pictured as spheres with distinct radii. For classical considerations to have any validity, it is necessary that the reduced wavelength of relative motion, $\lambda\equiv(\hbar/mv)$, be much smaller than nuclear dimensions; in the present experiments, $(\lambda/R)\sim(1/20)$, so that a classical picture should have some qualitative merit. So long as the path of the alpha particle does not allow the nucleus and alpha particle to overlap, a classical alpha particle ollows the well-known hyperbolic path due to pure Coulomb repulsion. For given energy and nuclear charge, the scattered angle in the center-of-mass system, ϕ, is uniquely related to the angular momentum, p, through $p=(ZZ'e^2/v)\cot(\phi/2)$. Further ϕ is uniquely related to the distance of closest approach or apsidal distance, D, by $D=(ZZ'e^2/2E)(1+\csc(\phi/2))$. In these relations, Ze is the nuclear charge, $Z'e=2e$ is the charge of the alpha particle, v is the relative velocity, and E is the energy in the center-of-mass system.

When $D\leqq R$, where $R=R_n+R_\alpha$, the sum of nuclear and alpha-particle radii, deviations from pure Coulomb scattering are expected.[3,4] In particular, if it is assumed that the alpha particles are strongly absorbed or broken up by the nucleus, very few alpha particles should then emerge unscathed from the nucleus. Thus at a given scattering angle, there will be a marked decrease in the scattering cross section as the energy is raised above the energy at which $D=R$. If D_0, the distance of closest approach at E_0, is chosen as a measure of R, radii of a reasonable order of magnitude are obtained although these are slightly larger than the sum of radii obtained by other means;[5] for example, the critical energy for gold at $\phi=96°$ corresponds to $D\cong13(10^{-13})$ cm.[2]

Two explanations seem plausible for the fact that the experimental curves of cross section *versus* energy show a finite slope after the "break." One is that the alpha particle may have a finite mean free path in nuclear matter. The second is that the relative motion is not strictly classical, but rather there will be some quantum-mechanical spread of the trajectory. The second suggestion seems more promising to pursue since it also provides an explanation for the large apparent radii mentioned above. We therefore proceed with a quantum-mechanical discussion of the scattering process.

The quantum-mechanical expression for the differential elastic scattering cross section is well known[6] in terms of partial waves representing the relative motion of the centers of mass of the nucleus and alpha particle:

$$d\sigma=\left|\frac{\lambda}{2i}\sum_{l=0}^{\infty}(2l+1)(\eta_l-1)P_l(\cos\phi)\right|^2 d\Omega. \qquad (1)$$

In this formula, η_l is the coefficient of the outgoing lth partial wave and is determined by the boundary conditions at the nuclear surface. For pure Coulomb scattering, $\eta_l=\exp(2i\sigma_l)$, where

$$\sigma_l=\sigma_0+\sum_{l''=1}^{l}\arctan(n/l'') \quad \text{and} \quad n=(ZZ'e^2/\hbar v).$$

* Partially supported by the U. S. Atomic Energy Commission.
[1] G. W. Farwell and H. E. Wegner, Phys. Rev. **93**, 356 (1954).
[2] G. W. Farwell and H. E. Wegner, Phys. Rev. **95**, 1212 (1954).
[3] E. Bieler, Proc. Roy. Soc. (London) **A105**, 434 (1924).
[4] E. Rutherford and J. Chadwick, Phil. Mag. **50**, 889 (1925).
[5] See J. M. Blatt and V. F. Weisskopf, *Theoretical Nuclear Physics* (John Wiley and Sons, Inc., New York, 1952), pp. 13–16.
[6] See Blatt and Weisskopf (reference 5), p. 323.

Moderate energy proton scattering has been previously investigated with models in which either (a) the interior of the nucleus is represented by a complex potential, thus allowing for both refraction and absorption of the proton wave,[7-9] or (b) the strong absorption of the wave is expressed by the boundary condition that there are no outgoing waves inside the nucleus.[7,9,10] It is difficult to use these models in the present problem, however, since η_l is a function of the Coulomb wave functions evaluated at the nuclear surface; such functions are not tabulated for values of Z and E which are here needed.[11]

As an alternative, the following crude semiclassical model is adopted: First, the nucleus and the alpha particle are again considered to be spherical particles with definite radii. Second, if the potential barrier of the lth wave allows the nucleus and alpha particle to overlap when considered classically, the outgoing lth wave is assumed to vanish. Third, if the barrier is such that the nucleus and alpha particle do not classically overlap the outgoing lth wave has the phase characteristic of pure Coulomb scattering. These assumptions may be more concisely stated:

$$\begin{aligned} &\eta_l=0 && \text{if} \quad l\leqq l', \\ &\eta_l=\exp(2i\sigma_l) && \text{if} \quad l>l', \end{aligned} \tag{2}$$

where $\hbar l'$ is defined as that angular momentum for which the classical turning point is equal to $R=R_n+R_\alpha$, i.e.,

$$E=(ZZ'e^2/R)+(\hbar^2 l'(l'+1)/2mR^2). \tag{3}$$

The crudity of the model is obvious. The drastic boundary condition when $l>l'$ neglects absorption due to penetration of the barrier. Further, the assumption $\eta_l=0$ for $l\leqq l'$ neglects reflection due to the sudden change of "refractive index" at the nuclear surface, as well as reflection due to the potential outside the nucleus. In support of the model, however, it should be mentioned that the assumptions of model (b) above lead to $\eta_l\to 0$ when l is so small that the Coulomb wave functions approach their asymptotic amplitudes at the nuclear surface and the change in kinetic energy at the surface is small compared to the energy itself. Correspondingly, it can be demonstrated that model (b) implies that $\eta_l\to\exp(2i\sigma_l)$ when $l\gg l'$. Akhieser and Pomeranchuk[12] and, recently, Clementel and Coen[13] have used this semiclassical model to study the elastic very small angle scattering of high-energy charged particles.

When the η_l are given by Eq. (2), the differential cross section becomes:

$$\begin{aligned} d\sigma=\tfrac{1}{4}\lambda^2\big|&[-in/\sin^2(\phi/2)] \\ &\times\exp[-in\ln\sin^2(\phi/2)+2i\sigma_0] \\ &-\sum_{l=0}^{l'}(2l+1)\exp(2i\sigma_l)P_l(\cos\phi)\big|^2 d\Omega. \end{aligned} \tag{4}$$

According to Eq. (4), the scattered amplitude is simply the amplitude for Coulomb scattering minus the contribution to Coulomb scattering of all outgoing waves up to l'. The ratio of the above cross section to that for pure Coulomb scattering, $(d\sigma/d\sigma_c)\equiv G$, has been computed as a function of l' (l' running from 1 to 30) and a variety of n for $\phi=90°$ and 60°. For a given R, Z, and ϕ, these curves can be used to find $d\sigma$ as a function of E since $l'=l'(E,Z,R)$ and $n=n(Z,E)$. (When the ratio G is computed, l' takes on only integer values. In what follows, however, l' is treated as a continuous variable and corresponding values of G are determined by interpolation.)

Before continuing with the detailed comparison between experimental and theoretical curves, let us discuss how the present model relates to the previous classical picture; this digression will be particularly worth while since it leads to a simple prescription for estimating R.

The parameter n can be considered a measure of how "classical" is the pure Coulomb scattering since it equals a distance characteristic of the classical solution, namely D evaluated at $\phi=180°$, divided by twice the reduced wavelength. In the present alpha-particle experiments n is of the order 10, so that for these values of n the quantum-mechanical should approach the classical description of Coulomb scattering. In particular, it is anticipated that the most important contribution to Coulomb scattering at a specific angle comes from those partial waves whose angular momentum is of the order of the classical angular momentum, p, i.e., from partial waves with l of the order $l_{cl}\equiv n\cot(\phi/2)$.

The plot of G *vs* (l'/l_{cl}) when $\phi=90°$, shown in Fig. 1, verifies this expectation. As was mentioned earlier, $d\sigma$ can be interpreted as the cross section obtained when the contributions of all partial waves with l up to l' are sliced out of the pure Coulomb scattering amplitude. Thus the graph of G *vs* (l'/l_{cl}) shows the relative contributions of the various partial waves to Coulomb scattering. It is seen in Fig. 1 that G is of the order unity for small l', rapidly decreases for l' of the order l_{cl}, and flattens out for l' much larger than l_{cl}. Further the decrease in G is relatively more abrupt with the larger n.

In addition it is observed that all of the curves in Fig. 1 cross at $l'=l_{cl}$ and the value of G at this point is approximately (1/4). This phenomenon is interpreted to mean that the pure Coulomb scattering amplitude is "centered" about l_{cl} in the sense that half of the scatter-

[7] R. E. LeLevier and D. S. Saxon, Phys. Rev. **87**, 40 (1952).
[8] R. Britten, Phys. Rev. **88**, 283 (1952).
[9] D. M. Chase and F. Rohrlich, Phys. Rev. **94**, 81 (1954).
[10] H. Feshbach and V. F. Weisskopf, Phys. Rev. **76**, 1550 (1949).
[11] Bloch, Hull, Broyles, Bouricius, Freeman, and Breit, Revs. Modern Phys. **23**, 147 (1951).
[12] A. Akhieser and I. Pomeranchuk, J. Phys. (U.S.S.R.) **9**, 471 (1945).
[13] E. Clementel and A. Coen, Nuovo cimento **10**, 988 (1953).

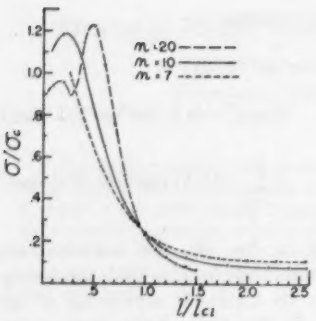

FIG. 1. Ratio of cross sections, σ/σ_c, plotted *versus* the ratio, l'/l_{c1}, for three values of n and $\phi=90°$. The ratio can be computed only for even integer values of l', indicated by the dots, and the smooth curves are interpolated.

ing amplitude is due to partial waves with $l<l_{c1}$; when these waves are removed from the scattered wave the resulting intensity is one-quarter of what it is when no partial waves are subtracted.

The above observation makes it possible to estimate R in a simple manner: The experimental cross section curves are examined to determine the energy at which $d\sigma/d\sigma_c=\frac{1}{4}$. Now it was just seen that the semiclassical strong absorption model predicts that $l'=l_{c1}$ when $d\sigma/d\sigma_c=\frac{1}{4}$ regardless of the value of n. Further, by definition, l_{c1} corresponds to the partial wave with classical turning point equal to D while l' corresponds to the partial wave whose classical turning point is R. Thus at the one-quarter point energy, $E_{1/4}$,

$$R=D_{1/4}\equiv(ZZ'e^2/2E_{1/4})[1+\csc(\phi/2)]. \qquad (5)$$

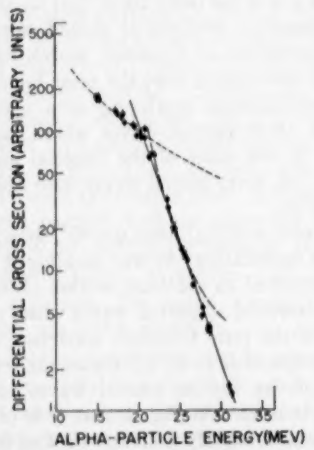

FIG. 2. Differential scattering cross section for gold at $\phi=90°$. The short dashed curve gives the Rutherford cross section; the computed cross section for $R=10.95(10^{-13})$ cm agrees with this for $E<20.5$ Mev but beyond this energy is given by broad dashed curve. The points give the experimental cross sections observed by Farwell and Wegner (reference 1) at the 90° port; the theoretical and experimental cross sections are normalized at 15 Mev. The straight line is the best straight line representing the experimental values beyond the critical energy.

The "one-quarter point" phenomenon can be described perhaps more pictorially as follows: The outgoing wave describing pure Coulomb scattering is centered about the classical trajectory in the sense that half of the contributions to the outgoing wave come from partial waves which classically penetrate closer to the origin than does the classical trajectory. When in addition to the Coulomb potential, there is present strongly absorbing nuclear matter extending to a distance $R=D$, the amplitude of the outgoing component of these waves is damped so that only half of the scattering amplitude remains, namely that contribution due to partial waves which do not classically penetrate beyond D.

For this "one-quarter point" recipe to have any meaning, the theory must also give the correct shape of the curve of cross section *vs* E, and predict the correct location of the critical energy, E_0; as will be seen later, these features are fairly well duplicated. It is also only fair to point out two inaccuracies of this one-quarter point recipe: (1) There is the familiar uncertainty of order one in l simply because quantum-mechanically the square of the angular momentum is not $(\hbar l)^2$ but $\hbar^2 l(l+1)$. Strict application of the definition of l', Eq. (3), leads to values of R which are of the order $0.2(10^{-13})$ cm larger than that given by Eq. (5). (2) For ϕ different from 90°, the plots of G *vs* (l'/n) are not so easily interpolated and thus make the analysis less certain. However, the best smooth curves at $\phi=60°$, for example, do not appear to cross exactly at $l'=l_{c1}$, and indicate that G is slightly higher than 0.25 at $l'=l_{c1}$. Thus the best over-all fits to the experimental curves at 60° are obtained with choices for R which are slightly larger than those predicted by the one-quarter point recipe. In the case of Pb, for example, the best fit is obtained for the choice $R\cong 10.6(10^{-13})$ cm while $D_{1/4}=10.26(10^{-13})$ cm.[2] The worst discrepancy between $D_{1/4}$ and the R giving the best fit occurs for the lightest element studied, Ag; in this case a fit to the data is obtained for R as large as $9.5(10^{-13})$ cm although $D_{1/4}=8.3(10^{-13})$ cm.[2]

We shall now continue with the detailed comparison of experimental and theoretical curves. In Fig. 2 the experimental cross section for scattering alpha particles from the 90° port is compared with the cross section computed for $R=10.95(10^{-13})$ cm and $\phi=90°$. The curves are normalized at 15 Mev, an energy well below the Coulomb barrier for "head-on" collisions; at such an energy, the scattering is anticipated to be purely Coulomb. The two curves agree fairly well except for large values of E. The change of slope at these energies can be traced to the leveling off of G for $l'>l_{c1}$. It is believed that this leveling off effect is due to the sharp transition from pure Coulomb phase shifts to complete absorption at $l=l'$, and is analogous to the "ringing" effect observed when a Fourier series is abruptly terminated. A more realistic boundary condition at R is expected to give a theoretical cross section which

decreases more rapidly at large E than does that computed from the present model.

Some caution should be exercised when comparing the theoretical and experimental curves of Fig. 2. For one thing, it is estimated that the theoretical curve may be uncertain by as much as 5 percent due to the graphical interpolation which was necessary to obtain G as a function of E. More important, it should be pointed out that the experimental and theoretical curves of Fig. 2 correspond to somewhat different situations: (a) The theoretical curve was computed for $\phi=90°$ in the center-of-mass system while it was later found that the average experimental ϕ corresponding to the 90° port was 97° in the center-of-mass system.[1,2] (b) Moreover, the experimental ϕ changes by perhaps 3° over the energy range here considered.

The points determining G do not lie on such smooth curves when ϕ is different from 90°. This is illustrated in Fig. 3 where the points give the value of G corresponding to the various integers l' when $n=10$ and $\phi=60°$. For purposes of graphical interpolation, a smooth curve is sketched which appears to give the best fit of the scattered points. It is felt that the uncertainty introduced when this smooth curve is used for interpolation is no worse than the uncertainty of any curve designed to pass through the limited number of points. Also, it is believed that a theory which incorporates a more realistic and less sharp boundary condition will predict that these oscillations are damped. Nonetheless, one should be careful in interpreting the cross sections resulting from use of a smooth curve of G *vs* l', since the points may deviate 10 percent from the smooth curve when G is of the order unity and may deviate as much as 50 percent when G is small.

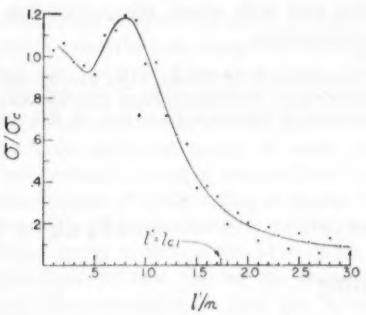

FIG. 3. Ratio of cross sections, σ/σ_c, plotted *versus* l'/n for $n=10$ and $\phi=60°$. The ratio can be computed only for integer values of l', indicated by the dots. The curve is judged to be the best smooth curve representing these points, and is the curve used for interpolation.

The comparisons of experimental and theoretical cross sections at the 60° port are shown in Fig. 4 and Fig. 5. One source of error present in the comparison at the 90° port is less important at 60°, namely, the average experimental scattering angle in the center-of-mass system is 61° which is only 1° larger than value chosen in the computations.

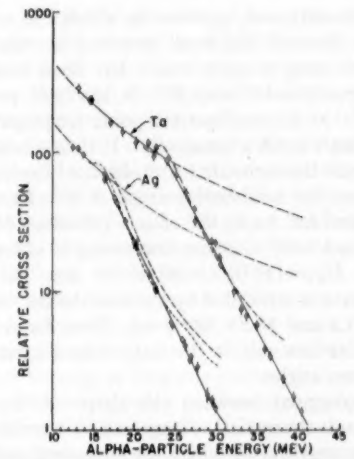

FIG. 4. Differential cross sections for Ag and Ta at $\phi=60°$ as a function of alpha-particle energy. In both cases the broad dashed curve gives the Rutherford cross section; the points and solid curves represent the experimental cross sections observed by Farwell and Wegner (see reference 2). In the case of Ta, the small dashed curve gives the theoretical cross section for $R=10.54(10^{-13})$ cm. In the case of Ag, two theoretical curves are shown; the finer dashed curve is for $R=9.67(10^{-13})$ cm and the larger dashed curve is for $R=8.84(10^{-13})$ cm. (One should not compare the relative magnitude of the Ta and Ag curves; their relative orientation is purely a matter of convenience.)

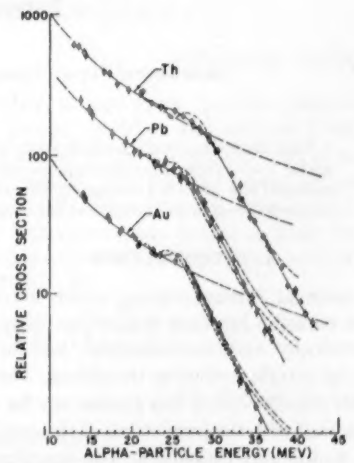

FIG. 5. Differential cross sections for Au, Pb, and Th at $\phi=60°$ as a function of alpha-particle energy. In all cases the broad dashed curves give the Rutherford cross section; the points and solid curves represent the experimental cross sections observed by Farwell and Wegner (see references 1 and 2). Two theoretical curves are shown for Au: the finer dashed curve corresponds to $R=10.58(10^{-13})$ cm while the larger dashed curve corresponds to $R=10.3(10^{-13})$ cm. Two theoretical curves are shown for Pb: the finer dashed curve corresponds to $R=10.87(10^{-13})$ cm while the larger dashed curve corresponds to $R=10.42(10^{-13})$ cm. The dashed theoretical curve in the case of Th corresponds to $R=11.01(10^{-13})$ cm.

There is only one instance in which the scattering from one element has been observed at two angles; this is the case of gold which has been studied for scattering angles 60° and 96°. It has been previously observed that the one-quarter point recipe provides a good estimate for R when $\phi=90°$. It then seems reasonable to trust the estimate for R obtained from this prescription at the neighboring angle of 96°; Farwell and Wegner find for Au at 96°, $D_{1/4}=(10.45\pm0.25)(10^{-13})$ cm.[2] When $\phi=60°$ it is now interesting to observe that, although $D_{1/4}=(10.05\pm0.16)(10^{-13})$ cm, the experimental curve is straddled by the two theoretical curves for $R=10.3$ and $10.58(10^{-13})$ cm. Thus for this single case, one radius will fit the data within experimental error at two angles.

The agreement between the shape of the experimental and theoretical cross section curves over a range of energy during which the cross section drops by more than a factor 10 suggests not only that the present semiclassical strong absorption model has more merit than its crudity would indicate, but also that it is possible to think of the alpha particle and nucleus as possessing fairly definite collision radii.

The values of R obtained by the "one-quarter point" prescription were given and discussed in the previous paper.[2] In general, these values of R yield theoretical curves whose over-all behavior is in fair agreement with the experimental cross sections. As mentioned before, however, the choice of somewhat larger R gives better agreement for $\phi=60°$ and the deviation between these values of R becomes larger as Z is decreased. It will be noted that, if one assumes a reasonable radius of the order $2(10^{-13})$ cm or less for the alpha particle, then the resulting nuclear collision radii can be fitted moderately well with the usual formula, $R_n=r_0A^{\frac{1}{3}}$, where $r_0\cong(1.5)(10^{-13})$ cm. This is in agreement with other estimates of nuclear collision radii and emphasizes the distinction between the "electromagnetic" and "nuclear force" radii.[14-16]

The author wishes to thank many members of the Department of Physics at the University of Washington for helpful comments. He is particularly indebted to Professor G. W. Farwell and Dr. H. E. Wegner who have made available the experimental data prior to publication and with whom the author has had invaluable discussions.

[14] L. N. Cooper and E. M. Henley, Phys. Rev. **92**, 801 (1953).
[15] V. L. Fitch and J. Rainwater, Phys. Rev. **92**, 789 (1953).
[16] F. Bitter and H. Feshbach, Phys. Rev. **92**, 837 (1953).

PHYSICAL REVIEW VOLUME 95, NUMBER 5 SEPTEMBER 1, 1954

Internal Bremsstrahlung*

R. E. CUTKOSKY
Department of Physics, Carnegie Institute of Technology, Pittsburgh, Pennsylvania
(Received November 4, 1953)

Some theorems are given which apply to the beta radiation and internal bremsstrahlung emitted by light nuclei. Use of these theorems simplifies the calculation of approximate spectra and angular correlations. The principal new result is a simple, explicit relation between the spectra and angular correlations of the internal bremsstrahlung of K capture and the spectra and angular correlations of positrons.

1. INTRODUCTION

THE internal bremsstrahlung which accompanies beta emission has been studied by many writers, both theoretically[1] and experimentally,[2] and for allowed as well as for certain forbidden transitions. The spectra and angular correlations of this gamma ray for all cases agree quite well with the predictions of the semiclassical theory of Knipp and Uhlenbeck. The spectrum of the internal bremsstrahlung of K capture, which has been given by Morrison and Schiff,[3] is also in agreement with the measured spectra,[4] but the theory of this process, which does not have a classical analog, has been given hitherto only for allowed transitions. The principal object of this study is to examine the properties of the internal bremsstrahlung of K capture for forbidden transitions; in particular, the spectra and the angular correlation with a subsequent (nuclear) gamma ray.

We show that one can obtain as much information about electron-capturing nuclei by studying the gamma rays they emit as one can obtain about beta-emitting

* Taken from a dissertation presented to the Carnegie Institute of Technology in partial fulfillment of the requirements for the degree of Doctor of Philosophy. This work was supported by a National Science Foundation Predoctoral Fellowship.
[1] J. K. Knipp and G. E. Uhlenbeck, Physica **3**, 425 (1936); F. Bloch, Phys. Rev. **50**, 272 (1936); C. S. Wang Chang and D. L. Falkoff, Phys. Rev. **76**, 365 (1949); J. M. Jauch, Oak Ridge National Laboratory Report ORNL 1102, 1951 (unpublished). Madansky, Lipps, Bolgiano, and Berlin, Phys. Rev. **84**, 596 (1951).
[2] T. B. Novey, Phys. Rev. **89**, 672 (1953); Bolgiano, Madansky, and Rasetti, Phys. Rev. **89**, 679 (1953).
[3] P. Morrison and L. I. Schiff, Phys. Rev. **58**, 24 (1940).
[4] Bradt *et al.*, Helv. Phys. Acta **19**, 222 (1946); D. Maeder and P. Preiswerk, Phys. Rev. **84**, 595 (1951); Anderson, Wheeler, and Watson, Phys. Rev. **87**, 608 (1952), and Phys. Rev. **90**, 606 (1953).

nuclei by studying their beta radiation. Experiments which make use of the internal bremsstrahlung are extremely difficult, but would provide invaluable information, as they are the only source of information about some of the properties of electron-capturing nuclei. The calculation of the spectra and angular correlations is greatly facilitated by two techniques, illustrated hereafter, which have applications to a much wider class of problems than that which is the chief concern of this paper. In Sec. 2 a way of treating the Coulomb wave functions will be introduced which is extremely convenient in the lowest approximation which does not neglect the large spin-orbit coupling effect. In Sec. 3, using this method, relationships between various radiative and nonradiative beta processes are given which enable one to obtain the spectra and angular correlations of the internal bremsstrahlung from those which have been given for beta decay.[5,6]

2. COULOMB WAVE FUNCTIONS

Those who have studied the effect of the Coulomb field on the processes of beta decay[6] have proceeded by expanding the electron wave functions in angular momentum eigenstates, and then at some point in the calculation have often made the assumption that Z is small and have neglected terms of order αZ, while keeping the dominant terms of order $\alpha Z/mR$ (m is the mass of the electron, R is the radius of the nucleus, and we let $\hbar=c=1$). This cumbersome procedure can be circumvented easily if one is not attempting to find exact expressions, by first making the above approximation and then summing to find the approximate solutions which asymptotically have the form of plane waves (with ingoing spherical waves). More precisely, we note that it is possible to write

$$\Psi(\mathbf{r};\mathbf{p},\sigma)=A(\mathbf{r},\mathbf{p})u(\mathbf{p},\sigma), \tag{1}$$

where $\Psi(\mathbf{r};\mathbf{p},\sigma)$ is the wave function with asymptotic momentum $\mathbf{p}$ and spin σ, $A(\mathbf{r},\mathbf{p})$ is a matrix function, and $u(\mathbf{p},\sigma)$ is a plane-wave spinor. If the states are restricted to have positive energy, A has the form

$$A=f_1(\mathbf{r},\mathbf{p})+\beta f_2(\mathbf{r},\mathbf{p})+i\boldsymbol{\alpha}\cdot\mathbf{r}[f_3(\mathbf{r},\mathbf{p})+\beta f_4(\mathbf{r},\mathbf{p})], \tag{2}$$

where the f's are ordinary scalar functions. We wish to find an approximate expression for A for $r<R$ and small Z, which may be done by comparing (1) with the expansion for a plane wave traveling along the z axis and then using the fact that A must be invariant in rotations.

One finds

$$A(\mathbf{r},\mathbf{p})=1+i(\mathbf{p}\cdot\mathbf{r})-\tfrac{1}{2}(\mathbf{p}\cdot\mathbf{r})^2+i\xi(\boldsymbol{\alpha}\cdot\mathbf{r}) -\tfrac{1}{2}\xi(\boldsymbol{\alpha}\cdot\mathbf{r})(\mathbf{p}\cdot\mathbf{r})+\cdots, \tag{3}$$

where $\xi=\alpha Z/2R$. To obtain Eq. (3) we have discarded terms strictly of order αZ or smaller, as well as terms which contribute only to third or higher forbidden transitions. We have also supposed that the velocity of the electron is greater than αZ, and that the radial wave function of a component with orbital angular momentum l is adequately represented inside the nucleus by a term of the form ar^l. The wave functions inside and outside of the nucleus have been matched in the naive fashion of equating this term ar^l to the value of the Coulomb wave function at $r=R$, which is equivalent to the usual procedure. We remark that (3) can also be obtained from the Furry wave function.[7] The matrix (3) applies to both spin states, and to states with either ingoing or outgoing scattered waves. It also applies to states with either positive or negative energy; we remember that the negative energy states are related to positive energy states by the operation of charge conjugation and observe that

$$A(\mathbf{r},\mathbf{p},Z)=CA^*(\mathbf{r},-\mathbf{p},-Z)C^{-1}. \tag{4}$$

In this equation the asterisk denotes the complex conjugate and C is the charge conjugation matrix. The utility of the matrix $A(\mathbf{r},\mathbf{p})$ arises from the fact that it enables one to perform all spin sums by the standard method of projection operators and spurs and thus exhibits the effect of the spin-orbit coupling in a particularly convenient form.

The interaction Hamiltonian density for beta decay may be written as

$$H_\beta=\sum_{ka} G_k(\bar{\psi}_N\lambda_a{}^k\psi_P)(\bar{\psi}_\nu\lambda_a{}^k\psi_e) +\text{Hermitian conjugate}, \tag{5}$$

where ψ_N, ψ_P, ψ_ν, and ψ_e are the field operators for the neutron, proton, neutrino, and electron fields, and $\lambda_a{}^k$ is the ath matrix of the kth covariant set of matrices in the Dirac algebra. The matrix element for emission of an electron with momentum $\mathbf{p}$, spin σ, and an antineutrino with momentum $\mathbf{q}$, spin ρ, while the nucleus makes a transition between the states with wave functions V and U, is

$$X_\beta=\bar{u}_e(\mathbf{p},\sigma)\sum_{ka} G_k\Big(U,\Big[\int\bar{\psi}_P\lambda_a{}^k\psi_N e^{-i\mathbf{q}\cdot\mathbf{r}} \times\bar{A}(\mathbf{r},\mathbf{p})d^3x\Big]V\Big)\lambda_a{}^k v(\mathbf{q},\rho) =\bar{u}(\mathbf{p},\sigma)\Lambda v(\mathbf{q},\rho). \tag{6}$$

With $Q_m{}^{k(\alpha)}(\mathbf{r})$ and $P_m{}^{k(\alpha)}(Z,\mathbf{p},\mathbf{q})$ denoting the mth components of the irreducible tensors[8] contained in (6),

$$\Lambda=\sum_{kam} G_k\Big(U,\Big[\int\psi_P{}^*Q_m{}^{k(\alpha)}(\mathbf{r})\psi_N d^3x\Big]V\Big) \times P_m{}^{k(\alpha)}(Z,\mathbf{p},\mathbf{q}). \tag{7}$$

[5] D. L. Falkoff and G. E. Uhlenbeck, Phys. Rev. **79**, 334 (1950).
[6] E. J. Konopinski and G. E. Uhlenbeck, Phys. Rev. **60**, 308 (1941); E. J. Konopinski, Revs. Modern Phys. **15**, 209 (1943); M. Fuchs, thesis, University of Michigan, 1951 (unpublished); E. Greuling and M. L. Meeks, Phys. Rev. **82**, 531 (1951).
[7] W. Furry, Phys. Rev. **46**, 391 (1934).
[8] D. L. Falkoff and G. E. Uhlenbeck, Phys. Rev. **79**, 323 (1950).

For first forbidden transitions, for example, the tensor interaction gives

$$\mathbf{Q}^{T(1a)}(\mathbf{r})=\boldsymbol{\beta\alpha},\quad \mathbf{P}^{T(1a)}(Z,\mathbf{p},\mathbf{q})=\boldsymbol{\alpha};\quad Q^{T(0)}(\mathbf{r})=\boldsymbol{\beta\sigma}\cdot\mathbf{r},$$

$$p^{T(0)}(Z)=\tfrac{1}{3}(-i\mathbf{p}-i\mathbf{q}+i\xi\boldsymbol{\alpha})\cdot\boldsymbol{\sigma}$$
$$=P^{T(0)}(Z=0)+i\xi P^{PS}(Z=0),$$

$$\mathbf{Q}^{T(1)}=\boldsymbol{\beta\sigma}\times\mathbf{r},$$

$$\mathbf{P}^{T(1)}(Z)=-\tfrac{1}{2}(-i\mathbf{p}-i\mathbf{q}+i\xi\boldsymbol{\alpha})\times\boldsymbol{\sigma}$$
$$=\mathbf{P}^{T(1)}(Z=0)+\xi\mathbf{P}^{T(1a)}(Z=0),\quad (8a)$$

$$Q_{ij}{}^{T(2)}=\beta(\tfrac{1}{2}\sigma_i r_j+\tfrac{1}{2}\sigma_j r_i-\tfrac{1}{3}\boldsymbol{\sigma}\cdot\mathbf{r}\delta_{ij}),$$

$$P_{ij}{}^{T(2)}=\tfrac{1}{2}(-ip_i-iq_i+i\xi\alpha_i)\sigma_j$$
$$+\tfrac{1}{2}(-ip_j-iq_j+i\xi\alpha_j)\sigma_i-P^{T(0)}(Z)\delta_{ij}$$
$$=P_{ij}{}^{T(2)}(Z=0);$$

the scalar interaction gives

$$\mathbf{Q}^{S}(\mathbf{r})=\boldsymbol{\beta}\mathbf{r},$$

$$\mathbf{P}^{S}(Z,\mathbf{p},\mathbf{q})=-i\mathbf{p}-i\mathbf{q}+i\xi\boldsymbol{\alpha}$$
$$=\mathbf{P}^{S}(Z=0)+i\xi\mathbf{P}^{T(1a)}(Z=0).\quad (8b)$$

For all first forbidden transitions, the terms in the P's which are proportioned to ξ are the same as other first forbidden P's for $Z=0$. The transition probabilities for all processes, which involve the P's quadratically, can therefore be obtained easily as linear combinations of corresponding transition probabilities for $Z=0$, in this approximation. Note that (8) and the similar relations for the other interactions give directly the well-known results that $\Delta I=0$, ±1 (yes) transitions will almost always have allowed spectra and allowed angular correlations, and that the $\Delta I=\pm2$ (yes) transitions are not so greatly affected by the Coulomb field. Second forbidden transitions are not quite as simple. The transition probabilities for small Z cannot always be expressed in terms of the transition probabilities for the same process in the limit $Z=0$. We easily find, however, that the ξ^2 terms in $|X_\beta|^2$ are always the same as the terms associated with the matrix elements A_{ij} and $A_{ij}{}^\beta$, with the neutrino momentum doubled, and the fact that there is no large Coulomb effect in $\Delta I=\pm3$ (no) transitions appears as a consequence of the anticommutativity of the Dirac matrices. Similar relations hold in nth forbidden transitions.

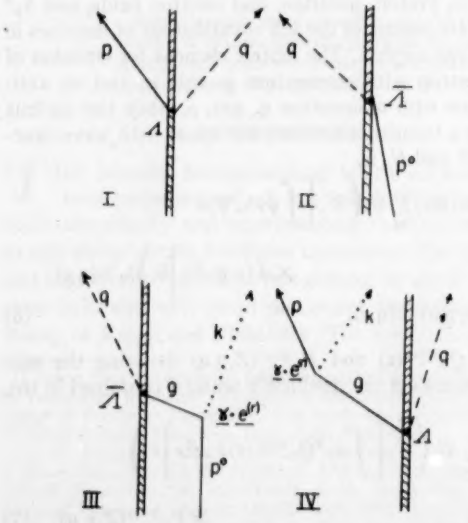

FIG. 1. Feynman diagrams for several beta-decay processes. The nucleus is supposed to be infinitely heavy and at rest.

3. INTERNAL BREMSSTRAHLUNG FOR LIGHT ELEMENTS

From Eq. (6), the beta-emission transition probability is proportional to

$$\sum|X_\beta|^2=\tfrac{1}{4}\,\mathrm{Tr}\left\{\int\bar{\Lambda}\left(i\gamma_0-\frac{i\boldsymbol{\gamma}\cdot\mathbf{q}}{q}\right)\right.$$
$$\left.\times\Lambda d\Omega_q\frac{m+i\gamma_0E-i\boldsymbol{\gamma}\cdot\mathbf{p}}{E}\right\}\quad (9)$$
$$=\tfrac{1}{4}\,\mathrm{Tr}\left\{N(\mathbf{p},q,\xi)\frac{m+i\gamma_0E-i\boldsymbol{\gamma}\cdot\mathbf{p}}{E}\right\}.$$

The Dirac matrix N which is thus introduced is a function of the nuclear quantum numbers and the coupling constants, as well as of $\mathbf{p}$, q, and ξ. Note that the matrix element (6) may be defined by diagram I of Fig. 1; through the use of the matrix A we may, in this approximation, consider the effect of the Coulomb field to be included in the interaction term Λ rather than in the propagation function of the electron, thus we consider the electron and neutrino to be both in plane wave states.

In the processes of radiative and nonradiative K capture we assume, in addition to the assumptions used in deriving (3), that the binding energy as well as the spread in momentum space and the small components of the K-electron wave function can be neglected, and that the gamma-emission matrix element is given by its value when $Z=0$. The errors thus introduced are all of order αZ or smaller compared to the terms which are kept, if in all continuum states the electron has a velocity $v\gg\alpha Z$.[9] If $p_\mu{}^0$ denotes the 4-momentum of an electron at rest and $\phi(0)$ the Schrödinger wave function of the K electron evaluated at the nucleus, the matrix element for the ordinary K capture, which is described

[9] The Coulomb field in intermediate states depends on whether there is an electron or a positron present. This also gives a small effect, which we disregard.

by diagram II, is

$$X_K=\bar{u}_\nu(\mathbf{q},\rho)\bar{\Lambda}u_e(0,\sigma)\phi(0), \tag{10}$$

where $\Lambda=\Lambda(0,-\mathbf{q},\xi)$; so that the transition probability is

$$P_K=(2\pi)^{-2}W^2\tfrac{1}{4}\,\mathrm{Tr}\{(1+\beta)N(0,-W,\xi)\}[\phi(0)]^2, \tag{11}$$

where W is the total energy liberated in the transition.

The radiative capture, described by diagram III, has the matrix element

$$X_{K\gamma}=ie(2\omega)^{-\frac{1}{2}}\phi(0)\bar{u}_\nu(\mathbf{q},\rho)\bar{\Lambda}\frac{-i\gamma_\mu g_\mu-m}{g_\mu{}^2+m^2}\mathbf{e}^{(r)}\cdot\boldsymbol{\gamma}u_e(0,\sigma), \tag{12}$$

where $g_\mu=p_\mu{}^0-k_\mu$, $\omega\equiv k_0$, and $\mathbf{e}^{(r)}$ is the polarization vector of the emitted photon. Squaring and summing gives

$$\begin{aligned}\sum|X_{K\gamma}|^2=&-\frac{2\pi\alpha}{\omega}[\phi(0)]^2\tfrac{1}{4}\,\mathrm{Tr}\left\{\left[\sum_r\frac{i\gamma_\mu g_\mu-m}{g^2+m^2}\boldsymbol{\gamma}\cdot\mathbf{e}^{(r)}\right.\right.\\&\left.\left.\times(1+i\gamma_0)\boldsymbol{\gamma}\cdot\mathbf{e}^{(r)}\frac{i\gamma_\mu g_\mu-m}{g^2+m^2}N(-\mathbf{k},-q,\xi)\right]\right\} \qquad (13)\\&=2\pi\alpha\omega^{-1}m^{-2}[\phi(0)]^2\tfrac{1}{4}\,\mathrm{Tr}\{(i\gamma_0-i\boldsymbol{\gamma}\cdot\boldsymbol{\varkappa})N\},\end{aligned}$$

where $\boldsymbol{\varkappa}=\omega^{-1}\mathbf{k}$. Referring to (9), we see that this is just equal to $2\pi\alpha\omega^{-1}m^{-2}[\phi(0)]^2$ times the corresponding expression for emission of a positron with momentum $\mathbf{k}$ and zero rest mass. The density of final states is also the same for a γ ray and such a positron, so the above calculation can be summarized by the following rule: Let P_γ be the probability for emission of a γ ray with momentum $\mathbf{k}$ in K capture, and let $P_{\beta+}$: be the probability for emission of a positron with the same momentum [and energy $E=(m^2+k^2)^{\frac{1}{2}}$] when the nucleus makes the same transition. The expression for $P_{\beta+}$ will of course involve the mass of the positron explicitly. *To obtain P_γ, set the rest mass equal to zero in $P_{\beta+}$, and multiply by $2\pi\alpha\omega^{-1}m^{-2}[\phi(0)]^2$.* For example, consider an allowed transition. Provided there is no Fierz interference,

$$N=4\pi i\gamma_0(\textstyle\sum G^2|M_{VU}|^2), \tag{14}$$

which with (13) gives the result of Morrison and Schiff,[3] and which with (9) gives the well-known allowed beta spectrum.

All radiative corrections to beta decay can be treated in a similar fashion by this method, when the same approximations are made. Consider for example the radiative beta emission, which is given by diagram IV. The matrix element is

$$X_{\beta\gamma}=ie(2\omega)^{-\frac{1}{2}}\bar{u}_e(\mathbf{p},\sigma)\boldsymbol{\gamma}\cdot\mathbf{e}^{(r)}\frac{i\gamma_\nu g_\mu-m}{g^2+m^2}\Lambda v_\nu(\mathbf{q},\rho). \tag{15}$$

The summed square has the form

$$\textstyle\sum|X_{\beta\gamma}|^2=2\pi\alpha\omega^{-1}\frac{1}{4}\,\mathrm{Tr}\{BN(\mathbf{p}+\mathbf{k},q,\xi)\}, \tag{16}$$

where, after some manipulation, one finds, with the notion $\mathbf{p}\cdot\mathbf{k}=pk\cos\theta$, $\Theta=1-pE^{-1}\cos\theta$:

$$\begin{aligned}B=&E^{-3}\omega^{-2}\Theta^{-2}\{mp^2\sin^2\theta+i\gamma_0[(E+\omega)p^2\sin^2\theta\\&+E\omega^2\Theta]-i\boldsymbol{\gamma}\cdot\mathbf{p}[p^2\sin^2\theta+E\omega\Theta]\\&-i\boldsymbol{\gamma}\cdot\boldsymbol{\varkappa}[(E+\omega)E\omega\Theta-m^2\omega]\}.\end{aligned} \tag{17}$$

The dominant term is (with $v=p/E$):

$$B_0=\frac{v^2\sin^2\theta}{\omega^2(1-v\cos\theta)^2}\left(\frac{m+i\gamma_0E-i\boldsymbol{\gamma}\cdot\mathbf{p}}{E}\right), \tag{18}$$

which should be compared with (9). The probability for emission of a low-energy photon, in this approximation, is thus

$$dP_{\beta\gamma}=\frac{\alpha}{4\pi^2}\frac{v^2\sin^2\theta}{\omega(1-v\cos\theta)^2}d\omega d\Omega_\gamma dP_\beta, \tag{19}$$

as has been shown for some special cases.[1] The calculation leading to (19) gives a quantum-mechanical verification that the classical theory gives a good description of this process. The corrections to (19) can be determined easily from (17).

The method explained above has been used to calculate the spectra and angular correlations of the K-capture bremsstrahlung for first and second forbidden transitions and for a mixture of the scalar, tensor, and pseudoscalar interactions. These results are not given here because their tabulation would require a great deal of space and because most of them can be obtained easily from the results of others[6] as indicated above. Of more importance than these particular results is the method used, which was found to be simpler than that of Fuchs,[6] whose results have been checked. The approach of Sec. 2 enables one to see easily how the spin-orbit coupling alters the character of many forbidden transitions, and the theorems of Sec. 3 provide a complete description of the internal bremsstrahlung of K capture and beta emission for light nuclei.

I am very grateful to Professor G. C. Wick for his kind interest, advice, and encouragement.

Scattering of Protons by Hydrogen Near 18 Mev*

J. L. YNTEMA† AND M. G. WHITE
Palmer Physical Laboratory, Princeton University, Princeton, New Jersey
(Received March 19, 1954)

The differential cross section for the scattering of 18.2±0.2-Mev protons by hydrogen has been measured over the angular range 30°–90° in the center-of-mass system. In order to reduce the over-all errors to less than 1 percent a 60-in. scattering chamber was used. Polyethylene, polystyrene, and nylon foils were used as scatterers while the proton-proton events were detected by observing coincidences between the scattered and recoil protons in anthracene photomultiplier counters. The incident proton beam was collimated to ±14 minutes of arc. Probable relative errors varied from 0.5 percent at 90° to about 1 percent at 30°, while the probable error in the absolute differential cross section at 90° is estimated to be 1 percent. The data show a significant deviation from pure S-wave scattering and are best fitted by taking S-, P-, and D-wave phase shifts to be $k_0=54.1°$, $k_1=+1.0°$, $k_2=+0.4°$, respectively.

I. INTRODUCTION

THE analysis of proton-proton scattering data obtained with incident proton energies of less than 10 Mev, using the method developed by Breit, Condon, and Present[1] has shown that in most cases these data are consistent with the assumption of only a S-wave phase shift. Breit and co-workers,[2] and Jackson and Blatt[3] have shown that, if one assumes that a central potential describes the interaction between protons adequately, the experimental data at these energies do not permit one to distinguish between different potential shapes. At higher energies one would expect to detect the presence of P- and D-wave phase shift, the magnitude of which would depend upon the assumed potential shape. Christian and Noyes[4] have shown that the data obtained by Panofsky and Fillmore,[5] and Cork, Johnston, and Richman[6] near 32 Mev do not show the expected P- and D-wave phase shift, but are consistent with the assumption of only a S-wave phase shift. Christian and Noyes have suggested the possibility of a masking of the P- and D-wave phase shifts, e.g., by a highly singular tensor interaction. If such a masking were present it might be less pronounced near 20 Mev than it would be at 30 Mev. However, the expected magnitude of the P- and D-wave phase shifts would be considerably smaller at 20 Mev than at 30 Mev and therefore harder to detect.

It was felt desirable to design the experiment so as to obtain a relative probable error of the order of one percent or less for the differential cross section between 30° and 90° in the center-of-mass system and to obtain an absolute probable error of one percent for the differential cross section at 90°.

II. DESIGN OF THE EXPERIMENT

The protons were supplied by the Princeton 35-in. synchrocyclotron. The available beam intensity after focusing by a magnetic lens system at 15 feet from the cyclotron was of the order of 10^{-9} amp over a 0.1-cm² area. The duty cycle of the cyclotron is about 2 to 5 percent depending upon the conditions of operation, with an average beam pulse length of about 15 microseconds. Hydrocarbon foils were used as target materials so as to obtain sufficient statistical accuracy in a reasonable time. The proton-proton events were detected by observing the coincidences between the scattered and recoil protons using anthracene crystals with photomultiplier tubes as detectors and a shorted line-type coincidence circuit.

The dimensions of the scattering chamber were determined by two requirements: (1) The solid angle subtended by the detector system was the one subtended by one of the apertures, which requires the solid angle subtended by the other, conjugate, aperture to be large enough to permit the entrance of all protons conjugate to the ones entering the defining aperture without introducing a prohibitively high single counting rate in either counter. (2) In determining the solid angle subtended by the defining counter one has to take into account the penetration of some protons through the edges of the aperture which causes the actual subtended aperture to be larger than the apparent one. In order for the effect to be negligible the area of the defining aperture should be large compared to the transparent area which sets a lower limit for the diameter of the aperture for a given permissible error. On the basis of these requirements a diameter of 60 in. was selected for the scattering chamber.

III. DESIGN OF THE 60-IN. SCATTERING CHAMBER

The scattering chamber, a vertical section of which is shown in Fig. 1, consists of a table B on which the target, defining apertures and detectors are mounted

* Supported in part by the U. S. Atomic Energy Commission and the Higgins Trust Fund.
† Present address: University of Pittsburgh, Pittsburgh, Pennsylvania.
[1] Breit, Condon, and Present, Phys. Rev. **50**, 825 (1936).
[2] G. Breit, Revs. Modern Phys. **21**, 238 (1951).
[3] J. Jackson and J. Blatt, Revs. Modern Phys. **22**, 77 (1950).
[4] R. S. Christian and H. P. Noyes, Phys. Rev. **79**, 85 (1950).
[5] W. K. H. Panofsky and F. L. Fillmore, Phys. Rev. **79**, 57 (1951); F. L. Fillmore, Phys. Rev. **83**, 1252(1951).
[6] Cork, Johnston, and Richman, Phys. Rev. **79**, 71 (1950).

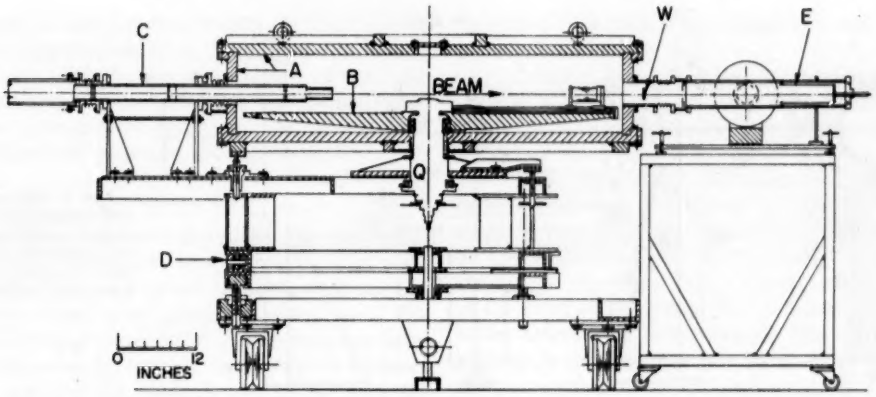

FIG. 1. The 60-inch scattering chamber. *A*, vacuum can; *B*, scattering table; *C*, beam collimating system; *D*, supporting structure; *E*, current collector; *Q*, table stem assembly; *W*, photographic plate holder.

and a collimation system *C*. It is necessary for the axis of the collimated beam to intersect with and be perpendicular to the axis of rotation of the chamber while the geometrical alignment obtained in air should not be affected by the evacuation of vacuum can *A*. This was achieved by having supporting structure *D* support both the collimation system *C* and, through table stem assembly *Q*, table *B*. The vacuum connection between *C* and *A* and *Q* and *A* are sylphon bellows which take up the deformation of *A* caused by evacuation without affecting the geometrical alignment obtained in air. Table stem assembly *Q* contained provisions for rotation of the table as well as for changing the angle between the two detectors while the system was evacuated.

1. Scattering Table *B*

The table was made out of aluminum 61ST6, its surface was machined flat to ± 0.005 in. and its thickness decreased from 2.75 in. at the center to 0.50 in. at the edge. Adjusting screws permit the table to be made accurately perpendicular to the axis of rotation of the table stem assembly *Q*. Care was taken to machine the central hole at the same time as the outer edge so as to insure concentricity. Graduation marks 0.012 in. wide were scratched in the outer edge every degree, or about 0.500 in. apart. Graduation accuracy was found to be better than two minutes of arc and by the use of a Bausch & Lomb microscope mounted outside the scattering chamber the angular position of the table could be located to better than 0.002 in.

2. Beam Collimation System

Adjustments for the beam collimation system are shown in more detail in Fig. 2. Collimating apertures 3 mm in diameter were mounted 75 cm apart inside a long, straight brass cylinder collimating the beam to ± 14 minutes of arc. Two lead baffle slits with 9-mm diameter apertures were used. One was located half-way in between the defining apertures and the other about 18 cm from the last aperture in a tube of smaller diameter so as to permit measurements to 172° in the laboratory system. The center line joining the two apertures must intersect and be perpendicular to the axis of rotation of the table with an accuracy greater than the spread in beam angle. This was achieved by the adjustments shown as follows. Translation in the horizontal plane is obtained through *A*, translation in the vertical plane through *B*. Rotation in the horizontal plane is obtained through *D* and in the vertical plane through *C* while spring *C'* presses the beam tube down on the top of screw *C*. After a satisfactory alignment has been obtained (perpendicular to the axis to better than 1 minute of arc and intersecting to ± 0.003 in.) the tube was clamped to the supporting brackets by rings as shown in Fig. 1. Sliding motion during evacuation was prevented by split-ring clamps around the tube.

3. Table Stem Assembly *Q*

The table stem assembly *Q* is shown in detail in Fig. 3. The main support for the table, 1, consists of a steel plate welded to a steel tube. This support was machined after the welding. The plate carries three arms which rest on the support structure through three tool steel, oil-hardened plates, one of which is flat, the second has a *V* groove and the third one a conical hole. The screws permit the leveling of support 1 and thus of the scattering table. The table has been bolted on to the steel ring which rests on a preloaded bearing. The tolerances on machining of these parts which locate the table position have been kept very small. The rotation of the table is made possible through Part 2. Part 3 is located with respect to Part 2 by a keyway and is press-fitted to the bearing. The vacuum seal between 1 and 2 is made through *V* rings as are the other vacuum seals in the table assembly. A worm gear system has been attached to Part 3. The latter can also be clamped so as to hold the table in place. Arm 5 is centered and rotated by a cylinder 4 which

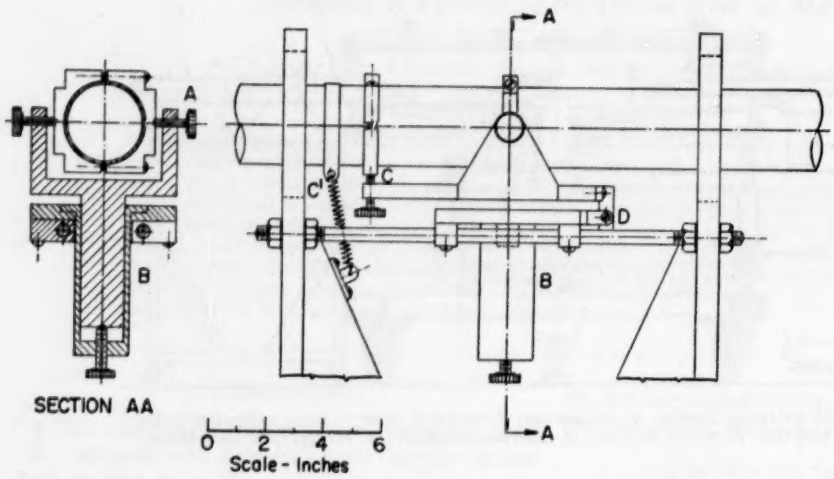

FIG. 2. Alignment of the collimating system. *A*, horizontal translation; *B*, vertical translation; *C*, *C'* rotation in vertical plane; *D*, rotation in horizontal plane.

also has a worm gear drive. Provisions were made to tie the motions of 2 to 4 by means of set screws. This required a clutch arrangement on the worm gear drive for arm 5. Arm 6 is centered by the upper bearing and is clamped to the edge of the table as shown.

The foil holder plate is carried by the top of the table stem assembly. Adjustments for lining up the axis of rotation in the plane of the foil have been provided for.

4. Supporting Structure

The motions required for aligning the scattering chamber with the deflected proton beam are translation, elevation, and leveling. The structure consists essentially of four frames. The bottom frame is made out of 6-in. ship channel. *V*-grooved swivel casters were bolted onto it. The vertical adjustment is made from this frame. A $\frac{1}{2}\times 20$ screw passes through a threaded block bolted to the channel. The height of the screw can be changed by turning a bolt which is supported by a ball bearing so as to eliminate unnecessary friction. A hardened steel ball rests on top of each screw and supports the second frame which has been made out of 4-in. ship channel. The balls rest against steel blocks, which have been bolted to the bottom of the second frame. On top of the channel, above the blocks, bearing plates have been mounted on which the third frame rests through ball bearings. These bearings are mounted in housings which have been bolted to columns welded to the top frame and are also bolted to the third frame. The two top frames thus form a unit which can rotate with respect to the two lower frames, over an angle of about 7°. This rotation is done by means of a screw with a fine thread. A bearing located under the second

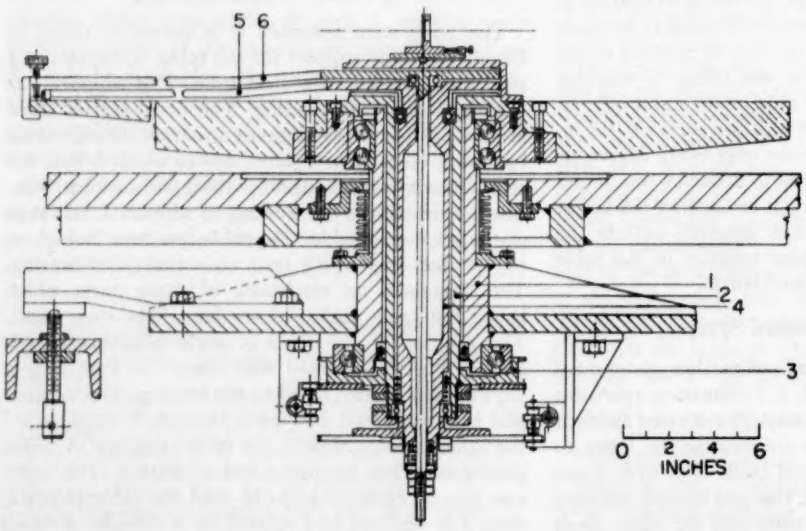

FIG. 3. Table stem assembly. *B*, scattering table; 1, table support; 5 and 6, arms for support of detectors.

frame keeps the two top frames from moving out. The top frame supports the beam collimating system and the scattering table. It also supports the vacuum can. The leveling of the vacuum can was accomplished through an arrangement similar to that used to level the structure with respect to the bottom frame.

5. Vacuum Can

The vacuum chamber consists of two reinforced steel plates and a cylinder. The cylinder is 12 in. high, $1\frac{7}{8}$ in. thick and has an interior diameter of 60 in. Top and bottom edges were machined down to a fine finish and two grooves for 0.210 O-rings were machined in. Two diametrically opposed holes serve as entrance and exit ports for the beam. A hole at 30° with the direction of the outgoing beam has been made to install a fixed angle monitoring counter. Two small holes for viewing the graduations at the edge of the scattering table were provided. The top and bottom plates are 1.5 in. thick; the top plate was reinforced with tack welded bars and the bottom plate with both bars and rings. The actual deflection measured with a dial indicator at the center of the bottom plate was 0.040 in. Holes have also been provided in the top and bottom plates for bringing in leads to the counters, for gas inlets, pressure gauges, and for the pumping unit.

IV. CURRENT INTEGRATOR

The collector cup is made of a heavy-wall 2.5-in. i.d. brass tube closed at one end by a heavy copper plate. On the inside the copper is covered with a sheet of graphite so as to reduce the fast neutron flux due to the stopping of 18-Mev protons. The cup is housed in a 4-in. o.d. brass tube, closed at the entrance by a 0.0015-in. Al foil which separates the vacuum inside the collector from that of the scattering chamber. At the back end the housing is closed by a polystyrene plate with a ground shield close to it. A 0.5-in. copper rod, screwed into the copper plate on the cup is brought out through an O-ring seal arrangement. The vacuum in the cup is generally held at 10^{-5} mm Hg. A magnet with 4-in. diameter pole tips is located as shown in Fig. 4. The magnetic field is approximately 300 gauss/amp in the normal region of operation. The current integration circuit is similar to the one constructed by Aamodt.[6] The copper rod is connected to a condenser and to an electrometer which is used as null indicating instrument. The collector cup is held very closely to ground potential through the compensating voltage supplied by batteries B through the intermediary of two 10-turn helipots of 500 and 150 ohms, respectively. The helipots are driven by a worm gear arrangement with a 1:60 reduction and operated by remote control. At the end of the run the voltage used to compensate for the charge due to the proton beam is measured on a Wolff-Feussner potentiometer, calibrated to 0.02 percent with a Leeds and Northrup Wenner potentiometer, through a 1:10 reduction provided by a volt box known to ±0.04 percent.

The capacitors were Unicon polystyrene capacitors ranging from 1.0 to 0.1 μf. They were calibrated by the National Bureau of Standards to ±0.2 percent using a time-constant current method. A recheck about one year after the original calibration of one of these capacitors showed a change of 0.5±0.2 percent in the originally reported value. The capacitors were calibrated at the temperature and relative humidity maintained during the experiment. The resistance was found to be of the order of 10^{14} ohms. Thus the time constants are of the order of 10^{7} to 10^{8} seconds. The upper limit for soakage in the dielectric was found to be 0.1 percent. Stray capacitances were found to have a negligible effect.

The electrometer used was a vibrating reed electrometer of the type described by Swank and Forstat.[7] With the input floating the resistance was of the order of 10^{16} ohm the input capacitance 10 μμf. The contact

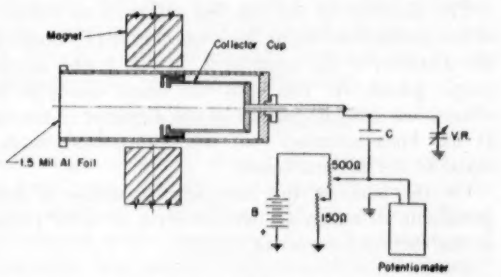

FIG. 4. Current integration circuit. C is calibrated condenser. $V.R.$ is vibrating reed electrometer. B is compensating voltage supply.

potential between reed and anvil was about 8 mv with a drift of less than 1 mv a day. The frequency of maximum converter efficiency was 292 cps. Since the instrument was used as null indicator only its absolute calibration was not important; usually it was operated at a sensitivity of about 5-mv full scale. This sensitivity permitted a fairly constant check on the current passing through the chamber.

It was felt desirable to make a certain number of checks on the consistency of the current integrator. In particular the integrated current should be independent of the voltage on the collector cup. Thin gold foils were used as targets and the detector was placed at an angle of about 7° with the outgoing beam. Since the cross section under those conditions varies to a good approximation with E_0^{-2}, where E_0 is the energy of the incident beam it was necessary to operate the cyclotron under constant conditions. The data given in Fig. 5 were obtained with a 0.0015-in. Al foil at the entrance and a field of approximately 500 gauss over the opening of the cup. The number of monitoring

[7] R. Swank and H. Forstat, Argonne National Laboratory Report CP3595 (unpublished).

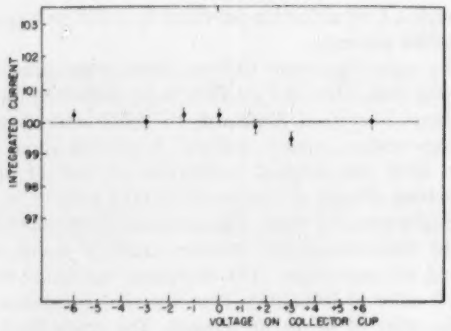

FIG. 5. Variation of integrated current as a function of voltage on the collector cup. The errors indicated are the standard deviation of the number of monitoring counts.

counts used was 300 000 and the error indicated is the standard deviation of the number of monitoring counts. In taking data the cup was always held within 0.5 v from ground potential.

The diameter of the cup was sufficient to collect all of the transmitted beam. This was checked by observing the diameter of the beam at W in Fig. 1 with spectroscopic plates. At this spot the beam diameter was always less than 10 percent of the diameter of the cup. It has been assumed that the transmitted beam is equal to the incident beam.

On the basis of the foregoing discussion it seems justifiable to assign an over-all error of ± 0.5 percent to the current integration circuit.

V. DETECTOR

The protons were detected by anthracene crystals in optical contact with RCA C7151 photomultiplier tubes. The pulses were clipped at the anode of the photomultiplier tube with a time constant of about 0.03 microsecond. Electrical breakdown around the photomultiplier tubes placed inside the vacuum can did not occur at pressures below 10^{-2} mm Hg.

The efficiency of the anthracene crystals has been checked by measuring the pulse height distribution of alpha particles from Po. It was assumed that the efficiency would be 100 percent for 5-Mev alpha particles. It was found that the average pulse height was about a factor 40 above the noise level. Varying the pressure in the system while keeping the geometry constant it was found that the probability for detecting 1.2-Mev alpha particles was 99 percent or higher. The effects of cracks in the crystal surface and other defects were investigated. These imperfections reduced the average pulse height by approximately 10 percent. Since the pulse height in anthracene at low energies is proportional to the range of the particle in the crystal and more or less independent of the nature of the particle, a 600-kev proton ought to be detected with more than 99 percent probability.

The protons scattered by hydrogen in the target are detected by observing the coincidences between the scattered and recoil protons. The problems of accidental coincidences and coincidence losses have been studied by Feather[8] and Westcott.[9] However it seems impractical to calculate the corrections and therefore the accidental coincidence rate was reduced as much as possible and the corrections were made experimentally. The coincidences were detected with a circuit similar to the one described by Bell, Graham, and Petch.[10] Since it was not possible to operate the photomultiplier tubes at very high voltages, the pulses were amplified by wide band amplifiers to produce the necessary pulse height for the cutoff of the tube.

The amplifiers which were used to amplify the pulses from the photomultiplier have been designed following Elmore's paper[11] and have a band pass of about 35 Mc/sec. The coincidence circuit had usually a resolving time of about 5×10^{-8} sec. The part of the pulse transmitted by the 1N34 diode in the case of a coincidence was amplified by a 25-Mc amplifier and from there fed in a scale of 16. The first stage of this scaler is identical to the one described by Fitch.[12] This stage will not trigger on pulses which are either much smaller or bigger than 5 volts. The fact that pulses smaller than 5 volts do not trigger this stage is used as a discriminator against the small pulses coming from the amplifier due to capacitive transmissions of single pulses by the biassed diode. Pulses bigger than 6 volts are limited by a diode circuit. The other stages of the scale of 16 are somewhat slower than the first stage but considerably faster than the usual design.

To count the number of accidental coincidences one changes the length of one of the cables from the cut-off tube to the shorted stub. If this length is increased by 15 meters coincidences due to proton-proton scattering are no longer recorded. The number of coincidences thus counted is taken to be the number of accidental coincidences.

The background can also be obtained if the included angle between the defining and conjugate counters is changed. In several cases this angle was changed from

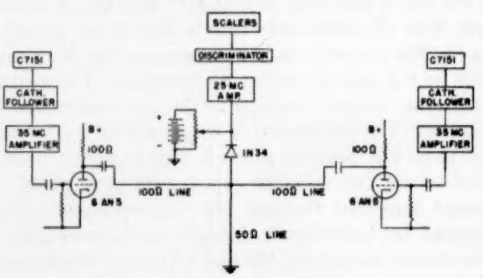

FIG. 6. Coincidence circuit.

[8] W. Feather, Proc. Cambridge Phil. Soc. **45**, 648 (1949).
[9] C. H. Westcott, Proc. Roy. Soc. (London) **A194**, 508 (1948).
[10] Bell, Graham, and Petch, Can. J. Phys. **30**, 35 (1952).
[11] W. C. Elmore, Nucleonics **5**, 48 (1949).
[12] Val Fitch, Rev. Sci. Instr. **20**, 942 (1950).

89.5° to about 86°. The results obtained were in substantial agreement with the delay line method, provided the beam intensity through the target was approximately the same. This may be taken to indicate that true coincidences, due to a $p,p\gamma$ reaction in carbon have a negligible effect.

The circuits were adjusted with a millimicrosecond pulse as described by Garwin.[13] This pulser was also used to check the behavior of the scale of 16. It was found that the first stage of this scaler will resolve two pulses separated by 0.07 μsec about 99 percent of the time.

When it was desirable to take single counting rates into any one channel the output of the cathode follower inside the vacuum can was connected directly to the input of a 25-Mc amplifier. The block diagram of the detection circuit is given in Fig. 6.

VI. DETERMINATION OF SOLID ANGLES

The solid angle subtended by the system is determined by the aperture of the defining counter and its distance from the center of the scattering. Circular apertures were used and their diameters measured both on a comparator and by direct comparison with a standard meter to about 1×10^{-3} mm. However, the effective diameter is different due to the slit edge penetration of the incident particles. It was felt desirable to estimate the effect of slit edge penetration experimentally. The number of particles which will be transmitted by the edges with an energy loss ΔE increases linearly with the diameter of the aperture while the solid angle subtended by the aperture increases with the square. Thus the relative effect decreases with r^{-1} if r is the radius of the aperture. Furthermore the effect, for small $\Delta E/E$, varies to a good approximation with E^2 where E is the energy of the particles incident on the aperture. Therefore the measurement of the cross section at, e.g., 25° and 65° with apertures with different radii ought to give an indication for the upper limit of the effect. If one compares runs 7 and 8 of Table II with runs 14 and 15 where the ratio of the aperture diameters was approximately 0.6 one can conclude that the effect is small. No corrections have been made for it in the final data.

The projected area of the defining aperture on the plane perpendicular to the radius vector from the scattering center will be fairly independent of the angle which the defining aperture makes with this plane, provided this angle be small. In general it has been possible to keep this angle smaller than 1° which gives an upper limit of error of 0.015 percent. The distance of the defining slit to the center of rotation of the scattering table was measured by two reading microscopes mounted on a rigid frame. The distance was measured by taking the difference between a standard length of 55.70 cm and the distance between the center and the aperture. This difference was of the order of a few millimeters and was measured with a traveling microscope. The target was placed at an angle of 45° with the scattered beam.

Since the solid angle subtended by the system was taken to be the solid angle $d\omega$ subtended by the defining aperture the angle subtended by the conjugate aperture $d\omega'$ has to be sufficiently large so as to admit all the protons conjugate to those entering the defining aperture. The geometrical relations are readily established. Another factor contributing to the spread of conjugate protons is the multiple scattering in the target. A reasonably good estimate for the required $d\omega'$ corresponding to a given $d\omega$ at an angle of scattering ϑ can be obtained. It was desirable, however, to ascertain experimentally that $d\omega'$ was large enough by measuring the cross sections for the different values of $d\omega'$ and increasing $d\omega'$ until the cross section remained constant. This could be done at all angles, except at the 30° point in the center-of-mass system. Though it appeared that the cross section remained constant and $d\omega'$ was larger than the calculated minimum value, it is felt that some uncertainty remains due to the limitations in the variation at this angle.

VII. TARGET MATERIAL

The target materials should be uniform over the area used, have negligible water absorption, accurately known chemical composition and be stable. These requirements seem to be met by polyethylene and polystyrene. The polyethylene was 0.0015 in. thick.[14] It has a very uniform gauge and no polymerizer is used in the polymerization. The polystyrene film used was 0.0005-in. cast polystyrene.[15] The water absorption was found to be less than 0.1 percent. A check on the presence of unpolymerized material was made and found to be less than 0.04 percent. No change in scattering cross section as a function of bombarding time was found. Both the polyethylene and polystyrene foils were analyzed by Mr. R. Paulsen of the National Bureau of Standards, Chemistry Division. The carbon and hydrogen content were determined by a semimacro method, using 0.5 to 0.8 gram per sample. The data are given in Table I, together with the estimated uncertainties.

The samples analyzed at the Bureau of Standards were considerably larger than the ones actually used in the experiments. The latter were about 1.00 in. ×1.75 in. and the polyethylene samples weighed about 36 mg each. However, since the composition is very well represented by CH_2 or CH as the case may be, there is little probability for a deviation from the chemical composition as determined by the semimacro method. The area of the foils used was measured to about 0.1 percent by direct comparison with the

[13] R. Garwin, Rev. Sci. Instr. **21**, 903 (1950).

[14] Obtained from E. I. Dupont de Nemours, Special Film Department.

[15] Obtained from Plax, Inc., Hartford, Connecticut.

TABLE I. Analysis of hydrocarbon foils.

Sample	%H	%C	Residue after combustion	%O
$(CH_2)^a$	14.38	85.59	0.03	0.08
	14.37	85.51	0.04	
	14.37	85.57	0.00	
$(CH)^a$	7.84	91.72	0.05	0.40
0.0005 in.	7.84	91.76	0.02	
$(CH)^a$	7.86	91.68	0.11	0.33
0.0008 in.	7.84	combustion	incomplete	
Estimated uncertainty	±0.02	±0.04		±0.02[a] ±0.04[b]

[a] For polyethylene.
[b] For polystyrene.

standard meter. The weight was determined to about 0.01 percent with a microbalance.[16] The uniformity of the polyethylene film was not measured directly. However, the cross sections obtained from three different foils and from different sections of the same foil are in excellent agreement and it is felt that a probable error of 0.4 percent describes the uniformity reliably. With polystyrene some idea of the uniformity may be obtained by observing green-light fringes in a Michelson interferometer. No high accuracy can be expected from such measurements. The data obtained with a 0.0005-in. polystyrene foil are in excellent agreement with the polyethylene data. In the measurements at 20°, 18°, and 15°, in the laboratory system it was desirable to use a somewhat thinner target. Targets of 0.0002-in. polyethylene[16] and 0.0005-in. nylon were used at these angles. Since the chemical composition of these foils was not known, the cross sections were calculated by comparison with respect to 25° or 30°.

VIII. ENERGY OF INCIDENT PROTONS

The energy of the incident beam was determined by a range measurement in Al of protons elastically scattered by carbon at 30°.[17] The protons were detected with a proportional counter 0.75 in. in diameter and filled at 32 cm with A and 2 percent of CO_2. The pulse-height discrimination was set so as to count only particles producing maximum ionization. The proportional counter was sealed with an Al foil of 7 mg/cm². The counter was placed 2 cm outside the scattering chamber. The peak of the distribution curve was found for a thickness of interposed Al of 458 mg/cm². The scattering foils used in these experiments were polyethylene films with a thickness of 0.00375 cm. The particles came out of the foil at a 30° angle and the mean loss of energy of the particles in the foil after scattering was estimated to be equivalent to 3 mg/cm² of Al. The protons thus have a total range of 472 mg/cm² in Al. If one uses the experimentally determined range of 18-Mev protons in Al[18] to correct the theoretically calculated range-energy curve one obtains a value for the energy of about 17.92 Mev. This corresponds to a value of 18.28 Mev for the energy of the incident protons, with an estimated error of ±0.2 Mev.

The proton beam is certainly not monoenergetic. However, since the cross section over the range 90° to 30° at this energy varies to a good approximation as E^{-1} some inhomogeneity will not affect the results. The results certainly would be affected by a variation in the mean value of the energy from run to run. There are indications that the mean value of the incident energy can be varied as much as 4 percent depending on the conditions of operation. However, since the value of the magnetic field was kept constant during the different runs and since the voltage on the deflector could not be varied much due to the strong collimation at the entrance of the chamber it is felt that the probable variation in mean energy is considerably smaller. Experiments in which gold was used as a scatterer and where the detector was placed at an angle where the cross section varies to a good approximation with E^{-2} indicated that the probable variation in E_0 was of the order of ±0.4 percent. One also has to consider the contribution to the cross section of a possible low-energy component in the beam. This component is mainly due to the collimating system of the scattering chamber. From calculations of Courant[19] it may be estimated that the apparent slit-widening effect is of the order of 0.5 percent. This estimate is based on the assumption that the detectors will not detect scattering due to particles with an energy of less than 75 percent of the mean energy of the incident beam. This assumption seems to be a reasonable one. The error due to this effect is negligible over the angular and energy range with which we are concerned in this experiment. There seems to be also a small low-energy tail at the exit of the cyclotron. This tail is, however, close enough to the mean value of the energy to be neglected.

IX. DATA

The cross sections have been calculated from

$$\sigma(\vartheta,E_0)=N\times10^{24}/nId\omega.$$

The data are given in Table II. N is the total number of counts after a correction for accidental coincidences which never amounted to more than 2 percent and in most cases was about 0.3 percent. The observed voltage is proportional to the number of incident protons I. The number of hydrogen nuclei per cm² in the foil was obtained by the area-weight method. Since the target was always at a 45° angle to the scat-

[16] We are indebted to Dr. H. White of the Textile Research Institute, Princeton, New Jersey for his cooperation in the weighing of the samples.
[17] We are indebted to Mr. K. G. Standing for his help in this measurement.
[18] E. L. Hubbard and K. R. MacKensie, Phys. Rev. **85**, 107 (1952).
[19] E. Courant, Rev. Sci. Instr. **22**, 1003 (1952).

TABLE II. Summary of experimental data.

Run No.	Target	Angle lab. sys.	Angle c.m.	Counts	Voltage observed	$d\omega \times 10^3$	Reference value	Cross section millibarns/sterad
1	Polyethylene No. 3	45°	90°	40 900	3.4714	0.876		27.32
2	Polyethylene No. 3	45°	90°	41 000	3.4824	0.876		27.42
3	Polystyrene	45°	90°	40 890	10.3748	0.876		27.23
4	Polyethylene No. 4	45°	90°	15 070	1.1847	0.9465		27.33
5	Polyethylene No. 4	40°	80°	10 120	0.7329	0.9465		27.28
6	Polyethylene No. 4	35°	70°	15 130	1.0036	0.9465		27.53
7	Polyethylene No. 4	30°	60°	10 170	0.6269	0.9465		27.49
8	Polyethylene No. 4	25°	50°	10 130	0.5855	0.9465		27.25
9	Polyethylene No. 4	20°	40°	10 070	0.5436	0.9465		26.40
10	Polyethylene No. 4	45°	90°	45 996	1.3649	2.501		27.40
11	Polyethylene No. 4	40°	80°	61 256	1.6780	2.501		27.30
12	Polyethylene No. 4	35°	70°	29 850	0.7524	2.501		27.42
13	Polyethylene No. 4	55°	110°	46 000	1.6541	2.501		27.45
14	Polyethylene No. 4	60°	120°	30 520	1.2396	2.501		27.35
15	Polyethylene No. 4	65°	130°	14 975	0.7342	2.501		27.30
16	Polyethylene No. 7	45°	90°	20 460	1.6223	0.9465		27.12
17	0.2-mil Polyethylene	25°	50°	6 144	2.3087		27.27	
18	0.2-mil Polyethylene	20°	40°	6 116	2.1833			26.69
19	0.2-mil Polyethylene	18°	36°	6 120	2.1903			25.86
20	0.2-mil Polyethylene	15°	30°	10 025	3.5525			25.00
21	0.2-mil Polyethylene	18°	36°	6 055	2.1450			26.12
22	0.2-mil Polyethylene	25°	50°	7 130	2.6764		27.27	
23	Nylon	25°	50°	3 562	1.6498		27.27	
24	Nylon	15°	30°	3 040	1.3310			24.89

tered beam, this number has to be divided by $\cos(45° - \vartheta)$ to give the number n of hydrogen nuclei per cm² in the target. The data of runs 1 to 16 have been obtained from measured values of n, N, I, $d\omega$ and ϑ. Runs 17 to 22 and runs 23 and 24 give relative data. The cross sections at 20°, 18°, and 15° were obtained from the cross section at 25° which, from runs 8 and 15, was 27.27 mb/sterad.

The errors occurring in the measurement can be separated into two groups, those which affect the absolute measurement only and those which affect both the absolute and relative measurements.

1. Errors Which Affect Both the Relative and Absolute Values

(a) Statistics of counting. The standard deviation is the square root of the number of counts N taken. This standard deviation is slightly too low for those runs where the number of accidental coincidences was of the order of 1 to 2 percent.

(b) Fluctuation of incident energy. The fluctuation of energy as a function of time seems to be adequately represented by an error of 0.4 percent.

(c) The independence of the collected charge as a function of the voltage on the collector cup shows that fluctuations in the current integrator circuit do not introduce appreciable error.

(d) Penetration of the slit edges. Comparison of runs 7 and 8 with runs 14 and 15, respectively, shows that the contribution from this effect is small and can be neglected.

(e) The angle of the scatterer with the transmitted beam. This angle is introduced in the factor $\cos(45° - \vartheta)$. The maximum value for this angle is 30°. The uncertainty at this value is estimated to be less than 0.2° or 0.2 percent.

The estimated probable errors due to these effects varies from 0.5 percent at 90° to about 1 percent at 30°.

2. Errors Affecting the Absolute Values Only

(a) The area of the scattering foil was determined by direct comparison with a standard meter. The limit of error is estimated to be 0.15 percent.

(b) Weight of the scattering foil was measured with a microbalance with an error of less than 0.05 percent.

(c) The estimated error in hydrogen content was 0.2 percent.

(d) On the basis of runs 1, 2, 3, 4, 10, 16 of Table II the error due to lack of uniformity of the foils is estimated to be 0.4 percent.

(e) The diameters of the defining apertures were measured on two different comparators. The error is estimated to be 0.05 percent contributing an error of 0.1 percent in $d\omega$. The position of the slit as discussed previously introduces another error of $+0$, -0.015 percent.

(f) The distance of the slit to the center of the chamber is known ± 0.1 percent or better.

(g) ϑ is measured to about 2 minutes of arc. The error introduced is negligible in all points considered here.

TABLE III. Probable values and errors.

Angle	90°	80°	70°	60°	50°	40°	36°	30°
Probable value (mb/sterad)$_{c.m.}$	27.32	27.29	27.47	27.42	27.27	26.50	25.98	25.00
Relative error	0.5%	0.5%	0.5%	0.6%	0.7%	0.8%	1%	1%

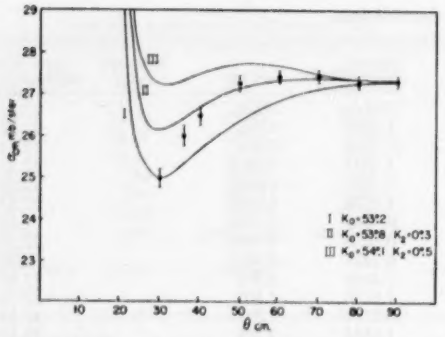

FIG. 7. Comparison of calculated distributions for various values of the S- and D-wave phase shifts with the experimental points. The S-wave phase shift was adjusted so as to give the experimental value for the cross section at 90°.

(h) Low energy component in the beam. On the basis of the discussion given above the error is estimated to be $+0, -0.2$ percent.

(i) The probable error in the current integration was estimated at ± 0.5 percent.

The combined rms error due to these effects is 0.8 percent and the estimated probable error in the cross section at 90° taking into account all errors is about 1 percent. The probable values of the cross section and the estimated probable errors are shown in Table III.

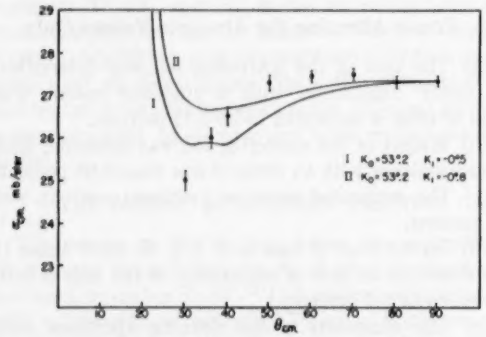

FIG. 8. Comparison of the calculated distribution for various combinations of S- and P-wave phase shifts. The S-wave phase shift was adjusted to give the experimental cross section at 90°.

X. THEORETICAL INTERPRETATION OF THE DATA

The theoretical distributions have been calculated using the formulas given by Breit, Condon, and Present.[1] The phase shifts were adjusted so as to give approximately the observed cross section at 90°. Figures 7, 8, and 9 give the distribution curves for the indicated values of the S-, P-, and D-wave phase shifts k_0, k_1, and k_2. Comparison of the distribution for an S-wave phase shift alone with the data, Fig. 7 curve I, shows that there is a deviation from S-wave scattering which we believe to be significant. It is seen that a combination of S- and D-wave phase shifts can give a reasonable agreement with the data if one assumes the observed 30° point to be about 3 or 4 percent low. Figure 8 shows that a combination of S- and P-wave phase shifts does not fit the data very well. If one adds an attractive P-wave phase shift to the $S+D$-wave distribution a very satisfactory fit may be obtained as shown in Fig. 9. If one uses the various values for the S-wave phase shift obtained by assuming 0°.0, 0°.3, and 0°.5 D-wave phase shifts one can calculate the f values which are found to be 23.7[4], 23.3[4], and 23.1[4]. These have been plotted in Fig. 10 on the curves of

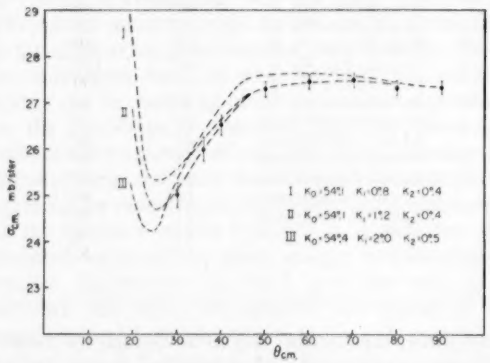

FIG. 9. Comparison of various combinations of S-, P- and D-wave phase shifts with the experimental values.

Yovits, Smith, Hull, Bengston, and Breit.[20] The estimated errors in the f values are ± 0.2. The value $k_0 = 53°.2$, obtained for $k_2 = 0$ has been included to permit comparison with f values obtained from data between 18 and 32 Mev by Cork,[21] where it was assumed that the cross section at 90° was due to S-wave scatter-

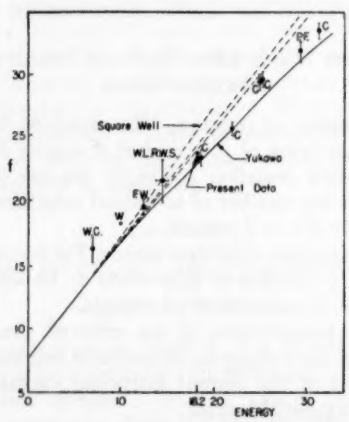

FIG. 10. Plot of the obtained values of the f function on the Fig. 1 of the paper by Yovits, Hull, Smith, Bengston, and Breit (see reference 20). The upper point corresponds to $K_0 = 53.2°$, the middle one to $K_0 = 53.8°$, and the lower one to $K_0 = 54.1°$. The error is about equal to the distance between two points.

[20] Yovits, Smith, Hull, Bengston, and Breit, Phys. Rev. **85**, 540 (1952).

[21] B. Cork, Phys. Rev. **80**, 321 (1950).

ing only. This shows that the S-wave scattering is of the magnitude expected from a Yukawa or exponential potential with the parameters fixed by the low-energy scattering. Figure 11 gives a comparison of the data with distribution curves to be expected from the potential proposed by Christian and Noyes.[22] It has been suggested that the discrepancy in the 90° values between the curves and the experimental point is not too important since a slight change in one of the available parameters could shift the curve vertically without any considerable change of shape. However, it is seen that the shape of the singlet square well plus triplet Yukawa tensor interactions is not satisfactory. The shape of the Gauss error potential plus triplet tensor interactions is satisfactory.

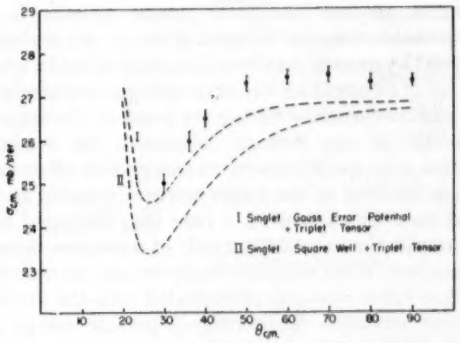

FIG. 11. Comparison of the experimental data with the potential proposed by Christian and Noyes (see reference 4).

ACKNOWLEDGMENTS

We are indebted to Dr. G. Breit for several very helpful discussions both on the experimental procedure and the interpretation of the data. The theoretical distribution curves given in Figs. 7, 8, and 9 were checked by Dr. M. H. Hull, Jr., Miss Smolen, Dr. Thaler, and Mr. Bengston. The assistance of Dr. J. C. D. Milton in the earlier stages of this work and of Mr. K. W. Brockman, Jr. in the taking of the data is gratefully acknowledged.

Most of the equipment was constructed in the shops of the Palmer Physical Laboratory. We are heavily indebted to the technical staff of the laboratory for their cooperation and many helpful suggestions.

[22] We are indebted to Dr. R. Christian for the calculation of the theoretical curves.

PHYSICAL REVIEW VOLUME 95, NUMBER 5 SEPTEMBER 1, 1954

Time-of-Flight Measurements on the Inelastic Scattering of 14.8-Mev Neutrons*

GERARD K. O'NEILL†
Laboratory of Nuclear Studies, Cornell University, Ithaca, New York
(Received May 25, 1954)

Measurements have been made of the energy spectra of neutrons inelastically scattered from 14.8 Mev into the interval 0.5–4 Mev. Carbon, aluminum, copper, tin, and lead scatterers were used. 100-kev deuterons were extracted from a cyclotron and allowed to strike a target of tritium absorbed in zirconium. The resulting reaction $T^3(d,n)He^4$ (17.7 Mev in the center-of-mass system) yielded a 14.8-Mev neutron accompanied by a recoil 3-Mev alpha particle. A scintillation counter within the vacuum system, subtending a solid angle of $4\pi/100$ at the target, detected recoil alpha particles with ~100 percent efficiency, delivering a fast signal whenever a neutron started on a path within a cone chosen to avoid scattering material for a distance of several meters. Within the cone and close to the target a scatterer was placed. The inelastically scattered neutrons emerged from the scatterer with approximate isotropy, while few elastically scattered neutrons were deflected through large angles. A proton-recoil neutron counter placed at ~90° to the cone axis was thus prevented from detecting almost all undesired neutrons. The distance from the scatterer to the counter was 50 to 100 centimeters, and neutron energies were obtained from the measured flight times over this path length, with the recoil alpha signal serving as a time zero. The flight times, which were from 20 to 65 millimicroseconds, were measured by a time analyzer having nine 4.7×10^{-9} second channels, recording directly on mechanical registers. Experimentally, neutron energies after scattering could be approximated by number/unit energy $E=E\exp(-E/T)$ with T, the "nuclear temperature" in Mev obtained from the raw data being: Pb, 0.75; Sn, 0.62; Cu, 0.84; Al, 1.06; C, 0.93. These results are in general agreement with photographic plate data. The experimentally observed angular distributions were isotropic within the limits of error of ~15 percent. Over-all limits of error of ±15 percent in the nuclear temperatures are assigned.

1. INTRODUCTION

IN studies of the internal structure of nuclei, measurements of inelastic neutron scattering (INS) are especially useful. Since neutrons do not interact with the Coulomb fields of nuclei or with atomic electrons, their scattering is a measure of nuclear properties alone and can be interpreted with few ambiguities.

In a complete inelastic scattering experiment, nuclei would be bombarded by monoenergetic neutrons, and the energy distributions of all subsequently emitted particles would be measured as functions of the angle from the incident neutron direction. For bombarding energies between 0.5 and 15 Mev, in all but the lightest

* Part of a Ph.D. thesis submitted to the faculty of the Graduate School of Cornell University. A preliminary report of this work was presented at the Spring, 1954, meeting of the American Physical Society, Phys. Rev. 95, 635(A) (1954).

† Present address: Physics Department, Princeton University, Princeton, New Jersey.

elements, charged particle or gamma emission is far less probable than the emission of one or two neutrons, followed by gamma rays from the decay of nuclei which are not of sufficient excitation to emit more neutrons.

Compound-nucleus models are based on the assumption that in any inelastic interaction the incoming neutron very quickly shares its energy with all or most of the nucleons in the target nucleus, forming an excited state which lasts for a time long compared with the transit time ($\sim 10^{-21}$ second) of a neutron through the nucleus. When this state finally decays, the emerging particle has a direction uncorrelated with the incident neutron direction. The emergent particle energy depends only on the matrix element for the transition from a bound to a free state, and on the density of available final states for the excited nucleus and the free particle.

This experiment was designed to check the compound-nucleus model at the high bombarding energy of 14 Mev, where, if anywhere, this model should be a good approximation. If all or a large number of the nucleons participate in the scattering process, and if they act as Fermi particles within a potential well of nuclear size, it can be shown[1-3] that the outcoming neutrons should have approximately the energy distribution $dN/dE = Ee^{-E/T}$, with T a constant for a given nuclide and excitation. In this energy distribution, with T between 0.5 and 1 Mev, most of the outcoming neutrons have energies between 0.5 and 5 Mev.

In the present experiment, only one excitation energy (14.8 Mev+the binding energy of one neutron) was used for each element. Thus changes in T with excitation were not measured. There was some evidence of the alternative shell-model mode of interaction in neutrons above 5 Mev, but resolution was not good enough to permit measurements on these neutrons. The experimental accuracy was also insufficient to allow the detection of effects due to $(n,2n)$ interactions.

2. METHOD

Measurements of neutron energy spectra in the Mev region are relatively difficult, since the individual neutrons can only be detected through their infrequent interactions with nuclei. Of several possible techniques for neutron energy measurement, that of time-of-flight (TOF) offers certain advantages and the following disadvantages.

(a) In the Mev region, flight times are very short, of the order of a few $\times 10^{-8}$ second for dimensions of the order of a meter.

(b) Since $dE/E = 2dt/t$, measurements of the flight time must be made with twice the relative precision of the resulting energy measurement.

(c) Two measurements on the neutron must be made, to establish the zero as well as the arrival time. In practice, it has been customary to use a pulsed neutron source to establish the time zero. For the required very short pulses, heavy and complex equipment is required. In the method to be described, the time zero is obtained without pulsing, and this disadvantage is avoided.

(d) The energy *vs* flight time conversion is very nonlinear, high energies being compressed to a small range of flight times.

Against these disadvantages, the TOF method can be made to have high efficiency, high resolution if intensity and background problems are overcome, and an energy sensitivity that is relatively easy to calculate. It is inherently clean since energy is measured in terms of the fundamental dimensions length and time.

For the experiment described here, the TOF method, in conjunction with a specific reaction for neutron production, was chosen. The technique[4] was: 100-kev deuterons were extracted from a cyclotron and used to bombard a T-Zr target. There the reaction T+D$\rightarrow n$+He+17.7 Mev (center of mass) yielded 14.8-Mev neutrons accompanied by 3-Mev recoil alpha particles. A scintillation counter within the vacuum system, subtending a solid angle of $\sim 4\pi/100$ at the target, detected recoil alphas with nearly 100 percent efficiency. The alpha signals thus supplied a time zero for 14.8-Mev neutrons and selected only those neutrons having directions within a cone free, for several meters, of all material except air, the vacuum chamber walls, and the desired scatterer. Within this cone a scatterer (S) was placed. The neutron counter, containing an organic scintillator, was placed outside the coincidence neutron beam, at a large angle from the cone axis so that most of the elastic scattering was avoided.

The advantages of this technique are:

(1) The time zero is obtained without the use of a pulsed neutron source, and with an uncertainty dependent only on electronics and on the alpha-path geometry.

(2) A beam of neutrons having a known and controllable direction is obtained without the use of absorbers and collimators. Thus the neutron beam is still monoenergetic after its direction is defined.

The disadvantages are:

(1) A practical restriction to machine-made neutrons, in particular to those neutrons made in two-body reactions with energetic recoils.

(2) Restriction to thin foils or gases as neutron-source targets.

(3) A limit on the source intensity, and so on the amount of data taken in a given time. This limit exists because one type of background, random n-α coincidences, has a component proportional to the square of the neutron detection rate. Although not serious in the experiment discussed here, such a limit might become important in measurements on scattered neutrons be-

[1] J. M. Blatt and V. F. Weisskopf, *Theoretical Nuclear Physics* (John Wiley and Sons, Inc., New York, 1952).
[2] D. B. Beard, Phys. Rev. **94**, 738 (1954).
[3] E. R. Graves and L. Rosen, Phys. Rev. **89**, 343 (1953).
[4] G. K. O'Neill, Phys. Rev. **92**, 853 (1953).

tween 5 and 14 Mev. A way of getting around this limit is discussed in Sec. 12.

3. APPARATUS

The target assembly (Fig. 1), placed at the end of a 36-inch snout on a small cyclotron, was provided with a beam collimator and a small metal door, operable through a vacuum seal. This door, when closed, shut off the target from the deuteron beam, and simultaneously exposed the alpha scintillator to a weak 5.3-Mev polonium alpha source. The scintillator,[5] 40 mils thick, was masked to $\frac{7}{8}$ in.$\times 1\frac{1}{8}$ in. by a brass plate and covered by a 1.09 mg/cm^2 bronze foil to stop scattered deuterons. Pulse-height spectra taken in the illustrated geometry showed a well resolved peak for the Po-alpha test source. The 5819 alpha counter was placed at the end of a 6-in. light pipe, so that a magnetic field could be maintained across the vacuum chamber. Such a field (*ca* 300 gauss) was used for a time to shield the alpha counter from the tritium beta rays, but improvements in electronics finally reduced the beta background to 500–1000 counts/second, and the magnet was removed to minimize scattering material.

The neutron counter (Fig. 1) was required to be large in volume for maximum counting rate and to be hydrogenous.[6] The housing was aluminum. Teflon (polytetrafluoroethylene) gaskets were used, since it was found that O-rings were attacked by the scintillator. Organic scintillators are strongly nonlinear, giving only weak light output for heavily ionizing slow protons, so there was also a light collection problem. At the time of construction of the counter, the high current photomultipliers (type 4646, etc.) were experimental and not yet fully reliable, so the large area type 5819's were used with subsequent distributed amplification. All three photomultipliers were operated at 1200–1500 volts, with equal dynode-to-dynode voltages and doubled photocathode-first dynode voltage. Experiments showed, however, that variations in the transit time of electrons from the photocathodes was still the most serious source of uncertainty in the entire time measuring process. The time resolution width due to transit time effects goes as (voltage)$^{-\frac{1}{2}}$, so that large

TABLE I. Scatterer dimensions.

Element	Source	t (cm)	L (cm)	W (cm)	Density
C	Pile graphite	5.4	15.4	17.5	1.59
Al	2S (99% pure)	5.1	16.2	17.9	2.73
Cu	Electrolytic	2.5	10.0	9.8	8.99
Sn	Chemically separated ingot	3.9	15.1	13.6	7.40
Pb	Electrolytic	2.9	9.3	10.0	10.7

[5] Plastifluor-B, Larco Nuclear Instrument Company.
[6] Scintillator mixing formula:

0.04 g/liter	diphenylhexatriene	(spectrum shifter)
3 g/liter	*p*-terphenyl	(scintillator)
1 liter	phenylcyclohexane	(carrier).

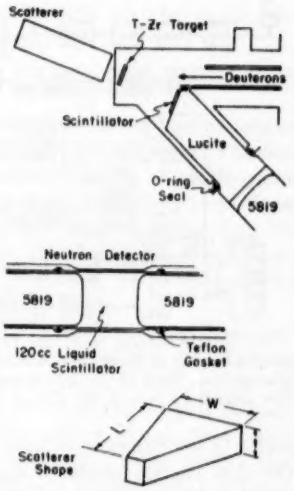

FIG. 1. Target assembly, neutron detector, and scatterer shape. (Sec. 3.)

area high voltage tubes would have helped this situation only slightly.

The scatterers (Fig. 1) were made with $L \approx W$, $L \approx \lambda$, $t \approx \frac{1}{4}\lambda$, λ being the inelastic mean free path for 14-Mev neutrons experimentally observed in the photographic plate work of Graves and Rosen.[3] An upper limit of 17 cm on L was, however, set to avoid uncertainty in the time zero due to the 14-Mev neutrons' flight time through the scatterer. Dimensions for the five scatterers used are given in Table I.

4. ELECTRONICS

In the design of the electronics, it was necessary to insure:

(1) Maximum speed (rise rate) of the fast pulses so that the time measurement could be made with the greatest possible precision.

(2) Easy and unambiguous measurement of all singles counting rates so that random coincidence backgrounds could be separated in measurements of the total background.

(3) Easy measurement of the minimum neutron counter pulse height accepted by the electronics, a quantity needed in the calculation of the (energy dependent) neutron sensitivity.

(4) Maximum discrimination against undesired signals. The process to be measured contributed only about $1/10^4$ of the counting rate in each neutron detecting photomultiplier, so that every advantage afforded by coincidence requirements had to be taken.

To achieve these ends, discriminations, counting rate, and efficiency measurements were made by stable slow circuits (rise times $\sim 0.2\times 10^{-6}$ second). Each fast circuit was operated at a gain sufficiently high that all pulses accepted by the slow circuits were also accepted by the fast elements. The register chronotron, which made the actual time measurements, was designed in such a way that every neutron-alpha pulse pair falling

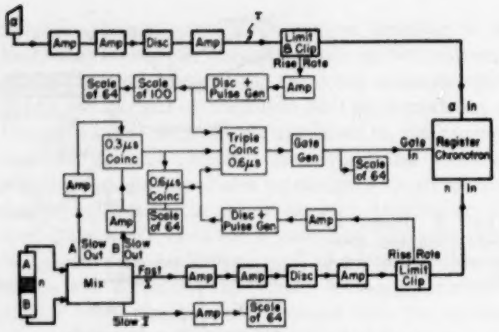

FIG. 2. Electronics, with fast (3-millimicrosecond rise time) circuits heavily outlined. The slow circuits have rise times of 0.2 microsecond. Each of the fast amplifiers has a gain of 10, each slow amplifier a gain of 10^4. (Sec. 4.)

within a 40-millimicroseconds range and accepted by the slow circuits produced one and only one register impulse. With this arrangement of the electronics, the fast neutron and alpha gains could each vary by ± 50 percent without changing the over-all counting efficiency for neutrons.

In the block diagram (Fig. 2) fast circuits are indicated by heavy lines. The chronotron will be discussed in the following section.

The alpha particles, having energies of about 2.2 Mev at the scintillator, were in the energy range of complete saturation (i.e., pulse height proportional to range and independent of energy loss). They produced pulses equivalent to electrons of about 40 kev. Thus high amplification was required in the alpha line. The signals passed through two distributed amplifiers (each with voltage gain of 10) to a fast discriminator of constant impedance. This device stopped all signals below a certain height V and passed all larger signals after subtracting V from their heights. It was designed so that signals of all heights, above or below V, were terminated in the characteristic impedance of the signal cable, thus preventing unwanted reflections and the pileup of many small pulses. This discriminator removed most of the tube noise, the pickup from the 8-Mc cyclotron rf, and most of the beta signals. After one more amplifier, the signals arrived at the chronotron pretreatment unit. Here their rise rate (volts/millimicrosecond) was measured by an RC network, and a tube carrying 50 mils was cut off to provide a positive 5-volt signal, clipped by a 65-cm shorted stub. A stretching circuit imposed a 1-microsecond dead time after the initial pulse to cut out ringing due to amplifier saturation or mismatch, and to remove after-pulse signals from the photomultiplier. Delay cables were inserted at τ (Fig. 2) to slide the chronotron's time zero to desired points. The impedance was 170 ohms throughout the fast line from the alpha 5819 to the register chronotron.

On the neutron side, signals observed by 5819's A and B were fed to a mixer. There the individual signals were sent to high impedance slow amplifiers and were added linearly to provide a third output (slow Σ) for monitoring and pulse-height analysis. These slow outputs were obtained without loading the input pulses. A fast addition of the A and B signals was also made, followed by moderate RC clipping (25 millimicroseconds) to prevent amplifier saturation. The rest of the fast circuits were nearly identical to those in the fast-alpha line.

The slow circuits operated as follows: alpha signals exceeding a fixed rise rate initiated uniform blocking oscillator pulses, which were applied to a triple coincidence circuit and simultaneously monitored for counting rate. Similar neutron-initiated signals were applied to the lowest input (Fig. 2) of this circuit. The individual A and B signals were sent through slow amplifiers to a faster coincidence circuit having pulse-height discriminators on its inputs. The output of the AB coincidence circuit led to the middle input of the triple coincidence circuit. An output of the latter unit fired another blocking oscillator (Gate Gen.) whose signal was used by the chronotron to initiate the various internal gate wave forms it required. Thus a gate fed to the chronotron implied:

(1) Fast rising pulses on both neutron and alpha lines.

(2) The presence of a neutron-side signal not due to photomultiplier noise.

In addition, the counting rates of alphas and AB coincidences were continuously monitored.

5. REGISTER CHRONOTRON

The chronotron, whose function of precise time interval measurement was basic to the entire experiment, was largely a new design but contained elements of a number of ideas found in the literature of fast electronics. It has been described in detail in an article, not yet published, for another journal.

Basically, the chronotron consisted of two fast-delay lines, one for the neutron and one for the alpha signal, arranged side by side with the neutron and alpha signals traveling in opposite directions. At intervals of 2.3 millimicroseconds on each line, a 6BN6 coincidence tube grid was attached. There were ten such tubes. When a pulse pair arrived, about three or four of the 6BN6's gave output signals, the largest indicating the point on the fast delay lines where the neutron and alpha signals most nearly met. These 6BN6 outputs were coded in time, amplified, and suitable circuits measured the position of the largest coincidence signal. After decoding, one of nine mechanical registers, each corresponding to a 4.7-millimicroseconds interval, fired. A tenth (Σ) register fired also, once for each pulse pair measured. The channel boundaries were stable to within 3×10^{-10} second. It was an essential property of the design that each channel register impulse corresponded to one and only one detected event in the neutron counter.

In order to test and adjust the chronotron, a sliding double pulser was built. This consisted of a wire-wound delay line with an internal grounded metal core. The coil was wound on threaded polystyrene tubing, had a length of 30 cm and a delay of ~1.5 microsecond/cm. The ends of the delay line were connected through an impedance matching network to cables which could be plugged into the chronotron's pretreatment unit inputs. A fast rising pulse, supplied by a thyratron or by a mercury switch, was introduced to the delay line by a sliding tap, whose position could be adjusted and read to 0.5 mm by a lead screw and a fixed 30-cm scale. Thus by moving the sliding tap through a 15-cm distance, the time difference between test pulses could be moved without jitter through the chronotron range of 40 millimicroseconds. The additional 15-cm range of adjustment allowed testing the behavior of the chronotron on pulse pairs falling just outside its nominal range and allowed movement of the whole time scale by the insertion of cables.

The calibration of chronotron channel widths and the absolute time measurements were made with the help of lengths of 170-ohm coaxial cable, fitted with standard cable connectors. The delay per unit length in these cables had been measured to ~1 percent in another experiment by Weil and Luckey.[7] The physical length of each cable was measured, and the electrical length calculated using the conversion factor measured in the experiment mentioned above. The delay introduced by the connectors was measured directly, and, as a further check, several pairs of these cables were compared for electrical length.

The chronotron time scale was measured in the following way: using the sliding double pulser, the pulser position for each of the ten channel boundaries was measured to $\sim 3\times 10^{-10}$ second. One of the standard cables was then inserted between the pulser and the pretreatment unit, sliding each of the 10 channel boundaries by the same fixed amount. After a remeasurement of the boundaries, the process was repeated with a different length of standard cable. Four such measurements were performed. None of the four results differed by more than 3 percent from the average value of 4.7×10^{-9} second/chronotron channel, and indicated a delay of 0.5 ± 0.1 millimicrosecond for each cable connector. Other measurements with the sliding double pulser confirmed the absence of gaps between channels of the chronotron. In the neutron energy measurement, five changes of the chronotron time zero were made to cover an interval longer than the chronotron total width and to average out small variations in individual channel widths. Thus the γ-ray peak, from which the time zero was obtained, and the neutron peak were measured in the same chronotron channels, so that the absolute time measurement depended mostly on the standard cables, relatively little on the chronotron channel width measurement.

6. ERRORS 1—BACKGROUND

Backgrounds may be divided into two groups, arising from scatterer-in and scatterer-out processes. The first group consists of register counts in the INS time region which are not the result of the desired process, single inelastic scattering in S, but which do depend on the presence of the scatterer. This background is difficult to measure and must, in general, be computed. The following processes contribute to it:

(1) Multiple scattering in S. Elastic processes contributed to a spread in the time resolution (by changing the total path length in S) but did not change the measured energy spectra. However, after a first inelastic scattering, a neutron might suffer a second. Assuming a constant INS cross section and a plane infinite slab geometry, the probability of a double INS was calculated by numerical integration. For this geometry, the only parameter required in the calculation was t/λ, the ratio of the slab thickness to the inelastic scattering mean free path. The probability that after a first inelastic scattering at a depth x, a neutron would emerge without suffering a second was calculated as a function of x for various t/λ. For the scatterer thicknesses used in this experiment, the fraction of once-scattered neutrons suffering a second scattering was found to be nearly $t/2\lambda$. Using the λ measured at 14 Mev by other experimenters,[3] the fraction of double scatterings was calculated to be 0.10–0.15. However, the most probable neutron energy after a first scattering is quite low (~1 Mev) and the INS cross section is known to decrease rapidly with decreasing energy. Thus an estimated upper limit of 5 percent on the double scattering ratio is reasonable.

(2) Processes in which a neutron scatters once in S, and again in nearby material (target assembly, cyclotron, floor, or walls). The nearest walls were at a distance of about 3 meters. This was far enough so that the earliest arrival time for a γ ray initiated in a wall was later than the arrival time for the latest neutron of interest. The walls were therefore neglected in the calculation. Processes in which a neutron scatters elastically in S may be estimated in the following way: Coon[8] has measured the angular distribution of the elastic scattering of 14-Mev neutrons and has found that less than 20 percent of the scattering is through angles of more than 20°. In the present experiment, all scatterings of less than 30° would have resulted in second scatterings at distances of not less than 3 meters. Gamma rays from such a scattering would have been outside the INS time region.

For the 20 percent or so of large angle elastic scatterings, an isotropic angular distribution was assumed. It was also assumed that when a 14-Mev neutron

[7] D. Luckey and J. W. Weil, Phys. Rev. **85**, 1060 (1952).

[8] J. Coon, Phys. Rev. **94**, 785 (1954).

TABLE II. Calculated double scattering backgrounds.

Source	Contribution
Floor	2%
Cyclotron	4%
Target assembly	1%
Total	7%

entered a thick slab of material it produced a secondary (gamma ray or neutron) with probability P of one. Further, such secondaries were assumed to be isotropically distributed and to escape the material without interaction.

For the low-energy neutrons from inelastic scatterings in S, the same assumptions were made except that P was taken to be $\frac{1}{2}$. The above assumptions are probably in error in such a direction as to cause an overestimate of these backgrounds.

The ratio of the number of inelastically scattered neutrons leaving S to the number of recoil alpha particles detected was calculated, including the effects of elastic outscattering; it was found to vary from 0.55 in Pb to 0.40 in C. Combining these calculations and estimates, the following (Table II) are the estimated double scattering backgrounds, with the location of the second scattering noted. The relative probability for this type of background event is roughly proportional to d, the distance between the scatterer and neutron counter. A distance of 50 cm was used in the estimate made in Table II. The uncertainty of this correction, as well as the falloff of counting rate with d, were the limiting factors on the useful working distance.

The scatterer-out backgrounds were measured directly, and are mentioned in a later section on experimental results. Since singles rates were monitored, these backgrounds could be computed; the computed backgrounds were in fairly good agreement with the measurements. One can distinguish:

(1) Background due to scattering of neutrons in the target backing and the vacuum chamber. This counting rate varied between 5 and 8 percent of the INS rate, and had a similar distribution in time.

(2) Random coincidences of alpha counter pulses with neutron signals. This was important mainly at the longer working distances and was uniformly distributed in time.

(3) Processes in which one 14-Mev neutron was received in the n counter in random coincidence with an alpha particle from a second neutron.

Since the deuterons of the cyclotron beam emerged in bunches at the cyclotron rf frequency, this background was somewhat peaked around the zero of time.

Under the operating conditions of this experiment, the background of type 2 was the most important. The total S-out background exceeded 20 percent of the true INS peak counting rate only at the longest working distance (100-cm flight path) and in angular distribution measurements on carbon.

7. ERRORS 2—ENERGY SENSITIVITY

Since measurements of the INS spectrum involved observations of neutrons over the energy range from 1 to 4 Mev, the apparatus had to be designed to allow easy calculation of the over-all efficiency. The effects to be considered are:

(1) Alpha counter efficiency. There was no correlation between scattered neutron energy and the recoil alpha direction, so no alpha counter effects needed to be considered.

(2) Probability of interaction in the n counter. The counter liquid was a mixture of hydrocarbons of known properties, so the number of C and H nuclei per cc was also known. The cross sections for both C and H are known and $n-p$ scattering is isotropic below 10 Mev.[9] Since the first excited state in carbon is at 4.5 Mev,[10] only elastic scattering had to be considered for the energies of interest. The maximum C^{12} recoil energy can be calculated immediately from momentum conservation, and is (neutron energy)/12.

(3) Pulse-height sensitivity and the response of organic scintillators. To make the calculation of efficiency as easy as possible, the neutron counter was designed and operated to have nearly uniform sensitivity over its entire volume. The relative sensitivity of the counter as a function of position was measured with a collimated radium gamma-ray source. For both the $\Sigma\epsilon$ and the AB counting systems (Sec. 4 and Fig. 2) there was less than a 15 percent variation in counting rate as the collimated beam was moved over the active length of the counter.

The fact that the response of organic scintillators to heavily ionizing radiation is nonlinear has been known for some time and a thorough experiment on the subject has been reported.[11] By assuming the liquid scintillator here employed to be stilbene-like, the relation of total pulse height (H) to particle energy for electrons, protons, and alpha particles was calculated from the data of reference 11.

Below 10 Mev for alphas, there is complete saturation (i.e., H proportional to range and independent of dE/dx). In order to compute H for C^{12} elastic recoils, it was necessary to know a range-energy relation for C^{12} nuclei. This was obtained by interpolation from the range-velocity relations for alphas, light fission fragments, and heavy fission fragments.[9]

In finding the sensitivity of the neutron counter as a function of energy, one quantity, the minimum scintillator pulse height accepted by the electronics, was measured directly. The relative response of the scintillator to protons from 0.3 to 14 Mev and to C^{12} nuclei from 0.5 to 5 Mev was calculated, and depends on

[9] *Experimental Nuclear Physics*, edited by E. Segrè (John Wiley and Sons, Inc., New York, 1953), Vol. I, p. 487.

[10] *Nuclear Data*, National Bureau of Standards Circular No. 499 (U. S. Government Printing Office, Washington, D. C., 1950).

[11] Taylor, Jentschke, Remley, Eby, and Kruger, Phys. Rev. **84**, 1034 (1951).

measurements of the response of solid organic scintillators. All effects due to geometry were calculated.

The measurement of minimum accepted pulse height was made in the following manner: the neutron counter photomultiplier voltages were adjusted so that the sensitivity was nearly uniform over the counter volume. Then, two measurements were made using the $\Sigma\epsilon$ slow linear pulse addition system (Sec. 4). In the first, the pulse height corresponding to 14-Mev recoil protons was measured, using direct 14-Mev neutrons from the target. In the second, a radium γ source was brought to a standard position, and an integral pulse-height spectrum was obtained with the same $\Sigma\epsilon$ system for this source. The source provided many low-energy pulses, presumably from Compton recoils, and the integral counting rate was a steep function of the minimum recording pulse height in the $\Sigma\epsilon$ system. Thus pulse height in the low-energy region was calibrated against counting rate from the source. Finally, the AB coincidence counting rate was measured; this measurement and the calibration just described allowed calculation of the minimum acceptable pulse height in units of the 14-Mev proton height. This minimum height was 1/300 of the 14-Mev height, with limits of error estimated as ± 50 percent.

With the help of the pulse height *vs* energy relation which has already been discussed, the minimum detectable proton and C^{12} energies were then calculated. They were: protons, 300 ± 100 kev; C^{12} nuclei, 1.5 ± 0.7 Mev. This most probable minimum detectable C^{12} energy was larger than the maximum recoil energy (1.2 Mev) from the most energetic neutron of interest (4 Mev).

The efficiency of the neutron counter as a function of energy was calculated, using the measured $n-p$ cross section (reference 9, pp. 486 and 507), the n-carbon cross section,[12] and the minimum detectable proton and C^{12} energies given above. The longest recoil-proton range involved (0.3 mm) was so short that no edge corrections had to be made. The probability of outscattering from the thin aluminum counter wall was also negligible ($\sim\frac{1}{2}$ percent). An upper limit on the effect of elastic outscattering by the carbon was calculated and found to be not more than 5 percent. The shape and size of the neutron counter were taken account of, and calculations of the efficiency were made on each of several assumptions as to minimum detectable pulse height.

To summarize the results of these calculations: the quantity needed in the interpretation of the neutron energy distributions was the variation in counter efficiency between 1 and 4 Mev. The effects of changing cross sections and the loss of low-energy pulses tended to cancel, and the net variation, a decrease of efficiency with increasing neutron energy, was not strongly dependent on the assumed low-energy cutoff. The calculated upper limit on the variation was about 35 percent of the mean efficiency, the lower limit about 20 percent. The variation was insensitive to the shape of the counter used in the calculation. If this were the only effect bearing on the nuclear temperature measurement, it would have had the effect of raising by not more than ~ 8 percent the temperatures obtained from the raw data alone. As will be shown in the next section, however, another effect tended partly to cancel the error due to the variation in energy sensitivity.

[12] *Neutron Cross Sections*, U. S. Atomic Energy Commission Report AECU-2040 (Office of Technical Services, Department of Commerce, Washington, D. C., 1952).

8. ERRORS 3—TIME AND ENERGY RESOLUTION

Uncertainties in the knowledge of neutron velocity came about through errors in both distance and time measurements. Uncertainties in the distance, which gave rise to constant relative errors $\Delta E/E$ over the E range, were due to:

$D1$. The finite size of the scatterer S along the line from S to the counter.

$D2$. Finite counter size.

$D3$. The shift in the effective center of the counter with energy.

Above one Mev, the distance uncertainties were small compared to the time uncertainties; of these, the most important were:

$T1$. The finite resolution width of the electronics, mostly due to photoelectron transit time variations.

$T2$. The transit time of 14.8-Mev neutrons through the scatterer.

$T3$. Variations in flight distance for recoil alphas.

In addition to these two groups of errors, there was one error affecting the energy directly: the variation in the $T(d,n)\alpha$ neutron energy with angle. The incoming deuterons, whose mean energy was measured as 95 ± 5 kev from the known cyclotron field strength, were monoenergetic within about 2 percent. However, the finite angular width of the scatterer resulted in an effective neutron beam energy distribution having a nearly rectangular shape and a width of 90 kev.

Since the INS data were taken at a scattering angle close to 90°, it was a good approximation to assume the independence of $D1$ and $T2$. $T3$ was made small by the design of the target assembly and was computed to be $\sim 3\times 10^{-10}$ second. The remaining errors were computed, the distance errors were combined and translated into times, and the three resulting time errors were combined to form a single resolution function.

The over-all resolution function was only slightly wider than that due to errors of the type $T1$ alone. It was approximately a Gaussian, with a full width at $1/e$ value of about 9 millimicroseconds.

In order to estimate the errors caused by the finite resolution width, it was necessary to assume a form for the neutron distribution being observed. The form $dN/dE=E\epsilon^{-E/T}$, to which the experimental points were compared, was used. In time units, $dN/dt=t^{-5}\exp[-(a/t)^2]$, a the flight time for neutrons of energy being equal to T. The measured value of

neutrons/unit time, dN/dt at $t=t_0$, could be written as the fold of dN/dt and the resolution function

$$\frac{dN}{dt}(t_0)_{\text{exp}}=\int_0^\infty t^{-b}\exp[-s(t-t_0)^2]\exp[-(a/t)^2]dt.$$

dN/dt was expanded in Taylor series around t_0, and term-by-term integration was used. All odd terms vanished, and the fractional error caused by the finite resolution width was taken as the ratio of the 2nd to the 0th order term.

The fractional error was computed for all cases of interest. In general, only the points at lowest t_0 were affected; for Pb (in which the effect was largest) the lowest t_0 point was 10 percent high due to this effect, and other points were affected by less than 5 percent.

To summarize the calculations on errors, it was concluded that systematic errors of types 1 and 3 were each less than 10 percent and were opposite to errors of type 2 between 1 and 4 Mev. Within that range, systematic errors of types 1, 2, and 3 were calculated as totaling between 0 and 20 percent in any measured point.

Since these errors were in general smaller than the estimates made of noncalculable error limits (e.g., variations in the electronics during operation) no corrections for them were made, and the nuclear temperatures were obtained from plots of the raw data, giving little weight to points outside the 1- to 4-Mev range. Systematic errors of 20 percent in the measured points could have made errors of at most ~7 percent in the nuclear temperatures.

9. PRELIMINARY EXPERIMENTS

Before taking any INS data, several measurements on systematic errors were made. First, the neutron counter sensitivity was measured, and pulse-height spectra were taken on monoenergetic neutrons and gamma rays. With the cyclotron off, the total neutron counter rate was ~35 counts/second, mostly due to small pulses. These may have been due to slow neutron capture from sources elsewhere in the building or to radioactivity in the counter liquid. Experiments with an anticoincidence Geiger counter umbrella, and with large thicknesses of lead and paraffin shielding, showed that this background was not due to cosmic rays. However, a small (0.5 count/second) component of large pulse height was consistent in rate and height with fast mu mesons from cosmic rays.

Using the Gate coincidence circuit, the neutron-alpha angular correlation was measured and is shown in Fig. 3.

A number of measurements of time resolution were made, using mu mesons, neutron-alpha coincidences, and the double-Compton scattering of radium gamma rays. By choosing different values of the photomultiplier high voltages, the distributed amplifier gains, and the conditions on minimum rise rate, it was possible to identify and measure the following sources of time-uncertainty.

(1) Variations in chronotron channel boundary positions. This effect was small compared to the next two.

(2) The variation in the center of gravity of a clipped pulse with the rise rate of the pulse before clipping. During operation this effect was made small by using high distributed amplifier gains and requiring high values of the rise rates.

(3) Variations in the transit time of electrons from photocathode to first dynode in each photomultiplier, due to statistical fluctuations in the photoelectrons' points of origin. This effect was the largest of the three; the over-all time resolution width was measured as 9 ± 1 millimicroseconds.

A number-bias spectrum for the gamma source was taken with a linear amplifier, and was used to calibrate the minimum acceptable pulse height for the entire system, as discussed in Sec. 7. With the n counter in the coincidence cone, the Gate counting rate was measured as a function of alpha-counter voltage, a plateau was obtained, and an operating point well onto the plateau was chosen.

The first distributed amplifier on the neutron side had an adjustable gain control. This control was calibrated, and it was found that above a certain value of the gain all signals accepted by the slow AB coincidence circuit also satisfied the rise-rate criterion. The plateau above this value had a width of about a factor three in gain. Maximum gain was used in operation.

Several preliminary INS runs on lead were made. The scatterer was built up of two layers, each ½ in. thick, and measurements were made with one and with two layers in use, the measured spectra being the same

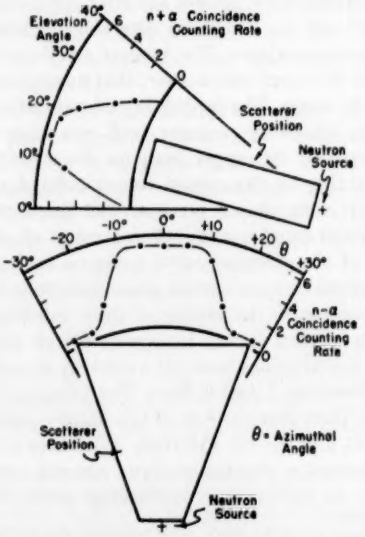

FIG. 3. Neutron-alpha angular correlations. The standard scatterer position for energy distribution measurements is shown.

within errors of ~10 percent. With a thick (1-in.) scatterer in place, ½-in. slabs of paraffin and of lead successively were placed halfway along the INS flight path. The paraffin had no effect on the shortest delay component, which had been identified by TOF as decay gamma rays; however, the paraffin reduced both the main INS and the 14-Mev elastic groups by ~30 percent. The latter group, not resolved by TOF alone, was thus identified. The ½-in. Pb slab had almost no effect on the neutrons, but reduced the gammas by ~70 percent.

A flight path of 71-cm average was chosen for the main energy-distribution measurements, a compromise between resolution, counting rate and scatterer-in background. Scatterer-out background was measured at the neutron-counter standard position (71 cm effective from the coincidence-cone axis, ~85° from that axis, and

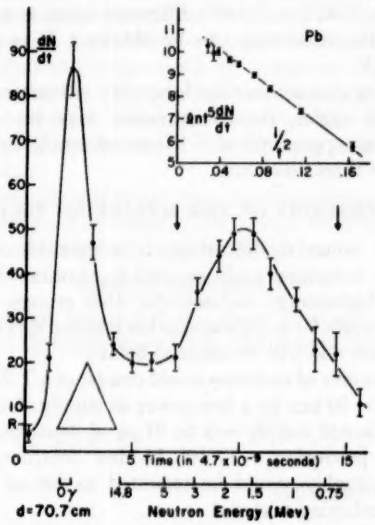

FIG. 4. Results of an energy distribution measurement with a Pb scatterer. Inset, plot for obtaining the "nuclear temperature" T from the measurement. (Sec. 10.)

160 cm from the concrete floor, the scatterer being at height 110 cm). The background was nearly uniform in time in the INS time region and consistent with the sources mentioned in a previous section. It was remeasured several times during the course of the experiment.

The external cyclotron beam was not focused and averaged 0.1 μa during the measurements. The neutron production rate was 1.5×10^5/sec, and about 1500 alpha particles/sec were incident on the alpha scintillator. Inelastically scattered neutrons were detected at a rate of ~1000 counts/hour.

Runs on each element at each distance required one day's operation, with actual data-taking times of 3 to 5 hours/day. Before each day's running an extensive schedule of standard tests was followed, in which

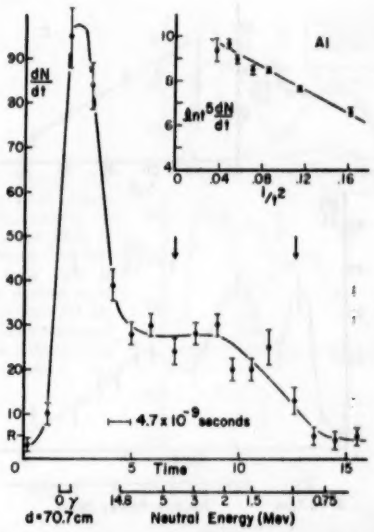

FIG. 5. Results of an energy distribution measurement using an Al scatterer. The results for Sn and Cu showed a smooth transition in the shape of the spectra from Pb to Al.

efficiencies and sensitivities were measured. This set of tests insured that the electronics was working properly before any data were taken. Although the nature of the chronotron made the INS results insensitive to running times, data were taken in units of a fixed number of detected 14-Mev neutrons, and experimental points represent the average of data from several (3 to 5) chronotron channels. No failures of the apparatus occurred during the three-week period required for collection of the data reported here.

10. ENERGY DISTRIBUTIONS

Two groups of runs were made on energy distributions. In the first, at a working distance of 71 cm, Pb, Al, Cu, C, and Sn were measured. The results for Pb, Al, and C are shown in Figs. 4–6, before subtraction of backgrounds. dN/dt for each figure is in arbitrary units, time in units of one chronotron channel width, with an arbitrary zero. The zero of time was measured by observation of the gamma rays from Pb, and was checked by the gammas from each element investigated. Below the time scale, an energy scale is given, and the time zero and gamma arrival time are noted. The equivalent resolution triangle is drawn in Fig. 4. R on the dN/dt scale indicates the measured scatterer-out background, and the arrows indicate the range of points which are plotted on the inset of each figure. The insets (plots of $\ln(t^5 dN/dt)$ *vs* $1/t^2$ with backgrounds subtracted) should be straight lines with slopes equal to $-a^2$, a being the flight time for neutrons of energy equal to the nuclear temperature T, if $dN/dE = Ee^{-E/T}$. Although the experimental errors are too large to permit the detection of small deviations from linearity, the measurements are consistent with the above form for dN/dE.

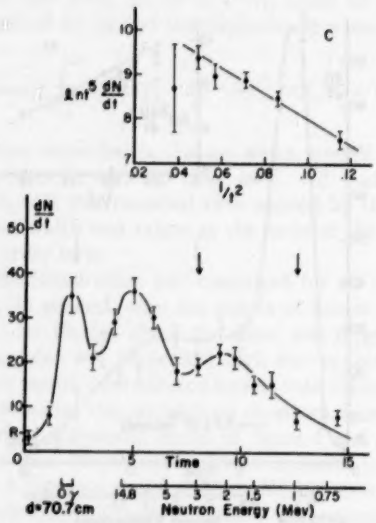

FIG. 6. An energy distribution measurement with a C scatterer. The number of observed decay gamma rays is small, presumably due to the simple level structure of carbon. The elastically scattered 14-Mev neutrons are well resolved from the gamma rays.

Another group of three energy measurements was also made, on the three lightest elements of the previous series. For Al, a working distance of 100 cm was used, with a distance of 88 cm for Cu and C. These measurements were made using different scattering angles and orientations from those of the previous measurement in an effort to obtain better resolution of the INS spectrum from the elastic scattering. An improvement was in fact obtained, but at the expense of scatterer-in/scatterer-out ratios and counting rates.

In Table III, the results of both these runs are given, together with average values which are adopted as the final results of the experiment.

It should be noted that these results come from straight lines drawn through sets of experimental points. The difference of 20 percent in the two measured values of T for Cu, and the difference of 9 percent and 6 percent for C and Al, indicate the uncertainties in drawing such lines. In order to allow for these uncertainties, estimated errors of ± 15 percent are assigned to each average value of T. Each of the average values is within 10 percent of the corresponding temperature obtained by photographic plate techniques.[3]

11. ANGULAR DISTRIBUTIONS

One of the easiest tests of the compound-nucleus model should be the measurement of isotropy in the INS. Although isotropy would not be expected for those neutron groups which do not follow an $Ee^{-E/T}$ law, the scattering of 14.8-Mev neutrons below 5 Mev should be nearly isotropic.

Using a working distance of 55 cm, with the scatterers suspended in the vertical plane, the distributions of neutrons from C, Al, and Pb were measured at laboratory angles of $\sim 48°$ and $\sim 130°$ (Fig. 7). In order to insure correct monitoring, an extra proton recoil counter was mounted in a fixed position, set at a bias of ~ 7 Mev, and used to monitor all angular distribution runs. Backgrounds were measured several times, and are shown at the top of Fig. 7. They were consistently higher at 130°, probably due to the increased n-counter rate near the cyclotron, and to the fact that for a fixed INS flight path, the T-target to n-counter distance decreased with increasing angle.

The rapid change of the 14-Mev elastic scattering with angle is clearly visible. The results for the INS in Pb were good enough to be plotted for nuclear temperature. The result (0.82 Mev) was within 10 percent of the more carefully measured value. The results for C are too poor to allow conclusions as to isotropy, but taking the sum of all counts below 5 Mev, with a positive $N(48°)-N(130°)$ difference taken as a positive effect, the anisotropy can be obtained. It is given in Table IV.

Taking into account the inequality of backgrounds at the two angles, the measurement may be taken as setting an upper limit of ~ 15 percent on the anisotropy in these three elements.

12. EXTENSIONS OF THE MEASURING TECHNIQUE

With minor modifications, it is probable that the present technique could be used to examine the interesting high-energy nonisotropic INS groups. A brief design study for a high-resolution neutron spectrometer was made and will be outlined below.

The source of neutrons would consist of a T-Zr target, held at -50 kev by a low-power dc supply. A deuteron source would supply ~ 5 to 10 μa of deuterons to the target, producing $\sim 3\times 10^6$ 14-Mev neutrons/second. This assembly would be mounted as far as possible from scattering material.

The target would be observed by two alpha counters; the first, which would be fixed, would subtend a solid angle $\Omega/4\pi$ of $\sim \frac{1}{6}$ and would apply a 0.2-microsecond anticoincidence signal whenever a neutron headed toward nearby parts of the laboratory or toward the neutron counter. Its counting rate would be $\sim 5\times 10^5$/

TABLE III. Measured nuclear temperatures.

Element	T (70.7-cm run) Mev	Distance d cm	T (run at d) Mev	Value of T adopted Mev
Pb	0.75			0.75
Sn	0.62			0.62
Cu	0.74	88	0.91	0.82
Al	1.03	100	1.10	1.06
C	0.89	88	0.97	0.93

TABLE IV. Anisotropy of inelastic neutron scattering.

Pb: $+8\pm 8\%$	Al: $-6\pm 13\%$	C: $+14\pm 18\%$

second. The second alpha counter would be a thin (slightly more than alpha range) layer of plastic scintillator on the glass envelope of a short-transit-time photomultiplier. This (coincidence and time zero) counter would be movable within the vacuum system to provide a coincidence neutron beam over a 120° range of angles, all directed away from the laboratory building. The scatterer would be outside the vacuum system. To cut down random background from cosmic rays, an array of Geiger counters in anticoincidence would shield the neutron detector.

Analysis would be carried out by a chronotron similar to the one already built, but with a channel width of 2×10^{-9} second to take advantage of the short-transit-time photomultipliers.

Estimates of the backgrounds to be expected indicate that 1000 counts/hour could be collected on a line having 2 percent of the total INS intensity, with a real-to-random ratio of 1:1. Since the main source of background would be random n-alpha coincidences, the true/background ratio could be improved in direct proportion to the time required to collect a specified number of counts. Energy resolution would be ~10 percent (full width) at 12 Mev, with a three-meter flight path.

It should be emphasized that the discussion above is the summary of a design study, not a description of apparatus already built or definitely planned.

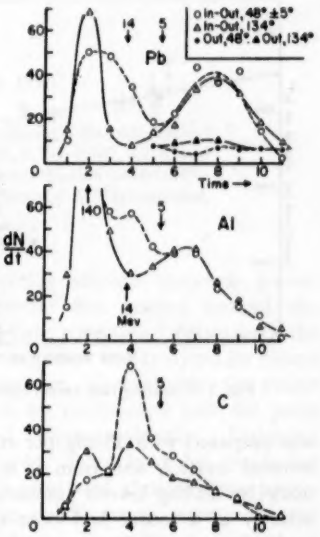

FIG. 7. Energy distributions, with backgrounds subtracted, at two angles for each of three elements. The first peak in each case is ascribed to gamma rays. The arrival time for 14-Mev elastically scattered neutrons is indicated on the graph for Al.

ACKNOWLEDGMENTS

The author would like to thank Professor B. D. McDaniel for suggesting work on the inelastic scattering problem, Mr. F. Turkot for operation of the cyclotron during part of the experiment, and Dr. D. B. Beard for sending a preprint of a letter before publication.

Special thanks are due Professor W. M. Woodward for his continued encouragement and for several helpful suggestions.

During part of this work the author received support from a U. S. Atomic Energy Commission predoctoral fellowship.

PHYSICAL REVIEW VOLUME 95, NUMBER 5 SEPTEMBER 1, 1954

Natural Radioactivity of Sm^{147}

GEORGE BEARD AND M. L. WIEDENBECK
Randall Laboratory of Physics, University of Michigan, Ann Arbor, Michigan

(Received May 3, 1954)

The half-life of Sm^{147} has been measured to be $1.25\pm0.06\times10^{11}$ years with an energy distribution corresponding to the emission of monoenergetic alpha particles.

A STUDY of the natural radioactivity of Sm^{147} has been made, including a determination of the half-life and an investigation of the energy spectrum of the alpha particles.

The activity of the samarium was measured using a 4π counter developed by Sawyer and Wiedenbeck.[1] The counter was originally designed for use in the Geiger region, but tests showed that with center wires of 4-mil diameter and a filling of 20 cm of CH_4 and 41 cm of argon it performs satisfactorily in the proportional region also. The sources were made of zapon films upon which aluminum was deposited by evaporation in a vacuum followed by a similarly deposited layer of samarium chloride. It was found that by using a molybdenum crucible quite efficient evaporation of the samarium chloride could be obtained.

When samarium chloride is evaporated, there is some question as to its final chemical composition.[2] Therefore, in order to determine the amount of samarium deposited, a spectroscopic analysis of each source was made.

A large quantity of 10 percent HCl stock solution

[1] G. A. Sawyer and M. L. Wiedenbeck, Phys. Rev. **79**, 490 (1950).

[2] L. L. Quill, *Nuclear Energy Series IV 19B* (McGraw-Hill Book Company, Inc., New York, 1950), pp. 125, 219.

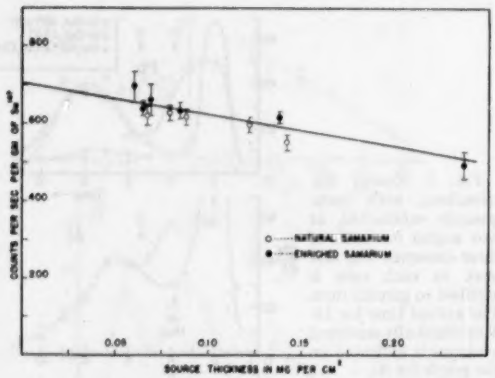

FIG. 1. Counting rate *versus* total source thickness.

was prepared with 15 mg per cc of Cu to act as the internal control, and from it several standards were made by adding known amounts of Sm_2O_3. After the activity of a source had been measured to within a probable error of 2 percent, the zapon film was immersed in a known quantity of the stock solution which dissolved the samarium chloride and aluminum. A large Littrow prism spectrograph was used with a spark source and the spectra recorded on a SA No. 1 photographic plate. By comparing the relative densities of the Cu control line at 3602.0 A and the Sm line at 3609.5 A, the concentration of the Sm in the sample was determined. In the best runs the accuracy was judged to be within 3 percent.

Both natural and enriched Sm were used as sources. The natural[3] Sm with 15.07 percent Sm^{147} was about 98 percent pure[4] Sm_2O_3 and the enriched[5] Sm with 78.35 percent Sm^{147} was over 99.6 percent pure Sm_2O_3.

Figure 1 shows the variation of the counting rate with the total source thickness. After extrapolation to zero thickness and application of a 2 percent correction to compensate for the counter inefficiency, one finds a counting rate of $7.19\pm0.36\times10^2$ counts per second per gram of Sm^{147}. This corresponds to a half-life of $1.25\pm0.06\times10^{11}$ years, a value somewhat lower than most results obtained in the past, particularly those which involved a measurement of the total number of tracks produced in a nuclear emulsion.[6-9]

To investigate the energy spectrum, 0.9 mg of enriched samarium chloride was evaporated onto a thin zapon film giving an average source thickness due to the samarium chloride of 0.008 mg/cm². The zapon film was then placed in contact with a fresh Eastman NTA 25 micron nuclear plate. After three weeks the plate and a blank control were examined. When a shrinkage factor of 2 was applied,[10,11] some 175 tracks were left which satisfied the criterion that their original penetration angles be less than 37.5°. Under these conditions an error of as much as 10 percent in the shrinkage factor would affect the length measurements by a maximum of about 4 percent. The resulting mean track length of 7.0 microns agrees with other nuclear emulsion measurements,[6,7,12] and the distribution shows that at least the large majority of the alpha particles are surely emitted at one energy which is also in agreement with previous work.[6,13,14]

[3] Inghram, Hess, and Hayden, Phys. Rev. **73**, 180 (1948).
[4] Fairmount Chemical Company (private communication).
[5] Obtained from the Carbide & Carbon Chemicals Company, Oak Ridge, Tennessee.

[6] C. M. G. Lattes and P. Cuer, Nature **158**, 197 (1946).
[7] E. Picciotti, Compt. rend. **229**, 117 (1949).
[8] R. Hosemann, Z. Physik. **99**, 405 (1936).
[9] W. F. Libby, Phys. Rev. **46**, 196 (1934).
[10] H. Yagoda, *Radioactive Measurements with Nuclear Emulsions* (John Wiley and Sons, Inc., New York, 1949), p. 257.
[11] A. Beiser, Revs. Modern Phys. **24**, 273 (1952).
[12] Waldron, Schultz, and Kohman, Phys. Rev. **93**, 254 (1954).
[13] F. Bestenreiner and E. Broda, Nature **164**, 658 (1949).
[14] K. K. Keller and K. B. Mather, Phys. Rev. **74**, 624 (1948).

Gamma-Ray Spectrum of Ac^{228}

HAROLD C. BOX AND G. STANLEY KLAIBER
University of Buffalo, Buffalo, New York

(Received May 15, 1954; revised manuscript received June 9, 1954)

The gamma radiation from a radioactively pure source of Ac^{228} has been studied using a NaI scintillation spectrometer. Gamma rays of 0.098, 0.127, 0.336, 0.410, 0.458, 0.907, 0.965, 1.587, 0.155, 0.220, 0.278, and 0.790 Mev are indicated, of which the last four are previously unreported. A double scintillation spectrometer is described which was used to investigate gamma-gamma coincidences. A decay scheme for Ac^{228} is suggested.

I. INTRODUCTION

THE analysis by Black[1] of the beta spectrum of Ac^{228} (MsTh II) indicated gamma-ray energies of 0.058, 0.080, 0.129, 0.184, 0.250, 0.319, 0.462, 0.915, and 0.970 Mev. Thibaud[2] examined the excited photoelectron spectrum of Ac^{228} mixed with the active deposit of thorium and found conversion lines corresponding to gamma-ray energies of 0.333, 0.461, 0.913, and 0.967 Mev. A recent investigation by Kyles *et al.*[3] showed that this spectrum is more complex than indicated by the earlier work. Their data suggest six beta end points of energies 0.450, 0.640, 1.100, 1.700, 1.850, and 2.180 Mev and seventeen gamma-rays of energies 0.057, 0.078, 0.098, 0.113, 0.127, 0.179, 0.184, 0.336, 0.410, 0.458, 0.907, 0.965, 1.035, 1.095, 1.587, and 1.640 Mev. These investigators have proposed a decay scheme based in part on coincidence measurements between the halves of a double beta spectrometer and between the beta spectrometer and a scintillation detector. The latter coincidence measurements were hampered by the poor energy resolution of the scintillation detector which was not of the NaI type. Jenkins and O'Kelley[4] have also analyzed the beta spectrum of Ac^{228} and found end-point energies of 2.030, 1.740, and 1.100 Mev. Because of the complexity of its disintegration neither the decay scheme nor even the gamma-ray spectrum of Ac^{228} is certain and for this reason further investigation seemed to be warranted.

In a recent investigation by the authors using a NaI scintillation spectrometer, not all of the reported gamma-ray energies were evident while some energies not previously reported were observed. In addition, coincidence measurements were made using two NaI scintillation spectrometers. A decay scheme based on these results is suggested which is not in agreement with that of Kyles *et al.*

II. APPARATUS AND TECHNIQUES

The scintillation detector consisted of a NaI crystal, 1½ inches in diameter by 1-inch thick, optically coupled to the photocathode of a 6292 DuMont photomultiplier tube using Dow Corning silicone stopcock grease. Magnesium oxide powder was packed around the crystal to insure good light collection.[5] Pulses from the detector were linearly amplified and analyzed by means of a single-channel analyzer. Alternatively, the pulses could be displayed on an oscilloscope and the pulse distribution obtained photographically. Unknown gamma-ray energies were determined by measuring the amplitude of their associated photoelectron peaks. A calibration of pulse height *versus* energy for the spectrometer was obtained by using a number of standard gamma-ray emitters. Among others, the 2.090-, 1.274-, and 1.085-Mev lines of In^{116}, the 0.794-Mev line of Cs^{134}, the 0.662-Mev line of Ba^{137}, the 0.411-Mev line of Au^{198}, the 0.137-Mev line of In^{116}, the 0.077-Mev line of Po^{210}, and the 0.059-Mev line associated with electron capture in W^{181} were used as energy references. The over-all energy resolution of the spectrometer was tested using the 0.794-Mev gamma ray of Cs^{134} and found to be about 8 percent.

A block diagram of the apparatus used for coincidence measurements is shown in Fig. 1. The apparatus is patterned in large part after the design of Johansson and Almquist.[6] The window of the single-channel analyzer in the lower channel is adjusted to straddle

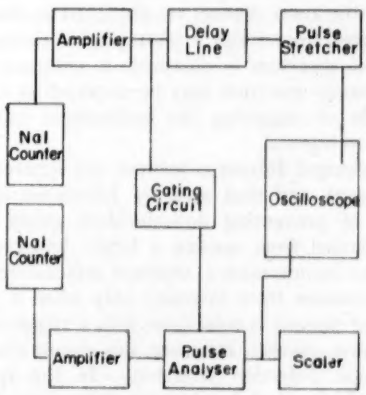

FIG. 1. Schematic diagram of the coincidence spectrometer.

[1] D. H. Black, Proc. Roy. Soc. (London) **A106**, 632 (1924).
[2] J. Thibaud, Ann. phys. **5**, 73 (1926).
[3] Kyles, Campbell, and Henderson, Proc. Phys. Soc. (London) **A66**, 519 (1953).
[4] W. A. Jenkins and G. D. O'Kelley (unpublished). See Hollander, Perlman, and Seaborg, Revs. Modern Phys. **25**, 469 (1953).
[5] C. J. Borkowski and R. L. Clark, Rev. Sci. Instr. **24**, 1046 (1953).
[6] S. A. E. Johansson and S. Almquist, Arkiv. Fysik **5**, 427 (1952).

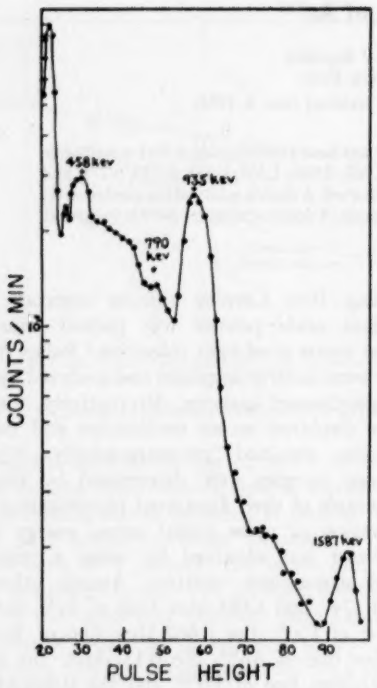

FIG. 2. High-energy portion of the gamma-ray spectrum of Ac^{228}.

the photopeak of a particular gamma ray in the spectrum and the output from the analyzer triggers the oscilloscope sweep. Pulses in the upper channel are delayed for 3 microseconds, in order to compensate for the delay in the lower channel caused by the single-channel analyzer, passed through a pulse stretcher, and applied to the vertical deflection plates of an oscilloscope. Pulses which are coincident with triggering pulses in the lower channel are displayed on the ocsilloscope screen from which a photographic record of the coincident spectrum is obtained. A reference picture of the normal spectrum may be obtained by changing the mode of triggering the oscilloscope trace from external to internal.

The principal difference between the apparatus used in this work and that used by Johannson is in the method of preventing noncoincident pulses in the lower channel from causing a bright base-line trace. Johansson incorporates a separate coincidence circuit which increases trace intensity only when a pulse in the upper channel is coincident with a triggering pulse in the lower channel. However, this circuit also affects oscilloscope deflection sensitivity. In the apparatus used for this work the gating circuit between channels, as shown in Fig. 1, prevents the single-channel analyzer from generating a triggering pulse except when coincident pulses occur and does not effect the gain of the system. Consequently, coincident and reference pictures of pulse distributions may be compared directly. The resolving time of the coincidence spectrometer is 1.5 microseconds.

The sources used in this investigation were prepared from a primary source of Ra^{228} (MsTh I) which has a half-life of 6.7 years. The Ra^{228} source was free from radium (Ra^{226}) contamination, having been prepared from a 13-year old sample of thorium nitrate. Radioactively pure sources of Ac^{228} were extracted from the primary source by using the method of Haissinsky[7] as improved by McLane and Peterson[8] whereby the isotopes of radium, thorium, lead, and bismuth are successively precipitated from a solution containing Ac^{228} and its decay products.

III. RESULTS AND CONCLUSIONS

With sufficient absorber placed between the source and the detector to remove the beta radiations, the pulse distribution from Ac^{228} was analyzed by means of the single-channel analyzer. The high-energy portion of the distribution is shown in Fig. 2 and the low-energy portion in Fig. 3. These spectra verify the existence of the following previously reported gamma-ray energies: 0.098, 0.127, 0.336, 0.410, 0.458, and 1.587 Mev. In addition, the gamma rays reported of 0.907 and 0.965 Mev are indicated, but not resolved, together yielding a broad maximum at 0.935 Mev. Previously unreported gamma rays of 0.220, 0.278, and 0.790 Mev are also present. A fourth unreported gamma ray of 0.155 Mev is hardly discernable in the normal spectrum but becomes evident when a coincidence spectrum is taken with the single-channel analyzer set on the 0.935-Mev maximum. The absence

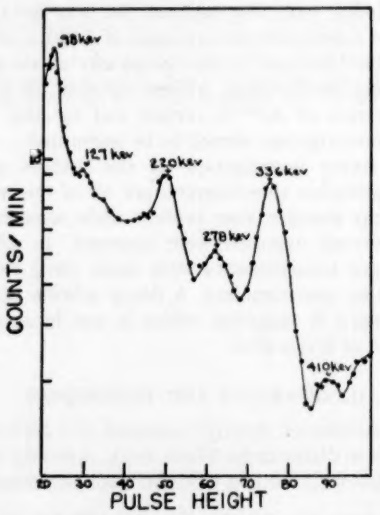

FIG. 3. Low-energy portion of the gamma-ray spectrum of Ac^{228}.

[7] M. Haissinsky, Compt. rend. **196**, 1778 (1933).
[8] C. K. McLane and S. Peterson, U. S. Atomic Energy Commission Report No. MDDC-1742, 1948 (unpublished).

from our spectrum of the 0.057- and 0.184-Mev gamma ray which have been established from internal conversion measurements might be accounted for by an extremely high conversion coefficient for these transitions.

Coincidences between gamma rays of the following energies have been observed: 0.336 and 0.790, 0.278 and 0.790, 0.220 and 0.127, 0.098 and 0.458, 0.098 and 0.410 Mev. Additional coincidence measurements between higher-energy radiation and the 0.220-Mev gamma ray have been hampered by radiation backscattered from one crystal to the other. The energy of the backscattered radiation is also in the neighborhood of 0.200 Mev and gives rise to false coincidences. Coincidences between the 0.935-Mev maximum and the 0.458, 0.410, 0.155, and 0.098 Mev radiations have also been observed. Efforts to split the 0.935-Mev maximum by measuring coincidences with the 0.458-Mev gamma ray indicate that the 0.907-Mev transition is coincident with that of 0.458 Mev and the 0.965-Mev transition is coincident with that of 0.410 Mev. Measurement of coincidences with the 0.098-Mev gamma ray does not appear to split the 0.935-Mev maximum.

These results are in agreement with the gamma-gamma coincidence measurements of Kyles *et al.* who found, using scintillation detectors, that gamma radiations of between 0.400 and 0.500 Mev are coincident with radiations of energies between 0.900 and 1.100 Mev and further, that gamma rays of under 0.900 Mev are coincident with gamma rays of less than approximately 0.400 Mev. These investigators also measured coincidences between gamma radiations and certain portions of the beta spectrum containing strong conversion lines. It was found that the 0.127, 0.184, and possibly the 0.098-Mev radiations are coincident with other gamma rays. The situation

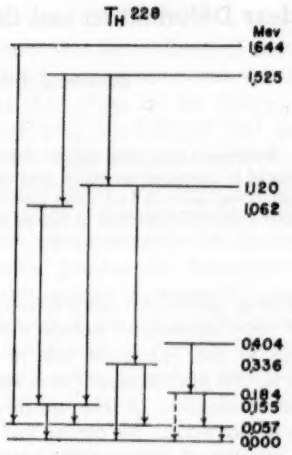

FIG. 4. Proposed decay scheme for Ac^{228}.

regarding the 0.098-Mev gamma ray was undecided because of the proximity of its conversion lines to the *K* conversion line of the 0.184-Mev radiation. There is no disagreement between our coincidence measurements and those made by Kyles *et al.* However, on the basis of more precise gamma-gamma coincidence relationships obtained with the NaI scintillation detectors, we are lead to conclude that the decay scheme proposed by these investigators is untenable.

A decay scheme consistent with all of the foregoing observations is given in Fig. 4. The 0.057- and 0.184-Mev transitions, not observed by us, have been included and are shown as broken lines.

The authors are pleased to acknowledge the assistance of the University of Buffalo Committee on Allocation of Research Funds which partially supported this research.

Nuclear Deformation and the Moment of Inertia of Nuclear Rotational States

KENNETH W. FORD
*Department of Physics, Indiana University, Bloomington, Indiana**
(Received May 19, 1954)

Evidence concerning nuclear deformation from isotope shifts and from rotational states in even-even nuclei is compared for nuclei near neutron number 82. It is concluded that the moment of inertia of the rotational states is 4 ± 1 times greater than the theory predicts, if the nuclear radius is $1.20\times10^{-13}A^{\frac{1}{3}}$ cm, and if the interpretation of isotope shifts in terms of nuclear deformation is correct.

THE recently published measurements by Arroe[1] of the (very anomalous) isotope shifts in cerium call attention to the significant role of the nuclear deformation in this phenomenon[2,3] and suggest that a more careful evaluation of the magnitude of the deformation be carried out for cerium and neighboring elements. A number of isotope shifts have been measured[3] relative to isotopes with 82 neutrons, among which only cerium includes neutron numbers both greater and less than 82.

A knowledge of nuclear deformation is important both for the detailed analysis of experiments which measure the distribution of charge in the nucleus[4] and for the interpretation of many collective phenomena[5,6] in the nucleus. We are concerned in this note in particular with the quantitative relationship between the nuclear deformation and the moment of inertia of nuclear rotational states—a relationship which has been shown previously to be qualitatively but not quantitatively in accord with theory.[6,7]

ISOTOPE SHIFTS

Nuclear deformations calculated from isotope shift data[1,3] are shown by circles in Fig. 1. In order to obtain these deformations, it was necessary to make several assumptions.

(1) Nuclei containing 82 neutrons have a negligible deformation. This assumption is based on the large energies (1.38 to 1.6 Mev) of the first excited states of $_{54}Xe^{136}$, $_{56}Ba^{138}$, $_{58}Ce^{140}$, and $_{60}Nd^{142}$, which are in good agreement with the weak coupling limit of the unified model of the nucleus.[6]

(1a) It is a corollary that the zero point oscillation of the nuclear surface is ignored. This is justified if the mean square amplitude of oscillation is nearly independent of the equilibrium shape of the nucleus.

(2) In the absence of deformation, the isotope shift is 0.40 times the predicted magnitude for incompressible uniform density spherical nuclei of radius $1.40\times10^{-13}A^{\frac{1}{3}}$ cm. This assumption is based on the trend of isotope shifts from $N=50$ to 126, and particularly on the fact that the shift due to deformation should be zero at $N\cong68$ and at $N=126$. A previous fit[2] used 0.50 as the "zero deformation ratio". Near $N=82$, however, the trend of shifts favors 0.4, with a probable error of about 0.05. (The value 0.4 is consistent with a nuclear electric radius of 1.1 to $1.2\times10^{-13}A^{\frac{1}{3}}$ cm and a nuclear compressibility in accord with theoretical estimates.[8,9])

(3) The nuclear electric radius is taken to be $1.20\times10^{-13}A^{\frac{1}{3}}$ cm.[10]

(4) The addition of two neutrons to a nucleus increases the volume occupied by the protons by an amount proportional to $2/A$ (but not necessarily equal to $2/A$). This is the vital assumption, for it implies that all deviations from constancy of the ratio of the observed isotope shifts to those predicted[11] by a model of a constant density spherical nucleus are due to deformation. Shell structure effects, on this assumption, manifest themselves in nuclear deformations but not in nuclear proton density. Deformations were computed from the data of references 1 and 3 with Eq. (21) of reference 2.

OTHER ELECTROMAGNETIC EVIDENCE

Nuclear deformations deduced from quadrupole moments[6,7] are shown by crosses in Fig. 1. Except at $N=90$, they are very much smaller than deformations based on isotope shifts. It seems likely that this anomaly stems from the changing sign of the quadrupole moment and the mixing of states of prolate and oblate shapes; Q is negative from $N=74$ to 77, should be positive just below $N=82$, should be negative just beyond $N=82$, and is positive at $N=88$ and 90. The importance of the quadrupole moment in the present discussion is that it corroborates the isotope shift evidence in suggesting a maximum deformation of about 25 percent just beyond $N=92$. Deformations from this source were calculated from Eq. (30b) of

* Supported in part by a joint program of the U. S. Office of Naval Research and the U. S. Atomic Energy Commission.
[1] H. Arroe, Phys. Rev. **93**, 94 (1954).
[2] Wilets, Hill, and Ford, Phys. Rev. **91**, 1488 (1953).
[3] P. Brix and H. Kopfermann, Festschr. Akad. Wiss. Göttingen, Math.-Physik Kl. 17 (1951); and Phys. Rev. **85**, 1050 (1952).
[4] Hofstadter, Fechter, and McIntyre, Phys. Rev. **92**, 978 (1953).
[5] D. L. Hill and J. A. Wheeler, Phys. Rev. **89**, 1102 (1953).
[6] A. Bohr and B. R. Mottelson, Kgl. Danske Videnskab. Selskab, Mat.-fys. Medd. **27**, No. 16 (1953).
[7] K. Ford, Phys. Rev. **90**, 29 (1953).
[8] Brueckner, Levinson, and Mahmoud, Phys. Rev. **95**, 217 (1954).
[9] E. Feenberg, Phys. Rev. **59**, 149 (1941).
[10] L. N. Cooper and E. M. Henley, Phys. Rev. **92**, 801 (1953).
[11] W. Humbach, Z. Physik **133**, 589 (1952).

reference 7, but with the numerical coefficient increased from 67.5 to 100 to account for the smaller electric radius of the nucleus now assumed.

The $E2$ transition rate from first excited to ground state in even-even nuclei[6] measures the nuclear deformation. Two values of β^2 found from this source[12,13] are shown by squares on Fig. 1 at $N=90$ and 94. They confirm the other electromagnetic sources of evidence as to the maximum deformations encountered in nuclei. The deformations were calculated from Eqs. (VII.1) and (VII.17) of reference 6. Total conversion coefficients of 0.95 for $_{62}Sm^{152}$ and 4.5 for $_{66}Dy^{160}$ were used.

MOMENTS OF INERTIA

The existence of rotational states in nuclei, especially in the rare earth region and in the region near uranium, seems to be well established.[6,14] If one accepts the deformations given by isotope shifts as approximately correct, however, the moments of inertia of these states are experimentally much greater than the theoretical expression,[15]

$$I=3B\beta^2,$$

where $B=(15/16\pi)$ times the moment of inertia of a rigid spherical nucleus. To illustrate this point we plot in Fig. 1 (as triangles) the quantity

$$\tfrac{1}{4}\beta_E{}^2=\tfrac{1}{4}(I/3B),$$

found from the energies of first excited states[16,17] of even-even nuclei near $N=82$ (excluding those with energies greater than 1 Mev, for which the rotational assumption should not be valid). These values are seen to be in fair agreement with deformations based on isotope shifts and transition rates. (For all nuclei for which more than one datum exists, the agreement is within the error of the electrically determined deformation).

Between 88 and 90 neutrons one observes a sharp decrease in energy of rotational states, a sharp increase in quadrupole moments, and very large isotope shifts, all corresponding to a marked increase in nuclear deformation. This sharp change, as seen nowhere else in the periodic table, is not understood. It is probably not due to the filling of the first two $i_{13/2}$ states because this should tend to produce negative quadrupole moments, while the observed moments are positive. It may be correlated, however, with the stabilization of the cylindrically symmetric form of deformation. Below 88 neutrons, the quadrupole moments are too small to be consistent with deformations of cylindrical symmetry.

[12] A. W. Sunyar, Phys. Rev. **95**, 626(A) (1954).
[13] F. K. McGowan, Phys. Rev. **85**, 151 (1952).
[14] F. Asaro and I. Perlman, Phys. Rev. **91**, 763 (1953).
[15] A. Bohr, Kgl. Danske Videnskab. Selskab, Mat.-fys. Medd. **26**, No. 14 (1952).
[16] G. Scharff-Goldhaber, Phys. Rev. **90**, 587 (1953).
[17] E. L. Church and M. Goldhaber, Phys. Rev. **95**, 626(A) (1954).

CONCLUSION

It is concluded that the moments of inertia of nuclear rotational states near neutron number 82 are 4 ± 1 times greater than given by the theory (for uniform density nuclei with $R=1.20\times10^{-13}A^{\frac{1}{3}}$ cm). The rotational interpretation of many nuclear levels has met with striking success[6] in explaining energy level ratios and transition rates. Nevertheless, the large discrepacny between theory and experiment as to the absolute values of the energies remains an important puzzle. All electromagnetic sources of evidence agree about the order of magnitude of the *charge deformation* (predicting a maximum deformation at $N\cong96$ of about 25 percent). The discrepancy exists, therefore, between the charge

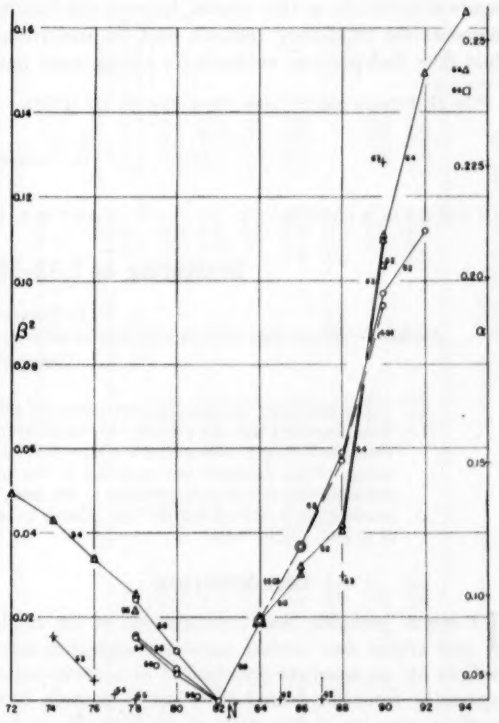

FIG. 1. Nuclear deformations vs neutron number. Left scale: square of deformation parameter β. Right scale (nonlinear): fractional deformation $\alpha(=|\Delta R|/R$ along nuclear symmetry axis). $\alpha=0.631\beta$. Z values indicated on graph. Circles: deformations calculated from isotope shifts, all relative to assumed zero deformation of nuclei with 82 neutrons. ($_{60}$Nd points, connected by dashed line, are only known relatively to each other and therefore contain an additional normalizing factor.) Crosses: deformations calculated from quadrupole moments, assuming cylindrically symmetric deformation and strong-coupling projection factor. Squares: deformations calculated from $E2$ transition rates, assuming rotational states. Triangles: *one-fourth* of deformations calculated from energy of first excited states of even-even nuclei, assuming strong coupling rotational states. All points use $R=1.20\times10^{-13}A^{\frac{1}{3}}$ cm. Isotope shifts and rotational energies determine $R^2\beta^2$. Quadrupole moments and transition rates determine $R^4\beta^2$.

deformation and the mass deformation as measured by the rotational energy.

Either of the following possibilities could increase the moment of inertia of the rotational state and thereby help to explain the existing discrepancy.

(1) Neutron structure different from proton structure. This could mean deformation of neutron structure greater than deformation of proton structure, for which there is no known reason, or neutron radius greater than proton radius, for which a qualitative argument has been advanced.[18] Such effects, together with possible effects of nonuniform density distribution, cannot reasonably account for all the factor four.

(2) Breakdown of the idea that the kinetic energy of collective motion is correctly described by an equivalent irrotational fluid flow. The observed moments of inertia lie, as they should, between the limiting moments for rigid-body rotation and for irrotational fluid flow. Independent evidence for a long mean path of nucleons within nuclear matter leads to the expectation that moments of inertia should lie close to the (small) moments of irrotational flow. The large observed moments, therefore, provide evidence against a complete independent particle picture.

It should be stressed that the very close agreement of theoretical and experimental energy ratios provides strong evidence for rotational states, (i.e., energy proportional to square of angular momentum), but does not check the unified (or collective) model in any fundamental way. Only the magnitudes of the energies test the independent particle assumption which underlies these models. The approximate proportionality of the moments of inertia to the square of the nuclear deformation favors the independent particle picture. The large values of the moments show that the picture is not wholly adequate.

Some helpful comments by Professor M. G. Mayer and Professor J. A. Wheeler caused this note to be written. The remarks here are based on earlier work with L. Wilets and D. L. Hill (reference 2).

[18] M. H. Johnson and E. Teller, Phys. Rev. **93**, 357 (1954).

PHYSICAL REVIEW VOLUME 95, NUMBER 5 SEPTEMBER 1, 1954

Scattering of 1.32-Mev Neutrons by Protons*

C. L. Storrs† and D. H. Frisch
Physics Department and Laboratory for Nuclear Science, Massachusetts Institute of Technology, Cambridge, Massachusetts

(Received April 29, 1954)

The total cross sections of polyethylene and graphite for scattering of neutrons of 1.315±0.003 Mev have been measured and are $\sigma(CH_2)=(9.542\pm0.035)\times10^{-24}$ cm² and $\sigma(C)=(2.192\pm0.020)\times10^{-24}$ cm². From these the hydrogen cross section is $\sigma(H)=(3.675\pm0.020)\times10^{-24}$ cm². If the best current values of the binding energy of the deuteron (see reference 3) the coherent scattering length (see reference 4) and the epithermal cross section (see reference 5) are used, the singlet effective range in the shape-independent approximation is $(2.4\pm0.3)\times10^{-13}$ cm. This is to be compared with the proton-proton singlet effective range of $(2.7\pm0.1)\times10^{-13}$ cm.

I. INTRODUCTION

It seems probable that consideration of the singlet and triplet zero orbital angular momentum states suffices for an accurate description[1] of neutron-proton scattering from the bound state up to neutron bombarding energies of the order of 15 Mev. If so, four independent measured quantities may determine[2] the strength and effective range of both the singlet and triplet S-wave interactions, and six independent quantities may begin to differentiate in both cases between interactions of qualitatively different shapes. Three accurate independent quantities known at present are the binding energy of the deuteron[3] and the thermal neutron-proton singlet and triplet scattering amplitudes.[4,5] If applied to a description of the interactions by static potentials, these may be used to determine the strength and range of a triplet potential of a given shape and to determine the approximate product of the magnitude times the square of the range for a singlet potential of a given shape.

Other independent measurements which may be made are the total neutron-proton cross sections for fast neutrons of different energies. The region of neutron

* Submitted to the Department of Physics, Massachusetts Institute of Technology in partial fulfillment of the requirements for the degree of Doctor of Philosophy for C. L. Storrs. This work has been supported in part by the joint program of the U. S. Office of Naval Research and the U. S. Atomic Energy Commission.

† Now at General Electric Company, ANP Project, Evendale, Ohio.

[1] J. D. Jackson and J. M. Blatt, Revs. Modern Phys. **22**, 77 (1950). That a tensor coupling of the triplet S state to a state of higher orbital angular momentum may be included effectively in the triplet S parameters is shown by J. M. Blatt and L. C. Biedenharn, Phys. Rev. **86**, 399 (1952).

[2] George Snow, Phys. Rev. **87**, 21 (1952).

[3] R. C. Mobley and R. A. Laubenstein, Phys. Rev. **80**, 309 (1950).

[4] Burgy, Ringo, and Hughes, Phys. Rev. **84**, 1160 (1950).

[5] E. Melkonian, Phys. Rev. **76**, 1744 (1949).

energy of around 1 Mev is particularly suited for giving an effective singlet range independent of singlet and triplet shape, because the singlet contribution to the total cross section is comparatively large at energies less than a few Mev, and because the effect of potential shape is small. At around 5 Mev the triplet contribution to the total cross section is dominant, so an accurate cross section may be used to indicate a triplet shape if the singlet range is known accurately. At around 15 Mev the triplet phase-shift is nearly 90°, and therefore the triplet contribution to the total cross section is quite insensitive to triplet parameters, giving an opportunity to obtain the singlet shape if the singlet range is known accurately.

The total n-p cross sections have been measured over a wide range of neutron energies in many previous experiments, of which only the most recent[6-9] have been sufficiently accurate to give information about even the singlet range. In this experiment, aiming for a determination of the singlet range to the order of 0.1×10^{-13} cm, we needed to know the energy to 10 kev and the cross section to 0.2 percent. At transmissions of $T=0.4$ the latter permits an error in transmission of 0.2 percent, or at $T=0.6$ an error of 0.1 percent. In this range of accuracy in transmission measurements many precautions must be taken and many small corrections made. Both of these are discussed in Sec. II, and the corrections are displayed in Table I.

The final accuracy achieved in the singlet range, of the order of 0.3×10^{-13} cm, is not enough to select any but extreme singlet shapes when used in conjunction with even the most accurate higher energy experiments.

II. EXPERIMENT

The total neutron cross sections of polyethylene and graphite were determined from many transmission measurements. We have, however, a very accurate experiment only at a transmission of 0.4 and in a single geometry.

Neutrons were produced by the Li(p,n) reaction[10] using the Rockefeller electrostatic generator at M.I.T. Neutron energy was determined by observing the oxygen resonance at 1.315 Mev.[11] For each scatterer the counting rate of a small, propane-filled proportional counter, relative to that of a BF_3 "long-counter"[12] monitor, was determined many times with the scatterer alternately shielding the propane counter and removed. The setup is shown in plan drawing in Fig. 1.

The hydrogen cross section was computed on the assumption that the polyethylene was pure CH_2 by

TABLE I. Scattering data, corrections, and cross sections.*

1	2	3	4	5	6	7	8	9	10	11	12	13	14	15	16	17	18
				Distance (inches)			Corrections to transmissions										
	Properties of scatterers Material	sample length (inches corrected to 23°C)		Source to scatterer	Scatterers to front of detector	Observed transmissions	Adjustment of length and density to 23°C	Background in detector	Background in monitor	Low-energy group of neutrons	Rate dependence of detector efficiency	Rate dependence of monitor efficiency	Scattering into detector	Scattering into monitor	Corrected transmission	Cross section in 10^{-24} cm² with statistical error only	Standard deviation of errors in columns 4 and 8–15
Date																	
10/9/51	CH_2	a	0.5411 ±0.0002	5.5 ±0.3	9.8 ±0.3	0.5982 ±0.0021	... ±0.0004	−0.0016 ±0.0004	...	+0.0007 ±0.0002	−0.0011 ±0.0006	...	−0.0007 ±0.0001	+0.0002 ±0.0001	0.5957	9.555 ±0.067	±0.028
12/14/51	CH_2	a	0.5411 ±0.0002	3.0 ±0.3	5.0 ±0.3	0.5997 ±0.0014	... ±0.0004	−0.0007 ±0.0002	...	+0.0008 ±0.0003	−0.0012 ±0.0006	...	−0.0023 ±0.0003	+0.0008 ±0.0002	0.5971	9.516 ±0.044	±0.028
12/14/51	CH_2	e	0.5478 ±0.0004	3.0 ±0.3	5.0 ±0.3	0.5960 ±0.0015	... ±0.0004	−0.0007 ±0.0002	...	+0.0008 ±0.0003	−0.0012 ±0.0006	...	−0.0023 ±0.0003	+0.0008 ±0.0002	0.5934	9.513 ±0.048	±0.029
1/15/52	CH_2	c	0.9802 ±0.0004	3.0 ±0.3	4.5 ±0.3	0.3958 ±0.0012	+0.0001 ±0.0003	−0.0009 ±0.0002	...	+0.0006 ±0.0002	−0.0012 ±0.0006	...	−0.0030 ±0.0004	+0.0001 ±0.0001	0.3915	9.556 ±0.031	±0.024
2/3/52	CH_2	c	0.9802 ±0.0004	3.0 ±0.3	5.0 ±0.3	0.3939 ±0.0009	+0.0005 ±0.0004	−0.0007 ±0.0002	−0.0002 ±0.0002	+0.0005 ±0.0002	...	+0.0004 ±0.0002	−0.0028 ±0.0004	+0.0001 ±0.0001	0.3917	9.551 ±0.023	±0.020
12/14/51	C	g	1.0004 ±0.0002	3.0 ±0.3	5.0 ±0.3	0.6284 ±0.0017	...	−0.0006 ±0.0002	...	+0.0008 ±0.0003	−0.0012 ±0.0006	...	−0.0012 ±0.0006	+0.0004 ±0.0002	0.6266	2.192 ±0.014	±0.008
12/14/51	C	1	0.9992 ±0.0002	3.0 ±0.3	5.0 ±0.3	0.6275 ±0.0017	...	−0.0006 ±0.0002	...	+0.0008 ±0.0003	−0.0012 ±0.0006	...	−0.0012 ±0.0006	+0.0004 ±0.0002	0.6257	2.192 ±0.014	±0.008

CH_2 average 9.542 (using both statistical and other errors) ±0.016 (statistical errors only)

C average 2.192 ±0.010 (statistical errors only)

* All errors statistical or estimated standard deviations.

[6] Lampi, Freier, and Williams, Phys. Rev. **80**, 853 (1950).
[7] Poss, Salant, Yuan, and Snow, Phys. Rev. **87**, 11 (1952).
[8] Hafner, Hornyak, Falk, Snow, and Coor, Phys. Rev. **89**, 204 (1952).
[9] Fields, Becker, and Adair, Phys. Rev. **89**, 908 (1953).
[10] Hanson, Taschek, and Williams, Revs. Modern Phys. **21**, 635 (1949).
[11] Freier, Fulk, Lampi, and Williams, Phys. Rev. **78**, 508 (1950).
[12] A. O. Hanson and J. L. McKibben, Phys. Rev. **72**, 673 (1947).

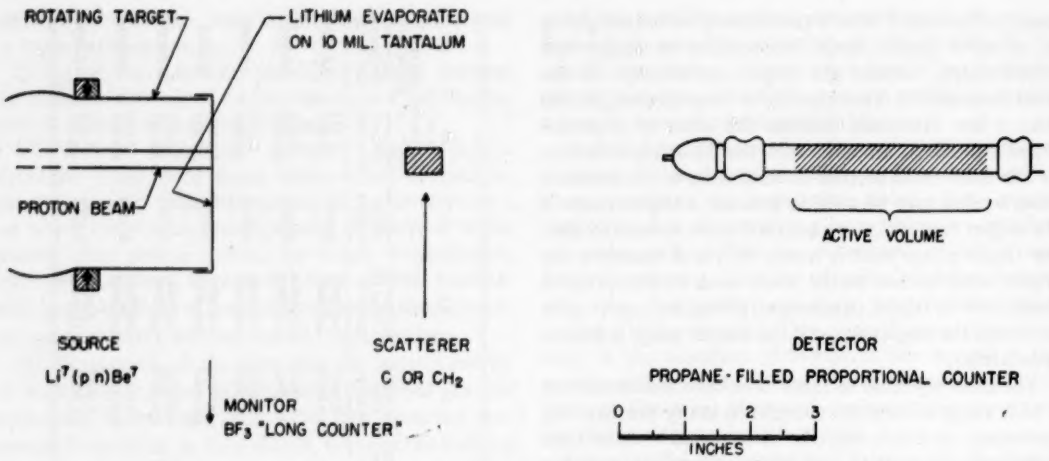

FIG. 1. Plan drawing of experiment.

subtracting the carbon cross section from that of polyethylene. In the final experiments the results were corrected for scattered neutrons entering the counters, the group of neutrons of lower energy from the Li(p,n) reaction, the change in efficiency of the counters as a function of counting rate, and background. A description of the salient experimental details follows.

A. Neutron Source

The electrostatic generator produced a proton beam of 10 microamperes and a fraction of a kilovolt spread in energy. This beam bombarded a thin film of lithium which had been evaporated on a rotating disk of 0.010-in. tantalum.

1. *Target Thickness*

The lithium target thickness—which chiefly determined the spread in energy of the resulting neutrons—was estimated roughly from the "geometrical resonance"[10] at threshold, both before and after using the target. In order to take into account more accurately the thickening and deterioration of the target, the neutrons produced in this manner were used to determine the transmission of an oxygen-containing scatterer as a function of proton beam energy. In the vicinity of 1.315 Mev the oxygen cross section for neutron scattering has a strong resonance. By locating this transmission minimum repeatedly throughout the experiment the average energy of the main group of neutrons from the Li(p,n) reaction was known at all times.

A discussion of the effect of the much smaller second group of neutrons will be given in Sec. 3 below. For the main group the very close approximation of the effective neutron energy to the energy of the center of the oxygen resonance is displayed schematically in Fig. 2. There $\epsilon(E)Y(E)$ is the counter efficiency times target yield for neutrons of each energy coming from the target. When weighted with the transmission T_{ox} of oxygen, this gives a counting rate for each machine energy proportional to $\int \epsilon(E)Y(E)T_{ox}(E)dE$. The ratio of this quantity to the unattenuated rate $\int \epsilon(E)Y(E)dE$ is minimized by changing the machine energy.

The machine energy corresponding to this minimum transmission is found by extrapolating from the two nearly straight parts of the observed transmission curve to their interaction as in Fig. 2. One thus sets the effective central energy $\bar{E}$ of the target, determined by the average of two approximately linear weightings with equal and opposite slopes, on the peak of the oxygen cross section, provided only that the resonance is approximately symmetric, and that the detector efficiency is (as observed) a linear function of energy over this small energy region, and that the relative yield from different parts of the target does not change rapidly with energy.

The central energy for polyethylene scattering is also very closely defined by a flat weighting, since the polyethylene cross section does not change by more than 10 percent over a 100-kev interval in this energy region.

The energy of a particular neutron resonance is thus chosen as the standard effective neutron energy for the experiment. It is believed that this method gives the effective energy to a few kev for any reasonable target yield profile and for targets up to 40-kev thickness. In practice targets of from 10 to 15-kev rise when fresh were used, thickening to 30 kev at most with use. The energy of the resonance was measured at Wisconsin[12] and checked by us as $E_n = 1.315 \pm 0.003$ Mev. If a future independent determination of the energy of this resonance gives a different value, the present data may be reassigned to that energy; a change of about 10 kev is required to change the singlet range by 0.1×10^{-13} cm.

After cleaning a used target only lightly with alcohol and steel wool, with 6 percent of the target activity remaining, the cross section was measured at the same

[12] R. K. Adair (private communication).

energy, and found (with insufficient statistics) to be greater than previously by 0.3 ± 0.4 percent. In this case of partial cleaning, the target may well have been thickened rather than thinned. After a thorough cleaning of another old target, only 0.15 percent of the activity remained and it gave the same transmission as the full target within the statistical error of 15 percent, reflecting a possible error of only 0.04 percent in cross section. In any case, unless there was target thickening of greater than about 50 kev, any effect from target nonuniformity would be included in the centering on the oxygen resonance.

2. *Scattering from Target and Nearby Material*

The 0.010-in. tantalum target backing was mounted on the end of a thin-walled steel cylinder, and there was an appreciable mass of scattering material several inches back of the target. The massive deflector magnet was several feet behind it. But because of the small scale of the experiment, and because of the sharp energy bias of the detector and the lower energy and yield of backward neutrons, the neutrons scattered back by this material were not expected to be observed. (All neutrons coming off at more than 85° had less than 10 percent counting efficiency relative to those at 0°, even if scattered elastically into the detector.) This was checked experimentally by background studies described below. An upper limit on forward scattering by the tantalum was set by observing that there was less than 0.1 percent difference in the number of neutrons counted with a $\frac{3}{8}$-in. shadow cylinder and with a $\frac{5}{8}$-in. cylinder.

3. *Monitoring of Source Strength*

The neutron intensity was monitored by a BF_3 "long counter" at 90° to the beam, with standard Model 100 pulse amplifier[14] and parallel lines of scaling circuits. Both monitor and detector scalers were turned off after a fixed number of monitor counts, usually of the order of 3×10^5 counts in a five-minute run.

B. Detector

Because the size of the beam spot on the target was not more than 4 millimeters in diameter under good operating conditions, the detector could be made quite small. It was placed as close to the target as compatible with sure shadowing of the whole detector and with keeping geometric corrections to less than 1 percent. The beam size and position were observed occasionally with a glass viewer. Some data were taken when there was poor control of the beam size, and gave lower cross sections because of incomplete shadowing.

1. *Counter Construction and Electronics*

The detector was a proportional counter $\frac{7}{16}$ in. in outside diameter with a 0.010-in. center wire. There were two sets of guard rings—0.035-in. hypodermic needles on the center wire and intermediate voltage rings on the end seals to aid in insulating the negative 12 kv on the outer electrode. The active volume was about 3 in. long. The filling gas was 5 atmospheres of cp propane, not purified in any way. This counter had an almost linear integral bias curve. The measured total efficiency was about 1.5 percent, but the discriminator bias was set sufficiently high to eliminate all but perhaps 20 percent of the pulses.

The pulses were amplified by a Model 100 preamplifier and amplifier. Two discriminators and scaling circuits in parallel followed the amplifier to provide a check on electronic malfunctions in these components. Scalers with discriminators, such as the Model 310, were used. The negative 12-kv power supply was a regulated-input half-wave rectifier and *RC* filter.

2. *Background in Detector*

Background studies were made using Lucite rods to attenuate the neutrons coming directly from the target to the counter. The true background was attributed to (1) scattering from the floor and walls of the room, essentially independent of small displacements of the counter; and (2) a small amount of reflection from the filter and preamplifier 30 in. behind the counter, depending on counter position and the amount of shielding afforded by a scatterer. It was also necessary to ascribe a transmission of 0.15 percent to the 12-in. Lucite cylinders used as attenuators, although this is a factor of

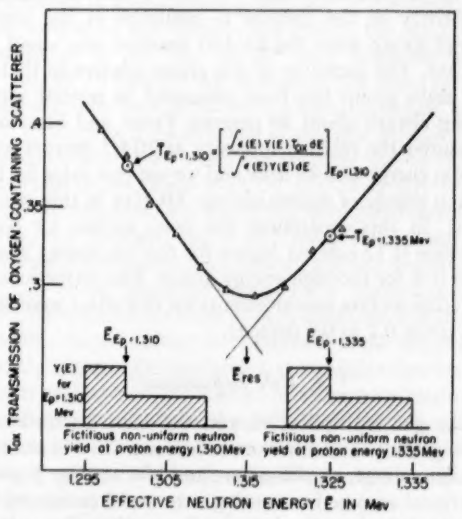

FIG. 2. Schematic drawing of method of determining effective neutron energy. The points are experimental transmissions with a target with approximately 14 kev "geometric" rise at threshold. The average transmission is shown, by circles, for a nonuniform target with the neutron yield shown, for two different values of the proton energy. The effective neutron energy of the target is $\bar{E}(E_p=1.310)$ at the lower energy and $\bar{E}(E_p=1.335)$ at the upper. These energies correspond closely to the effective energies for *n-p* scattering, as explained in the text.

[14] W. C. Elmore and M. Sands, *Electronics: Experimental Techniques* (McGraw-Hill Book Company, Inc., New York, 1949).

five higher than had been anticipated on a simple exponential attenuation basis. Cutting off 1½ in. of the back end of a cylinder, while keeping the counter position fixed, increased the background by a larger amount than anticipated, also suggesting that at many mean free paths the neutrons were diffusing forward in appreciable numbers.

In most cases the desired geometry for transmission measurements had the counter too close to the source to permit placing a 12-in. cylinder between them. The background for these cases was extrapolated from the measurements with the counter farther back, approximately a factor of 2 in effective distance from the target. The validity of this extrapolation is based on detailed studies as a function of counter and shadow cylinder location and cylinder diameter and length.[15] Using the two true sources of background plus a small leakage through the shadow cylinder, the background could then be analyzed quite consistently (to 0.04 percent of the unattenuated rate) for various diameters of shadow cylinder and locations of cylinder and detector. The observed slight decrease of background by 0.12±0.08 percent of the unattenuated rate on adding additional tantalum (0.18 in.) next to the target was also compatible with these studies.

The background correction to the cross section was usually about 0.3 percent and introduced an uncertainty estimated at considerably less than 0.1 percent.

3. *Correction for Binergy of Neutron Source*

The discriminator bias was set so that the relative sensitivity of the counter to neutrons of the lower-energy group from the Li(p,n) reaction was about 10 percent. The intensity of this group relative to that of the main group has been measured in several ways, giving always about 10 percent. Freier and Stratton[16] measured the relative intensity as 10±3 percent at a proton energy of 3.49 Mev and we use this value for the proton energy of approximately 3.0 Mev in this experiment. In this experiment the cross section for polyethylene is 12 percent higher for the low-energy group than it is for the high-energy group. The corrections to the cross-section measurements for this effect were thus only from 0.1 to 0.3 percent.

4. *Rate Dependence*

The gas multiplication and the high discriminator setting made the counter extremely sensitive to changes in high voltage, amplification, and bias setting. A given fractional change in counting rate could be caused by one third the fractional change in amplification or bias, or by 1/15 the fractional change in high voltage. Precautions such as long warmup, heating the filaments of the amplifier tubes with a battery, avoiding air currents, and careful selection of components made it possible to reproduce transmission measurements to within statistical errors of less than 1 percent, each measurement taking 10 or 20 minutes. The counting rate usually stayed constant to the order of 1 percent for several hours.

A major source of error in the earlier stages of the experiment was the change of detector efficiency as a function of counting rate. Since the discriminators on the propane counter were biased very high, a slight change in gain of the electronics made a large fractional difference in counting rate—the price exacted for fast counting combined with good rejection of background and low-energy group. The first results we obtained gave quite high transmissions because of this effect, and while the effect was reduced considerably by working over the electronics, it was never completely understood. After testing with a sinusoidal signal generator, we felt that the possible shift of bias of the discriminators when counting at these rates would be sufficient to cause this effect. Self-biasing of the counter, by insulators charging up, and missing by scalers were also possible contributors. Instead of its expected resolving time of about 4 μsec, measured with a double pulser, the whole detector system had an "effective resolving time" of about 15 μsec, defined by the losses between two very high rates used to study it. In order to use this result in the real experiment at lower counting rates, the assumption must be made that there is a known dependence of lost counts on rate.

The following scheme to eliminate rate dependence of detector efficiency was finally used. The machine was run at low current when the scatterer was out, and at high current when the scatterer was in, in such a way as to keep the propane counter working at the same rate. The long counter monitor thus showed the variation of counting rate, and because of its flat bias curve, should not give such a large rate dependence of efficiency as the detector. But since the long counter might still have given trouble because it was run at a very high rate in order to get good monitor statistics, its efficiency was actually checked between the approximate rates used by bringing up and removing two equivalent radium-beryllium sources in sequence, finding the very slight nonadditivity of their counting rates. (This method was also used in a more complex way between transmissions ⅔ and 1.) Thus the relative efficiency of the long counter and its whole electronic equipment was found at the two rates used, and the experiment did not depend on any assumption about efficiency of counters or electronics as a function of counting rate.

The result on the one high-accuracy run (0.22 percent statistics) taken by this constant detector count method agrees well within statistics with the other high-accuracy run on the same scatterer (0.33 percent statistics) using the resolving time derived from ratios of detector to monitor counts at two different very high detector rates,

[15] C. L. Storrs, thesis, Massachusetts Institute of Technology, February, 1952 (unpublished).
[16] G. Freier and T. F. Stratton, Phys. Rev. **79**, 721 (1950).

and assuming a conventional quadratic dependence of lost counts on rate.

C. Scatterers

1. *Composition of Scatterers*

Most of the CH_2 scatterers for this experiment were cut from the same stock used by Lampi, Freier, and Williams,[6] and some from the stock used by Hafner *et al.*[8] The carbon scatterers were cut from pile graphite sent from Brookhaven. The chemical analysis of the particular scatterers used revealed no significant differences between them. The hydrogen to carbon ratio was measured as two to one by numbers, to well within the maximum error of 0.1 percent, by Dr. R. A. Paulson of the Bureau of Standards. The scatterers were less than 0.1 percent oxygen by weight and had negligible ash. At this energy the high cross section of oxygen makes the oxygen impurity especially unimportant.

2. *Dimensions of Scatterers*

From the standpoint of statistics alone[17] a transmission of $T \cong 0.2$ would be desirable for determining cross sections with the low background present in this experiment. But at low transmissions the corrections to the cross section for neutrons multiply scattered but still counted becomes large, and possible errors in interpretation of background are magnified. A reasonable compromise between best use of time and background corrections seemed to be to work at $0.4 \leq T \leq 0.6$.

Five polyethylene cylinders were used with diameters of $\frac{3}{8}$ in. and $\frac{5}{8}$ in., and transmissions of 0.4 and 0.6, there being two of the smallest cylinders. Most of these were machined on a lathe, but one of the smallest was faced with a grinder.

The dimensions of the cylinders were determined by comparing them with size blocks by means of a dial indicator gauge. It was estimated by inspection with a microscope that the scatterer with the ground ends had irregularities of not more than 0.0003 in. The length of this scatterer was measured with a size block on top of it to distribute the force of the dial indicator gauge, with the dial gauge pressing directly on the plastic, and with an 0.11-in. size block edgewise beneath it. The three results indicated that the plastic was deformed about 0.0005 in. when the force of the dial gauge was concentrated in a small area. The true length of the ground scatterer was taken to be the one observed with size block on top of the plastic and this small correction for deformation was applied to measurements of the other CH_2 scatterers.

3. *Density of Scatterers*

A major source of uncertainty in this whole experiment was caused by the interchangeable use of two previously intercalibrated thermometers, one of which was found to be off by the order of 4°C at the end of the experiment. Despite accurate density and length measurements there is thus an uncertainty in the temperature at which the experiment was carried out, displayed in the errors in the adjustment of length and density in Table I.

4. *Single and Multiple Scattering-in Corrections*

A lower limit for the scattering correction is obtained by computing the relative number of neutrons from the target which were scattered into the detector by each point in the scatterer, taking into consideration attenuation both before and after scattering, and integrating. The scatterer is thus considered to be a secondary source of neutrons, and its total strength per neutron incident on it from the target is given by this integration to be $T \ln(1/T)$, where T is the transmission. This gives quite accurately the effect of singly scattered neutrons.

A high upper limit for the secondary source intensity in the forward direction, including multiple scattering if there is a reasonable angular distribution of scattering, is to assume that the secondary source is comprised by the $1-T^{-N\sigma X}$ neutrons which are scattered per incident neutron, and has the angular distribution of singly scattered neutrons. Since the detector discriminated strongly against neutrons which had lost energy by multiple scattering, the lower limit is a much better first approximation.

The scattering correction depends upon the angular distributions of the scattered neutrons. For hydrogen the scattering is approximately isotropic in the center-of-mass system at this energy. For carbon the ratio of scattering at 0° to that at 90° was measured as $\sigma_C(0°)/\sigma_C(90°) = 2.0 \pm 0.5$ by increasing the mass of a graphite scatterer by a factor of 10, without changing its length, by slipping a coaxial shell of graphite around it. The monitor was at 90°, and the graphite was in this case so close to the target that the scattering into the monitor just cancelled the scattering into the detector. Actually, the monitor was at 40° when the graphite cross sections were taken, so a smooth angular distribution[18] had to be assumed to make the scattering-in correction for carbon for those runs in which the monitor was at 90°. (As pointed out in reference 8, if the monitor were at the same angle throughout, the angular distribution from carbon would not enter into single scattering at all.) The assumptions were $\sigma_C(0°)/\sigma_C(45°) \cong 1.5$, and $\sigma_C(90°) \cong (1/4\pi)\sigma_{C\ total}$. A factor of two in the assumed anisotropy would make a difference of only 0.0001 in the CH_2 transmission.

The very small effect on cross section of the scattering by the air displaced by the polyethylene was compensated to less than 0.02 percent by the longer average path length in the scatterer for neutrons going through

[17] M. E. Rose and M. M. Shapiro, Phys. Rev. **74**, 1853 (1948).

[18] Feld, Feshbach, Goldberger, Goldstein, and Weisskopf, Atomic Energy Commission Report AEC NYO-636, 1951 (unpublished).

the scatterer at a slight angle to the axis. The energy of the neutrons at these small angles is not significantly lower than in the exact forward direction.

An estimate was made of the secondary source strength due to doubly scattered neutrons, taking into account the fact that the detector would not count neutrons which were scattered from hydrogen by more than 30° and then scattered back in by hydrogen. The inclusion of these doubly scattered neutrons raises the hydrogen cross section by not more than 0.07 percent. More double scattering than computed could raise the hydrogen cross section further by only about 0.2 percent before reaching the upper limit of multiple scattering discussed above. Since in the final measurements the scattering correction was about 0.8 percent, the uncertainty in the result from this source was thus shown experimentally to be not more than about 0.3 percent. It is our belief that the actual uncertainty in cross section due to scattering-in correction, using the correction estimated theoretically, is not more than 0.1 percent.

Some of the formulas used in this experiment are tabulated in the Appendix.

III. RESULTS

The best determinations of polyethylene and graphite transmissions are shown with corrections in Table I. In early runs a series of measurements was made with scatterers of various lengths and diameters with scattering corrections from 0.3 percent to 3 percent of the cross sections. Within the standard deviation of about 0.5 percent, these measurements all give the same cross section around 9.52×10^{-24} cm^2, when corrected for rate effects as well as possible in retrospect. Only one of the earlier runs is included, because only it had a very small rate correction, and because it was taken in a geometry for which background was observed directly and for which scattering into the monitor (then at 40°) was known to be small. We do not feel that we understand the other runs well enough to use their data, the average of which lies within the final error we will quote for the best runs.

Some data taken on scatterer a around the 12/14/51 run showed rather large fluctuations in the direction of higher transmission, and it is possible that the transmissions tabulated for a and e on that data are high because of incomplete shadowing of the target. The accuracy of the previous measurements cannot rule out a possible undiscovered systematically higher transmission for shorter scatterers, but in the absence of any positive evidence we average these runs in as if their higher transmissions arose from statistics alone.

The corrections are as discussed in Sec. II. Using the statistical standard deviation as the sole source of error, the resultant n-p cross section at this energy is found to be $(3.675\pm0.008)\times10^{-24}$ cm^2. This error will be raised by uncertainties in the corrections, and, to a much lesser extent, by the uncertainty in the energy by assigning the cross section to the definite energy $T_n=1.315$ Mev. A reasonable final estimate is $\sigma_{np}=(3.675\pm0.16)\times10^{-24}$ cm^2.

IV. DISCUSSION

A. Relativistic Corrections

We may put the above value of the total cross section, together with the binding energy of the deuteron and the thermal scattering amplitudes, into a consistent shape-independent approximation by using, for the k of the reduced mass $\mu=m_pm_n/(m_p+m_n)$, the momentum p of either particle in the center-of-momentum system. Then $\hbar^2k^2/2\mu$ is given by $p^2/2\mu=\frac{1}{2}T_n\{1-[(m_n-m_p)/2m_n]\}$, where T_n is the neutron bombarding energy $E_n-m_nc^2$. If m_n and m_p are taken as equal, this expression is the same as that used by Snow[6] to the approximation used, i.e., neglect of β^4 compared with unity. We hope, by using the value of the relativistic momentum in the center-of-momentum system for $\hbar k$ wherever it appears in the shape-independent approximation, to separate out kinematic relativistic corrections from those effects possibly arising from a velocity-dependent force field.

B. Comparison with Proton-Proton Effective Range

The best value of the p-p singlet S-wave effective range comes at present from a shape-independent fit to data[19] in the 2- to 4-Mev region. This effective range is an average taken at a somewhat higher energy than the combination of present data and other n-p parameters represents, and so shape-dependence may affect the local slope of $k\cot\delta$ in a given energy region. There is the possibility of a change compatible with the data of not more than 0.1×10^{-13} cm in the p-p effective range, depending on what shape-dependent parameter is chosen.

In addition to this uncertainty in interpreting the p-p data, there are two small differences to be expected between the n-p and p-p singlet S-wave systems. The first is that if the observed π-mesons give rise to nuclear forces in even approximately the manner which led to Yukawa's original suggestion, the p-p intrinsic range may possibly be longer than the n-p intrinsic range. If neutral mesons are exchanged in the p-p case, and charged mesons, among others, in the n-p case, the lighter mass of the neutral meson might give a longer p-p range. For example, in a symmetric scalar theory the fractional difference would be $\frac{2}{3}(m^{\pm}-m_0)/m^{\pm}$, so the n-p range would be 2.59×10^{-13} cm for a p-p range of 2.65×10^{-13} cm.

A second difference comes from the influence of the electromagnetic interactions on the effective range. For example,[20] turning off the Coulomb interaction but keeping the same nuclear well parameters changes the

[19] Worthington, Findley, and McGruer, Phys. Rev. **87**, 223 (1952).

[20] J. D. Jackson and J. M. Blatt, Revs. Modern Phys. **22**, 108 (1950).

effective range by only 0.2 percent for a Yukawa well, but by 5.6 percent, i.e., from 2.64 for p-p to 2.79×10^{-13} for n-p, for a square well. The effect of a repulsive core should be to minimize this difference.

V. CONCLUSION

Using the value $\sigma=(3.675\pm0.016)\times10^{-24}$ cm^2 at $T_n=1.315$ Mev, we get $r_s=(2.36\pm0.20)\times10^{-13}$ cm in the shape-independent approximation. It should be pointed out that the quoted errors in the measurements of the other quantities that enter into the present evaluation of the singlet range, particularly the coherent thermal scattering amplitude, give a minimum uncertainty of almost 0.2×10^{-13} cm in r_s, so that several different experiments are now at about the same limit of accuracy as far as their application to the singlet n-p range. A reasonable figure for our result is therefore $(2.4\pm0.3)\times10^{-13}$ cm. This value[21] touches the p-p singlet range discussed in IV–B and is compatible with charge independence of singlet S-wave effective ranges.

No attempt at a comparison of singlet ranges obtained from other n-p scattering experiments will be made here, except to remark that a simple interpretation of a succession of experiments of comparable accuracy is that they average out to give a singlet n-p range that is of the order of 0.2×10^{-13} cm less than the p-p range.

VI. ACKNOWLEDGMENTS

We are grateful to E. E. Lampi, J. H. Williams, and Clarke Williams for scattering materials, to R. Paulson of the National Bureau of Standards for accurate analysis of the scatterers, to C. Goodman, W. Preston, and P. Stelson for making available the Rockefeller generator and helping us use it, to R. Adair, J. Blatt, S. Drell, H. Feshbach, G. Snow, and F. Villars for discussions and calculations, and to D. I. Cooper, T. Romanowski, and R. L. Zimmerman for very great help in running the experiment.

APPENDIX

Formulas Used in Experiment

1. Correction to transmission for background in detector in typical geometry:

$$\Delta T=(1-T)[(2.7\pm0.3)+(1.5\pm0.3)]\times10^{-3},$$

where the first term is from reflection from the walls and floors of the room, and the second term is from unshadowed and partially shadowed parts of the detector preamplifier, etc.

2. Correction to transmission for single scattering into detector and monitor:

$$T_{\text{observed}}=T_{\text{true}}\left[1+\frac{4\pi\sigma(0^\circ)}{\sigma_{\text{tot}}}\frac{\omega_{sq}\omega_{ds}}{\omega_{dq}}\ln\frac{1}{T}-\frac{I(0^\circ)}{I(\theta)}\frac{4\pi\sigma(\theta)}{\sigma_{\text{tot}}}\omega_{sq}(1-T)\right].$$

Here $4\pi\sigma(0^\circ)/\sigma_{\text{tot}}$ is the ratio of scattering at zero degrees to the average scattering for all other angles. $I(0)/I(\theta)$ is the ratio of source intensity in the 0° and θ directions. ω_{sq} is the solid angle subtended by scatterer at source, ω_{ds} by detector at scatterer, and ω_{dq} by detector at source.

3. Estimate of upper limit on double scattering: detector assumed to have a linear response as a function of energy, starting from zero at E_e.

$$\frac{N_{\text{doubly scattered}}}{N_{\text{singly scattered}}}\leqq\bar{\epsilon}\sin^2\theta_e\left(\frac{1-T}{T\ln(1/T)}-1\right).$$

Here $\bar{\epsilon}$ is average efficiency, taken to be $\frac{1}{2}$, for those doubly scattered neutrons which are counted. θ_e is the scattering angle for which the energy of the doubly scattered neutron drops to E_e. Since $\sin^2\theta_e$ is about 0.3, for $T=0.4$ the double scattering gives not more than 0.07 percent correction to the transmission.

4. Calibration of rate dependence of monitor efficiency ϵ with two natural sources:

(a) Between rates R and $2R$: bring up source A to a distance such that the monitor counts at Rate $[A]\cong R$. Then bring up B so that $[A+B]\cong2R$. Remove A, giving $[B]\cong R$. Thus, $\epsilon_{2R}/\epsilon_R=[A+B]/([A]+[B])$. Note that the locations of A and B need not be measured or reproduced.

(b) Between rates $2R$ and $3R$: proceed as above for first three steps. Then, without moving B, move A up to a closer position than before, such that $[A'+B]\cong3R$. Then remove B, giving $[A']\cong2R$. Thus,

$$\frac{\epsilon_{3R}}{\epsilon_{2R}}=\frac{[A']+[B]\{[A+B]/([A]+[B])\}-[A'+B]}{[A']+[B]\{[A+B]/([A]+[B])\}}.$$

Again no distances need to be measured or locations reproduced.

[21] In progress reports $r_s=2.2\pm0.3$ was computed tentatively from almost the same cross section. This error arose in part from use of $T_n=1.320$ Mev, the neutron energy computed without relativistic corrections to the reaction energy measurement.

Uranium Photofission Yields*†

ROMAN A. SCHMITT‡ AND NATHAN SUGARMAN
Institute for Nuclear Studies, University of Chicago, Chicago, Illinois

(Received April 19, 1954)

The photofission yield-mass curve of natural uranium for 48-Mev x-rays was determined radiochemically. Isolation of selected peak and trough fission products at various maximum x-ray energies, 7 Mev, 10 Mev, 16 Mev, 21 Mev, 48 Mev, 100 Mev, and 300 Mev showed that the peak-to-trough ratio decreased from 300 to 4 as the maximum x-ray energy increased from 7 Mev to 300 Mev. The observed photofission yield curves may be quantitatively interpreted as the superposition of two components, a low-energy asymmetric (double-humped) curve and a high-energy single-humped curve. The average cross section for symmetric fission for photons in the energy range 16 Mev to 300 Mev is about 7 millibarns.

I. INTRODUCTION

MANY investigations of high-energy fission, induced by particles and x-rays, have been reported.[1–12] One striking feature of these studies is the decrease in the peak-to-trough yield ratio of the yield-mass curve as the energy of the bombarding particle increases, resulting in the one hump yield-mass curve as the energy of the particle enters the hundred-Mev range. A systematic investigation of the photofission of a heavy nuclide at various energies has not been reported.

The purpose of this work was essentially threefold; (1) to determine the yield-mass curve of natural uranium for 48-Mev maximum x-rays by the comparison method;[4,13,14] (2) to study the changes in the photo-yield curve of uranium as a function of increasing maximum x-ray energy from 7 Mev to 300 Mev; and (3) to study the change in the neutron-to-proton ratio of primary fission fragments with increasing x-ray energy. On the assumption that the observed fission-yield curves are composites of two idealized curves,[14] one very asymmetric and the other symmetric, the excitation function and probability for symmetric fission as a function of energy were calculated.

II. EXPERIMENTAL PROCEDURE

A. Irradiation Setups

The University of Chicago 100-Mev betatron, described by Westendorp and Charlton,[15] was used primarily in this research. Ten-gram samples of analytical reagent grade uranyl nitrate (Mallinckrodt) in plastic vials were placed about 32 cm from the tungsten target (about 3 cm from the Pyrex glass doughnut) directly along the x-ray axis and within the half-angle of the x-ray beam. Average intensities of the x-ray beams at (21±1) Mev, (48±1) Mev, and (100±1) Mev, in roentgens/min at one meter from the target, were about 20, 250, and 1000, respectively. About 50 irradiations, most of them at 48 Mev, were performed.

Twenty gram samples in glass vials were irradiated at the University of Illinois 22-Mev betatron. A total of 10 irradiations were made at energies of 7 Mev (6.8±0.1), 10 Mev (9.7±0.1), 16 Mev (15.5±0.1), and 21 Mev (21.3±0.1). X-ray intensities at one meter for the 7, 10, 16, and 21 Mev x-ray beams were about 2.5, 9, 20, and 65 roentgens/min, respectively.

Six irradiations at 300 Mev were performed at the University of Illinois 340-Mev betatron. Cylindrical glass vials, containing 2.5 g of powdered uranyl nitrate, were placed about 55 cm from the platinum target. The intensity was about 1500 roentgens/min at one meter.

Since the photofission yields were determined by comparison with thermal-neutron yields,[4,13,14] it was necessary to obtain thermal-neutron irradiations of uranyl nitrate. These were performed at the Argonne Heavy-water Pile (CP-3) and at the University of Chicago 37-inch cyclotron. Six irradiations were performed at the pile, in each of which about 2 g of uranyl nitrate was bombarded in the thermal column for about 20 min at an average neutron flux of about 3×10^{11} neutrons/cm² sec. Ten irradiations were made at the

* This work was supported in part by a grant from the U. S. Atomic Energy Commission.
† Part of this document is based on work performed at the University of Illinois, Urbana, Illinois, supported by a grant from the U. S. Office of Naval Research.
‡ Presented in partial fulfillment for the Ph.D. degree in the Department of Chemistry, University of Chicago. Now at the University of Illinois, Urbana, Illinois.

[1] P. R. O'Connor and G. T. Seaborg, Phys. Rev. **74**, 1189 (1948).
[2] A. S. Newton, Phys. Rev. **75**, 17 (1949).
[3] R. H. Goeckermann and I. Perlman, Phys. Rev. **76**, 628 (1949).
[4] R. W. Spence, *Brookhaven Conference Report*, Chemistry Conference No. 3, Brookhaven National Laboratory, 1949 (unpublished), pp. 43–51.
[5] N. Sugarman, Phys. Rev. **79**, 532 (1950).
[6] H. G. Richter and C. D. Coryell, Phys. Rev. **90**, 389 (1953).
[7] Fowler, Jones, and Paehler, Phys. Rev. **88**, 71 (1952).
[8] Turkevich, Niday, and Tompkins, Phys. Rev. **89**, 552 (1953).
[9] D. M. Hiller and D. S. Martin, Jr., Phys. Rev. **90**, 581 (1953).
[10] R. A. Schmitt and N. Sugarman, Phys. Rev. **89**, 1155 (1953).
[11] R. W. Spence and G. P. Ford, Ann. Rev. Nuclear Sci. **2**, 399–410 (1953).
[12] H. A. Tewes and R. A. James, Phys. Rev. **88**, 860 (1952).
[13] Finkle, Hoagland, Katcoff, and Sugarman in *Radiochemical Studies: The Fission Products*, edited by C. D. Coryell and N. Sugarman (McGraw-Hill Book Company, Inc., New York, 1951), Paper No. 216 National Nuclear Energy Series, Plutonium Project Record, Vol. 9, Div. IV, p. 1368.
[14] A. Turkevich and J. B. Niday, Phys. Rev. **84**, 52 (1951).
[15] W. F. Westendorp and E. E. Charlton, J. Appl. Phys. **16**, 581 (1945).

cyclotron. About 30 g embedded in 4 inches of paraffin was irradiated for about 20 min to 4 hr at a neutron flux of about 10^9 neutrons/cm² sec.

B. General Radiochemical Procedure

After irradiation, the uranyl nitrate was dissolved in $6N$ HNO_3 and was diluted to $3N$. Radiochemical analyses were performed on solutions containing about 20 mg of carrier and aliquots yielding an initial counting rate of about 1000 to 8000 counts per minute for the nuclide isolated. The radiochemical analyses, after slight modifications because of larger amounts of uranyl nitrate, were the same as those employed on the Plutonium Project.[16] Duplicate analyses for each nuclide from a given bombardment were carried out.

The final precipitates of about 25 mg were filtered onto 1.8-cm diameter filter paper disks, which were subsequently mounted on rectangular cardboards 6.3 cm ×7.6 cm and 60 mg/cm² thick. Cellophane of about 2.5 mg/cm² covered the precipitates. The radioactive samples, all beta emitters, were counted by a standard end-window (~2.5 mg/cm²) Geiger-Mueller Tube (Tracerlab TGC-1) in a lead shield.

The nuclides isolated from betatron irradiations were also isolated from thermal-neutron bombardments. They were identified by tested radiochemical procedures,[16] by counting them for at least 3 to 4 half-lives, and by absorption curves when necessary. In some cases it was advantageous to follow the decay curves of a nuclide isolated from x-ray and neutron fission through a selected aluminum absorber.

III. SECONDARY NEUTRON FISSION

Since fast-neutron fission tends towards more symmetric cleavage of the nucleus,[4,8,17] it was important to show that the high photofission trough yields which are observed were not due to high-energy neutrons, resulting from (γ,n) reactions in the electron target, the doughnut, and the sample. The high (~15 Mev) potential barrier for protons and the small number of protons above 15 Mev excludes any appreciable proton-fission competition.

In order to determine the fast-neutron flux in the 10 g sample, and thereby, the fast-neutron fission contribution, a number of experiments were performed on the activation of phosphorus. The radioactivity from the reaction $P^{31}(n,p)S^{31}$ ($Q=-1.0$ Mev) was detected as 170-min Si^{31}. It was assumed that the average cross section[18,19] for the (n,p) reaction is 0.10×10^{-24} cm² from ~2 Mev to 14 Mev.

Experiments at 48 Mev were performed to determine the fast-neutron flux resulting from (γ,n) reactions in the sample, and in the electron target and the Pyrex doughnut. About 1.1 g of red phosphorus was sandwiched between two plastic cylinders each of which contained 4.3 g of powdered uranyl nitrate. An identical setup, but with no uranyl nitrate, was irradiated for 10 min immediately after the first setup and at the same betatron intensity.

TABLE I. Fast-neutron measurements.

Sandwich	(nv), cm^{-2} min^{-1}	Fission rate, min^{-1}
(U−red P−U)	1.1×10^8	6.5×10^7
(no U−red P−no U)	5.3×10^7	

After irradiation, the phosphorus samples (Si^{31}) were counted. 85-min Ba^{139} was isolated from the combined uranyl nitrate samples of the first irradiation from which the total fission rate was calculated. The results are given in Table I, where (nv) is the fast-neutron flux from ~2 Mev to 14 Mev, and the fission rate is that observed in the uranium samples. Assuming an (nv) of 1.1×10^8 cm^{-2} min^{-1} in the sample and a fission cross section[20] of 0.5×10^{-24} cm², we calculate that 1 percent of the total fissions at 48 Mev is due to fast-neutron fission. Similar results were obtained at 100 Mev. This low percentage of neutron fission is about the same as that found by Richter[21] using 16-Mev x-rays.

Experiments with 300-Mev x-rays yield a maximum value of 1 percent for the fast-neutron fission contribution. The thermal-neutron fission contribution, resulting either from external neutrons or internal neutrons was shown to be unimportant by cadmium shielding and indium foil activation experiments. If it is assumed that the peak-to-trough ratio for the fast-neutron fission is 6, as found with 14-Mev neutrons,[4] then the maximum error in the observed peak-to-trough ratios is 5 percent.

IV. EXPERIMENTAL RESULTS

The comparison method[4,13,14] was used in this research to determine the photofission yields in order to circumvent absolute beta and gamma counting. The ratio of two photofission yields is given by the equation:

$$\frac{Y'(N)}{Y'(S)}=\frac{Y(N)}{Y(S)}\cdot\frac{A^{\infty}(S)}{A^{\infty}(N)}\cdot\frac{A^{\infty\prime}(N)}{A^{\infty\prime}(S)}.$$

In this equation (N) and (S) designate, respectively, the nuclide isolated and the standard nuclide isolated (67-hr Mo^{99}); A^{∞} and $A^{\infty\prime}$, the saturation activities for

[16] *Radiochemical Studies: The Fission Products* (McGraw-Hill Book Company, Inc., New York, 1951), National Nuclear Energy Series, Plutonium Project Record, Vol. 9, Div. IV.
[17] J. Jungerman and S. C. Wright, Phys. Rev. **76**, 1112 (1949).
[18] B. L. Cohen, Nucleonics **8**, No. 2, 29 (1951).
[19] E. B. Paul and R. L. Clarke, Report CRP-527, Atomic Energy of Canada, Ltd., Chalk River Project, Ontario (unpublished).
[20] Ladenburg, Kanner, Barschall, and Van Voorhis, Phys. Rev. **56**, 168 (1938); National Research Council of Canada, Atomic Energy Project, Can, J. Phys. **29**, 203 (1951).
[21] H. G. Richter, Ph.D. thesis, Massachusetts Institute of Technology, August 16, 1952 (unpublished), showed by a modified technique that less than 0.8 percent of the fission of uranium with 16-Mev x-rays from the linear accelerator was caused by fast neutrons.

TABLE II. Natural uranium photofission yields.

Mass No.	Nuclide isolated and measured[a]	Thermal-neutron yield in U^{235}[b]	7 Mev	10 Mev	16 Mev	21 Mev	48 Mev	100 Mev	300 Mev
77	12-hr Ge→38-hr As	0.0067[c]					0.032±0.004[d]		
78	86-min Ge→91-min As[e]	0.020[b,c]					0.059±0.002		
83	2.4-hr Br	0.48					0.59±0.06	0.62±0.07	0.73±0.08
84	31-min Br	0.65					1.03±0.17	1.04±0.15	1.09±0.18
89	53-day Sr	4.3				2.6±0.1	2.8±0.1	2.8±0.1	3.0±0.1
91	9.7-hr Sr[f]	5.5					3.9±0.1		
97	17.0-hr Zr→74-min Nb[g]	6.0				5.7±0.2	5.8±0.2	5.8±0.2	
99	67-hr Mo[h]	6.8	6.6[i]	6.6[i]	6.6[i]	6.6[i]	6.6	6.6[i]	6.6[i]
103	38.5-day Ru	2.2				3.0±0.3	2.9±0.2	3.2±0.2	3.4±0.3
105	4.5-hr Ru	0.9					2.5±0.1		
106	1.0-yr Ru→30-sec Rh[g]	0.52				2.1±0.3	2.0±0.2	2.6±0.2	3.0±0.2
111	7.6-day Ag	0.018	0.046±0.004	0.065±0.007	0.30±0.01	0.43±0.01	0.77±0.02	1.02±0.02	1.88±0.06
112	3.2-hr Ag[j]	0.011	0.031±0.005	0.047±0.005	0.16±0.01	0.26±0.02	0.52±0.03	0.71±0.04	1.14±0.08
113	5.2-hr Ag	0.011[k]					0.60±0.03	0.77±0.04	1.21±0.06
115	54-hr Cd[l]	0.011		0.030±0.004	0.16±0.01	0.25±0.01	0.047±0.02	0.67±0.03	1.15±0.05
	43-day Cd	8×10^{-4}			0.013±0.001	0.018±0.001	0.041±0.002	0.048±0.002	0.20±0.02
117	2.83-hr Cd→1.95-hr In[m]	0.010		0.027±0.007			0.50±0.02	0.69±0.02	1.04±0.04
127	94-hr Sb	0.094[p]				0.70±0.02[p]	0.93±0.02[p]	1.07±0.03[p]	1.49±0.09[p]
131	8.0-day I	2.8				4.1±0.2	4.3±0.1	4.4±0.2	4.6±0.2
132	2.4-hr I[j]	4.2				5.0±0.1	4.9±0.1	4.6±0.1	4.3±0.1
133	22.4-hr I[m]	6.3					6.2±0.3		
137	33-yr Cs	6.1					4.7±0.3		
139	85-min Ba	6.3					4.6±0.1	5.1±0.1	
140	12.8-day Ba→40-hr La[g]	6.2	5.8±0.3	5.7±0.2	5.0±0.1	4.9±0.1	5.0±0.3	5.3±0.1	4.8±0.2
141	30-day Ce[n]	5.9					4.9±0.3		
143	33-hr Ce[o]	5.3				4.0±0.1	3.8±0.3	3.8±0.1	3.6±0.1
144	275-day Ce→17.5-min Pr[g]	4.6				3.8±0.2	3.4±0.2		

[a] The observed half-lives are given. For literature values, see reference 16 and "Table of Isotopes," Hollander, Perlman, and Seaborg, Revs. Modern Phys. 25, 469 (1953).
[b] Yields above 2 percent and below 2 percent were taken from references 22 and 23, respectively.
[c] Yield of 38-hr As^{77} as reported by N. Sugarman, Phys. Rev. 89, 570 (1953).
[d] Yield of 38-hr As^{77}, calculated by assuming that the branching ratio of 12-hr Ge^{77} to 59-sec Ge^{77} is 0.52 as reported in reference c.
[e] Activity mixture counted. Half-lives of Ge and As are those of reference c.
[f] Counted through 199 mg/cm² Al to emphasize 9.7-hr Sr^{91}.
[g] Counted equilibrium mixture.
[h] Counted through 21.0 mg/cm² Al to absorb radiations of 6.0-hr Tc^{99m} daughter.
[i] Assumed yield; other yields normalized to it.
[j] The daughters 3.2-hr Ag^{112} and 2.4-hr I^{132} were separated from their parents during equilibrium. The yields of 112 and 132 are therefore the yields of their parents.
[k] Interpolated yield from smooth yield curve of reference 23.
[l] Counted through 91.0 mg/cm² Al to absorb radiations of 4.5-hr In^{115m} daughter.
[m] Counted through 56.9 mg/cm² Al to emphasize 22.4-hr I^{133}.
[n] Counted through 24.9 mg/cm² Al to absorb soft components of 30-day Ce^{141}.
[o] Counted through 67.4 mg/cm² Al to emphasize 33-hr Ce^{143}.
[p] The thermal-neutron yield of 0.15 percent reported by A. C. Pappas [Massachusetts Institute of Technology Technical Report No. 63, September 15, 1953 (unpublished)] raises the photoyields by a factor of 1.6.

thermal-neutron and x-ray irradiations, respectively; and Y and Y', the thermal-neutron and x-ray fission yields, respectively.

The thermal-yield values, $Y(N)$ and $Y(S)$, above 2 percent, obtained by Glendenin *et al.*,[22] and those below 2 percent, found by workers on the Plutonium Project,[23] were taken as absolute values (Table II). The absolute photo-yield of 67-hr Mo^{99}, $Y'(S)$, was found to be 6.6 percent for 48-Mev x-rays by normalizing the fission yield curve to 200 percent.

The most important advantage to be gained from the comparison method is the elimination of the need for absolute beta and gamma counting. The major disadvantages of the method are: (1) the photoyield curve is at best no more accurate than the assumed thermal-neutron yield curve, and (2) the yield determined in this manner, or by absolute counting, may not represent the full yield of the chain,[24,25] especially at higher energies where the most probable charge for a given mass is closer to stability.[3,26,27]

The photofission yield data of natural uranium at 7, 10, 16, 21, 48, 100, and 300 Mev are given in Tab e II, where, for the most part, the errors are the mean deviations of duplicate samples of an individual run. In some cases, such as Ru^{106}, Ag^{111}, Ag^{112}, Sb^{127}, and others, the yields at 48 Mev are the averages obtained from two or more experiments. In these cases, the errors are not appreciably different from those of a single run. Photofission values at 48 Mev are normalized to a total yield of 200 percent. The 7, 10, 16, 21, 100, and 300-Mev photoyields were calculated by arbitrarily assuming a yield for 67-hr Mo^{99} of 6.6 percent, the normalized 48-Mev value.

The experimental results of Table II are graphically represented in Figs. 1 and 2. Construction of the best 48-Mev photocurve (Fig. 1) was accomplished as follows. A binary fragment sum of 234, amounting to the emission of 4 neutrons per fission, was found by reflecting the experimental values of near-peak yields that are sensitive to the mass sum assumed, *viz.*, masses 89, 91, 140, 141, 143, and 144. A larger mass sum[28] of 237 is a better fit to the experimental yields of near-trough masses 111 and 127. Construction of the intermediate portion of the curve was accomplished by assuming that the mass sum ranged from 234 to 237. Similar

[22] Glendenin, Steinberg, Inghram, and Hess, Phys. Rev. 84, 860 (1951).
[23] Reference 16, Appendix B.
[24] Glendenin, Coryell, and Edwards, reference 16, paper 52.
[25] L. E. Glendenin, Ph.D. thesis, Massachusetts Institute of Technology, Technical Report No. 35, July 29, 1949 (unpublished).
[26] P. Kruger, Ph.D. thesis, University of Chicago, January, 1954 (unpublished).
[27] L. Jodra, University of Chicago (unpublished).
[28] The effect of the apparent change in the number of neutrons emitted in other fission-yield curves was observed earlier by L. E. Glendenin and E. P. Steinberg of the Argonne National Laboratory, and C. D. Coryell of the Massachusetts Institute of Technology (private communication).

results were also found for the 21- and 100-Mev photoyield curves.

Since the 48-Mev curve is normalized to 200 percent and since the asymmetric yields at 16, 21, 100, and 300 Mev did not change appreciably when normalized to a yield of 6.6 percent for Mo^{99}, it is necessary to displace these photocurves vertically about +4, +3, −2, and −8 percent, respectively, to take account of the changing yields in the trough. These changes, however, do not affect the peak-to-trough yield ratios.

Table III presents data on independent yields of selected nuclides and their fractions of the chain yields for the thermal-neutron fission of U^{235} and for the x-ray work of this research. The species studied were 36.0-hr Br^{82}, 3.2-hr Ag^{112}, 52.5-min I^{134}, and 13.6-day Cs^{136}. It is noted that the independent yields of Br^{82} and Cs^{136} increase markedly at the higher energies. This effect is discussed in Sec. V. D.

V. DISCUSSION

A. General Observations of Photofission Results

Baldwin and Klaiber[29] determined the photofission excitation curve for uranium and reported a peak in the curve at about 16 Mev and a negligibly small cross section beyond 33 Mev. This peak at about 16 Mev was interpreted by Goldhaber and Teller[30] as a resonance in the photoabsorption cross section. Relative cross-section data of the photofission of U^{235} and U^{238} obtained by McElhinney and Ogle[31] indicate that in the 12-Mev

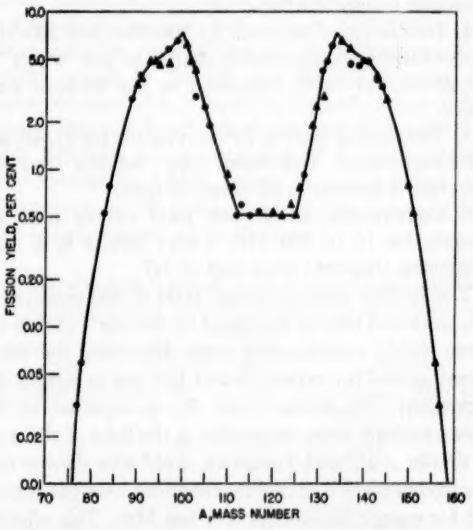

FIG. 1. Photofission yield curve for 48-Mev x-ray fission of natural uranium. ●, observed 48-Mev photoyields; ▲, reflected 48-Mev yields assuming that the fragment sum was 237 for masses 111 through 127, 234 for asymmetric masses, and mass sums in the 234 to 237 range for near-trough masses. Total fission yield is 200 percent.

[29] G. C. Baldwin and G. S. Klaiber, Phys. Rev. **71**, 3 (1947).
[30] M. Goldhaber and E. Teller, Phys. Rev. **74**, 1046 (1948).
[31] J. McElhinney and W. E. Ogle, Phys. Rev. **81**, 342 (1951).

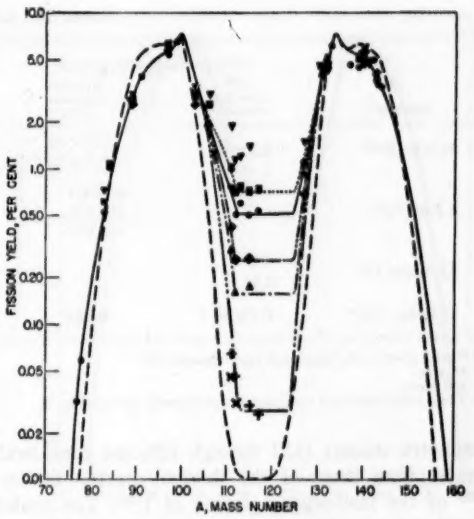

FIG. 2. Photofission yield curves for natural uranium as a function of x-ray energy. ×, 7 Mev; +, 10 Mev; ▲, 16 Mev; ◆, 21 Mev; ●, 48 Mev; ■, 100 Mev; and ▼, 300 Mev. The 7, 10, 16, 21, 100, and 300 Mev yields are normalized to 6.6 percent yield for mass 99 (48-Mev yield). ——, thermal-neutron U^{235} curve; – – – – –, 10-Mev curve; — — —, 16-Mev curve; — — —, 21-Mev curve; ————, 48-Mev curve; and – – – – –, 100-Mev curve.

to 22-Mev maximum x-ray interval the isotope U^{238} in natural uranium is responsible for about 99 percent of the fissions. Jungerman and Steiner[32] obtained similar results at 335 Mev.

The fission yield curve in uranium was extensively investigated with 48-Mev x-rays so that excitation over the entire resonance region[33] could occur. Following are some comparisons of the 48-Mev x-ray fission curve of U^{238} with the thermal-neutron fission curve of U^{235} and other specified curves. The thermal-neutron fission curve of U^{235} is used for comparison since the fragment mass sum for the most probable mode of fission appears to be the same as that from 48-Mev x-rays and U^{238}.

1. The very-asymmetric yields of masses 77 through 84 are substantially higher than the corresponding thermal-neutron yields in U^{235} and the 10-Mev and 16-Mev x-ray yields[21] in U^{238}, where determined (see Table II and Fig. 3).

2. The light-peak yields of masses 89 through 106 and the yields of the complementary masses on the heavy peak are approximately equal to the corresponding yields of the fission-neutron (Fig. 4) or the 16-Mev photofission (Fig. 3) of U^{238}, and the 14-Mev neutron and ~20-Mev x-ray fission of U^{235} (Fig. 4).

3. Yields of the near-symmetric (111 and 127) and

[32] J. Jungerman and H. Steiner, Phys. Rev. **93**, 949(A) (1954).
[33] As discussed later in this paper, the cross section beyond the resonance region is small but measurable. J. Gindler, Ph.D. thesis, University of Illinois, February, 1954 (unpublished), using a different experimental approach from that reported here, has arrived at the same conclusion.

TABLE III. Independent fission yields.

Nuclide	Independent yield, percent: U^{235} thermal neutrons[a]	Independent yield, percent: Natural uranium, x-rays	Chain yield, percent: U^{235} thermal neutrons[a]	Chain yield, percent: Natural uranium, x-rays	Fraction of chain yield: U^{235} thermal neutrons[a]	Fraction of chain yield: Natural uranium, x-rays
36.0-hr Br^{82}	3.5×10^{-6}	1.8×10^{-4}[b] 2.7×10^{-2}[c]	0.20	0.38[d] 0.40[i]	1.75×10^{-4}	4.7×10^{-4}[b] 6.5×10^{-2}[c]
3.2-hr Ag^{112}		<0.01[b] <0.02[c] <0.07[e]		<0.53[b] <0.73[c] <1.21[e]		<1.9×10^{-2}[b] <2.8×10^{-2}[c] <5.8×10^{-2}[e]
52.5-min I^{134}	1.0 0.9[f]		5.5 7.9[f]	7.4[d]	0.19[g] 0.11[f]	0.20[b,h]
13.6-day Cs^{136}	6.2×10^{-5}	0.044[b]	6.0	6.2[b,d]	1.0×10^{-3}	7.1×10^{-3}[b]

[a] Taken after L. E. Glendenin (see reference 25).
[b] 48 Mev.
[c] 300 Mev.
[d] These yields are read from smooth photoyield curves (Fig. 2).
[e] 100 Mev.
[f] A. C. Pappas and C. D. Coryell, Phys. Rev. 81, 329 (1951).
[g] The yield becomes 0.13 if 7.9 is assumed for the total chain yield.
[h] Obtained by repeated separations of I^{131}.

symmetric masses (112 through 126) are considerably greater than those of the thermal-neutron fission of U^{235} or the fast-neutron fission of U^{238}. The peak-to-trough ratio for 48-Mev maximum x-rays is 11.

4. Fine structure, which has been shown[22] to be present in the thermal-neutron fission of U^{235} at masses 100 and 134, may also be present in the x-ray fission of U^{238} at about the same masses. Tewes and James[12] have reported the existence of fine structure in the proton fission of thorium.

Analysis of the 7, 10, 16, 21, 100, and 300-Mev photofission results given in Tables II, III, IV (where the peak-to-trough ratios at various energies are reported) and Figs. 2 and 3 leads to the following observations:

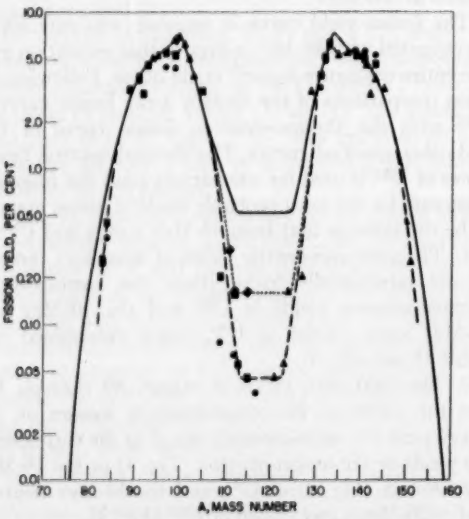

FIG. 3. Natural uranium photofission yield-mass curves. ●, 10-Mev and ■, 16-Mev photoyields by H. G. Richter (see reference 21). ▲, 16-Mev reflected photofission yields (arbitrarily assumed that the fragment mass-sum is 236 for masses 110 to 126 and 234 for all other masses). ◆, 16-Mev photoyields of this research. ———, 16-Mev curve of H. G. Richter, normalizing his curve to the 48-Mev photoyield of mass 139; – – – –, 16-Mev curve of this research, and ————, 48-Mev curve of this research (see Fig. 1).

1. The peak-to-trough ratios at 7, 10, 16, 21, 48, 100, and 300 Mev are: >300, 200, 38, 23, 11, 8, and 4, respectively. The lower limit to the 7-Mev ratio was obtained by assuming the same yield ratio of Pd^{112} to Cd^{115} at 7 Mev and 10 Mev.

2. Relative to the yield of Mo^{99} at 48 Mev (6.6 percent), the asymmetric peak yields of masses 89 through 103, and the yields of their complementary masses, for the x-ray energies 21 to 300 Mev hardly changed outside the experimental error.

3. The trough photoyields in U^{238} approach the thermal-neutron yields (0.01 percent) in U^{235} as the maximum x-ray energy decreases and approaches the threshold energy, 5.2 Mev.[34]

4. Irradiation of uranium by 100-Mev and 300-Mev x-rays caused no appreciable change in the "wings" of the photoyield curve, compared to the 48-Mev x-ray curve.

5. The ratio of Mo^{99} to Zr^{97} is constant for 21, 48, and 100-Mev x-rays. This result may indicate that fine structure is present at all three energies.

6. Construction of smooth yield curves near the troughs for 16 to 300 Mev x-rays results in a near-symmetric fragment mass sum of 237.

The 10-Mev peak-to-trough ratio of 200 observed in this work and that of 150 found by Richter[21] (Table IV) agree within experimental error. However, the corresponding 16-Mev ratios, 38 and 120, are in serious disagreement. The former ratio 38, as reported in this paper, appears more reasonable in the light of the work of Fowler *et al.*[7] and Turkevich *et al.*[8] who showed that the trough yield is markedly enhanced near the threshold for energy increments of a few Mev. This effect is mostly dependent upon the extent of nuclear excitation and is fairly independent of the incident particle and the heavy fissionable nucleus involved. The ~20-Mev and 21-Mev photo peak-to-trough ratios in U^{235} and U^{238} of 20 and 23, respectively, and the 48-Mev and

[34] Koch, McElhinney, and Gasteiger, Phys. Rev. 77, 329 (1950); R. E. Anderson and R. B. Duffield, Phys. Rev. 85, 728 (1952).

69-Mev ratios in U^{238} and Th^{232}, of 11 and 10, respectively, support this conclusion.

B. Quantitative Interpretation of X-Ray Fission in U^{238}

The observed photofission yield curves (Fig. 2) may be interpreted as the superposition of two components, a low-energy asymmetric (double-humped) curve and a high-energy single-humped curve, produced by the absorption of high-energy photons. This postulate was suggested by Turkevich *et al.*[14] in order to interpret the observed neutron-fission yield curves of Th^{232} and U^{238}. The decrease in the peak-to-trough ratio with increasing energy (Table IV) will be assumed to be the result of an increasing contribution of high-energy fission. The cross section for high-energy fission may be obtained by calculating the fraction of high-energy fission and by assuming the measured cross section for photofission at the resonance energy.

The low-energy curve adopted for this analysis is essentially the photoyield curve observed at 7 to 10 Mev (Figs. 2 and 3) but with a peak-to-trough ratio of 600. This value was chosen to be roughly the same[16,35] as that found with thermal neutrons and U^{233} or U^{235}. In these cases the fissioning nucleus is excited by about 1 Mev above the fission threshold of 5.2 Mev.[34] With 7-Mev x-rays most of the excitation is at about 1–2 Mev (because of the resonance nature of the photoabsorption) where the contribution from symmetric fission would be expected to be higher.[7,36]

The single-humped high-energy photofission yield curve may be calculated from the differences in the trough yields of the 48- and 100-Mev curves. The value obtained, 2.4, is equal to the percentage of high-energy fission induced by the photons of 48 to 100 Mev with 100-Mev maximum x-rays. If it is assumed that only symmetric fission occurs in this interval, then 97.6 percent of the fissions for 100-Mev x-rays occur in the energy interval up to 48 Mev.

TABLE IV. Peak-to-trough ratios at various x-ray energies.

Energy of x-rays, Mev	Nuclide irradiated	Peak-to-trough ratio	Reference
2.6, fission neutrons	U^{238}	100	Engelkemeir, Seiler, Steinberg, and Winsberg, see reference 16, paper 218.
7	U^{238}	>300	This paper.
10	U^{238}	200	This paper.
10	U^{238}	150	See reference 21.
16	U^{238}	38	This paper.
16	U^{238}	120	See reference 21.
~20	U^{235}	20	See reference 4.
21	U^{238}	23	This paper.
48	U^{238}	11	This paper.
69	Th^{232}	10	See reference 9.
100	U^{238}	8	This paper.
300	U^{238}	4	This paper.

[35] W. E. Grummitt and G. Wilkinson, Nature **161**, 520 (1948).
[36] P. Fong, Phys. Rev. **89**, 332 (1953).

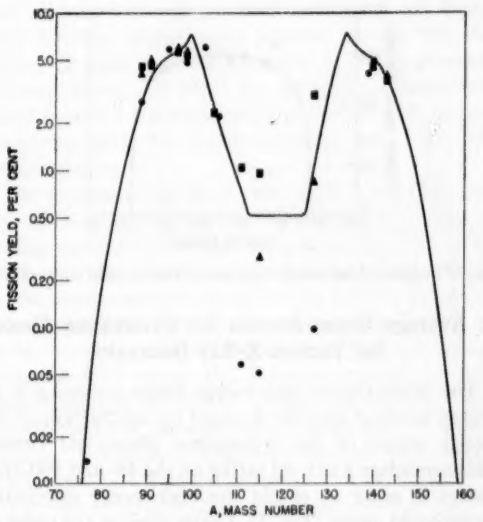

FIG. 4. X-ray and fast-neutron induced fission yields. ●, fission-neutrons and U^{238} (see reference 16); ■, 14-Mev neutrons and U^{235} (see reference 4); ▲, ~20-Mev x-rays and U^{235} (see reference 4). Solid curve is the normalized 48-Mev photofission curve of natural uranium of this research (see Fig. 1). The yields of reference 16 were normalized to the 48-Mev x-ray curve at mass 140 and those of reference 4 at mass 97.

The yields of masses 111, 112, 115, 117, and 127 of the high-energy yield curve, calculated from the percentage of fissions[37] occurring in the energy interval 48 to 100 Mev and the observed fission yields of the trough species at 48 and 100 Mev, are 11.8, 9.1, 10.0, 9.6, and 7.3 percent, respectively. The proposed high-energy symmetric fission-yield curve is presented in Fig. 5. A curve of similar shape and roughly of the same yield values is found by like treatment of the 100- and 300-Mev trough data. The curve was assumed to approach zero at masses 106 and 130 because of the approximate constancy of the yield values at masses 103, 106, 131, and 132 (Table II).

The half-width (full width at half-height) of the proposed high-energy symmetric curve of U^{238} is ~21 mass-units. Sugarman,[5] investigating the photofission of Bi^{209} with 85-Mev x-rays, reported a half-width of ~20 mass-units for the symmetric yield curve. This contrasted sharply with a half-width of ~40 mass-units, found by Goeckermann and Perlman,[3] who determined the 190-Mev deuteron-induced yield curve in Bi^{209}. O'Connor and Seaborg,[1] bombarding uranium with 380-Mev alpha-particles, found a similarly shaped symmetric distribution of the fission products with a half-width of ~40 mass-units. Perhaps the 40 mass-unit widths result from a superposition of many narrow symmetric curves like that of Fig. 5.

[37] The percentage of symmetric fissions changes from 2.4 to 2.2 when correction is made for the change in bremsstrahlung spectrum for 48- and 100-Mev maximum energies.

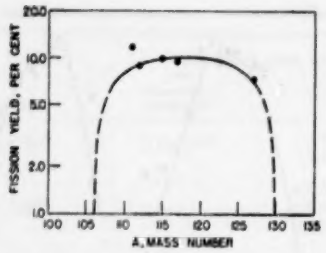

FIG. 5. Proposed high-energy symmetric fission-yield curve of U^{238}.

C. Average Cross Section for Symmetric Fission for Various X-Ray Intervals

The percentage of high-energy fission occurring in an energy interval may be obtained by subtraction of the trough values of the appropriate photoyield curves. This procedure was used earlier on the 48- and 100-Mev curves in order to obtain the high-energy symmetric fission-yield curve (Fig. 5). Corrections of the order of 10 percent are necessary for the change in the bremsstrahlung spectrum with energy. These data are given in column 2 of Table V where the energy intervals are given in column 1. The measured cross section[38] for the resonance absorption can be used to calculate the average cross section for high-energy fission for the various energy intervals. These values are given in column 3 of Table V, where it is seen that the cross section is roughly constant for photon energies above 16 Mev, with a value of about 7 millibarns. Thus, the assumption that was made on the analysis of the observed fission yield curve into low- and high-energy components leads to a total cross section for photofission that is constant at a value of about 8 millibarns from 48 to 300 Mev.

Gindler and Duffield[39] have made measurements on the photofissions of uranium in the energy ranges 10 to 22 and 125 to 300 Mev, by observation of the ionization from the fission fragments in scintillating crystals.

TABLE V. Symmetric fission data for various energy intervals.

Energy interval	Percentage of high-energy fission by subtraction of yield curves[a]	Average cross section for high-energy fission, barns	Average total fission cross section,[b] barns	Branching ratio for "symmetric fission"
5–10	0.2		0.03	
10–16	1.1		0.14	
16–21	1.0	0.006	0.06	0.1
21–48	2.4	0.006	0.02	0.3
48–100	2.2	0.007	0.02	0.3
100–300	5.2	0.009	0.05	0.2

[a] Subtracted values corrected for change in bremsstrahlung spectrum with energy.
[b] From upper curve of Fig. 6, taken from reference 39.

[38] R. B. Duffield and J. R. Huizenga, Phys. Rev. **89**, 1042 (1953).
[39] J. Gindler and R. B. Duffield, Phys. Rev. **94**, 759 (1954); J. Gindler, Ph.D. Thesis, University of Illinois, February, 1954 (unpublished).

Because of the absence of data from 22 Mev to 125 Mev two possible cross-section curves may be drawn depending upon the interpolated cross-section curve assumed for the unmeasured energy interval. These curves are given in Fig. 6. It is seen that the lower curve (dashed) agrees favorably with the cross-section value for the range 100 to 300 Mev given in column 3 of Table V, implying that high-energy fission is mostly symmetric. The upper curve, however, has cross-section values at high energy higher than those given in column 3 of Table V and are given in column 4. The values of the total cross section in the interval 21 to 300 Mev are about a factor of 3 greater than the average cross section as calculated on the assumption that only symmetric fission occurred in this interval. We may interpret the ratio of the cross section, found on the assumption that only symmetric fission occurred, to the total cross section as the branching ratio for "symmetric fission" (column 5).

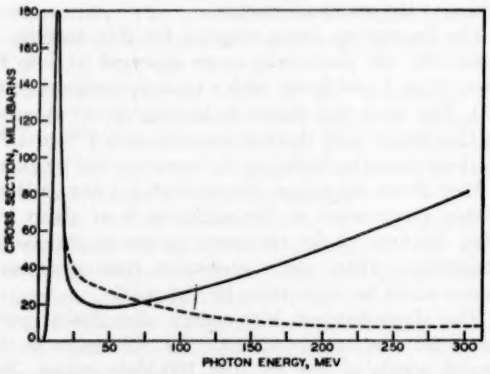

FIG. 6. Photofission cross section of U^{238}. Solid curve from 8 Mev to 19 Mev determined by Duffield and Huizenga (see reference 38); remainder of solid and dashed curves from 19 Mev to 300 Mev determined by J. Gindler (see reference 39).

Here, the term "symmetric fission" simply refers to the mass region 106 to 131.

A branching ratio of 0.3 for "symmetric fission" in the high-energy region implies that the fission-yield curve is still asymmetric, but with a small peak-to trough ratio. A nearly symmetric curve of 50 mass-unit width with a dip at symmetric fission corresponding to a peak-to-trough ratio of about 1.5 satisfies the experimental data.

D. Variation of Independent Fission Yields with Energy

Measurements of the independent fission yields of the nuclides, Br^{82}, Ag^{112}, I^{134}, and Cs^{136}, were made at various x-ray energies and are given in Table III. For comparison, the independent yields of these nuclides in the thermal-neutron fission of U^{235} are also presented.[25] The fraction of the chain yield measures the probability that fission leading to a given mass will result directly in the charge represented by the nuclide

studied. The fact that the values for Br^{82} and Cs^{136} from x-ray fission are higher than those from slow neutron fission of U^{235} means that the primary fission fragments from high-energy x-ray fission of U^{238} are formed closer to stability. These data, and the observed change in the ratio of the yields of the Cd^{115} isomers in the region 100 to 300 Mev, may be used to estimate the most probable neutron-to-proton ratio for a given mass. If it is assumed that the neutron-to-proton ratio does not change in high-energy fission,[3,40] the neutron-to-proton ratio of the fissioning nucleus for photons of 100 to 300 Mev is thus obtained. The assumption that the neutron-to-proton ratio of the primary fragments in high-energy fission is constant appears to be questionable in the light of recent experiments.[26]

The ratio of 54-hr Cd^{115} to 43-day Cd^{115m} for 300-Mev x-rays was found to be 5.7 as compared to 14 for x-rays below 100 Mev. A ratio of ~14 is also observed[14,16] in the fission of U^{235} and Th^{232} with low-energy neutrons. If it is assumed that the ratio changed above 100 Mev because of the independent formation of Cd^{115} isomers, whereas below 100 Mev all of the Cd^{115} was formed from decay of Ag^{115}, then we may calculate the fraction of the chain formed at Cd^{115}. The ratio of 54-hr Cd^{115} to 43-day Cd^{115m} formed independently in high energy proton fission of heavy elements[26] (tantalum to gold) is 0.36. Using this ratio and an increase of 20 percent in the total fissions as the energy is increased from 100 to 300 Mev (upper curve of Fig. 6), then it is found that 7 percent of the chain of mass 115 is formed directly at cadmium. This fraction of the chain yield corresponds to a charge displacement of 1.7 from the most probable charge if the variation of fractional yield with charge displacement is the same as that found in thermal-neutron fission[24,25] of U^{235}. The neutron-to-proton ratio for the most probable charge of 46.3 for mass 115 is calculated to be 1.49. If the neutron-to-proton ratio of the fissioning uranium nucleus is taken to be 1.49, then it is found that there is associated with the fission of uranium with photons of 100 to 300 Mev, the emission of 9 neutrons. For an increase of 5 percent in the total fissions, such as is found if it is assumed that only symmetric fission occurs at high energy (Table V), calculations lead to 12 neutrons emitted.

The high fractional yield of the shielded nuclide Br^{82} with 300-Mev x-rays may be ascribed exclusively to the energy range 100 to 300 Mev. Below 48 Mev the yield is low, and only about 5 percent of the fissions with 300-Mev x-rays occur between 48 and 100 Mev where the yield may be expected to be intermediate between 48 and 300 Mev. The neutron-to-proton ratio found from the fractional yield of Br^{82} is 1.46, in good agreement with the value obtained from the Cd^{115} measurements.

The measurements at 48 Mev on I^{134} and Cs^{136} both lead to neutron-to-proton ratios of about 1.57. The fissioning nucleus of the same ratio would be U^{236}, which agrees well with the observed mass sum of 234 (Fig. 1) for the fission ascribed mainly to the 14-Mev resonance absorption. The higher independent yield of Cs^{136} for 48-Mev x-rays on U^{238} relative to thermal-neutron fission of U^{235}, where the fissioning nucleus in both cases is thought to be U^{236}, in this analysis is ascribed to a difference in the splitting of the nucleus. At higher energies, a constant neutron-to-proton ratio fission process results in a higher independent yield for Cs^{136}.

The upper limits to the independent yields of Ag^{112} at 48, 100, and 300 Mev are not inconsistent with values calculated from the neutron-to-proton ratios of 1.57 and 1.49 for the energy intervals 5 to 48 Mev, and 100 to 300 Mev, respectively. The normalized fission yield of Te^{132} decreases from 5.2 percent with 21-Mev x-rays to 4.0 percent with 300-Mev x-rays, whereas the yield of I^{131} for this energy interval is constant at 4.3 percent. This may be interpreted on the basis that I^{132} is being formed independently in increasing yield. The fractional yield of I^{132} found in the 100- to 300-Mev interval agrees well with that expected.

It is thus seen that there are increased yields of products closer to stability in the fission of U^{238} with x-rays of 48 Mev or greater. For 48-Mev x-rays, the increased yields can be explained by an unchanged neutron-to-proton ratio in the fission process. For 100–300 Mev x-rays, there is evidence for the emission of about 9 neutrons in the fission act.

ACKNOWLEDGMENTS

We wish to acknowledge the assistance of Mr. B. C. Cook and the Betatron Group, Mr. M. Fielding and the staff of the 37-inch cyclotron of the University of Chicago, and the personnel of the Argonne National Laboratory responsible for the thermal-neutron irradiations. The irradiations at the 22-Mev and the 340-Mev betatrons of the University of Illinois were accomplished through the generous cooperation of Professor D. W. Kerst, Mr. T. J. Keegan, Mr. T. B. Elfe, and the Betatron Groups.

[40] W. F. Biller, University of California Radiation Laboratory Report UCRL-2067, 1953 (unpublished).

Nuclear Radii from Inelastic Cross-Section Measurements*

G. P. MILLBURN, W. BIRNBAUM,† W. E. CRANDALL,† AND L. SCHECTER†
Radiation Laboratory, Department of Physics, University of California, Berkeley, California
(Received April 9, 1954)

Inelastic cross sections for high-energy protons, deuterons, He^3 particles, and alpha particles accelerated in the 184-inch cyclotron were measured by an attenuation technique. All the cross sections vary as the square of the nuclear radius and indicate that if the nucleus has a fringe it increases as $A^{\frac{1}{3}}$. The derived value of the nuclear radius constant a_0 depends on the nuclear model and the particular bombarding particle. The effect of the nucleus is found to extend at least to a radius given by $a_0=(1.68\pm0.04)\times10^{-13}$ cm. Deuteron stripping cross sections were derived and found to vary approximately as the square root of the mass number.

I. INTRODUCTION

THE total inelastic cross sections of high-energy charged particles for several elements have been determined by an attenuation technique. Much of the emphasis in this report has been concentrated on the behavior of 190-Mev deuterons while traversing an absorbing medium, but the experimental technique has been extended to include the attenuation of 340-Mev protons, 490-Mev He^3 particles, and 380-Mev alpha particles. The latter cross sections have been determined with somewhat less precision because of the limitations of the experimental method and the consequent uncertainties in the interpretation of the data.

These attenuation cross sections are fundamental in the general understanding of nuclear processes. A comparison of the respective inelastic cross sections gives further information regarding the structure of the nucleus and the effects of nuclear transparency.[1] Furthermore, from the deuteron data, stripping cross sections[2] can be determined for the different elements serving as attenuators.

A summary of the high-energy neutron inelastic cross sections,[3–6] as well as the proton attenuation cross sections of Kirschbaum and Hicks,[7] and Chen *et al.*,[8] are presented together with the results of this experiment.

II. THEORY OF THE EXPERIMENTAL METHOD

A. Definition of Symbols

The following symbols will be used throughout the paper:

σ_{1p} = an effective attenuation cross section for protons.
σ_2 = the total inelastic or attenuation cross section for deuterons.
σ_3 = the total inelastic cross section for He^3 particles.
σ_4 = the total inelastic cross section for He^4 (alpha) particles.
σ_{2sp} = the cross section for the production of stripped protons from incident deuterons ($\sigma_{2sp}=\sigma_2-\sigma_{1p}$).
σ_{3sp} = the cross section for the production of one stripped proton from an incident He^3 particle [$\sigma_{3sp}=2(\sigma_3-\sigma_{1p})$].
R_1 = range of protons.
R_2 = range of deuterons.
R_{3He} = range of He^3.
R_4 = range of alpha particles.
r = nuclear radius, assumed to be given by $r=a_0A^{\frac{1}{3}}$.
t = absorber thickness.

B. Definition of an Inelastic Event

The definition of an inelastic event in this experiment is based upon range measurements. A particle is said to have suffered an inelastic collision if its range in the absorbing medium is shortened by a measurable amount. For the energies involved, the range-energy relation is approximately $R=\text{const}T^{1.8}$.[9] Therefore, the relative energy loss is given by $(\Delta T/T)=(1/1.8)\times(\Delta R/R)$. For 190-Mev deuterons, a change of range of 4 percent is easily detected: a deuteron event is considered inelastic only if the energy loss is 4 Mev or greater. In any case, because of its low binding energy, any inelastic collision will probably cause the deuteron to split up into its component nucleons. For 340-Mev protons, 490-Mev He^3 particles, and 380-Mev alpha particles, inelastic events are defined as those in which energy losses occur which are greater than 15 Mev.

C. Deuterons

The deuteron beam current I_0 enters the absorber, is attenuated, and leaves with a reduced value, I. The following assumptions are made in the interpretation of the deuteron attenuation data:

* This work was performed under the auspices of the U. S. Atomic Energy Commission.
† California Research and Development Company, Livermore, California.
[1] Fernbach, Serber, and Taylor, Phys. Rev. **75**, 1352 (1949).
[2] R. Serber, Phys. Rev. **72**, 1008 (1947).
[3] J. DeJuren and N. Knable, Phys. Rev. **77**, 606 (1950).
[4] J. DeJuren, Phys. Rev. **80**, 27 (1950).
[5] W. P. Ball, thesis, University of California Report UCRL-1938 (unpublished).
[6] Bratenahl, Fernbach, Hildebrand, Leith, Moyer, de Juren, and Knable, Phys. Rev. **77**, 597 (1950).
[7] A. J. Kirschbaum, thesis, University of California Report UCRL-1967 (unpublished).
[8] F. F. Chen (private communication).
[9] Aron, Hoffman, and Williams, Atomic Energy Commission Report AECU-663 (unpublished).

1. All cross sections are assumed to be independent of energy in the region between 20 and 200 Mev.

2. The charged secondary particles are protons produced by the stripping of the deuterons.

3. The number of secondary charged particles other than stripped protons is negligible for the high-Z elements.

The current I for a high-Z element is given by

$$I=I_0e^{-\sigma_2 t}+\int_{t-\tau_1}^{t} I_0e^{-\sigma_2 x}\sigma_{2sp}e^{-\sigma_{1p}(t-x)}dx, \qquad (1)$$

where t = the thickness of the attenuator, x = the distance traveled by a deuteron in the attenuator before suffering an inelastic collision, and $t-\tau_1$ = the maximum depth in the attenuator from which secondary protons can escape. The most probable value of the kinetic energy $\langle T_p\rangle$ of the stripped proton is obtained by assuming that the proton has half the energy of the deuteron at the instant of stripping, plus the electrostatic energy gained by the proton due to the Coulomb barrier, minus half the binding energy ϵ_d of the deuteron

$$\langle T_p\rangle=\frac{1}{2}\left(T_d-\frac{Ze^2}{r'}\right)+\frac{Ze^2}{r'}-\frac{\epsilon_d}{2}=\frac{1}{2}\left(T_d+\frac{Ze^2}{r'}-\epsilon_d\right), \qquad (2)$$

where r' is the distance between the center of the target nucleus and the incident particle; $\tau_1=t$ for $t<R_1(\langle T_p\rangle)$; and $\tau_1=R_2(T_d)-t$ for $t>R_1(\langle T_p\rangle)$, where $R_1(\langle T_p\rangle)$ and $R_2(T_d)$ are the mean ranges of the proton and deuteron of energies $\langle T_p\rangle$ and T_d, respectively, in the absorber.

Integrating Eq. (1) yields

$$I=I_0e^{-\sigma_2 t}\left[1+\frac{\sigma_{2sp}}{\sigma_1-\sigma_2}(1-e^{-(\sigma_1-\sigma_2)\tau_1})\right]. \qquad (3)$$

If one defines Δ_d as the number of deuterons affected per unit thickness of absorber by inelastic collisions of the incident number of deuterons N_d, one may write $\Delta_d=\sigma_2N_d$. Since each deuteron contains one proton, the number of affected protons is $\Delta_p=\sigma_2N_d=\sigma_2N_p$. The number of protons Δ_p' being attenuated is $\Delta_p'=\sigma_{1p}N_p=\sigma_{1p}N_d$, if it is assumed that the coupled proton acts as a free particle because of its weak binding. Therefore the total number of stripped protons Δ_{2sp} leaving the absorber becomes

$$\Delta_{2sp}=(\Delta_p-\Delta_p')=\sigma_{2sp}N_d. \qquad (4)$$

Solving for an effective stripping cross section, one obtains

$$\sigma_{2sp}=\sigma_2-\sigma_{1p}. \qquad (5)$$

Substituting in Eq. (3), we have

$$I=I_0\exp(-\sigma_2 t+\sigma_{2sp}\tau_1).$$

Therefore,

$$I=I_0e^{-\sigma_1 t} \quad \text{for} \quad t<R_1(\langle T_p\rangle), \qquad (6a)$$

and

$$I=I_0\exp-(\sigma_2+\sigma_{2sp})t+\sigma_{2sp}R_2(T_d)$$
$$=I_0'\exp-(\sigma_2+\sigma_{2sp})t \quad \text{for} \quad t>R_1(\langle T_p\rangle). \qquad (6b)$$

Thus, for high-Z elements, if the above assumptions are correct, a semilogarithmic plot of I/I_0 *vs* t should give an integral range curve composed of two straight-line segments with the change in slope at $t=R_1(\langle T_p\rangle)$.[10]

For the lower-Z elements, assumption (3) no longer holds. Consequently, interpretation of the integral range curves becomes difficult because of the large number of secondary knock-on charged particles. In order to minimize this effect, the following technique was employed (see Fig. 1). The integral range curve for uranium was first obtained. The uranium was then replaced by another element Z_i whose fixed thickness t_i (usually about half a range) reduced the incident beam energy from T_0 to T. Increments of uranium absorbers were then added between the absorber Z_i and the detector to obtain a series of integral range curves for different Z_i+U combinations. Many of the secondaries produced in the so-called primary absorber were then effectively prevented from being detected by the presence of the secondary uranium attenuator. For absorber thicknesses approximately $\frac{3}{4}$ the range of the incident deuteron no protons stripped in the absorber Z_i would be detected.

The number of deuterons leaving absorber Z_i is $I_i'=I_0e^{-\sigma_i t_i}$, and the number leaving the uranium is $I_i=I_0\exp(-\sigma_i t_i-\sigma_U t_U)$, where t_i and t_U are the respective thicknesses of the primary Z_i and secondary U attenuators, and σ_i is the total deuteron attenuation cross section for the ith element. A comparison of the value of the relative current I_i/I_0 at the end of the integral range curve of the Z_i+U combination with that of the total uranium relative current I_U/I_0 allows one to determine σ_i in terms of σ_U. For a complete range thickness R_U of uranium (aside from the usual range straggling), the number of deuterons left unattenuated is $I_U=I_0\exp(-\sigma_U R_U)$. Therefore at the ends

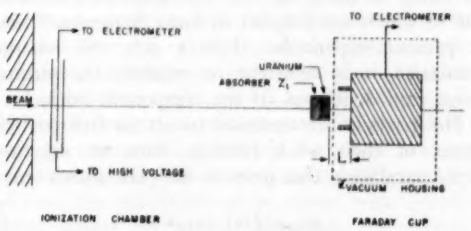

FIG. 1. Schematic diagram of experimental arrangement.

[10] An experiment by W. J. Knox at this laboratory first showed the tendency for the deuteron attenuation curve to fall on two straight lines with a break at the point $t=0.5R_2$. Only limits on the cross sections were determined because of the preliminary nature of his work.

of the ranges of the two curves, one can write the ratio,

$$\frac{I_i/I_0}{I_U/I_U}=\frac{\exp(-\sigma_i t_i)}{\exp\{-\sigma_U(R_U-T_U)\}}. \tag{7}$$

In the above equation, t_i and t_U are known experimental parameters, and I_i/I_0, I_U/I_0, and R_U are directly observable; therefore, one can easily solve for σ_i as a function of σ_U.

D. Protons

There appears to be no simple mechanism by which one can describe the production of secondary charged particles when high-energy protons traverse an absorber. The presence of such secondaries and/or a variation in the inelastic cross section with energy will introduce curvature into the integral range curves. Unlike the case for deuterons, there seems to be no basis one can use to test which of these two effects predominates. Thus the inelastic proton cross sections calculated from the integral range curves are subject to greater uncertainties than the deuteron cross sections.

The main purpose in measuring the proton inelastic cross sections was to test the agreement between the present method and that of Kirschbaum and Hicks.[7] To do this it is sufficient to measure an average cross section by assuming that a negligible number of secondary charged particles leaves the absorber for thicknesses nearly the range of the protons. Then the ratio I/I_0 for $t=R_1$ is given by

$$I/I_0=e^{-\sigma_1 R_1}, \tag{8}$$

which permits the calculation of σ_1, an average inelastic cross section.

The cross sections for various elements may be measured just as for deuterons, with Z_i+U absorbers, since there are essentially no secondary charged particles for $t_i+T_U\sim R_1$.

E. He^3 Particles

When a He^3 particle suffers an inelastic collision it is very likely to break up into its component nucleons, some of which are coupled to form deuterons.[11] Since the present experiment detects only the charged secondaries, it is sufficient to consider the stripped protons and deuterons. If the component nucleons of the He^3 particle are assumed to act as free particles because of their weak binding, then an argument exactly paralleling that given in Sec. IIC shows that

$$\sigma_{3sp}=2(\sigma_3-\sigma_{1p}), \tag{9}$$

where σ_{3sp} is the cross section for producing one stripped proton and σ_3 is the inelastic cross section for He^3 particles. The factor of 2 arises from the fact that the He^3 nucleus contains 2 protons. The most probable values of the kinetic energies of the stripped particles, neglecting small binding energy effects, may be expressed as

$$\langle T_p\rangle=\tfrac{1}{3}T_{He^3}+\tfrac{1}{3}Ze^2/r', \tag{10a}$$

$$\langle T_d\rangle=\tfrac{2}{3}T_{He^3}-\tfrac{1}{3}Ze^2/r'. \tag{10b}$$

If it is assumed that all secondary particles are produced with these energies, and the Coulomb energies are neglected, then the stripped protons produced will have a range 4/3 the residual range of the He^3 particles, whereas the stripped deuterons will have a range 8/3 the residual range of the He^3 particle. These secondary particles can be easily accounted for in calculating the inelastic cross sections from the integral range curves.

An analytic expression for the current as a function of absorber thickness ($0<t<8/3R_{2He^3}$) can be derived by using the techniques and results of Sec. IIC.[12]

F. Alpha Particles

Since the alpha particle is much more tightly bound than either the deuteron or the He^3 particle, an application of the previous method of calculating the current as a function of absorber thickness is not likely to prove fruitful.

If protons are "stripped" from an alpha particle during an inelastic collision, their residual range should be equal to the residual range of the alpha particle; because of the expected energy distribution of such stripped protons, their presence should tend to broaden the end of the integral range curve.

In spite of these difficulties the average inelastic cross section σ_4 may be determined from the discontinuity in beam current at the end of the alpha-particle range.

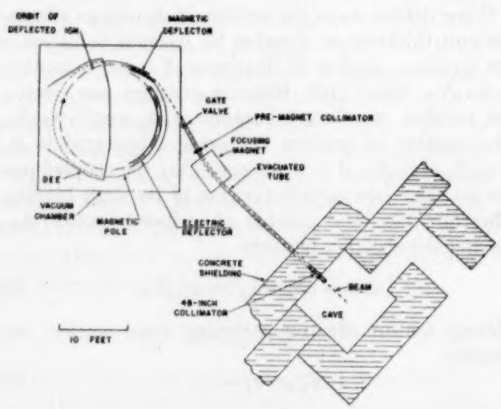

FIG. 2. Schematic diagram of the cyclotron, deflected beam path, and shielded enclosure.

[11] J. Ise *et al.*, University of California Report UCRL-2319 2nd Rev., Rev. Sci. Instr. **25**, 437 (1954).

[12] W. Birnbaum *et al.*, California Research and Development Company Report LRL-85 (unpublished) gives a more detailed report of this experiment.

III. EXPERIMENTAL METHOD

A. Procedure

The high-energy charged particles were electrically and magnetically deflected out of their circular orbits in the 184-inch cyclotron, and passed through a pre-magnet collimator, a focusing magnet, and a 48-inch collimator into the external experimental area. A plan view is shown in Fig. 2. The particles in the various deflected beams are essentially monoenergetic with probable energy spreads about their respective means of less than 1 percent.

The beams were monitored externally by a parallel-plate ionization chamber filled with helium to a pressure of 75 cm. For the beam levels employed in the present study, the chamber showed negligible recombination effects over a wide region of collection voltages (500–2500 volts). Figure 1 is a schematic diagram of the experimental apparatus. After passing through the monitor, the beam impinged upon the attenuating material. That portion of the beam which traversed the absorber was collected in a Faraday cup. The operating characteristics of the cup and the details of its behavior have been discussed previously by Aamodt *et al.*[13]

The charges collected by the monitor and the Faraday cup were placed on low leakage condensers connected to the inputs of integrating electrometers. The electrometer was of the 100 percent inverse feedback type; the electrometer signal was measured and recorded on a Leeds and Northrup Speedomax which automatically calibrated itself against a standard cell at frequent intervals. Since only the ratios of voltages entered into the final calculations, absolute calibration of the electrometers with their associated condensers and recorders was unnecessary. The procedure followed in the experiment was then to measure the ratio of the charges I and I_0 collected by the Faraday cup and ionization chamber, respectively, as a function of absorber thickness.

B. Scattering Corrections

For thick absorbers, the elastic scattering of the emergent unattenuated particles may be large enough to cause a decrease in the charge collected by the cup. This tends to give an apparent value for the inelastic cross section which is too high. To correct for this effect for incident deuterons and protons, the distance L (see Fig. 1) between the absorber and the Faraday cup was varied. This allowed an extrapolation of the ratio I/I_0 to the point where $L=0$. The corrections due to multiple Coulomb scattering were determined analytically by a graphical integration method.[14] Figure 3 shows the excellent agreement between the experimental points and the analytical curves for deuterons incident on two typical absorber thicknesses (carbon plus uranium, and uranium alone). It is to be noted that the scattering corrections are essentially negligible because of the large diameter of the Faraday cup. These small corrections as calculated by the graphical method were applied for absorber thicknesses up to 98 percent of the full range of the incident particle. Beyond that point, the magnitude of the scattering correction increases quite rapidly, introducing large uncertainties in its determination; the corrections were applied for $t/R>0.98$ by extrapolation, but this was done only to determine the mean range. (The cross section is insensitive to the precise location of the mean range point.) As will be discussed below, exact interpretation of the experimental points beyond 95 percent of the range was not attempted.

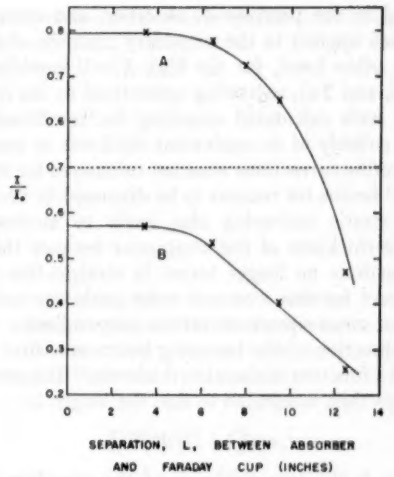

FIG. 3. Observed and calculated multiple scattering effect for 190-Mev deuterons. A. 28.0 g/cm² uranium ($t/R_2=0.88$). B. 6.526 g/cm² plus 17.20 g/cm² uranium ($t_U/R_{2U}'=0.96$). Crosses are the observed points.

For the low-Z elements, the agreement between the experimental points and the calculated scattering curve was not satisfactory. For 190-Mev deuterons incident on carbon, an attenuator 0.95 of a range thick showed a current loss of 10 percent when the separation L was increased from 3.5 to 12.5 in. A calculation predicted no drop in I/I_0 due to multiple scattering. The observed effect is believed to be caused by the relatively large number of charged secondary particles present in the beam of attenuated deuterons for low-Z absorbers. Since the experimental curve showed such a gentle fall, and since the calculated curves agreed with the experimental points for high-Z absorbers, the calculated corrections are used for the low-Z absorbers instead of attempting to determine an empirical correction. The calculated corrections to I/I_0 for beryllium and carbon were all zero for $t/R<0.98$.

For the Z_i+U combinations, where $Z_i \leq 29$, it was assumed that a negligible amount of Coulomb scattering

[13] R. L. Aamodt *et al.*, University of California Report UCRL-1400 (unpublished).

[14] W. C. Dickinson and D. C. Dodder, Los Alamos Report LA-1182 (unpublished).

occurred in the primary Z_i absorber, and corrections were then applied to the secondary uranium absorber. On the other hand, for the high Z_i+U combinations (Pb, Bi, and Ta), scattering corrections to the relative current were calculated assuming the combination to consist entirely of its equivalent thickness in uranium.

Scattering corrections were not calculated for the He^3 and He^4 beams for reasons to be discussed in Sec. IV.

The elastic scattering also tends to increase the effective thickness of the attenuator because the incident particles no longer travel in straight-line paths. To correct for this a second order path was assumed. The root-mean-square deviations perpendicular to the initial direction of the incoming beam were first calculated as a function of absorber thickness.[15] The parabolic path was then integrated to find the length t_e:

$$t_e = t_0[1+(2/9)\langle\theta^2\rangle],$$

where t_0 is the true thickness of the absorber, and t_e may be considered the effective thickness traversed by the incident particle; $\langle\theta^2\rangle$ is the mean square scattering angle for the thickness t_0. Since the corrections were small, the choice of the path was unimportant.

The number of very large-angle single-scattering events are considered to be negligible as is borne out by the excellent agreement between the experimental points and the multiple Coulomb scattering theory. This is especially true for the case of the deuteron where the associated small impact parameters required for large-angle scattering would probably cause the deuteron to break up into its component nucleons.

C. Range Straggling and Collimation

The shape of the integral range curve near its end is influenced by at least six effects: (1) range straggling, (2) small energy-transfer inelastic events, (3) scattering in the collimator, (4) energy distribution of the incident beam, (5) variation of cross section with energy, and (6) multiple scattering. The last has been discussed in the previous section. The result of these effects is to introduce a rounding off of the end of the curve. The variation of cross section with energy cannot be treated

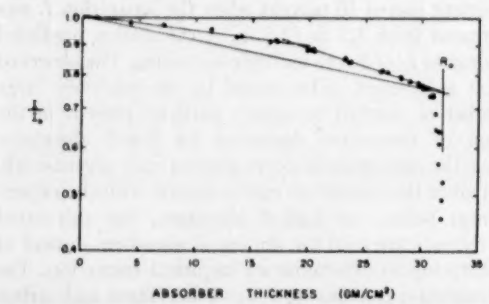

FIG. 4. Integral range curve for 190-Mev deuterons incident on uranium. The straight lines were fitted by least squares.

[15] B. Rossi and K. Greisen, Revs. Modern Phys. 13, 240 (1941).

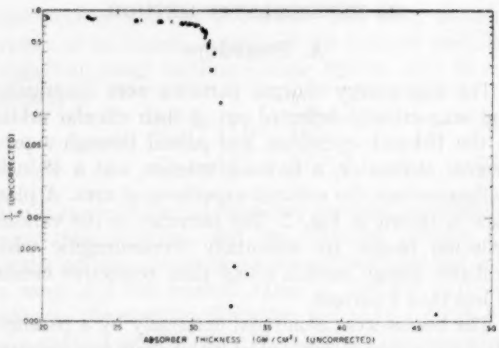

FIG. 5. Integral range curve for 190-Mev deuterons incident on uranium. Results of three runs are shown.

in this experiment and is felt to be a minor consideration in the energy regions with which we are concerned.

The mean range is taken as the point where energy losses due to ionization alone would reduce the current of particles to half its initial value; nuclear attenuation, etc., must be taken into account when the true current is measured. The mean range so defined is the center of an essentially Gaussian distribution whose width is a measure of the range straggling. Thus such straggling should result in rounding off the integral range curve. For 190-Mev deuterons and 340-Mev protons the half-width at half-maximum of the straggling curve is about 1 percent of the range.[16] The range straggling has been neglected in all the integral range curves, since points within 2 percent of the end of the range were not used.

If a particle undergoes an inelastic nuclear event in which it loses a very small amount of energy, then its final range will be only slightly shorter than its original range. Such particles would then stop near the end of the integral range curve and cause a rounding superimposed on the other effects, mainly range straggling and multiple scattering. After corrections for multiple scattering have been applied, the extent to which range straggling can be detected imposes a limit on the energy loss a particle must suffer to be counted as having had an inelastic event. Thus range straggling is the basis for the definitions of inelastic events for this experiment as given in Sec. II.

Scattering of the beam by the 48-inch collimator was reduced by adjusting the premagnet collimators; the energy selection of the focusing magnet prevented deuterons with degraded energies from passing through the 48-inch collimator. Under these conditions points were reproduced for different runs to within one percent for $t/R<0.95$.

Only points for $t/R<0.95$ were used in the final calculations. This procedure was followed as a precaution against uncertainties in I/I_0 near the end of the range.

[16] E. Segrè, *Experimental Nuclear Physics* (John Wiley and Sons, Inc., New York, 1953), Vol. 1.

The points for $0.95<t/R<0.98$ showed a tendency to fall below the straight line through the other points, but the discrepancies were not significant and were less than 4 percent for all cases.

IV. ANALYSIS OF DATA

A. Deuterons

1. Uranium

The experimental attenuation curves obtained for 190-Mev deuterons incident upon uranium (Fig. 4) show the characteristics discussed in Sec. IIC. Two straight lines were fitted by the method of least squares to the experimental points for $0<t<15$ g/cm^2 and $20<t<30$ g/cm^2, respectively, and extended until they intersected. The point of intersection at $t=0.57R_2$ ($t=18.2\pm0.7$ g/cm^2, $R_2(T_d)=31.8$ g/cm^2) allows one to calculate $T_{p\,\max}=103\pm2$ Mev. Substitution in Eq. (2) yields a value for the Coulomb barrier for uranium of 18 ± 4 Mev. If stripping is assumed to occur only at the edge of the nucleus, and if the charge is concentrated at the center, then the radius of the uranium nucleus is 7.3×10^{-13} cm, and $a_0=(1.2\pm0.3)\times10^{-13}$ cm. If, instead, stripping is assumed to occur throughout the volume, then the radius is 11×10^{-13} cm, and $a_0=(1.8\pm0.4)\times10^{-13}$ cm.

The straight-line fit applied to the latter half of the range is then extended to the end of the range. The inelastic deuteron cross section for an average deuteron energy of 120 Mev is determined from the slope of the straight line drawn from $t=0$ to $t=R_2$. These two points were chosen, since at $t=0$ no secondary particles have yet been produced, while at $t\geqq R_2$ the number of secondaries present is negligible as shown by Fig. 5. This gives a value for σ_2 of 3.81 ± 0.06 barns. The errors quoted above are statistical standard errors.

TABLE I. Inelastic cross sections for high-energy particles.

A. Neutrons

	84 Mev[a] (upper limits)	95 Mev[b] (lower limits)	270 Mev[c] (lower limits)	300 Mev[d]
Carbon	···	0.222 ±0.009	0.145 ±0.006	0.203 ±0.033
Aluminum	0.50 ±0.05	0.418 ±0.017	···	0.390 ±0.023
Copper	0.91 ±0.05	0.782 ±0.013	0.573 ±0.024	0.755 ±0.033
Lead	1.85 ±0.18	1.75 ±0.05	1.42 ±0.06	1.72 ±0.08

B. Protons (10 percent errors)

	305 Mev[e]	240 Mev[e]	185 Mev[e]	290 Mev	870 Mev[f]
Beryllium	0.151	0.169	0.172	···	0.171
Carbon	0.187	0.202	0.204	0.199	0.222
Aluminum	0.334	0.383	0.408	0.416	0.394
Copper	0.608	0.667	0.746	0.717	0.708
Lead	1.48	1.57	1.55	···	1.62
Uranium	1.60	1.77	1.90	1.85 2.03 (230 Mev)	

C. Deuterons, He^3, and alpha particles

	160-Mev H^3	315-Mev He^3	240-Mev He^4
Beryllium	0.512 ±0.025	···	···
Carbon	0.667 ±0.033	0.59 ±0.10	0.64 ±0.10
Aluminum	0.996 ±0.050	0.91 ±0.15	···
Copper	1.76 ±0.17	1.8 ±0.3	1.8 ±0.3
Tantalum	3.13 ±0.30	3.5 ±0.5	3.6 ±0.5
Lead	3.44 ±0.17	···	···
Bismuth	3.55 ±0.18	···	···
Uranium	3.81 ±0.15	4.4 ±0.7	···

[a] See reference 6.
[b] See reference 3.
[c] See reference 4.
[d] See reference 5.
[e] See reference 7.
[f] See reference 8.

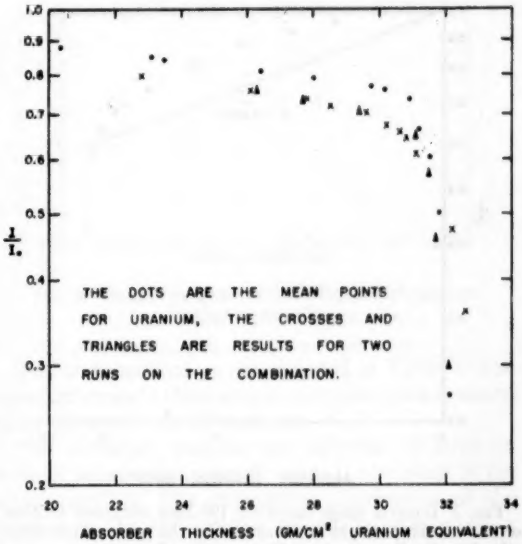

FIG. 6. Apparent attenuation of 190-Mev deuterons incident on carbon backed by uranium compared with the integral range curve for uranium.

The measurement of σ_1 for protons in uranium from the slope of the first part of the integral range curve [Eq. (6a)] is consistent with the proton attenuation work described below, and with the independent experiment of Kirschbaum and Hicks.[7] The slope $\sigma_1-2\sigma_2$ of the other straight-line segment [Eqs. (6b), (5)] gives another measurement of the deuteron inelastic cross section: $\sigma_2=3.95\pm0.12$ barns. The excellent agreement obtained from these different measurements of σ_2 and σ_1 indicates that the number of charged secondary particles other than stripped protons must be quite low.

2. U+Z_i Combinations

The C+U integral range curve is compared directly with the uranium curve in Fig. 6. The relative current $(I/I_0)_{C+U}$ has been plotted as a function of the absorber thickness in g/cm^2 uranium equivalent. The conversion to equivalent uranium thickness was made from the range R_2 in uranium and the range R_2' in Z_i+U. As above, a straight line is fitted to the latter half of the experimental data up to $0.95R_2$ and then extrapolated to the mean range point. Table I gives the inelastic cross sections for all the absorbers used. The standard errors shown in Table I for the deuteron cross sections are not statistical errors, but have been increased to take account of possible systematic effects by doubling the statistical error for the uranium cross section.

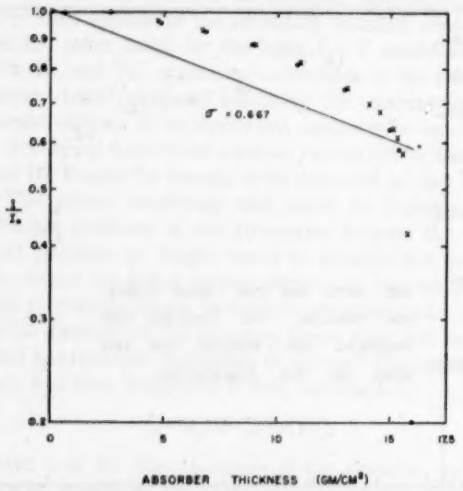

FIG. 7. Integral range curve for 190-Mev deuterons incident on carbon. The straight line is drawn for the cross section determined by C+U attenuation. Two runs are shown.

3. Carbon

The curve for C is presented in Fig. 7. As discussed in Sec. IIC, the presence of a large number of charged secondaries causes this integral range curve to show a continuously changing slope. Hence, the theory which is applicable for uranium is no longer suitable. Only rough estimates of σ_2 can be made from this curve since the location of the mean range points is uncertain. The slope of the straight line superimposed on the experimental data represents the inelastic cross section calculated from the U+Z_i combination method. The straight line is not inconsistent with the experimental points, and illustrates the effectiveness of the combination method in reducing uncertainties arising from the secondaries.

B. Protons

The inelastic cross sections for high energy protons were determined essentially as in Part A. The integral range curve for uranium, Fig. 8, shows a smoothly varying slope and there appears to be no simple theory to explain the shape. Instead, the shape was assumed to result from a combination of the variation of the cross section with energy and the detection of secondary particles. Since there should be essentially no secondary particles for $t \geqq R_1$, the average cross section was determined by a straight line joining $\log(I/I_0)$ at $t=0$ and $t=R_2$. The mean energy was 230 Mev for this case.

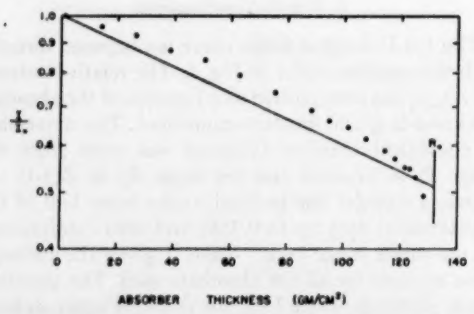

FIG. 8. Integral range curve for 340-Mev protons incident on uranium. The straight line is drawn for the cross section determined by extending the end of the curve to R_0 (mean range point). Corrections for multiple scattering were applied.

The attenuation cross section for protons in carbon, aluminum and copper were determined by Z_i+U combinations as in Part A for deuterons. A typical attenuation curve for carbon plus uranium is shown in Fig. 9. The mean energy of protons in the Z_i primary attenuator was 290 Mev, so the inelastic cross section for uranium had to be extrapolated to 290 Mev. This was done by using the curve drawn through plots of $\log\sigma_1$ *vs* energy shown in Fig. 10.

The proton inelastic cross sections determined in this experiment are listed with those determined by Kirschbaum and Hicks[7] in Table I. The present values tend to be systematically higher; since the effect of secondary particles in the attenuated proton beam would be to decrease the measured cross section, a possible explanation is in the difference between the definition of inelastic events in the two experiments. Kirschbaum and Hicks call an event inelastic if the proton loses 10 percent of its incident energy (34 Mev), whereas it is believed that this experiment measures an event as inelastic if the energy loss is 15 Mev. The systematic difference between the two sets of measurements may be a measure of the number of inelastic events in which the proton loses between 34 and 15 Mev of energy. The present measurements may be low if there are many inelastic events with energy loss between 0 and 15 Mev.

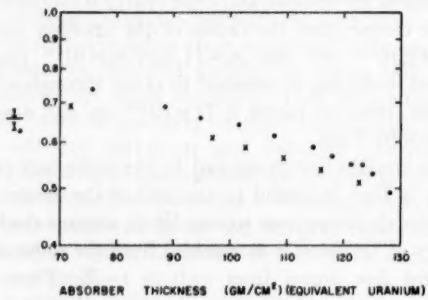

FIG. 9. Apparent attenuation of 340-Mev protons incident on carbon backed by uranium compared with the integral range curve for uranium. The dots are for uranium, the crosses for carbon backed by uranium.

C. He^3 Particles

The secondary particles formed when an incident He^3 particle breaks up have residual ranges greater than the residual range of the He^3 particle (Sec. IIE). Thus

to determine the inelastic cross sections σ_3, the integral range curve must be measured for each element individually instead of using the Z_i+U combination technique. A typical integral range curve is shown in Fig. 11.

Although the experimental points do not allow sharp differentiation between the secondary protons and deuterons, it appears qualitatively from the residual range analysis that a significant fraction of the secondaries are deuterons.

The cross section is determined by subtracting I/I_0 for $t=R_{3\mathrm{He}}+\delta$ from I/I_0 for $t=R_{3\mathrm{He}}-\delta$ (δ is a small increment of absorber around the mean range point)

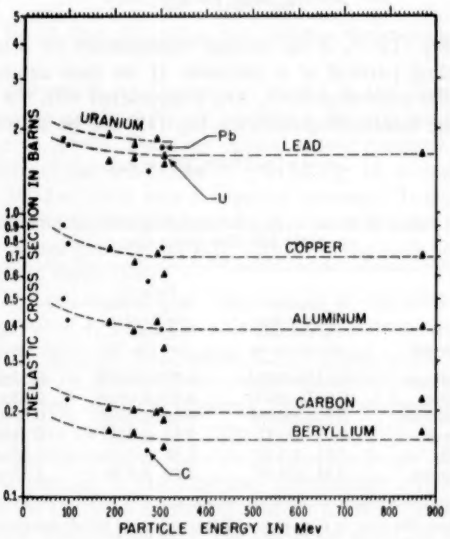

FIG. 10. Inelastic cross sections for high energy protons (triangles) and neutrons (dots) plotted as a function of the energy. The lines were drawn to give smoothed values; the slope of the line for uranium was drawn equal to that for lead; the slopes of the lines for carbon and beryllium, equal to that for aluminum. References for the points are given in Table I.

and assuming the cross section to be independent of the energy. The cross sections σ_3 are listed in Table I. No scattering corrections were made since the subtraction removes their effect. The effect of multiple scattering on the range is much smaller than the uncertainty in the location of the mean range point, and hence can be neglected.

It is assumed that a 15 percent standard error is a conservative estimate of the uncertainties in the measured cross sections for all elements.

D. Alpha Particles

To measure the inelastic cross section σ_4 for alpha particles, the same technique was used as for He^3 particles. The number of secondary particles is much lower as shown in a typical integral range curve, Fig. 12.

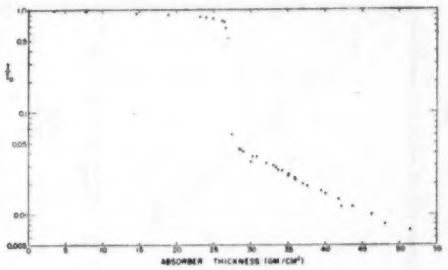

FIG. 11. Integral range curve for 490-Mev He^3 particles incident on tantalum.

The cross sections σ_4 are included in Table I. The standard errors in these cross sections are again assumed to be 15 percent for all elements.

The secondary protons are expected to have an average range approximately equal to the range of the alpha particles. The momentum distribution of the protons in the He^4 nucleus should be reflected in a broad distribution of the proton ranges. The absence of secondary protons is shown by the sharp fall-off of the integral range curves at $t=R_4$ and the low current for $t>R_4$. If such protons were present, the cross sections measured would be too low.

V. INTERPRETATION OF THE DATA

A. Deuteron Stripping Cross Sections

As shown in Sec. IIC, the quantity $\sigma_{2p}\approx\sigma_2-\sigma_{1p}$ may be taken as a cross section for stripping a proton from an incident deuteron. σ_{1p} for a proton of half the mean energy of the deuterons should be used, and in this energy region $\sigma_{1p}\approx\sigma_{1n}$ so that the inelastic cross sections for 80-Mev neutrons from Fig. 10 may be used. Table II gives the difference $\sigma_2-\sigma_{1n}$ for elements whose cross sections are known, and these are plotted against the mass number A in Fig. 13. The stripping cross section varies approximately as $A^{\frac{1}{3}}$ in disagreement with the variation expected if the stripping process were a pure edge ($A^{\frac{2}{3}}$) interaction. The effects of

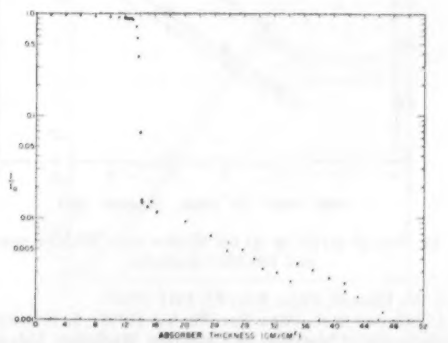

FIG. 12. Integral range curve for 380-Mev alpha particles incident on tantalum.

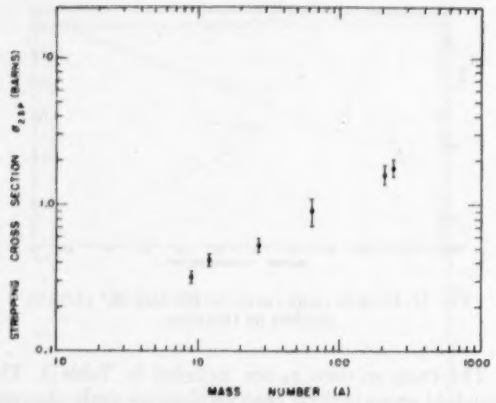

FIG. 13. The cross section for producing a stripped proton from 160-Mev deuterons ($\sigma_2-\sigma_{1p}$) plotted as a function of the mass number A.

electric stripping are less than the standard errors of the cross sections.[17]

These stripping cross sections, inferred from a measurement of the deuteron attenuation, are in reasonable agreement with those inferred from a measurement of the angular distribution of the secondary protons at relatively large angles.[18] The present method avoids the necessity of choosing a specific model for the stripping process.

The relative stripping cross sections measured by W. J. Knox[19] agree with this variation with A.

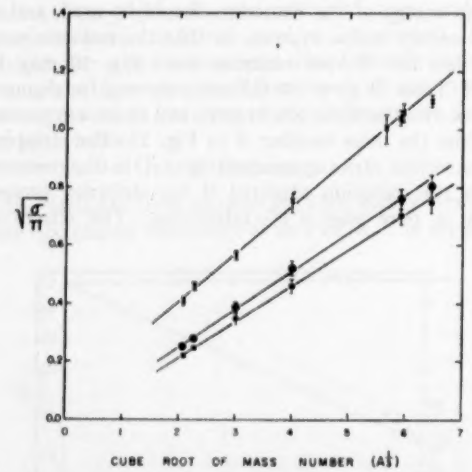

FIG. 14. Plot of $(\sigma/\pi)^{\frac{1}{2}}$ vs $A^{\frac{1}{3}}$ for 80-Mev and 300-Mev neutrons, and 160-Mev deuterons.

[17] S. M. Dancoff, Phys. Rev. **72**, 1017 (1947).
[18] L. Schecter *et al.*, Phys. Rev. **90**, 633 (1953); L. Schecter and W. Heckrotte, University of California Radiation Laboratory Report UCRL-2516 [Phys. Rev. **94**, 1086 (1954)].
[19] W. J. Knox, Phys. Rev. **81**, 687 (1951).

B. Inelastic Cross Sections

Figures 14, 15, and 16 clearly show that the inelastic cross section for a bombarding particle of n nucleons can be written

$$\sigma_n=\pi(a_nA^{\frac{1}{3}}+r_n')^2. \tag{11}$$

The parameters a_n and r_n' were determined by the method of least squares and are listed in Table III. Equation (11) is open to certain interpretations. If one takes $r=a_nA^{\frac{1}{3}}$ as the radius of the nucleus, then r is a function of the bombarding particle. It appears to us that a more satisfying assumption is that r is independent of n, and that $r=a_0A^{\frac{1}{3}}$, where we write

$$a_n=a_0(1-\tau_n)^{\frac{1}{3}}. \tag{12}$$

In Eq. (12) τ_n is the nuclear transparency for a bombarding particle of n nucleons. If we then assume a similar expression for r_n' (r_n is associated with the size of the bombarding particle), Eq. (11) can be written

$$\sigma_n=\pi(a_0A^{\frac{1}{3}}+r_n)^2(1-\tau_n). \tag{13}$$

TABLE II. Cross section for producing stripped protons from 160-Mev deuterons.

Element	Inelastic cross section for 160-Mev deuterons, σ_2	Inelastic cross section for 80-Mev neutrons, σ_1 (see Fig. 10)	σ_{2sp} $(\sigma_2-\sigma_1)$
Beryllium	0.512±0.025	0.185±0.019	0.33±0.03
Carbon	0.667±0.033	0.237±0.024	0.43±0.04
Aluminum	0.996±0.050	0.465±0.047	0.53±0.05
Copper	1.76 ±0.17	0.85 ±0.09	0.91±0.19
Lead	3.44 ±0.17	1.81 ±0.18	1.63±0.25
Uranium	3.81 ±0.15	2.06 ±0.20	1.75±0.25

Note: The error in σ_1 was estimated as 10 percent for all elements.

The behavior exhibited by the inelastic cross sections is of value in determining the structure of the nucleus and its interactions with bombarding particles. We first consider how the optical model of the nucleus proposed by Fernbach, Serber, and Taylor[1] is affected by the present data. In their model they assume $a_0=1.4\times10^{-13}$ cm and a nuclear transparency τ which varies with A; these parameters were chosen to fit the total neutron cross sections. In Fig. 17 two curves calculated from the model with $a_0=1.35\times10^{-13}$ cm, $K=3.0\times10^{12}$ cm^{-1}, and $a_0=1.7\times10^{-13}$ cm, $K=1.0\times10^{12}$ cm^{-1} are shown together with the data from Fig. 10 for 80-Mev neutrons. The agreement with the first curve is satisfactory, since the systematic difference for the lighter elements could be due to a failure of the model. The figure clearly shows that the second curve cannot be considered satisfactory. The curves have a very straight portion for $2<A^{\frac{1}{3}}<6$ which is not changed for wide variations in a_0 or K. The slope of this portion is governed by the choice of a_0 and the position by the choice of K; the lines are insensitive to K for $\infty>K>10^{12}$ cm^{-1}, but begin to curve for

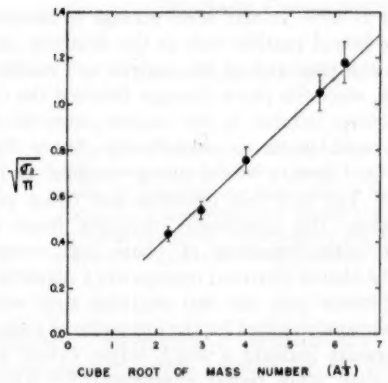

FIG. 15. Plot of $(\sigma_3/\pi)^{\frac{1}{2}}$ *vs* $A^{\frac{1}{3}}$ for 315-Mev He^3 particles.

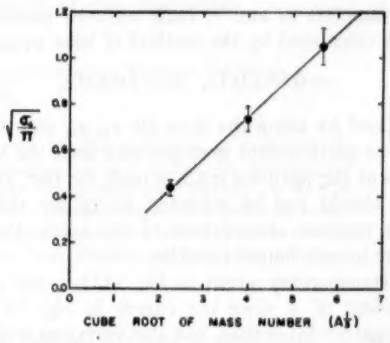

FIG. 16. Plot of $(\sigma_4/\pi)^{\frac{1}{2}}$ *vs* $A^{\frac{1}{3}}$ for 240-Mev alpha particles.

$K<10^{12}$ cm^{-1}. An interesting feature is the negative intercept obtained by extrapolating the straight portions to $A^{\frac{1}{3}}=0$. Thus the optical model produces the important features shown by $\sqrt{\sigma_1}$ in Fig. 14: a straight line for $2<A^{\frac{1}{3}}<6$ with a negative intercept. It should be mentioned that the curve for $K=\infty$, $a_0=1.25\times10^{-13}$ cm (a straight line through zero), fits the data better than the curve shown.

The optical model of Fernbach *et al.* explains the variation of σ_1 with A in a satisfactory manner, but it is clear from the magnitudes of σ_2, σ_3, and σ_4 that the model in its present form cannot be entirely correct. Considering σ_2, it is apparent that the nucleus must extend to a radius of the order of $1.7\times10^{-13}A^{\frac{1}{3}}$ cm, and the magnitudes of σ_3 and σ_4 show that the larger radius is not peculiar to the deuteron. Independent evidence from the Coulomb scattering of alpha particles tends to confirm this conclusion.[20] The curve for $a_0=1.7\times10^{-13}$ cm in Fig. 17 indicates that the nucleus cannot be considered as a sphere of constant density.

Thus a simple square-well potential for a nucleus of constant density does not appear to be capable of explaining the present results in a consistent manner, but the agreement between σ_1 as observed and as calculated from the optical model leads one to believe that a potential not radically different from a square-well might be appropriate. A modified potential with a fringe extending to the outermost radius of the nucleus appears to be a reasonable assumption. The results for σ_2, σ_3, and σ_4 indicate that such a fringe should increase linearly with $A^{\frac{1}{3}}$.

The assumption of constant density over the entire nucleus would probably need modification for such a potential, but the data do not permit determination of the form of the nuclear density distribution.

The nuclear transparency resulting from the optical model was based on a constant-density, spherical nucleus. It is interesting to consider a transparency which is an average over the entire nucleus including the fringe. It is assumed that the nucleus interacts with the individual nucleons in a bombarding particle, and that if τ is the transparency for a single-nucleon particle, then τ^2 is the transparency for a two-nucleon particle, etc. Equation (13) can then be written

$$a_n=\pi(a_0A^{\frac{1}{3}}+r_n)^2(1-\tau^n). \tag{14}$$

TABLE III. Slopes and intercepts for straight-line fits of inelastic cross sections.

Particle	Mean energy (Mev)	Slope $\times10^{13}$ (cm)	Intercept $\times10^{13}$ (cm)
Neutron	80	1.37 ± 0.07	-0.33 ± 0.20
Neutron	300	1.26 ± 0.06	-0.41 ± 0.18
Deuteron	160	1.68 ± 0.04	0.64 ± 0.08
He^3	315	1.92 ± 0.18	-0.12 ± 0.61
Alpha	240	1.84 ± 0.42	0.35 ± 1.1

[20] G. W. Farwell and H. E. Wegner, Phys. Rev. **93**, 356 (1954).

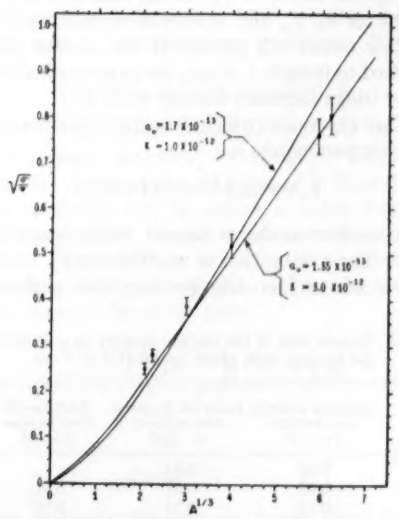

FIG. 17. Calculated (curves) and observed (dots) values of $(\sigma_1/\pi)^{\frac{1}{2}}$ for *vs* $A^{\frac{1}{3}}$ 80-Mev neutrons. K was chosen to fit curves to dots near $A^{\frac{1}{3}}=4$.

The parameters a_0 and τ, both assumed independent of A, as calculated by the method of least squares are

$$\tau=0.55\pm0.12, \quad a_0=2.0\pm0.3, \tag{15}$$

as obtained by using the data for σ_1, σ_2, and σ_3 only. The alpha particle data were not used since the binding energies of the particles reach a peak for He^4, and this system should not be expected to satisfy the independent nucleon assumptions to the same degree as the more loosely bound particles.

The transparency given in Eq. (15) is not strictly independent of A since the curves in Fig. 14 for σ_1 have negative intercepts, but the variation with A is not extreme. Equation (14) can be rewritten

$$(\sigma_n/\pi)^{\frac{1}{2}}=(a_nA^{\frac{1}{3}}+r_n)(1-\tau^n)^{\frac{1}{2}}. \tag{16}$$

The ratio

$$[1-\tau_n(A)]^{\frac{1}{2}}=(\sigma_n/\pi)^{\frac{1}{2}}/a_0A^{\frac{1}{3}}+r_n,$$

with $a_0=2.0\times10^{-13}$ cm, $r_1=0$, $r_2=0.75\times10^{-13}$ cm, $r_3=0$, is given in Table IV for $n=1$, 2, and 3.

The values calculated from $\tau=0.55\pm0.12$ are $(1-\tau)^{\frac{1}{2}}=0.67\pm0.08$, $(1-\tau^2)^{\frac{1}{2}}=0.84\pm0.07$, and $(1-\tau^3)^{\frac{1}{2}}=0.91\pm0.05$. The agreement shows that the assumption $\tau_n=\tau^n$ is not inconsistent with the data.

VI. SUMMARY AND CONCLUSIONS

The inelastic cross section for a particle of n nucleons bombarding a nucleus of mass number A can be accurately represented by the equation

$$\sigma_n=\pi(a_nA^{\frac{1}{3}}+r_n')^2, \tag{11}$$

where a_n and r_n' vary with n.

Although the data for σ_1 are explained satisfactorily by the optical model of Fernbach, Serber, and Taylor,[1] the data for σ_2, σ_3, and σ_4 require nuclear radii larger than their model will permit. If the nuclear potential is modified to include a fringe, the present data indicate that the fringe increases linearly with $A^{\frac{1}{3}}$.

Another expression which describes the cross sections with fewer parameters is

$$\sigma_n=\pi(a_0A^{\frac{1}{3}}+r_n)^2(1-\tau^n), \tag{14}$$

but no nuclear model is known which leads to this relation. The assumption of $\tau_n\neq0$ for $n>1$ introduces the idea of nuclear transparency for multinucleon particles as such. It may seem strange to assume that a loosely bound particle such as the deuteron can pass through the potential of the nucleus and emerge as a deuteron, since the phase changes between the component nucleons induced by the nuclear potential at first thought would seem to preclude the chance that the neutron and proton would emerge coupled to form a deuteron. The fact that deuteron and triton pickup[21] occur when the component nucleons have widely different initial relations of phase and momentum makes the idea of deuteron transparency plausible since in the present case the two nucleons start with the initial relations required for the formation of a deuteron.

Our results indicate a much larger extent for the nucleus than other recent experiments.[22,23] Fitch and Rainwater find $a_0=1.2\times10^{-13}$ cm from experiments with μ mesons and a high energy electron scattering experiment of Hofstadter *et al.* gives approximately $a_0=1.1\times10^{-13}$ cm. These two experiments of course do not measure the same part of the nucleus as our experiment; in particular, they measure the charge distribution and in any case would be insensitive to the nuclear fringe. The argument advanced that neutron scattering experiments measure the outer range of the nucleus is not consistent with our results. It may be that the recent model of the distribution of neutrons and protons in the nucleus proposed by Teller and Johnson[24] will explain the difference between the experiments, or it may be that a suitable choice of the shape of the nuclear potential in itself will be sufficient. As is shown by Heckrotte[25] in the following paper, even the choice of a crude nuclear potential which has the features of a fringe area seems to give better agreement between the different experiments than one would expect.

The stripping cross section derived from the present data varies approximately as $A^{\frac{1}{3}}$, which indicates that an interaction which varies as $A^{\frac{2}{3}}$ probably should be added to Serber's expression.

TABLE IV. Square root of the nuclear opacity as a function of $A^{\frac{1}{3}}$ for nuclear radii given by $2.0A^{\frac{1}{3}}\times10^{-13}$ cm.

$A^{\frac{1}{3}}$	Ratio for neutron cross sections $(1-\tau_1)^{\frac{1}{2}}$	Ratio for deuteron cross sections $(1-\tau_2)^{\frac{1}{2}}$	Ratio for He^3 cross sections $(1-\tau_3)^{\frac{1}{2}}$
2.03	0.60	0.82	...
2.26	0.62	0.87	0.96
3.00	0.64	0.83	0.90
3.99	0.65	0.86	0.95
5.92	0.64	0.82	0.93 ($A^{\frac{1}{3}}=5.65$)
6.20	0.65	0.84	0.95

VII. ACKNOWLEDGMENTS

The authors are happy to acknowledge the encouragement and assistance of Dr. C. M. Van Atta. We are indebted to Dr. Warren Heckrotte for stimulating discussions concerning the interpretation of the data, and to Mr. Donald Hicks, Dr. John Ise, Mr. Robert Main, and Dr. Robert Pyle for assistance in collecting the data and in maintaining the equipment. Finally, thanks are due to Mr. James Vale, members of the cyclotron crew, and the electrometer maintenance group of the University of California Radiation Laboratory.

[21] J. Hadley and H. York, Phys. Rev. **80**, 345 (1950).
[22] V. L. Fitch and J. Rainwater, Phys. Rev. **92**, 789 (1953).
[23] L. I. Schiff, Phys. Rev. **92**, 988 (1953).
[24] M. H. Johnson and E. Teller, Phys. Rev. **93**, 357 (1954).
[25] Warren Heckrotte, University of California Radiation Laboratory Report UCRL-2510, following paper [Phys. Rev. **95**, 1279 (1954)].

Nuclear Cross Sections and the Size of the Nucleus*

WARREN HECKROTTE
Radiation Laboratory, Department of Physics, University of California, Berkeley, California
(Received April 9, 1954)

The recent experiments on the total inelastic cross sections for 190-Mev deuterons on various target nuclei demand a considerably larger nuclear radius than is usually accepted to explain the experimental results. It is shown that this result is not inconsistent with the total nuclear cross sections for 90-Mev neutrons if a nonsquare-well nuclear shape is taken. Taking for numerical simplicity a parabolic shape, the radius (measured to the edge of the distribution) that is obtained is $R=1.6A^{\frac{1}{3}}\times10^{-13}$ cm. The average radius is $R=1.0A^{\frac{1}{3}}\times10^{-13}$ cm. This result is compared with other determinations of the nuclear radius.

THE recent experiment of Millburn *et al.*[1] on the total inelastic cross sections for 190-Mev deuterons on various target nuclei yields the following expression for this cross section as a function of A, the mass number of the target nuclei:

$$\sigma_D=(1.68A^{\frac{1}{3}}+0.64)^2\times10^{-26}\ \text{cm}^2. \tag{1}$$

The principal contribution to this inelastic cross section is from the breakup of the deuteron.

If it is assumed that the interaction of either of the nucleons of the deuteron with the target nucleus always leads to the breakup of the deuteron,[2] then the cross section is given by

$$\sigma_D=\pi R^2+\tfrac{1}{2}\pi R_D R, \tag{2}$$

where R is the nuclear radius and R_D is the mean distance of separation of the particles of the deuteron. The term $\pi R_D R/2$ comes from Serber's calculation of the stripping process.[3] Equation (2) can be written as

$$\sigma_D=\pi(R+\tfrac{1}{4}R_D)^2-\tfrac{1}{16}\pi R_D^2.$$

It is a good approximation to neglect the latter term; thus for the deuteron inelastic cross section one may write

$$\sigma_D=\pi(R+\tfrac{1}{4}R_D)^2. \tag{3}$$

Comparing this with Eq. (1), the nuclear radius and R_D are given by

$$R=1.68A^{\frac{1}{3}}\times10^{-13}\ \text{cm},\quad R_D=2.56\times10^{-13}\ \text{cm}. \tag{4}$$

This is a reasonable value for R_D, but the value for the nuclear radius is considerably larger than values usually mentioned. Also, this is the minimum value to be deduced from the data. If there is an effective transparency for deuterons, the extent of nuclear matter is even greater.

Although this value for the radius is large, it is not incompatible with the idea of a fringe region about the main bulk of the nuclear matter, where the nuclear density falls off from its interior value to zero. That is, the nucleus is not of a square-well configuration, but is in a sense smoothed out. This outer fringe, though of smaller density than the interior region, is capable of stripping deuterons.

To understand further the above experimental results and interpretation, the total nuclear cross sections for 90-Mev neutrons[4] have been interpreted in terms of a nonsquare-well configuration for the nucleus. The optical model of Fernbach, Serber, and Taylor[5] has been used. As in FST, it is assumed that the incident neutron wave passes through the nucleus with negligible refraction. The change in phase of the incident wave as it passes through the nucleus is then readily calculated. The change in phase of that part of the wave which strikes the nucleus at an impact parameter y and travels the distance $2S=2(R^2-y^2)^{\frac{1}{2}}$ through the nucleus is given by

$$\phi=\int_{-S}^{S}\left(k+k_1+i\frac{K}{2}\right)dS', \tag{5}$$

where k is the wave number of the incident wave, $(k+k_1)$ the real part of the wave number inside the nucleus, and K the absorption coefficient. Then k_1 is given by

$$k_1=k[(1+V/E)^{\frac{1}{2}}-1]\simeq\tfrac{1}{2}kV/E, \tag{6}$$

where V is the nuclear potential and E is the energy of the incident neutrons. In order to simplify the calculations the approximate value of k_1 is used.

It is necessary now to choose a radial dependence for $V(r)$ and $K(r)$, the potential and the absorption coefficient. These will be taken to be proportional to the nuclear-density distribution $\rho(r)$, which in turn will be chosen to be of the form

$$\rho(r)=C\left(1-\frac{r^2}{R^2}\right),\quad 0\le r\le R,$$
$$C=\frac{A}{\frac{2}{5}(4\pi R^3/3)}. \tag{7}$$

* This work was performed under the auspices of the U. S. Atomic Energy Commission.

[1] Millburn, Birnbaum, Crandall, and Schecter, preceding paper [Phys. Rev. **95**, 1268 (1954)].

[2] This would imply that the deuteron is also broken up without the excitation of the target nucleus.

[3] R. Serber, Phys. Rev. **72**, 1008 (1947).

[4] Cook, McMillan, Peterson, and Sewell, Phys. Rev. **75**, 7 (1949).

[5] Fernbach, Serber, and Taylor, Phys. Rev. **75**, 1352 (1949), hereafter referred to as FST.

Other than the square well, this is the simplest distribution to handle and was chosen for this reason. $V(r)$ and $K(r)$ become then,

$$V(r)=V_0[1-(r^2/R^2)],$$
$$K(r)=\sigma\rho(r)=K_0[1-(r^2/R^2)], \quad (8)$$
$$K_0=\sigma C,$$

where σ is the mean neutron-nucleon cross section in nuclear matter.

The change in phase ϕ is then readily evaluated from Eq. (5), which yields

$$\phi=2kS+2\frac{\alpha S^3}{R^2}+i\frac{\bar{K}_0}{R^3}S^3, \quad \alpha=-\frac{1}{3}\frac{kV_0}{E}, \quad \bar{K}_0=\tfrac{3}{5}K_0. \quad (9)$$

Here α and $\bar{K}_0$ represent, in a sense, average values of k_1 and K, respectively.

From this expression for ϕ, expressions for the diffraction and absorption cross sections can be written down in the same manner as in FST. These become

$$\sigma_d=2\pi R^2\int_0^1|1-\exp(-\bar{K}_0R\zeta^3+2i\alpha R\zeta^3)|^2\zeta d\zeta,$$
$$\sigma_a=2\pi R^2\int_0^1[1-\exp(-2\bar{K}_0R\zeta^3)]\zeta d\zeta. \quad (10)$$

The total cross section is the sum of the two and is given by

$$\frac{\sigma_t}{\pi R^2}=2-4I,$$
$$I=\int_0^1\exp(-\bar{K}_0R\zeta^3)\cos(2\alpha R\zeta^3)\zeta d\zeta. \quad (11)$$

If we let $\bar{K}_0R=x$ and $2\alpha/K_0=\beta$, the integral I can be expressed in the following power series form:

$$I=\sum_{n=0}^{\infty}\frac{(-)^n}{n!}\frac{x^n}{3n+2}(1+\beta^2)^{n/2}\cos(n\theta),$$
$$\theta=\tan^{-1}\beta. \quad (12)$$

For values of x and β larger than one, the evaluation of the series becomes rather tedious. However, the integral can be expressed as the solution of the following differential equation:

$$\frac{dI}{dx}=\frac{2}{3x}[\tfrac{1}{2}e^{-x}\cos(x\beta)-I], \quad I(x=0)=\tfrac{1}{2}. \quad (13)$$

This equation may be easily solved on the differential analyzer at the Radiation Laboratory; solutions were found for values of $x>1$. The results of the calculation are given in Fig. 1, where $\sigma_t/\pi R^2$ is plotted as a function of x for various values of β; $\sigma_a/\pi R^2$ is also shown as a function of x.

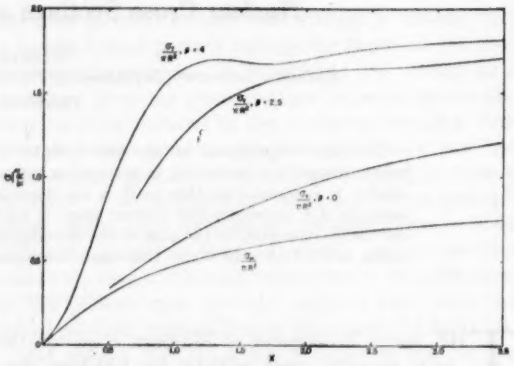

FIG. 1. Plot of the total and absorption cross sections as a function of $x=\bar{K}_0R$. The total cross sections are plotted for several values of $\beta=2kV_0/3E\bar{K}_0$.

From these numerical results, and using the experimental cross sections,[4] the variation of R with $A^{\frac{1}{3}}$ can be determined. This dependence is plotted in Fig. 2 for the values $\bar{K}_0=3.2\times10^{12}$ cm^{-1} and $\beta=2.5$. These values of the parameters yield an adequate straight-line fit to the experimental points. The slope of the line is 1.6, which yields

$$R=1.6A^{\frac{1}{3}}\times10^{-13}\text{ cm} \quad (14)$$

for the nuclear radius as a function of mass number.

If $\bar{K}_0$ and β are varied so as to keep the product $\bar{K}_0\beta$ constant, a considerable range of values for these parameters still yields satisfactory straight-line fits of essentially the same slope to the experimental points. As the product $\bar{K}_0\beta$ is proportional to V_0, the total cross sections determine only V_0 and not the absorption coefficient.[5] The absorption coefficient is of course to be determined from the neutron-absorption cross sections. The values of the radius obtained from the nuclear-absorption cross sections for 84-Mev neutrons[6] and the above parameters are shown in Fig. 2 also. Because of the uncertainties in the absorption cross sections, the value of $\bar{K}_0$ can only be regarded as falling in the range between 3.6×10^{12} cm^{-1} and 2.7×10^{12} cm^{-1}.

The angular distributions of the elastically scattered neutrons have also been calculated. It was found that this model yields essentially the same angular distributions as the square-well model.[6] For the lighter target nuclei the experimental angular distributions show greater peaking in the forward directions than is obtained from either model, although the agreement for the heavier target nuclei is reasonably good.

The values of V_0 and σ obtained from β and $\bar{K}_0$ are

$$V_0=52\text{ Mev}, \quad \sigma=3.3\times10^{-26}\text{ cm}^2.$$

The value of V_0 is considerably larger than the usual value of 30 Mev. The average value of the potential, however, as given by Eq. (9), is about 35 Mev. The

[6] Bratenahl, Fernbach, Hildebrand, Leith, and Moyer, Phys. Rev. 77, 597 (1950).

mean value of σ that would be expected from the 125(90+35)-Mev nucleon-nucleon cross sections is about 4.5×10^{-26} cm^2. When this is multiplied by a factor of $\frac{2}{3}$ to account for the exclusion principle,[7] the agreement with the above result is satisfactory.

The value of the nuclear radius obtained from the neutron data is still smaller than the value obtained from the inelastic-deuteron cross-section experiments. However, the model here adopted still suffers from the same defect as the square-well model; i.e., a cutoff at some distance R. The main point is that the inelastic-deuteron cross sections demand an extended nuclear-density distribution, and it appears that the 90-Mev neutron total and absorption cross sections can be fitted by an extended distribution. A more extensive analysis is needed using various well shapes that tail off. This program is, however, more suited to high-speed machine computation. This is also true from the point of view of accuracy, since the errors introduced by the neglect of refraction are probably not altogether negligible.[8] Such a program of computation is being undertaken by S. Fernbach at the University of California Radiation Laboratory, Livermore.

TABLE I. Comparison of the average and root-mean-square radii for the square well model and the parabolic well model.

	Square-well distribution $R=1.37A^{\frac{1}{3}}\times10^{-13}$ cm	Parabolic distribution $R=1.6A^{\frac{1}{3}}\times10^{-13}$ cm
$\bar{R}$	$1.03A^{\frac{1}{3}}\times10^{-13}$ cm	$1.04A^{\frac{1}{3}}\times10^{-13}$ cm
$\langle R^2\rangle_{Av}^{\frac{1}{2}}$	$1.06A^{\frac{1}{3}}\times10^{-13}$ cm	$1.05A^{\frac{1}{3}}\times10^{-13}$ cm

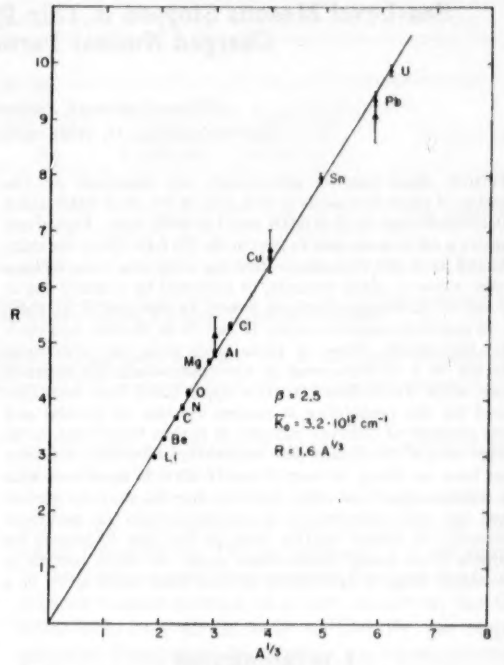

FIG. 2. Nuclear radii deduced from the total nuclear cross sections for 90-Mev neutrons (circular points) and from the absorption cross sections for 84-Mev neutrons (triangular points) as a function of the cube root of the mass number.

Finally, a comparison between these results and other determinations of nuclear radii should be noted. The radius of the square well distribution used by FST to fit the 90-Mev neutron scattering data is $R=1.37A^{\frac{1}{3}}\times10^{-13}$ cm. Though the extent of the parabolic well is greater than this, a comparison of the average and/or root-mean-square radius is more significant. This comparison is given in Table I. These values of the first two moments for the two models agree rather closely, though it appears that a smoothing out of the square well causes a reduction of the average and rms radii.

These values of the rms radius can be compared with the results of the electron scattering and mesic-atom experiments, which effectively measure the rms radius of the charge distribution.[9] The rms radius obtained in these experiments is about $R=0.9A^{\frac{1}{3}}\times10^{-13}$ cm, or about 15 percent less than the rms radius obtained from the optical model. Now it may be that with the introduction of a well shape which extends to infinity, the optical model will yield an rms radius of about this value and resolve the difference between these two types of measurements.[10] On the other hand, Johnson and Teller[11] have recently suggested that such a difference in the radius of the proton distribution and neutron distribution might exist. However, the existence of such an effect would be better resolved, not by the considerations of the optical model which admits of many variations, but by resort to experimental measurements which in some way would depend on the n/p ratio at the surface of the nucleus.

I wish to express my appreciation to Dr. Birnbaum, Dr. Crandall, Dr. Millburn, and Dr. Schecter for the many discussions pertaining to the experimental data on the scattering of particles from nuclei. I am also indebted to the various members of the computing group who assisted in the numerical computation.

[7] M. L. Goldberger, Phys. Rev. **74**, 1268 (1948).

[8] For example, a Gaussian-shaped well may be considered in the same manner as was the parabolic well. However, the real potential obtained is such as to render the approximations invalid.

[9] F. Bitter and H. Feshbach, Phys. Rev. **92**, 837 (1953).

[10] Some of this difference can certainly be ascribed to the finite range of the nucleon-nucleon potential, which is implicitly contained in the size of the nucleus as defined by the optical model.

[11] M. Johnson and E. Teller, Phys. Rev. **93**, 357 (1954).

Sea-Level Mesons Stopped in Thin Pb and Al Foils. I. Possible Emission of Charged Nuclear Particles and Related Events

W. Y. CHANG
Physics Department, Purdue University, Lafayette, Indiana

(Received January 18, 1954; revised manuscript received May 13, 1954)

Further cloud-chamber experiments are described on the stopping of sea-level mesons in thin foils of Pb (5 of 0.009 and 6 of 0.018 inch) and Al (8 of 0.004 and 3 of 0.032 inch). Eighty-one negative μ mesons are seen to stop in the Pb foils (50 in the thick foils and 31 in the thin ones). *Only two cases show some evidence of slow proton or alpha emission*, as indicated by a heavy dot at the end of the stopped negative meson. In the case of Al, there are 36 negative mesons stopped, 12 and 24 in the thin and thick foils, respectively. None of these cases gives any observable evidence of a nuclear event at the place where the negative meson stops. From these statistics, upper limits have been estimated for the probability of nuclear ejection of protons and alpha particles of different energies. It is thus found that, to be ejected from a Pb nucleus with reasonable probability, a proton must have an energy between 3 and 12 Mev, in agreement with the emulsion results of other workers. For Al, since no nuclear event has been observed, it is concluded that the maximum probability of nuclear ejection must be less than 10 percent for a proton of an energy in the above range. An alpha particle in this energy range is improbably emitted from either an Al or a Pb nucleus. As in the previous experiments, no long-track and narrow-angle electron pairs have been observed in either Pb or Al which can be attributed to high-energy photons over 15 Mev emitted from the stopped negative μ meson (or decaying meson). Thus we find no high-energy gamma rays and evidence for the rarity of even low-energy nuclear events. Consequently we draw the same conclusions as in earlier less extensive experiments: that following the nuclear interaction *only a small part of the μ meson's rest energy is imparted to the nucleus*, and that the remaining part must go off as neutral, nonelectromagnetic radiation, to escape observation in the cloud chamber.

Altogether, 87 decaying mesons have been actually found from the two (previous and present) series of experiments. None of the decay electrons has been seen to move toward any one of the anticoincidence counters below the chamber. From this fact, the solid angle covered by the anticoincidence counters, and the absorbing material above the counters, one argues that the proportion of μ-decay electrons with energy smaller than 10 Mev is of the order of 1 in 60 or less.

I. INTRODUCTION

IN our previous communications,[1] cloud-chamber experiments were described on the absorption of slow μ mesons by thin foils of Al (0.002 and 0.032 inch), Fe (0.028 inch), and Pb (0.018 inch). Continuous operation of the chamber for an effective period of over 2600 hours showed the following: (1) No protons were observed for the 53 negative μ mesons stopped at the Pb, Fe, and Al foils (except one doubtful case from Pb). (2) No long-track and narrow-angle electron pairs of total energy, say, over 15 Mev, were observed from these elements which could be due to high-energy photons associated with the stopped negative μ mesons (or with the decaying mesons). Such photons would have been easily observed in the chamber because of the large absorption coefficient, particularly of Pb, for such high-energy gamma rays. Therefore, we were led to the following conclusions: (1) only a small portion of the rest energy ($\sim$100 Mev) of the stopped negative μ meson is imported to the nucleus and (2) the remaining portion must come off as neutral, nonelectromagnetic radiation, in order to escape observation in the cloud chamber.

Besides, evidence of low-energy gamma rays (1–5 Mev) was obtained from the observation of the meson-oriented electrons and pairs from Pb and Fe. They were "meson-oriented" in the sense that the single electron track or apex of the pair made an angle less than $\pm 20°$ with the imaginary line running back to the end point where the meson was stopped. Stray tracks were shown unable to account for these events. The energy and frequency of occurrence of these electrons were compatible with those predicted in Wheeler's theory[2] of meson transitions between the Bohr orbits before μ-meson capture and with those expected after capture due to de-excitation of the transformed nucleus. No evidence of such gamma rays was found for Al.

Since these results were reported, our experimental conditions have been somewhat improved in the hope that more definite and detailed information could be gained about the results mentioned above, particularly better statistics about the low-energy (1–5 Mev) photons associated with the stopped negative meson. Subsequent experiments with Al and Pb were completed in 1949 at Princeton. Part of the cloud-chamber pictures were examined also at Princeton, and the results were partly analyzed there and briefly reported on several occasions.[3] The examination of the pictures and analysis of the results were continued at Purdue and recently completed. They will be reported now in a more detailed and systematic manner. As will be seen, these new results substantially support all the previous results and conclusions.

It may be noted that similar findings to those obtained in these experiments have also been reported later by other workers, using μ mesons from both cosmic

[1] W. Y. Chang, Phys. Rev. **74**, 1236 (1948); Revs. Modern Phys. **21**, 166 (1949).

[2] J. A. Wheeler, Revs. Modern Phys. **21**, 133 (1949).

[3] W. Y. Chang, Phys. Rev. **76**, 170 (1949); Princeton Biennial Report, 1 July 1947–30 June 1949 (unpublished); Proceedings of the Echo Lake Cosmic-Ray Symposium (sponsored by U. S. Office of Naval Research and the U. S. Atomic Energy Comsion), 23–28 June 1949 (unpublished); Phys. Rev. **79**, 205 (1950).

TABLE I. Summary of results for μ-mesons stopped in Pb foils. A μ-o-e means a meson-oriented electron seen at another foil; similarly for μ-o-pair. Figures in each column give number of mesons stopped at a thick or thin foil. An A track means that the track has a proper variation of ionization and remains in a well-illuminated region. A B track means that the above two conditions for the track are less certain but are still good enough to identify the track.

Effective working period ~1500 hours	I. Meson stopped; nothing seen from the end		II. Meson stopped; μ-o-e or μ-o-pair seen at other foil		III. Meson stopped; a heavy dot from the end	IV. Meson stopped; a thin curved short track from the end	V. Meson decay	
	A	*B*	*A*	*B*			*A*	*B*
Thick Pb foils: (6×0.018 inch)	26	10	8[a] (+1)[b]	3[c]	1	2[e]	19 (45)[f]	8
Thin Pb foils: (5×0.009 inch)	16	6	5[d]	1	1[e]	1	10[e] (25)[f]	5

[a] One stopped meson track has 2 μ-o-e's. Three have a μ-o-pair each.
[b] This particular event is classified with the μ-o-e and μ-o-pair events because a secondary electron emerges at the end of the stopped negative meson track, moves upward through 2 foils, and suffers multiple scattering twice near the end (see Fig. 1 of Part II); energy is ~5 Mev.
[c] One has a μ-o-pair.
[d] One has both a μ-o-pair and a μ-o-e.
[e] One in each group has a μ-o-e from a thick foil. The one associated with the decaying meson (column V) may be due to either a photon from the decay positron, i.e., bremsstrahlung produced in the same foil where the positive meson undergoes decay, or a stray electron.
[f] Figures in parentheses represent roughly the numbers of decaying mesons, which would have been observed, had the bottom anticoincidence counters not been used.

rays and high-energy machines. These will be mentioned in the sections concerning the results and their analysis.

For convenience of discussion, the results related with the possible emission of charged nuclear particles will be analyzed and discussed in this paper (to be called Part I), and the results for the low-energy gamma rays will be reported in Part II, a separate paper to follow.[4]

II. EXPERIMENTAL ARRANGEMENT

The apparatus and the experimental setup were practically the same as before,[1] except that the depth of the cloud chamber was increased from 5 inches to 8 inches and the solid angle of the defining counter telescope was increased accordingly. The number of mesons entering the chamber via the telescope was found to increase to about 150 per hour, being approximately 2 to 3 times larger than that in the previous cases (see Table II of the following paper). The details concerning the electronic controls and the construction of the cloud chamber used have been published elsewhere.[5]

Two series of experiments were carried out, one with thin Pb foils and the other with thin Al foils. In the experiments with the Pb foils, five 0.009-inch foils (half the thickness in the previous experiments)[1] alternated with six 0.018-inch foils inside the chamber. They were not covered with any thinner foils of Al or other material. With the thinner Pb foils, one would have a larger chance to observe low-energy protons (if any) emitted by the Pb nuclei after capturing negative μ mesons. Also, more detail might be revealed of the μ-meson-oriented electrons and pairs. The length of the electron tracks in the gas would be longer because of smaller absorption in the foils and the direction of the tracks could be better determined because of smaller multiple scattering in the foils. The absence of the 0.002-inch reflecting Al foils used in previous experiments removed a slight ambiguity as to which material gave rise to the events.

In the experiments with Al foils, eight 0.004-inch and three 0.032-inch foils were symmetrically placed inside the chamber. This arrangement was the same as in the previous experiments except that here the thinner foils were twice as thick as before. As before, the three 0.032-inch foils served only to identify the stopped particles. Using eight thicker foils, we hoped to increase (1) the statistics of the stopped mesons which were rather small in the previous experiments, and (2) the chance of observing the μ-meson-oriented electrons and pairs which were not found before.

The same techniques as used before were employed here also to identify the particles stopped at the foils, i.e., the variation of ionization in the different gas spaces supplemented by the multiple scattering in the foils and knock-on electrons in the gas.

III. RESULTS AND DISCUSSION

About 7500 pictures were taken in an effective working period of about 1500 hours in the experiment with Pb, and about 6000 pictures in about 1400 hours in the case of Al, the different types of results being presented in Tables I and II. In the following, these different kinds of results will be discussed briefly and conclusions will be compared with those reached in the previous experiments. As mentioned before, the results

TABLE II. Summary of results for μ mesons stopped in Al foils.

Effective working period ~1400 hours	I. Meson stopped; nothing seen from the end[a]		II. Meson stopped; μ-e decay	
	A	*B*	*A*	*B*
Thick Al foils: (3×0.032 inch)	18	6	11 (23)[b]	3
Thin Al foils: (8×0.004 inch)	9	3	4 (9)[b]	1

[a] *A* and *B* are used to indicate the quality of the cloud chamber pictures. For definitions see Table I.
[b] The figures in parentheses represent the numbers of decay positrons (some of them perhaps are decay electrons) corrected roughly for those excluded by the anticoincidence counters.

[4] W. Y. Chang, following paper, Phys. Rev. **95**, 1288 (1954).
[5] W. Y. Chang and J. R. Winckler, Rev. Sci. Instr. **20**, 276 (1949).

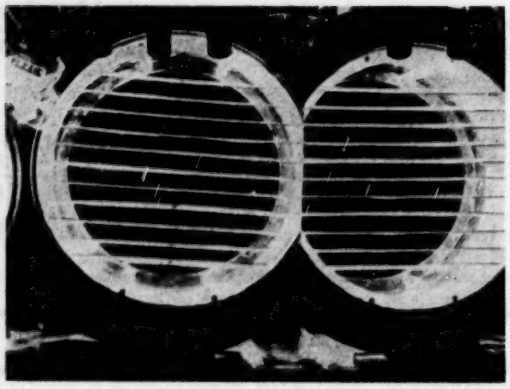

FIG. 1. A μ meson stops in the seventh Pb foil (0.018 inch). It undergoes decay with the decay electron moving upward to the top of the chamber. Neither of the two "stray" tracks is of the same age. See Fig. 2. (The thin and long line in the stereoscopic picture is due to a scratch in the negative.)

for the low-energy gamma rays will be presented in a separate paper (see reference 4).

1. Mesons Decaying at the Foils

Figures 1 and 2 are two typical μ-decay pictures out of a number of cases where a slow meson undergoes radioactive decay in a Pb or Al foil. In Fig. 1 the meson stops and decays in the seventh Pb foil (0.018 inch), while in Fig. 2 the event takes place in the ninth Al foil (0.032 inch). In both cases (like many others), the decay electrons (thinner tracks) move approximately upwards, for the reasons discussed below. The variation in ionization of these decaying meson tracks serves as a very reliable standard of reference to identify those other mesons which stop in the foils and give rise to nothing observable at their end points.

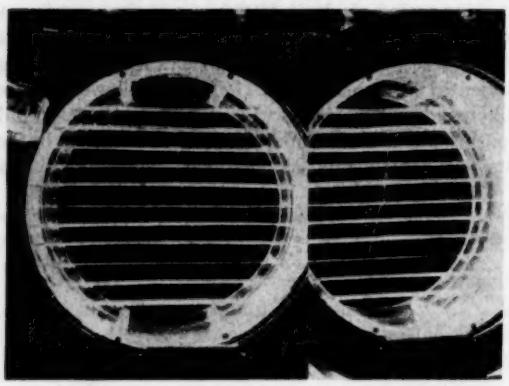

FIG. 2. A μ meson stops in the ninth Al foil (0.032 inch) with the decay electron moving to the chamber top. The variation of ionization of decaying mesons such as this is usually taken as a reliable standard of reference for identifying mesons stopped in Al or Pb foils without decay. (See Fig. 1.)

The numbers of mesons decaying in the Pb and Al foils are shown in the last columns of Tables I and II, respectively. It is seen that in each element fewer decaying mesons have actually been observed than the stopped negative mesons. This was noticed also in our first experiments and was then and is now, too, due to the fact that the bottom circumference of the cloud chamber has been surrounded with the anticoincidence counters which have covered roughly $\frac{2}{3}$ of the entire solid angle and thus have excluded those decay electrons moving into this solid angle. This is evidenced by the fact that in all of the μ-decay pictures none of the 87 decay-electron tracks, observed in both the previous and present experiments, is seen directed toward any one of the anticoincidence counters below the chamber.

The figures in parentheses are the values corrected by this solid angle factor and hence represent roughly the numbers of decay electrons which would have been actually observed had the bottom anticoincidence counters not been used. These figures are now closer to those of the stopped negative μ mesons; the difference is comparable with the statistical fluctuation if allowance is made for the rough estimate of the above solid angle.

As just mentioned above, none of the 87 decay electrons is seen to move toward any one of the anticoincidence counters below the chamber. This fact may be taken as a basis for obtaining information about the proportion of the low-energy μ-decay electrons: The chamber and counter walls, etc., are estimated to be about 5 g/cm^2 thick (Cu equivalent), corresponding roughly to the range of a 10-Mev electron. The geometrical disposition of the anticoincidence counters as discussed above shows that approximately $0.4\times87/(1-0.4)\sim60$ decay electrons moving toward the anticoincidence counters would have been observed if their energy were smaller than 10 Mev. Therefore, one may argue that the proportion of μ-decay electrons with energies smaller than 10 Mev is of the order of 1 in 60 or less. This proportion of the low-energy ($\sim$10 Mev) delay electrons deduced from our experiments is in approximate agreement with the extrapolated portion of the experimental curves.[6]

2. Meson Stopped; Nothing Seen at the End

Figures 3 and 4 are two representative pictures out of many pictures which do not show any observable charged particle coming out from the end of the stopped negative μ mesons. In Fig. 3 a μ meson is stopped at the fifth Pb foil (0.018 inch) and nothing is seen at its end. Figure 4 is a similar picture showing a μ meson stopped at the sixth Pb foil (0.009 inch) again without anything accompanying its end; a thinner track

[6] Leighton, Anderson, and Seriff, Phys. Rev. **75**, 1432 (1949); Sagane, Gardner, and Hubbard, Phys. Rev. **82**, 557 (1951); H. Bramson and W. W. Havens, Phys. Rev. **83**, 861 (1951); Bramson, Selfert, and Havens, Phys. Rev. **88**, 304 (1952); R. W. Williams, Phys. Rev. (to be published).

appears in the gas space between the eighth and ninth foils and is obviously a much younger track.

In the case of Pb foils, we have actually observed a total of 123 stopped mesons as shown in Table I. Seventy-six of these, as seen in columns 1 and 2 (48 from the 0.018-inch foils, and 28 from the 0.009-inch foils), do not appear to give rise to any observable[7] particle from the place of the foils where they stopped. This number (plus those in columns 3 and 4) which do not decay is approximately equal to the number of mesons which do decay at the foils after correction for those excluded by the anticoincidence counters below the cloud chamber, as shown in the last column of the table. Therefore, these 76 (+5) mesons are regarded as negative μ mesons. The failure to observe any proton emitted except the two possible cases in column 3, when a negative μ meson is captured by a Pb nucleus, is exactly what was found in our first experiments,[1] where

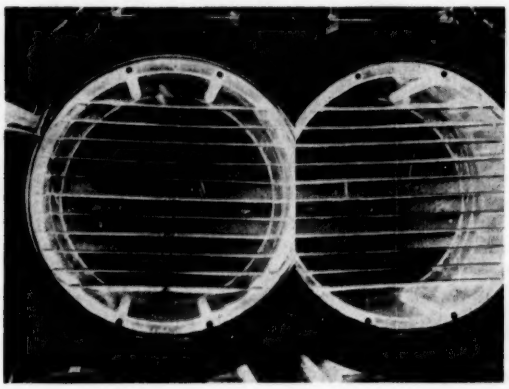

FIG. 3. A μ meson stops in the fifth Pb foil (0.018 inch). No charged particle is observed to come out from the end. The thickness of the foil is about the range of an 11-Mev proton. It is a picture of quality *A* (see Table I for definition), without being accompanied by any tracks of the same age.

no proton was observed from 27 negative μ mesons stopped at 0.018-inch Pb foils. Of course, in the present experiments, the statistics are more than twice as good and the data give information about foils having half the previous thickness, i.e., only 0.009 inch.

It may be noted that soon after the report of our first results,[1] Wang and Jones[8] also announced similar negative results for much thicker foils, i.e., 0.032-inch Al and 0.25-inch Pb.

In the Al foils (Table II), altogether 55 μ mesons have been found to stop. Of these, 36 (24 from the 0.032-inch foils and 12 from the 0.004-inch foils) do not emit any observable particle from the end of their range. Since this number is roughly equal to the

[7] Except one, which has been attributed to an electron of approximately 5 Mev ejected by a photon from the stopped negative μ meson. See reference b of Table I and Fig. 1 of the following paper (reference 4).

[8] K. C. Wang and S. B. Jones, Phys. Rev. **74**, 1547 (1948).

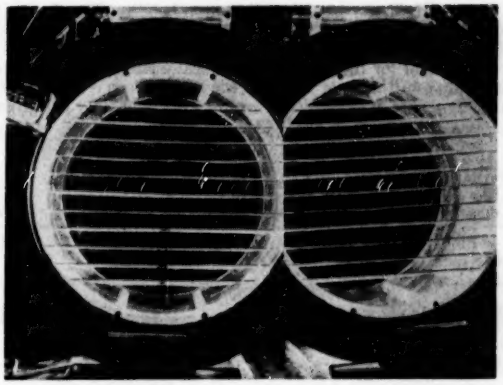

FIG. 4. A μ meson stops in the sixth Pb foil (0.009 inch). No observable charged particle is emitted from the end, though the foil thickness is only about the range of a 5-Mev proton. None of the few "stray" tracks has the same age.

corrected number of mesons decaying in the Al foils, the 36 mesons are reasonably regarded as negative μ mesons stopped in the foils as in the case of Pb. The absence of proton emission in the nuclear capture of a negative μ meson by Al checks our first experiments.

3. Possible Emission of a Heavy Charged Particle. Discussion of the Stopped Negative μ Meson

So far, we have found only two cases (and these only in Pb) where a very slow, heavily ionizing particle could be emitted after the nuclear capture of a negative μ meson. These are shown in column 3 of Table I. The identification in each of the two cases cannot be entirely certain, for the heavy dot does not extend far in the gas space from the end of the stopped meson. However, it seems reasonable to attribute the heavy dot to the short track of a proton or alpha particle of extremely

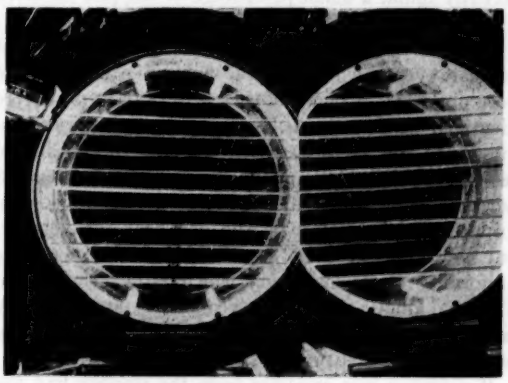

FIG. 5. A star of more than 15 particles produced in the seventh Pb foil (0.018 inch). Total kinetic energy involved is probably larger than 400 Mev, if the star particles are protons. It is very probably produced by a fast proton, or a locally produced fast π meson.

TABLE III. Heavy-particle emission probability. The observed rate of events which admit interpretation as heavy particles is considered to be the product of the probability that the heavy particle will escape from the foil and the probability that the heavy particle will be emitted from the nucleus. The first factor is calculated. From its value and from the observed rate is then deduced an estimate or upper limit for the probability for heavy particle emission from the nucleus. In the calculation it is assumed that the probability distribution of the point at which the meson stops is uniform from top to bottom of the foil. Energy values lower than those listed in the table are not considered because the probability of barrier penetration would then seem negligibly small.

Material and foil thickness	Observed probability for μ^- to produce event interpretable as ejection of heavily ionizing particle	Conceivable interpretation of particle	Conceivable energy in Mev	Range[a] in g/cm²	Calculated probability to be seen if emitted	Upper limit to probability of nuclear ejections deduced from experiments
Pb			12	0.51	0.4	0.05
0.018 inch	1/50	Proton	5.5	0.13	0.15	0.1
0.51 g/cm²			3.7	0.07	0.06	0.3
		Alpha	10	$\sim 30\times10^{-3}$	0.02	(~1)
			5	$\sim 10\times10^{-3}$	0.005	(~4)
Pb			8	0.26	0.4	0.08
0.009 inch	1/31	Proton	3.7	0.07	0.15	0.2
0.26 g/cm²						
		Alpha	10	$\sim 30\times10^{-3}$	0.06	(~0.5)
			5	$\sim 10\times10^{-3}$	0.01	(~3)
Al						
0.032 inch	<1/24	Proton	11.5	0.22	0.4	< 0.1
0.22 g/cm²			5.5	0.055	0.15	< 0.3
			3.5	0.027	0.06	< 0.7
		Alpha	5	$\sim 4\times10^{-3}$		
			1.5	$\sim 1\times10^{-3}$		
Al			3.5	0.027	0.4	< 0.2
0.004 inch	<1/12	Proton	1.5	6.5×10^{-3}	0.15	< 0.6
0.027 g/cm²			1.0	3.3×10^{-3}	0.06	<(1.4)
		Alpha	5	$\sim 4\times10^{-3}$		
			1.5	$\sim 1\times10^{-3}$		
Emulsion results of			Proton energy		% of stopped μ^- mesons	
George and Evans[b]			1–10 Mev		8.7±1.7	
Fry[c]			1–10 Mev		~5	
			With max. int. at ~5 Mev			

[a] E. Segrè, *Experimental Nuclear Physics* (John Wiley and Sons, Inc., New York, 1953), Vol. I.
[b] See reference 9.
[c] See reference 10.

low energy. It should be noted that George and Evans[9] and also Fry,[10] using the emulsion technique, have also recently found a small percentage of stopped negative μ mesons which give rise to a low-energy proton.

Figure 5 shows one of a few cases so far obtained of nuclear events where several nuclear particles have been observed, but none of these cases can be positively identified as due to nuclear capture of a negative μ meson. In this picture, where the event occurs in the seventh Pb foil (0.018 inch), there are more than 15 particles in the star that are presumably protons. The initiating particle may be the one near the vertical, but its nature cannot be decided because of the uniformity of its ionization which is near minimum. The total kinetic energy involved in the star is probably larger than 400 Mev, and the event is very probably produced by a fast proton or π meson.

If a proton just escaping from the nucleus had too small an energy, it would be absorbed by the foil which has a finite thickness. Hence, no proton track could be observed in the chamber at the end of the negative μ meson range. One may estimate the range and the average solid angle and hence the probability that a proton of a given energy can come out of the foil, as indicated in Table III. For the convenience of calculation, the values for the foil-penetration probability as given in column 6 are calculated by assuming the initial proton energy (just escaping from the nucleus) to have a range equal to the foil thickness, about $\frac{1}{4}$ and about $\frac{1}{8}$ of the foil thickness, respectively. For an alpha particle, they are estimated from the ranges of the given energies (see column 4). The figures for the nuclear-emission probability as shown in the last column are obtained by dividing the observed possible rates in column 2 by the above probabilities. They represent the experimental upper limits to the probability of nuclear ejection corresponding to the different *initial* energies in column 4.

In the case of the thick Pb foils, if the one nuclear event observed is a proton of an energy between 5 Mev

[9] E. P. George and J. Evans, Proc. Phys. Soc. (London) **A64**, 193 (1951).
[10] W. F. Fry, Phys. Rev. **85**, 677 (1952); **91**, 481 (1953); H. Movinnaga and W. Fry, Nuovo cimento **10**, 308 (1953).

TABLE IV. Number of electron pairs expected if 15-Mev photons were emitted at the point where the meson stops. The photons are assumed to emerge in random directions, one photon from each stopped μ meson. The experiments show the *absence* of such electron pairs.

Material	Equivalent[a] number of spherical shells of foil system	Total effective path in g/cm²	Mean-free-path in g/cm² of 15-Mev photon	Number of stopped μ mesons not decaying	Number of stopped μ mesons decaying	Number of electron pairs expected from 15-Mev photons if emitted from Those not decaying	Those decaying
Pb foils	~3-thin (0.78 g/cm²) ~3.5-thick (1.79 g/cm²)	2.57	14	81	42	15	8

[a] The figures given here are estimated only approximately from (1) the solid angle of the foil system to intercept the photons and (2) the effectively traversed path in the foils corrected for the secθ effect, where θ is the angle made with the vertical by the assumed photon, both (1) and (2) being averaged over different points in the chamber.

and 12 Mev (very probably it is), its probability of escaping the nuclear barrier, as seen from the last column, is between 10 and 5 percent. This percentage for the ejection probability seems reasonable theoretically, because a proton needs only roughly 10 Mev to surmount the Coulomb barrier of the Tl^{208} nucleus. Also, it is consistent with the emulsion results of George and Evans[9] and Fry,[10] as can be seen from the bottom table of Table III (of course in the latter case one has to allow too for certain absorption by the grains of the emulsion). Similar considerations show that it is much less probable that the event represents a proton of 3 Mev or less because of the unreasonably large barrier transmission probability for this energy, and that for the same reason it cannot represent an alpha particle of 5 or 10 Mev. Similarly, the event obtained from the thin Pb foil is very probably a proton of an energy between 4 and 8 Mev and it is very improbable that it is an alpha particle of 5–10 Mev. If the blobs observed in Pb were alpha particles of, say, 10 Mev, the probability of escaping nuclear barrier as deduced from the experiment would be 50 or 100 percent. This value is impossibly large when one remembers the potential barrier of Tl^{208} for an alpha particle. In fact, experimentally these blobs do not seem to have sufficient ionization to be very slow alpha particles.

So far no nuclear event has been observed in association with the μ^- mesons stopped at Al foils, and consequently no definite upper limit can be deduced from our experiments for the nuclear-ejection probability. It seems a little surprising that Al shows no nuclear event. The potential barrier of Mg^{27} (about 3 Mev) for a proton is much smaller than that of Tl^{208} and is also much smaller than the neutron binding energy in Mg^{27}. For this reason one would expect proton emission with probability comparable with that of the neutron emission, the latter being actually observed from Pb.[11]

[11] M. F. Crouch and R. D. Sard, Phys. Rev. **85**, 120 (1952), and earlier papers of Sard and co-workers.

4. Absence of High-Energy Photons

In the present experiments, as in the previous ones, we have not observed in Pb or Al any meson-oriented electron pair which can be attributed to a photon of energy greater than 15 Mev emitted from the stopped negative μ meson (or from the decaying mesons). If high-energy photons were actually emitted in these cases, we should have observed many pictures showing long and narrow-angle electron pairs associated directionally with the stopped μ mesons, because of the large absorption coefficient of the foils, particularly of Pb, for such high-energy photons. In Table IV, we have made some estimates to see how many high-energy electron pairs would have been actually observed in our present Pb esperiments, if high-energy photons were emitted from the stopped μ mesons. Both the efficiency of detection and the probability of conversion into pairs have been approximately allowed for. Only one such photon is assumed to be emitted (in a random direction) from each stopped μ meson. It is seen that we should have observed about 23 such long and narrow-angle pairs in our experiments, and more if the assumed photons had energy higher than 15 Mev.

The absence of high-energy photons and the rare evidence of only two possible low-energy nuclear events lead us to the same conclusions as found before that *the negative μ meson*, when captured by a nucleus, *only imparts a small fraction of its rest energy* ($\sim$100 Mev) *to the nucleus* and that *the remaining portion must go off as neutral, nonelectromagnetic radiation* in order to escape cloud-chamber observation. A theoretical account of this result has been given by Tiomno and Wheeler,[12] in terms of the charge exchange reaction $\mu^-+p\rightarrow n+\nu$. Our results are consistent with the theoretical predictions.

[12] J. Tiomno and J. A. Wheeler, Revs. Modern Phys. **21**, 153 (1949).

Sea-Level Mesons Stopped in Thin Pb and Al Foils. II. Low-Energy (1–5 Mev) Gamma Rays

W. Y. Chang
Physics Department, Purdue University, Lafayette, Indiana
(Received January 18, 1954; revised manuscript received May 13, 1954)

Low-energy gamma rays (1–5 Mev) associated with the stopped negative μ mesons, similar to those reported before, have been observed also in these experiments. Twenty-five meson-oriented electrons and pairs have been found in Pb associated with 23 of the 81 stopped negative μ mesons. They are "meson-oriented" in the sense that the single electron track (or apex of the pair) makes an angle less than $\pm 20°$ with the imaginary line running back to the end point where the meson is stopped. None of such events has been obtained from Al. Of the 25 directed events, 4 are single electrons emitted directly from the end point of the stopped negative μ mesons, one being fairly energetic and the other three rather slow. The other 21 are single electrons and pairs observed in each case at a foil different from that where the meson stops and are meson-oriented in the above sense. The reality of this angular correlation follows from the fact that the 81 photographs of negative mesons stopped in Pb show only 6 electron tracks which make an angle of $90° \pm 20°$ with the line back to the end point of the meson track (6/21 as many tracks for 6 times as much solid angle). An independent determination of the rate of the strays was made by examining a film of 575 pictures to see how many tracks point by chance toward or away from an arbitrary point in the chamber with a 20° tolerance. From both ways of counting accidentals it is concluded that, of the 21 meson oriented events, at most about $\frac{1}{3}$ can be explained as stray tracks. A crude analysis of the electron range in the Pb foils indicates that the majority of the "oriented electrons" and "oriented pairs" may be interpreted as having an energy of about 5 Mev and the rest an energy probably below 3 Mev. The multiplicity of the photons producing these electrons has also been estimated, after a correction has been made for the multiple scattering of the electrons in the first foil, where they are emitted, so as to include all the electrons other than those counted within the cone ($\pm 20°$) in the forward direction of the photons. *The value for the multiplicity obtained is about 4·5* per negative meson stopped. The energy and frequency of occurrence of these photons are thus consistent with that predicted in Wheeler's theory of meson transition between the Bohr orbits and with that expected from nuclear de-excitation following the μ-meson capture.

I. INTRODUCTION

IN Part I, the preceding paper,[1] we have reported 81 and 36 negative μ mesons stopped respectively in thin Pb and Al foils. These events were obtained from continuous operation of a cloud chamber for an effective period of nearly 3000 hours. Only two pictures for Pb show some evidence of slow proton emission, and none has been found for Al. Moreover, no energetic electron pairs have been observed in either Pb or Al which can be attributed to high-energy photons of, say, over 15 Mev emitted from the stopped negative meson (or decaying meson). Therefore, we have concluded there as well as in our first reports[2] that following capture by a nucleus, the negative μ meson imparts only a small portion of its rest energy to the nucleus and that the remaining part must go off as neutral, nonelectromagnetic radiation, in order to escape observation in the cloud chamber.

In the present paper (Part II), we should like to discuss in some detail the low-energy (1–5 Mev) photons associated with the stopped negative μ mesons, for which much better statistics have been obtained now than in our first experiments.[2] Twenty-five single electrons and pairs have been found in Pb associated with 23 of the 81 stopped negative μ mesons, and none has been observed for Al. These electrons and pairs are lined up with a tolerance of $\pm 20°$ with the point at which the μ meson stops and hence will be called "oriented electrons" and "oriented pairs," respectively. In Sec. II we shall discuss the energies of these electrons and pairs, the chance coincidence of the stray tracks, the origins of the gamma rays responsible for the oriented electrons and pairs, and the mean multiplicity of the photons.

In Sec. III, the absolute rate of stopping of mesons is calculated for both Pb and Al in the present and previous[2] experiments. The results are compared with that of other workers in order to get a supplementary check that the experimental setup was in correct operation.

II. RESULTS AND DISCUSSION

All the data for the low-energy photons have been necessarily presented together with the stopped mesons in Table I of Part I, the preceding paper.[1] Since there is no satisfactory way to separate these data and show them here, we shall have to, when it is necessary, refer to this table of Part I in the following discussions.

Coming from the Pb foils are 20 meson-oriented electrons and pairs (see column II, Table I in Part I) with energy estimated ranging from 1 to 5 Mev similar to those found and discussed in our first experiments.[2] Their tracks are of the same age as the stopped meson tracks and are found pointing toward the end points of the stopped mesons within a cone of half-angle $\sim 20°$ as examined from both the direct and stereoscopic pictures. Thirteen are associated with twelve negative μ mesons stopped at the thick (0.018-inch) Pb foils, and seven with six mesons stopped at the thin (0.009-inch) Pb foils; and as before, none has been observed from the Al foils. Some of these are electron pairs and the rest are single tracks. Of the single electron tracks, one case, as presented in Fig. 1, is obtained which is

[1] W. Y. Chang, preceding paper, Phys. Rev. **95**, 1282 (1954).
[2] W. Y. Chang, Phys. Rev. **74**, 1236 (1948); Revs. Modern Phys. **21**, 166 (1949).

quite similar in direction and energy (perhaps slower) to that shown in Fig. 7 of our first publication;[2] an electron track comes upward from the place where the meson stops and passes through two foils before it twice suffers large-angle scattering. In addition to the twenty, a similar oriented electron has been associated with an event in column III and another one with one event in column IV both of Table I in the preceding paper.[1] Both occur at thick foils, while the μ mesons stop, respectively, at thin and thick ones.[3] Three more slower electrons are observed to be emitted directly from the end of the stopped mesons (see column IV, Table I, Part I) as will be discussed in the following. So, altogether we have twenty-five meson-oriented electrons and pairs.

1. The Rough Energy Distribution of the μ-Oriented Electrons and Pairs

The estimation of the energy of these oriented electrons and pairs from the absorption in the foils is extremely difficult, because of the following reasons: (1) In the energy region concerned, the radiation loss is almost as important as the ionization loss. Since the thickness of each foil is much smaller than the radiation length, the radiation loss may fluctuate greatly. Therefore, it is difficult to allow a mean value for this loss. (2) The electron may suffer multiple scattering within each foil, and thus the actual path traversed in the foil may be greater than that determined from the direction of emergence. (3) The location of the end points of the electron track is uncertain (due to finite foil thickness). No attempt will be made to allow for these corrections nor for the energy loss in the gas. For the estimate of energy, we have used the range-energy curve given in Montgomery's book,[4] which is for the ionization loss only. We have also applied the correction $\sec\theta$ in order to obtain the actual straight path in the foil, i.e., $l = t\sec\theta$, where t is the foil thickness and θ the angle made with the vertical by the electron track. The energy value obtained in this way may be expected to be smaller than the real value. The way of grouping of these oriented electrons and pairs is summarized in Table I(a), (b), (c), and (d), and the rough energy distribution is given in Table I(d). The lower limit to the possible range in each group of Table I(c) is obtained by assuming the track to begin and end at the midpoint of the foil thickness. The rough energy distribution in Table I(d) seems to show a general trend towards a maximum around 5 Mev. However, no great weight should be attached to this distribution, because of the crudeness of the method of measurement and hence of the analysis.

TABLE I. Rough energy distribution of μ-o-e's and μ-o-pairs.

(a) Range-energy relation (Al). We assume that it is approximately the same for Pb.

	Range in g/cm²				
	0.5	1	1.5	2	2.5
Energy in Mev	1.1	2.1	3.5	4.6	~5.6

(b) Distribution of track length (in units of gas space).

	Track length in No. of gas spaces between foils			
	<1	1	2	3
Single (19)	3	9	6	1
Pair (6)	0	6	0	0

(c) Possible range in the foil. Note: (1) Thin foils (0.26 g/cm² each) and thick foils (0.51 g/cm²) alternately placed. (2) The secθ effect on the path.

	Track length in No. of gas spaces between foils[a]		
	1	2	3
Possible range in g/cm²	0.75–1.5	1.5–2.5 1.5–2	2.25–3

(d) Rough energy distribution. Total track length of each pair = 2 gas spaces.

	Energy in Mev			
	~1–2	1.5–3.5	3.5–5	5–6.5
No. of μ-oriented electrons and pairs	3[b]	9	12	1[b]

[a] The lower limit is obtained by assuming the event to begin and end at a point half way of the foil thickness.
[b] These four electron tracks are observed to emerge from the end of four stopped μ^- mesons.

[3] A μ-oriented electron is also found at a thick foil with a meson decaying at a thin foil. This oriented electron may be due to either a photon from the radiation of a decay position, or a stray electron; see column V, Table I, Part I (not included in our statistics).

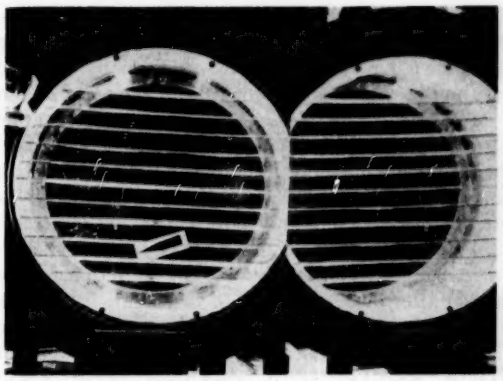

FIG. 1. A μ meson stops in the last Pb foil (0.018 inch), and a thin track is emitted from the end and moves upwards. After passing through two foils, it suffers scattering twice first from the eighth foil and then from the ninth and back to stop in the eighth foil. It is almost certainly an electron and its kinetic energy is probably between 5 and 6 Mev [see Table I(d)]. This is one of four such cases found in the present experiments. They are very probably Compton electrons, each ejected by a photon absorbed by the same foil in which the μ meson stops. See also Figs. 2 and 3. See text for discussion.

2. The Electron from the End Point of the Stopped Negative Meson

In addition to the electron listed in Table I of Part I (column II, top row) and also shown in Fig. 1 of the present paper, we have observed 3 other cases, all from the Pb foils (see column IV, Table I of Part I), where a thin, curved, and short track of the right age appears

[4] D. J. X. Montgomery, *Cosmic Ray Physics* (Princeton University Press, Princeton, New Jersey, 1949), Appendix E.

at the end of the track of the stopped negative μ meson. If the particle is an electron, its energy, after coming out of the foil, may be only of the order of a few hundred kev, and its initial energy could be of the order of 1 or 2 Mev [see Table I(d)] if it came from the atom (Auger effect or internal conversion) which has captured the negative μ meson or from a neighboring atom. It is not probable that both these 3 low-energy particles, presumably electrons, and those 3 more energetic ones (2, 1 for Pb and 1 for Fe, reported before in reference 2) are β particles emitted by the β-radioactive isotope formed after nuclear capture of the negative μ meson, because the sensitive time ($\sim$0.1 sec) of the cloud chamber is very much shorter than the mean life ($Tl^{206}\,\beta^-$, $\tau\sim$3.5 yr; $Tl^{207}\,\beta^-$, $\tau\sim$4.8 min; $Tl^{208}\,\beta^-$, $\tau\sim$3.1 min) of the radioactive isotope and the chance is extremely small for the beta and meson tracks to have the *same age*. Moreover, if they were the low-energy μ-decay positrons (1–5 Mev) from decaying positive μ mesons, their proportion to the total number of μ-decay positrons so far actually observed would be 5/52 for Pb and 1/9 for Fe, which are unbelievably large (see Part I), where 52 and 9 are the total numbers of μ-decay events observed respectively for Pb and Fe in both our present and previous[2] experiments. Furthermore, the fact that none of such low-energy electrons has been found from Al, where 26 μ-decay events have been obtained, also supports the above conclusion that these electrons cannot be low-energy μ-decay positrons.

Slow electrons (10–100 kev) associated with μ mesons stopped in emulsions have been observed by Cosyns and co-workers[5] and by Fry.[6] These have been interpreted as Auger electrons ejected from the radiationless transitions of the μ mesons. The theory of the more energetic Auger transitions for μ-meson capture was first worked out by Wheeler[7] and more recently by Burbidge and De Borde[8] for the elements in photographic emulsions. The agreement with the experimental results is not too close, comparison being made, however, only on the basis of the small number of tracks so far observed.

As were the two previous cases interpreted in our former report,[2] the present four cases, where the electron appears at the end of the stopped meson, may also more satisfactorily be attributed to Compton recoil or photoelectron tracks, which are ejected by photons emitted in the interaction of the negative μ mesons with the nucleus. The energetic one [see Table I(d), last column] may be a Compton recoil ejected from a neighboring atom by a photon emitted either when the μ meson makes the 6-Mev $2p\rightarrow 1s$ jump, or when the μ-excited nucleus falls to the ground state. The 3 low-energy ones [see Table I(d), first column] may be Compton recoils ejected from the same foil by photons of the same group emitted from either the $2p\rightarrow 1s$ transition or the nuclear de-excitation, and the electron energy may be degraded to the lower value by radiation and ionization loss. Or, some of the tracks may be due to photons from the $3d\rightarrow 2p$ and $2s\rightarrow 2p$ transitions. The observed frequency corresponds roughly to one photon from each μ-meson capture (see the following section on multiplicity). Of course, the statistics of these oriented electrons from the same foil are poor, and one may not put too much weight on the figure estimated for the multiplicity in this case. However, it is not inconsistent, considering statistics, with more accurate result on multiplicity as calculated from the larger number of the μ-oriented electrons and pairs from other foils.

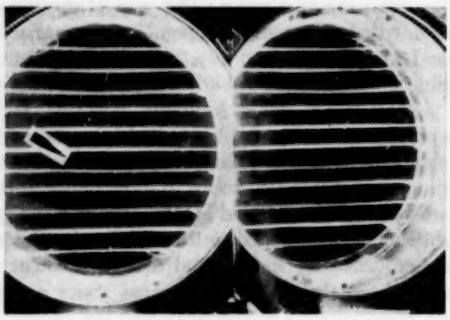

FIG. 2. The thin track between the sixth and seventh foils, as indicated by the arrow, appears to be oriented toward the end point of the stopped meson, which is the bent track ended at the fifth foil. It has the same age as the track of the stopped meson. It is very probably an electron ejected from the foil by a photon associated with the stopped meson. It is one of more than 20 similar cases so far observed (see Fig. 3) in the present experiments. The straight track through the chamber may be a faster μ meson or proton.

3. The μ-Oriented Electrons and Pairs Observed at a Different Foil

Figures 2 and 3 show 3 μ-oriented electrons and pairs out of the total 21 observed at foils different from those at which the negative μ mesons stop. In Fig. 2 a negative μ meson stops at the fifth Pb foil (0.018 inch), and in the gas space between sixth and seventh foils a thin track of *the right age*, presumably an electron track, is oriented toward the end point of the stopped meson. The energy of the electron is probably below 3 Mev. Figure 3 shows one oriented electron and one oriented pair both of the *right age* associated with one negative μ meson stopped at the fifth Pb foil (0.018 inch). The single electron between the second and third foils is reasonably assigned an energy below 2 Mev, while the pair between the eighth and ninth foils is estimated to have an energy of the order of 5 Mev. (See Table I.)

[5] Cosyns, Dilworth, Occhialini, Schoenberg, and Page, Proc. Phys. Soc. (London) **A62**, 801 (1949).
[6] W. F. Fry, Phys. Rev. **83**, 594 (1951).
[7] J. A. Wheeler, Revs. Modern Phys. **21**, 133 (1949); E. Fermi and E. Teller were the first to analyze the lower-energy Auger processes [Phys. Rev. **72**, 399 (1947)].
[8] G. R. Burbidge and A. H. De Borde, Phys. Rev. **89**, 189 (1953).

(i) *Angular Correlation*

The 21 oriented electrons and pairs which are found coming from the foils different from those where the negative mesons stop, have a definite angular correlation with the end points of the stopped mesons. As mentioned before, these 21 electrons and pairs have been found within a cone of half-angle $\sim 20°$ about the line joining the end point of the stopped meson to the beginning point of the electron. Practically it is not possible to determine a significant angular distribution of these tracks, because of the small number and because of the difficulty in measuring the angle due to small length of the tracks. Instead, we have counted the electron tracks within a similar cone in a direction perpendicular to the above line from the 81 pictures containing the stopped negative μ mesons. The number found in this way is about 6, which is much smaller than the 21 found in the forward cone and is about the "chance coincidence" of the stray tracks (see following). This is 6/21 as many tracks for about 6 times as much solid angle.

It is well known that the emission of a secondary electron (a pair or a Compton electron) produced by a high-energy photon has as its direction of preference the direction of the photon. The root-mean-square angle is of the order of magnitude of $[\langle\phi^2\rangle_{Av}]^{\frac{1}{2}} \propto mc^2/E$, where E is the energy of the primary photon and m the mass of the electron. For 6-Mev photons the expected spread in angle from this source is only about $\frac{1}{12}$ radian, negligible in comparison with the 20° or $\frac{1}{3}$ radian tolerance adopted in our definition of "μ-meson-oriented electron and pair." More important is the spread due to multiple scattering. To demonstrate this effect, we may estimate the root-mean-square *projected* angle of scattering of a 6-Mev electron in the foils from the following formula:[9]

$$[\langle\phi_{y}^{2}\rangle_{Av}]^{\frac{1}{2}} = (\zeta/2)^{\frac{1}{2}} 21/\beta cp, \qquad (1)$$

where ζ is the foil thickness in radiation units and βcp in Mev. The rms projected angles are thus found to be about 36° and 25° for the electrons in the thick (0.51-g/cm²) and thin (0.26-g/cm²) foils, respectively. These angles are of such a size as to make the observed spread in angles seem not too unreasonable. Thus, as will be seen, in calculating the multiplicity of the photons we have corrected the observed number of the oriented electrons and pairs for the spread in angles due to multiple scattering.

(ii) *Chance Coincidence of Stray Tracks; the Origins of the Photons*

To study the effect of the stray electron tracks, we took 575 pictures by using a single tray of counters. It is found from examining these 575 pictures that, on the average, there are about 13 stray electron tracks of the *right age* in each 10 pictures. The probability that such an electron track point accidentally toward or away from the end point of the stopped negative μ-meson track is approximately

$$1.3\times 2\times \pi(20/57.3)^2/4\pi \sim 6/80. \qquad (2)$$

By comparing this figure with 21/81, it becomes evident that the stray electrons are far from being able to account for the 21 μ-oriented electrons and pairs observed in our present experiments. To check the above calculation, we have re-examined the same roll of film to see how many of the stray electron tracks point (within a cone of half-angle $\sim 20°$) accidentally toward or away from an arbitrary point inside the chamber. It has been found that there are about 9 such tracks in 575 stray tracks, i.e., $9/575 \sim 1/63$, still smaller than 21/81.

It, therefore, seems to us that these 21 μ-oriented electrons and pairs found in the present experiments are much more reasonably interpreted in the same way as the other four electrons which are observed to be emitted from the end points of the stopped negative μ mesons. That is, they appear to be much better attributed to the photons from the two following sources: (1) the extra-nuclear transitions between the Bohr orbits by the incoming negative μ meson, and (2) the nuclear-de-excitation of the nucleus, to which a small fraction of the negative μ meson's rest energy has been imparted (see Part I) and which may have been left excited after the emission of 1 or 2 neutrons.[10] The energies of these electrons are compatible with those predicted in Wheeler's theory[11] and with those expected from the nuclear de-excitation (see our previous paper[2]

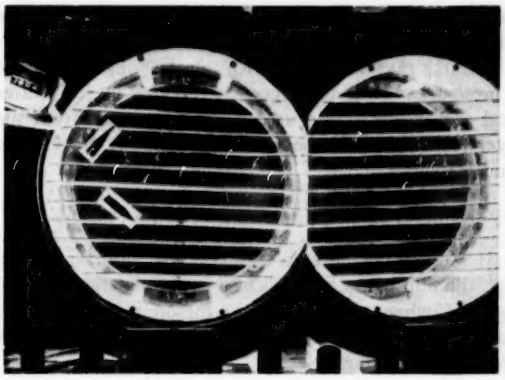

FIG. 3. A pair and a single electron, both of the same age as the track of the stopped meson are seen oriented toward the end point of the single stopped meson, which is ended at the fifth foil. They are indicated by the arrows in the direct view. The energy of the single electron may be below 3 Mev and that of the pair is probably about 5 Mev or less. They are very probably ejected by two photons emitted from the stopping of the negative μ meson (compare Fig. 2).

[9] B. Rossi, *High Energy Particles* (Prentice-Hall, Inc., New York, 1952), p. 68.

[10] M. F. Crouch and R. Sard, Phys. Rev. **85**, 120 (1952), and earlier papers of Sard and co-workers.

[11] J. A. Wheeler, Revs. Modern Phys. **21**, 133 (1949).

and the following discussion of multiplicity in this paper).

Gamma rays associated with the stopping of negative μ mesons have also been recently reported by Rainwater and co-workers,[12] who used a μ-meson beam from the cyclotron, and have been discussed briefly by Cooper and Henley.[13]

(iii) *The Mean Multiplicity of the Photons*

It is of importance to estimate the multiplicity, m, i.e., the number of photons of a certain energy actually emitted when one negative μ meson is stopped and captured by a nucleus. It may be calculated by the following equation:

$$Nmt/L=n/\sigma, \tag{3}$$

where N is the number of negative mesons stopped; t, the effective path traversed by the photons calculated as if the foil system consisted of spherical shells (see Table IV, Column I, Part I); L, the mean free path of the photon; n, the number of μ-oriented electrons and pairs of the corresponding energy actually observed, and σ is the ratio of this number to the total number, that would be expected from Gaussian distribution; i.e., σ is a correction for the multiple scattering of the electrons just ejected through the foil and will be called the M.S. correction factor. No correction is made for the angular spread of the electron emission involved in the processes of conversion from photons to electrons, the root-mean-square angle being only of the order of 6°.

It may be noted that the application of multiple scattering theory to the present case cannot be too significant statistically, because, in the first place, the number of the oriented electrons and pairs observed is small, and secondly, the energies of these electrons have been only roughly estimated. Moreover, only a crude estimate has been made for the value of t. However, it may be still possible and of interest to get a general idea, however crude it may be, of the multiplicity as a check on the origin of these photons.

As mentioned before, the rough energy distribution of the electrons as shown in Table I(d) has indicated a general trend towards a maximum around 5 Mev. Therefore, for the convenience in calculating the photon multiplicity, we may take all of the 21 electrons and pairs as having an energy of 5 Mev corresponding approximately to the photons from the $2p\rightarrow 1s$ transition. Of course, part of these may come from the nuclear de-excitation and also probably from the other extra-nuclear orbital transitions such as $3d\rightarrow 2p$ and $2s\rightarrow 2p$. To calculate the M.S. correction factor, σ, we have to calculate first the root-mean-square total angle[9] of multiple scattering of the electrons in the foils, which may be obtained from a formula similar to Eq. (1):

$$[\langle\phi^2\rangle_{Av}]^{\frac{1}{2}}=21\xi^{\frac{1}{2}}/\beta cp, \tag{4}$$

where ξ is half the foil thickness in radiation units, assuming the electron to be emitted from this point and βcp in Mev. It is found that $[\langle\phi^2\rangle_{Av}]^{\frac{1}{2}}=46°$ for a thick foil (0.51 g/cm²) and 32° for a thin one (0.26 g/cm²). The root-mean-square value of these two angles is about 41°, allowing for the fact that about $\frac{2}{3}$ of the electrons and pairs are emitted from the thick foils and $\frac{1}{3}$ from the thin ones. The value of σ corresponding to $[\langle\phi^2\rangle_{Av}]^{\frac{1}{2}}=41°$ is found to be about 0.39; i.e., the number counted within a cone of half-angle approximately 20° includes only 0.39 of the total area under the Gaussian curve. The effective path length $t\sim 2.57$ g/cm² (see Table IV, column 2 and footnote in Part I); $L\simeq 20$ g/cm², $N=81$; $n=21-6=15$, where 6 is assumed to be the maximum possible number of the stray tracks. Hence, the multiplicity is found to be

$$m=\frac{15}{0.39}\times\frac{20}{81\times 2.57}\simeq 3.5. \tag{5}$$

As to the multiplicity of the photons absorbed in the same foil in which the meson is stopped (as discussed at the end of Sec. 2), it may be estimated as follows: Taking 22 g/cm² as the mean free path of a (2–4 Mev) photon and one g/cm² (corrected for the secθ effect) as the average path traversed in the stopping foil, one would then expect one secondary electron emitted at the same foil from a total of about 22 stopped negative μ mesons, or 4 in 88. In order to compare with the observed 4 in 81, it is sufficient to assume, on the average, only about one such photon emitted per negative μ-meson capture. Actually, one would expect two photons (instead of one) per stopped meson, namely one from the $2p\rightarrow 1s$ transition and another from the nuclear rearrangement. The figure one as estimated above is not inconsistent, within the poor statistics, with the figure two that would be expected.

The total multiplicity obtained from the two cases is, therefore, 4.5 per negative meson stopped with a probable uncertainty of a factor of 1.5 ± 1.

A total multiplicity of around 5 seems fairly reasonable, if one allows for the crudeness of the calculation, for two photons may satisfactorily be attributed to the extra-nuclear origin[11]—transition between the Bohr orbits, such as $2p\rightarrow 1s$ and $3d\rightarrow 2p$—and two or three to the nuclear de-excitation. A photon multiplicity of 2 for the nuclear rearrangement radiation does not seem to be incompatible with the nuclear models usually used.[14]

It may be noted that, using cosmic ray μ mesons, Hincks[15] (counting method) and more recently Harris and Shanley[14] (cloud chamber in a magnetic field) have

[12] James Rainwater, Phys. Rev. **90**, 349 (1953); V. L. Fitch and J. Rainwater, Phys. Rev. **92**, 789 (1953).
[13] L. N. Cooper and E. M. Henley, Phys. Rev. **91**, 480 (1953); **92**, 801 (1953).
[14] G. Harris and B. Shanley, Phys. Rev. **89**, 983 (1953).
[15] E. P. Hincks, Phys. Rev. **81**, 313 (1951).

TABLE II. Number of mesons arriving per second at sea level within a unit solid angle about the vertical, and stopped in one gram of Pb.

Experiments	Working period, sec	Effective solid angle,[a] sterad	Material	Grams in chamber	Equivalent[b] in grams of Pb	Number of mesons stopped (+ and −)	Number stopped per gram Pb per sec per sterad
Previous	3.35×10^6	0.011	Pb	5.6	5.6	44	1.4×10^{-6}
Previous	3.74×10^6	0.019	Al	0.76	1.5	23	1.4×10^{-6}
Present	5.40×10^6	0.027	Pb	4.3	4.3	151	1.2×10^{-6}
Present	5.04×10^6	0.027	Al	0.88	1.7	68	1.5×10^{-6}
George and Evans[c]							4×10^{-6}air(2×10^{-6})[d]
Rossi[e]							4.6×10^{-6}air(2.3×10^{-6})[d]

[a] The solid angle Ω is calculated from $\Omega=N/(I_v A)$; N = observed number of all mesons (fast and slow) entering the telescope and the foil system per sec. N is 45/(3600) and 85/(3600) for Pb and Al, respectively, in the previous experiments and 150/(3600) in the present experiments. A is the average area of the foils ~150 cm² and 200 cm², respectively, for the previous and present experiments. I_v is the vertical intensity of hard component at sea level $=0.83\times10^{-3}$ cm^{-2} sec^{-1} sterad^{-1}. See reference e.

[b] Specifically, 0.85 g of Al has the same stopping power for 10-Mev mesons as 1.6 g of Pb. See reference d. 10 Mev is the typical energy of a meson which will stop in a foil half-way through the chamber.

[c] E. P. George and F. Evans, Proc. Phys. Soc. (London) **A63**, 1249 (1950).

[d] See reference 4.

[e] B. Rossi, Revs. Modern Phys. **20**, 537 (1948).

also confirmed the existence of these (1–5 Mev) gamma rays associated with the stopping of μ mesons.

Our results, analyzed along the above lines, seem to indicate that the total gamma-ray energy emitted per negative μ meson stopped in Pb may be about 15 Mev (tentatively, we assume, on the average, two 5-Mev lines and two 2.5-Mev lines emitted from each stopped negative meson). This figure is somewhat larger than the values obtained by Hincks[15] and by Harris and Shanley.[14] Assuming that about half of this total energy comes from the nuclear de-excitation, and taking the fact that usually about two neutrons[10] with kinetic energy presumably about 3 Mev each are emitted (very rarely a slow proton), then the energy imparted to the Pb nucleus by the captured negative μ meson is probably $2(3+6)+7+3=28$ Mev, where the number 6 in the parenthesis is the binding energy in Mev in Pb of a neutron and the last number 3 is the energy in Mev required to change Pb^{208} to Tl^{208}.

III. ABSOLUTE COUNTING RATE

To get a supplementary check that the experimental setup was operating correctly, we can calculate back from the total number of mesons stopped in the foils, from the working period, from the mass and atomic number of the stopping foils, and from the solid angle, and obtain a value for the absolute rate of stopping of mesons, in the present and the previous experiments for both Pb and Al. The results of such a calculation are presented in Table II, the values for the absolute stopping rate being given in the last column. The experimental results obtained by George and Evans (originally for emulsion and converted by these authors to values for air) and by Rossi (from analysis of many data) are included. For comparison with our own results, we have converted these workers' results to values for Pb as shown in parentheses. The consistency of our rates with each other and with the values of the other investigators is better than expected and does encourage belief that the μ mesons stopped in Pb and Al have received an unbiased investigation. Our rates are systematically smaller than those of George and Evans and Rossi, the average being about 30 percent smaller than the average of the two groups. This difference may easily be attributed, in addition to statistical error in our case, to the errors involved in estimating the effective working periods and solid angles in our experiments and in the conversion of stopping power from one element to another.

These experiments were completed at Princeton in 1949. The writer would like to take this opportunity to express his gratitude to his colleagues in the Cosmic Ray Laboratory at Princeton for their help in various ways, and, in particular, to Professor J. A. Wheeler for his enthusiastic support and profitable discussion in this work, and to Dr. J. R. Winckler, now at the University of Minnesota, for his valuable help in building the electronic controls. He also wishes to express his sincere thanks to Professor K. Lark-Horovitz, Head of the Physics Department at Purdue University, for his interest and support in the study of elementary particles.

Low-Energy Events in Cosmic Radiation

L. Reiffel and G. M. Burgwald
Armour Research Foundation of Illinois Institute of Technology, Chicago, Illinois
(Received May 6, 1954)

The intensity of low-energy events in the cosmic radiation has been examined as a function of altitude with an energy gated scintillation counter. Events selected were those giving pulses the equivalent of 0.2-Mev to 2.0-Mev electron energy loss in the scintillation crystal. Compared with data for total radiation, the present results show a shift toward lower altitudes by an almost constant fraction of a radiation length.

OBSERVATIONS have been made on the distribution with altitude of low-energy interactions between cosmic rays and a Harshaw NaI(Tl) scintillation crystal. Six balloon flights at geomagnetic latitude 39.8° north were made during a 14-day period. The resulting altitude curve obtained by averaging all data is shown in Fig. 1 together with a normalized curve for the omnidirectional total flux at 38.5° north as registered by a balloon electroscope.[1]

The low-energy events in the 1½-in. diameter by 2 in. long crystal were selected by means of fixed differential pulse-height discriminators in the balloon units. The circuitry was set to accept pulses corresponding to between 0.2-Mev and 2.0-Mev energy loss. The counting rate so obtained results primarily from the intense low-energy gamma-ray component[2] for which the crystal has high detection efficiency.[3] A smaller contribution is due to grazing collisions with energetic charged particles.

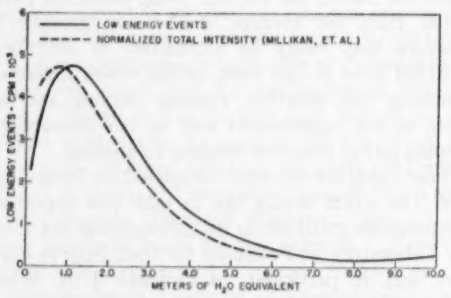

FIG. 1. Low-energy events *vs* altitude.

The gamma rays represent the low-energy end of the cascade process further degraded by multiple Compton scattering. It is of interest to note that the Pfotzer maximum for low-energy events occurs at 1.08 meters of water equivalent or approximately 51 900 feet pressure altitude, while the data of Millikan indicate a maximum for total radiation at 0.76 meters of water equivalent or 60 000 feet pressure altitude. This shift in the position of the maximum is considered to be well established since the mean deviation for six flights was only 1500 feet.

In essence, the low-energy distribution retains all features of the gross radiation curve and is of almost identical shape, but is shifted deeper into the atmosphere by slightly less than one radiation length. Such behavior is indicative of the very small dependence of the degradation of the soft component on the history of the cascade. It is presumed that a cascade theory including multiple Compton scattering and possibly the energy dependence of ionization loss would account for these results. The rise in counting rate between eight and ten meters is, of course, due to the natural radioactivity of the earth and lower atmosphere.

The authors are indebted to Mr. J. C. Beynon for assistance in these experiments.

[1] Millikan, Neher, and Pickering, Phys. Rev. **66**, 295 (1944).

[2] Rest, Reiffel, and Stone, Phys. Rev. **81**, 894 (1951).

[3] Reiffel, Stone, and Rest, Phys. Rev. **82**, 121 (1951).

Total Cross Section for Charge Exchange Scattering of π^- Mesons by Hydrogen at 42, 30, and 20 Mev*

W. J. Spry
Physics Department, University of Rochester, Rochester, New York
(Received April 30, 1954)

A measurement of the total cross section for the reaction $p(\pi^-,\pi^0)n$ has been made at three energies using polyethylene and carbon targets in a difference experiment. The values obtained for the cross sections are $\sigma(42\text{ Mev})=6.9\pm1.2$ mb; $\sigma(30\text{ Mev})=5.7\pm0.9$ mb; and $\sigma(20\text{ Mev})=5.0\pm0.8$ mb. The results are analyzed under the assumption of charge independence in an attempt to determine the energy dependence of the *S*-wave phase shifts.

INTRODUCTION

Cross sections for charge-exchange scattering of π^- mesons by hydrogen, $(\pi^-+p\rightarrow\pi^0+n)$, have been measured at 120 and 144 Mev by Anderson *et al.*[1] and at 65 Mev by Bodansky *et al.*[2] The total cross section has also been measured at 34 Mev by Roberts and Tinlot.[3] This experiment was a continuation of the latter work with the intent of measuring the energy dependence of the total cross section at the mean meson energies of 42, 30, and 20 Mev in the laboratory system.

Both single and double photon coincidences were detected from the π^0 decay, $(\pi^0\rightarrow2\gamma)$, but the total cross sections were computed from the much larger yield of single photons. At these meson energies the resultant single-photon angular distribution is only slightly affected by the initial π^0 angular distribution, and this permits measuring the total cross section without a detailed knowledge of the π^0 differential scattering behavior.

In the process of measuring the hydrogen cross section some data were collected concerning charge-exchange scattering of π^- mesons by carbon. Here only those events in which both decay photons were detected could be assigned unambiguously to π^0 decay.

EXPERIMENTAL ARRANGEMENT

The hydrogen cross sections were measured by doing a difference experiment with polyethylene and carbon targets. The experiment utilized an external 50-Mev meson beam produced in the 240-Mev Rochester cyclotron by protons impinging on an aluminum target. This beam was moderated to the appropriate energies by absorbers and was focused both vertically and horizontally by two focusing magnets. Figure 1 shows the general arrangement of the focusing magnets, shielding, and counter assembly with relation to the cyclotron.

Counter Assembly and Targets

The procedure with either target consisted of measuring two counting rates: first, the flux of mesons incident on the target; and second, the number of gamma rays that emerged from the target in coincidence with incoming mesons. A single meson telescope performed the first task, while the gamma rays were detected by three gamma telescopes arranged symmetrically around the target.

Figure 2 shows two views of this counter assembly. The meson telescope consisted of two scintillation counters, No. 1 and No. 2. The three gamma telescopes each consisted of two scintillation counters also and are numbered No. 4 through No. 9. For clarity the side view omits two of these three telescopes.

In order to reduce the background it was necessary to subtract those mesons from the beam which did not interact in the target and to shield the gamma telescopes from ionizing particles produced by meson stars in carbon. Counter No. 3 does this by being placed in anticoincidence with the other counters. It was a "bucket"-shaped scintillation counter that surrounded the target in all but the forward direction.

The targets were chosen to have equal stopping power for π^- mesons. This choice was made because the differ-

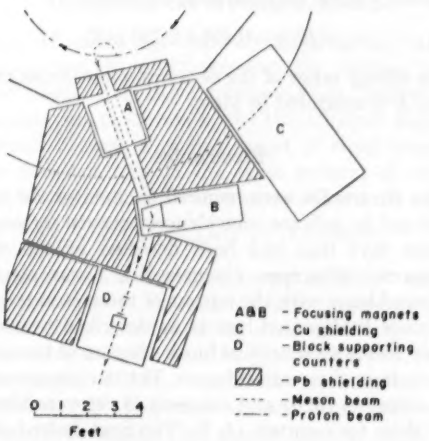

FIG. 1. General arrangement of the apparatus and shielding.

* This work was supported by the U. S. Atomic Energy Commission.

[1] Anderson, Fermi, Martin, and Nagle, Phys. Rev. **91**, 155 (1953).

[2] Bodansky, Sachs, and Steinberger, Columbia University, Nevis Cyclotron Laboratories, Nevis 1, 1953, Phys. Rev. **93**, 1367 (1954).

[3] A. Roberts and J. Tinlot, Phys. Rev. **90**, 951 (1953).

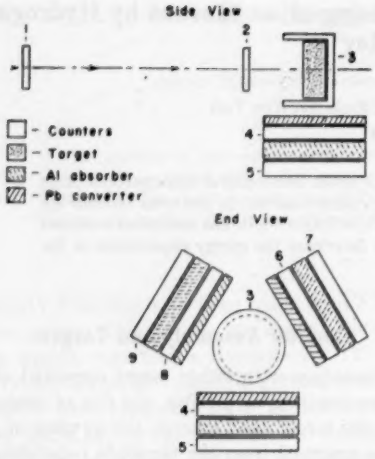

FIG. 2. Counter assembly.

ence in energy loss in passing through CH_2 and C targets with equal numbers of carbon nuclei is not negligible at the mean meson energy of 20 Mev. In this energy range the cross section for charge-exchange scattering in carbon might vary rapidly since the kinematic threshold is 12 Mev in the laboratory system. Table I shows the energy spread through the targets for the various mean meson energies.

Gamma-Ray Telescopes

The gamma-ray telescopes detect photons by virtue of electron showers produced in lead converters. They were designed so that Wilson's[4] "Monte Carlo" results could be applied, that is, the two elements of each telescope were separated by an aluminum absorber that cut-off electrons of less than 8-Mev energy. Using Wilson's results the efficiency of the telescopes (when sensitive to minimum ionization particles) *versus* gamma-ray energy could be approximated closely by

$$\epsilon(E) = -0.494 + 0.228 \ln E,$$

in the energy range of the decay photons in this experiment. E is measured in Mev.

Electronics

The electronics were required to monitor the meson beam and to indicate coincidences between mesons and gamma rays that had been detected in one of the gamma-ray telescopes. Counter No. 3 was placed in anticoincidence with the output of the meson telescope to reduce background counts as described previously. Figure 3 shows a simplified block diagram of the circuits used to form these coincidences. The circuits associated with counters (6, 7) and counters (8, 9) were identical with those for counters (4, 5). The final desired coincidence was among counters (1, 2, $\bar{3}$) plus either (4, 5) or (6, 7) or (8, 9). The bar above 3 indicates anticoincidence.

Variation of the cyclotron beam intensity made it necessary to subtract random coincidences at the same time that the data were being recorded. This was done by connecting the output of each gamma telescope to one input of each of two coincidence circuits. These coincidence circuits had approximate resolving times of 3×10^{-8} and 5×10^{-7} second, respectively. The common (1, 2, $\bar{3}$) output pulse was split also and fed to the other input of each of these circuits. Prior to entering the slow circuit the (1, 2, $\bar{3}$) pulse was delayed sufficiently so that true counts produced no output. The observed counting rate in the slow circuit divided by the known ratio of resolving times between the two circuits gave the random rate in the fast circuit.

When both decay photons from a π^0 meson were detected in two separate gamma-ray telescopes the event was recorded on a separate scaler by using a "threefold and two" Garwin[5] circuit that is not indicated in the simplified block diagram. The output pulses from counters (1, 2, $\bar{3}$, 4, 5), from (1, 2, $\bar{3}$, 6, 7), and from counters (1, 2, $\bar{3}$, 8, 9) were connected to the three input grids of this circuit. This Garwin coincidence circuit was similar to the other coincidence circuits except that the plate load resistances were adjusted to produce an output when any two of the three grids were negatively pulsed. The output from this circuit provided evidence of true π^0 decay and gave the only plausible information about charge-exchange scattering in carbon.

PROCEDURE

Calibration of the Counters

The meson rate was sensitive to the current through the focusing magnets and this was adjusted for a maximum flux at the start of each operating period. The photomultiplier voltages for counters No. 1, No. 2, and No. 3 were then adjusted until plateaus of meson rate *versus* counter voltages were determined for each counter.

The energy of the meson beam was measured by range curves with the absorbers placed in front of counter No. 3. The beam was contaminated by several sources and it was not possible to determine accurately either the nature or the amount of beam contamination from range curves alone. This contamination also could have changed from one operating period to the next or

TABLE I. Meson energies at the target, in Mev.

Nominal energy	Incident energy	Outgoing energy
42	45.6	39.0
30	34.0	26.0
20	25.0	14.5

[4] R. Wilson, Phys. Rev. **86**, 261 (1952).

[5] R. Garwin, Rev. Sci. Instr. **21**, 569 (1950).

even during a single period. From the tails of the range curves, however, it was estimated that the total contamination was 18±7 percent, and it was assumed that the associated error was sufficient to account for any fluctuation throughout the experiment.

The sensitivity of the gamma-ray telescopes to minimum ionization particles was determined by their response to cosmic rays. Each counter was first tested for uniform sensitivity over its entire volume by using a collimated gamma-ray source. Each telescope then was calibrated by placing it between two smaller test counters so that every cosmic-ray particle that passed through the two test counters would also pass through it. All of the counters could be set at voltages such that the telescopes were 98±2 percent efficient for minimum ionization particles. In operation these telescopes were in the presence of strong radiation from the cyclotron and checks were made to show that there were no efficiency losses due to dead time or pileup in the circuits.

Reliability of the Data

During each operating period the targets and meson energies were changed at roughly hour intervals and no set pattern was followed. The number of counts for a given energy and target were always compared with the mean of previous runs, and no drifts ever were noticed that could not be explained by statistical variation. A "column" check also was possible since three separate gamma telescopes were used. If the three telescopes remained equally sensitive throughout the experiment then the total number of true counts recorded by any telescope should equal the total recorded by any other. The "column" totals for the three telescopes were equal within statistics.

All of the data also were analyzed for random variation about their mean values. This required plotting the deviation, run by run, of the rate recorded in each run from the mean rate for that target and energy. This was done for all targets and energies and finally all such plots were adjusted to the same scale. The expected second moment of the resulting distribution on this scale was 3.5. The actual second moment of the distribution was 3.6. The first moment of the distribution was zero within statistics. It is believed that there was no long term drift or any erratic excess or deficiency of counts due to unstable operation of the apparatus.

TABLE II. The corrected experimental data in counts per million mesons.

Period	CH_2	C	0
	42-Mev meson energy		
4	116.0±7.0	83.0±7.0	29.0±12.0
5	124.0±6.0	87.0±6.0	37.0± 7.0
	30-Mev meson energy		
Period	CH_2	C	0
4	85.4±8.5	66.4±7.2	12.0± 7.0
5	86.2±3.8	50.0±4.2	20.0± 5.0
6	88.5±3.9	59.2±4.4	25.0± 4.0
	20-Mev meson energy		
Period	CH_2	C	0
4	67.0±4.9	47.2±3.6	10.0± 4.0
5	76.5±3.3	40.3±3.2	21.0± 5.0
6	68.3±5.7	44.7±6.7	18.0± 8.0

Column headings show the target material and the operating period. CH_2 refers to counts obtained with a CH_2 target. C refers to counts obtained with a C target. 0 refers to counts obtained with no target in place.

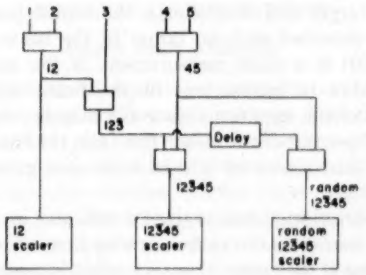

FIG. 3. Simplified block diagram of electronics. Circuits associated with counters (6, 7) and (8, 9) are identical to those used with counters (4, 5).

ANALYSIS OF THE DATA

The data were analyzed in three steps. First, the counts due to carbon nuclei and other spurious effects were subtracted from the number of counts obtained with the CH_2 target to obtain the total hydrogen effect. Second, the number of counts due to the competing process $p(\pi^-,\gamma)n$ were subtracted from the total hydrogen effect. Finally, the gamma-ray distribution that results from the initial π^0 distribution at 40 Mev[6] was obtained from the kinematics of π^0 decay. This distribution, weighted by the telescope efficiency *versus* gamma-ray energy and integrated over the surfaces of the telescopes, transforms the counting rate for charge exchange to a cross section.

Computing the Hydrogen Effect

Table II shows the data obtained during various operating periods after correction for random background counts and beam contamination. Subtracting the counts due to carbon in the polyethylene target is not direct because a carbon target of equal stopping power does not contain the same number of carbon nuclei. The subtraction was done as follows:

$$N_{H\gamma}=N(CH_2)-\alpha N(C)-(1-\alpha)N(0).$$

$N_{H\gamma}$ equals the number of counts per million π^- mesons due to hydrogen in the polyethylene target. α equals the ratio of the number of carbon nuclei in the polyethylene target to the number of carbon nuclei in the carbon target. $N(CH_2)$ equals the total number of counts from the polyethylene target per million π^- mesons. $N(C)$ equals the similar number from the

[6] A. Roberts and J. Tinlot, Phys. Rev. **94**, 766 (1954).

carbon target and $N(0)$ equals the counts per million mesons recorded with no target in the beam. In this case $N(0)$ is a valid measurement of the number of counts due to interactions of the beam with other sections of the apparatus since the targets remove less than 2.7 percent of the meson flux from the beam. In all cases a lead converter is used with each gamma telescope.

This description has omitted a difficulty in subtracting the counts due to carbon arising from second-order scattering in the target. One such effect is meson-carbon scattering followed by capture in a carbon nucleus. This can occur whenever the scattered meson has insufficient range to escape from the target in its new direction. This effect might invalidate the method described for subtracting counts due to carbon since it is not proportional to the number of carbon nuclei present. It is energy dependent because at low energies a greater fraction of the first scattered mesons will have insufficient range to leave the target. Counter No. 3 discriminated against this, however, by cancelling meson produced stars in carbon, and it was demonstrated during the experiment that with counter No. 3 in operation this effect was negligible.

A similar effect occurs when a scattered meson is subsequently captured by a hydrogen nucleus in the CH_2 target. To determine the magnitude of this effect the number of mesons that scatter and stop in the target was estimated from the data of Byfield, Kessler, and Lederman.[7] The number of such stopped mesons that were captured by a hydrogen nucleus was determined experimentally.[8] This effect produced approximately a 4 percent correction to the observed hydrogen effect.

The observed counting rate from hydrogen also will be increased at the 20-Mev point by those mesons that stop in the target due to ordinary range straggling. The report of Caldwell[9] was used to estimate this effect and the required correction was negligible.

Correcting for the Reaction $p(\pi^-,\gamma)n$

An estimate of the effect of the competing reaction $p(\pi^-,\gamma)n$ was made. The results of Jacobson, Schulz, and White[10] indicate that for the purpose of this correction the cross section for the reaction $p(\gamma,\pi^+)n$ can be considered equal to the cross section for the reaction $n(\gamma,\pi^-)p$. Detailed balancing, this assumption, and the results of Bernardini[11] for the reaction $p(\gamma,\pi^+)n$ at the appropriate energies make it possible to compute the required correction. This process is responsible for approximately a 5 percent correction to the results at each energy.

[7] Byfield, Kessler, and Lederman, Phys. Rev. **86**, 17 (1952).
[8] The observed probability for the capture of a π^- meson by a hydrogen nucleus in CH_2 was 0.3 ± 0.2 percent.
[9] D. Caldwell, Phys. Rev. **88**, 131 (1952).
[10] Jacobson, Schulz, and White, Phys. Rev. **88**, 836 (1952).
[11] G. Bernardini, Phys. Rev. **93**, 930 (1954).

Kinematics of Charge-Exchange

The resultant gamma-ray distribution was computed for arbitrary S and P wave scattering distributions of the π^0 mesons. If the initial π^0 distribution is expressed in the form

$$J(\theta')d\Omega' = \sum_l a_l P_l(\cos\theta')d\Omega',$$

in the center-of-mass system, it can be shown that the resultant gamma-ray distribution in the center-of-mass system is of the form:

$$I(\theta',E')dE'd\Omega' = \sum_l (2\pi\beta\gamma\mu)^{-1} a_l P_l(\cos\theta') \times P_l\left(\frac{1}{\beta}-\frac{\mu}{2\beta\gamma E'}\right)dE'd\Omega'.$$

The decay gamma rays fall between the energy limits

$$\tfrac{1}{2}\mu\gamma(1-\beta) \le E' \le \tfrac{1}{2}\mu\gamma(1+\beta).$$

μ is the rest energy of the π^0 meson ($\mu=138$ Mev). βc is the velocity of the π^0 meson in the center-of-mass system, and $\gamma=1/(1-\beta^2)^{\frac{1}{2}}$. $I(\theta',E')$ is normalized to one π^0 meson (two gamma rays).

The probability of observing a π^0 meson by detecting one of its decay photons in a gamma telescope is given by

$$\text{Eff.} = \int_{\Omega'} d\Omega' \int_{E'} I(\theta',E')\epsilon(E')dE'.$$

All integrations are to be carried out in the center-of-mass system. $\epsilon(E')$ is the detection efficiency of a gamma telescope *versus* gamma-ray energy. In order to reduce the labor involved this integral was approximated by

$$\text{Eff.} = \int_{\Omega} d\Omega \int_{E'} I(\theta,E')\epsilon(E')dE'.$$

The unprimed quantities refer to the laboratory system. The coefficients associated with $I(\theta,E')$ were those of the π^0 distribution as it appeared in the laboratory system, $J(\theta)=\sum_l a_l P_l(\cos\theta)$. These were obtained from the observed $J(\theta')$ for 40-Mev π^- mesons.[6] The approximate solution for a 40-Mev π^- meson differed by less than 1 percent from the exact solution in the center-of-mass system.

The distribution of the meson flux over the target surface normally needs to be applied as a weighting factor in computing telescope efficiencies. In this case, however, due to the location of the gamma telescopes the average solid angle did not vary greatly over the surface of the target. The resultant error introduced by any reasonable flux distribution was less than ±1 percent.

The effect of the actual π^0 distribution measured at 40 Mev has been used in computing the value of the cross section at 42 Mev. The same π^0 distribution applied at 30 Mev and 20 Mev raises these cross

sections 1 percent and 0.6 percent, respectively, over the cross sections obtained by assuming an isotropic π^0 distribution. At 30 and 20 Mev the cross sections were computed on the basis of the 40-Mev π^0 distribution and the percentage change between this value and that obtained for an isotropic π^0 distribution was assigned as an additional error.

Errors and Corrections

Two sets of errors must be attached to the cross sections. Each measurement can be used singly as an absolute value or the three values can be considered together as a relative measurement of the energy dependence.

Each cross section as an absolute value was assigned the following major sources of error in addition to those already discussed: (1) Statistical fluctuations contribute a standard deviation of ± 10 percent at each energy. (2) It is assumed that the detection efficiencies of the gamma telescopes *versus* gamma-ray energy are known within ± 10 percent. (3) From range curves it is estimated that the uncertainty in the mean meson energies is ± 2 Mev at each point.

If the three cross sections are considered together as a relative measurement of the energy dependence only the statistical standard deviations produce a significant contribution to the error.

In addition to those previously mentioned the following corrections were also applied to the data: (1) A correction of 3 percent for gamma conversion in the target. (2) A correction of 1.5 percent for the alternate mode of π^0 decay.[12]

Results

With the preceding corrections and assigned errors the total cross sections for hydrogen are:

6.9 ± 1.2 mb at 42 ± 2 Mev,

5.7 ± 0.9 mb at 30 ± 2 Mev,

5.0 ± 0.8 mb at 20 ± 2 Mev.

The errors refer to each value as an absolute measurement.

Charge-Exchange Scattering in Carbon

A rough estimate of charge-exchange scattering in carbon could be determined from the number of double photon coincidences observed with a carbon target. It can be estimated roughly that the ratio of the number of detected double photons from charge exchange in carbon to the total cross section in carbon is the same as the similar ratio for scattering in hydrogen. Using the ratio observed for hydrogen the order of magnitude of the total cross section in carbon is 8 mb at 42 Mev, 6 mb at 30 Mev, and 3 mb at 20 Mev.

[12] Lindenfield, Sacks, and Steinberger, Phys. Rev. **89**, 531 (1953).

DISCUSSION OF THE RESULTS

Phase Shift Analysis

The experimental results for hydrogen can be discussed in terms of a phase shift analysis. Two assumptions are made: (1) only S- and P-wave scattering contribute appreciably and (2) the total isotopic spin is a good quantum number. Under these assumptions all meson-nucleon interactions in the appropriate energy range can be explained in terms of six phase shifts. The notation of Ashkin[13] is used to describe these phase shifts. In this notation all states of isotopic spin $T=\frac{3}{2}$ are designated by β_J^L and all states with $T=\frac{1}{2}$ by α_J^L. $\alpha_{\frac{1}{2}}^1$ is the $T=\frac{1}{2}$, $J=\frac{3}{2}$, and $L=1$ state.

Anderson *et al.*[1] analyzed their data in the region of 120 Mev in terms of a phase shift analysis and gave "first solutions" for the six phase shifts at each of their energies. These solutions have an energy dependence for $\beta_{\frac{1}{2}}^1$ of $16^\circ\ \eta'^3$ while $\beta_{\frac{1}{2}}^1$, $\alpha_{\frac{1}{2}}^0$, and $\alpha_{\frac{1}{2}}^1$ have values less than $\pm 6^\circ$. $\eta'=p'c/\mu_0c^2$, μ_0c^2 is the rest energy of a $\pi^\pm$ meson, and p' is the momentum of the π^- meson in the center-of-mass system. If these solutions are assumed to be correct in the region of 120 Mev then the following approximations can be made at lower energies: (1) Since $\beta_{\frac{1}{2}}^1$, $\alpha_{\frac{1}{2}}^1$, and $\alpha_{\frac{1}{2}}^1$ are small it is a reasonable first approximation to set these three phase shifts equal to zero in the energy range between 20 and 42 Mev. (2) It is assumed that $\beta_{\frac{1}{2}}^1=16^\circ\ \eta'^3$ in this lower-energy interval. (3) With this assumed energy dependence for $\beta_{\frac{1}{2}}^1$ it is a consistent further assumption that $\beta_{\frac{1}{2}}^0-\alpha_{\frac{1}{2}}^0$ is proportional to η' at sufficiently low energies.

With these assumptions the cross sections from this experiment were used to solve for the energy dependence of $\beta_{\frac{1}{2}}^0-\alpha_{\frac{1}{2}}^0$. The values obtained at 20, 30, and 42 Mev were $-(16.2^\circ)\eta'$, $-(16.7^\circ)\eta'$, and $-(16.6^\circ)\eta'$, respectively, with an average value of $(-16.5^\circ \pm 1.5^\circ)\eta'$. The limits assigned to the average value correspond to the two values of $\beta_{\frac{1}{2}}^0-\alpha_{\frac{1}{2}}^0$ for which the resulting predicted cross sections fall outside the assigned experimental errors of any cross section. A total cross section for charge exchange of $(4.4 \pm 0.9)v_0/v$ millibarns is predicted if this energy dependence of the phase shifts is extrapolated to very low energies. v_0 is the relative velocity of the π^0 meson and the neutron while v is the relative velocity of the π^- meson and the proton.

CONCLUSIONS

A discrepancy exists if the present results are extrapolated to the energy of Panofsky's[14] experiment under the assumption that $\beta_{\frac{1}{2}}^0-\alpha_{\frac{1}{2}}^0$ remains proportional to η'. This has been discussed by Fermi[15] for an extrapolation of $\beta_{\frac{1}{2}}^0$ and $\alpha_{\frac{1}{2}}^0$ under the same assumption. The extrapolation predicts a capture rate for charge exchange from the lowest Bohr orbit of hydrogen. From

[13] J. Ashkin and S. Vosko, Phys. Rev. **91**, 1248 (1953).
[14] Aamodt, Hadley, and Panofsky, Phys. Rev. **81**, 565 (1951).
[15] H. Anderson and E. Fermi, Phys. Rev. **86**, 794 (1952).

the results of this experiment $R=\sigma_0 v/\pi b^2=(1.0\pm0.2)\times10^{15}$ sec^{-1} if the limits placed on $\beta_{\frac{1}{2}}^0-\alpha_{\frac{1}{2}}^0$ are taken seriously. This assumes the radius of the mesonic Bohr orbit $b=2.2\times10^{-11}$ cm and that $v_0=8\times10^9$ cm/sec; $\sigma_0=(8\pi/9k^2)(v_0/v)(\beta_{\frac{1}{2}}^0-\alpha_{\frac{1}{2}}^0)^2$. Panofsky's experiment shows that this capture rate should equal the capture rate for the competing process $p(\pi^-,\gamma)n$.

Bernardini[11] has discussed the cross sections for $p(\gamma,\pi^+)n$, $d(\gamma,\pi^+)2n$, and $d(\gamma,\pi^-)2p$ for E_γ between 170 and 190 Mev in the laboratory system. If it is assumed that the ratio of π^- to π^+ production obtained from the second reaction is the same as the photoproduction ratio between the free neutron and free proton then the principle of detailed balance and this ratio can be used to predict the corresponding cross sections for $p(\pi^-,\gamma)n$. If these cross sections are extrapolated to the energy of Panofsky's experiment Bernardini obtains a capture rate that requires the initial slope of $\beta_{\frac{1}{2}}^0-\alpha_{\frac{1}{2}}^0$ to be $\pm(9.2°)\eta'$ in contrast to the value of $-(16.5°)\eta'$ obtained from this experiment.

Bethe and Noyes[16] have given an argument to explain this discrepancy in terms of Marshak's[17] suggestion. In brief this argument assumes that the slope of $\beta_{\frac{1}{2}}^0-\alpha_{\frac{1}{2}}^0$ obtained from this experiment cannot be extrapolated to the energy of Panofsky's experiment, but that this initial slope is $\pm(9.2°)\eta'$. They then fit this initial slope and the data of this experiment with a smooth curve for $\beta_{\frac{1}{2}}^0-\alpha_{\frac{1}{2}}^0$ *versus* η'. When the values of $\beta_{\frac{1}{2}}^0$ and $\alpha_{\frac{1}{2}}^0$ from higher energies are extrapolated with this restriction on their difference, it is difficult to fit the data without assuming that $\alpha_{\frac{1}{2}}^0$ varies less rapidly than η' and that $\beta_{\frac{1}{2}}^0$ varies more rapidly than η' in the energy region between 20 and 42 Mev. For the most probable fit under these assumptions $\beta_{\frac{1}{2}}^0$ changes sign between 20 and 30 Mev. This energy dependence for $\beta_{\frac{1}{2}}^0$ suggests a Jastrow[18] potential for this phase shift.

[16] H. Bethe and H. P. Noyes, Proceedings of the Fourth Annual Rochester Conference, 1954, University of Rochester.
[17] R. Marshak, Phys. Rev. **88**, 1208 (1952).

ACKNOWLEDGMENTS

A number of people aided the author in this experiment. Thanks are due especially to Dr. A. Roberts and Dr. J. Tinlot for their help and advice throughout the experiment. The author also wishes to thank Dr. J. French and Dr. H. P. Noyes for their helpful discussions of the results. Others who assisted and who contributed numerous suggestions were Dr. E. Hafner, Dr. F. Tenney, R. Santirocco, and D. Nelson. W. Coombs, K. Enslein, L. Braun, H. VonThenen, and F. Palmer were responsible for construction of parts of the equipment and for the reliable operation of the cyclotron.

[18] R. Jastrow, Phys. Rev. **81**, 1165 (1951).

PHYSICAL REVIEW VOLUME 95, NUMBER 5 SEPTEMBER 1, 1954

Quantum Electrodynamics at Small Distances*

M. GELL-MANN† AND F. E. LOW
Physics Department, University of Illinois, Urbana, Illinois

(Received April 1, 1954)

The renormalized propagation functions D_{FC} and S_{FC} for photons and electrons, respectively, are investigated for momenta much greater than the mass of the electron. It is found that in this region the individual terms of the perturbation series to all orders in the coupling constant take on very simple asymptotic forms. An attempt to sum the entire series is only partially successful. It is found that the series satisfy certain functional equations by virtue of the renormalizability of the theory. If photon self-energy parts are omitted from the series, so that $D_{FC}=D_F$, then S_{FC} has the asymptotic form $A[p^2/m^2]^n[i\gamma\cdot p]^{-1}$, where $A=A(e_1^2)$ and $n=n(e_1^2)$. When all diagrams are included, less specific results are found. One conclusion is that the *shape* of the charge distribution surrounding a test charge in the vacuum does not, at small distances, depend on the coupling constant except through a scale factor. The behavior of the propagation functions for large momenta is related to the magnitude of the renormalization constants in the theory. Thus it is shown that the unrenormalized coupling constant $e_0^2/4\pi\hbar c$, which appears in perturbation theory as a power series in the renormalized coupling constant $e_1^2/4\pi\hbar c$ with divergent coefficients, may behave in either of two ways:

(a) It may really be infinite as perturbation theory indicates;
(b) It may be a finite number independent of $e_1^2/4\pi\hbar c$.

1. INTRODUCTION

IT is a well-known fact that according to quantum electrodynamics the electrostatic potential between two classical test charges in the vacuum is not given exactly by Coulomb's law. The deviations are due to vacuum polarization. They were calculated to first order in the coupling constant α by Serber[1] and Uehling[2] shortly after the first discussion of vacuum polarization by Dirac[3] and Heisenberg.[4] We may express their results by writing a formula for the potential energy be-

* This work was supported by grants from the U. S. Office of Naval Research and the U. S. Atomic Energy Commission.

† Now at Department of Physics and Institute for Nuclear Studies, University of Chicago.

[1] R. Serber, Phys. Rev. **48**, 49 (1935).
[2] A. E. Uehling, Phys. Rev. **48**, 55 (1935).
[3] P. A. M. Dirac, Proc. Cambridge Phil. Soc. **30**, 150(1934).
[4] W. Heisenberg, Z. Physik **90**, 209 (1934).

tween two heavy point test bodies, with renormalized charges q and q', separated by a distance r:

$$V(r)=\frac{qq'}{4\pi r}\left\{1+\frac{\alpha}{3\pi}\int_{(2m)^2}^{\infty}\exp\left[-r\left(\frac{M^2c^2}{\hbar^2}\right)^{\frac{1}{2}}\right]\times\left(1+\frac{2m^2}{M^2}\right)\left(1-\frac{4m^2}{M^2}\right)^{\frac{1}{2}}\frac{dM^2}{M^2}+O(\alpha^2)+\cdots\right\}. \quad (1.1)^5$$

Here $\alpha=e_1^2/4\pi\hbar c\cong 1/137$ is the renormalized fine structure constant and m is the renormalized (observed) rest mass of the electron.

If $r\ll\hbar/mc$, then (1.1) takes the simple asymptotic form,

$$V(r)=\frac{qq'}{4\pi r}\left\{1+\frac{2\alpha}{3\pi}\left[\ln\left(\frac{\hbar}{mcr}\right)-\tfrac{5}{6}-\ln\gamma\right]+O(\alpha^2)+\cdots\right\}, \quad (1.2)^5$$

where $\gamma\cong 1.781$. We shall discuss the behavior of the entire series (1.2), to all orders in the coupling constant, making use of certain simple properties that it possesses in virtue of the approximation $r\ll\hbar/mc$. These properties are intimately connected with the concept of charge renormalization. The relation between (1.2) and charge renormalization can be made clear by the following physical argument:

A test body of "bare charge" q_0 polarizes the vacuum, surrounding itself by a neutral cloud of electrons and positrons; some of these, with a net charge δq, of the same sign as q_0, escape to infinity, leaving a net charge $-\delta q$ in the part of the cloud which is closely bound to the test body (within a distance $\hbar/mc$). If we observe the body from a distance much greater than $\hbar/mc$, we see an effective charge q equal to $(q_0-\delta q)$, the renormalized charge. However, as we inspect more closely and penetrate through the cloud to the core of the test body, the charge that we see inside approaches the bare charge q_0, concentrated in a point at the center. It is clear, then, that the potential $V(r)$, in Eqs. (1.1) and (1.2), must approach $q_0q_0'/4\pi r$ as r approaches zero. Thus, using (1.1), we may write

$$q_0q_0'=qq'\left\{1+\frac{2\alpha}{3\pi}\left[\ln\left(\frac{\hbar/mc}{0}\right)-\tfrac{5}{6}-\ln\gamma\right]+O(\alpha^2)\right\}, \quad (1.3)$$

where the individual terms in the series diverge logarithmically in a familiar way. The occurrence of these logarithmic divergences will play an important role in our work.

Such divergences occur in quantum electrodynamics whenever observable quantities are expressed in terms of the bare charge e_0 and the bare (or mechanical) mass m_0 of the electron. The renormalizability of the theory consists in the fact that, when the observable quantities are re-expressed in terms of the renormalized parameters e_1 and m, no divergences appear, at least when a power series expansion in $e_1^2/4\pi\hbar c$ is used. The proof of renormalizability has been given by Dyson,[6] Salam,[7] and Ward.[8] We shall make particular use in Secs. III and IV of the elegant techniques of Ward.

We shall show that the fact of renormalizability gives considerable information about the behavior of the complete series (1.2). It may be objected to an investigation of this sort that while (1.2) is valid for $r\ll\hbar/mc$, the first few terms should suffice for calculation unless r is as small as $e^{-137}\hbar/mc$, a ridiculously small distance. We have no reason, in fact, to believe that at such distances quantum electrodynamics has any validity whatever, particularly since interactions of the electromagnetic field with particles other than the electron are ignored. However, a study of the mathematical character of the theory at small distances may prove useful in constructing future theories. Moreover, in other field theories now being considered, such as the relativistic pseudoscalar meson theory, conclusions similar to ours may be reached, and the characteristic distance at which they become useful is much greater, on account of the largeness of the coupling constant.

In this paper we shall be mainly concerned with quantum electrodynamics, simply because gauge invariance and charge conservation simplify the calculations to a considerable extent. Actually, our considerations apply to any renormalizable field theory, and we shall from time to time indicate the form they would take in meson theory.

2. REPRESENTATIONS OF THE PROPAGATION FUNCTIONS

The modified Coulomb potential discussed in Sec. I can be expressed in terms of the finite modified photon propagation function $D_{FC}(p^2,e_1^2)$ that includes vacuum polarization effects to all orders in the coupling constant. (Here p^2 is the square of a four-vector momentum $p\mu$.) The function D_{FC} is calculated by summing all Feynman diagrams that begin and end with a single photon line, renormalizing to all orders. The potential is given by[9]

$$V(r)=\frac{qq'}{(2\pi)^3}\int d^3p e^{i\mathbf{p}\cdot\mathbf{r}}D_{FC}(p^2,e_1^2), \quad (2.1)$$

where $\mathbf{p}$ is a three-dimensional vector.

If we were to sum all the Feynman diagrams that make up D_{FC} without renormalizing the charge we

[5] J. Schwinger, Phys. Rev. **75**, 651 (1949).

[6] F. J. Dyson, Phys. Rev. **75**, 1756 (1949).

[7] A. Salam, Phys. Rev. **84**, 426 (1951).

[8] J. C. Ward, Proc. Phys. Soc. (London) **A64**, 54 (1951); see also Phys. Rev. **84**, 897 (1951).

[9] From this point on, we take $\hbar=c=1$.

would obtain the divergent function $D_F'(p^2,e_0^2)$, which is related to the finite propagation function by Dyson's equations

$$D_F'(p^2,e_0^2)=Z_2D_{FC}(p^2,e_1^2), \tag{2.2}$$

$$e_1^2=Z_3e_0^2, \tag{2.3}$$

where Z_3 is a power series in e_1^2 with divergent coefficients. The bare and renormalized charges of a test body satisfy a relation similar to (2.3):

$$q_1^2=Z_3q_0^2, \tag{2.4}$$

so that Z_3^{-1} is just the bracketed quantity in (1.3).

The function D_{FC} can be represented in the form

$$D_{FC}(p^2,e_1^2)=\frac{1}{p^2-i\epsilon}+\int_0^\infty f\left(\frac{M^2}{m^2},e_1^2\right)\frac{dM^2}{M^2}\frac{1}{p^2+M^2-i\epsilon}, \tag{2.5}$$

where f is real and positive; the quantity Z_3 may be expressed in terms of f through the relation

$$Z_3^{-1}=1+\int_0^\infty f\left(\frac{M^2}{m^2},e_1^2\right)\frac{dM^2}{M^2}. \tag{2.6}$$

These equations have been presented and derived, in a slightly different form by Källén.[10] Their derivation is completely analogous to the derivation given in Appendix A of Eqs. (2.8) and (2.9) for the propagation function of the electron, which is discussed below.

We see from (2.5) and (2.6) that a virtual photon propagates like a particle with a probability distribution of virtual masses. In D_{FC}, the distribution is not normalized, but in the unrenormalized propagation function $D_F'=Z_3D_{FC}$ the probabilities are normalized to 1. The normalization integral is just the formally divergent quantity Z_3^{-1}. In D_{FC}, it is the coefficient of $1/(p^2-i\epsilon)$ that is 1, corresponding to the fact that the potential $V(r)$ in (2.1) at large distances is simply $qq'/4\pi r$.

It has been remarked[10,11] that Z_3^{-1} must be greater than unity, a result that follows immediately from Eq. (2.6). To this property of the renormalization constant there corresponds a simple property of the finite function D_{FC}, to wit, that as $p^2\to\infty$, the quantity p^2D_{FC} approaches Z_3^{-1}. If Z_3^{-1} is in fact infinite, as it appears to be when expanded in a power series, then D_{FC} is more singular than the free photon propagation function $D_F=1/(p^2-i\epsilon)$. In any case, D_{FC} can never be less singular than D_F, nor even smaller asymptotically. This is a general property of existing field theories; it is of particular interest in connection with the hope often expressed that in meson theory the exact modified propagation functions are less singular, or smaller, for large momenta, than the corresponding free-particle propagation functions.

The propagation functions for the electron behave quite similarly to the photon functions we have been discussing. Analogous to D_F' is the divergent electron propagation function $S_F'(p,e_0^2)$. It is obtained by summing all Feynman diagrams beginning and ending in a single electron line, renormalizing the mass of the electron, but not its charge, to all orders. Corresponding to D_{FC} there is the finite function $S_{FC}(p,e_1^2)$, related to S_F' by an equation similar to (2.2):

$$S_F'(p,e_0^2)=Z_2S_{FC}(p,e_1^2). \tag{2.7}$$

The quantity Z_2, like Z_3, appears as a power series in e_1^2 with divergent coefficients. It does not, however, contribute to charge renormalization.

A parametric representation of S_{FC}, resembling Eq. (2.5) for D_{FC}, is derived in Appendix A and reproduced here:

$$S_{FC}(p,e_1^2)=\frac{1}{i\gamma p+m-i\epsilon}+\int_m^\infty\frac{g(M/m,e_1^2)}{i\gamma p+M-i\epsilon}\frac{dM}{M}+\int_m^\infty\frac{h(M/m,e_1^2)}{i\gamma p-M+i\epsilon}\frac{dM}{M}. \tag{2.8}$$

Both g and h are real; in meson theory they are positive, but in quantum electrodynamics they may assume negative values. Z_2 can be expressed in terms of g and h through the relation

$$Z_2^{-1}=1+\int_m^\infty g\left(\frac{M}{m},e_1^2\right)\frac{dM}{M}+\int_m^\infty h\left(\frac{M}{m},e_1^2\right)\frac{dM}{M}. \tag{2.9}$$

Again we have a sort of probability distribution of virtual masses with a formally divergent normalization integral. As before, the modified propagation function is more singular, or at least asymptotically greater, than the free-particle propagation function, since $Z_2^{-1}\geq 1$, except possibly in quantum electrodynamics.

Equations (2.8) and (2.9), like (2.5) and (2.6), are similar to ones derived by Källén.[10] However, our notation and approach are perhaps sufficiently different from his to warrant separate treatment.

It should be noted that Källén's paper contains a further equation, (70), which, in our notation expresses the mechanical mass m_0 of the electron in terms of g and h:

$$m_0=\left[m+\int_m^\infty Mg\frac{dM}{M}+\int_m^\infty(-M)h\frac{dM}{M}\right]\times\left[1+\int_m^\infty g\frac{dM}{M}+\int_m^\infty h\frac{dM}{M}\right]^{-1}. \tag{2.10}$$

We see that m_0 is simply the mean virtual mass of the electron.

[10] G. Källén, Helv. Phys. Acta **25**, 417 (1952).
[11] J. Schwinger (private communication from R. Glauber).

It may be remarked that a quantity analogous to m_0 can be constructed for the photon field, that is, the mean squared virtual mass of the photon:[12]

$$\mu_0^2=\left[\int_0^\infty fM^2\frac{dM^2}{M^2}\right]\left[1+\int_0^\infty f\frac{dM^2}{M^2}\right]^{-1}. \quad (2.11)$$

While gauge invariance forbids the occurrence of a mechanical mass of the photon in the theory, it is well known that a quadratically divergent quantity that looks like the square of a mechanical mass frequently turns up in calculations and must be discarded. That quantity is just μ_0^2, as given by (2.11). An equation similar to (2.11) holds in pseudoscalar meson theory, where μ_0^2 is really the square of a mechanical mass:

$$\mu_0^2=\left[\mu^2+\int_{9\mu^2}^\infty fM^2\frac{dM^2}{M^2}\right]\left[1+\int_{9\mu^2}^\infty f\frac{dM^2}{M^2}\right]^{-1}. \quad (2.12)$$

Here μ^2 is the observed meson mass. Evidently (2.12) implies that $\mu_0^2>\mu^2$.

3. EXAMPLE: QUANTUM ELECTRODYNAMICS WITHOUT PHOTON SELF-ENERGY PARTS

Before examining the asymptotic forms of the singular functions in the full theory of quantum electrodynamics let us consider a simplified but still renormalizable form of the theory in which all photon self-energy parts are omitted. A photon self-energy part is a portion of a Feynman diagram which is connected to the remainder of the diagram by two and only two photon lines. By omitting such parts, we effectively set

$$D_{FC}(p^2)=D_F(p^2)=1/(p^2-i\epsilon). \quad (3.1)$$

Moreover, there is no charge renormalization left in the theory, so that

$$Z_3=1$$

and

$$e_0^2=e_1^2. \quad (3.2)$$

Although some finite effects of vacuum polarization (such as its contribution to the second-order Lamb shift) have been left out, others (such as the scattering of light by light) are still included.

If the mass of the electron is now renormalized the only divergence remaining in the theory is Z_2. It has been shown by Ward[8] that in the calculation of any observable quantity, such as a cross section, Z_2 cancels out. We shall nevertheless be concerned with Z_2 since it does appear in a calculation of the electron propagation function S_F'.

In order to deal with Z_2, a divergent quantity, we shall make use of the relativistic high-momentum cut-off procedure introduced by Feynman, which consists of replacing the photon function D_F by a modified function $D_{F\lambda}$ defined by

$$D_{F\lambda}(p^2)=D_F(p^2)\lambda^2/(\lambda^2+p^2-i\epsilon).$$

In a given calculation, if λ^2 is large enough, quantities that would be finite in the absence of a cutoff remain unchanged while logarithmically divergent quantities become finite logarithmic functions of λ^2.

Thus, if we calculate $S_F'(p)$ using a Feynman cutoff with $\lambda^2\gg|p^2|$ and $\lambda^2\gg m^2$, and drop terms that approach zero as λ^2 approaches infinity, we must find a relation similar to (2.7):

$$S_{F'\lambda}(p)=z_{2\lambda}S_{FC}(p), \quad (3.3)$$

where the finite function S_{FC} has remained unchanged by the cut-off process, while the infinite constant Z_2 has been converted to the finite quantity $z_{2\lambda}$, which is a function of λ^2/m^2. (The reader who is not impressed with the rigor of these arguments should refer to the next section, where a more satisfactory cut-off procedure is introduced.)

Calculation to the first few orders in the coupling constant indicates that $z_{2\lambda}$ has the form

$$z_{2\lambda}=1+e_1^2\left(a_1+b_1\ln\frac{\lambda^2}{m^2}\right)+e_1^4\left[a_2+b_2\ln\frac{\lambda^2}{m^2}+c_2\left(\ln\frac{\lambda^2}{m^2}\right)^2\right]+\cdots. \quad (3.4)$$

The propagation function S_{FC} may also be calculated to fourth order in e_1; for $|p^2|\gg m^2$ it has the form

$$|p^2|\gg m^2\colon\ S_{FC}(p)\ \frac{1}{i\gamma p}\{1+e_1^2[a_1'+b_1'\ln(p^2/m^2)]+e_1^4[a_2'+b_2'\ln(p^2/m^2)+c_2'(\ln(p^2/m^2))^2]+\cdots\}. \quad (3.5)$$

In order to obtain some understanding of the properties of Eq. (3.3), let us substitute these approximate expressions into that equation. Let us then examine what happens in the limit $m\to 0$. We see that in neither of the expressions (3.4) and (3.5) can m be set equal to zero with impunity; that is to say, both factors on the right-hand side of (3.3) contain logarithmic divergences as $m\to 0$. Thus we should naively expect that the left-hand side have no limit as $m\to 0$. Rather, we should expect to find logarithmic divergences to each order in e_1^2, unless fantastic cancellations, involving the constants a_1, a_1', etc., should happen to occur.

But such cancellations must indeed occur, since a direct calculation of $S_{F\lambda}'$ with m set equal to zero exhibits no divergences whatever. Instead, each Feynman diagram yields a term equal to $1/i\gamma p$ times a finite function of λ^2/p^2. It is clear that this must be so, since λ

[12] We are indebted to Dr. Källén for a discussion of this point.

provides an ultraviolet cutoff for every integral, while μ provides an infrared cutoff.

Let us now make use of the remarkable cancellations that we have discussed, but in such a way that we do not rely on the specific forms of (3.4) and (3.5), for which we have so far claimed no validity beyond fourth order in e_1. We shall consider the asymptotic region $\lambda^2 \gg |p^2| \gg m^2$. We may write

$$S_{FC} = (1/i\gamma p) s_C(p^2/m^2) \tag{3.6}$$

and

$$z_{2\lambda} = z_2(\lambda^2/m^2). \tag{3.7}$$

Moreover, in the asymptotic region, we may drop m entirely in $S_{F'\lambda'}$, since a limit exists as m^2/λ^2 and m^2/p^2 approach zero, with $\lambda^2 \gg |p^2|$. Thus we have

$$S_{F'\lambda} \approx (1/i\gamma p) s(\lambda^2/p^2). \tag{3.8}$$

Equation (3.3) then implies the following functional equation:

$$s(\lambda^2/p^2) = z_2(\lambda^2/m^2) \cdot s_C(p^2/m^2). \tag{3.9}$$

The functional equation has the general solution[13]

$$z_2(\lambda^2/m^2) = A(\lambda^2/m^2)^{-n} = A \exp[-n \ln(\lambda^2/m^2)], \tag{3.10}$$

$$s_C(p^2/m^2) = B(p^2/m^2)^n = B \exp[n \ln(p^2/m^2)], \tag{3.11}$$

$$s(\lambda^2/p^2) = AB(\lambda^2/p^2)^{-n} = AB \exp[-n \ln(\lambda^2/p^2)]. \tag{3.12}$$

Here A, B, and n are functions of e_1^2 alone. If all three constants are expanded in power series in e_1^2, then formulas like (3.4) and (3.5) can be seen to be valid to all orders in e_1^2. The constants are given, to second order in e_1, by the equations

$$n = \frac{e_1^2}{16\pi^2} + \cdots, \tag{3.13}$$

$$A = 1 + \frac{e_1^2}{16\pi^2}\left[\tfrac{3}{2} + \int_{m^2}^{\infty} \frac{dM^2}{M^4(M^2-m^2)}(5m^2M^2 - m^4)\right], \tag{3.14}$$

$$B = 1 - \frac{e_1^2}{16\pi^2}\int_{m^2}^{\infty} \frac{dM^2}{M^4(M^2-m^2)}(5m^2M^2 - m^4) + \cdots. \tag{3.15}$$

It is now apparent that we have glossed over a difficulty, although it turns out to be a minor one. While AB is perfectly finite, A and B separately contain infrared divergences that must be cut off by the introduction of a small fictitious photon mass μ. These divergences are well-known and arise from the requirement that $(i\gamma p + m)S_{FC}(p)$ approach unity as $i\gamma p + m$ tends to zero, while the point $i\gamma p + m = 0$ is in fact a singularity of the function $(i\gamma p + m)S_F'(p)$.

From the asymptotic form for S_{FC},

$$S_{FC}(p) \approx \frac{B}{i\gamma p}\left(\frac{p^2}{m^2}\right)^n, \tag{3.16}$$

we may derive an asymptotic form for the vertex operator[6] $\Gamma_{\mu C}(p,p')$ for equal arguments.

We use Ward's[8] relation

$$\Gamma_{\mu C}(p,p) = \frac{1}{i}\frac{\partial}{\partial p_\mu}[S_{FC}(p)]^{-1}, \tag{3.17}$$

and obtain

$$\Gamma_{\mu C}(p,p) = B^{-1}(p^2/m^2)^{-n}(\gamma_\mu - 2np_\mu\gamma p/p^2). \tag{3.18}$$

A result similar to this was found by Edwards,[14] who summed a small subset of the diagrams we consider here. We may note that corresponding to the increase in the singularity of S_F there is a decrease in that of Γ_μ. The two are obviously tied together by (3.17). It is therefore highly inadvisable to take seriously any calculation using a modified Γ_μ and unmodified S_F', or vice versa.

It is unfortunate that the inclusion of photon self-energy parts (omitted in this section) invalidates the simple results we have obtained here. In Sec. V we shall derive and solve the functional equations that replace (3.9) in the general case, but the solutions give much less detailed information than (3.16). In order to treat the general case, we must first develop (in Sec. IV) a more powerful cut-off technique than the one we have used so far.

4. WARD'S METHOD[8] USED AS A CUTOFF[15]

The starting point of Ward's method of renormalization is a set of four integral equations derived by summing Feynman diagrams. The equations involve four functions: $S_F'(p)$, $D_F'(k)$, the vertex operator $\Gamma_\mu(p_1,p_2)$, and a function $W_\mu(k)$ defined by

$$W_\mu = (\partial/\partial k_\mu)[D_F'(k)]^{-1}. \tag{4.1}$$

Two of the equations are trivial, following from (4.1) and (3.17), respectively:

$$[S_F'(p)]^{-1} = i\int_0^1 dx(p_\mu - p_\mu') \times \Gamma_\mu(px + p'(1-x), px + p'(1-x)) \tag{4.2}$$

and

$$[D_F'(k)]^{-1} = \int_0^1 dy k_\mu W_\mu(ky), \tag{4.3}$$

where p' is a free electron momentum, i.e., after integration p'^2 is to be replaced by $-m^2$ and $i\gamma p'$ by $-m$, where m is the experimental electron mass. No further mass renormalization is necessary.

[13] J. C. Maxwell, Phil. Mag. (Series 4) **19**, 19 (1860).

[14] S. F. Edwards, Phys. Rev. **90**, 284 (1953).

[15] The purpose of this section is to justify the use of a cutoff when photon self-energy parts are included. The reader who is willing to take this point for granted need devote only the briefest attention to the material between Eqs. (4.3) and (4.6). The remainder of the section contains some simple but important algebraic manipulation of the cut-off propagation functions.

The two remaining equations are nonlinear power-series integral equations for Γ_μ and W_μ in which each term describes an "irreducible" Feynman diagram. An irreducible diagram, as defined by Dyson, is one which contains no vertex or self-energy parts inside itself. When the complete series of irreducible diagrams for Γ_μ or W_μ is written down, and in each one S_F' is substituted for S_F, D_F' for D_F, Γ_μ for γ_μ, and W_μ for $2k_\mu$, then the complete series of *all* diagrams for Γ_μ or W_μ is generated. We give below the first two terms of each of the integral equations. Equation (4.4) corresponds to Fig. 1 and Eq. (4.5) to Fig. 2.

$$\Gamma_\mu(p_1,p_2)\equiv\gamma_\mu+\Lambda_\mu(p_1,p_2)$$
$$=\gamma_\mu+\frac{ie_0^2}{(2\pi)^4}\int\Gamma_\lambda(p_1,p_1-k)$$
$$\times S_F'(p_1-k)\Gamma_\mu(p_1-k,p_2-k)\cdot S_F'(p_2-k)$$
$$\times\Gamma_\lambda(p_2-k,p_2)D_F'(k)d^4k+\cdots, \quad (4.4)$$

$$W_\mu(k)\equiv 2k_\mu+Tk_\mu$$
$$=2k_\mu+\frac{e_0^2}{(2\pi)^4}\cdot\tfrac{1}{3}\,\mathrm{Tr}\int\Gamma_\nu(p,p+k)$$
$$\times S_F'(p+k)\Gamma_\mu(p+k,p+k)S_F'(p+k)$$
$$\times\Gamma_\nu(p+k,p)S_F'(p)d^4p+\cdots. \quad (4.5)$$

The factor of one-third arises in (4.5) because we are interested only in the coefficient of $\delta_{\nu\lambda}$ in the tensor $[\delta_{\nu\lambda}-(k_\nu k_\lambda/k^2)]D_F'(k)$.

The heavy lines and dots have been drawn as a reminder that the complete S_F', D_F', and Γ_μ are to be inserted.

The symbols Λ_μ and T_μ are simply a convenient shorthand for the sum of all the integrals occurring on the right in (4.4) and (4.5), respectively.

The properties of (4.4) and (4.5) that are crucial for the possibility of renormalization are the following:

(i) All divergences that occur in the power series solution of the equations are logarithmic divergences. (W_μ is actually formally linearly divergent but on grounds of covariance the linear divergence will vanish.)

(ii) In (4.4), each terms with coefficient $(e_0^2)^n$ conexactly nD_F' functions and contains one more Γ_μ function than S_F' functions.

(iii) In (4.5), each term with coefficient $(e_0^2)^n$ contains $(n-1)$ more D_F' functions than W_μ functions, and contains equal numbers of Γ_μ and S_F' functions.

At this point Ward introduces a subtraction procedure which alters Eqs. (4.4) and (4.5) so that the solutions of the new equations are finite functions S_{FC}, D_{FC}, $\Gamma_{\mu C}$, and $W_{\mu C}$. He then shows that the modifications introduced are equivalent to charge renormalization. The method that we shall present here is a slight generalization of Ward's involving two cut-off parameters λ and λ'. When $\lambda=0$ and $\lambda'=im$, our method reduces to Ward's.

FIG. 1. The sequence of irreducible diagrams for Γ_μ.

From the right-hand side of (4.4) we subtract $\int dx\Lambda_\mu(l'x+p'(1-x),\, l'x+p'(1-x))$, where p' has the same significance as in (4.2) and l' is a vector parallel to p' but with $(l')^2$ set equal to $(\lambda')^2$ and $\gamma\cdot l'$ set equal to λ' after the integration. This choice of subtraction procedure may appear arbitrarily complicated, so that a remark about our motivation may be in order. Since Λ_μ consists of logarithmically divergent integrals, the quantity

$$\Lambda_\mu{}^x=\Lambda_\mu(p_1,p_2)-\Lambda_\mu(l'x+p'(1-x),\, l'x+p'(1-x))$$

is certainly finite. Therefore so is

$$\Lambda_{\mu l'}=\int_0^1 dx\Lambda_\mu{}^x=\Lambda_\mu(p_1,p_2)$$
$$-\int\Lambda_\mu(l'x+p'(1-x),\, l'x+p'(1-x))dx,$$

which is the quantity of interest. However, referring to (4.2), we see that if we replace Γ_μ by $\gamma_\mu+\Lambda_{\mu l'}$, $S_F'(p)$ will have the value $1/(i\gamma p+m)$ at $p=l'$. This subtraction procedure therefore provides a convenient normalization for the cut-off functions.

Similarly, from the right-hand side of (4.5) we subtract $k_\mu\int_0^1 2ydyT(ly)$, where $l^2=\lambda^2$. (The motivation is the same here as before.) Let us denote the solutions of the modified equations by the symbols $S_{F\lambda'\lambda}$, etc. Like Ward's functions, they are finite to all orders in the coupling constant, the logarithmic divergences having disappeared in the course of the subtraction. In the modified equations, let us everywhere replace the coupling constant e_0^2 by another one, e_2^2. Then we may show that if e_2^2 is a properly chosen function of e_0^2, λ^2, and m^2 the modified functions are multiples of the

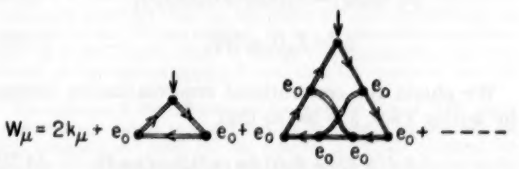

FIG. 2. The sequence of irreducible diagrams for W_μ. Notice that there is no irreducible diagram in fourth order.

original divergent functions. In fact, we have the relations:

$$\Gamma_\mu(p_1,p_2;e_0^2)=Z_2^{-1}(\lambda,\lambda';e_2^2)\Gamma_{\mu\lambda\lambda'}(p_1,p_2;e_2^2), \quad (4.6)$$

$$S_F'(p;e_0^2)=Z_2(\lambda,\lambda';e_2^2)S_{F\lambda\lambda'}(p,e_2^2), \quad (4.7)$$

$$W_\mu(k,e_0^2)=Z_3^{-1}(\lambda;e_2^2)W_{\mu\lambda}(k,e_2^2), \quad (4.8)$$

$$D_F'(k,e_0^2)=Z_3(\lambda;e_2^2)D_{F\lambda}(k,e_2^2), \quad (4.9)$$

$$e_2^2=Z_3(\lambda;e_2^2)e_0^2. \quad (4.10)$$

These relations can be proved by substituting them into the original integral Eqs. (4.2) through (4.5) and making use of the properties (ii) and (iii). Z_2 and Z_3 are then given by

$$\gamma_\mu Z_2(\lambda,\lambda';e_2^2)=\gamma_\mu-\int_0^1 dx\times$$

$$\Lambda_{\mu\lambda\lambda'}(l'x+p'(1-x),l'x+p'(1-x);e_2^2) \quad (4.11)$$

and

$$Z_3(\lambda,e_2^2)=1-\int_0^1 ydyT_\lambda(ly,e_2^2). \quad (4.12)$$

Here Λ and T stands for the series of integrals on the right-hand side of (4.4) and (4.5) calculated *with the cut-off functions.*

We note that the photon functions are independent of λ'. This is of course due to the fact that Z_2 cancels out in calculating these functions. Furthermore,

$$[(i\gamma p+m)S_{F\lambda\lambda'}(p)]_{\gamma p=\lambda'}=1, \quad (4.13)$$

and

$$[k^2D_{F\lambda}(k)]_{k=\lambda}=1. \quad (4.14)$$

It is clear, then, that for $\lambda'=im$ and $\lambda=0$ our modified functions reduce to the usual convergent functions as defined by Ward. Furthermore, when λ and λ' are both infinite our modified functions are (in some sense which we need not worry about) the original divergent functions S_F', D_F', etc. We may now relate our functions to the usual convergent functions very simply. (From now on we shall limit our discussion to S_F' and D_F', since Γ and W are obtained from them by differentiation.)

We rewrite (4.7), (4.9), and (4.10):

$$S_F'(p,e_0^2)=Z_2(\lambda,\lambda';e_2^2)S_{F\lambda\lambda'}(p,e_2^2), \quad (4.7)$$

$$D_F'(k,e_0^2)=Z_3(\lambda,e_2^2)D_{F\lambda}(k,e_2^2), \quad (4.9)$$

$$e_2^2=Z_3(\lambda,e_2^2)e_0^2. \quad (4.10)$$

We obtain the conventional renormalization theory by setting $\lambda=0$, $\lambda'=im$, so that

$$S_F'(p,e_0^2)=Z_2(0,im;e_1^2)S_{FC}(p,e_1^2), \quad (4.7)'$$

$$D_F'(k,e_0^2)=Z_3(0,e_1^2)D_{FC}(k,e_1^2), \quad (4.9)'$$

and

$$e_1^2=Z_3(0,e_1^2)e_0^2, \quad (4.10)'$$

where e_1 is the observed electronic charge.

Dividing the unprimed equations by the primed ones leads to the relations:

$$S_F(\lambda,\lambda',p;e_2^2)=z_2(\lambda,\lambda';e_1^2)S_{FC}(p,e_1^2), \quad (4.7)''$$

$$D_F(\lambda,k;e_2^2)=z_3(\lambda,e_1^2)D_{FC}(k,e_1^2), \quad (4.9)''$$

$$e_1^2=z_3(\lambda,e_1^2)e_2^2. \quad (4.10)''$$

In these last equations all the quantities involved are finite. As λ' and λ approach ∞, however, they approach their original divergent values. We have therefore established a cutoff which is useful in the presence of photon self-energy parts and which has the desired renormalization property for any values of the cut-off parameters. We may call attention to the essential simplicity of the cutoff. For example, if we had used it in Sec. III instead of the Feynman cutoff we would have found $s=(p^2/\lambda^2)^n$ to all orders in Eq. (3.12), i.e., $AB=1$.

For our purposes it is convenient to eliminate the trivial $1/(i\gamma p+m)$ dependence of S_{FC} and the $1/k^2$ dependence of D_{FC}. We therefore set, as in Sec. III:

$$S_{FC}(p)=\frac{1}{i\gamma p+m}s_C(p), \quad (4.15)$$

$$D_{FC}(k)=(1/k^2)d_C(k), \quad (4.16)$$

and

$$S_{F\lambda\lambda'}(p)=\frac{1}{i\gamma p+m}s(\lambda,\lambda',p) \quad (4.15)'$$

$$D_{F\lambda}(k)=(1/k^2)d(\lambda,k). \quad (4.16)'$$

Equations (4.13) and (4.14) are now very useful. Using them together with (4.7)'', (4.9)'', (4.10)'', and the definitions (4.15), (4.16), we find:

$$z_2^{-1}(\lambda,\lambda';e_1^2)=[s_C(p,e_1^2)]_{\gamma p=\lambda'}, \quad (4.17)$$

$$z_3^{-1}(\lambda,e_1^2)=[d_C(k,e_1^2)]_{k=\lambda}. \quad (4.18)$$

z_2 is thus independent of λ since the right-hand side of (4.17) is independent of λ.

Our final equations are therefore

$$s(\lambda,\lambda',p,e_2^2)=s_C(p,e_1^2)/s_C(\lambda',e_1^2), \quad (4.19)$$

$$d(\lambda,k,e_2^2)=d_C(k,e_1^2)/d_C(\lambda,e_1^2), \quad (4.20)$$

and

$$e_2^2=d_C(\lambda,e_1^2)e_1^2. \quad (4.21)$$

The renormalization constants are seen to be the convergent functions calculated at infinite values of their arguments. This confirms the results of Sec. II and Appendix A.

Before closing this section we might remark that the entire treatment presented here can be very easily transcribed to meson theory. The situation in that case

is somewhat more complicated since both Z_2 and Z_5 (the renormalization constant for Γ_5) contribute to charge renormalization, which is present even in the absence of closed loops (as is well known). The renormalization of Γ_5 must be carried through somewhat differently from that of Γ_μ, since we shall want $\Gamma_{5\lambda\lambda'}(p,p';g_2^2)$ to equal γ_5 at $\gamma p=\lambda'$. The equations analogous to (4.19)–(4.21) for pseudoscalar meson theory are:

$$s(\lambda,\lambda',p,g_2^2)=s_C(p,g_1^2)/s_C(\lambda',g_1^2), \tag{4.19$'$}$$

$$\delta(\lambda,\lambda',k,g_2^2)=\delta_C(k,g_1^2)/\delta_C(\lambda,g_1^2), \tag{4.20$'$}$$

$$\gamma_5(\lambda,\lambda',p,g_2^2)=\gamma_{5C}(p,g_1^2)/\gamma_{5C}(\lambda',g_1^2), \tag{4.22}$$

$$g_2^2=g_1^2[s_C(\lambda',e_1^2)\gamma_{5C}(\lambda',g_1^2)]^2\delta_C(\lambda,g_1^2), \tag{4.21$'$}$$

where

$$\Gamma_{5C}(p,p,g_1^2)=\gamma_5\cdot\gamma_{5C}(p,g_1^2), \text{ etc.},$$

and where $\Delta=\delta/(k^2+\mu^2)$ is the meson propagation function.

We shall not investigate these equations further; we shall confine our attention to the much simpler case of quantum electrodynamics.

5. ASYMPTOTIC BEHAVIOR OF THE PROPAGATION FUNCTIONS IN QUANTUM ELECTRODYNAMICS

With the aid of the cut-off procedure introduced in the previous section, we may return to the discussion, begun in Sec. III, of the behavior of the propagation functions in the asymptotic region ($|p^2|\gg m^2$). In Sec. III photon self-energy parts were omitted and it was sufficient to use a Feynman cutoff in order to find the functional equation (3.9) satisfied asymptotically by the electron propagation function S_F'. The new cutoff enables us to include all Feynman diagrams. We shall now find a new functional equation for S_F' and one for D_F' as well.

Our starting point is the set of Eqs. (4.19)–(4.21) that express the cut-off propagation functions in terms of renormalized quantities. [In Sec. III, we used Eq. (3.3) instead.] We must first observe, as in Sec. III, that in a power series calculation of the cut-off functions the results remain finite when the electron mass is set equal to zero. The quantities λ and λ' provide, of course, ultraviolet cutoffs, while p provides an infrared cutoff for all Feynman integrals. Thus in the asymptotic region we may drop the electron mass in a calculation of the cut-off functions, which then take the forms

$|p^2|,\lambda^2,\lambda'^2\gg m^2$:

$$s(p/\lambda,p/\lambda',m^2/p^2,e_2^2)\approx s(p/\lambda,p/\lambda',0,e_2^2), \tag{5.1}$$

$|k^2|,\lambda^2\gg m^2$:

$$d(k^2/\lambda^2,m^2/k^2,e_2^2)\approx d(k^2/\lambda^2,0,e_2^2). \tag{5.2}$$

It should be noted that the asymptotic form of s depends only on p^2 and not on $i\gamma p$.

Equations (4.19)–(4.21) now give us at once the required functional equations:

$$|p^2|,\lambda^2,\lambda'^2\gg m^2\colon\ s(p^2/\lambda^2,p^2/\lambda'^2,e_2^2)=\frac{s_C(p^2/m^2,e_1^2)}{s_C(\lambda'^2/m^2,e_1^2)} \tag{5.3}$$

$$|k^2|,\lambda^2\gg m^2\colon\qquad d(k^2/\lambda^2,e_2^2)=\frac{d_C(k^2/m^2,e_1^2)}{d_C(\lambda^2/m^2,e_1^2)} \tag{5.4}$$

$$e_2^2=e_1^2d_C(\lambda^2/m^2,e_1^2). \tag{5.5}$$

(We have omitted the argument $m^2/p^2=0$ in s and d.)

In Appendix B it is shown that the general nontrivial solution of these equations is given by:

$$e_1^2d_C(k^2/m^2,e_1^2)=F((k^2/m^2)\phi(e_1^2)), \tag{5.6}$$

$$s_C(p^2/m^2,e_1^2)=A(e_1^2)H((p^2/m^2)\phi(e_1^2)). \tag{5.7}$$

Here F, H, ϕ, and A are unknown functions of their arguments. (A contains an infrared divergent factor, which is always canceled, in calculations, by a similar factor in the vertex operator $\Gamma_{\mu C}$.) It is evident that we have obtained much less information here than we did in Sec. III. Also, the results of Sec. III are not correct in the general case, since Eq. (3.11) is not a special case of (5.7), but corresponds rather to a trivial solution of the functional equations (5.3)–(5.5), peculiar to the case of no charge renormalization.[16]

At least one striking result has emerged from the work in this section, however. The quantity on the left-hand side of Eq. (5.6) is, as remarked in the introduction, the Fourier transform of the Laplacian of the potential energy of two heavy point charges. It represents, therefore, the Fourier transform of a kind of effective charge density for the cloud of pairs surrounding a test body in the vacuum. Equation (5.6) states, in effect, that the *shape* of the charge distribution, at distances much smaller than $\hbar/mc$, is independent of the coupling constant $e_1^2/4\pi$, which enters only into the *scale factor* $\phi(e_1^2)$.

This result has an important consequence for the magnitude of e_0^2, the square of the bare charge, which is associated with the strength of the singularity at the center of the effective charge distribution. We have learned in Sec. II that e_0^2 is given by

$$e_0^2=e_1^2d_C(\infty,e_1^2) \tag{5.8}$$

[16] It should be noted that, in any simplified form of the theory in which a restricted class of diagrams is summed, our results are unchanged provided that the conditions for renormalizability, as discussed in Sec. IV, are fulfilled. If, in a renormalizable approximation to the theory, there is charge renormalization, then the results of this section apply; if not, then the results of Sec. III apply.

For example, if the full integral equations (4.4) and (4.5), when renormalized, should turn out not to have solutions, it may be that solutions will exist for the integral equations obtained by cutting off the sequences on the right-hand sides after a finite number of terms and renormalizing. Such a procedure would be renormalizable and would not affect our functional equations.

and that $e_1^2 d_C(k^2/m^2, e_1^2)$ is a positive increasing function of k^2/m^2. Equation (5.6) tells us, then, that $F(\phi(e_1^2)k^2/m^2)$ is an increasing function of k^2/m^2 and that:

(a) If as $k^2/m^2 \to \infty$, $F(\phi k^2/m^2) \to \infty$, then e_0^2 is infinite, and the singularity at the center of the charge distribution is stronger than the δ function that corresponds to a finite point charge. This is the result indicated by perturbation theory.

(b) If, as $k^2/m^2 \to \infty$, $F(\phi k^2/m^2)$ approaches a finite limit, then e_0^2 equals that limit, which is *independent of the value of* e_1^2. The singularity at the center of the effective charge distribution is then a δ function with a strength corresponding to a finite bare charge e_0.

We shall return, at the end of this section, to the discussion of cases (a) and (b). Meanwhile, let us look at the solution of the functional equations from another point of view.

While the functions F and ϕ are unknown, certain of their properties can be deduced from the perturbation expansion of d_C. In the asymptotic region, d_C appears as a double power series in e_1^2 and $\ln(k^2/m^2)$ with finite numerical coefficients. (Of course, the convergence properties of this series are unknown. We have assumed throughout, however, that it defines a function which satisfies the same functional equations that we have derived for the series.) To facilitate comparison of (5.6) with the series, let us make use of the alternative form derived in Appendix B:

$$|k^2| \gg m^2: \quad \ln\frac{k^2}{m^2} = \int_{q(e_1^2)}^{e_1^2 d_C(k^2/m^2, e_1^2)} \frac{dx}{\psi(x)}. \tag{5.9}$$

In Eq. (5.9) both unknown functions q and ψ have power series expansions in their arguments and the first few terms of these series may be determined from the first few orders of perturbation theory. (The functions F and ϕ do not have this property.)

Perturbation theory yields for d_C in the asymptotic region the expansion

$$|k^2| \gg m^2: \quad d_C\left(\frac{k^2}{m^2}, e_1^2\right) = \left[1 - \frac{e_1^2}{12\pi^2}\left(\ln\frac{k^2}{m^2} - \frac{5}{3}\right) - \frac{e_1^4}{64\pi^4}\left(\ln\frac{k^2}{m^2} + c\right) + \cdots\right]^{-1}. \tag{5.10}$$

The fourth-order calculation was performed by Jost and Luttinger,[17] who did not compute c. Comparison of (5.9) and (5.10) yields the expansions of q and ψ:

$$\psi(x) = \frac{1}{12\pi^2}\left[x^2 + \frac{3}{16\pi^2}x^3 + \cdots\right], \tag{5.11}$$

$$q(e_1^2) = e_1^2 - \frac{5}{36\pi^2}e_1^4 + \cdots. \tag{5.12}$$

[17] R. Jost and J. M. Luttinger, Helv. Phys. Acta **23**, 201 (1950).

For the actual value of the coupling constant in quantum electrodynamics, $q(e_1^2)$ is presumably well approximated by e_1^2 and need not concern us very much. The crucial function is $\psi(x)$, which is given by (5.11) for very small x but is needed for large x in order to determine the behavior of the propagation function at very high momenta and to resolve the question of the finiteness of the bare charge.

We can restate, in terms of the properties of ψ, the two possibilities (a) and (b) for the behavior of the theory at high momenta:

(a) The integral $\int dx/\psi(x)$ in (5.9) does not diverge until the upper limit reaches $+\infty$. In that case $\ln(k^2/m^2) = +\infty$ corresponds to $e_1^2 d_C(k^2/m^2, e_1^2) = +\infty$ and the bare coupling constant $e_0^2/4\pi$ is infinite.

(b) For some finite value x_0 of the upper limit, $\int^{x_0} dx/\psi(x)$ diverges; for this to happen, $\psi(x)$ must come down to zero at $x = x_0$. Then $e_1^2 d_C(k^2/m^2, e_1^2) \to x_0$ as $\ln(k^2/m^2) \to \infty$, so that $e_0^2 = x_0$, a finite number independent of e_1^2. Since $e_1^2 < e_0^2$, the theory can exist only for e_1^2 less than some critical value $e_c^2 \leq e_0^2$, where $q(e_c^2) = e_0^2$. As $q(e_1^2)$ approaches its maximum value e_0^2, $\psi(q(e_1^2)) \to 0$, so we learn from Eq. (B.26) in Appendix B that the asymptotic form of $e_1^2 d_C(k^2/m^2, e_1^2)$ reduces simply to the constant e_0^2. A constant asymptotic form of $e_1^2 d_C(k^2/m^2, e_1^2)$ means that the weighting function $f(M^2/m^2, e_1^2)$ in Eq. (2.5) must vanish in the asymptotic region to order $1/M^2$. If the bare charge is finite, then the effective coupling at high momenta varies in a strange way with $q(e_1^2)$, increasing at first with increasing $q(e_1^2)$ and then decreasing to zero at $q(e_1^2) = e_0^2$, beyond which point the theory is meaningless.

Since we cannot discriminate between cases (a) and (b), the methods we have developed have not really served to settle fully the question of the asymptotic character of the propagation function D_{FC}. However, it is to be hoped that these methods may be used in the future to obtain more powerful results.

Recently Källén[18] has investigated the question of the finiteness of the bare charge. His result is that of the three renormalization quantities Z_2^{-1}, e_0^2, and m_0, at least one is infinite. Unfortunately, it is not possible to conclude from Källén's work that case (b) must be rejected.

APPENDIX A. CONSTRUCTION OF PARAMETRIC REPRESENTATIONS FOR THE PROPAGATION FUNCTIONS

The function $S_{F'\alpha\gamma}(x-y)$ is given by the matrix element

$$S_{F'\alpha\gamma}(x-y) = \epsilon(x_0 - y_0)(\Psi_0, P[\psi_\alpha(x), \bar{\psi}_\gamma(y)]\Psi_0). \tag{A.1}$$

Here $\psi(x)$ is the electron (or nucleon) field operator at the space-time point x in the Heisenberg representation; $\bar{\psi}(y)$ is the Dirac adjoint $\psi^*(y)\beta$ of $\psi(y)$; P is Dyson's

[18] G. Källén, Kgl. Danske Videnskab. Selskab, Mat.-fys.Medd. **27**, 12 (1953).

time-ordering operator; $\epsilon(t)$ is $t/|t|$; and Ψ_0 is the vacuum state of the coupled electron and photon (or nucleon and meson) fields.

In quantum electrodynamics S_F' is a gauge-variant function and for that reason one may easily be misled in dealing with it. To avoid such difficulties let us first discuss the function in meson theory (say the neutral pseudoscalar theory).

For $x_0>y_0$ we may write (A.1) in the form

$$S_{F'\alpha\gamma}(x-y)=\sum_{\mathbf{p},M,s,\Pi,n}(\Psi_0\psi_\alpha(x)\Psi_{\mathbf{p},M,s,\Pi,n})\times(\Psi_{\mathbf{p},M,s,\Pi,n}\bar{\psi}_\gamma(y)\Psi_0) \quad (A.2)$$

where the Ψ's are a complete set of eigenstates of the coupled-field Hamiltonian and momentum. The momentum eigenvalue is denoted by $\mathbf{p}$ and the energy eigenvalue is given by $(M^2+p^2)^{\frac{1}{2}}$, so that the system described by the state Ψ has the energy M in its rest frame. For those states which contribute nonvanishing matrix elements to (A.2), the angular momentum of the system in its rest frame is $\frac{1}{2}$ and may have z component $\pm\frac{1}{2}$, denoted by the values ±1 of the index s. Π is the parity of the system in its rest frame and may be $+1$ or -1. The remaining index n labels all the other (invariant) quantum numbers necessary to specify the state.

We may list some of the simplest types of states that contribute:

(1) one nucleon: $M=m$, the renormalized nucleon mass, and $\Pi=+1$ by convention.

(2) one nucleon, one meson: $M=(m^2+k^2)^{\frac{1}{2}}+(\mu^2+k^2)^{\frac{1}{2}}$, where μ is the renormalized meson mass and k is the relative momentum in the rest frame. The parity Π is $+1$ for a meson in a p state and -1 for a meson in an s state relative to the nucleon. It should be emphasized that in the latter case the matrix element does not vanish. For more complicated systems, more quantum numbers n are needed.

The space-time dependence of the matrix elements in (A.2) is determined by the energy and momentum eigenvalues of the Ψ's and so we have, for $x_0>y_0$,

$$S_{F'\alpha\gamma}(x-y)=\frac{1}{(2\pi)^3}\int d^3p\sum_M\times\exp\{i[\mathbf{p}\cdot(\mathbf{x}-\mathbf{y})-(M^2+p^2)^{\frac{1}{2}}(x_0-y_0)]\}\times\sum_{n,s,\Pi}u_\alpha(\mathbf{p},M,s,\Pi,n)u_\delta^*(\mathbf{p},M,s,\Pi,n)\beta_{\delta\gamma}. \quad (A.3)$$

We may consider first only those states with $\mathbf{p}=0$ and later discuss the others by means of Lorentz transformations. For states of zero momentum the sum over spins must give simply

$$\sum_s u_\alpha(0,M,s,\Pi,n)u_\delta^*(0,M,s,\Pi,n)=\tfrac{1}{2}(1+\beta)_{\alpha\delta}U(M,n) \quad \text{if } \Pi=+1$$
$$=\tfrac{1}{2}(1-\beta)_{\alpha\delta}V(M,n) \quad \text{if } \Pi=-1, \quad (A.4)$$

since for such a state the parity operator is β. That all U's and V's are both real and positive follows from taking the trace of both sides of (A.4).

The generalization of (A.4) to the case of $\mathbf{p}\neq0$ is easily calculated by transforming both sides with the Lorentz transformation matrix for velocity $-\mathbf{p}/(p^2+M^2)^{\frac{1}{2}}$. We obtain

$$\sum_s u_\alpha(\mathbf{p},M,s,\Pi,n)u_\delta^*(\mathbf{p},M,s,\Pi,n)=\left(\frac{\boldsymbol{\alpha}\cdot\mathbf{p}+\beta M+(p^2+M^2)^{\frac{1}{2}}}{2(p^2+M^2)^{\frac{1}{2}}}\right)_{\alpha\delta}U(M,n) \quad \text{if } \Pi=+1,$$
$$=\left(\frac{\boldsymbol{\alpha}\cdot\mathbf{p}-\beta M+(p^2+M^2)^{\frac{1}{2}}}{2(p^2+M^2)^{\frac{1}{2}}}\right)_{\alpha\delta}V(M,n) \quad \text{if } \Pi=-1. \quad (A.5)$$

Before substituting these expressions into the formula for S_F', let us make use of the relations

$$\frac{1}{2\pi i}\int_{-\infty}^{\infty}\frac{dp_0\exp(-ip_0t)}{i\gamma_\mu p_\mu+M-i\epsilon}=\frac{\boldsymbol{\alpha}\cdot\mathbf{p}+\beta M+(p^2+M^2)^{\frac{1}{2}}}{2(p^2+M^2)^{\frac{1}{2}}}\beta\times\exp[-i(p^2+M^2)^{\frac{1}{2}}t], \quad (t>0), \quad (A.6)$$

and

$$\frac{1}{2\pi i}\int_{-\infty}^{\infty}\frac{dp_0\exp(-ip_0t)}{i\gamma_\mu p_\mu-M+i\epsilon}=\frac{\boldsymbol{\alpha}\cdot\mathbf{p}-\beta M+(p^2+M^2)^{\frac{1}{2}}}{2(p^2+M^2)^{\frac{1}{2}}}\beta\times\exp[-i(p^2+M^2)^{\frac{1}{2}}t] \quad (t>0). \quad (A.6')$$

Here ϵ is a positive infinitesimal quantity.

We may now rewrite (A.3) as follows:

$$S_{F'}(x)=\frac{1}{(2\pi)^4i}\int d^4p\exp(ip_\mu x_\mu)\sum_M\times\left[\frac{1}{i\gamma_\lambda p_\lambda+M-i\epsilon}\sum_{\Pi=1}^{n}U(M,n)+\frac{1}{i\gamma_\lambda p_\lambda-M+i\epsilon}\sum_{\Pi=-1}^{n}V(M,n)\right]. \quad (A.7)$$

Let us separate off the contribution to S_F' of one-nucleon states, which are associated with $M=m$; the coefficient U for that case is the formally divergent constant called Z_2. For all other values of M, let us put

$$\sum_{\Pi=+1}^{n}U(M,n)=Z_2g(M)/M \quad (A.8)$$

and

$$\sum_{\Pi=-1}^{n}V(M,n)=Z_2h(M)/M. \quad (A.9)$$

Evidently Z_2, g, and h are all real and positive. We now have

$$S_{F'}(x)=\frac{Z_2}{(2\pi)^4 i}\int d^4p\,\exp(ip_\mu x_\mu)\times\left\{\frac{1}{i\gamma p+m-i\epsilon}+\int_{m+\mu}^{\infty}\frac{g(M)}{i\gamma p+M-i\epsilon}\frac{dM}{M}+\int_{m+\mu}^{\infty}\frac{h(M)}{i\gamma p-M+i\epsilon}\frac{dM}{M}\right\}\quad(x_0>0).\quad\text{(A.10)}$$

It follows from the invariance of the theory under charge conjugation that the Eq. (A.10), which we have derived for $x_0>0$, holds also for $x_0<0$.

We must still find an expression for Z_2 in terms of g and h. So far, we have used nothing but relativistic invariance; now we must make use of the anticommutation rules for ψ and ψ^*. Let us calculate the quantity

$$\text{disc}\,S_F'\equiv\lim_{t\to 0^+}[S_F'(\mathbf{x},t)-S_F'(\mathbf{x},-t)].\quad\text{(A.11)}$$

We utilize the relation

$$\text{disc}\,\frac{1}{(2\pi)^4 i}\int\frac{d^4p\,\exp(ip_\mu x_\mu)}{i\gamma p+M-i\epsilon}=\text{disc}\,\frac{1}{(2\pi)^4 i}\int\frac{d^4p\,\exp(ip_\mu x_\mu)}{i\gamma p-M+i\epsilon}=\beta\delta(\mathbf{x}).\quad\text{(A.12)}$$

Equation (A.10) then yields

$$\text{disc}\,S_F'=Z_2\beta\delta(\mathbf{x})\times\left(1+\int_{m+\mu}^{\infty}\frac{dM}{M}[g(M)+h(M)]\right).\quad\text{(A.13)}$$

Another expression for disc S_F' can be obtained from Eq. (A.1):

$$\text{disc}\,S_F'=\langle\Psi_0,\{\psi(\mathbf{x},t),\bar{\psi}(0,t)\}\Psi_0\rangle=\beta\delta(\mathbf{x}).\quad\text{(A.14)}$$

Comparison of (A.13) and (A.14) yields

$$Z_2^{-1}=1+\int_{m+\mu}^{\infty}\frac{dM}{M}[g(M)+h(M)].\quad\text{(A.15)}$$

With the aid of (A.10) and Dyson's Eq. (2.7) we have for the Fourier transform of the renormalized propagation function the representation

$$S_{FC}(p)=\frac{1}{i\gamma p+m-i\epsilon}+\int_{m+\mu}^{\infty}\frac{g(M)dM/M}{i\gamma p+M-i\epsilon}+\int_{m+\mu}^{\infty}\frac{h(M)dM/M}{i\gamma p-M+i\epsilon}.\quad\text{(A.16)}$$

The meson propagation functions Δ_F' and Δ_{FC} can be dealt with by methods entirely analogous to those we have used for the nucleon functions. In place of (A.1) we have

$$\Delta_F'(x-y)=\langle\Psi_0,P[\phi(x),\phi(y)]\Psi_0\rangle.\quad\text{(A.17)}$$

Considerations of relativistic invariance lead us to the result

$$\Delta_F'(x)=Z_3\frac{1}{(2\pi)^4 i}\int d^4k\,\exp(ik_\mu x_\mu)\times\left[\frac{1}{k^2+\mu^2-i\epsilon}+\int_{(2\mu)^2}^{\infty}\frac{dM^2}{M^2}\frac{f(M^2)}{k^2+M^2-i\epsilon}\right]\quad\text{(A.18)}$$

corresponding to (A.10). Utilizing the canonical commutation rule for ϕ and $\partial\phi/\partial t$ at equal times, we obtain, in complete analogy with (A.15),

$$Z_3^{-1}=1+\int_{(2\mu)^2}^{\infty}\frac{dM^2 f(M^2)}{M^2}.\quad\text{(A.19)}$$

In quantum electrodynamics, S_F' must be calculated, according to Gupta[19] and Bleuler,[20] from the equation

$$S_F'(x-y)=\epsilon(x_0-y_0)\langle\Psi_0,\eta P[\psi(x),\bar{\psi}(y)]\Psi_0\rangle\quad\text{(A.20)}$$

rather than (A.1). Here $\eta=(-1)^{N_4}$ and N_4 is the operator describing the number of "temporal photons." The only effect of the introduction of η into our previous work is to remove the requirement that g and h be positive.

The photon propagation function D_F' satisfies the relation

$$\langle\Psi_0,\eta P[A_\mu(x),A_\nu(y)]\Psi_0\rangle=\delta_{\mu\nu}D_F'(x-y)+\frac{\partial^2}{\partial x_\mu\partial x_\nu}G(x-y),\quad\text{(A.21)}$$

analogous to (A.17). Here G is gauge-variant but D_F' is not. We may determine D_F', moreover, from the transverse part of $A_\mu(x)$ alone, so that the operator η does not disturb us. The results are then identical with (A.18) and (A.19) with $\mu=0$; f is positive as in meson theory.

The functions S_{FC} and D_{FC} in quantum electrodynamics are given, to first order in the coupling constant $\alpha=e_1^2/4\pi$, by

$$S_{FC}(p)=\frac{1}{i\gamma p+m-i\epsilon}+\frac{e_1^2}{16\pi^2}\int_m^{\infty}\frac{dM}{M^3(M^2-m^2)}\times\left[\frac{(M+m)^3(M^2+m^2-4mM)}{i\gamma p+M-i\epsilon}+\frac{(M-m)^2(M^2+m^2+4mM)}{i\gamma p-M+i\epsilon}\right]\quad\text{(A.22)}$$

[19] S. W. Gupta, Proc. Phys. Soc. (London) **63**, 681 (1950).
[20] K. Bleuler, Helv. Phys. Acta **23**, 567 (1950).

and

$$D_{FC}(k)=\frac{1}{k^2}+\frac{e_1^2}{12\pi^2}\int_{4m^2}^{\infty}\frac{dM^2}{M^2}\times\frac{(1+2m^2/M^2)(1-4m^2/M^2)^{\frac{1}{2}}}{k^2+M^2-i\epsilon}. \quad (A.23)$$

It will be seen that the function $g(M)$ in (A.22) is not always positive. This is in contrast with the situation in meson theory. In the scalar symmetric theory with $\mu=0$ we have

$$S_{FC}(p)=\frac{1}{i\gamma p+m-i\epsilon}+\frac{3g_1^2}{16\pi^2}\int_m^{\infty}\times\frac{dM}{M^3(M^2-m^2)}\left[\frac{(M+m)^2(M^2+m^2)}{i\gamma p+M-i\epsilon}+\frac{(M-m)^2(M^2+m^2)}{i\gamma p-M+i\epsilon}\right], \quad (A.24)$$

while in the pseudoscalar symmetric theory we have

$$S_{FC}(p)=\frac{1}{i\gamma p+m-i\epsilon}+\frac{3g_1^2}{16\pi^2}\int_m^{\infty}\frac{dM}{2M^3}(M^2-m^2)\times\left[\frac{1}{i\gamma p+M-i\epsilon}+\frac{1}{i\gamma p-M+i\epsilon}\right]. \quad (A.25)$$

APPENDIX B. SOLUTION OF THE FUNCTIONAL EQUATIONS[21]

We may solve Eqs. (5.4) and (5.5) for the photon propagation function without reference to Eq. (5.3). For convenience we reproduce the equations:

$$d(k^2/\lambda^2,e_2^2)=d_C(k^2/m^2,e_1^2)/d_C(\lambda^2/m^2,e_1^2), \quad (5.4)$$

$$e_2^2=e_1^2d_C(\lambda^2/m^2,e_1^2). \quad (5.5)$$

Combining the equations, we obtain

$$e_1^2d_C(k^2/m^2,e_1^2)=e_1^2d_C(\lambda^2/m^2,e_1^2)\times d(k^2/\lambda^2,e_1^2d_C(\lambda^2/m^2,e_1^2)). \quad (B.1)$$

Giving new names to the left- and right-hand sides of (B.1), we may write

$$g(k^2/m^2,e_1^2)=Q(k^2/\lambda^2,g(\lambda^2/m^2,e_1^2)) \quad (B.2)$$

or

$$g(x,e_1^2)=Q(x/y,g(y,e_1^2)). \quad (B.3)$$

Except in trivial cases we may invert the function g and put

$$x=h(g,e_1^2), \quad y=h(g',e_1^2). \quad (B.4)$$

[21] We would like to thank Dr. T. D. Lee for suggesting the form of the solution to us.

Then (B.3) becomes

$$g=Q(h(g,e_1^2)/h(g',e_1^2),\,g'). \quad (B.5)$$

If the functional form of Q is nontrivial, then $h(g,e_1^2)/h(g',e_1^2)$ must be independent of e_1^2. Thus

$$h(g,e_1^2)=G(g)/\phi(e_1^2), \quad (B.6)$$

which implies that

$$g(x,e_1^2)=F(x\phi(e_1^2)), \quad (B.7)$$

where F is the inverse function to G. In terms of the original labels, we have

$$e_1^2d_C(k^2/m^2,e_1^2)=F((k^2/m^2)\phi(e_1^2)). \quad (B.8)$$

Substituting (B.8) into (5.5), we obtain

$$e_2^2=F((\lambda^2/m^2)\phi(e_1^2)). \quad (B.9)$$

Using (B.8) and (B.9) we find

$$F\left(\frac{k^2}{m^2}\phi(e_1^2)\right)=F\left(\frac{k^2}{\lambda^2}\frac{\lambda^2}{m^2}\phi(e_1^2)\right)=F((k^2/\lambda^2)G(e_2^2)). \quad (B.10)$$

Since F and G are inverse functions, there is only one arbitrary function in (B.10). It is now evident that (B.1) is indeed satisfied, with

$$e_2^2d(k^2/\lambda^2,e_2^2)=F((k^2/\lambda^2)G(e_2^2)). \quad (B.11)$$

In a power series calculation, e_2^2d appears as a double series in e_2^2 and $\ln(k^2/\lambda^2)$. Let us transform (B.11) so that comparison with the series solution becomes possible:

$$G(e_2^2d)=(k^2/\lambda^2)G(e_2^2), \quad (B.12)$$

$$\ln k^2/\lambda^2=\ln G(e_2^2d)-\ln G(e_2^2), \quad (B.13)$$

$$\ln\frac{k^2}{\lambda^2}=\int_{e_2^2}^{e_2^2d}\frac{dx}{\psi(x)}. \quad (B.14)$$

Here

$$\psi(x)=G(x)(dG/dx)^{-1}. \quad (B.15)$$

Differentiating both sides of (B.14) with respect to $\ln(k^2/\lambda^2)$, we have

$$1=\frac{1}{\psi(e_2^2d)}\frac{\partial(e_2^2d)}{\partial(\ln(k^2/\lambda^2))}, \quad (B.16)$$

or

$$\psi(e_2^2d)=\frac{\partial(e_2^2d)}{\partial(\ln(k^2/\lambda^2))}. \quad (B.17)$$

If in (B.17) we put $\ln(k^2/\lambda^2)=0$, we obtain

$$\psi(e_2^2)=\frac{\partial(e_2^2 d)}{\partial(\ln(k^2/\lambda^2))}\bigg|_{\ln(k^2/\lambda^2)=0}. \tag{B.18}$$

Evidently the double series expansion of $e_2^2 d$ yields a power series expansion of $\psi(e_2^2)$. In fact the entire double series can be rewritten in terms of $\psi(e_2^2)$. If we differentiate both sides of (B.14) with respect to e_2^2, we get

$$0=\frac{1}{\psi(e_2^2 d)}\frac{\partial(e_2^2 d)}{\partial(e_2^2)}-\frac{1}{\psi(e_2^2)}. \tag{B.19}$$

Combining this result with (B.17) yields

$$\psi(e_2^2)=\frac{\partial(e_2^2 d)}{\partial(\ln(k^2/\lambda^2))}\Big/\frac{\partial(e_2^2 d)}{\partial e_2^2}, \tag{B.20}$$

whence

$$e_2^2 d\left(\frac{k^2}{\lambda^2},e_2^2\right)=\sum_{n=0}^{\infty}\frac{[\ln(k^2/\lambda^2)]^n}{n!}\left[\psi(e_2^2)\frac{d}{de_2^2}\right]^n e_2^2. \tag{B.21}$$

Representations similar to (B.14) and (B.21) can be found for $e_1^2 d_C(k^2/m^2,e_1^2)$. We transform (B.8) as follows:

$$G(e_1^2 d_C)=(k^2/m^2)\phi(e_1^2), \tag{B.22}$$

$$\ln(k^2/m^2)=\ln G(e_1^2 d_C)-\ln\phi(e_1^2), \tag{B.23}$$

$$\ln(k^2/m^2)=\int_{q(e_1^2)}^{e_1^2 d_C} dx/\psi(x) \tag{B.24}$$

where ψ is the same function as before and

$$q(e_1^2)=F(\phi(e_1^2)). \tag{B.25}$$

A comparison of (B.24) and (B.14) shows that the functional dependence of $e_1^2 d_C$ on k^2/m^2 and $q(e_1^2)$ is the same as the dependence of $e_2^2 d$ on k^2/λ^2 and e_2^2. Therefore, we have, from Eq. (3.21), the series expansion

$$e_1^2 d_C\left(\frac{k^2}{m^2}e_1^2\right)=\sum_{n=0}^{\infty}\frac{[\ln(k^2/m^2)]^n}{n!}\times\left\{\left[\psi(y)\frac{d}{dy}\right]^n y\right\}_{y=q(e_1^2)}. \tag{B.26}$$

The representation (B.26) may easily be compared with the double series in e_1^2 and $\ln(k^2/m^2)$ obtained from perturbation theory. We see that when $\ln(k^2/m^2)$ is set equal to 0 we obtain for the right-hand side just $q(e_1^2)$, so that the perturbation theory gives a power series expansion for $q(e_1^2)$.

So far our discussion has been confined to the photon propagation function. We must now solve the functional equation (5.3) for the electron propagation function:

$$s(p^2/\lambda^2,p^2/\lambda'^2,e_2^2)=\frac{s_C(p^2/m^2,e_1^2)}{s_C(\lambda'^2/m^2,e_1^2)}. \tag{5.3}$$

Using (B.9), we can write the left-hand side as

$$s(p^2/\lambda^2,p^2/\lambda'^2,e_2^2)=s(p^2/\lambda^2,p^2/\lambda'^2,F(\phi(e_1^2)\lambda^2/m^2)). \tag{B.27}$$

By virtue of (5.3) this must be independent of λ^2 and may be written

$$s(p^2/\lambda^2,p^2/\lambda'^2,e_2^2)=R((p^2/m^2)\phi(e_1^2),(\lambda'^2/m^2)\phi(e_1^2)). \tag{B.28}$$

Since the quotient on the right-hand side of (5.3) depends on its arguments only through $(p^2/m^2)\phi(e_1^2)$ and $(\lambda'^2/m^2)\phi(e_1^2)$, we must have

$$s_C(p^2/m^2,e_1^2)=A(e_1^2)H(p^2/m^2\phi(e_1^2)). \tag{B.29}$$

Tamm-Dancoff Method

J. C. TAYLOR
Peterhouse, Cambridge, England
(Received April 26, 1954)

The Tamm-Dancoff equations are expressed in a concise four-dimensional form. The difficulty of renormalizing the new Tamm-Dancoff equation of Dyson is discussed. The Lévy-Klein approximation to the Bethe-Salpeter equation is derived as an approximation to the old Tamm-Dancoff equation, and a new renormalizable equation is derived analogously as an approximation to the new Tamm-Dancoff equation. The latter approximation is better than the former.

1. INTRODUCTION

DYSON[1] has shown that the Tamm-Dancoff equation in its original form (to be called O.T.D.) is not renormalizable. He has given a modified theory[2] (N.T.D.) from which the divergencies can be removed in the second order. In Part 3, we show that Dyson's result cannot be extended to the fourth order. The reasons for this are discussed.

Use is made of a concise reformulation of Cini's[3] covariant form of Tamm-Dancoff. The new formulation is due to Matthews and Salam,[4] and is quoted in Part 2. It shows up more clearly the precise approximations which are being made and the relation of the theory to the perturbation method.

Lévy[5] and Klein[6] have developed a technique for approximating to the Bethe-Salpeter equation by using an ansatz for the dependence of the wave function on the relative time of the two particles. They obtain a three-dimensional equation (to be called L.K.), which gains physical plausibility from its resemblance to O.T.D. Because of the divergence difficulties in Tamm-Dancoff, L.K. has sometimes been used along with or instead of O.T.D.

In the past, L.K. has mainly been considered as derived from the Bethe-Salpeter equation, its similarity to O.T.D. being accepted as a fortunate accident. In Parts 4 and 5, we analyze the relation between L.K. and O.T.D. Two distinct approximations are required to get the one from the other. The second approximation is cruder than the first. In the case of N.T.D., however, an approximation of the first kind, by itself, gives a new renormalizable equation. This equation, like L.K., can be derived from the Bethe-Salpeter equation, but only after the application of an analytic continuation process of the sort used by Dyson[7] in his study of Heisenberg operators.

We conclude that, starting from the Tamm-Dancoff method, there is available a better renormalizable approximation to N.T.D. than the L.K. approximation to O.T.D. Since the Tamm-Dancoff method is better understood physically than the Bethe-Salpeter equation, the new approximation may be preferable to L.K.

2. THE EQUATIONS

In this section, we quote the Matthews-Salam formulation of the Cini-Tamm-Dancoff equations.

Let $|t\rangle$ be the state vector of the system in the interaction representation at time t. Then

$$|t\rangle=|-\infty\rangle-i\int_{-\infty}^{t}H(t_1)|t_1\rangle dt_1, \tag{1}$$

where $H(t)$ is the interaction Hamiltonian. Iterating (1) n times,

$$\begin{aligned}|t\rangle=|-\infty\rangle+\sum_{m=1}^{n-1}(-i)^m\int_{-\infty}^{t}dt_1\int_{-\infty}^{t_1}dt_2\cdots\\ \times\int_{-\infty}^{t_{m-1}}dt_mH(t_1)\cdots H(t_m)|-\infty\rangle\\ +(-i)^n\int_{-\infty}^{t}dt_1\int_{-\infty}^{t_1}dt_2\cdots\\ \times\int_{-\infty}^{t_{n-1}}dt_nH(t_1)\cdots H(t_n)|t_n\rangle.\end{aligned} \tag{2}$$

We now specialize to the deuteron. Multiply (2) on the left by ${}_0\langle\psi^+(x')\psi^+(x'')$, where ${}_0\langle$ is the bare particle vacuum. For a bound state, all terms containing $|-\infty\rangle$ vanish, by an argument of Cini's.[3] There remains an exact equation for the Cini amplitude

$$\begin{aligned}{}_0\langle\psi^+(x')\psi^+(x'')|t\rangle=(-i)^n\int_{-\infty}^{t}dt_1\cdots\\ \times\int_{-\infty}^{t_{n-1}}dt_n\,{}_0\langle\psi^+(x')\psi^+(x'')H(t_1)\cdots H(t_n)|t_n\rangle.\end{aligned} \tag{3}$$

The right-hand side of (3) can be expanded in terms of normal products, each term giving rise to a Cini amplitude multiplied by a c-number kernel. The approximation which gives an integral equation is to

[1] F. J. Dyson, Phys. Rev. **91**, 421 (1953).
[2] F. J. Dyson, Phys. Rev. **91**, 1543 (1953).
[3] M. Cini, Nuovo cimento **10**, 526 (1953).
[4] The author is deeply indebted to Dr. P. T. Matthews and Dr. Abdus Salam for the opportunity to see their unpublished work and their kind permission to quote from it.
[5] M. Lévy, Phys. Rev. **88**, 72 (1952).
[6] A. Klein, Phys. Rev. **90**, 1101 (1953).
[7] F. J. Dyson, Phys. Rev. **82**, 428 (1951).

neglect all terms on the right except those containing the two-particle amplitude. This is equivalent to the two approximations: (i) All amplitudes that cannot be linked to the original amplitude (in our case the two-particle amplitude) by $\frac{1}{2}n$ operations of the Hamiltonian are neglected (the "true" Tamm-Dancoff approximation). (ii) Higher amplitudes are systematically eliminated to give an integral equation, whose kernel is taken to the nth order (the method used, for instance, by Lévy[6]). By "the Tamm-Dancoff equation" we will always mean the result of both these approximations.

The Tamm-Dancoff equation was originally given in three-dimensional form. If our equation is transformed to momentum space, the equivalence is evident; for each of the successive time integrations in (3) brings down a characteristic energy denominator.

We may formulate N.T.D. in an analogous way. Let $|t\rangle_0$ be the vacuum state vector of the interacting fields. Then, for any operator Q,

$$ {}_0\langle t|Q|t\rangle = {}_0\langle -\infty|Q|-\infty\rangle + i\int_{-\infty}^{t} dt_1\, {}_0\langle t_1|[H(t_1),Q]|t_1\rangle. \quad (4) $$

Iterating (4) n times:

$$ \begin{aligned} {}_0\langle t|Q|t\rangle = {}_0\langle -\infty|Q|-\infty\rangle &+ \sum_{m=1}^{n-1}(i)^m\int_{-\infty}^{t}dt_1\cdots\int_{-\infty}^{t_{m-1}}dt_m \\ &\times {}_0\langle -\infty|[H(t_m),\cdots[H(t_1),Q]\cdots]|-\infty\rangle \\ &+(i)^n\int_{-\infty}^{t}dt_1\cdots\int_{-\infty}^{t_{n-1}}dt_n \\ &\times {}_0\langle t_n|[H(t_n),\cdots[H(t_1),Q]\cdots]|t_n\rangle. \quad (5) \end{aligned} $$

For the deuteron, $Q=\psi(x')\psi(x'')$. When the the right-hand side of (5) is expanded in terms of normal products, the terms containing $|-\infty\rangle$ are of two sorts: (i) those with only destruction operators and (ii) those with at least one creation operator. For a bound state, the terms (i) vanish by Cini's argument. The terms (ii) correspond to incoming "minus" particles. They are unphysical, and we shall suppose them to be zero. This would come out of the formalism if we had, for instance,

$$ |-\infty\rangle_0 = \rangle_0. \quad (6) $$

This question is connected with the "spurious poles" discussed by Dyson.[2]

We have then the exact equation for the Dyson amplitude

$$ {}_0\langle t|\psi(x')\psi(x'')|t\rangle = (i)^n\int_{-\infty}^{t}dt_1\cdots\int_{-\infty}^{t_{n-1}}dt_n \times {}_0\langle t_n|[H(t_n),\cdots[H(t_1),\psi(x')\psi(x'')]\cdots]|t_n\rangle. \quad (7) $$

The approximate integral equation is obtained in the same way as for O.T.D.

3. RENORMALIZATION

We begin this section by giving an example of a term in N.T.D. from which the divergence cannot be removed by the usual methods. Afterwards we discuss the reason for this difficulty.

Consider the N.T.D. one-particle equation in three-dimensional momentum space. This has the form

$$ (W-H_p)\chi(\mathbf{p}) = K(\mathbf{p},W)\chi(\mathbf{p}). \quad (8) $$

W is the total energy, and $H_p=\eta_p E_p=\boldsymbol{\alpha}\cdot\mathbf{p}+M\beta$. Otherwise the notation is Dyson's.[2] Four time-ordered graphs which represent fourth-order contributions to $K(\mathbf{p},W)$ are shown in Fig. 1.

Picking out terms from these graphs characterized by certain matrix elements in their numerators (which are sufficiently independent of terms not written down for there is to be no possibility of cancellation), the contribution to $K(\mathbf{p},W)$ is

$$ \lambda^2\int d\mathbf{k}d\mathbf{k}'(4\omega_k\omega_{k'})^{-1}\Lambda_p{}^{+}\gamma\Lambda_{p-k}{}^{+}\gamma(\Lambda_{p-k-k'}{}^{+}-\Lambda_{p-k-k'}{}^{-}) \times\gamma\Lambda_{p-k}{}^{-}\gamma\Lambda_p{}^{+}(W-E_{p-k}-\omega_k)^{-1}f, \quad (9) $$

where the contributions to f from the four graphs are, respectively,

$$ f_a=f_b=-\tfrac{1}{2}(W-E_p-2E_{p-k})^{-1} \times(W-E_p-E_{p-k}-E_{p-k-k'}-\omega_{k'})^{-1}; \quad (9a) $$

$$ f_c=\tfrac{1}{2}(W-E_{p-k-k'}-\omega_k-\omega_{k'})^{-1} \times(W-E_p-E_{p-k}-E_{p-k-k'}-\omega_{k'})^{-1}; \quad (9b) $$

$$ f_d=\tfrac{1}{2}(W-E_p-2E_{p-k})^{-1}\{(E_{p-k}-E_{p-k-k'}-\omega_{k'})^{-1} -(E_{p-k}+E_{p-k-k'}+\omega_{k'})^{-1}\}. \quad (9c) $$

(9c) gives the correct value of the rest mass counter term δM. We have taken advantage of the identity,

$$ \Lambda_{p-k}{}^{+}\gamma(\Lambda_{p-k-k'}{}^{+}+\Lambda_{p-k-k'}{}^{-})\gamma\Lambda_{p-k}{}^{-}=0, $$

to produce a uniform antisymmetry in Eqs. (9).

When Eqs. (9) are combined we have, as well as terms which are convergent over the $\mathbf{k}'$ integration, a term containing the logarithmically divergent integral,

$$ \tfrac{1}{2}\lambda\int d\mathbf{k}'(2\omega_{k'})^{-1}(\Lambda_{p-k-k'}{}^{+}-\Lambda_{p-k-k'}{}^{-}) \times\{E_{p-k}{}^2-(E_{p-k-k'}+\omega_{k'})^2\}^{-1}. \quad (10) $$

Expression (10) is *not* a constant and so cannot be interpreted as any usual sort of renormalization. It is certainly not a charge renormalization term, for such terms cannot appear in this example.

To see the reason for the unrenormalizability, we return to the four-dimensional formalism. The general

form of the one-particle integral equation derived from the one-particle analog of (3) or (7) is

$$\chi_t(x)=\int K_1(x,x')\chi_{t'}(x')dx' + \int K_2(x,x',x'')\chi_{t''}(x')dx'dx'', \quad (11)$$

where χ_t is the Cini or Dyson amplitude. $x=(\mathbf{x},t)$ is a four-vector. If we pass to momentum space with the help of

$$\chi_{t''}(x')=\int d\mathbf{p}\exp\{i(\mathbf{p}\cdot\mathbf{x}'-Wt') +i(W-H_{\mathbf{p}})(t'-t'')\}\chi(\mathbf{p}), \quad (12)$$

we get Eq. (8). From (11) and (12), it is clear that the contribution to $K(\mathbf{p},W)$ from $K_2(x,x',x'')$ cannot contain $(\mathbf{p},W)$ as a four-vector. Therefore, the usual renormalization process, based upon the subtraction of a covariant linear form from $K(\mathbf{p},W)$, cannot be expected to succeed in general.

The second-order N.T.D. equation is exceptional, because there are no terms of the sort of K_2 in (11).

The renormalization difficulty may be understood in a more physical way as follows. Consider, for simplicity, the second-order O.T.D. equation. Effectively this iterates the time-ordered graphs (a) and (b) of Fig. 2. In contrast, the corresponding renormalizable equation, the Dyson integral equation in the theory of the S matrix, iterates the Feynman graph (c). But the iteration of (c) is not equivalent to the iteration of (a) and (b). For example, the second iterate of (c) contains, when time-ordered, in addition to the second iterates of (a) and (b), such graphs as (d). This graph, which

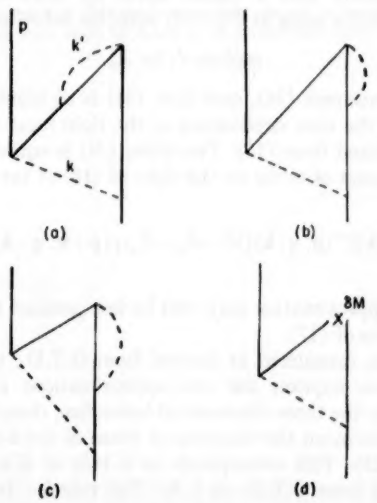

FIG. 1. Time-ordered graphs describing a nonrenormalizable fourth-order self-energy term in N.T.D.

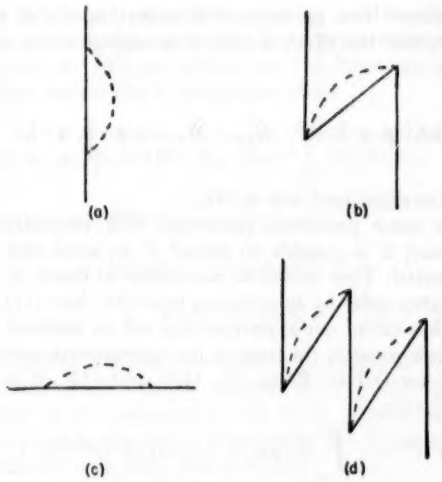

FIG. 2. Time-ordered graphs [(a), (b), and (d)] and a Feynman graph (c) relevant to the question of renormalization.

only appears in a higher-order Tamm-Dancoff term, is needed to complete the renormalization of (b). Thus, the Tamm-Dancoff approximation separates from the iteration of (c) a subset of time-ordered graphs in a noncovariant way.

The same argument applies to N.T.D., with, for example, the graphs of Fig. 1 replacing graph (b) of Fig. 2.

4. APPROXIMATE EQUATIONS

Let $\chi_t(x',x'')$ be a Cini or Dyson amplitude for the two-particle system. Define

$$\chi(x',x'')=\chi_{t'}(x',x''), \quad t'<t'' \\ =\chi_{t''}(x',x''), \quad t'>t''. \quad (13)$$

Then our basic approximation is to

$$\text{replace } \chi_t(x',x'') \text{ by } \chi(x',x'') \quad (14)$$

in the right-hand side of the Tamm-Dancoff integral equation.

The validity of this approximation can be estimated most easily in the three-dimensional formalism. From the definition of the amplitudes,

$$\chi_t(x',x'')=\int d\mathbf{p}d\mathbf{q}\exp\{i(\mathbf{p}\cdot\mathbf{x}'+\mathbf{q}\cdot\mathbf{x}''-H_{\mathbf{p}}t'-H_{\mathbf{q}}t'') -i(W-H_{\mathbf{p}}-H_{\mathbf{q}})t\}\chi(\mathbf{p},\mathbf{q}). \quad (15)$$

[In the case of O.T.D., $\chi(\mathbf{p},\mathbf{q})$ is to be understood to contain the factor $\Lambda_{\mathbf{p}}^{+}\Lambda_{\mathbf{q}}^{+}$.] With the use of (15), the integral equation takes the form

$$(W-H_{\mathbf{p}}-H_{\mathbf{q}})\chi(\mathbf{p},\mathbf{q}) =\int d\mathbf{k}K(\mathbf{p},\mathbf{q};\mathbf{k})\chi(\mathbf{p}+\mathbf{k},\mathbf{q}-\mathbf{k}). \quad (16)$$

It follows from the manner of derivation of (16) using (15), that the effect of (14) is to neglect terms of the form

$$\int d\mathbf{k}K'(\mathbf{p},\mathbf{q};\mathbf{k})(W-H_{\mathbf{p}+\mathbf{k}}-H_{\mathbf{q}-\mathbf{k}})\chi(\mathbf{p}+\mathbf{k},\mathbf{q}-\mathbf{k}) \quad (17)$$

on the right-hand side of (16).

In some problems, concerned with nonrelativistic regions, it is possible to regard K as some sort of a potential. Then it will be reasonable to throw K' into a higher order by substituting from (16) into (17), and to that extent our approximation will be justified.

Now consider the form of the approximate equation, first for O.T.D. From (3), (13), and (14), it is (for $t', t''>t$):

$$\chi_t(x',x'')=-\int_{-\infty}^{t}dx_1'dx_1''S^+(x'-x_1')S^+(x''-x_1'')$$

$$\times\int_{-\infty}^{+\infty}dx_2'dx_2''J_t(x_1',x_1'';x_2',x_2'')\chi(x_2',x_2''), \quad (18)$$

where J_t is defined by

$$\int_{-\infty}^{t}dx_1'dx_1''S^+(x'-x_1')S^+(x''-x_1'')\int_{-\infty}^{+\infty}dx_2'dx_2''$$

$$\times J_t(x_1',x_1'';x_2',x_2'')S^+(x_2'-y')S^+(x_2''-y'')$$

$$=(-i)^n\int_{-\infty}^{t}dt_1\cdots\int_{-\infty}^{t_{n-1}}dt_n\,{}_0\langle T(\psi^+(x')\psi^+(x'')$$

$$\times H(t_1)\cdots H(t_n)\bar{\psi}^-(y')\bar{\psi}^-(y''))\rangle_0. \quad (19)$$

T denotes a chronologically ordered product. In spite of the form of the right-hand side of (19), Eq. (18) is not renormalizable by the usual methods because of the incomplete time integration.

Second, consider the form of the approximate N.T.D. equation. From (7), (13), and (14), it is

$$\chi_t(x',x'')=\int I(x',x'';x_1',x_1'')\chi(x_1',x_1'')dx_1'dx_1'', \quad (20)$$

where

$$-\int dx_1'dx_1''I(x',x'';x_1',x_1'')S^+(x_1'-y')S^+(x_1''-y'')$$

$$=(i)^n\int_{-\infty}^{t}dt_1\cdots\int_{-\infty}^{t_{n-1}}dt_n\,{}_0\langle[H(t_n),\cdots$$

$$\times[H(t_1),\psi(x')\psi(x'')]\cdots]\bar{\psi}^-(y')\bar{\psi}^-(y'')\rangle_0. \quad (21)$$

In (20), we may write $t'=t''=t$ without loss of generality. Then (21) is similar to a term arising in the expansion of Heisenberg operators. It is easy to see that the theory given by Dyson[7,8] is equally applicable to the particular product of two fermion field variables appearing here, and thus affords a method for renormalizing Eq. (20). The theory also provides a method of evaluating I. In our case, we first define a function I_F,

$$-\int dx_1'dx_1''I_F(x',x'';x_1',x_1'')S^+(x_1'-y')S^+(x_1''-y'')$$

$$=(1/n!)(-i)^n\int_{-\infty}^{+\infty}dt_1\cdots dt_n\,{}_0\langle T(H(t_1)\cdots$$

$$\times H(t_n)\psi(x')\psi(x''))\bar{\psi}^-(y')\bar{\psi}^-(y'')\rangle_0. \quad (22)$$

Then the momentum space forms of I and I_F are related by a certain analytical continuation process.

5. RELATION TO THE BETHE-SALPETER EQUATION

Lévy[5] and Klein[6] have obtained a three-dimensional approximation to the Bethe-Salpeter equation, by means of an ansatz for the relative-time dependence of the wave function. The ansatz used means, physically, that the "later" particle propagates freely beyond the "earlier" one. From Eqs. (13) and (15), our function $\chi(x',x'')$ has, for the case of O.T.D., just this relative-time dependence.

Define J_∞ by Eq. (19) with t replaced by $+\infty$. Then the Bethe-Salpeter equation in the nth order may be written

$$X(x',x'')=\int dx_1'dx_1''dx_2'dx_2''S_F(x'-x_1')S_F(x''-x_1'')$$

$$\times J_\infty(x_1',x_1'';x_2',x_2'')X(x_2',x_2''). \quad (23)$$

The L.K. equation is obtained from (23) by approximating to X by χ, and throwing the negative energy components into a higher order by iteration. The result is the same as Eq. (18) with the substitution:

$$\text{replace } J_t \text{ by } J_\infty. \quad (24)$$

To interpret (24), note that (18) is an identity in t, and so the time dependence of the right-hand side can be deduced from (15). Therefore, (24) is equivalent to the neglect of terms on the right of (16) of the form

$$\int d\mathbf{k}K''(\mathbf{p},\mathbf{q};\mathbf{k})(W-E_{\mathbf{p}}-E_{\mathbf{q}})\chi(\mathbf{p}+\mathbf{k},\mathbf{q}-\mathbf{k}). \quad (25)$$

This approximation may well be less justified than the omission of (17).

Thus, considered as derived from O.T.D., the L.K. equation requires the two approximations (14) and (24). In the three-dimensional formalism, these approximations mean the dropping of terms of the forms (17) and (25). This corresponds to a rule of Klein's[6] for passing from O.T.D. to L.K. The rule is "In energy denominators corresponding to intermediate states for which the two nucleons are in their initial or final

[8] F. J. Dyson, Phys. Rev. 83, 608 (1951).

state, the combined energy of the two nucleons is to be taken as W."

We now give the corresponding relation for the case of N.T.D. If, in (20), we approximate to I by I_F and to χ by X, it follows from (22) that we have exactly the Bethe-Salpeter equation. Reversing this procedure, we have the following prescription for deriving our approximate N.T.D. equation from the Bethe-Salpeter equation. "Calculate the nth order Bethe-Salpeter kernel. Apply the Dyson analytic continuation process to it. Then insert the ansatz χ for the wave function X." The ansatz χ, defined by (13) and (15), has the same sort of physical interpretation as in the O.T.D. case. However, the free particle propagation is according to single-particle theory and not to hole theory.[9]

Thus, an equation [our Eq. (20)] closely related to the Bethe-Salpeter equation can be derived from N.T.D. by the single approximation (14). This approximation is less drastic than the one required to give L.K., but the equation is also renormalizable.

Finally, we illustrate, by means of the ladder approximation, the prescription for deriving our approximate N.T.D. equation from the Bethe-Salpeter equation. After putting the times equal on the right-hand side, the Bethe-Salpeter equation may be written, in momentum space,

$$\begin{aligned}\int X(\mathbf{p},\mathbf{q};p_0)dp_0 &= \lambda(2\pi i)^{-1}(W-H_p-H_q)^{-1}\int dp_0'dk_0d\mathbf{k}(2\omega_k)^{-1}\\ &\times\{(\tfrac{1}{2}W+p_0'-k_0-H_p)^{-1}+(\tfrac{1}{2}W-p_0'+k_0-H_q)^{-1}\}\\ &\times\{(k_0-\omega_k)^{-1}-(k_0+\omega_k)^{-1}\}\\ &\times\gamma^P\gamma^N X(\mathbf{p}+\mathbf{k},\mathbf{q}-\mathbf{k};p_0'),\end{aligned}\tag{26}$$

[9] The suggestion that such an ansatz should be required for N.T.D. has been made by Klein in an unpublished note.

where p_0 and p_0' are relative energies, and superfixes P and N distinguish the two nucleons where necessary. The poles in (26) are defined by the Feynman prescription, and so the k_0 integration gives

$$\begin{aligned}\int X(\mathbf{p},\mathbf{q};p_0)dp_0 &= \lambda(W-H_p-H_q)^{-1}\int dp_0'd\mathbf{k}(2\omega_k)^{-1}\\ &\times[\{\tfrac{1}{2}W+p_0'-\eta_p(E_p+\omega_k)\}^{-1}\\ &+\{\tfrac{1}{2}W-p_0'-\eta_q(E_q+\omega_k)\}^{-1}]\\ &\times\gamma^P\gamma^N X(\mathbf{p}+\mathbf{k},\mathbf{q}-\mathbf{k};p_0').\end{aligned}\tag{27}$$

The Dyson analytic continuation process applied to the kernel of (27) simply changes the Feynman prescription to the prescription that W be given a small positive imaginary part. The ansatz for the p_0 dependence of X is, from (15) and (13),

$$\{(\tfrac{1}{2}W+p_0-H_p+i\epsilon)^{-1}+(\tfrac{1}{2}W-p_0-H_q+i\epsilon)^{-1}\}\chi(\mathbf{p},\mathbf{q}).\tag{28}$$

Inserting (28) into (27) and integrating over the remaining energy components, we find

$$\begin{aligned}\chi(\mathbf{p},\mathbf{q}) &= \lambda(W-H_p-H_q)^{-1}\int d\mathbf{k}(2\omega_k)^{-1}\\ &\times[\gamma^N\{W-H_{q-k}-\eta_p(E_p+\omega_k)\}^{-1}\gamma^P\\ &+\gamma^P\{W-H_{p+k}-\eta_q(E_q+\omega_k)\}^{-1}\gamma^N]\\ &\times\chi(\mathbf{p}+\mathbf{k},\mathbf{q}-\mathbf{k}),\end{aligned}\tag{29}$$

which is the exact second-order N.T.D. equation. In this simple case the approximation (14) has no effect.

The author is indebted to Dr. R. J. Eden, Dr. P. T. Matthews, and Dr. Abdus Salam for many discussions.

Hyperquantization of Feynman Amplitudes

F. COESTER*
Institute for Advanced Study, Princeton, New Jersey
(Received May 7, 1954)

A hyperquantization formalism is presented which employs an occupation-number representation for the set of all Feynman amplitudes. The relation between the amplitudes and the occupation number representation is quite similar to that between the Fock amplitudes and the occupation number representation commonly used in the theory of quantized fields. The differential equations for the Feynman amplitudes can be written and manipulated in a more compact form in this representation. Formal solutions of these equations are given and the connection with the S-matrix formalism is discussed.

I. INTRODUCTION

IN the relativistic description of elementary particles, space-time functions akin to the wave functions of nonrelativistic quantum mechanics have been widely used. Feynman[1] used them intuitively without giving a formal definition relating them to quantized fields. Such a definition was first given for two-particle amplitudes by Gell-Mann and Low.[2] Many-particle amplitudes have been studied by Gell-Mann and Goldberger[3] who proposed the name "Feynman amplitudes" and a formal definition in terms of quantized fields. Feynman's kernel functions[1] and Schwinger's Green's functions[4] are closely related to these amplitudes. Recently several authors[5-7] have studied independently the equations satisfied by general Feynman amplitudes and their interpretation. The analogy between these many-particle amplitudes and the many-body wave functions of nonrelativistic quantum mechanics is quite limited. Nevertheless, this analogy can be exploited advantageously in formal considerations. It is well known that a considerable formal simplification results from the use of an occupation number representation for the state vector and the introduction of particle creation and annihilation operators.[8] The purpose of this note is to show that a similar step greatly simplifies formal operations with Feynman amplitudes.[9] To be specific about the particles described we treat only pseudoscalar mesons in interaction with nucleons. The methods can, of course, be applied as well to other types of particles and other interactions.

II. THE FUNDAMENTAL EQUATIONS

Let $\chi(x_n\cdots x_1; y_1\cdots y_m; z_1\cdots z_k)$ be the Feynman amplitude for n nucleons, m antinucleons, and k mesons. We need not, at this point, discuss its definition in terms of field operators; we merely note its transformation properties. Under Lorentz transformations, the amplitude χ transforms by definition like a product of n spinors, m adjoint spinors (usually denoted by $\bar{\psi}$), and k pseudoscalars. To every variable x and y belongs a spinor index which takes the values $1\cdots4$.

The fundamental step in our hyperquantization formalism is the introduction of a "state vector" Φ such that the components of Φ are the Feynman amplitudes:

$$\Phi=\sum_{nmk}(n!m!k!)^{-1}\int dx_n\cdots\int dx_1\int dy_1\cdots$$
$$\times\int dy_m\int dz_1\cdots\int dz_k\chi(x_n\cdots x_1;y_1\cdots y_m;$$
$$\times z_1\cdots z_k)\mathbf{c}^+(z_k)\cdots\mathbf{c}^+(z_1)\mathbf{b}^+(y_m)\cdots$$
$$\times\mathbf{b}^+(y_1)\mathbf{a}^+(x_1)\cdots\mathbf{a}^+(x_n)\Omega_0, \quad (1)$$

where $\mathbf{a}^+(x)$, $\mathbf{b}^+(y)$, and $\mathbf{c}^+(z)$ are creation operators depending on the space-time points x, y, z. Ω_0 is a "vacuum state" defined by the condition that any annihilation operator operating on Ω_0 gives zero. Space-time and four-momentum space are treated here in much the same way as the three-dimensional position and momentum spaces in the ordinary theory. In addition to the usual periodicity cube of volume V in x space we have a finite time interval of length T and therefore a point lattice in four-momentum space with $VT/(2\pi)^4$ lattice points per unit volume:

$$\lim_{VT\to\infty}\frac{1}{VT}\sum_p\cdots=(2\pi)^{-4}\int dp\cdots,$$

where p is a four-vector and dp is a four-dimensional volume element. We can define creation and annihilation operators satisfying the usual commutation rules at every lattice point. For the mesons we have the creation and annihilation operators $\mathbf{c}^+(p)$ and $\mathbf{c}(p)$

* Permanent address: Department of Physics, State University of Iowa, Iowa City, Iowa.
[1] R. P. Feynman, Phys. Rev. **80**, 440 (1950).
[2] M. Gell-Mann and F. Low, Phys. Rev. **84**, 350 (1951).
[3] M. Gell-Mann and M. L. Goldberger, Phys. Rev. **87**, 218 (1952) (A).
[4] J. Schwinger, Proc. Natl. Acad. Sci. **37**, 452 (1951); Phys. Rev. **82**, 664, 914 (1951); **91**, 713, 728 (1953); **92**, 1283 (1953); **93**, 615 (1954).
[5] P. T. Matthews and A. Salam, Proc. Roy. Soc. (London) **A221**, 128 (1953).
[6] E. Freese, Z. Naturforsch **8a**, 776 (1953); Nuovo cimento **11**, 312 (1954); Acta Phys. Austriaca **8**, 289 (1954).
[7] K. Nishijima, Progr. Theoret. Phys. **10**, 549 (1953).
[8] V. Fock, Z. Physik **75**, 622 (1934).
[9] Creation and annihilation operators of the type to be discussed here have been used by M. Gell-Mann and M. L. Goldberger. I am indebted to Dr. Goldberger for telling me about this unpublished work.

satisfying the relations

$$[\mathbf{c}(p),\mathbf{c}(p')]=0, \tag{2}$$

and

$$[\mathbf{c}(p),\mathbf{c}^{+}(p')]=\delta(p,p'), \tag{3}$$

where $^{+}$ indicates the Hermitian conjugate. In order to describe nucleons and antinucleons we need the operators $\mathbf{a}_\rho(p)$ and $\mathbf{b}_\rho(p)$ satisfying the anticommutation rules,

$$\{\mathbf{a}_\rho(p),\mathbf{a}_{\rho'}{}^{+}(p')\}=\{\mathbf{b}_\rho(p),\mathbf{b}_{\rho'}{}^{+}(p')\}=\delta_{\rho\rho'}\delta(p,p'). \tag{4}$$

All other combinations anticommute. The space-time dependent operators occurring in (1) are defined by a Fourier transformation:

$$\mathbf{c}(x)=(VT)^{-\frac{1}{2}}\sum_p \mathbf{c}(p)e^{ipx}, \tag{5}$$

$$\mathbf{a}_\rho(x)=(VT)^{-\frac{1}{2}}\sum_p \mathbf{a}_\rho(p)e^{ipx}, \tag{6}$$

$$\mathbf{b}_\rho(x)=(VT)^{-\frac{1}{2}}\sum_p \mathbf{b}_\rho(p)e^{ipx}. \tag{7}$$

Here ρ plays a part of a four-valued spinor index. Spinor indices have been dropped from the notation in (1) for convenience. Summation over the spinor index is implied whenever there is an integration over x or y. Equation (1) can easily be solved for the amplitudes:[10]

$$\chi(x_n\cdots x_1;y_1\cdots y_m;z_1\cdots z_k)=(\Omega_0,\mathbf{a}(x_n)\cdots \times\mathbf{a}(x_1)\mathbf{b}(y_1)\cdots\mathbf{b}(y_m)\mathbf{c}(z_1)\cdots\mathbf{c}(z_k)\Phi). \tag{8}$$

The operators $\mathbf{a}_\rho$ and $\mathbf{b}_\rho$ cannot transform as spinors since this would be inconsistent with the commutation rules (4). There is, however, no difficulty on that account. We may assume for instance that they are the same functions of p in all Lorentz frames. Φ' and Φ represent the same state in two different Lorentz frames if Φ' is given by (1) with χ' substituted for χ, and χ' is obtained from χ by Lorentz transformation.

Matthews and Salam[5] and Freese[6] have derived differential equations for the Feynman amplitudes from the field equations for the Heisenberg operators:

$$\mathfrak{D}(x)\psi(x)=g\gamma_5\psi(x)\phi(x), \tag{9}$$

$$\mathfrak{D}(-x)\bar{\psi}(x)=g\bar{\psi}(x)\gamma_5\phi(x), \tag{10}$$

$$\mathfrak{K}(x)\phi(x)=g\tfrac{1}{2}[\bar{\psi}(x),\gamma_5\psi(x)]. \tag{11}$$

$\mathfrak{D}(x)$ and $\mathfrak{K}(x)$ are, respectively, the Dirac operator and the Klein Gordon operator:

$$\mathfrak{D}(x)=i\left(\gamma^\mu(x)\frac{\partial}{\partial x^\mu}+m\right), \tag{12}$$

$$\mathfrak{K}(x)=-i(\Box-\kappa^2). \tag{13}$$

The notation $\gamma(x)$ means the Dirac matrix γ is to be multiplied by the x-dependent spinor following it. For instance,

$$\gamma_5(x)\psi(y)\psi(x)=\psi(y)(\gamma_5\psi(x)), \tag{14}$$

and

$$\gamma_5(x)\bar{\psi}(x)=\bar{\psi}(x)\gamma_5.$$

We could proceed now and derive equations for Φ from the differential equations for the amplitudes. There is some advantage, however, in deriving the equations for Φ by considering the matrix element,

$$(\Psi_0,T(\psi(x_n)\cdots\psi(x_1)\bar{\psi}(y_1)\cdots\bar{\psi}(y_m)\phi(z_1)\cdots\phi(z_k))\Psi) =T(x_n\cdots x_1;y_1\cdots y_m;z_1\cdots z_k). \tag{15}$$

Ψ_0 is the physical vacuum state and Ψ is any state in the Heisenberg representation. $T(\psi(x_n)\cdots)$ is Wick's T product[11] of the field operators. These T products satisfy a set of differential equations given by Matthews and Salam[5] which is somewhat simpler than that for the Feynman amplitudes.

$$\mathfrak{D}(x)T(x_n\cdots x_1x;y_1\cdots y_m;z_1\cdots z_k) =g\gamma_5(x)T(x_n\cdots x_1x;y_1\cdots y_m;xz_1\cdots z_k) +\sum_{j=1}^{m}\delta(x-y_j)T(x_n\cdots x_1;y_j{}^{-1}y_1\cdots y_m;z_1\cdots z_k), \tag{16}$$

where, by definition,

$$T(x_n\cdots x_1;y_j{}^{-1}y_1\cdots y_m;z_1\cdots z_k) =(-1)^{j-1}T(x_n\cdots x_1;y_1\cdots y_{j-1}y_{j+1}\cdots y_m;\times z_1\cdots z_k), \tag{17}$$

$$\mathfrak{D}(-y)T(x_n\cdots x_1;yy_1\cdots y_m;z_1\cdots z_k) =g\gamma_5(y)T(x_n\cdots x_1;yy_1\cdots y_m;yz_1\cdots z_k) +\sum_{i=1}^{n}\delta(x_i-y)T(x_n\cdots x_1x_i{}^{-1};y_1\cdots y_m;z_1\cdots z_k), \tag{18}$$

and

$$\mathfrak{K}(z)T(x_n\cdots x_1;y_1\cdots y_m;zz_1\cdots z_k) =-g\gamma_5(z)T(x_n\cdots x_1z;zy_1\cdots y_m;z_1\cdots z_k) +\sum_{h=1}^{k}\delta(z-z_h)T(x_n\cdots x_1;y_1\cdots y_m;z_1\cdots z_h{}^{-1}\cdots z_k). \tag{19}$$

These equations follow from (9)–(11) and the canonical commutation rules at equal times.

In formulating the equations for Φ it will be useful to *define* operators ψ, $\psi^\dagger$, ϕ as follows:

$$\psi(x)=\mathbf{a}(x)-\int dy S_F(x-y)\mathbf{b}^{+}(y) =(VT)^{-1/2}\sum_p[\mathbf{a}(p)-S_F(p)\mathbf{b}^{+}(-p)]e^{ipx}, \tag{20}$$

[10] We assume that χ has no δ-like singularities for equal arguments.

[11] G. C. Wick, Phys. Rev. **80**, 268 (1950).

$$\psi^\dagger(x)=\mathbf{b}(x)+\int dy\mathbf{a}^+(y)S_F(y-x)$$

$$=(VT)^{-\frac{1}{2}}\sum_p[\mathbf{b}(p)+\mathbf{a}^+(-p)S_F(-p)]e^{ipx}, \quad (21)$$

$$\phi(x)=\mathbf{c}(x)+\int dyD_F(x-y)\mathbf{c}^+(y)$$

$$=(VT)^{-1/2}\sum_p[\mathbf{c}(p)+D_F(p)\mathbf{c}^+(-p)]e^{ipx}, \quad (22)$$

where the Feynman propagators S_F and D_F are defined by[12,13]

$$S_F(x)=(2\pi)^{-4}\int dpe^{ipx}S_F(p),$$
$$S_F(p)=-i(i\gamma p+m-i\epsilon)^{-1}, \quad (23)$$

and

$$D_F(x)=(2\pi)^{-4}\int dpe^{ipx}D_F(p), \quad (24)$$

$$D_F(p)=-i(p^2+\kappa^2-i\eta)^{-1}. \quad (25)$$

The quantities ϵ and η are small positive parameters which tend to zero at the end of any calculation. They remain different from zero while V and T go to infinity. The matrices $\mathbf{a}$, $\mathbf{b}^+$, and ψ are column matrices with respect to the spinor index; $\mathbf{b}$, $\mathbf{a}^+$, and $\psi^\dagger$ are row matrices. The operators ψ, $\psi^\dagger$, and ϕ are defined by (20)–(22) and should not be confused with the Heisenberg field operators ψ, $\bar{\psi}$, and ϕ. According to their definition ψ, $\psi^\dagger$, and ϕ satisfy the remarkably simple commutation relations:

$$\{\psi(x),\psi(x')\}=\{\psi^\dagger(x),\psi^\dagger(x')\}=0, \quad (26)$$

$$\{\psi(x),\psi^\dagger(x')\}=0, \quad [\phi(x),\phi(x')]=0, \quad (27)$$

which will be important throughout the following development. The S product of such operators is defined exactly as Wick's S product of field operators in the interaction representation.[11]

It is now easy to see that the functions

$$(\Omega_0,\psi(x_n)\cdots\psi(x_1)\psi^\dagger(y_1)\cdots\psi^\dagger(y_m)\phi(z_1)\cdots\phi(z_k)\Phi) \quad (28)$$

satisfy the differential equations (16), (18), and (19) if we require the following equations for Φ:

$$(\mathfrak{D}(x)\mathbf{a}(x)-g\gamma_5\psi(x)\phi(x))\Phi=0, \quad (\mathrm{I})$$

$$(\mathfrak{D}(-x)\mathbf{b}(x)-g\psi^\dagger(x)\gamma_5\phi(x))\Phi=0, \quad (\mathrm{II})$$

$$(\mathfrak{K}(x)\mathbf{c}(x)-g:\psi^\dagger(x)\gamma_5\psi(x):)\Phi=0. \quad (\mathrm{III})$$

The colons in (III) indicate Wick's S product. To prove that (28) satisfies (16) as a consequence of (I) we point out that $\mathfrak{D}(x)\psi(x)=\mathfrak{D}(x)\mathbf{a}(x)-\mathbf{b}^+(x)$. The first term is shifted to the right until it stands next to Φ and can be replaced by the second term in (I). $\mathbf{b}^+(x)$ is shifted to the left. By similar operations one obtains (18) and (19) from (II) and (III), respectively. According to the definition of ψ, $\psi^\dagger$, and ϕ the product occurring in (28) is related to the S product of these operators in the same way in which the T product and the S product of free fields are related in the ordinary theory. The amplitudes χ [see Eq. (8)] are therefore identical to the Feynman amplitudes as defined by Matthews and Salam.[5] It is also easy to verify from (I)–(III) that the χ's satisfy the required equations.

Φ is obviously not fully determined by the Eqs. (I)–(III). On the other hand, Eqs. (16), (18), and (19) hold for any matrix element of the T product of Heisenberg fields. Identification of (28) with (15) implies the selection of a particular Φ satisfying (I)–(III). Other matrix elements of the same T product would be equal to (28) with a different Φ also satisfying (I)–(III). We are concerned here mainly with the Feynman amplitudes and therefore the particular matrix element (15), but it might be of interest to consider, for instance, a Φ such that

$$(\Psi,\tfrac{1}{2}[\bar{\psi}(x),\gamma_5\psi(x)]\Psi)=(\Omega_0,\mathbf{b}(x)\gamma_5\mathbf{a}(x)\Phi). \quad (29)$$

Matthews and Salam define the Feynman amplitudes in terms of T-product amplitudes and the free-particle propagators S_F and D_F. Other authors[6,7] propose amplitudes defined in the same way except that

$$S_F'(x-y)=\langle T(\psi(x)\bar{\psi}(y))\rangle_0, \quad (30)$$

and

$$D_F'(x-y)=\langle T(\phi(x)\phi(y))\rangle_0 \quad (31)$$

are substituted for S_F and D_F. These amplitudes satisfy more complicated equations and it has not been demonstrated that they are useful. Nevertheless, it may be of interest to point out possible modifications of our formalism. We define ψ', $\psi^{\dagger\prime}$, and ϕ' by substituting S_F' and D_F' for S_F and D_F in (20), (21), and (22). The equations for a modified vector Φ' are then written in the form

$$(\mathfrak{D}(x)\psi'(x)+\mathbf{b}^+(x)-g\gamma_5\psi'(x)\phi'(x))\Phi'=0, \quad (\mathrm{I}')$$

$$(\mathfrak{D}(-x)\psi^{\dagger\prime}(x)-\mathbf{a}^+(x)-g\psi^{\dagger\prime}(x)\gamma_5\phi'(x))\Phi'=0, \quad (\mathrm{II}')$$

$$(\mathfrak{K}(x)\phi'(x)-\mathbf{c}^+(x)-g:\psi^{\dagger\prime}(x)\gamma_5\psi'(x):)\Phi'=0. \quad (\mathrm{III}')$$

These equations are obviously identical to (I)–(III) if we leave the prime off everywhere. On the other hand, the expression (28) formed with ψ', $\psi^{\dagger\prime}$, ϕ', and Φ' still satisfies Eqs. (16), (18), and (19). To verify (16), for instance, we shift $\mathfrak{D}\psi'$ to the right until it stands next to Φ'; it can then be replaced by $-\mathbf{b}^+ + g\gamma_5\psi'\phi$. Then $\mathbf{b}^+$ is shifted all the way to the left and $g\gamma_5\psi'\phi'$ shifted to the place where $\mathfrak{D}\psi'$ stood in the beginning.

[12] These definitions of S_F and D_F differ from Dyson's (see reference 13) by a factor $-\frac{1}{2}$ and $\frac{1}{2}$, respectively. Our $S_F(x)$ and $D_F(x)$ are identical with those of reference 2 and with the functions $s(x)$ and $d(x)$ of reference 5.

[13] F. J. Dyson, Phys. Rev. **75**, 1736 (1949).

Equations (18) and (19) can be verified in the same way. $(\Omega_0, \psi'(x_n)\cdots\psi'(x_1)\psi'(y_1)\cdots\psi^{\dagger\prime}(y_m)\phi'(z_1)\cdots\phi'(z_k)\Phi')$ can therefore again be identified with (15). The amplitudes,

$$\chi'(x\cdots)=(\Omega_0,\mathfrak{a}(x)\cdots\Phi'), \tag{32}$$

are, of course, different. Their differential equations can be easily derived from (I')–(III'). The properties of S_F' and D_F' have not been used in these arguments and they need not be defined by (30) and (31).

III. FORMAL SOLUTIONS

For $g=0$ Eqs. (I)–(III) are easily interpreted. They require that only particles with the experimental mass values may be present. Let Ω be any vector satisfying the equations with $g=0$;

$$\mathfrak{D}(x)\mathfrak{a}(x)\Omega=0, \tag{I_0}$$

$$\mathfrak{D}(-x)\mathfrak{b}(x)\Omega=0, \tag{II_0}$$

$$\mathfrak{K}(x)\mathfrak{c}(x)\Omega=0. \tag{III_0}$$

We can construct a formal solution of (I)–(III) by putting

$$\Phi=(\exp\mathfrak{L})\Omega, \tag{33}$$

where

$$\mathfrak{L}=g\int dx{:}\psi^\dagger(x)\gamma_0\psi(x){:}\phi(x)-\mathfrak{L}_0. \tag{34}$$

$\mathfrak{L}_0$ is a constant defined by the condition,

$$(\Omega_0,(\exp\mathfrak{L})\Omega_0)=1. \tag{35}$$

In order to show that (33) is a solution of (I) we multiply (I_0) by $\exp\mathfrak{L}$ and use the identity,

$$(\exp\mathfrak{L})\mathfrak{D}\mathfrak{a}=\{\mathfrak{D}\mathfrak{a}+[\mathfrak{L},\mathfrak{D}\mathfrak{a}] +\tfrac{1}{2}[\mathfrak{L},[\mathfrak{L},\mathfrak{D}\mathfrak{a}]]+\cdots\}\exp\mathfrak{L}. \tag{36}$$

From the commutation rules (4), it follows that

$$[\mathfrak{L},\mathfrak{D}\mathfrak{a}]=-g\gamma_0\psi\phi. \tag{37}$$

The right-hand side of (37) commutes with $\mathfrak{L}$ according to (26)–(27) and the commutator series in (36) breaks off. This shows that $\Phi=(\exp\mathfrak{L})\Omega$ satisfies (I). In the same manner one can easily see that (II) and (III) are also satisfied.

From the formal solution (33) we can easily derive integral equations for the Feynman amplitudes.[6,14] The derivation of these integral equations can be sufficiently explained by considering the two-nucleon amplitude $\chi(x_1x_2;-;-)$. We define the amplitude $\chi^0(x_1x_2;-;-)$ by

$$\chi^0(x_1x_2;-;-)=(\Omega_0,(\exp\mathfrak{L})\mathfrak{a}(x_1)\mathfrak{a}(x_2)\Omega), \tag{38}$$

and use the identity

$$(\Omega_0,(\exp\mathfrak{L})\mathfrak{a}(x_1)\mathfrak{a}(x_2)\Omega) =(\Omega_0,\mathfrak{a}(x_1)\mathfrak{a}(x_2)\Phi)+(\Omega_0,[\mathfrak{L},\mathfrak{a}(x_1)\mathfrak{a}(x_2)]\Phi) +\tfrac{1}{2}(\Omega_0,[\mathfrak{L},[\mathfrak{L},\mathfrak{a}(x_1)\mathfrak{a}(x_2)]]\Phi). \tag{39}$$

After evaluation of the commutators, we have

$$\begin{aligned}\chi(x_1x_2;-;-)&=\chi^0(x_1x_2;-;-)\\&+g\int dyS_F(x_1-y)\gamma_0(y)\chi(yx_2;-;y)\\&+g\int dyS_F(x_2-y)\gamma_0(y)\chi(x_1y;-;y)\\&+g^2\int dy_1\int dy_2S_F(x_1-y_1)\gamma_0(y_1)S_F(x_2-y_2)\gamma_0(y_2)\\&\times\{\chi(y_1y_2;-;y_1y_2)+D_F(y_1-y_2)\\&\qquad\times\chi(y_1y_2;-;-)\}.\end{aligned} \tag{40}$$

χ^0 satisfies the free Dirac equation with respect to both variables as a consequence of (I_0). The generalization to other amplitudes is straight forward. For N particles the commutator series breaks off after the Nth term.

Formal solutions of (I')–(III') can be constructed in a similar way. We do not leave S_F' and D_F' completely arbitrary but require that they satisfy equations of the form:

$$\begin{aligned}S_F'(p)&=S_F(p)+S_F(p)\xi(p)S_F'(p),\\D_F'(p)&=D_F(p)+D_F(p)\zeta(p^2)D_F'(p),\end{aligned} \tag{41}$$

where ξ and ζ are arbitrary except for the requirements $\zeta(-\kappa^2)=0$ and $\xi(p)u(p)=0$; $u(p)$ is a spinor satisfying $(i\gamma p+m)u(p)=0$. A formal solution of (I')–(III') is given by

$$\Phi'=(\exp\mathfrak{L}')\Omega, \tag{42}$$

if

$$\begin{aligned}\mathfrak{L}'=g\int dx{:}\psi^{\dagger\prime}(x)\gamma_0\psi'(x){:}\phi'(x)\\-\int dx\int dy\psi^{\dagger\prime}(x)\xi(x-y)\psi'(y)\\-\tfrac{1}{2}\int dx\int dy\phi'(x)\zeta(x-y)\phi'(y)-\mathfrak{L}_0'.\end{aligned} \tag{43}$$

That (42) is indeed a solution of (I')–(III') is easily verified with the aid of the relations:

$$[\mathfrak{L}',\mathfrak{b}^+(x)]=-g\gamma_0\psi'(x)\phi'(x)+\int dy\xi(x-y)\psi'(y), \tag{44}$$

$$[\mathfrak{L}',\mathfrak{a}^+(x)]=g\psi^{\dagger\prime}(x)\gamma_0\phi'(x)-\int dy\psi^{\dagger\prime}(y)\xi(y-x), \tag{45}$$

$$[\mathfrak{L}',\mathfrak{c}^+(x)]=g{:}\psi^{\dagger\prime}(x)\gamma_0\psi'(x){:}-\int dy\zeta(x-y)\phi'(y). \tag{46}$$

[14] R. J. Eden, Proc. Cambridge Phil. Soc. (to be published).

Inserting (42) in (I′) and shifting $\exp\mathfrak{L}'$ to the left, we get for the left-hand side of (I′):

$$(\exp\mathfrak{L}')\left(\mathfrak{D}(x)\psi'(x)+\mathbf{b}^+(x)-\int dy\xi(x-y)\psi'(y)\right)\Omega$$

$$=(\exp\mathfrak{L}')\left(\mathfrak{D}(x)\mathbf{a}(x)-\int dy\xi(x-y)\mathbf{a}(y)\right)\Omega=0. \quad (47)$$

This vanishes on account of (I_0) and our assumption about ξ. The same procedure yields from (II′) and (III′), respectively:

$$(\exp\mathfrak{L}')\left(\mathfrak{D}(-x)\psi^{\dagger\prime}(x)-\mathbf{a}^+(x)-\int dy\psi^{\dagger\prime}(y)\xi(y-x)\right)\Omega$$

$$=(\exp\mathfrak{L}')\left(\mathfrak{D}(-x)\mathbf{b}(x)-\int dy\mathbf{b}(y)\xi(y-x)\right)\Omega=0, \quad (48)$$

and

$$(\exp\mathfrak{L}')\left(\mathfrak{K}(x)\phi'(x)-\mathbf{c}^+(x)-\int dy\zeta(x-y)\phi'(y)\right)\Omega$$

$$=(\exp\mathfrak{L}')\left(\mathfrak{K}(x)\mathbf{c}(x)-\int dy\zeta(x-y)\mathbf{c}(y)\right)\Omega=0. \quad (49)$$

IV. THE S MATRIX

The form of the operator $\exp\mathfrak{L}$ suggests a close relationship between this operator and the S matrix as calculated in the interaction representation. In discussing this relationship we restrict ourselves to meson-nucleon scattering for the sake of definiteness in our formulas. The same arguments apply to other cases.

Some attention must be paid to the limiting process involved in calculating transition rates form the S matrix. In agreement with the usual trick of switching on the interaction adiabatically we assume a time dependent coupling constant,

$$g(x)=\begin{cases} g\exp(\alpha x^0) & \text{if } x^0<t \\ 0 & \text{if } x^0>t, \end{cases} \quad (50)$$

with the understanding that $\alpha\to 0$, $t\to\infty$ and $\alpha t\to 0$.

$$S=\lim S(\alpha,t).$$

The transition rate for the transition $a\to b$ is then given by

$$\lim_{\alpha t\to 0,\, t\to\infty}\frac{\partial|S_{ba}(\alpha,t)|^2}{\partial t}. \quad (51)$$

The asymptotic Feynman amplitude $\chi(\mathbf{x},\infty;\mathbf{z},\infty)$ is defined by

$$\chi(\mathbf{x},\infty;\mathbf{z},\infty)=\lim(\alpha t\to 0,\, t\to\infty,\, x^0>t,\, z^0>t)\times\chi(x,z;\alpha,t), \quad (52)$$

$$\chi(x,z;\alpha,t)=(\Phi^0,\psi_f(x)\phi_f(x)S(\alpha,t)\Phi_i)\times(\Phi^0,S(\alpha,t)\Phi^0)^{-1}, \quad (53)$$

if $x^0>t$ and $z^0>t$. Here Φ^0 is the free-particle vacuum; ψ_f and ϕ_f are field operators in the interaction representation. Φ_i is the initial state; for instance,

$$\Phi_i=a^+(p,\sigma)c^+(k)\Phi^0, \quad (54)$$

for definite initial momenta $\mathbf{p}$ and $\mathbf{k}$ and spin orientation σ. a^+ and c^+ are the creation operators of the ordinary field theory. In our hyperquantization formalism we have

$$\mathfrak{L}=\lim\mathfrak{L}(\alpha,t), \quad (55)$$

according to (50). There are several limits implied: $VT\to\infty$; $\epsilon\to 0$, $\eta\to 0$; $\alpha t\to 0$, $t\to\infty$. They must be taken in this order when the order is relevant. The expression to be compared with (53) is

$$\chi(x,z;\alpha,t)=(\Omega_0,\mathbf{a}(x)\mathbf{c}(z)(\exp\mathfrak{L}(\alpha,t))\Omega), \quad (56)$$

where

$$\Omega=\int dx'\int dx''\mathbf{a}^+(x')\mathbf{c}^+(z')\chi^0(x',z')\Omega_0, \quad (57)$$

and

$$\chi^0(x,z)=V^{-1}(2\nu)^{-1/2}u(\mathbf{p},\sigma)e^{ipx}e^{ikz}, \quad (58)$$

u being a spinor describing a free nucleon with momentum $\mathbf{p}$ and spin orientation σ. $\nu=(|\mathbf{k}|^2+\kappa^2)^{\frac{1}{2}}$. Comparison of (53) and (56) establishes the precise relationship between $\exp\mathfrak{L}$ and the S matrix. It is easy to see that the usual Feynman rules obtain if one expands $\exp\mathfrak{L}$ in powers of $\mathfrak{L}$ and expresses the terms of the power series in S products. Comparison of (56) and (53) incidentally also elucidates the significance of the constant $\exp\mathfrak{L}_0$. It is equal to $(\Phi^0, S\Phi^0)$ and serves to eliminate disconnected closed loops from the transition amplitudes. In order to have a simple illustration, we expand (56) up to the second order in g and obtain

$$\chi(x,z;\alpha t)=\chi^0(x,z)+\int dx'\int dx''g(x')g(x'')\times S_F(x-x')\gamma_5 S_F(x'-x'')\gamma_5 u(\mathbf{p},\sigma)(2\nu)^{-\frac{1}{2}}e^{ipx''}\times(D_F(z-x')e^{ikx'}+D_F(z-x'')e^{ikx''}). \quad (59)$$

The Feynman propagators $S_F(x-x')$ and $D_F(z-x')$ assure the correct mass values for the outgoing waves provided $x^0>x'^0$ and $z^0>z'^0$. The same approximation follows from (53) and the usual perturbation expansion of the S matrix.

In the case discussed here, the amplitude $\chi'(x,z)$ defined by (32) is identical to $\chi(x,z)$:

$$\chi(x,z)=\chi'(x,z)=(\Psi_0,T(\psi(x)\phi(z))\Psi). \quad (60)$$

If we expand in powers of $\mathfrak{L}'$ [see Eq. (43)] rather than $\mathfrak{L}$, modified Feynman rules obtain and one might hope to gain an improvement over straightforward perturbation theory in this way.

The close relationship between $\exp\mathfrak{L}$ and the S matrix makes it obvious that Dyson's renormalization procedure[13,15] can be applied to our formalism without difficulty.

I wish to thank the Institute for Advanced Study for a grant-in-aid and Professor J. Robert Oppenheimer for the hospitality extended to me at the Institute. I have benefited from many conversations with the members of the Institute, in particular Dr. G. Källén. I am indebted to Dr. M. L. Goldberger for several stimulating discussions.

[15] A. Salam, Phys. Rev. 82, 217 (1951).

PHYSICAL REVIEW VOLUME 95, NUMBER 5 SEPTEMBER 1, 1954

Some Generalizations of the Foldy-Wouthuysen Transformation

K. M. Case
Randall Laboratory of Physics, University of Michigan, Ann Arbor, Michigan

(Received April 30, 1954)

A canonical transformation similar to that given by Foldy and Wouthuysen is obtained for the spin zero and one theories. For free particles positive and negative charge states are separately described by one or three component wave functions. It is found that the resulting forms for operators and the nonrelativistic limits are quite similar to that for spin ½. The resulting similarity is found to carry over to still higher spins. Particles moving in magnetic fields are described most simply using the transformed representation.

I. INTRODUCTION

FOLDY and Wouthuysen[1] have shown that, by means of a canonical transformation, it is possible to transform the Dirac equation for a free particle into a form in which the paradoxical properties disappear. More precisely, they have shown that in the transformed representation it is particularly clear how to associate operators with classical dynamical variables so that these operators go over into the expected nonrelativistic form and so that these operators have reasonable properties. For the case in which external fields are present they have shown that the nonrelativistic approximation is most conveniently obtained by means of canonical transformations suggested by their field free work.

While the point is not usually emphasized, it is well known that Klein-Gordon and Proca particles also exhibit peculiar properties. For example (with the most natural definition of the relevant operators), the eigenvalues of the velocity operator for a spin-zero particle are all zero, while the eigenvalues of the *square* of the velocity operator of a spin-one particle are zero or *negative*. (This is possible since the corresponding operators are not Hermitian.)

The question arises as to the possibility of transforming these equations so as to circumvent the difficulties. It may be expected that, if an appropriate transformation is possible, the resulting equations for spin 0, ½ and 1 will have a very similar form. Moreover, the nonrelativistic approximation for integral spin should be particularly easy to obtain from this point of view. It will be seen that these expectations are indeed borne out. The resulting symmetry of the wave equations is also found to hold for particles of spin higher than one.

While most of the usefulness of the transformation lies in discussing questions of interpretation, it will be seen in Sec. VI that the transformation considerably facilitates computations involving spin 0 and ½ particles in magnetic fields. It is shown that the relevant transformations can be obtained in closed form. The resulting equations for wave functions and operators are then particularly simple.

[1] L. L. Foldy and S. A. Wouthuysen, Phys. Rev. 78, 29 (1950).

II. PARTICLE FORM OF INTEGRAL SPIN EQUATIONS

Since we are concerned with particle properties a Hamiltonian form of the wave equations should be used. A suitable form is given by Taketani and Sakata and others.[2] The equations (involving two or six component wave functions for spin 0 and 1, respectively,) are

$$ih\partial\psi/\partial t=3\mathcal{C}\psi, \tag{1}$$

where

$$3\mathcal{C}=e\phi+\rho_3\{mc^2+\Pi^2/2m-(eh/2mc)\mathbf{S}\cdot\mathbf{H}\}$$
$$+i\rho_1\{\Pi^2/2m-(\mathbf{S}\cdot\Pi)^2/m-(eh/2mc)\mathbf{S}\cdot\mathbf{H}\}. \tag{2}$$

Here ϕ is the scalar potential, Π is the gauge invariant momentum operator, and $\mathbf{H}$ is the external magnetic field. ρ_1, ρ_2, ρ_3 are a set of three 2×2 Pauli matrices. The three Hermitian matrices $\mathbf{S}$, which commute with the ρ matrices, are the angular momentum matrices for particles of spin 0 (0 matrices) or one (3×3).

[2] M. Taketani and S. Sakata, Proc. Phys.-Math. Soc. (Japan) 22, 757 (1940); I. Tamm, Compt. rend. acad. sci. (U.R.S.S.) 29, 551 (1940); W. Heitler, Proc. Roy. Irish Acad. 49, 1 (1943).

They satisfy the relations

$$S_jS_jS_k+S_kS_jS_j=\delta_{ij}S_k+\delta_{kj}S_i, \tag{3}$$

$$[S_i,S_j]=i\epsilon_{ijk}S_k. \tag{4}$$

We must add to these equations the additional facts that the metric is to be defined as

$$M=\int\psi^*\rho_3\psi dV=(\psi^*,\rho_3\psi), \tag{5}$$

and the expectation of an operator O is

$$\bar{O}=\int\psi^*\rho_3O\psi dV=(\psi^*,\rho_3O\psi). \tag{6}$$

The physical interpretation is that the total charge Q described by our wave function is

$$Q=e(\psi^*,\rho_3\psi). \tag{7}$$

The introduction of the indefinite metric (5) necessitates some slight changes in the properties of operators associated with physical quantities as compared with those encountered in nonrelativistic quantum mechanics. For example, we may ask what kind of operators are to be associated with real dynamical variables. The requirement[3]

$$\bar{O}^*=\bar{O} \tag{8}$$

gives, on using (6),

$$(\psi^*,\rho_3O\psi)^*=(\psi^*,O^\dagger\rho_3\psi)=(\psi^*,\rho_3O\psi). \tag{9}$$

Since this must be true for all ψ,

$$\rho_3O=O^\dagger\rho_3, \tag{10}$$

or

$$O=\rho_3O^\dagger\rho_3. \tag{11}$$

That is, these operators must be *pseudo-Hermitian*. As an example it may be noted that the occurrence of the factor i in conjunction with ρ_1 in Eq. (2) is just right to make $\mathcal{H}$ pseudo-Hermitian and hence the interpretation of this as the energy consistent.

Transformation theory must also be slightly reformulated. Let ψ be a wave function representing a given state in a certain representation. Then the wave function representing the same state in a different representation (ψ') is connected with ψ by

$$\psi=U\psi', \tag{12}$$

where U is some linear operator.

If the transformation is to be canonical it must leave invariant the fundamental metric form. On inserting (12) in

$$(\psi^*,\rho_3\psi)=(\psi'^*,\rho_3\psi'), \tag{13}$$

we have

$$(U^*\psi'^*,\rho_3U\psi')=(\psi'^*,U^\dagger\rho_3U\psi')=(\psi'^*,\rho_3\psi'), \tag{14}$$

i.e.,

$$U^\dagger\rho_3U=\rho_3 \tag{15}$$

or

$$\rho_3U^\dagger\rho_3=U^{-1}. \tag{16}$$

Thus, just as real dynamical variables are associated with pseudo-Hermitian operators, canonical transformations are produced by pseudo-unitary operators [defined by (16)].

The transformation of operators proceeds in the ordinary way. If the wave function ψ in the original representation satisfies (1) the transformed wave function ψ' satisfies

$$i\hbar\partial\psi'/\partial t=\mathcal{H}'\psi', \tag{17}$$

where

$$\mathcal{H}'=U^{-1}\mathcal{H}U-i\hbar U^{-1}\partial U/\partial t. \tag{18}$$

If O is the representative of a given operator in the original representation, then

$$O'=U^{-1}OU \tag{19}$$

is the representative of the *same* operator in the new representation.

In order to define the time derivative of an operator O which is not explicitly time dependent we can proceed as in conventional quantum mechanics and define it as that operator whose expectation is the same as the time derivative of the expectation of O. Thus:

$$d\bar{O}/dt=\overline{dO/dt}. \tag{20}$$

Using (6), we have:

$$d\bar{O}/dt=(\partial\psi^*/\partial t,\rho_3O\psi)+(\psi^*,\rho_3O\partial\psi/\partial t). \tag{21}$$

Equation (1) and its complex conjugate are

$$\partial\psi/\partial t=(\mathcal{H}\psi)/i\hbar;\quad \partial\psi^*/\partial t=-(\mathcal{H}^*\psi^*)/i\hbar. \tag{22}$$

By substitution in (18),

$$d\bar{O}/dt=(i/\hbar)(\psi^*,(\mathcal{H}^\dagger\rho_3O-\rho_3O\mathcal{H})\psi). \tag{23}$$

But since $\mathcal{H}$ is pseudo-Hermitian,

$$\mathcal{H}^\dagger\rho_3=\rho_3\mathcal{H}.$$

Thus

$$d\bar{O}/dt=(\psi^*,\rho_3(i/\hbar)[\mathcal{H},O]\psi). \tag{24}$$

Comparison with (20) gives then just the usual relation,

$$dO/dt=(i/\hbar)[\mathcal{H},O]. \tag{25}$$

To see the difficulties of interpretation which arise, let us consider the field-free case. The Hamiltonian simplifies to

$$\mathcal{H}=\rho_3\{mc^2+\mathbf{P}^2/2m\}+i\rho_1\{\mathbf{P}^2/2m-(\mathbf{S}\cdot\mathbf{P})^2/m\}. \tag{26}$$

[3] * will mean complex conjugate, † Hermitian conjugate.

If to the position of the particle we associate as customary the operator $\mathbf{x}$ (multiplication by the coordinate) we obtain for the corresponding velocity operator:

$$\begin{aligned}\mathbf{v}&\equiv d\mathbf{x}/dt\\&=(i/\hbar)[\mathcal{H},\mathbf{x}]\\&=(\mathbf{P}/m)(\rho_3-i\rho_2)+i(\rho_2/m)(\mathbf{SS}\cdot\mathbf{P}+\mathbf{S}\cdot\mathbf{PS}).\end{aligned}\tag{27}$$

If $\mathbf{n}$ is a unit vector in an arbitrary direction, (27) and the relations (3) give

$$(\mathbf{n}\cdot d\mathbf{x}/dt)^2=-(1/m^2)(\mathbf{n}\times\mathbf{P}\cdot\mathbf{S})^2.\tag{28}$$

For spin 0 this states that the square of any component of the velocity operator is zero. Taken literally this might lead to the absurd interpretation that the particle is always at rest.

For spin one we see that two different components of the velocity operator do not commute. Hence, just as in the theory of the Dirac equation, one could not simultaneously specify the values of both. Since the eigenvalues of any component of $\mathbf{S}$ are 1, 0, -1 we see that the eigenvalues of the square of any component of the velocity operators are

$$(\mathbf{n}\cdot d\mathbf{x}'/dt)^2=-(\mathbf{n}\times\mathbf{P})^2/m^2\begin{Bmatrix}1\\0\end{Bmatrix}.\tag{29}$$

It might be remarked that these peculiar results occur because the operators are *not* Hermitian. The eigenvalues can all be zero and the operator still need not vanish identically. Moreover, the eigenvalues can be imaginary (and thus have negative squares). Of course, the expectation values are all real as guaranteed by the pseudo-Hermiticity.

Using (25) and (27) we can immediately find the acceleration operator $(d^2\mathbf{x}/dt^2)$. The essential point is that even in the absence of external fields it is not zero.

Similarly, if we associate with the intrinsic angular momentum the matrix $\mathbf{S}$ we find that even in the absence of external fields it is not constant. Indeed

$$\begin{aligned}d\mathbf{S}/dt&=(i/\hbar)[\mathcal{H},\mathbf{S}]\\&=(i\rho_1/2m)\{\mathbf{S}\cdot\mathbf{P}(\mathbf{P}\times\mathbf{S})+(\mathbf{P}\times\mathbf{S})\mathbf{S}\cdot\mathbf{P}\}.\end{aligned}\tag{30}$$

That is, the spin angular momentum is not a constant of motion, nor is the orbital angular momentum. Of course, again as in the Dirac case, the sum of the two is a constant of motion.

III. TRANSFORMATION OF THE FIELD FREE EQUATIONS

Following Foldy and Wouthuysen we seek a canonical transformation to a new representation in which the "natural" association of operators with classical dynamical variables leads to operators with somewhat less paradoxical properties. As a guide we use the requirement that in the transformed representation the Schrödinger equation shall be free of "odd" operators. (In our notation this means that only the operators 1 and ρ_3 in ρ space are to appear.) In the vector (scalar) case this will result in the positive and negative charge states being separately described by three (one) component wave functions.

In the field-free case the transformation is readily found by means of the following trivial, but useful, generalization of a theorem used in reference 1.

Theorem

Let

$$O=\rho_1O_1+\rho_3O_3,\tag{31}$$

where O_1, O_3 are commuting operators which commute with ρ_1 and ρ_3, then there exists a similarity transformation such that

$$O'=U^{-1}OU=\rho_3(O^2)^{\frac{1}{2}}.\tag{32}$$

The proof follows by construction. We need only to perform a rotation in ρ space around the 2 axis. Let

$$U=e^{\frac{1}{2}i\rho_2\varphi},$$

where φ commutes with all ρ operators and with O_1 and O_3. Then

$$\begin{aligned}O'&=e^{-(i\rho_2/2)\varphi}Oe^{(i\rho_2/2)\varphi}\\&=\rho_1'O_1+\rho_3'O_3,\end{aligned}$$

where

$$\rho_1'=e^{-\frac{1}{2}i\rho_2\varphi}\rho_1e^{\frac{1}{2}i\rho_2\varphi}=\rho_1\cos\varphi-\rho_3\sin\varphi,$$

$$\rho_3'=e^{-\frac{1}{2}i\rho_2\varphi}\rho_3e^{\frac{1}{2}i\rho_2\varphi}=\rho_3\cos\varphi+\rho_1\sin\varphi.$$

Then

$$O'=\rho_1\{O_1\cos\varphi+O_3\sin\varphi\}+\rho_3\{-O_1\sin\varphi+O_3\cos\varphi\}.$$

Choose φ so that

$$\tan\varphi=-O_1/O_3.$$

Then

$$\begin{aligned}O'&=(\rho_3/\cos\varphi)\{-O_1\tan\varphi+O_3\}\\&=\rho_3(O_1^2+O_3^2)/(O_1^2+O_3^2)^{\frac{1}{2}}\\&=\rho_3(O^2)^{\frac{1}{2}}.\end{aligned}$$

This similarity transformation may be applied directly to the integral spin Hamiltonian (26) on noting that this is of the form (31) with

$$O_1=i\{\mathbf{P}^2/2m-(\mathbf{S}\cdot\mathbf{P})^2/m\},\quad O_3=\{mc^2+\mathbf{P}^2/2m\}.\tag{33}$$

Noticing that $i^*=-i$ and that ρ_2 anticommutes with ρ_3 we readily see that the operator

$$U=e^{\frac{1}{2}i\rho_2\phi},\tag{34}$$

with

$$\varphi=-\tan^{-1}i\{\mathbf{P}^2/2m-(\mathbf{S}\cdot\mathbf{P})^2/m\}/\{mc^2+\mathbf{P}^2/2m\}\tag{35}$$

is pseudo-Hermitian and, hence, that the similarity transformation (32) is canonical.

Since the relations (3) and the form (26) have as consequence

$$\mathcal{H}^2=m^2c^4+c^2\mathbf{P}^2=E_P^2,\tag{36}$$

we obtain

$$\mathcal{H}'=\rho_3 E_P. \tag{37}$$

It is remarkable that in the transformed representation the Hamiltonian (37) has identically the same form for spin 0, $\frac{1}{2}$, 1. [Of course there is implicitly a unit $(2S+1)$ dimensional matrix multiplying this for spin S.]

The operator which we tentatively identified as the position operator and which was "multiplication by $\mathbf{x}$" in the original representation is quite complicated in the new representation.

$$\mathbf{x}'=\mathbf{x}-(\hbar\rho_2/2)\{\quad\},$$

$$\begin{aligned}\{\quad\}=&-ic^2\mathbf{P}/E_P^2-2ic^2\mathbf{P}(\mathbf{S}\cdot\mathbf{P})^2/mE_P^2(E_P+mc^2)\\&+(i/mE_P)(\mathbf{SS}\cdot\mathbf{P}+\mathbf{S}\cdot\mathbf{PS})\\&+\rho_2(E_P-mc^2)(\mathbf{P}\times\mathbf{S})/mE_P(E_P+mc^2).\end{aligned} \tag{38}$$

The momentum operator is unchanged in form

$$\mathbf{P}'=\mathbf{P}. \tag{39}$$

It is suggestive to consider as position operator, the operator $\mathbf{X}$ whose representative in the *new* representation is "multiplication by $\mathbf{x}$":

$$\mathbf{X}'=\mathbf{x}. \tag{40}$$

Since the form of this operator in the old representation is just obtained by applying the transformation reciprocal to (32), $\mathbf{X}$ is just the right-hand side of (38) with ρ_2 replaced by $-\rho_2$.

The velocity operator corresponding to $\mathbf{X}$ is readily found in the new representation as

$$\begin{aligned}d\mathbf{X}'/dt&=(i/\hbar)[\mathcal{H}',\mathbf{x}]\\&=\partial\mathcal{H}'/\partial\mathbf{P}=\rho_3c^2\mathbf{P}/E_P.\end{aligned} \tag{41}$$

This has just the classically expected form and again is the same for spin 0, $\frac{1}{2}$, and 1. The corresponding acceleration operator is zero,

$$d^2\mathbf{X}'/dt^2=0, \tag{42}$$

as we would expect for a field-free particle. The operator $\mathbf{X}$ is then for integral spin the Foldy-Wouthuysen mean position operator. It is the corresponding set of operators which go over into the nonrelativistic position, velocity, and acceleration operators.

Similar considerations hold for the spin operator. If $\mathbf{\Sigma}$ be the operator such that

$$\mathbf{\Sigma}'=\mathbf{S}, \tag{43}$$

one sees immediately that

$$d\mathbf{\Sigma}/dt=0, \tag{44}$$

i.e., it is a constant of motion. In the old representation this mean spin operator is

$$\begin{aligned}\mathbf{\Sigma}=&\mathbf{S}(mc^2+\mathbf{P}^2/2m)/E_P\\&-\mathbf{PS}\cdot\mathbf{P}(E_P-mc^2)/2mE_P(E_P+mc^2)\\&+(i\rho_2/2mE_P)(\mathbf{P}\cdot\mathbf{SP}\times\mathbf{S}+\mathbf{P}\times\mathbf{SP}\cdot\mathbf{S}).\end{aligned} \tag{45}$$

The mean orbital angular momentum operator, defined as

$$\mathfrak{L}=\mathbf{X}\times\mathbf{P}, \tag{46}$$

is also separately a constant of motion.

In summary it can be said that despite the initial formal difference between the spin $\frac{1}{2}$ case and the integral spin cases the considerations of Foldy and Wouthuysen can be carried over almost unchanged. Indeed, in the transformed representations the theories are identical in form. (It might be noted that the transformation that we have carried out is essentially the Pauli-Weisskopf[4] transformation in unquantized form.)

IV. THE NONRELATIVISTIC LIMIT FOR INTEGRAL SPIN EQUATIONS

In the presence of arbitrary external fields it is, of course, not possible to perform a transformation in closed form which eliminates the odd components. However, by means of a sequence of transformations it is possible, just as in the spin $\frac{1}{2}$ case, to eliminate "odd" terms to any desired power in the reciprocal of the mass. Thus suppose the Hamiltonian in general to be of the form

$$\mathcal{H}=\rho_3mc^2+\mathcal{E}^{(0)}+\mathcal{O}^{(0)}+\mathcal{E}^{(1)}+\mathcal{O}^{(1)}+\cdots, \tag{47}$$

where $\mathcal{E}$ and $\mathcal{O}$ denote even and odd terms, respectively. The superscripts denote the order of the term in reciprocal powers of the mass. Suppose $\mathcal{O}^{(l)}$ is the lowest order nonvanishing odd term. By means of the time-dependent transformation given by

$$U=e^{iS}, \tag{48}$$

where

$$S=i\rho_3\mathcal{O}^{(l)}/2mc^2, \tag{49}$$

we obtain a new Hamiltonian.

$$\mathcal{H}'=\rho_3mc^2+(\text{even terms})+\mathcal{O}'^{(l+1)}+\cdots, \tag{50}$$

where the new odd terms are all of order $l+1$ or higher in the reciprocal mass. By means of a sequence of such transformations the desired order of eliminations is readily obtained. The only difference between the spin $\frac{1}{2}$ and the integral spin cases arises because the first nonvanishing odd terms are of order $(1/m)^0$ and $(1/m)^1$, respectively. This occasions a much more rapid elimination in the integral spin cases. Carrying the elimination out we obtain correct to terms of order $(1/m)^3$

[4] W. Pauli and V. Weisskopf, Helv. Phys. Acta 7, 709 (1934).

inclusive the nonrelativistic Hamiltonian.

$$\mathcal{H}=\rho_3 mc^2+e\phi+\rho_3\{\boldsymbol{\Pi}^2/2m-(e\hbar/2mc)\mathbf{S}\cdot\mathbf{H}\}-(\rho_3/2m^3c^2)\{(\boldsymbol{\Pi}^2/2)^2+E\}. \quad (51)$$

Here the first term of order $(1/m^3)$ is just the relativistic mass correction of the order that would be expected. The second term of that order (E) vanishes both for spin 0 and for no external magnetic field. Explicitly it is

$$E=(\mathbf{S}\cdot\boldsymbol{\Pi})^4-[\boldsymbol{\Pi}^2/2,\ (\mathbf{S}\cdot\boldsymbol{\Pi})^2]_+-(e\hbar/4c)[\mathbf{S}\cdot\mathbf{H},\ \boldsymbol{\Pi}^2]_+ +(e\hbar/2c)[\mathbf{S}\cdot\mathbf{H},\ (\mathbf{S}\cdot\boldsymbol{\Pi})^2]_+ +(e\hbar/2c)^2(\mathbf{S}\cdot\mathbf{H})^2. \quad (52)$$

By means of the relations (3) and (4), E may be expressed in terms of the zero, first, and second powers of the spin matrices. For a constant magnetic field this simplifies to

$$E=3(e\hbar\mathbf{S}\cdot\mathbf{H}/2c)^2+(e\hbar\mathbf{H}/c)^2/2+(e\hbar/2c)\mathbf{S}\cdot\boldsymbol{\Pi}\mathbf{H}\cdot\boldsymbol{\Pi} -(e\hbar/c)\boldsymbol{\Pi}^2(\mathbf{S}\cdot\mathbf{H}). \quad (53)$$

It is of interest to note that there are no contributions of order $(1/m^2)$. In the Dirac case these are essentially the spin-orbit coupling terms. The nonappearance of comparable terms for a vector particle is readily understood on the basis of the semiclassical derivation of the Thomas factor.[5] A particle of angular momentum $\hbar\mathbf{S}$, gyromagnetic ratio $ge/2mc$ has a magnetic energy

$$E^{(m)}=-(g)(e\hbar/2mc)\mathbf{S}\cdot\mathbf{H}. \quad (54)$$

If the particle is moving in an electric field it sees in its rest system an effective magnetic field,

$$\mathbf{H}'=\mathbf{H}+\mathbf{E}\times\mathbf{v}/c. \quad (55)$$

Thus, in addition to (54) we should have a term in the Hamiltonian,

$$-g(e\hbar/2mc)\mathbf{S}\cdot(\mathbf{E}\times\mathbf{v})/c. \quad (56)$$

In addition to (56) there must be a term in the Hamiltonian describing the Thomas precession. This is

$$(e\hbar/2mc)\mathbf{S}\cdot(\mathbf{E}\times\mathbf{v})/c. \quad (57)$$

Adding (56) and (57), expressing $\mathbf{v}$ in terms of the gauge invariant momentum, and symmetrizing noncommuting quantities leads us to expect a $(1/m)^2$ term in the Hamiltonian which is

$$-(e\hbar/4m^2c^2)(g-1)\{\mathbf{S}\cdot(\mathbf{E}\times\boldsymbol{\Pi})-\mathbf{S}\cdot(\boldsymbol{\Pi}\times\mathbf{E})\}. \quad (58)$$

For the electron $g=2$ and (58) gives the ordinary spin-orbit coupling. For a vector particle we see from (51) that $g=1$ and hence (58) would be expected to vanish. It has been shown[6] that, for particles of arbitrary spin, $g=1/s$ where s is the magnitude of the spin. Hence, this cancellation of the spin-orbit terms is completely fortuitous for the vector case and will occur nowhere else.

V. EXTENSIONS TO HIGHER SPIN

The formal similarity of the equations for the Hamiltonian, position, velocity, and spin operators for field-free spin 0, $\frac{1}{2}$, and 1 particles in the transformed representations shown by the equations of Sec. III and those of reference 1 suggest that the form is quite general. It looks as if there are transformations which will put the equations for arbitrary spin into precisely the same form.

It will be shown elsewhere[7] that the field-free equations given by Dirac, Fierz, and Pauli[8] describing particles of spin $k+\frac{1}{2}$ can by elimination of redundant components be put in the form

$$i\hbar\partial\psi/\partial t=\mathcal{H}\psi, \quad (59)$$

where

$$\mathcal{H}=\rho_1\mathcal{O}_1(\mathbf{S}\cdot\mathbf{P})+\rho_3\mathcal{O}_2(\mathbf{S}\cdot\mathbf{P}). \quad (60)$$

Here ρ_1, ρ_3 are the same as in (2), while $\mathbf{S}$ are the appropriate spin matrices.

Since the original forms of the equations are obtained in part by requiring each component of the wave function to satisfy the Klein-Gordon equation it follows that

$$\mathcal{H}^2=m^2c^4+c^2\mathbf{P}^2. \quad (61)$$

Hence the conditions of the theorem of Sec. III are satisfied and there exists a canonical transformation such that in the new representation,

$$\mathcal{H}'=\rho_3(m^2c^4+c^2\mathbf{P}^2)^{\frac{1}{2}}. \quad (62)$$

If we define as position operator $\mathbf{X}$ (multiplication by $\mathbf{x}$ in the new representation) the results of III for velocity, acceleration, and orbital angular momentum are immediately carried over to arbitrary half-integral spin. Defining the spin operator as $\mathbf{S}$ acting in the new representation, gives the result that the spin is separately a constant of motion.

Since we have now obtained operators which go over into the expected nonrelativistic form it is fairly clear that the nonrelativistic limit of these theories is readily obtained by a sequence of transformations as in IV. The only gap is in proving that an equation like (47) holds. This will be shown in another place.[7]

VI. COMPUTATIONAL APPLICATIONS

If the external fields acting on a particle reduce to a time-independent magnetic field no energy is being

[5] L. H. Thomas, Nature **117**, 514 (1926).
[6] K. M. Case, Bull. Am. Phys. Soc. Detroit-Ann Arbor Meeting (March 1954).
[7] K. M. Case (to be published).
[8] P. A. M. Dirac, Proc. Roy. Soc. (London) **A155**, 447 (1936). M. Fierz, Helv. Phys. Acta **12**, 297 (1939). M. Fierz and W. Pauli, Proc. Roy. Soc. (London) **A173**, 211 (1939).

imparted to the particle. This indicates a decomposition into positive and negative energy (or charge) states is possible. Alternatively, this suggests that here, as in the field-free case, the appropriate canonical transformations can be obtained in closed form.

In such fields the Hamiltonians for spin 0 and $\frac{1}{2}$[9] are

$$\begin{aligned} &\mathcal{H}=\rho_3\{mc^2+\boldsymbol{\Pi}^2/2m\}+i\rho_1\{\boldsymbol{\Pi}^2/2m\}, && \text{(spin 0)}\\ &\mathcal{H}=\rho_3 mc^2+\rho_1 c\boldsymbol{\sigma}\cdot\boldsymbol{\Pi}. && \text{(spin } \tfrac{1}{2}\text{)}. \end{aligned} \tag{63}$$

By means of the canonical transformation obtained with

$$U=e^{\frac{1}{2}i\rho_2\varphi}, \tag{64}$$

where

$$\varphi=\begin{cases} -\tan^{-1}(i\boldsymbol{\Pi}^2/2m)/(mc^2+\boldsymbol{\Pi}^2/2m) & \text{(spin 0)},\\ -\tan^{-1}(\boldsymbol{\sigma}\cdot\boldsymbol{\Pi})/mc & \text{(spin } \tfrac{1}{2}\text{)}, \end{cases} \tag{65}$$

we obtain, in the transformed representation:

$$\mathcal{H}'=\rho_3(m^2c^4+c^2\boldsymbol{\Pi}^2)^{\frac{1}{2}}, \tag{66a}$$

$$\mathcal{H}'=\rho_3(m^2c^4+c^2\boldsymbol{\Pi}^2-ehc\boldsymbol{\sigma}\cdot\mathbf{H})^{\frac{1}{2}}. \tag{66b}$$

The most important example is that when the magnetic field is also spatially constant. Let ψ_n be the eigenfunctions of a nonrelativistic Schrödinger particle in a constant magnetic field. Then

$$(\boldsymbol{\Pi}^2/2m)\psi_n=(n+\tfrac{1}{2})\hbar\omega\psi_n, \tag{67}$$

where

$$\omega=eH/mc. \tag{68}$$

Choosing a representation in which ρ_3 is diagonal, we see from (66a) that the eigenfunctions for a spin 0 particle are

$$\Psi^+=\begin{pmatrix}\psi_n\\0\end{pmatrix}, \quad \Psi^-=\begin{pmatrix}0\\\psi_n\end{pmatrix}, \tag{69}$$

and the corresponding eigenvalues are

$$E_n{}^{\pm}=\pm[m^2c^4+2m\hbar\omega(n+\tfrac{1}{2})]^{\frac{1}{2}}. \tag{70}$$

If for the Dirac case we also choose the component of the spin matrix in the direction of the magnetic field diagonal the eigenfunctions and eigenvalues are

$$\begin{aligned} \Psi_n{}^{(+)(1)}&=\begin{bmatrix}\psi_n\\0\\0\\0\end{bmatrix}, \quad \Psi_n{}^{+(-1)}=\begin{bmatrix}0\\\psi_n\\0\\0\end{bmatrix},\\ \Psi_n{}^{(-)(1)}&=\begin{bmatrix}0\\0\\\psi_n\\0\end{bmatrix}, \quad \Psi_n{}^{(-)(-1)}=\begin{bmatrix}0\\0\\0\\\psi_n\end{bmatrix}, \end{aligned} \tag{71}$$

$$E_n{}^{(\pm)(s)}=\pm(m^2c^4+2m\hbar\omega[n+(1-s)/2])^{\frac{1}{2}}. \tag{72}$$

For both spin 0 and $\frac{1}{2}$ we thus see that in the transformed representation the wave functions are particularly simple. They are just the nonrelativistic wave functions. No linear combinations are necessary.

Equation (66b) is also of interest in discussing the behavior of the spin of the electron in magnetic moment experiments. Defining spin as the operator $(\frac{1}{2}\hbar\boldsymbol{\sigma})$ acting in the *new* representation [this is just the gauge-invariant generalization of (43)] we obtain as equations for the spin precession

$$\begin{aligned} d\boldsymbol{\sigma}/dt&=(i/\hbar)[\mathcal{H}',\boldsymbol{\sigma}]\\ &=(\rho_3/\hbar)(E_+-E_-)\boldsymbol{\sigma}\times\mathbf{H}/H, \end{aligned} \tag{73}$$

where

$$E_\pm=(E_r{}^2\pm ehcH)^{\frac{1}{2}}, \quad E_r=(m^2c^4+c^2\boldsymbol{\Pi}^2)^{\frac{1}{2}}. \tag{74}$$

Expanding $E_\pm$ and dropping all but the first nonvanishing term in the difference (the omitted terms are completely negligible for all practical magnetic fields), we obtain

$$d\boldsymbol{\sigma}/dt=\boldsymbol{\mu}\times\mathbf{H}, \tag{75}$$

where the magnetic moment operator is

$$\boldsymbol{\mu}=(ec/E_r)\rho_3\boldsymbol{\sigma}. \tag{76}$$

Thus we see that the spin precesses just as in the nonrelativistic Pauli approximation, with the single difference that the rest mass is to be replaced by the relativistic mass.

VII. CONCLUSION

It has been shown that the transformations of reference 1 can be extended to integral-spin particles and indeed to particles of arbitrary half-integral spin. The various paradoxical properties of operators disappear. All the resulting theories become strikingly similar. The nonrelativistic approximations are extremely easy to obtain using the new representations. Computations involving particles in time-independent magnetic fields are simplified.

[9] We have not been able to find the appropriate transformation in the case of spin one.

Some Special Examples in Renormalizable Field Theory

T. D. LEE
Department of Physics, Columbia University, New York, New York
(Received May 4, 1954)

Some special problems of interacting fields that contain removable divergences are treated in detail. Comparisons with the power series renormalization procedures are made. Examination of the closed forms of the solutions before and after renormalization shows that, in one special case solved, coupling-constant renormalization cannot be obtained by any limiting processes that involve only real values of the unrenormalized coupling constant.

I. INTRODUCTION

EVER since the overwhelming success of the applications of renormalization technique in quantum electrodynamics, the problem of understanding this renormalization procedure without the use of perturbation methods has been of great interest. Unfortunately, in all physically realistic cases the Hamiltonians are quite complicated in structure, and so far no solution other than the power series method has been found. Yet the renormalization methods as developed by Dyson,[1] Ward,[2] and others can certainly be applied to a large class of field-theoretical problems that involve removable divergencies. Thus some deeper insight as to the nature of the renormalization procedure may, perhaps, be obtained by examining problems that are similar to, but not as rich as, either the quantum electrodynamics or the relativistic pseudoscalar meson theory. With this motive we shall in this paper treat some simple problems of interacting fields that are both renormalizable and solvable.

We consider first a problem that involves the interactions between two neutral nonrelativistic fermion fields and one relativistic boson field. Although the Hamiltonian of this problem does involve infinities, the Schroedinger equation can still be solved directly. A close examination of the solutions indicates that all the divergent quantities can be removed by both a mass renormalization and a coupling-constant renormalization. The scattering amplitude is then calculated after renormalization and is indeed found to be finite (i.e., not zero). This problem can also be treated by the application of the customary power series renormalization procedure whereby identical conclusions concerning the nature of renormalization quantities are reached. Furthermore, even outside its radius of convergence, the formal sum of the power series can still be used to give the correct closed form. A rather unexpected and quite surprising feature is obtained by comparing the renormalized coupling constant with the unrenormalized coupling constant. In this particular case it can be shown that the result of the renormalization process *cannot* be obtained by any limiting process that involves only *real* values of the unrenormalized coupling constant. This difficulty may, however, be overcome by a modification of the present rules of quantum mechanics.

Next, the well-known soluble problem of neutral scalar mesons with fixed nucleons is studied. The closed forms of the nucleon propagation functions and vertex functions are listed in Appendix I.

In Appendix II, the charged scalar theory together with some interesting identities between the customary matrix elements and the renormalization quantities Z_1, Z_2 are discussed.

II. HAMILTONIAN

Let us consider the interaction between two neutral fermion fields, V and N, and a neutral scalar boson field, θ. The Hamiltonian for the free fields is

$$H_0=m_V\int\psi_V^\dagger\psi_V d\tau+m_N\int\psi_N^\dagger\psi_N d\tau+\tfrac{1}{2}\int[\pi^2+(\nabla\varphi)^2+\mu^2\varphi^2]d\tau, \quad (1)$$

where $\psi_V^\dagger$, ψ_V and $\psi_N^\dagger$, ψ_N obey the usual anticommutation relation and represent the field variables of V and N, φ and π are the field variable and conjugate momentum of the θ particles. The "observed" masses of V, N, and θ are denoted by m_V, m_N, and μ. Recoil effects of V and N are not included.

It is convenient to write

$$\varphi=A(\mathbf{r})+A^\dagger(\mathbf{r}),$$

where

$$A(\mathbf{r})=\sum(2\omega\Omega)^{-\frac{1}{2}}\alpha_k\exp(i\mathbf{k}\cdot\mathbf{r}),$$
$$A^\dagger(\mathbf{r})=\sum(2\omega\Omega)^{-\frac{1}{2}}\alpha_k^\dagger\exp(-i\mathbf{k}\cdot\mathbf{r}).$$

α_k and $\alpha_k^\dagger$ are the annihilation and creation operators of the θ particle with wave number k. Ω is the volume of the system and ω is $(k^2+\mu^2)^{\frac{1}{2}}$. The interaction Hamiltonian H_1 that represents the reaction

$$V\rightleftarrows N+\theta \quad (2)$$

can be written as

$$H_1=g\int[\psi_V^\dagger(\mathbf{r})\psi_N(\mathbf{r})A(\mathbf{r})+\psi_N^\dagger(\mathbf{r})\psi_V(\mathbf{r})A^\dagger(\mathbf{r})]d\tau+\delta m_V\int\psi_V^\dagger\psi_V d\tau, \quad (3)$$

[1] F. J. Dyson, Phys. Rev. **75**, 1736 (1949).
[2] J. C. Ward, Proc. Phys. Soc. (London) **A64**, 54 (1951); Phys. Rev. **84**, 897 (1951).

where δm_V is used to cancel any change in mass of the V particle due to the reaction (2).

Upon examining the total Hamiltonian

$$H=H_0+H_1, \tag{4}$$

one sees that this system possesses two simple conservation laws:

$$\begin{aligned} &\mathfrak{N}_V+\mathfrak{N}_N=\text{constant}, \\ \text{and} \quad &\\ &\mathfrak{N}_V+\mathfrak{N}_\theta=\text{constant}, \end{aligned} \tag{5}$$

with $\mathfrak{N}_V$, $\mathfrak{N}_N$, $\mathfrak{N}_\theta$ the total number of V, N, and θ particles, respectively. Because of (5) the eigenfunctions of H contain only a finite number of particles and consequently can be solved directly.

III. GROUND STATES

In the following, we denote the state of a "bare" V particle and that of a "bare" N particle by $|V\rangle$ and $|N\rangle$ while the states of the corresponding "physical" particles are indicated by $|\mathbf{V}\rangle$ and $|\mathbf{N}\rangle$. Thus $|\mathbf{V}\rangle$ and $|\mathbf{N}\rangle$ are eigenstates of the Hamiltonian and satisfy

$$\begin{aligned} H|\mathbf{N}\rangle&=m_N|\mathbf{N}\rangle, \\ H|\mathbf{V}\rangle&=m_V|\mathbf{V}\rangle. \end{aligned} \tag{6}$$

In order that V be a stable particle we assume $m_V-m_N<\mu$. Using (5), one see that

$$|\mathbf{N}\rangle=|N\rangle,$$

and

$$|\mathbf{V}\rangle=Z_2^{\frac{1}{2}}[|V\rangle+g\textstyle\sum_k f(k)\alpha_k^\dagger|N\rangle], \tag{7}$$

where $Z_2^{\frac{1}{2}}$ is a normalization constant and $f(k)$ is proportional to the probability amplitude for finding a θ particle with wave number k in a physical V state.

Applying the Hamiltonian (4) on $|\mathbf{V}\rangle$ and requiring that the eigenvalue should be the "observed" mass m_V, one finds

$$\delta m_V=-g^2\textstyle\sum(2\omega\Omega)^{-1}(m_V-m_N-\omega)^{-1}, \tag{8}$$

$$f(k)=(2\omega\Omega)^{-1}(m_V-m_N-\omega)^{-1}, \tag{9}$$

and

$$Z_2^{-1}=1+g^2\textstyle\sum(2\omega\Omega)^{-1}(m_V-m_N-\omega)^{-2}. \tag{10}$$

We remark that the divergent quantity δm_V serves as the renormalization in mass such that the eigenvalue m_V of the Hamiltonian is now finite. The divergent quantity Z_2^{-1} is related to the coupling-constant renormalization and will be studied in the next section.

IV. SCATTERING STATE

We consider first the scattering process

$$N+\theta\rightarrow N+\theta.$$

The eigenfunction $|\mathbf{N}+\theta\rangle$ that represents this process can be written in terms of the physical one-particle states as

$$|\mathbf{N}+\theta\rangle=\textstyle\sum_k\chi(k)\alpha_k^\dagger|\mathbf{N}\rangle+c|\mathbf{V}\rangle, \tag{11}$$

and furthermore it satisfies the Schroedinger equation,

$$H|\mathbf{N}+\theta\rangle=(m_N+\omega_0)|\mathbf{N}+\theta\rangle. \tag{12}$$

On using the special form of H together with (6) and (7), the Schroedinger equation can be readily solved and one obtains

$$c=-\langle\mathbf{V}|\textstyle\sum\chi(k)\alpha_k^\dagger|\mathbf{N}\rangle, \tag{13}$$

and

$$(\omega-\omega_0)\chi(k)=g^2Z_2\int K(k,k')\chi(k')d^3k', \tag{14}$$

where

$$\begin{aligned} K(k,k')&=(m_V-m_N-\omega_0)(4\omega\omega')^{-\frac{1}{2}} \\ &\times[8\pi^3(m_V-m_N-\omega)(m_V-m_N-\omega')]^{-1}. \end{aligned}$$

One observes that although Z_2^{-1} involves a divergent sum, the cross section will not vanish if the renormalized coupling constant, given by

$$g_c^2=g^2Z_2, \tag{15}$$

is chosen to be finite. Equation (14) can then be easily solved, and the phase shift δ for the scattering process is

$$\begin{aligned} \tan\delta=&\frac{g_c^2k_0}{4\pi(m_V-m_N-\omega_0)} \\ &\times\left[1-\frac{g_c^2}{16\pi^3}\mathcal{P}\int\frac{d^3k(m_V-m_N-\omega_0)}{\omega(\omega-\omega_0)(m_V-m_N-\omega)^2}\right]^{-1}, \end{aligned} \tag{16}$$

where $\mathcal{P}$ indicates that in the integration the principal value is to be taken. Thus if g_c is finite the expression for the phase shift is indeed free from divergent quantities.

Next we consider the scattering process,

$$V+\theta\rightarrow V+\theta. \tag{17}$$

Again, the corresponding eigenstate that satisfies

$$H|\mathbf{V}+\theta\rangle=(m_V+\omega_0)|\mathbf{V}+\theta\rangle \tag{18}$$

can be written in terms of the physical one-particle states as

$$|\mathbf{V}+\theta\rangle=\sum_k\psi(k)\alpha_k^\dagger|\mathbf{V}\rangle+\sum_{k_1,k_2}\phi(k_1,k_2)\alpha_{k_1}^\dagger\alpha_{k_2}^\dagger|\mathbf{N}\rangle. \tag{19}$$

The Schroedinger equation can also be solved and one finds

$$(\omega-\omega_0)h(\omega)\psi(k)=g^2Z_2\int K'(k,k')\psi(k')\alpha^2k', \tag{20}$$

where

$$\begin{aligned} &K'(k,k')=(16\pi^3)^{-1}(\omega\omega')^{-\frac{1}{2}}(\omega+\omega'-\omega_0-m_V+m_N)^{-1}, \\ &h(\omega)=1-g^2Z_2(16\pi^3)^{-1} \\ &\times\int\frac{d^3k'}{(\omega+\omega'-\omega_0-m_V+m_N)(m_V-m_N-\omega')^2\omega'}, \end{aligned}$$

and

$$(\omega_1+\omega_2-\omega_0-m_V+m_N)\phi(k_1,k_2) = -\tfrac{1}{2}(gZ_2^{\frac{1}{2}})[(\omega_1-\omega_0)\psi(k_1)f(k_2) + (\omega_2-\omega_0)\psi(k_2)f(k_1)]. \quad (21)$$

$f(k)$ is given by Eq. (9). By counting the powers of ω and ω' in the kernel K' one sees that the solution $\psi(k)$ and $\phi(k_1,k_2)$ would be free from divergent integrals if the renormalized coupling constant $g_e=gZ_2^{\frac{1}{2}}$ is finite.

V. COMPARISON WITH POWER SERIES METHOD

The above problem can also be renormalized by the power series method. By constructing the S matrix in the interaction representation and commuting all the time ordered operators into S products[1,3] one finds the following rules for the Feynman diagram:

(i) Each V line gives a factor $(p_0-m_V+i\epsilon)^{-1}$, where p_0 is $-i$ times the fourth component of the momentum vector carried by the V particle. ϵ is a positive infinitesimal quantity.

(ii) Each N line gives a factor $(p_0-m_N+i\epsilon)^{-1}$.

(iii) Each θ line gives a factor $(-k_\mu{}^2-\mu^2+i\epsilon)^{-1}$ and each variable momentum k_μ gives an integration $\int d^4k/(2\pi)^4$.

(iv) Each vertex gives a factor g.

Let S_N', S_V', and Γ denote the sum of all diagrams that contribute to the propagation function of N, the propagation function of V, and the vertex function, respectively. From the nature of the interaction (2), these quantities can be calculated readily and they are

$$\Gamma=1, \quad (S_N')^{-1}=p_0-m_N, \quad (S_V')^{-1}=p_0-m_V-\delta m_V-\Sigma(p_0), \quad (22)$$

where

$$\Sigma(p_0)=g^2\textstyle\sum_k(2\omega\Omega)^{-1}(p_0-m_N-\omega)^{-1}.$$

Thus, both Γ and S_N' need no renormalization. The renormalization of mass and propagation function of V are given by

$$(S_V')^{-1}=0 \quad \text{at} \quad p_0=m_V,$$

and

$$Z_2^{-1}=d[(S_V')^{-1}]/dp_0 \quad \text{at} \quad p_0=m_V. \quad (23)$$

Hence δm_V and S_V' can be written as

$$\delta m_V=-\textstyle\sum(p_0=m_V)=-g^2\sum(2\omega\Omega)^{-1}(m_V-m_N-\omega)^{-1},$$

and

$$S_V'(p_0)=Z_2S_{Ve}(p_0), \quad (24)$$

where

$$Z_2^{-1}=1+g^2\textstyle\sum(2\omega\Omega)^{-1}(m_V-m_N-\omega)^{-2},$$

$$S_{Ve}^{-1}(p_0)=(p_0-m_V)\left[1-g^2Z_2\sum\frac{p_0-m_V}{(2\omega\Omega)(p_0-m_N-\omega)(m_V-m_N-\omega)^2}\right]. \quad (25)$$

[3] G. C. Wick, Phys. Rev. 80, 268 (1950).

If, as in (15), g^2Z_2 is set to be g_e^2 and remains finite, then the renormalized propagation function $S_{Ve}(p_0)$ will be free from divergent quantities.[4]

For any other physical processes it can then be shown that one needs only to consider the irreducible diagrams and use S_{Ve}, $S_{Ne}=S_N'$, and g_e for the propagation lines of V, N, and the vertex, respectively. Although the number of irreducible diagrams may still be infinite, the contribution of each diagram will be free from divergent integrals. In this case, using (25), one can compute the scattering processes in powers of g_e and one obtains indeed the same results as discussed in the previous section.

Thus, identical conclusions concerning both the mass renormalization and coupling-constant renormalization are obtained either by the power series method or by directly solving the Schroedinger equation. A comparison between these two methods shows that Z_2, which in the power series method is defined as the residue of S_V' at its pole, is actually the probability[5] of finding a "bare" V particle in the state of a "physical" V particle as shown by (7). It may be of interest to notice that, for example, in (25) the radius of convergence for the power series expansion of $S_{Ve}(p_0)$ in g_e^2 depends on the variable p_0 and it is 0 if $p_0=\infty$. Yet, the power series can always be summed formally and still gives the correct result.

VI. DISCUSSION OF COUPLING CONSTANT RENORMALIZATION

The nature of the coupling constant renormalization may be investigated by expressing g^2 and Z_2 in terms of the renormalized coupling constant g_e. Using (10) and (15) one finds

$$g^2=g_e^2[1-g_e^2\textstyle\sum(2\omega\Omega)^{-1}(m_V-m_N-\omega)^{-2}]^{-1}, \quad (26)$$

and

$$Z_2=1-g_e^2\textstyle\sum(2\omega\Omega)^{-1}(m_V-m_N-\omega)^{-2}. \quad (27)$$

Hence, if g_e does not vanish and remains finite, the unrenormalized coupling constant becomes

$$g=i\infty^{-1},$$

while Z_2 which, being a probability, should be between 0 and 1 is actually

$$Z_2=-\infty.$$

This shows that the result of coupling-constant renormalization in this problem cannot be realized by any limiting process if g is restricted to be on the real axis. Instead, the expressions for cross sections in previous sections may be obtained by allowing in the original Hamiltonian an unrenormalized coupling constant

[4] It is of interest to notice that if g_e^2 is finite, then S_{Ve} has another pole besides $p_0=m_V$. This pole corresponds to another stable state for the V particle. Identical conclusions can be obtained either by studying the bound state solutions for the state $|\mathbf{N}+\mathbf{\theta}\rangle$ or by examining the energy of the outgoing θ particle in the scattering state $|\mathbf{V}+\mathbf{\theta}\rangle$.

[5] See Appendix II for a general discussion of this property.

which is pure imaginary and which approaches zero while the upper limit of the sum in momentum space approaches infinity as described by (26).

This raises immediately the question as to what changes in the present rules of quantum mechanics we have made by allowing the Hamiltonian to be non-Hermitian. As shown in the preceding sections, the eigenvalues of the Hamiltonian and the matrix elements of the collision matrix are only functions of the renormalized coupling constant g_e, which is always real. Thus, even if g is imaginary, the unitarity of the collision matrix and the reality of the energy spectrum can still be preserved. Consequently, it is possible to transform this non-Hermitian Hamiltonian into a Hermitian matrix by a similarity transformation. As is well known, a similarity transformation preserves all relations between matrices and vectors; the laws of quantum mechanics may still be applied to this non-Hermitian Hamiltonian provided some attention is given to the formal differences between a unitary transformation and a similarity transformation. In particular, the transformation between the bare particle states and the physical particle states is not unitary, which explains why Z_2 as shown by (27) is not confined between 0 and 1.

The author wishes to thank Professors R. Serber and N. Kroll for discussions.

APPENDIX I[6]

Another soluble problem is that of the neutral scalar meson with fixed nucleon. The Hamiltonian is H_0+H_1, where

$$H_0=\int m\psi_N^\dagger\psi_N d\tau+\tfrac{1}{2}\int[\pi^2+(\nabla\varphi)^2+\mu^2\varphi^2]d\tau,$$

and

$$H_1=g\int\psi_N^\dagger\psi_N\varphi d\tau+\delta m\int\psi_N^\dagger\psi_N d\tau,$$

where $\psi_N^\dagger$, ψ_N describe the nucleon field and π, φ the meson field, g the coupling constant, and m the physical mass of the nucleon. While the Schroedinger equation of the above Hamiltonian is well known to be solvable, it is of some interest to examine the nucleon propagation function S', the vertex function Γ, and the renormalization quantities δm and Z_1, Z_2.

The mass renormalization is

$$\delta m=-g^2\textstyle\sum(2\omega^2\Omega)^{-1}, \tag{A1}$$

where Ω is the volume of the system. The nucleon propagation function can be expressed as[7]

$$\mathbf{S}'(x-x')=T\langle\mathrm{vac}|\psi_N(x)\psi_N^\dagger(x')|\mathrm{vac}\rangle, \tag{A2}$$

where ψ_N and $\psi_N^\dagger$ are operators in the Heisenberg representations and T is the T product as defined by Wick.[8]

Using the known solutions in the Heisenberg representation, one finds

$$\mathbf{S}'(x-x')=Z_2\mathbf{S}_e(x-x'), \tag{A3}$$

where

$$Z_2=\exp[-g^2\textstyle\sum(2\omega^2\Omega)^{-1}] \tag{A4}$$

and

$$\mathbf{S}_e(x-x')=\delta^3(r-r')\exp[-im(t-t')]\times\exp[g^2\textstyle\sum(2\omega^2\Omega)^{-1}e^{-i\omega(t-t')}]\text{ if }t>t';\quad=0\text{ if }t<t'. \tag{A5}$$

It is of interest to notice that Z_2 is again the probability of finding the bare nucleon in the state of a physical nucleon.[5] If $t\neq t'$, $\mathbf{S}_e(x-x')$ is always free from divergent quantities; furthermore it can always be expanded into convergent power series in g.

For convenience we shall in the following omit the trivial spatial dependence of $\mathbf{S}'(x)$ and denote its Fourier transform by $S'(p_0)$. The vertex function $\Gamma(p_0,p_0')$ is related to $S'(p_0)$ by[8]

$$\Gamma(p_0,p_0')(p_0-p_0')=[S'(p_0)]^{-1}-[S'(p_0')]^{-1}. \tag{A6}$$

Following Dyson's notation,[1] we write

$$\Gamma=Z_1^{-1}\Gamma_e. \tag{A7}$$

If we use (A3), Γ_e would be free from a divergent sum if

$$Z_1=Z_2. \tag{A8}$$

Thus, no coupling-constant renormalization is needed in this case and Z_2 is actually ∞^{-1} for any finite value of g.

APPENDIX II

There exist some interesting relations between the renormalization quantities Z_1, Z_2, etc., and the ordinary matrix elements. In this section we shall illustrate the proof of these relations by considering the problem of the charged scalar meson field with a fixed nucleon. For simplicity, we shall set the nucleon at the origin. The Hamiltonian is

$$H=(m+\delta m)\psi^\dagger\psi+\tfrac{1}{2}\int\sum_{i=1}^{2}[\pi_i^2+(\nabla\varphi_i)^2+\mu^2\varphi_i^2]d\tau+(g/\sqrt{2})\sum_{i=1}^{2}\psi^\dagger\tau_i\psi\varphi_i(0), \tag{A9}$$

where

$$\psi=\begin{pmatrix}\psi_P(t)\\ \psi_N(t)\end{pmatrix}$$

describes the nucleon field and τ_1, τ_2 are the Pauli matrices.

By applying the power-series renormalization method, one can prove that this problem can be renormalized by both a mass renormalization and a coupling-constant

[6] Some of the results obtained in the appendices have been obtained by other authors: M. Gell-Mann and F. Low (private communication); S. Edwards and R. Peierls (to be published).

[7] M. Gell-Mann and F. Low, Phys. Rev. 84, 350 (1951).

[8] This can be obtained by generalizing the arguments used in proving Ward's identity. The author wishes to thank Dr. C. N. Yang for informing him of this generalization.

renormalization. The nucleon propagation function $S'(p_0)$ and the vertex function $\Gamma(p_0,p_0')$ can be written as

$$S'(p_0)=Z_2S_c(p_0), \tag{A10}$$

$$\Gamma(p_0,p_0')=Z_1^{-1}\Gamma_c(p_0,p_0'). \tag{A11}$$

The quantities Z_2 and Z_1 are determined by the conditions

$$(p_0-m)S_c(p_0)=1 \quad \text{when} \quad p_0=m, \tag{A12}$$

and

$$\Gamma_c(m,m)=1, \tag{A13}$$

where m is the physical mass of the nucleon. The renormalized coupling constant g_c is connected to the unrenormalized coupling constant g by

$$gZ_2Z_1^{-1}=g_c. \tag{A14}$$

S_c and Γ_c are then finite functions of g_c and p_0.

Let $|\mathbf{P}\rangle$ (or $|\mathbf{N}\rangle$) and $|P\rangle$ (or $|N\rangle$) represent one physical proton (neutron) state and one bare proton (neutron) state, respectively. Z_2 and Z_1 are related to these state vectors through the following theorems.

Theorem 1.

$$Z_2=|\langle P|\mathbf{P}\rangle|^2=|\langle N|\mathbf{N}\rangle|^2, \tag{A15}$$

Theorem 2.

$$Z_2Z_1^{-1}=\langle\mathbf{N}|\tau_-|\mathbf{P}\rangle, \tag{A16}$$

where τ_- is the operator $\frac{1}{2}(\tau_1-i\tau_2)$ which transforms a bare proton into a bare neutron.

(i) Proof of Theorem 1. The propagation function of a proton (or neutron) in time can be written as[7]

$$\mathbf{S}'(t_1-t_2)=T\langle\text{vac}|\,\psi_P(t_1)\psi_P^\dagger(t_2)\,|\text{vac}\rangle$$

in the Heisenberg representation. For convenience one chooses $t=0$ as the time when the Heisenberg representation coincides with the interaction representation; i.e.,

$$\psi_P(t=0)=\boldsymbol{\psi}_P(t=0), \tag{A17}$$

where ψ_P is in the Heisenberg representation and $\boldsymbol{\psi}_P$ in the interation representation.

$\mathbf{S}'(t_1-t_2)$ can be rewritten as

$$\mathbf{S}'(t_1-t_2)=\sum_n\langle\text{vac}|\,\psi_P(0)\,|n\rangle\langle n|\,\psi_P^\dagger(0)\,|\text{vac}\rangle \times\exp[-iE_n(t_1-t_2)] \text{ if } t_1>t_2, \tag{A18}$$

where $|n\rangle$ is eigenstate of the total Hamiltonian with eigenvalue E_n ($E_{\text{vac}}=0$). Thus,[9]

$$\underset{\substack{t_2\to-\infty\\ t_1\to+\infty}}{\mathfrak{L}} \exp[im(t_1-t_2)]\mathbf{S}'(t_1-t_2)=|\langle\text{vac}|\boldsymbol{\psi}_P(0)\,|\,\mathbf{P}\rangle|^2.$$

By using (A12) and noticing that $\mathbf{S}'(t)$ is the Fourier transform of $S'(p_0)$, one has

$$Z_2=|\langle\mathbf{P}|P\rangle|^2.$$

[9] $\mathfrak{L}$ represents an operator of the type $\operatorname{Lim}_{t\to\pm\infty} t^{-1}\int_t^{2t}dt$ such that all oscillating terms can be taken to be zero.

(ii) To prove Theorem 2, we consider the quantity A_k defined by

$$A_k=T\langle\text{vac}|\,\psi_N(t_1)\alpha_k(t_2)\psi_P^\dagger(t_2)\,|\text{vac}\rangle, \tag{A19}$$

where all operators are in the Heisenberg representation. We denote by $\alpha_k(t)$ the annihilation operator of a positive meson in the interaction representation and by $\boldsymbol{\alpha}_k(t)$ the corresponding operator in the Heisenberg representation. Similarly to (A17), we have

$$\boldsymbol{\alpha}_k(t=0)=\alpha_k(t=0). \tag{A17'}$$

By making similar arguments to those used by Gell-Mann and Low[7] in proving (A2), one can prove that

$$A_k=g\int\mathbf{S}'(t_1-t)\boldsymbol{\Gamma}(t-t'',t'-t'') \times\mathbf{S}'(t'-t_2)f(t''-t_3)dtdt'dt'', \tag{A20}$$

where $\boldsymbol{\Gamma}$, $\mathbf{S}'$ are Fourier transforms of Γ and S'. The function $f(t''-t_3)$ represents the retarded part of the propagation of a positive meson with wave number k from time t'' to time t_3. It can be written as

$$f(t''-t_3)=\frac{1}{2\pi}\int\frac{\exp[ip_0(t''-t_3)]}{(p_0-\omega+i\epsilon)(2\omega\Omega)^{\frac{1}{2}}}dp_0,$$

where Ω is the volume of the system. The factor $(2\omega\Omega)^{\frac{1}{2}}$ arises because we use α_k in the definition for A_k. Equation (A20) thus represents the totality of all diagrams in which a nucleon propagates from t_2 to t' and then a vertex part from t' to t with an emission of a positive meson at t''. The positive meson, then, propagates from t'' to t_3 and the nucleon from t to t_1.

As in the previous proof, we wish to examine the part of A_k that oscillates like $\exp[-im(t_1-t_2)]$ as $t_1\to+\infty$ and $t_2\to-\infty$. This can be achieved by two different ways. On the one hand, we can express the definition of A_k (A19) in terms of the eigenstates $|n\rangle$ of the total Hamiltonian. A_k can then be written as

$$A_k=\sum_{n,m}\langle\text{vac}|\,\psi_N(0)\,|n\rangle\langle n|\,\boldsymbol{\alpha}_k(0)\,|m\rangle\langle m|\,\psi_P^\dagger(0)\,|\text{vac}\rangle$$

$$\times\exp[-iE_n(t_1-t_3)]\exp[-iE_m(t_3-t_2)]; \text{ if } t_1>t_3>t_2.$$

Using (A17) and (A15), we have

$$\underset{\substack{t_1\to+\infty\\ t_2\to-\infty}}{\mathfrak{L}} \exp[im(t_1-t_2)]A_k=Z_2\langle\mathbf{N}|\boldsymbol{\alpha}_k(0)\,|\,\mathbf{P}\rangle. \tag{A21}$$

On the other hand, by (A18) and the definitions of $\mathbf{S}'$ and $\boldsymbol{\Gamma}$, one has

$$\underset{t_1\to+\infty}{\mathfrak{L}} \exp(iml_1)\mathbf{S}'(t_1-l)=Z_2\exp(iml),$$

$$\underset{t_2\to-\infty}{\mathfrak{L}} \exp(-iml_2)\mathbf{S}'(l'-t_2)=Z_2\exp(-iml'),$$

and

$$\Gamma(m,m)=\int \mathbf{\Gamma}(t,t')\exp[im(t-t')]dtdt'.$$

By using (A20), the same limit becomes

$$\mathop{\mathfrak{L}}_{\substack{t_1\to+\infty\\ t_2\to-\infty}} \exp[im(t_1-t_2)]A_k=gZ_2^{\frac{3}{2}}\Gamma(m,m)(-\omega)^{-1}(2\omega\Omega)^{-\frac{1}{2}}, \quad (A22)$$

which, together with (A21), gives

$$Z_2\Gamma(m,m)=g^{-1}(-\omega)(2\omega\Omega)^{\frac{1}{2}}\langle \mathbf{N}|\alpha_k(0)|\mathbf{P}\rangle. \quad (A23)$$

The left-hand side of (A23) is the ratio of the renormalization constants, Z_2/Z_1. The k dependence of the right-hand side can be eliminated by using the identity:

$$\langle \mathbf{N}|[\alpha_k,H]|\mathbf{P}\rangle=0.$$

By commuting α_k with the total Hamiltonian, we have

$$\langle \mathbf{N}|\alpha_k|\mathbf{P}\rangle=-g\omega^{-1}(2\omega\Omega)^{-\frac{1}{2}}\langle \mathbf{N}|\tau_-|\mathbf{P}\rangle. \quad (A24)$$

By comparing (A24) with (A23), we can express the coupling constant renormalization (A14) as

$$g_e/g=Z_2/Z_1=\langle \mathbf{N}|\tau_-|\mathbf{P}\rangle.$$

Thus g_e/g, if real, must be less than unity.

These proofs can be obviously generalized to other renormalizable field theoretical problems. In the charged scalar theory these identities can be applied to calculate formally the values of Z_1 and Z_2 by using both the weak-coupling and strong-coupling solutions.[10] They are:

(i) weak-coupling solution:

$$Z_2=1-g_e^2\sum(2\omega^3\Omega)^{-1}+\cdots,$$
$$Z_2/Z_1=1-g_e^2\sum(2\omega^3\Omega)^{-1}+\cdots;$$

(ii) strong-coupling solution:

$$Z_2=\tfrac{1}{2}\exp[-g_e^2\sum(2\omega^3\Omega)^{-1}]+\cdots,\quad Z_2/Z_1=\tfrac{1}{2}.$$

[10] G. Wentzel, Helv. Phys. Acta **13**, 269 (1940); **14**, 633 (1941); R. Serber and S. Dancoff, Phys. Rev. **63**, 143 (1943); S. Tomonaga, Progr. Theoret. Phys. (Japan) **1**, 109 (1946).

PHYSICAL REVIEW VOLUME 95, NUMBER 5 SEPTEMBER 1, 1954

Fierz-Pauli Theory of Particles of Spin 3/2

SURAJ N. GUPTA
Department of Physics, Purdue University, Lafayette, Indiana
(Received April 14, 1954)

The Fierz-Pauli field corresponding to particles of spin 3/2 is quantized, and its interaction with the electromagnetic field is investigated. It is also shown how the elements of the S matrix for collision processes, involving photons and charged particles of spin 3/2, can be obtained in a simple way.

1. INTRODUCTION

A THEORY of particles of arbitrary spin was first developed by Dirac,[1] Fierz and Pauli,[2] and since then several other theories have also been proposed.[3] Such theories are of special interest at the present time, because a number of new particles have been observed in recent years, and some of them may have a spin higher than one. However, except in the case of the gravitational field,[4] the interaction of a quantized field of spin higher than one with other fields has never been investigated.

We shall, therefore, discuss in some detail the Fierz-Pauli theory of particles of spin 3/2. We shall first carry out the quantization of the Fierz-Pauli field, and consider its interaction with the electromagnetic field. It will then be shown that in the present case, too, the contribution of any collision process can be obtained from the S matrix by means of simple rules, which are similar to the Feynman-Dyson[5] rules of quantum electrodynamics.

2. FIELD EQUATION FOR PARTICLES OF SPIN 3/2

According to Fierz and Pauli,[2] a field corresponding to particles of spin 3/2 is described by the symmetrical spinors

$$a^{\dot\alpha}{}_{\beta\nu}=a^{\dot\alpha}{}_{\nu\beta} \quad \text{and} \quad b_\nu{}^{\dot\alpha\dot\beta}=b^{\dot\beta\dot\alpha}, \quad (1)$$

and the auxiliary spinors c_α and $d^{\dot\alpha}$. The Lagrangian density for the field is

$$\begin{aligned}L=&-(a^{*\nu}{}_{\dot\alpha\dot\beta}\,p^{\dot\beta\rho}\,a^{\dot\alpha}{}_{\nu\rho}+b^{*}{}_{\dot\rho}{}^{\alpha\beta}\,p_{\alpha\dot\beta}\,b_\beta{}^{\dot\rho\dot\beta})\\ &+\kappa(a^{*\nu}{}_{\dot\alpha\dot\beta}\,b_\nu{}^{\dot\alpha\dot\beta}+b^{*}{}_{\dot\rho}{}^{\alpha\beta}\,a^{\dot\rho}{}_{\alpha\beta})+(p_{\dot\rho}{}^{\beta}\,d^{*\alpha}\,a^{\dot\rho}{}_{\alpha\beta}\\ &+p_\beta{}^{\nu}\,c^{*}{}_{\dot\alpha}\,b_\nu{}^{\dot\alpha\dot\beta}-a^{*\nu}{}_{\dot\alpha\dot\beta}\,p_\nu{}^{\dot\beta}\,d^{\dot\alpha}-b^{*}{}_{\dot\rho}{}^{\alpha\beta}\,p_\beta{}^{\dot\rho}\,c_\alpha)\\ &+3(d^{*\alpha}\,p_{\alpha\dot\beta}\,d^{\dot\beta}+c^{*}{}_{\dot\alpha}\,p^{\dot\alpha\beta}\,c_\beta)+6\kappa(d^{*\alpha}\,c_\alpha+c^{*}{}_{\dot\alpha}\,d^{\dot\alpha}), \quad (2)\end{aligned}$$

[1] P. A. M. Dirac, Proc. Roy. Soc. (London) **A155**, 447 (1936).
[2] M. Fierz and W. Pauli, Proc. Roy. Soc. (London) **A173**, 211 (1939).
[3] A specially interesting field equation for particles with two different mass states has recently been given by H. J. Bhabha, Phil. Mag. **43**, 33 (1952).
[4] S. N. Gupta, Proc. Phys. Soc. (London) **A65**, 161, 608 (1952).
[5] F. J. Dyson, Phys. Rev. **75**, 486, 1736 (1949).

$$\psi = \begin{pmatrix} a^{i}_{11} \\ \sqrt{2}\, a^{i}_{12} \\ a^{i}_{22} \\ a^{\dot{i}}_{11} \\ \sqrt{2}\, a^{\dot{i}}_{12} \\ a^{\dot{i}}_{22} \\ 3\sqrt{2}\, d^{i} \\ 3\sqrt{2}\, d^{\dot{i}} \\ b^{ii}_{1} \\ \sqrt{2}\, b^{i\dot{i}}_{1} \\ b^{\dot{i}\dot{i}}_{1} \\ b^{ii}_{2} \\ \sqrt{2}\, b^{i\dot{i}}_{2} \\ b^{\dot{i}\dot{i}}_{2} \\ 3\sqrt{2}\, c_{1} \\ 3\sqrt{2}\, c_{2} \end{pmatrix}$$

FIG. 1. Components of the matrix ψ.

whence we obtain the field equations:

$$\begin{aligned} -p^{\dot{\beta}\rho}\, a^{\dot{\alpha}}{}_{\nu\rho} - p^{\dot{\alpha}\rho}\, a^{\dot{\beta}}{}_{\nu\rho} - p_{\nu}{}^{\dot{\beta}}\, d^{\dot{\alpha}} - p_{\nu}{}^{\dot{\alpha}}\, d^{\dot{\beta}} + 2\kappa\, b_{\nu}{}^{\dot{\alpha}\dot{\beta}} &= 0, \\ -p_{\alpha\dot{\beta}}\, b_{\beta}{}^{\dot{\beta}\dot{\beta}} - p_{\beta\dot{\beta}}\, b_{\alpha}{}^{\dot{\beta}\dot{\beta}} - p_{\beta}{}^{\dot{\beta}}\, c_{\alpha} - p_{\alpha}{}^{\dot{\beta}}\, c_{\beta} + 2\kappa\, a^{\dot{\beta}}{}_{\alpha\beta} &= 0, \\ -p_{\nu}{}^{\beta}\, a^{\dot{\beta}}{}_{\alpha\beta} + 3p_{\alpha\dot{\beta}}\, d^{\dot{\beta}} + 6\kappa\, c_{\alpha} &= 0, \\ -p_{\dot{\beta}}{}^{\nu}\, b_{\nu}{}^{\dot{\alpha}\dot{\beta}} + 3p^{\dot{\alpha}\dot{\beta}}\, c_{\beta} + 6\kappa\, d^{\dot{\alpha}} &= 0. \end{aligned} \tag{3}$$

The field Eqs. (3) can easily be expressed in a form analogous to that of the Dirac equation.[6] For, using the relations

$$\begin{aligned} p_{1\dot{1}} &= -p_{1}{}^{\dot{1}} = -p_{\dot{1}}{}^{1} = p^{\dot{1}2} = -i\partial/\partial x_3 + \partial/\partial x_4, \\ p_{1\dot{2}} &= -p_{\dot{2}}{}^{1} = p_{1}{}^{\dot{1}} = -p^{\dot{1}2} = -i\partial/\partial x_1 + \partial/\partial x_2, \\ p_{2\dot{1}} &= p_{\dot{1}}{}^{1} = -p_{2}{}^{\dot{1}} = -p^{\dot{2}1} = -i\partial/\partial x_1 - \partial/\partial x_2, \\ p_{2\dot{2}} &= p_{\dot{2}}{}^{1} = p_{2}{}^{\dot{1}} = p^{\dot{1}1} = i\partial/\partial x_3 + \partial/\partial x_4, \end{aligned} \tag{4}$$

we can express (3) as a set of sixteen equations involving only the ordinary space and time derivatives of the field quantities. We can then write these sixteen equations as

$$\alpha_{\mu}(\partial\psi/\partial x_{\mu}) + \kappa\psi = 0, \tag{5}$$

where ψ is the one-column matrix shown in Fig. 1, and the α_{μ} are given in Fig. 2.

By actual multiplication of the matrices α_{μ}, it can be verified that they satisfy the relation

$$\sum(\alpha_{\mu}\alpha_{\nu} - \delta_{\mu\nu})\alpha_{\lambda}\alpha_{\rho} = 0, \tag{6}$$

where $\sum$ denotes a sum over all possible permutations of the indices μ, ν, λ, and ρ. Multiplying (5) by $\alpha_{\rho}\alpha_{\lambda}\alpha_{\nu}\partial^{3}/\partial x_{\rho}\partial x_{\lambda}\partial x_{\nu}$, we get

$$\begin{aligned} \alpha_{\rho}\alpha_{\lambda}\alpha_{\nu}\alpha_{\mu}(\partial^{4}\psi/\partial x_{\rho}\partial x_{\lambda}\partial x_{\nu}\partial x_{\mu}) \\ + \kappa\alpha_{\rho}\alpha_{\lambda}\alpha_{\nu}(\partial^{3}\psi/\partial x_{\rho}\partial x_{\lambda}\partial x_{\nu}) = 0 \end{aligned} \tag{7}$$

which gives, on using (6),

$$\alpha_{\nu}\alpha_{\mu}(\partial^{4}\psi/\partial x_{\lambda}{}^{2}\partial x_{\nu}\partial x_{\mu}) + \kappa\alpha_{\rho}\alpha_{\lambda}\alpha_{\nu}(\partial^{3}\psi/\partial x_{\rho}\partial x_{\lambda}\partial x_{\nu}) = 0. \tag{8}$$

Further, using field equation (5), we obtain from the above equation

$$\kappa^{2}(\partial^{2}\psi/\partial x_{\lambda}{}^{2}) - \kappa^{4}\psi = 0$$

or

$$(\Box^{2} - \kappa^{2})\psi = 0, \tag{9}$$

which shows that ψ satisfies the second-order wave equation.

3. LAGRANGIAN FORMALISM

In order to derive field equation (5) from a Lagrangian density, it is necessary to define an adjoint of ψ in the usual way. For this, we note that the nonsingular Hermitian matrix η of Fig. 3 satisfies the relations

$$\eta^{-1}\alpha_{i}{}^{*}\eta = -\alpha_{i}, \quad \eta^{-1}\alpha_{4}{}^{*}\eta = \alpha_{4}, \tag{10}$$

where an asterisk denotes the Hermitian conjugate. Further, taking the Hermitian conjugate of (5), we get

$$-(\partial\psi^{*}/\partial x_{4})\alpha_{4}{}^{*} + (\partial\psi^{*}/\partial x_{i})\alpha_{i}{}^{*} + \kappa\psi^{*} = 0, \tag{11}$$

which, on being multiplied by η, can be written as

$$\begin{aligned} -(\partial\psi^{*}/\partial x_{4})\eta(\eta^{-1}\alpha_{4}{}^{*}\eta) + (\partial\psi^{*}/\partial x_{i})\eta(\eta^{-1}\alpha_{i}{}^{*}\eta) \\ + \kappa\psi^{*}\eta = 0. \end{aligned} \tag{12}$$

Hence, using (10), we have

$$(\partial\bar{\psi}/\partial x_{\mu})\alpha_{\mu} - \kappa\bar{\psi} = 0, \tag{13}$$

where the adjoint $\bar{\psi}$ denotes the quantity

$$\bar{\psi} = \psi^{*}\eta. \tag{14}$$

The field equations (5) and (13) can be obtained by means of the usual variational principle from the Lagrangian density

$$L = -ch[\bar{\psi}\alpha_{\mu}(\partial\psi/\partial x_{\mu}) + \kappa\bar{\psi}\psi]. \tag{15}$$

[6] The above procedure for writing the Fierz-Pauli equation in the Dirac form is due to K. K. Gupta, Proc. Indian Acad. Sci. **A35**, 255 (1952). However, our choice of the components of ψ and the representation for the α's is slightly different.

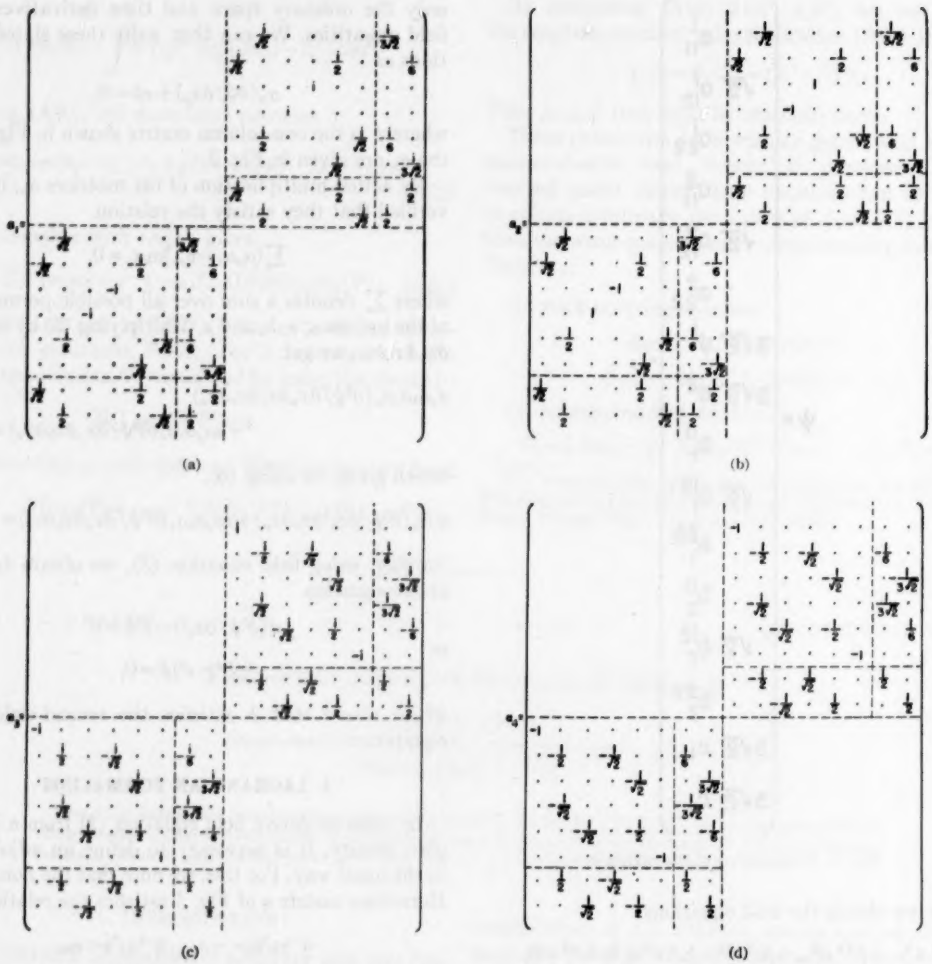

FIG. 2. The matrices α_μ. In these matrices a dot or a blank space indicates a zero or a block of zeros.

Although the field quantity ψ transforms in a rather complicated manner under a Lorentz transformation, we can prove the Lorentz invariance of the above Lagrangian density by showing that (15) is equal to the invariant quantity (2) apart from a constant factor. This also establishes the covariance of all the results obtained from the Lagrangian density (15).

From (15) we obtain in the usual way for the current density four-vector j_μ and the canonical energy-momentum tensor $S_{\mu\nu}$:

$$j_\mu = iec\bar{\psi}\alpha_\mu\psi, \tag{16}$$

$$S_{\mu\nu} = ch\bar{\psi}\alpha_\nu(\partial\psi/\partial x_\mu). \tag{17}$$

According to (16) and (17), the charge density and the Hamiltonian density of the field are

$$\rho = j_4/ic = e\bar{\psi}\alpha_4\psi = e\psi^\dagger\psi, \tag{18}$$

$$H = -S_{44} = ich\bar{\psi}\alpha_4(\partial\psi/\partial x_0) = ich\psi^\dagger(\partial\psi/\partial x_0), \tag{19}$$

where

$$\psi^\dagger = \bar{\psi}\alpha_4 = \psi^*\eta\alpha_4. \tag{20}$$

4. SOLUTION OF THE FIELD EQUATION

Since ψ satisfies the wave equation (9), a solution of (5) must be of the form

$$\psi = \psi^+(\mathbf{k})\exp[i(\mathbf{k}\cdot\mathbf{x}-\omega x_0)]$$
$$\text{or} \tag{21}$$
$$\psi = \psi^-(\mathbf{k})\exp[-i(\mathbf{k}\cdot\mathbf{x}-\omega x_0)],$$

where $\mathbf{k}$ is an arbitrary real vector, and

$$\omega = (\mathbf{k}^2+\kappa^2)^{\frac{1}{2}}. \tag{22}$$

For simplicity, let us first consider the solutions of (5) corresponding to $\mathbf{k}=0$, which are of the form

$$\psi = \psi^+(0)\exp(-i\kappa x_0) \quad \text{or} \quad \psi = \psi^-(0)\exp(i\kappa x_0). \tag{23}$$

Substituting (23) in (5), we get

$$(\alpha_4-1)\psi^+(0)=0 \quad \text{and} \quad (\alpha_4+1)\psi^-(0)=0. \tag{24}$$

Further, denoting the sixteen components of the one-column matrix $\psi^+(0)$ as $c_1, c_2, \cdots, c_{16}$, and making use of the explicit representation for α_4, we can decompose the first relation in (24) into the following four sets involving sixteen algebraic equations:

$$c_1+c_9=0, \qquad c_1+c_9=0; \tag{25}$$

$$c_6+c_{14}=0, \qquad c_6+c_{14}=0; \tag{26}$$

$$\begin{aligned} \sqrt{2}c_3+c_{13}+\tfrac{1}{3}c_{16}&=0, \\ c_5-\tfrac{1}{3}c_8+\sqrt{2}c_{11}&=0, \\ 2c_5+\sqrt{2}c_{11}+c_{13}-\tfrac{1}{3}c_{16}&=0, \\ 2c_8+\sqrt{2}c_{11}-c_{13}-c_{16}&=0, \\ \sqrt{2}c_3+c_5+\tfrac{1}{3}c_8+2c_{13}&=0, \\ \sqrt{2}c_3-c_5+c_8-2c_{16}&=0; \end{aligned} \tag{27}$$

$$\begin{aligned} c_2+\tfrac{1}{3}c_7+\sqrt{2}c_{12}&=0, \\ \sqrt{2}c_4+c_{10}-\tfrac{1}{3}c_{15}&=0, \\ c_2+\sqrt{2}c_4-\tfrac{1}{3}c_7+2c_{10}&=0, \\ c_2-\sqrt{2}c_4+c_7-2c_{15}&=0, \\ 2c_2+c_{10}+\sqrt{2}c_{12}+\tfrac{1}{3}c_{15}&=0, \\ 2c_7+c_{10}-\sqrt{2}c_{12}-c_{15}&=0. \end{aligned} \tag{28}$$

In order to solve the above simultaneous equations we have to regard one of the c's in each of the four sets as an arbitrary quantity. Thus, taking c_1, c_3, c_6, and c_{12}

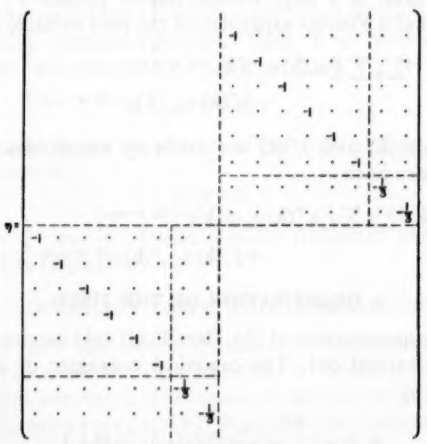

FIG. 3. The matrix η.

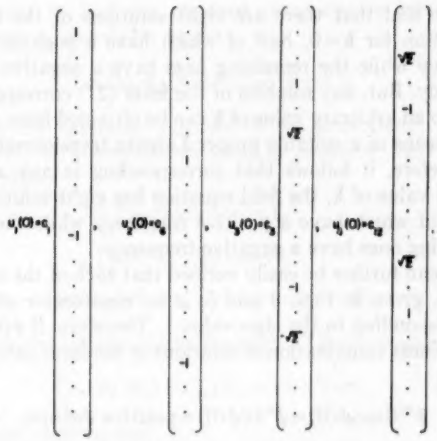

FIG. 4. The four independent solutions for $\psi^+(0)$.

as an arbitrary quantities, we easily find

$$c_1=\text{arbitrary}, \quad c_9=-c_1; \tag{29}$$

$$c_6=\text{arbitrary}, \quad c_{14}=-c_6; \tag{30}$$

$$\begin{aligned} c_3&=\text{arbitrary}, & c_5&=\sqrt{2}c_3, \\ c_{11}&=-c_3, & c_{13}&=-\sqrt{2}c_3, \\ c_8&=0, & c_{16}&=0; \end{aligned} \tag{31}$$

$$\begin{aligned} c_{12}&=\text{arbitrary}, & c_{10}&=\sqrt{2}c_{12}, \\ c_4&=-c_{12}, & c_2&=-\sqrt{2}c_{12}, \\ c_{15}&=0, & c_7&=0. \end{aligned} \tag{32}$$

Hence, there are four independent solutions of the first relation in (24), which are given in Fig. 4. Similarly, it can be shown that there are four independent solutions of the second relation in (24), which are given in Fig. 5.

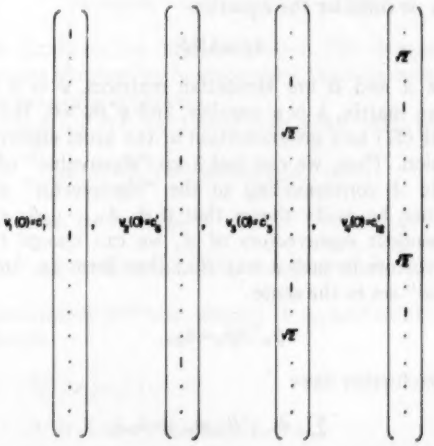

FIG. 5. The four independent solutions for $\psi^-(0)$.

We find that there are eight solutions of the field equation for $\mathbf{k}=0$, half of which have a positive frequency while the remaining ones have a negative frequency. But, any solution of the form (21) corresponding to an arbitrary value of $\mathbf{k}$ can be obtained from (23) by means of a suitable proper Lorentz transformation. Therefore, it follows that corresponding to any arbitrary value of $\mathbf{k}$, the field equation has eight solutions, four of which have a positive frequency while the remaining ones have a negative frequency.

It can further be easily verified that each of the solutions, given in Figs. 4 and 5, is an eigenvector of $\eta\alpha_4$ corresponding to the eigenvalue 1. Therefore, if $\psi(0)$ is any linear combination of solutions of the form (23), we have

$$\psi^*(0)\eta\alpha_4\psi(0)=\psi^*(0)\psi(0)=\text{positive definite}. \quad (33)$$

Thus, according to (18), the charge density due to the component $\psi(0)$ of the field is

$$\rho(0)=j_0(0)/c=e\psi^*(0)\eta\alpha_4\psi(0)=\text{positive definite}, \quad (34)$$

where we have taken e as a positive quantity. Moreover, there being no privileged direction for the vector $\mathbf{k}=0$, the current density vector due to the component $\psi(0)$ must vanish, i.e.,

$$j_i(0)=iec\psi^*(0)\eta\alpha_i\psi(0)=0. \quad (35)$$

Since $j_i(0)$ and $ic\rho(0)$ form components of a timelike four vector, it follows that under any proper Lorentz transformation the positive quantity $\rho(0)$ will transform again into a positive quantity, which shows that

$$\psi^*(\mathbf{k})\eta\alpha_4\psi(\mathbf{k})=\text{positive definite}, \quad (36)$$

where $\psi(\mathbf{k})$ denotes any linear combination of solutions of the form (21).

5. FOURIER EXPANSION OF THE FIELD VARIABLES

Let us consider the equation

$$A\psi=\lambda B\psi, \quad (37)$$

where A and B are Hermitian matrices, ψ is a one-column matrix, λ is a number, and $\psi^*B\psi>0$. We can regard (37) as a generalization of the usual eigenvalue equation. Thus, we can call λ an "eigenvalue" of the matrix A corresponding to the "eigenvector" ψ. It can then be easily shown that if $\psi_1, \psi_2, \cdots, \psi_n$ are n independent eigenvectors of A, we can choose these eigenvectors in such a way that they form an "orthonormal" set in the sense

$$\psi_m^*B\psi_n=\delta_{mn}, \quad (38)$$

and we further have

$$\sum_m \psi_{m,\gamma}^*B_{\gamma\alpha}\psi_{m,\beta}=\delta_{\alpha\beta}, \quad (39)$$

where $\psi_{m,\gamma}^*$, $B_{\gamma\alpha}$, and $\psi_{m,\beta}$ denote elements of the matrices ψ_m^*, B, and ψ_m, respectively, and the indices α, β, γ can take the values $1, 2, \cdots, n$.

Substituting (21) in (5), we get

$$(ik_1\alpha_1+ik_2\alpha_2+ik_3\alpha_3-\omega\alpha_4+\kappa)\psi^+(\mathbf{k})=0, \quad (40)$$

$$(ik_1\alpha_1+ik_2\alpha_2+ik_3\alpha_3-\omega\alpha_4-\kappa)\psi^-(\mathbf{k})=0, \quad (41)$$

which give, on being multiplied by η,

$$(ik_1\eta\alpha_1+ik_2\eta\alpha_2+ik_3\eta\alpha_3+\kappa\eta)\psi^+(\mathbf{k})=\omega\eta\alpha_4\psi^+(\mathbf{k}), \quad (42)$$

$$(ik_1\eta\alpha_1+ik_2\eta\alpha_2+ik_3\eta\alpha_3+\kappa\eta)\psi^-(-\mathbf{k})=-\omega\eta\alpha_4\psi^-(-\mathbf{k}). \quad (43)$$

The above equations are of the same form as (37), where the Hermitian operators $ik_1\eta\alpha_1+ik_2\eta\alpha_2+ik_3\eta\alpha_3+\kappa\eta$ and $\eta\alpha_4$ correspond to A and B, respectively, ω and $-\omega$ are the eigenvalues, and $\eta\alpha_4$ satisfies the condition (36). Hence, all possible solutions of (42) and (43) can be chosen in such a way that

$$\begin{aligned} u_r^\dagger(\mathbf{k})u_s(\mathbf{k})&=v_r^\dagger(-\mathbf{k})v_s(-\mathbf{k})=\delta_{rs},\\ u_r^\dagger(\mathbf{k})v_s(-\mathbf{k})&=v_s^\dagger(-\mathbf{k})u_r(\mathbf{k})=0, \end{aligned} \quad (44)$$

and

$$\sum_r[u_{r,\alpha}^\dagger(\mathbf{k})u_{r,\beta}(\mathbf{k})+v_{r,\alpha}^\dagger(-\mathbf{k})v_{r,\beta}(-\mathbf{k})]=\delta_{\alpha\beta}, \quad (45)$$

where the $u_r(\mathbf{k})$'s are the independent solutions for $\psi^+(\mathbf{k})$, the $v_r(\mathbf{k})$'s are the independent solutions for $\psi^-(\mathbf{k})$, and

$$u_r^\dagger(\mathbf{k})=u_r^*(\mathbf{k})\eta\alpha_4, \quad v_r^\dagger(\mathbf{k})=v_r^*(\mathbf{k})\eta\alpha_4. \quad (46)$$

Since we have shown in the preceding section that corresponding to any value of $\mathbf{k}$ there are four independent solutions for $\psi^+(\mathbf{k})$ as well as for $\psi^-(\mathbf{k})$, the indices r and s in (44) and (45) can take the values 1, 2, 3, 4. On the other hand, the indices α and β in (45) can take the values $1, 2, \cdots, 16$.

We can now assume in the usual way that the field is enclosed in a large cubical box of volume V, and carry out a Fourier expansion of the field variable ψ as

$$\psi_\alpha=V^{-\frac{1}{2}}\sum_{\mathbf{k}}\sum_r[a_r(\mathbf{k})u_{r,\alpha}(\mathbf{k})e^{i(\mathbf{k}\cdot\mathbf{x}-\omega x_0)}+b_r^*(\mathbf{k})v_{r,\alpha}(\mathbf{k})e^{-i(\mathbf{k}\cdot\mathbf{x}-\omega x_0)}], \quad (47)$$

where $a_r(\mathbf{k})$ and $b_r^*(\mathbf{k})$ are arbitrary amplitudes. We then also have

$$\psi_\alpha^\dagger=V^{-\frac{1}{2}}\sum_{\mathbf{k}}\sum_r[a_r^*(\mathbf{k})u_{r,\alpha}^\dagger(\mathbf{k})e^{-i(\mathbf{k}\cdot\mathbf{x}-\omega x_0)}+b_r(\mathbf{k})v_{r,\alpha}^\dagger(\mathbf{k})e^{i(\mathbf{k}\cdot\mathbf{x}-\omega x_0)}]. \quad (48)$$

6. QUANTIZATION OF THE FIELD

The quantization of the Fierz-Pauli field can now be easily carried out. The canonical conjugate of ψ_α is given by

$$\pi_\alpha=\frac{\partial L}{\partial(\partial\psi_\alpha/\partial t)}=ih\bar{\psi}_\beta(\alpha_4)_{\beta\alpha}=ih\psi_\alpha^\dagger. \quad (49)$$

Since fields of half-integral spin obey Fermi statistics, the appropriate commutation relations in the present case are

$$\{\psi_\alpha(\mathbf{x},t),\psi_\beta(\mathbf{x}',t)\}=0,\quad \{\psi_\alpha^\dagger(\mathbf{x},t),\psi_\beta^\dagger(\mathbf{x}',t)\}=0, \tag{50}$$

$$\{\psi_\alpha(\mathbf{x},t),\psi_\beta^\dagger(\mathbf{x}',t)\}=\delta_{\alpha\beta}\delta(\mathbf{x}-\mathbf{x}'). \tag{51}$$

Substituting (47) and (48) in (50) and (51), and using (44), we get

$$\begin{aligned}\{a_r(\mathbf{k}),\, a_s^*(\mathbf{k}')\}&=\delta_{rs}\delta_{\mathbf{k},\mathbf{k}'},\\ \{b_r(\mathbf{k}),\, b_s^*(\mathbf{k}')\}&=\delta_{rs}\delta_{\mathbf{k},\mathbf{k}'},\end{aligned} \tag{52}$$

while any other anticommutator involving a pair of the operators $a_r(\mathbf{k})$, $a_r^*(\mathbf{k})$, $b_r(\mathbf{k})$, or $b_r^*(\mathbf{k})$ vanishes.

Again, substituting (47) and (48) in (18) and (19), and using (44), we obtain for the total Hamiltonian and the total charge of the field

$$\mathcal{H}=\sum_{\mathbf{k}}\sum_r ch\omega[a_r^*(\mathbf{k})a_r(\mathbf{k})-b_r(\mathbf{k})b_r^*(\mathbf{k})], \tag{53}$$

$$\int\rho dV=\sum_{\mathbf{k}}\sum_r e[a_r^*(\mathbf{k})a_r(\mathbf{k})+b_r(\mathbf{k})b_r^*(\mathbf{k})]. \tag{54}$$

Using the commutation relations (52), and ignoring the zero-point energy and charge, we can write (53) and (54) as

$$\mathcal{H}=\sum_{\mathbf{k}}\sum_r ch\omega[a_r^*(\mathbf{k})a_r(\mathbf{k})+b_r^*(\mathbf{k})b_r(\mathbf{k})], \tag{55}$$

$$\int\rho dV=\sum_{\mathbf{k}}\sum_r e[a_r^*(\mathbf{k})a_r(\mathbf{k})-b_r^*(\mathbf{k})b_r(\mathbf{k})]. \tag{56}$$

It follows in the usual way that the quantities $a_1^*(\mathbf{k})a_1(\mathbf{k})$, $b_1^*(\mathbf{k})b_1(\mathbf{k})$, $a_2^*(\mathbf{k})a_2(\mathbf{k})$, $b_2^*(\mathbf{k})b_2(\mathbf{k})$, . . . can have only the eigenvalues 0 or 1, so that the present field describes particles of positive energy obeying Pauli's exclusion principle. Moreover, the $a_r(\mathbf{k})$ are the absorption operators for particles of energy $ch\omega$ and charge e, while the $b_r(\mathbf{k})$ are the absorption operators for particles of energy $ch\omega$ and charge $-e$. The Hermitian conjugates of these operators are the corresponding emission operators. Thus, if no particles of charge e are present in a state Ψ, we have

$$\psi^+\Psi=0, \tag{57}$$

and similarly, in the absence of particles of charge $-e$ in a state Ψ,

$$\bar{\psi}^+\Psi=0, \tag{58}$$

where ψ^+ and $\bar{\psi}^+$ denote positive frequency parts of ψ and $\bar{\psi}$, respectively.

7. COVARIANT COMMUTATION RELATIONS

We shall now obtain covariant commutation relations between the field variables at different times. For this purpose it is necessary to use the variables ψ_α and $\bar{\psi}_\alpha$ instead of ψ_α and $\psi_\alpha^\dagger$. It is, of course, evident that

$$\{\psi_\alpha(x),\psi_\beta(x')\}=\{\bar{\psi}_\alpha(x),\bar{\psi}_\beta(x')\}=0. \tag{59}$$

In order to find the required commutation relation between ψ_α and $\bar{\psi}_\beta$ let us put

$$\{\psi_\alpha(x),\bar{\psi}_\beta(x')\}=f_{\alpha\beta}\Delta(x-x'), \tag{60}$$

where the quantity $f_{\alpha\beta}$ has to be determined, and $\Delta(x-x')$ is a well-known singular function with the properties

$$(\Box^2-\kappa^2)\Delta(x-x')=0, \tag{61}$$

$$\begin{aligned}[\Delta(x-x')]_{x_0'=x_0}&=0,\\ [\partial\Delta(x-x')/\partial x_0]_{x_0'=x_0}&=-\delta(\mathbf{x}-\mathbf{x}').\end{aligned} \tag{62}$$

Since $\psi_\alpha(x)$ satisfies the field equation (5), we must have

$$[\alpha_\mu(\partial/\partial x_\mu)+\kappa]_{\alpha\beta}f_{\beta\gamma}\Delta(x-x')=0. \tag{63}$$

We also observe that

$$\begin{aligned}&[\alpha_\mu(\partial/\partial x_\mu)+\kappa][\alpha_\nu\alpha_\lambda\alpha_\rho(\partial^3/\partial x_\nu\partial x_\lambda\partial x_\rho)\\ &\quad-\kappa\alpha_\lambda\alpha_\rho(\partial^2/\partial x_\lambda\partial x_\rho)]\Delta(x-x')\\ &\quad=\alpha_\lambda\alpha_\rho(\partial^2/\partial x_\lambda\partial x_\rho)(\Box^2-\kappa^2)\Delta(x-x')=0,\end{aligned} \tag{64}$$

which suggests that $f_{\beta\gamma}$ should be of the form

$$\begin{aligned}f_{\beta\gamma}=C[&\alpha_\nu\alpha_\lambda\alpha_\rho(\partial^3/\partial x_\nu\partial x_\lambda\partial x_\rho)\\ &-\kappa\alpha_\lambda\alpha_\rho(\partial^2/\partial x_\lambda\partial x_\rho)]_{\beta\gamma},\end{aligned} \tag{65}$$

where C is a constant. We have now to verify that the commutation relation, given by (60) and (65), agrees with (51), and for this we shall derive a relation between $\bar{\psi}$ and $\psi^\dagger$.

We note that the relation (6) gives us

$$\alpha_4^2-\alpha_4^4=0 \tag{66}$$

$$\alpha_4^3\alpha_i+\alpha_4^2\alpha_i\alpha_4+\alpha_4\alpha_i\alpha_4^2+\alpha_i\alpha_4^3-\alpha_4\alpha_i-\alpha_i\alpha_4=0, \tag{67}$$

$$\begin{aligned}&\alpha_4^2\alpha_k\alpha_i+\alpha_4\alpha_k\alpha_4\alpha_i+\alpha_4\alpha_k\alpha_i\alpha_4-\delta_{ik}\alpha_4^2+\alpha_k\alpha_i\alpha_4^2\\ &\quad+\alpha_k\alpha_4\alpha_i\alpha_4+\alpha_k\alpha_4^2\alpha_i-\alpha_k\alpha_i+(i\rightleftarrows k)=0,\end{aligned} \tag{68}$$

where $(i\rightleftarrows k)$ on the left-hand side of (68) denotes an expression obtained by interchanging the indices i and k in the preceding expression.

Multiplying (13) by $\alpha_4-\alpha_4^3$, and using (66), we get

$$\kappa\bar{\psi}(\alpha_4-\alpha_4^3)=(\partial\bar{\psi}/\partial x_i)\alpha_i(\alpha_4-\alpha_4^3),$$

which gives, on using (67),

$$\kappa\bar{\psi}\alpha_4(1-\alpha_4^2)=(\partial\bar{\psi}/\partial x_i)\alpha_4(\alpha_4^2\alpha_i+\alpha_4\alpha_i\alpha_4+\alpha_i\alpha_4^2-\alpha_i). \tag{69}$$

Differentiating (69) with respect to x_4, and using (13), we obtain

$$\begin{aligned}&\kappa[\kappa\bar{\psi}-(\partial\bar{\psi}/\partial x_i)\alpha_i](1-\alpha_4^2)\\ &\quad=(\partial/\partial x_i)[\kappa\bar{\psi}-(\partial\bar{\psi}/\partial x_k)\alpha_k]\\ &\qquad\times(\alpha_4^2\alpha_i+\alpha_4\alpha_i\alpha_4+\alpha_i\alpha_4^2-\alpha_i),\end{aligned}$$

or

$$\bar{\psi}=\bar{\psi}\alpha_4{}^3+\frac{1}{\kappa}\frac{\partial\bar{\psi}}{\partial x_i}(\alpha_4{}^2\alpha_i+\alpha_4\alpha_i\alpha_4)$$
$$-\frac{1}{\kappa^2}\frac{\partial^2\bar{\psi}}{\partial x_i\partial x_k}\alpha_k(\alpha_4{}^2\alpha_i+\alpha_4\alpha_i\alpha_4+\alpha_i\alpha_4{}^2-\alpha_i).$$

Further, using (66) and (68), we can write the above relation as

$$\bar{\psi}=\bar{\psi}\alpha_4{}^4+\frac{1}{\kappa}\frac{\partial\bar{\psi}\alpha_4}{\partial x_i}(\alpha_4\alpha_i+\alpha_i\alpha_4)$$
$$+\frac{1}{\kappa^2}\frac{\partial^2\bar{\psi}\alpha_4}{\partial x_i\partial x_k}(\alpha_4\alpha_i\alpha_i+\alpha_i\alpha_4\alpha_i+\alpha_i\alpha_i\alpha_4-\delta_{ik}\alpha_4{}^3),$$

or

$$\bar{\psi}=\psi^\dagger\alpha_4{}^3+\frac{1}{\kappa}\frac{\partial\psi^\dagger}{\partial x_i}(\alpha_4\alpha_i+\alpha_i\alpha_4)$$
$$+\frac{1}{\kappa^2}\frac{\partial^2\psi^\dagger}{\partial x_i\partial x_k}(\alpha_4\alpha_i\alpha_i+\alpha_i\alpha_4\alpha_i+\alpha_i\alpha_i\alpha_4-\delta_{ik}\alpha_4{}^3). \quad (70)$$

From (70) and (51) we get

$$\{\psi_\alpha(\mathbf{x},t),\bar{\psi}_\beta(\mathbf{x}',t)\}$$
$$=\left[\alpha_4{}^3+\frac{1}{\kappa}\frac{\partial}{\partial x_i'}(\alpha_4\alpha_i+\alpha_i\alpha_4)+\frac{1}{\kappa^2}\frac{\partial^2}{\partial x_i'\partial x_k'}\right.$$
$$\left.\times(\alpha_4\alpha_i\alpha_i+\alpha_i\alpha_4\alpha_i+\alpha_i\alpha_i\alpha_4-\delta_{ik}\alpha_4{}^3)\right]_{\alpha\beta}\delta(\mathbf{x}-\mathbf{x}')$$
$$=\left[\alpha_4{}^3-\frac{1}{\kappa}\frac{\partial}{\partial x_i}(\alpha_4\alpha_i+\alpha_i\alpha_4)+\frac{1}{\kappa^2}\frac{\partial^2}{\partial x_i\partial x_k}\right.$$
$$\left.\times(\alpha_4\alpha_i\alpha_i+\alpha_i\alpha_4\alpha_i+\alpha_i\alpha_i\alpha_4-\delta_{ik}\alpha_4{}^3)\right]_{\alpha\beta}\delta(\mathbf{x}-\mathbf{x}'). \quad (71)$$

On the other hand, substituting (65) in (60), putting $x_0'=x_0$, and using (61) and (62), we obtain

$$\{\psi_\alpha(\mathbf{x},t),\bar{\psi}_\beta(\mathbf{x}',t)\}$$
$$=iC\left[\kappa^2\alpha_4{}^3-\kappa\frac{\partial}{\partial x_i}(\alpha_4\alpha_i+\alpha_i\alpha_4)\right.$$
$$+\frac{\partial^2}{\partial x_i\partial x_k}(\alpha_4\alpha_i\alpha_i+\alpha_i\alpha_4\alpha_i+\alpha_i\alpha_i\alpha_4)$$
$$\left.-\frac{\partial^2}{\partial x_i{}^2}\alpha_4{}^3\right]_{\alpha\beta}\delta(\mathbf{x}-\mathbf{x}'). \quad (72)$$

Comparing (71) and (72), we find that the commutation relation (60) agrees with (51), provided that we choose the constant C in (65) as

$$C=-i/\kappa^2. \quad (73)$$

Thus, from (60), (65), and (73) we obtain the commutation relation:

$$\{\psi_\alpha(x),\bar{\psi}_\beta(x')\}$$
$$=-\frac{i}{\kappa^2}\left(\alpha_\nu\alpha_\lambda\alpha_\rho\frac{\partial^3}{\partial x_\nu\partial x_\lambda\partial x_\rho}-\kappa\alpha_\lambda\alpha_\rho\frac{\partial^2}{\partial x_\lambda\partial x_\rho}\right)_{\alpha\beta}$$
$$\times\Delta(x-x'). \quad (74)$$

8. ELECTROMAGNETIC INTERACTION OF PARTICLES OF SPIN 3/2

Following the usual procedure, we can write the Lagrangian density for the Fierz-Pauli field interacting with the electromagnetic field as

$$L=-\frac{1}{4}\left(\frac{\partial A_\nu}{\partial x_\mu}-\frac{\partial A_\mu}{\partial x_\nu}\right)^2-\frac{1}{2}\left(\frac{\partial A_\mu}{\partial x_\mu}\right)^2$$
$$-c\hbar\left[\bar{\psi}\alpha_\mu\left(\frac{\partial}{\partial x_\mu}-\frac{ie}{c\hbar}A_\mu\right)\psi+\kappa\bar{\psi}\psi\right], \quad (75)$$

which gives us the field equations:

$$\alpha_\mu(\partial\psi/\partial x_\mu)+\kappa\psi=(ie/c\hbar)A_\mu\alpha_\mu\psi,$$
$$(\partial\bar{\psi}/\partial x_\mu)\alpha_\mu-\kappa\bar{\psi}=(-ie/c\hbar)A_\mu\bar{\psi}\alpha_\mu, \quad (76)$$
$$\Box^2A_\mu=-ie\bar{\psi}\alpha_\mu\psi.$$

In order to obtain the rules for writing down the elements of the S matrix in the present case, it will be very convenient to follow the treatment of Yang and Feldman.[7] We first observe that the relation (6) gives us

$$\left(\alpha_\mu\frac{\partial}{\partial x_\mu}+\kappa\right)\left(\alpha_\nu\frac{\partial}{\partial x_\nu}-\kappa\right)$$
$$\times\left(\frac{1}{\kappa^2}\alpha_\lambda\alpha_\rho\frac{\partial^2}{\partial x_\lambda\partial x_\rho}-\frac{1}{\kappa^2}\Box^2+1\right)=\Box^2-\kappa^2, \quad (77)$$

so that, defining $R^{\rm ret}(x-x')$ by

$$R^{\rm ret}(x-x')=\left(\alpha_\nu\frac{\partial}{\partial x_\nu}-\kappa\right)$$
$$\times\left(\frac{1}{\kappa^2}\alpha_\lambda\alpha_\rho\frac{\partial^2}{\partial x_\lambda\partial x_\rho}-\frac{1}{\kappa^2}\Box^2+1\right)\Delta^{\rm ret}(x-x'), \quad (78)$$

we get

$$[\alpha_\nu(\partial/\partial x_\nu)+\kappa]R^{\rm ret}(x-x')=-\delta(x-x'). \quad (79)$$

Similarly, we define a function $R^{\rm adv}$ by replacing $\Delta^{\rm ret}$ in (78) by $\Delta^{\rm adv}$, so that $R^{\rm adv}$ also satisfies the relation (79).

[7] C. N. Yang and D. Feldman, Phys. Rev. **79**, 972 (1950). We also refer to this paper for the definitions of the functions $\Delta^{\rm ret}$, $\Delta^{\rm adv}$, $D^{\rm ret}$, and $D^{\rm adv}$, which we shall be using here.

Further, we define "incoming field operators" ψ^{in}, $\bar{\psi}^{\text{in}}$, and $A_\mu{}^{\text{in}}$ by the set of integral equations

$$\psi(x)=\psi^{\text{in}}(x)-(ie/c\hbar)\times\int R^{\text{ret}}(x-x')dx'A_\nu(x')\alpha_\nu\psi(x'),$$

$$\bar{\psi}(x)=\bar{\psi}^{\text{in}}(x)-(ie/c\hbar)\times\int\bar{\psi}(x')\alpha_\nu A_\nu(x')dx'R^{\text{adv}}(x'-x),\quad(80)$$

$$A_\nu(x)=A_\nu{}^{\text{in}}(x)+ie\times\int D^{\text{ret}}(x-x')dx'\bar{\psi}(x')\alpha_\mu\psi(x'),$$

and the "outgoing field operators" ψ^{out}, $\bar{\psi}^{\text{out}}$, and $A_\mu{}^{\text{out}}$ by the set of integral equations:

$$\psi(x)=\psi^{\text{out}}(x)-(ie/c\hbar)\times\int R^{\text{adv}}(x-x')dx'A_\nu(x')\alpha_\nu\psi(x'),$$

$$\bar{\psi}(x)=\bar{\psi}^{\text{out}}(x)-(ie/c\hbar)\times\int\bar{\psi}(x')\alpha_\nu A_\nu(x')dx'R^{\text{ret}}(x'-x),\quad(81)$$

$$A_\nu(x)=A_\nu{}^{\text{out}}(x)+ie\times\int D^{\text{adv}}(x-x')dx'\bar{\psi}(x')\alpha_\mu\psi(x').$$

It can then be easily shown that both the incoming as well as the outgoing field operators satisfy the free-field equations and the free-field commutation relations.

We can now define the S matrix for the interaction of photons and particles of spin 3/2 as the unitary operator, given by

$$\psi^{\text{out}}(x)=S^{-1}\psi^{\text{in}}(x)S,\quad\bar{\psi}^{\text{out}}(x)=S^{-1}\bar{\psi}^{\text{in}}(x)S,\quad A_\nu{}^{\text{out}}(x)=S^{-1}A_\nu{}^{\text{in}}(x)S.\quad(82)$$

One can obtain the matrix elements of the S matrix by solving (80) by successive approximations in powers of e, and then using (81) and (82). However, as pointed out by Yang and Feldman,[7] in practice one need not take this trouble. For, if we compare the set of Eqs. (80), (81), and (82) with similar equations in quantum electrodynamics, it is evident that the rules for obtaining the elements of the S matrix in the present case will be exactly analogous to the Feynman-Dyson rules of quantum electrodynamics,[5] except that the γ_μ matrices of Dirac have to be replaced by the α_μ matrices of Fig. 2, and the function

$$S_F(x-x')=[\gamma_\mu(\partial/\partial x_\mu)-\kappa]\Delta_F(x-x')\quad(83)$$

has to be replaced by

$$R_F(x-x')=\left(\alpha_\nu\frac{\partial}{\partial x_\nu}-\kappa\right)\times\left(\frac{1}{\kappa^2}\alpha_\lambda\alpha_\rho\frac{\partial^2}{\partial x_\lambda\partial x_\rho}-\frac{1}{\kappa^2}\Box^2+1\right)\Delta_F(x-x'),\quad(84)$$

where $\Delta_F(x-x')$ is Feynman's singular function, as defined by Dyson.[5] It is interesting to note that if we replace α_μ by γ_μ in (84), $R_F(x-x')$ reduces to $S_F(x-x')$.

Since $R_F(x-x')$ involves third space and time derivatives of $\Delta_F(x-x')$, it seems at first sight that the divergencies in the present case are even stronger than those in the case of charged particles of spin 1. However, in order to see whether the renormalization theory is really unsuccessful in the case of charged particles of spin 3/2, it would be necessary to carry out actual calculations of the various possibly divergent matrix elements.

We have seen that the quantization of the Fierz-Pauli field does not present any special difficulty. Therefore, it seems to us by no means certain that particles of spin higher than one do not exist in nature, and it would be interesting to carry out further investigations of the properties of such particles. In this connection it should be noted that the intrinsic magnetic moment of charged particles of spin 3/2 has recently been calculated by Belinfante,[8] and shown to be equal to $e\hbar/2mc$, where m is the rest mass of the particles. As pointed out by Belinfante, this seems to suggest that the intrinsic magnetic moment of every elementary particle of nonzero spin is given by the same expression $e\hbar/2mc$, which depends only on the charge and the rest mass of the particle.

[8] F. J. Belinfante, Phys. Rev. **92**, 997 (1953).

Letters to the Editor

PUBLICATION of brief reports of important discoveries in physics may be secured by addressing them to this department. The closing date for this department is five weeks prior to the date of issue. No proof will be sent to the authors. The Board of Editors does not hold itself responsible for the opinions expressed by the correspondents. Communications should not exceed 600 words in length and should be submitted in duplicate.

Electron Multiplication in Germanium at Low Temperature

E. J. RYDER, I. M. ROSS, AND D. A. KLEINMAN
Bell Telephone Laboratories, Murray Hill, New Jersey
(Received July 8, 1954)

IN measurements on germanium and silicon at 300°K and 77°K, Ryder[1] has found that the current density is proportional to the electric field E provided the drift velocity is below a critical value, which for electrons in germanium is 3.2×10^6 cm/sec. For higher drift velocities the current density becomes proportional to $E^{\frac{1}{2}}$ and this has been explained by Shockley[2] as caused by the heating of the electron gas. Ryder's data at 30° differed from that at 77° and 300° in that the transition to the $E^{\frac{1}{2}}$ behavior showed an initial steep rise with field. This steep rise has been seen in new data on n-type germanium at 12.1°, 13.9°, and 20.3°. A similar effect was observed by Gerritsen[3] at 1.7° in p-type germanium at fields above 4.1 volt/cm. Recently Sclar, Burstein, Turner, and Davisson[4] have observed such an effect at 4.2° and 6.4 volt/cm which they[5] interpret as a breakdown by the mechanism of impact ionization of neutral donors. In the explanation of Ryder's 20° data advanced by Conwell,[6] the rise in current is attributed to an increase in mobility. This theory is based on the assumption that at low fields the mobility is limited by impurity scattering, so that when the electrons are heated with increasing field the impurity scattering decreases and the mobility increases until it becomes limited by lattice scattering. In a recent private communication Miss Conwell says that she now believes that the acceptor density required to explain the Ryder data as a mobility change is implausibly high. She has gone on to suggest[7] that measurements on different samples at the same temperature, or on the same sample at different temperatures, should reveal whether electron multiplication is taking place.

Figure 1 shows the current density as a function of electric field for one sample of n-type germanium at the temperatures 12.1°, 13.9°, 20.3°, 77°, 300°. The sample was in the form of a bar 0.194 in.×0.026 in.×0.026 in. with very heavily doped n-type ends on which copper was plated. This type of contact has been found to be nonrectifying and noninjecting at all the temperatures studied. The current and voltage was measured by

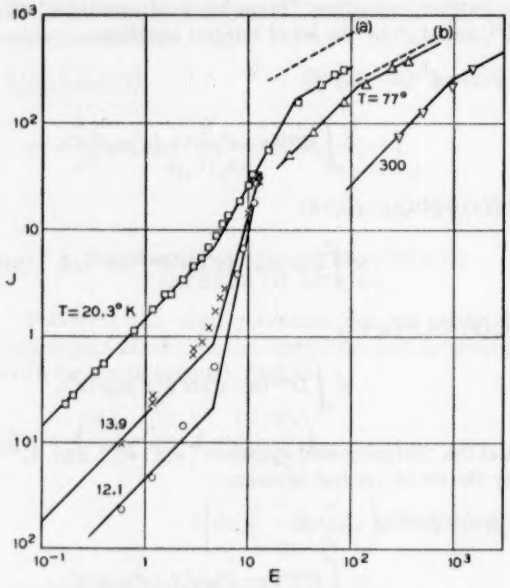

FIG. 1. Current density (amp/cm²) as a function of electric field (volt/cm) in n-type germanium.

Ryder's pulse technique and the current density and electric field calculated from the dimensions of the sample. Normal behavior was found at 300° and 77°. The previously reported steep rise with field at 20° is confirmed by the new data. We find in addition that at 12° and 14° the rise is even steeper, and the current densities at 13 volt/cm are about the same for all three temperatures. If the rising portions of the curves are extrapolated to meet the low-field portions the intersections are all at 4.5 volt/cm. The effective conductivities at 12 volt/cm are greater than the low-field values by the factors 2.1, 13, 50 for 20°, 14°, 12°, respectively.

Table I gives the low-field resistivities of our sample for the five temperatures. It turns out that our sample is very similar to sample No. 49 of Debye and Conwell,[8] as shown in the table, which provides a basis for estimating the carrier density. The carrier density at 300° can be estimated independently from the observed current density 240 amp/cm² at the knee of the curve and the previously measured critical drift velocity 3.2×10^6 cm/sec, which gives 4.7×10^{14} cm^{-3} in good agreement with sample No. 49. Were it not for the freezing out of carriers at lower temperatures the critical current density would be constant in temperature. Since the critical current density at 77° seems to be 200 amp/cm², we conclude that the uncompensated donors are about 83 percent ionized at 77° in our sample. According to the Conwell theory the current is limited by lattice scattering in the $E^{\frac{1}{2}}$ region. Assuming that lattice mobility varies at $T^{-\frac{3}{2}}$ and that ionization is complete at 300°, we find that the $E^{\frac{1}{2}}$ lines correspond-

TABLE I. Resistivity of our sample compared with sample No. 49 of Debye and Conwell (see reference 8) and the carrier density of sample No. 49 by Hall effect.

Temperature	Resistivity Our sample	Resistivity Sample 49	Carrier density Sample 49
12.1°K	23 ohm-cm	16 ohm-cm	3×10^{13} cm^{-3}
13.9	5.5	4.3	9×10^{12}
20.3	0.71	0.67	9×10^{13}
77	0.53	0.55	
300	3.8	4.0	4.8×10^{14}

ing to complete ionization are the lines (a) and (b) in Fig. 1 for 20° and 77°, respectively. Comparing (a) with the 20° data shows that ionization is about 50 percent in the E^1 region, whereas at low fields we estimate from sample No. 49 that ionization is about 19 percent. This is our most direct evidence for electron multiplication. Indirect evidence is provided by the large increase in conductivity with field at 14° and 12°. We believe that this cannot be attributed to an increase in mobility. A simple interpretation can be given for a steady-state ionization of 50 percent at high fields. Let n be the electron density, v the velocity, N_0 the density of neutral donors, N_+ the density of ionized donors, and σ_0 the cross section for impact ionization, σ_+ the cross section for recombination with an ionized donor. We shall neglect the acceptors. Then if R is the thermal rate of production of carriers we have

$$R+vn\sigma_0N_0-vn\sigma_+N_+=0.$$

At high field we may assume R is small compared to the other terms, so we have

$$\sigma_0N_0=\sigma_+N_+.$$

Now 50 percent ionization corresponds to

$$N_0\sim N_+\sim\tfrac{1}{2}N_D,$$

where N_D is the donor concentration. Thus our simple interpretation is that σ_0 and σ_+ are approximately equal,

$$\sigma_0\sim\sigma_+.$$

[1] E. J. Ryder, Phys. Rev. **90**, 766 (1950).
[2] W. Shockley, Bell System Tech. J. **30**, 990 (1951).
[3] Gerritsen, Physica **15**, 427 (1949).
[4] Sclar, Burstein, Turner, and Davisson, Phys. Rev. **91**, 215 (1953).
[5] Sclar, Burstein, and Davisson, Phys. Rev. **92**, 858 (1953).
[6] E. M. Conwell, Phys. Rev. **90**, 769 (1953).
[7] E. M. Conwell, Phys. Rev. **94**, 1068 (1954).
[8] P. P. Debye and E. M. Conwell, Phys. Rev. **93**, 693 (1954).

Electron Spin Resonance in Beryllium*

G. FEHER AND A. F. KIP
Department of Physics, University of California, Berkeley, California
(Received, June 22, 1954)

THE electron spin resonance in beryllium was observed at 300 and 9000 Mc/sec. The sample was in the form of particles embedded in paraffin. The particles were large in comparison to a skin depth (of the order of 1 mm) so that Dyson's[1] theory for the absorption in bulk metals could be applied. A typical trace of the derivative of the power absorption *vs* field at 300 Mc/sec and room temperature is shown in Fig. 1. The ratio of the maximum to minimum deflection A/B (see Fig. 1) depends on T_D/T_2, where T_D is the time it takes an electron to diffuse through the skin depth and T_2 is the electron spin relaxation time. T_2 was found to be 2×10^{-8} sec and taking the velocity of the electrons at the Fermi surface, we find $T_D/T_2=0.14$. Corresponding to this value, A/B should be [1,2] 7.0. The observed value is 7.5 ± 0.5. This agreement is a definite proof that the observed resonance is due to conduction electrons rather than to stationary paramagnetic impurities throughout the metal, which for a Lorentzian line would give a value for A/B of 2.7 and for a Gaussian 2.0.

At 300 Mc/sec the temperature was varied between 296°K and 4°K. T_2 was found to be temperature independent for the entire range and had a value of

$$T_2=2.0\times10^{-8}\text{ sec}.$$

The same value was obtained at 9000 Mc/sec at room temperature.

The electronic g value was determined at 9000 Mc/sec by comparison with the free radical α,α-diphenyl β-picryl hydrazyl. Taking Hutchison and Pastor's[3] value of $g=2.0037$ for the hydrazyl we found the g for beryllium to be

$$g=2.0032\pm0.0001.$$

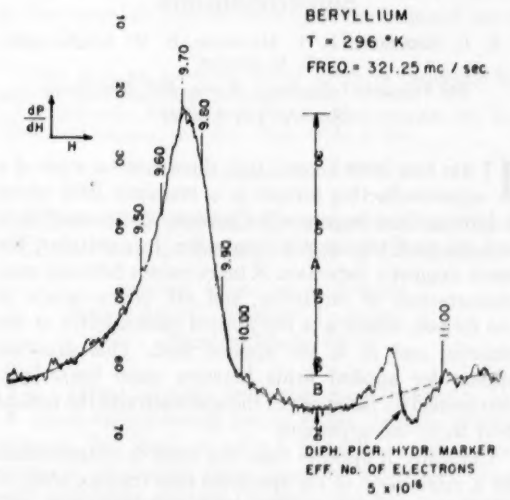

FIG. 1. The derivative of the power absorption *vs* field in beryllium. Vertical markers are proportional to magnetic field. 1 unit = 11.77 oersteds. The free radical resonance is displaced in field to avoid interference with the main line.

Thus the g shift is in the opposite direction from that found in sodium.[2]

The temperature independence of T_2 suggests that impurity scattering via spin-orbit coupling[4] is responsible for the electron spin relaxation time. The situation seems similar to that in lithium in which the broadening effect of impurities was experimentally demonstrated.[3] Another evidence of the importance of the impurities is the fact that in some samples obtained from different sources no resonance was observed. This presumably is due to the higher impurity concentration which would broaden the line and decrease the signal. This could also explain the failure of Gutowsky and Frank[5] to observe the resonance in beryllium. The sample in which we observed the resonance was supplied by the French company Pechiney[6] and quoted to be 99.5 percent pure.

Because of the unknown particle size distribution of the sample we were unable to determine the absolute value of the susceptibility. Attempts to observe a resonance in beryllium sheets have been successful so far, probably again because of impurities.

We are indebted to Professor E. Segrè for supplying us with the beryllium sheets.

* Assisted in part by the U. S. Office of Naval Research and the U. S. Signal Corps.

[1] F. J. Dyson (to be published).
[2] G. Feher and M. Browne (to be published).
[3] C. A. Hutchison and R. C. Pastor, Phys. Rev. **81**, 282 (1951).
[4] R. J. Elliott (to be published).
[5] H. S. Gutowsky and P. S. Frank, Phys. Rev. **94**, 1067 (1954).
[6] U. S. representative of Pechiney Company, International Selling Corporation, 122 East 42nd St., New York 17, New York.

Structure of the Intermediate State in Superconductors

A. L. Schawlow, B. T. Matthias, H. W. Lewis, and G. E. Devlin
Bell Telephone Laboratories, Murray Hill, New Jersey
(Received July 9, 1954)

IT has long been known[1] that there exists a state of a superconducting sample in a magnetic field which is intermediate in properties between the normal state and the pure superconducting state. In particular, the mean magnetic induction B takes values between zero, characteristic of the latter, and μH, characteristic of the former, where μ is the normal permeability of the material and H is the applied field. This situation applies for applied fields between some lower limit determined by the shape of the specimen and the critical field H_c at the upper end.

Currently it appears that this state is characterized by a subdivision of the specimen into regions, some of which are superconducting, with induction zero, and some normal, with induction μH_c, and that the relative total volumes of these two types of region is determined by the mean induction. Contrary to what was for a time thought to be the case, it is now believed that this subdivision extends to the surface of the specimen and can be observed there. This has been done with bismuth microprobes.[1]

We have succeeded in making these domains visible by distributing a superconducting niobium powder on the surface of a tin sample in the intermediate state.

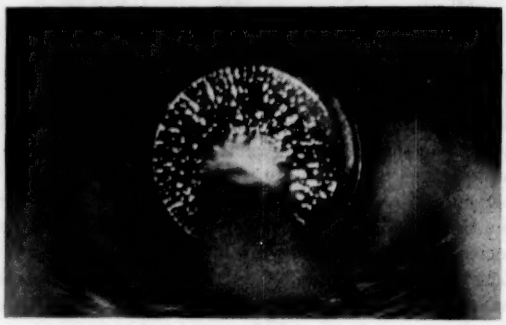

FIG. 1. Island pattern. The light spots are regions from which flux emerges.

The powder, in view of its perfect diamagnetism, migrates to the regions of the surface in which there is no field, and leaves the others relatively bare. The "island" type pattern previously mapped by the bismuth probe technique was directly observed, and a photograph of a typical example is shown in Fig. 1. The sample here was in the shape of a horizontal circular disk, 2 cm in diameter and 1 cm thick, with a hole drilled through

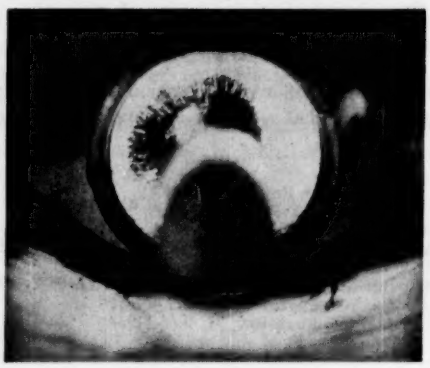

FIG. 2. Radial spoke pattern.

the center for mounting purposes, and was in a vertical magnetic field. One sees the region between the mounting rod and the periphery of the disk.

During the exploration, various transient patterns, such as that of Fig. 2, were seen and are still only imperfectly explained. The one shown was produced after the field was turned off.

We feel that this technique furnishes a useful tool for the study of the intermediate state, and we are pressing the work with a view to contributing to the understanding of both the statics and dynamics of the transition.

[1] See D. Shoenberg, *Superconductivity* (Cambridge University Press, Cambridge, 1952), for a full discussion.

Distribution of the Mass Transported from a Collector into a Germanium Crystal by the Forming Process*

M. W. Aarons, M. Pobereskin, J. E. Gates, and E. B. Dale
Battelle Memorial Institute, Columbus, Ohio
(Received July 8, 1954)

A MAJOR problem in transistor physics is the elucidation of the effects of the forming process in point contact crystal triodes. An hypothesis for the high α's observed in formed collectors is the "hook" theory of Shockley.[1] The combination of mass transfer and thermal effects during the forming pulse have been proposed as a possible mechanism for "hook" formation. The purpose of this note is to report preliminary results of experiments measuring the distribution of the transported mass in the crystal.

Rough estimates of the number of atoms expected to be transferred indicated 10^9 atoms into a volume of 10^{-8} cm^3. In order to detect so small a quantity of matter, carrier-free radio isotopes were considered. A survey of available isotopes resulted in the selection of gold 199 as a suitable tracer material.

Very briefly, the experiments proceeded as follows: Gold 199 and 197 were separated from irradiated platinum and plated on a tungsten needle. The plated needle was used to "form" single crystals of 7 ohm-cm n-type germanium. The amount of gold transferred was measured by counting with an end-window Geiger tube, and the area of gold distribution was measured from an autoradiograph. Microphotographs of the autoradiographs were subsequently analyzed by a photodensitometer to obtain the area and distribution of the gold at that level. The surface was then precisely lapped and counted and an autoradiograph taken. By repeating this procedure to a depth in the crystal at which no activity could be detected, the concentration of gold atoms as a function of depth was obtained. The results of two forming experiments are presented in Tables I and II.

Table I. The distribution of Au in crystal 1 after forming. The forming pulse was 0.053 seconds long, with an average current of 65 ma at 240 volts. A total of 1.6×10^9 Au atoms was transferred into a volume of about 10^{-7} cm^3. There was no visible damage to the crystal surface.

Thickness of layer lapped off, microns	Diameter of formed region at top of layer, microns	Average Au concentration in formed region of layer, atoms/cm^3
5	180	1.9×10^{16}
2.5	72	8.9×10^{14}
2.5	72	2.8×10^{15}

Table II. The distribution of Au in crystal 2 after forming. The forming pulse was 0.053 seconds long, at a peak voltage of 400 volts. A total of 7.4×10^{10} Au atoms was transferred into a volume of about 10^{-6} cm^3. A crater 230 microns in diameter and about 15 microns deep was observed in the crystal surface after forming. A conical protuberance was noted in the center of the crater.

Thickness of layer lapped off, microns	Diameter of formed region at top of layer,* microns	Average Au concentration in formed region of layer, atoms/cm
5	Broad and diffuse	3.3×10^{17}
10	232	1.3×10^{15}
9	198	1.6×10^{15}
9	153	5.7×10^{14}

* The diameter of the active region on the crystal surface after the last lap was 108 microns.

Crystal 1 was destroyed after the third lap. To compute the concentration of gold in the third layer, the formed region in that layer was assumed to be conical, with a base equal to the exposed active area after the second lap, and a height equal to the thickness of the third layer.

Crystal 2 was destroyed after the fourth lap. At that time 4.6×10^7 foreign atoms remained in the crystal.

From these results, it appears that the distribution in depth of the transferred gold atoms was as follows: a high concentration region at the surface, followed by a region of diminished concentration, terminating in a region of somewhat higher concentration than the minimum. The concentration drops abruptly beyond this point.

Experiments on the effects of emitter current flowing in the crystal during the forming of the collector are in progress.

* This work was sponsored by the Air Force Cambridge Research Center, Cambridge, Massachusetts.

[1] W. Shockley, *Electrons and Holes in Semiconductors* (D. Van Nostrand Company, Inc., New York, 1950), p. 108.

Effect of Chemical Combination on the Characteristic Energy Loss of Electrons*

Lewis B. Leder and L. Marton
National Bureau of Standards, Washington, D. C.
(Received July 6, 1954)

IN a recent note we presented measurements of the characteristic energy loss of 30-kev electrons passing through thin films of solids.[1] There have been some attempts to explain these losses by associating them with secondary electron emission,[2] by electron plasma oscillation,[3] and by comparison with x-ray absorption data.[4,5] The data available are not complete enough to verify any of the possible explanations. We have, there-

TABLE I. Characteristic energy losses (in ev) of 30-kev electrons passing through thin films of Si, Te, Pb, Sb, Mg, and compounds of these metals.

Material	Energy loss (ev) E_1	E_2	E_3
Si	4.8	16.9	
SiO_2	5.4	19.4	
Te	4.6	16.0	
TeO_2	9.5	17.5	
Pb	5.1	12.1	21.8
PbS	6.8	14.7	21.9
Sb	4.3	14.9	30.6
Sb_2S_3	6.3	18.0	35.4
Mg	9.7	20.3	
MgO*	11.4	25.0	

* H. Watanabe (private communication).

fore, been engaged in determining the properties of these losses.

As shown in the data of our previous communication these losses have been observed in insulators (collodion and quartz) as well as in metals, and in examining these results we noticed that the spectrum for quartz (SiO_2) was in all respects similar to that of silicon, except that the positions of the peaks were shifted to higher energy losses. In view of this we felt it would be of interest to pursue this line of investigation, and therefore, measured the energy losses in several other compounds. The resulting data are given in Table I. In Fig. 1 a representative set of spectra are shown. These are the superimposed microphotometer tracings of the Sb and Sb_2S_3 spectra. It is seen from the figure that the characteristics of the spectrum remain the same with the peaks shifted to higher energies. This trend was observed in all four pairs.

It has been known for a long time that a shift, such as we have observed, occurs in the K and L x-ray emission or absorption edge.[6] The shift in the K x-ray absorption edge of Si has been attributed to the effect of crystal structure by Barton and Lindsay;[7] and on the other hand, Das Gupta[8] has shown some correlation of the K-valence emission band shift with the heat of formation. While we are not prepared at present to discuss the source of the shift or to subscribe implicitly to Das Gupta's hypothesis, in Table II we have tabulated our observed shifts and in column four have given the shift expected using the formula of Das Gupta. These latter appear to be at least of the right order of magnitude.

TABLE II. The shift, ΔE, of the characteristic energy loss of Si, Te, Pb, Sb, and Mg as a result of chemical combination. In the fourth column are given the values calculated using the formula of Das Gupta.

Material	Shift of the energy loss (ev) ΔE_1	ΔE_2	ΔE_3	calc. ΔE_4
Si	0.6	2.5		3.7
Te	5.0	1.5		1.6
Pb	1.7	2.6	0	1.9
Sb	2.0	3.1	4.8	2.2
Mg	1.7	4.7		4.7

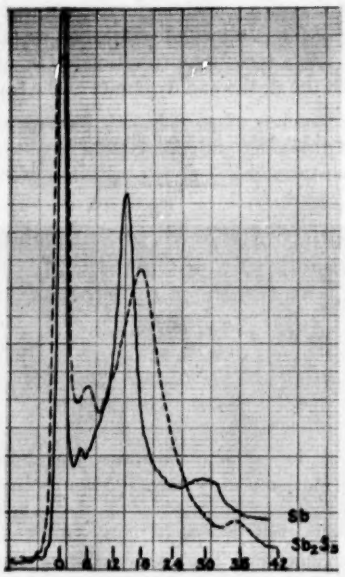

FIG. 1. Superimposed microphotometer tracings of the energy loss spectra of Sb and Sb_2S_3. The solid line is the spectrum of Sb, and the dashed line that of Sb_2S_3. The scale shown on the bottom is in electron volts. The ordinates are relative intensities.

We have also measured the energy losses in several alkali halides. However, the results are difficult to analyze because (1) although the alkali metals Na and K were evaporated directly in the vacuum of the analyzer, they may have oxidized during the time of observation, (2) in all cases the materials were deposited on a substrate and the effect of the substrate is as yet an unknown factor, (3) the spectra are more complex than for the other materials, and (4) the intensities of some of the peaks are radically different in the alkali metal and the alkali halide and thus make it difficult to correlate the various loss lines. Nevertheless, a shift of the peaks is indicated.

This evidence suggests that some of the characteristic energy losses that we are observing are not due to electron plasma interaction,[3] since there would be no plasma in the compound, but are rather due to excitations of some outer orbit electrons.

* This work was supported by the U. S. Office of Naval Research.

[1] L. Marton and L. B. Leder, Phys. Rev. **94**, 203 (1954).
[2] O. W. Richardson, Proc. Roy. Soc. (London) **A128**, 63 (1930).
[3] D. Bohm and D. Pines, Phys. Rev. **92**, 609 (1953); D. Pines, Phys. Rev. **92**, 626 (1953); and preceding papers.
[4] Y. Cauchois, Acta Cryst. **5**, 351 (1952).
[5] A. Nilsson, Arkiv Fysik **6**, No. 6 (1953).
[6] M. Siegbahn, *Spectroskopie der Rontgenstrahlen* (Verlag Julius Springer, Berlin, 1931), second edition, pp. 278–306.
[7] V. P. Barton and G. A. Lindsay, Phys. Rev. **71**, 406 (1947).
[8] K. Das Gupta, Phys. Rev. **80**, 281 (1950).

Plastic Flow and the Low-Frequency Dispersion in the Alkali Halide Crystal

MASAKAZU ISHIGURO, FUJIO ODA, AND TAKUZO FUJINO
The Institute of Scientific and Industrial Research, Osaka University, Sakai, Osaka, Japan
(Received May 17, 1954; revised manuscript received July 13, 1954)

IN the study of the influence of plastic flow on the ionic and electronic properties of the alkali halide crystals, Seitz proposed that vacancies are generated during a lattice flow process and condense to form clusters during the subsequent period of time.[1] According to Breckenridge, who has made an extensive study of the low-frequency dispersion in the alkali halides, the free paired vacancies are the cause of the anomalous dispersion in a pure sodium chloride crystal.[2] However, Kojima has lately proposed a model in which the paired vacancies are trapped on the dislocation segments.[3] Neither apparently deny that Breckenridge's anomalous dispersion is caused by the imperfections present in crystals in which dislocations play an important role. The authors have carried out an experiment to find a correlation between the plastic flow and the low-frequency dispersion.

A conventional bridge method at 1000 cycles/second was employed in measuring the loss tangent in order to compare our results with those obtained by Breckenridge. The sodium chloride specimens we used were prepared from 99.98 percent pure well-annealed single crystals which showed initially no anomalous dispersion [Fig. 1(a)]. The loss measurements were made at 1°C

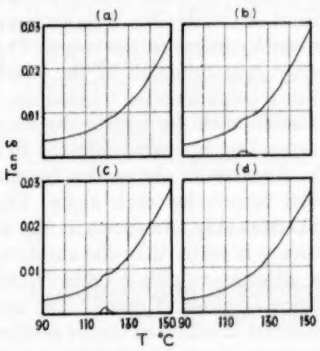

FIG. 1. The loss tangent *vs* temperature: (a) normal, (b) plastically deformed, (c) quenched, and (d) annealed.

intervals throughout the experiments. Figure 1(b) shows the results obtained two hours after producing plastic flow by the application of bending or tension forces to the specimen prepared as mentioned above. After the first thirty minutes, the height of the loss peaks showed no change, which is a prerequisite for making these measurements. Figure 1(c) shows the results obtained by using a quenched crystal, and it indicates that there is no substantial difference between the curve shown in Fig. 1(b) and that in Fig. 1(c). When the plastically deformed specimen is subjected to a heat treatment at 500°C for 3 hours, the loss peak at about 120°C disappears, as shown in Fig. 1(d), and is completely absent thereafter.

By irradiation with x-rays, the crystal is darkened if it is either plastically deformed or quenched. With this sample the anomalous dispersion peak which appeared at 120°C as shown in Fig. 1(b) or 1(c) is completely extinguished and the results are indicated in Fig. 2(a). However, when this specimen is bleached either by

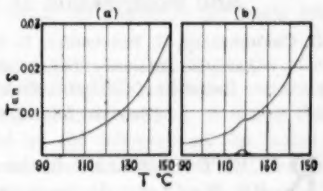

FIG. 2. The loss tangent *vs* temperature: (a) darkened by x-ray, and (b) after bleaching.

heating or illumination, the dispersion peak reappears as shown in Fig. 2(b).

No significant difference of dispersion characteristics was observed between the specimen plastically deformed and quenched and this fact leads us to propose the following idea. When the crystal is subjected to plastic flow, numerous vacancies are generated from the jogs of the dislocation lines as suggested by Seitz. The free vacancies thus created diffuse into the crystal to some extent because of the local temperature rise in the vicinity of moving dislocation lines. Before long, the vacancies adhere to the irregular dislocation segment and as a result they are unstable. In the quenching process, super-saturated thermal vacancies adhere to the dislocation lines and also make very irregular segments. Therefore, it is suggested that the irregular dislocation segments resulting from the localization of free vacancies are the cause of the anomalous dispersion. Thus the extinction of the loss peaks by annealing for several hours at 500°C can be explained by considering that the irregular dislocation segments become stable, smooth lines.

An explanation for the disappearance of the anomalous dispersion by x-ray darkening is that the electrons, holes, or excitons liberated by it are trapped on the irregular segments which are subsequently changed into smooth ones by the solvent action of the liberated particles with the resulting formation of free isolated color centers. The fact that the dispersion peak is reproduced when the darkened crystal is bleached might be interpreted as a result of the regeneration of the irregular segments having polarizability.

Some information on the relation between plastic deformation and low-frequency dispersion has been obtained. However, it seems to be necessary to undertake further investigation by other methods in order to obtain conclusive evidence. The measurements of low-frequency dispersion at various frequencies and

the spectroscopic study which we are now performing are expected to give us more knowledge in the near future.

[1] F. Seitz, Phys. Rev. **80**, 239 (1950).
[2] R. G. Breckenridge, J. Chem. Phys. **16**, 959 (1948).
[3] K. Kojima, presented at the lecture meeting of the Japan Physical Society in April, 1953 (unpublished).

Small-Angle *p-p* Cross Sections and Polarization at 300 Mev*

O. Chamberlain, G. Pettengill, E. Segrè, and C. Wiegand
Radiation Laboratory, Department of Physics, University of California, Berkeley, California
(Received July 12, 1954)

RECENT experiments[1] in the energy region 100 to 400 Mev have demonstrated the extreme constancy against energy and angle of the proton-proton differential scattering cross section. Because of the severe experimental difficulties, however, the angles below 20 degrees center of mass, where the nuclear and Coulomb terms in the cross section might reasonably be expected to interfere, have not been thoroughly investigated.

Since the major experimental difficulties in the small-angle region arise mainly from the high background, it is necessary either to take unusual care in the collimation or to define an allowed trajectory for the beam through counters in coincidence. In this experiment we have chosen the latter method. An accompanying paper[2] describes an experiment using the former method.

By using the 312-Mev polarized proton beam[3] from the Berkeley synchrocyclotron, we have been able to measure simultaneously the differential cross section and the asymmetry for polarized protons scattering from a liquid hydrogen target. The experimental arrangement is shown schematically in Fig. 1. Counter No. 3 is a

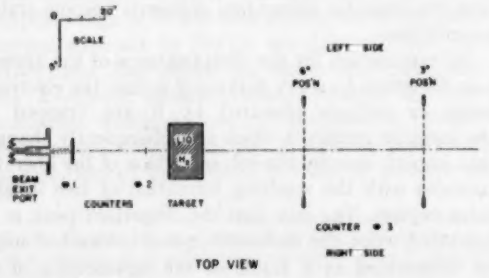

FIG. 1. Schematic representation of scattering arrangement. Note lateral expansion of scale.

symmetrical ring, divided into two parts along a vertical diameter parallel to the polarization of the incident beam. Provision is made for rotating this counter about an axis parallel to the incident beam in order to verify that the response of the two counter halves is equal.

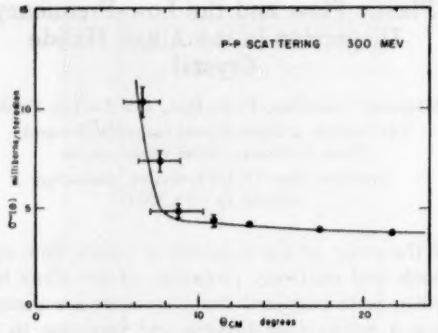

FIG. 2. The differential proton-proton scattering cross section plotted as a function of angle in the center-of-mass system. The solid curve is a visual fit to the data.

The incident beam was monitored by a fast coincidence and scaling system reading the output of the beam defining counters, Nos. 1 and 2. The 1–2 counting rate for all the cross-section data and the bulk of the asymmetry data was held at approximately 800 per second. At this level approximately 3½ percent of the 1–2 counting rate was due to pileup, i.e., two protons passing through the defining system within one resolving time of the counters.

Protons scattered into the left and right halves of counter No. 3 were counted independently, each in coincidence with counters Nos. 1 and 2. A typical value of the fraction of protons scattered into one-half of the counter by the 2.80 grams per square centimeter of hydrogen in the target was 2×10^{-4}. At each angle, data were taken with the target both full and empty. Part of the target empty data was taken with additional absorber inserted in front of counter No. 3 to simulate the stopping power of the hydrogen in the target. The possibility of low-energy contamination of the beam was thus checked. No such contamination was found.

The cross section was obtained by adding the fractions of the beam scattered by hydrogen into the two halves of counter No. 3 and multiplying this by the appropriate geometrical factors for each angle. The results, with statistical errors only, are shown in Fig. 2. Since the relative accuracy is better than the absolute, the values have been adjusted to give 3.7×10^{-27} cm^2 per steradian at 20 degrees (center of mass).[4] The approximate angular resolution is indicated for the smaller angles where it is of interest. The solid curve is a rough fit to the data, taking the angular resolutions into account.

The asymmetry was obtained from the formula, $\epsilon=[(f_L-f_R)/(f_L+f_R)](\phi/\sin\phi)$, where f_L, f_R are the fractions of beam protons scattered into the left and right sides of counter No. 3, respectively, and 2ϕ is the azimuthal angle covered by either half of counter No. 3. Since the beam polarization has been previously measured[3] in elastic scattering experiments, we may calculate directly the polarizations arising from the *p-p*

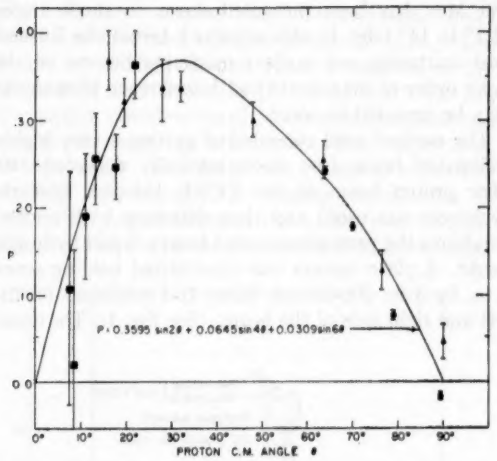

FIG. 3. Polarization produced by proton-proton scattering at 300 Mev, plotted as a function of center-of-mass scattering angle. ● Chamberlain *et al.* (reference 6); ▲ Chamberlain *et al.* (reference 5); ■ Present work.

scattering in this experiment through the relation $P=e/P_B$, where P_B has been taken to be $0.74+0.01$. The results are plotted in Fig. 3 in conjunction with previous p-p polarization data[5,6] taken at larger angles. The solid curve, a Fourier analysis of the previous data, seems still in agreement with the new points at smaller angles.

* This work was performed under the auspices of the U. S. Atomic Energy Commission.

[1] For a more complete list of references than is possible here, see for example, R. M. Thaler and J. Bengston, Phys. Rev. **94**, 679 (1954).

[2] D. Fischer and G. Goldhaber, following letter [Phys. Rev. **95**, 1350 (1954)].

[3] Chamberlain, Segrè, Tripp, Wiegand, and Ypsilantis, Phys. Rev. **95**, 1348 (1954).

[4] Chamberlain, Pettengill, Segrè, and Wiegand, Phys. Rev. **93**, 1424 (1954).

[5] Chamberlain, Segrè, Tripp, Wiegand, and Ypsilantis, Phys. Rev. **93**, 1430 (1954).

[6] Chamberlain, Donaldson, Segrè, Tripp, Wiegand, and Ypsilantis, Phys. Rev. **95**, 850 (1954).

Proton-Proton Scattering Experiments at 170 and 260 Mev*

OWEN CHAMBERLAIN AND JOHN D. GARRISON†
Radiation Laboratory, Department of Physics, University of California, Berkeley, California

(Received July 12, 1954)

THE differential proton-proton scattering cross section has been measured at 170 and 260 Mev for laboratory scattering angles of 4.4 to 40 degrees with the University of California synchrocyclotron. This experiment is an extension to smaller scattering angles of work completed earlier at this laboratory[1] and is essentially in agreement with this earlier work. The angular region of the differential p-p scattering cross section presented here is of interest because it is in this region that the experimental results are at greatest variance with the theory.[2]

The 340-Mev full-energy proton beam from the cyclotron was reduced in energy by using beryllium absorbers. Following the absorbers the proton beam was collimated and analyzed in a magnet to provide a beam reasonably parallel and homogeneous in energy. A liquid hydrogen target was used.[3] The target presented 5.6 inches of liquid hydrogen to the beam for scattering.

The scattered protons were counted by means of a telescope consisting of two liquid scintillation counters in coincidence. The first counter served to define the solid angle subtended by the telescope at the target. The second counter was placed to the rear of the first and was larger, so that multiple-scattering losses would be small.

The background coincidence counts, consisting primarily of protons scattered from the collimator system and hydrogen target walls, were determined by using a dummy target to simulate the empty hydrogen target. It was found that the dummy target gave a false measure of the true counting background because the stopping power of the full liquid hydrogen exceeded that of the dummy target by the stopping power of the liquid hydrogen. Some of the low-energy protons contributing to the counter background coincidences had insufficient

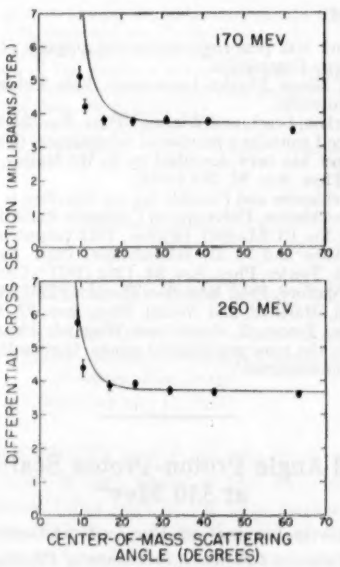

FIG. 1. Center-of-mass differential p-p scattering cross sections *versus* center-of-mass scattering angle. The points represent the experimental results, with errors as they apply to the angular distribution. The solid lines show the sum of a constant nuclear cross section and pure Coulomb scattering cross section. Energies are given for the laboratory system.

range to count when the hydrogen target was in the proton beam, but were able to count when the dummy was in the beam. This effect was appreciable at scattering angles close to the proton beam and was corrected by placing an absorber with just the stopping power of the liquid hydrogen between the two scintillation counters when counts were taken with the dummy target in the proton beam.

The beam was monitored by an ionization chamber, which was calibrated by a Faraday cup.[4] The Faraday cup calibration was done with varying amounts of absorber placed before it, permitting a determination of the energy distribution and mean range of the proton beam. The nuclear loss corrections in the absorber were determined with the use of the absorption cross sections of Kirschbaum.[5]

The measured differential cross sections are shown in Fig. 1. The differential cross section was found to be the same at both energies, within the accuracy of the experiment. The cross sections presented here are much lower than those of some previous workers;[6] however, they are in agreement with more recent work.[7] Figure 1 includes curves drawn for Coulomb scattering plus a constant nuclear cross section. Deviations from the curves should represent interference between Coulomb and nuclear scattering.

The errors indicated in the figure are those determined by combining the known errors affecting the shape of the angular distribution. The errors in the total cross sections are estimated to be about eight percent.

A complete account of the experiment will be published later.

* This work was performed under the auspices of the U. S. Atomic Energy Commission.

† Now at Sloane Physics Laboratory, Yale University, New Haven, Connecticut.

[1] Chamberlain, Segrè, and Wiegand, Phys. Rev. **83**, 923 (1951).

[2] Reference 1 contains a number of references on this subject.

[3] The target has been described by J. W. Mather and E. A. Martinelli, Phys. Rev. **92**, 785 (1953).

[4] The ion chamber and Faraday cup are described in reference 1

[5] A. J. Kirschbaum, University of California Radiation Laboratory Report No. UCRL-1967, October, 1952 (unpublished).

[6] C. L. Oxley and R. D. Schamberger, Phys. Rev. **85**, 416 (1952); O. A. Towler, Phys. Rev. **84**, 1262 (1951); Cassels, Pickavance, and Stafford, Proc. Roy. Soc. (London) **214**, 262 (1952).

[7] Marshall, Marshall, and Nedzel, Phys. Rev. **92**, 834 (1953); Chamberlain, Pettengill, Segrè, and Wiegand, Phys. Rev. **93**, 1424 (1954); also some unpublished results, Gordon H. Pettengill (private communication).

Small Angle Proton-Proton Scattering at 330 Mev*

DAVID FISCHER AND GERSON GOLDHABER
Radiation Laboratory, Department of Physics, University of California, Berkeley, California

(Received July 12, 1954)

IN conjunction with the program on p-p and n-p cross-section measurement, the p-p scattering at 330 Mev has been measured down to small angles (2.2° to 14° lab). In this angular interval the Rutherford scattering and nuclear scattering become of the same order of magnitude and interference phenomena may be expected to occur.

The method used consisted of getting a very highly collimated beam (the electrostatically deflected 340-Mev proton beam of the UCRL 184-inch synchrocyclotron was used) and then detecting with nuclear emulsions the protons scattered from a liquid hydrogen target. A plate camera was constructed holding seven 1 in. by 3 in. 200-micron Ilford G-5 emulsions on the left and right side of the beam. (See Fig. 1.) The emulsions were placed lengthwise in a horizontal row with the emulsion plane inclined at an angle of 43° with the proton beam. Exposures to an integrated flux of 5×10^{10} protons were made with target filled and with target empty. A copper absorber $2\frac{1}{2}$ in. thick was placed in front of the emulsions. During the target-empty exposure additional absorber was added to compensate for the energy loss and attenuation in the liquid hydrogen. One of the plates at 14° (lab) was not covered by absorber so that the attentuation could be determined and the absolute cross section evaluated.

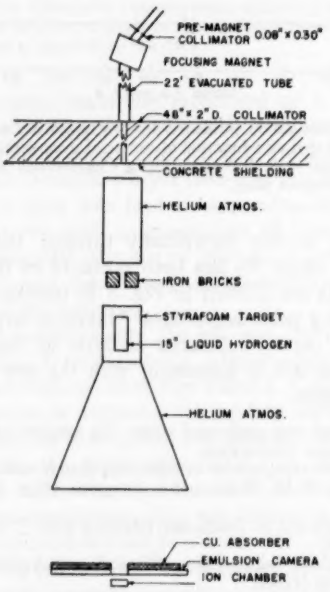

FIG. 1. Plan of the target and camera geometry.

In scanning the plates, the protons were counted as they entered the surface of the emulsion. Since there was a $2\frac{1}{2}$-in. copper absorber in front of the plates, the tracks were more than twice minimum ionizing and quite easily counted. The ratio of "target filled" to "target empty" counts varied from 7.0 to 2.5. The angular resolution at the camera varied from ±0.5° lab to ±0.9° lab.

The absolute cross-section determination gives 3.8 ± 0.25 mb/sterad for angles above 20° (c.m.). The principal uncertainty in this value is because of the calibration of the attenuation ($I/I_0=0.79\pm0.04$) in the $2\frac{1}{2}$-in. copper absorber ahead of the emulsions and the scanning efficiency ($\epsilon=0.95\pm0.05$). This value is in good agreement with the recent Berkeley value[1] of 3.72 ± 0.15 mb/sterad. Our angular distribution is shown in Fig. 2, normalized to the 3.7 mb/sterad value. In Fig. 2 is also shown the sum of the Rutherford scattering (calculated) and the nuclear scattering (considered constant at 3.7 mb/sterad). If one considers the differential cross section separated into three terms,[2] $P_{\text{nuc.}}+P_{\text{Ruth.}}+P_{\text{int.}}$, i.e., the nuclear scattering, the Rutherford scattering, and the interference between them, then the difference between the solid curve and the experimental points should represent $P_{\text{int.}}$. There appears to be a net effect of destructive interference in the region of 6° to 14° (c.m.).

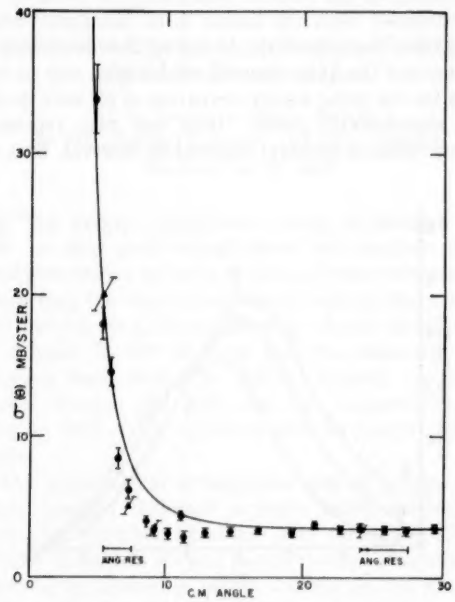

FIG. 2. Differential cross section for 330-Mev p-p scattering normalized to 3.7 mb/sterad in the region of pure nuclear scattering. The circles and triangles represent measurements on plates placed on the right and left side of the beam, respectively. The errors indicated are the statistical standard deviations. The solid curve represents the sum of Rutherford scattering and a constant nuclear scattering of 3.7 mb/sterad.

It is interesting to note that the interference term $P_{\text{int.}}$ is extremely sensitive to the relativistic corrections used for Rutherford scattering. The curve in Fig. 2 was drawn according to Møller's[3] formula. In the small-angle approximation this is identical with a modified form of Mott's formula.[4] The latter is obtained when the wavelength of relative motion $\hbar$ is factored out and replaced by its relativistic value,[2] leaving the remaining velocity dependence unchanged. If Mott's formula is evaluated without any relativistic corrections, the resulting scattering is larger by a factor $2\gamma^2/(\gamma+1)=1.55$, and the interference term then appears increased correspondingly. The relativistic approximation used by Van Hove[5] gives a value larger than that given by Møller's formula by a factor $(\gamma+1)/2=1.18$.

We were able to fit the experimental points fairly well by a selection of one s and three p wave phase shifts. In the symbols of Thaler and Bengston[2] for instance ${}^1K_0=31°$, $\alpha=1.2$, $\beta=0.28$ can give possible sets of phase shifts, where ${}^1K_0$ is the s wave phase shift[6] and α and β are functions of the p wave phase shifts. However, as was pointed out by Fried,[7] without the use of additional phase shifts this type of analysis is not able to account for the recent[8] polarization data, and a more detailed analysis will be required.

We wish to thank Professors Segrè and Chamberlain for their help and cooperation in this work, and Miss Sheila Livingston for her contribution to the scanning of the plates.

* This work was performed under the auspices of the U. S. Atomic Energy Commission.

[1] Chamberlain, Pettengill, Segrè, and Wiegand, Phys. Rev. **93**, 1424 (1954).

[2] R. M. Thaler and J. Bengston, Phys. Rev. **94**, 679 (1954).

[3] C. Møller, Ann. Physik **14**, 531 (1932).

[4] At small angles Mott's formula (nonrelativistic) for p-p scattering, c.m. system, can be expressed as

$$P_{\text{Mott}}=(e^4/M_p^2v^4)\sin^{-4}(\theta/2)\ \text{cm}^2/\text{sterad},$$

and Møller's formula can be reduced to

$$P_{\text{Mott}}(\gamma+1)/2\gamma^2,$$

where e is the electron charge, M_p the proton mass, v the relative velocity, θ the c.m. angle and $\gamma=(1-v^2/c^2)^{-\frac{1}{2}}$.

[5] L. Van Hove, Phys. Rev. **88**, 1359 (1952).

[6] The estimate of the singlet s phase shift was made by Dr. H. P. Noyes using the low-energy meson well parameters of Hall and Powell [Phys. Rev. **90**, 912 (1953)].

[7] B. D. Fried, Phys. Rev. **95**, 85 (1954).

[8] Chamberlain, Donaldson, Segrè, Tripp, Wiegand, and Ypsilantis, Phys. Rev. **95**, 850 (1954).

Recoil Spectrum in the Beta Decay of Ne^{19}†

W. PARKER ALFORD* AND DONALD R. HAMILTON
Palmer Physical Laboratory, Princeton University, Princeton, New Jersey

(Received July 15, 1954)

MEASUREMENTS of the electron-recoil angular correlation in beta decay of He^6 have shown[1,2] that the Gamow-Teller part of the beta interaction is tensor. In the Ne^{19} decay both Fermi and Gamow-Teller components should be present; to identify the Fermi part as scalar or vector we have measured the spectrum of Ne^{19} recoils emitted at nearly 180° from (and in time coincidence with) the positrons.

Figure 1 shows the apparatus used. Recoils, accelerated to 2-kev energy, are detected by a silver

magnesium electron multiplier; positrons are counted by a terphenyl crystal and 5819 photomultiplier. Ne^{19}, produced by a (p,n) reaction on magnesium fluoride, diffused without carrier down an evacuated line from the cyclotron, through a liquid air trap, into the electron-multiplier vacuum chamber. A 0.4-mg/cm² polyethylene foil on which a conducting coating of aluminum

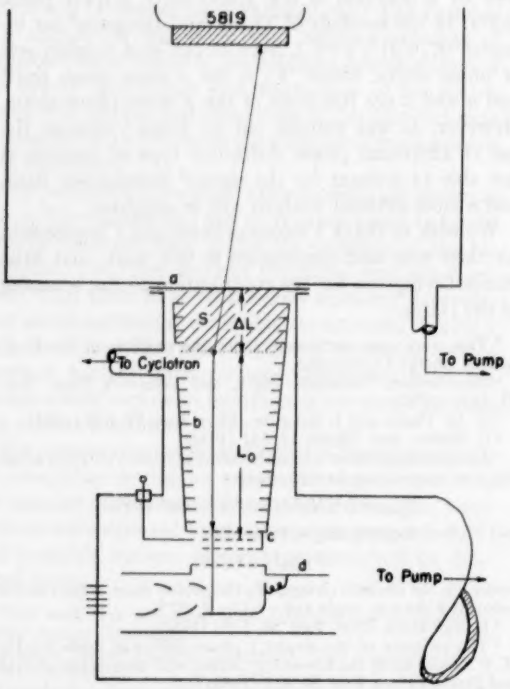

FIG. 1. Diagram of the apparatus used in the measurements. Only electron-recoil coincidences originating in the region "S" are recorded.

was evaporated separated the chambers containing the two detectors. Wall scattering was minimized by Lucite lining in the photomultiplier chamber, and by mechanical baffles in the recoil chamber.

Neon gas fills the recoil chamber and recoil multiplier; the volume sensitive to coincidences is limited as follows by a combination of transit-time and energy discrimination. An electron count signals the formation of a recoil ion ($t=0$). We consider recoils of energy $V<V_0$ (V_0=maximum recoil energy) formed at $t=0$ at a distance L_0 from G_2, and travelling toward G_2 normal to G_2. They arrive at G_2 at $t=L_0(m/2\,eV)^{\frac{1}{2}}$. Suppose there be on G_2 a repulsive voltage $V_2(t)$ given by

$$V_2=V_0, \quad t<t_0=L_0(m/2\,eV_0)^{\frac{1}{2}},$$
$$V_2=V_0(t_0/t)^2=V, \quad t>t_0;$$

it is seen that for this $V_2(t)$, recoils from distance L_0 and any energy V arrive at just such a time as to encounter a retarding voltage V. Recoils starting at $t=0$ closer to (further from) G_2 find $V_2>V(V_2<V)$ and are reflected by (get past) G_2. By choice of t_0 the sensitive volume is thus limited to the region $L_0<L<L_0+\Delta L$, where $L_0+\Delta L$ is distance from G_2 to the polyethylene foil. The distribution in transit time of the recoils passing G_2 then gives the distribution in energy of recoils from the sensitive volume.

Figure 2 shows the spectra predicted for the indicated values of α, the electron-neutrino angular correlation coefficient, on the basis of beta theory; a value of V_0 was deduced from the known beta end point[3] after corrections for geometry, including the finite source volume and the finite detector solid angles, and corrections for the finite energy resolution of G_2 were made. The experimental points (from one run) represent counts within a constant momentum interval. Bars on

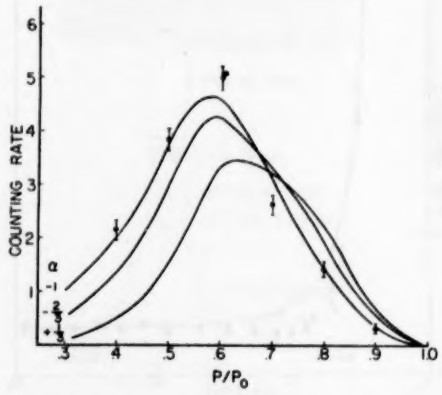

FIG. 2. Calculated recoil spectra for various values of α. The points represent data from one run, and each curve is normalized to the best least-squares fit to these points.

the measured points are standard deviations of counting statistics; the curves are normalized to give the best least-squares fit to the data for the various values of α. The weighted mean of six runs gave $\alpha=-0.8$. The scatter in the values of α for various runs was somewhat greater than that to be expected from statistics; on the basis of this scatter we assign a final value from present measurements of

$$\alpha=-0.8\pm0.4.$$

For a mixture of tensor and scalar interactions, $-1<\alpha<+\frac{1}{3}$; for a tensor-vector mixture, $+\frac{1}{3}<\alpha<1$. Thus the present result indicates that the Fermi part of the beta interaction is scalar. From the ft values of Ne^{19} and O^{14},[4] one predicts $-0.1<\alpha<0$ for a tensor-scalar mixture and $0.5<\alpha<0.55$ for a tensor-vector mixture.

Measurements of the electron spectrum in coincidence with recoils are now being initiated and it is

expected that these will allow a more accurate determination of α.

† Supported by the U. S. Atomic Energy Commission and The Higgins Scientific Trust Fund.
* Socony-Vacuum Fellow 1952–53.
[1] S. L. Ruby and B. M. Rustad, Phys. Rev. **89**, 880 (1953).
[2] J. S. Allen and W. K. Jentschke, Phys. Rev. **89**, 902 (1953).
[3] G. Schrank and J. R. Richardson, Phys. Rev. **86**, 248 (1952).
[4] J. B. Gerhart, Phys. Rev. **95**, 288 (1954).

Equilibrium Charge Distribution of Stripped 26-Mev Nitrogen Ions

H. L. Reynolds and A. Zucker
Oak Ridge National Laboratory, Oak Ridge, Tennessee
(Received July 12, 1954)

THE average equilibrium charge of nitrogen ions as they pass through nickel foils has been measured previously.[1] In order to obtain further information concerning the capture and loss of orbital electrons by fast moving ions, the equilibrium charge distribution of stripped 26-Mev nitrogen ions was measured. The nitrogen beam from the ORNL 63-inch Cyclotron passed through thin foils and was analyzed by the fringing field of the cyclotron into its charge components.

The experimental arrangement was as follows: the triply charged deflected nitrogen beam entered an evacuated chamber 12 inches long through a 0.5 in. $\times$0.001 in. carbon slit and passed through a thin foil of Formvar or aluminum placed directly on the slit. An average fringing field of approximately 2000 oersteds gave a separation of about 4 mm between charge states. The analyzed beam was detected at the end of the chamber with Ilford C-2 emulsions. The deflected beam was parallel enough so that a second collimating slit was not necessary. The foils used for stripping were 0.16 mg/cm² Al, and 100, 50, 25, 5 μg/cm² Formvar. In all cases except that of the thinnest Formvar, the same ratio of charges was observed, indicating that an equilibrium state is reached in foils thicker than 25 μg/cm².

The lines on the photographic plates were scanned with a photodensitometer. Several scans were made across each set of lines in order to obtain an average density ratio. Some lightly exposed plates were scanned with a microscope and the nitrogen tracks per unit area counted. The track counting results were in agreement with the photodensitometer data.

The relative abundance of charge states for 26-Mev nitrogen ions after passing through a thin foil is $N^{7+}=0.38$, $N^{6+}=0.46$, $N^{5+}=0.16$, $N^{4+}=<0.01$. The estimated error is 0.02 in each case. The average charge thus obtained is $6.2e$, in agreement with the average charge measured previously.[1]

The experiment is being extended in order to determine the charge ratios as a function of energy. A measurement of the charge ratios after passing through a foil which is thin enough so that equilibrium is not reached, will permit an evaluation of the capture and loss cross sections for the K shell electrons.

[1] Reynolds, Scott, and Zucker, Phys. Rev. **95**, 671 (1954).

Limits on π^- Meson Mass from Mesonic X-Rays*

M. Stearns, M. B. Stearns, S. DeBenedetti, and L. Leipuner
Carnegie Institute of Technology, Pittsburgh, Pennsylvania
(Received July 16, 1954)

IN a previous Letter,[1] we have reported that the energies of π^- mesonic x-rays, as determined with a multichannel pulse-height selector and a NaI detector, agree within 10 percent with the result of an elementary computation. More accurate energy measurements of selected mesonic lines are now being made by using the critical x-ray absorption technique. The primary aim of this work is the investigation of possible specifically nuclear interactions between the π^- meson and various nuclei. The results of this work will be described in a later communication. Here, we will report on an upper and lower limit for the π^- mass, obtained in the course of these experiments.

For the critical absorption measurements the absorbers were inserted between the target producing the mesonic x-rays and the NaI detector; the transmission of the mesonic line was measured as a function of the absorber Z. The absorbers were thin-walled Lucite cells, 1 cm thick, containing an aqueous solution of a salt of the absorbing element. The concentration (for a given absorber) was adjusted so that x-rays of energy immediately below its K-absorption edge would be transmitted four times more intensely than x-rays of

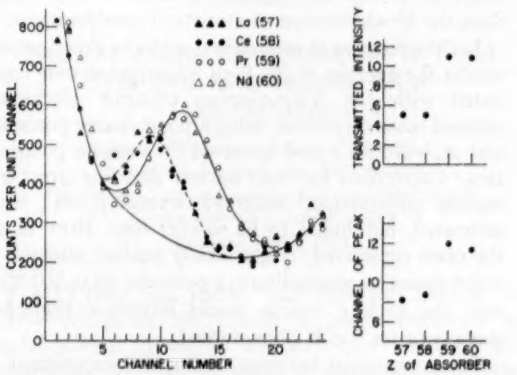

FIG. 1. Pulse-height distribution for the M line of π^- mesons in phosphorus. Absorbers: $Z=57$, 58, 59, and 60. Also shown as a function of Z are the transmitted intensities and the positions of the peaks.

energy immediately above the edge. The cells were placed in contact with the NaI counter, and, as a consequence, one could detect about 30 percent of the fluorescent radiation following the photoelectric absorption process.

The results of a typical run are plotted in Fig. 1. This shows the pulse-height distributions obtained when the π-mesonic M line of phosphorus is observed with the sequence of absorbing cells, $Z=57$, 58, 59, and 60. In each case the data are reduced to 2×10^6 stopping mesons. A transmission discontinuity is apparent between $Z=58$(Ce), and $Z=59$(Pr), indicating that the phosphorus mesonic line lies between the K edges[2] of these two elements. The peaks observed for

TABLE I. Comparison between theory and experiment.

	Line studied	P $4f\rightarrow3d$		Al $4f\rightarrow3d$		K $4f\rightarrow3d$
Theoretical	Klein-Gordon energy (kev) (for $m_\pi=272.5m_e$)	40.39		30.31–		64.90
	Vacuum polarization correction[a] (kev)	0.100		0.065		0.190
	Computed energy (kev)	40.49		30.37		65.09
Experimental	Absorbers bracketing transmission discontinuity	Ce(58)	Pr(59)	Sn(50)	Sb(51)	Hf(72)
	K edges[b] (kev)	40.45	42.00	29.19	30.49	65.35
	Meson mass limits	$\geq 272.2m_e$		$\leq 273.6m_e$		$\leq 273.6m_e$

[a] See reference 3. [b] See reference 2.

$Z=57$ and 58 are due, in part, to the fluorescent x-rays of the absorption cells, as evidenced by their magnitude and by their displacement to lower energies.

The absorption discontinuity of this line is due to the $4f\rightarrow3d$ transition. Higher lines of the M series, such as $5\rightarrow3$, $6\rightarrow3$, etc., would appear at higher energy and thus be strongly absorbed by all the cells used. Other transitions between the total quantum numbers 4 and 3 (such as $4s\rightarrow3p$ etc.) should be much less probable than the $4f\rightarrow3d$ because of statistical considerations.

For the purpose of comparison with the experimental results the energies of the lines investigated were computed with the Klein-Gordon equation (including reduced mass correction, using a point charge potential and $m_\pi=272.5m_e$) and corrected for vacuum polarization.[3] Corrections for finite nuclear size, fine structure, nuclear polarization,[4] electronic screening, etc., were estimated, but found to be smaller than 10 ev in all the cases considered. A specifically nuclear interaction of the meson corresponding to a potential up to 100 Mev over the nuclear volume would introduce negligible corrections for the M lines studied.

The comparison between theory and experiment is shown in Table I.

As one can see, from this experiment one obtains the following limits for the mass of the π^- meson:

$$272.2m_e\leqslant m_{\pi^-}\leqslant 273.6m_e.$$

(This value is in good agreement with the determination at Berkeley,[5] but does not agree well with a recent publication from Columbia.[6]) The greatest error in these limits is due to the uncertainty in our knowledge of the electronic K edges (which we hope to have remeasured) and of the vacuum polarization correction.

* Supported in part by the U. S. Atomic Energy Commission.

[1] Stearns, DeBenedetti, Stearns, and Leipuner, Phys. Rev. **93**, 1123 (1954).

[2] The K-absorption edges were taken from a recent compilation of Lewis Slack, Naval Research Laboratory. They are in satisfactory agreement with those reported by Hill, Church, and Mihelich, Rev. Sci. Instr. **23**, 523 (1952).

[3] H. C. Corben and A. Mickelwait (private communication).

[4] Wilbur Lakin (private communication).

[5] Smith, Birnbaum, and Barkas, Phys. Rev. **91**, 765 (1953).

[6] Cornelius, Sargent, Rinehart, Lederman, and Rogers, Phys. Rev. **92**, 1583 (1953).

Decay Scheme of Pb^{204m}

V. E. KROHN AND S. RABOY
Argonne National Laboratory, Lemont, Illinois

(Received July 8, 1954)

IN the course of investigating the angular correlation of the gamma rays of the 68-min isomer of Pb^{204}, we have found that the decay scheme consists of three, rather than two, gamma rays in cascade [Fig. 1(a)].

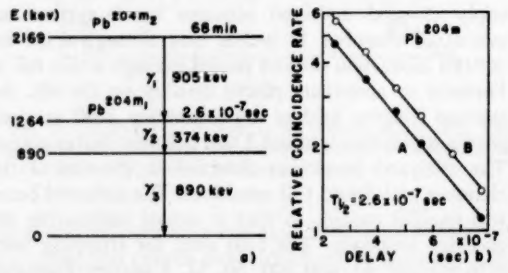

FIG. 1. (a) Proposed decay scheme for Pb^{204m}. (b) Decay of the intermediate state of the 905–890-kev cascade (curve A) and the 905–374-kev cascade (curve B).

The order of the two gamma rays following the 2.6×10^{-7} second state has not been determined experimentally.

Part of our study of the decay scheme was performed with apparatus which used two NaI(Tl) scintillation crystals together with a fast-slow coincidence scheme. The fast coincidence circuit had a resolving time of 10^{-7} second and the slow ($\sim2\times10^{-6}$ second) triple coincidence circuit received the output of the fast circuit plus pulses which had passed through discriminators operated as either differential or integral pulse-height analyzers. 1500-ohm delay lines were inserted as desired ahead of the fast coincidence unit.

The pulse-height distribution of the gamma rays following the 2.6×10^{-7} second state of Pb^{204m} was

obtained as follows: One discriminator was set with an integral bias at 500 kev and the corresponding input to the fast coincidence circuit was delayed 2.4×10^{-7} second. The other discriminator had a 50-kev window whose bias was varied with the results shown in Fig. 2.

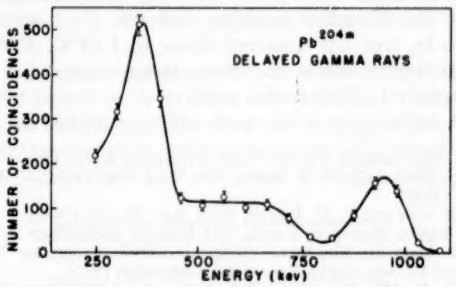

FIG. 2. Delayed coincidence spectrum of the gamma rays following the 2.6×10^{-7} second state of Pb^{204m}. The curve was taken with $\frac{1}{8}$ in. of lead shielding each NaI crystal from the source, and the data were corrected for the 68-min decay of the source and for chance coincidences.

The relative heights of the two full-energy peaks in the figure indicate that the second and third gamma rays of Fig. 1(a) are of approximately equal intensity. As the sources used for this work contained a variety of activities produced by bombardment of thallium with 22-Mev deuterons, several checks were made to verify the assignment of three gamma rays to Pb^{204m}.

First, the intermediate lifetimes of the 905–374-kev cascade and the 905–890-kev cascade were measured and found identical within two percent. This result was obtained by setting one discriminator with an integral bias at 500 kev and varying the corresponding delay [Fig. 1(b)]. The second discriminator was set with an integral bias at 500 kev for the 905–890-kev cascade (curve A) and then with a 250-kev window centered at 374 kev in order to maximize the contribution of the 905–374-kev coincidences (curve B). These curves indicate a half-life of $2.6\pm0.2\times10^{-7}$ seconds in agreement with the result of Sunyar *et al.*[1]

Second, the energies of the first gamma ray of the 905–890-kev cascade and the first gamma ray of the 905–374-kev cascade were compared by coincidence techniques similar to those used to obtain Fig. 2. The results were identical within 1 percent. The energies of the first and second gamma rays of the 905–890-kev cascade were compared by means of similar coincidence techniques. The results indicated that the second high-energy gamma ray of this cascade has 15 ± 5 kev less energy than the first. As there is no evidence of two gamma rays with energy near 900 kev in the internal conversion spectra of Sunyar *et al.*,[1] we have assumed that the internal conversion coefficients of the second high-energy gamma ray are small compared to those of the gamma ray originating from the 68-min state. Hence, 905 kev has been tentatively retained for the energy of the first gamma ray.

Third, the lifetime of the delayed 905–374-kev and 905–890-kev cascades was found to be approximately 68 min.

Fourth, the decay of one of the sources was observed in an apparatus which added the light output of thirteen 2-in. NaI cubes surrounding the source. There is evidence of interference from shorter and longer lived sum lines, but the presence of the expected sum line of about 2170-kev energy and 68-min half-life is demonstrated (Fig. 3).

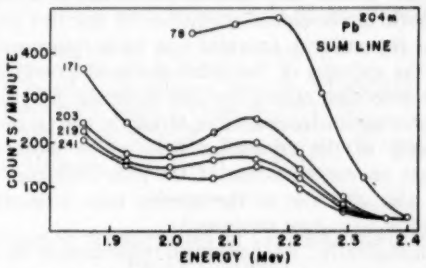

FIG. 3. The 2170-kev sum line of Pb^{204m}. The numbers to the left of the curves indicate the time at which the curves were taken, in minutes, after the end of a 20-min cyclotron irradiation.

The presence of an extra gamma ray in the cascade probably does not affect the measurements[2,3] of the gyromagnetic ratio of the 2.6×10^{-7} sec state of Pb^{204m}. At present our result for the gyromagnetic ratio is $+0.055\pm0.01$ nuclear units.

We would like to express our gratitude to Mr. Jay Wolf for valuable assistance with the electronic circuitry, to Dr. Paul Mooring and Dr. Robert Holland for use of the multicrystal NaI spectrometer, and to the crew of the Argonne cyclotron for their cooperation.

[1] Sunyar, Alburger, Friedlander, Goldhaber, and Scharff-Goldhaber, Phys. Rev. **79**, 181 (1950).
[2] Frauenfelder, Lawson, and Jentschke, Phys. Rev. **93**, 1126 (1954).
[3] V. Krohn and S. Raboy, Phys. Rev. **95**, 1354 (1954).

Nuclear Magnetic Resonance in Solid Hydrogen with Various *Ortho*-Concentrations

TADASHI SUGAWARA, YOSHIKA MASUDA,*
TEINOSUKE KANDA,* AND EIZO KANDA
The Research Institute for Iron, Steel, and Other Metals, Tohoku University, Sendai, Japan
(Received July 6, 1954)

HATTON and Rollin,[1] and Reif and Purcell[2] investigated the proton magnetic resonance in solid normal hydrogen. We performed[3] the same experiments using an autodyne detector technique near 8 Mc/sec in the temperature range from the triple point to 1.2°K. Experimental results were as follows: Only one peak was obtained with a line width of about

1 gauss above 10°K; at about this temperature the width increased abruptly to 5.4 gauss and remained constant down to 1.55°K. At 1.55°K two side peaks with a separation of about 39.5 gauss began to appear, and at 1.4°K two additional humps with a separation of about 75.5 gauss. As the temperature was reduced further there was a marked decrease in the intensity of the central line with a corresponding increase in the side peak intensity. These results are in agreement with those of references 1 and 2. The observed fine structure at low temperatures can be explained by the magnetic dipole-dipole interaction of the two protons in the lowest level, provided one takes into consideration the splitting of the rotational level ($J=1$) of the *ortho*-molecules caused by the potential field of the neighboring molecules. The strength and symmetry property of the crystalline field which most likely depend on concentration of the *ortho*-molecules probably also give rise to the specific heat anomaly observed in *ortho-para* mixtures.[4]

Consequently, we performed experiments on solid hydrogen samples with different *ortho*-concentrations. In 11, 16, and 34 percent *ortho*-hydrogen the observed line widths at 4.2°K were 1.2, 1.6, and 3.3 gauss, respectively. Only the central line appeared with no fine structure down to 1.20°K. In 55 percent *ortho*-hydrogen, the circumstances were the same, but the line width at 4.2°K was 5.0 gauss and remained unchanged down to 1.19°K. In 67 percent *ortho*-hydrogen, the line was a simple one with a width of 5.6 gauss down to 4.2°K. At 1.33°K, however, the side peaks appeared. At 1.20°K the separations of these side peaks and two humps were 39.5 gauss and 75.5 gauss, respectively. In 70 percent *ortho*-hydrogen, the line was a simple one with a width of 5.1 gauss down to 4.2°K. The side peaks appeared at 1.43°K. At 1.24°K, in addition to the two side peaks of the separation of 39.5 gauss, two humps with a separation of 75.5 gauss appeared. The interesting result is that the temperature at which the fine structure appeared depends on *ortho*-concentration. This temperature shifted to lower temperatures with falling *ortho*-concentration. The line width of the center peak also depends on *ortho*-concentration, but the observed line width in high *ortho*-concentration was broader than that calculated by Van Vleck's formula assuming the intermolecular broadening of *ortho*-molecules with $I=1$. The experiments should be extended to lower temperatures for the samples in which no fine structure was observed above 1.2°K.

Recently, Hill and Ricketson[5] reported the existence of a λ-type specific heat anomaly and a sharp dependence of its critical temperature on *ortho*-concentration in solid hydrogen. In 74 percent *ortho*-hydrogen the specific heat maximum occurs at 1.6°K, while in 66 percent *ortho*-hydrogen it is shifted to 1.35°K. It is interesting to note that there is a coincidence between the observed λ-point of the specific heat anomaly and the temperature at which the side peaks begin to appear in our nuclear magnetic resonance experiments.

We also made experiments with solid normal D_2 near 4 Mc/sec. The results were in agreement with those of references 1 and 2. The line at 4.2°K was a simple one with a width of about 1.4 gauss. The fine structure resulting from the $J=1$ state of *para*-D_2 was not observed down to 1.19°K. Further experiments down to lower temperatures will be necessary to confirm this point.

A full account of this work will be published shortly.

* Department of Physics, Kobe University, Kobe, Japan.

[1] J. Hatton and B. V. Rollin, Proc. Roy. Soc. (London) **A199**, 222 (1949).
[2] F. Reif and E. M. Purcell, Phys. Rev. **91**, 631 (1953).
[3] Kanda, Sugawara, Kanda, and Masuda, Symposium on Nuclear Magnetic Resonance (International Conference on Theoretical Physics, Osaka University, September, 1953).
[4] R. W. Hill, *Proceedings of the International Conference on Low Temperature Physics* (Oxford University Press, London, 1951), p. 8.
[5] R. W. Hill and B. W. A. Ricketson, Phil. Mag. **45**, 277 (1954).

Spins and Hyperfine Splittings of Ag^{111} and Cu^{64}†

AARON LEMONICK AND FRANCIS M. PIPKIN
Palmer Physical Laboratory, Princeton University, Princeton, New Jersey
(Received July 8, 1954)

FOLLOWING a suggestion by Professor Donald R. Hamilton, we have constructed an atomic beam magnetic resonance apparatus for the measurement of the spins and magnetic moments of radioactive nuclei in which the conventional A and B deflecting magnets[1] have been replaced by six-pole magnets similar to the focusing magnet constructed by Friedburg and Paul.[2] The A magnet acts as a converging lens for atoms having a negative strong field moment; the B magnet acts as a diverging lens for atoms having a positive strong field moment. By arranging the stops as shown schematically in Fig. 1, only atoms which have undergone a transition in the C field resulting in a change in the sign of the strong field moment can reach the detector. Each atom

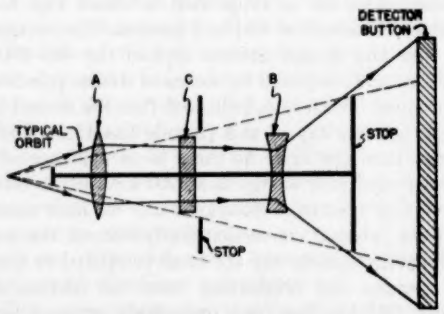

FIG. 1. Schematic of atom optics.

must cross the dotted line twice. Calculation showed that this arrangement of optics enabled us to compensate sufficiently for the chromatic aberration caused by the Maxwellian distribution, so that we were able to obtain an effective solid angle of $(5\times10^{-5})\ 4\pi$ steradians for flopped atoms reaching the detector from the oven and having a kinetic energy between 300°K and 1200°K.

A point on a resonance curve is taken by inserting a copper button in the position shown in Fig. 1. We collect for 5 min and then count for 5 min with a 2π Geiger counter. A typical resonance for Cu^{64} is shown in Fig. 2. The spin of Cu^{64} was found to be 1; a tentative

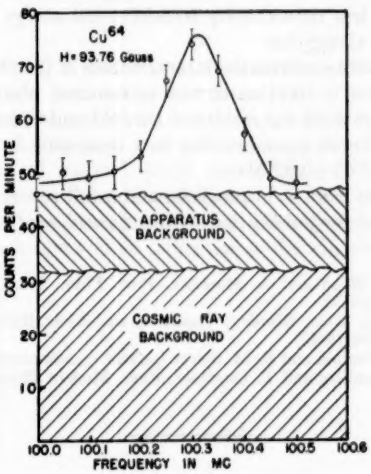

FIG. 2. Typical Cu^{64} resonance curve.

value for the hyperfine splitting is 1278±20 Mc/sec. Because of a dependence, which is not understood, of the line center upon the rf power level, at present we cannot say what the sign of the moment is. Using the hyperfine splitting of 0.195 cm^{-1} observed spectroscopically by Ritschl,[3] an average of the gyromagnetic ratios of Cu^{63} and Cu^{65},[4] and the Fermi-Segrè formula,[5] we obtain for the magnetic moment of Cu^{64},

$$|\mu| = 0.40 \pm 0.05 \text{ nm}.$$

A definitive interpretation must await the determination of the sign of the moment.

The spin of Ag^{111} is $\frac{1}{2}$; a tentative value of the hyperfine splitting is 2180±100 Mc/sec. Using the data of Wessel and Lew[6] on the hyperfine splitting of Ag^{107} and Ag^{109}, the nuclear magnetic moments measured by Sogo and Jeffries,[7] and the Fermi-Segrè formula, we obtain for the magnetic moment of Ag^{111}

$$|\mu| = 0.144 \pm 0.007 \text{ nm}.$$

This confirms the spin assignment of McGinnis,[8] and gives further evidence that the addition of two neutrons does not substantially change the nuclear state.

We are indebted to Professor Donald R. Hamilton for suggesting the possibility of constructing a focusing atomic beam apparatus and for his continued advice throughout the conduct of the experiment. We also wish to express our thanks to R. D. Petti and R. L. Christensen for their help in constructing the apparatus and taking data. A more complete report on the apparatus and further measurements now in progress will be submitted in the near future.

† This work was supported in part by the U. S. Atomic Energy Commission and the Higgins Scientific Trust Fund.

[1] J. M. B. Kellogg and S. Millman, Revs. Modern Phys. **18**, 323 (1946).
[2] H. Friedburg and W. Paul, Naturwiss. **38**, 159 (1951).
[3] R. Ritschl, Z. Physik **79**, 1 (1932).
[4] R. E. Sheriff and D. Williams, Phys. Rev. **82**, 651 (1951).
[5] E. Fermi and S. Segrè, Z. Physik **82**, 729 (1933).
[6] G. Wessel and H. Lew, Phys. Rev. **92**, 641 (1953).
[7] P. B. Sogo and C. D. Jeffries, Phys. Rev. **93**, 174 (1954).
[8] C. L. McGinnis, Phys. Rev. **81**, 734 (1948).

Resonance Absorption of Gamma Radiation by O^{16} Nuclei

J. G. CAMPBELL
Physics Department, University of Melbourne, Melbourne, Australia
(Received July 6, 1954)

RESONANCE absorption of gamma radiation was detected by Moon and Storruste[1] in the scattering of Hg^{198} radiation by the same nuclei. A high linear speed, mechanically attained, compensated for energy lost to recoil in emission and absorption. In this case, however, Doppler broadening due to thermal motion greatly exceeded the level width.

The occurrence of resonance absorption by individual levels in light nuclei has been inferred by Haslam *et al.*[2] from discontinuities in the slope of the betatron excitation curve for the reaction $O^{16}(\gamma,n)O^{15}$. Some uncertainty remains in this interpretation, however, owing to the energy spread in the betatron radiation.

This note reports preliminary experiments using gamma radiation from the reaction $Li^7(p,\gamma)Be^8$. The photonuclear reaction $O^{16}(\gamma,n)O^{15}$ was chosen for investigation because it has recently been the subject of a careful betatron study by Penfold and Spicer.[3]

The gamma radiation, produced by a 40-μa proton beam from the University of Melbourne 700-kv electrostatic generator striking thin lithium nitride targets, could be varied over a limited energy range by variation of proton energy. Only the highest energy component of this radiation (transitions to the ground state of Be^8) is above the photodisintegration threshold. The yield of this radiation exhibits the well-known resonance at 441 kev, above which it drops to a low but nearly constant level.

The oxygen irradiated was combined chemically in p-dioxane, in which was dissolved p-terphenyl to make a scintillating solution. O^{15} was detected by its positron

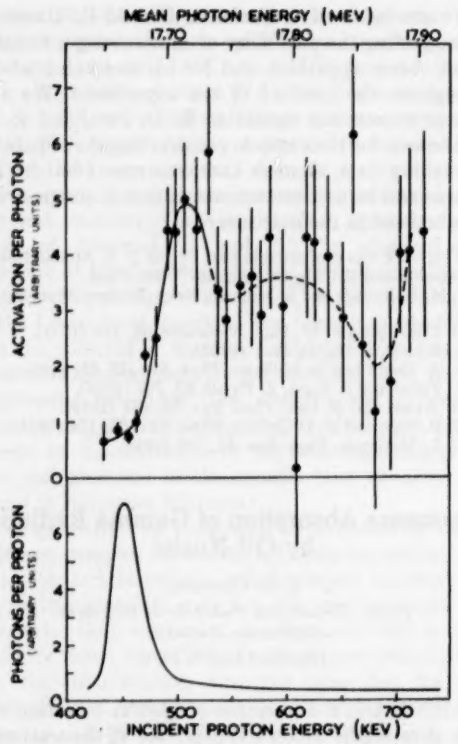

FIG. 1. Upper curve: Excitation function for the reaction $O^{16}(\gamma,n)O^{15}$. Statistical uncertainties are indicated by vertical lines. Lower curve: Available gamma intensity plotted against energy.

decay after the proton beam was interrupted, the scintillations being counted with a photomultiplier.

In the first experiments, gamma radiation at 90° to the proton beam was used. When the activation per photon was plotted against energy, the curve was flat in the region of high gamma intensity, but appeared to rise at higher energy, where the weakness of gamma intensity caused proportionately greater statistical fluctuations.

The radiation at 0° was then used to study this rise more carefully. Since the lifetime of the excited state of Be^8 is very short, this nucleus emits the gamma radiation when still travelling at the full velocity of recoil from proton absorption. At proton energy 500 kev, this results in a Doppler increase of 72 kev in photon energy in the forward direction. The scintillator was in the form of a truncated cone with apex at the target and semi-angle 45°, so that the mean Doppler shift was about 62 kev, with a total spread of 20 kev.

A set of results so obtained is shown in Fig. 1, with the gamma intensity plotted below. The sharp rise in activation per photon, to a peak at 510±10 kev incident proton energy, is quite clear. (The subsequent shape of the curve is partially obscured by statistical fluctuations, but there appears to be a broad unresolved hump around 610 kev, followed by a dip and a further sharp rise at 700 kev.)

To relate incident proton energy to photon energy, the Q-value of the reaction $Li^7(p,\gamma)Be^8$ is taken as 17.242 Mev.[4] The mean proton energy was less than the incident energy by 10 kev (half the target thickness) and, of this, seven-eighths is available for excitation. In the gamma emission, about 21 kev is lost to the recoiling Be^8 nucleus.

Thus we conclude that the peak at 510-kev incident proton energy corresponds to a resonant in the absorption of gamma radiation by O^{16} at a photon energy of 17.721±0.010 Mev, the width of which is estimated as about 20 kev. The corresponding excitation energy of O^{16} is less than this by 10.5 kev, the energy lost to recoil on absorption.

This work confirms the interpretation of the "breaks" in betatron activation curves as resonant absorption, and agrees with the results of Penfold and Spicer, who found a break corresponding to a resonance at photon energy 17.69±0.02 Mev.

Further work is in progress, and a full report will be submitted for publication to the *Australian Journal of Physics*.

[1] P. B. Moon and A. Storruste, Proc. Phys. Soc. (London) **A66**, 585 (1953).
[2] Haslam, Katz, Horsley, Cameron, and Montalbetti, Phys. Rev. **87**, 196 (1952).
[3] A. S. Penfold and B. M. Spicer (private communication).
[4] F. Ajzenberg and T. Lauritsen, Revs. Modern Phys. **24**, 321 (1952).

Ground State of Re^{186}†

LEO KOERTS
Columbia University, New York, New York
(Received July 7, 1954)

THE decay scheme of Re^{186} has been established by Metzger and Hill.[1] They found three negatron branches of end-point energies 1.06, 0.92, and 0.3 Mev leading to 0^+, 2^+, and 1^- levels in osmium. The assignment for the ground and first excited states is deduced from the even-even character of Os^{186}; that for the second excited state, from the approximately equal intensities of the gamma rays to the ground and first excited states. Since the two more energetic beta groups did not display a forbidden shape, 1^- was assigned to the Re^{186} ground state (Fig. 1).

Recently, however, the unique ($\Delta I = 2$, yes) shape was reported[2] for the 0.92-Mev group with consequently a 0^- assignment for the Re^{186}. Since this result was obtained by subtraction and the end points of the two groups are rather close, it seemed worthwhile to investigate this spectrum in the magnetic coincidence spectrometer. The fact that no positron emission occurs and the high energetic gamma rays are very weak makes the case quite clear cut for this type of experiment.

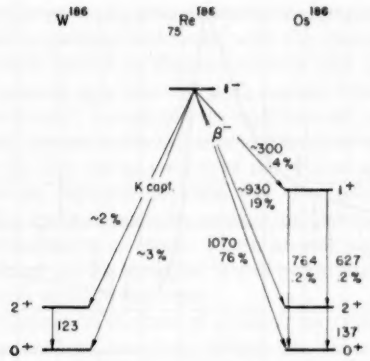

FIG. 1. Decay scheme of Re^{186}.

Sources of 3 mm diameter consisting of the active material in perrhenate form were used. The 926-kev group was measured in coincidence with the 137-kev gamma during four runs on two evaporated sources and was of allowed shape in all cases [Fig. 2(a)]. The total spectrum was followed for four half lives, while the low-situated conversion lines showed a 2 percent resolution and no indication of deformation of the spectrum. A subtraction was made, giving both the 1063- and 926-kev groups allowed shapes consistent with the coincidence runs [Fig. 2(b)]. An experiment was also made to establish the 0.3-Mev group more directly by partially discriminating against the 137-kev gamma ray, thus making the 0.3-Mev group relatively more pronounced [Fig. 2(c)]. The gamma-ray spectrum was checked in the crystal spectrometer.

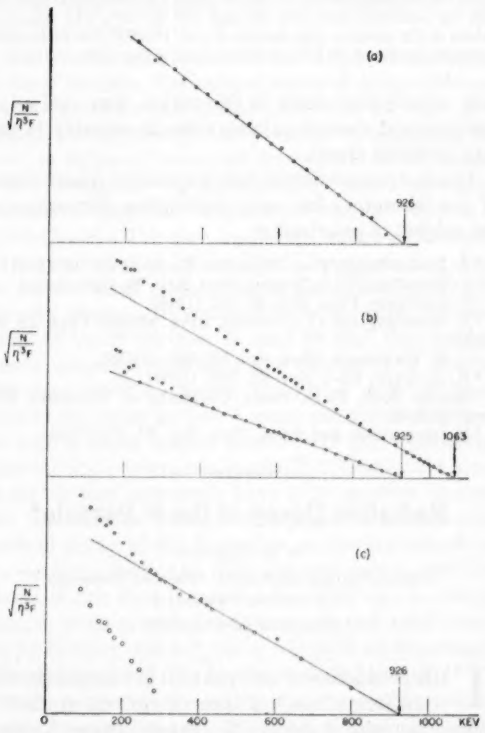

FIG. 2. (a) Kurie plot of the 926-kev spectrum taken in coincidence with the 137-kev gamma. (b) Kurie plots of total spectrum and two groups by subtraction. (c) Kurie plot of coincidence spectra; 0.3-Mev group more pronounced by stronger discrimination.

One concludes from the Kurie plots shown in Fig. 2 that no evidence has been found for a forbidden shape in any of the negatron branches and that consequently the unit spin and odd parity assignment for the Re^{186} ground state should be retained.

The author wishes to thank Professor Chien-Shiung Wu for her continued advice and stimulating interest in the problem, and Miss Noemie Benczer and R. Gold for their help in obtaining the data.

† This work was partially supported by the U. S. Atomic Energy Commission.

[1] F. R. Metzger and R. D. Hill, Phys. Rev. **82**, 646 (1951).
[2] Guss, Killion, and Porter, Phys. Rev. **95**, 627 (1954).

Polarization of Fast Neutrons from Nuclear Reactions

HARVEY B. WILLARD, JOE K. BAIR, AND JOE D. KINGTON
Oak Ridge National Laboratory, Oak Ridge, Tennessee
(Received July 13, 1954)

BLIN-STOYLE[1] and Simon and Welton[2] have pointed out the general theorem that polarized particles may be produced in nuclear reactions by the interference of nuclear states involving spin-orbit coupling. In particular, polarized neutrons may be produced by (p,n) reactions and analyzed by elastic scattering.[3] If the neutrons are emitted at angle θ_1 with respect to the proton beam, and elastically scattered through $+\theta_2$ and $-\theta_2$ in the plane of the reaction, the resultant asymmetry is

$$r_{\pm}=\frac{1-P_1(\theta_1)P_2(\theta_2)}{1+P_1(\theta_1)P_2(\theta_2)},$$

where $P_1(\theta_1)$ is the polarization of the first reaction, and $P_2(\theta_2)$ is the polarization of the second reaction.

The $Li^7(p,n)Be^7$ reaction[4] has a resonance at a proton energy of 2.22 Mev (all angles and energies stated are in the laboratory system) which could produce polarized neutrons by interference with either the known level below 1.88 Mev, or the very broad level at 4.89 kev. Neutrons elastically scattered by O^{16} have a $P_{\frac{1}{2}}$[5,6] resonance at 435 kev which interferes with the $S_{\frac{1}{2}}$ potential scattering. These reactions were used to investigate the degree of polarization obtainable.

Figure 1 shows the geometry of the experiments. A 12-kev thick rotating lithium target was bombarded by protons from the 5.5-Mev Van de Graaff and the re-

sultant neutrons emitted at 42° were elastically scattered through +90° and −90° by a 5-mil wall nickel cylinder, 1 in. in diameter and 4 in. long, containing H_2O and located 8 in. from the target. The scattered neutrons were detected by a hydrogen recoil counter (1 atmos of propane gas) whose sensitive volume was 1 in. in diameter and 4 in. long. This counter was placed a mean distance of 4 in. from the center of the scattering sample and shielded by paraffin wedges from the neutrons coming directly from the target. A bias was chosen so as to discriminate against neutrons multiply scattered by the H^1, but a small correction[7] was necessary for the multiple scattering in the O^{16}. As a check on this correction, an H_2O sample ½ in. in diameter and 2 in. long was used to measure the asymmetry at its maximum value. Backgrounds, ranging from 40 to 70 percent, were measured by removing the H_2O from the cylinder.

The total cross section of O^{16} was calculated by use of the observed[5,6] values of the level parameters and is shown in the lower part of Fig. 2. Its maximum value

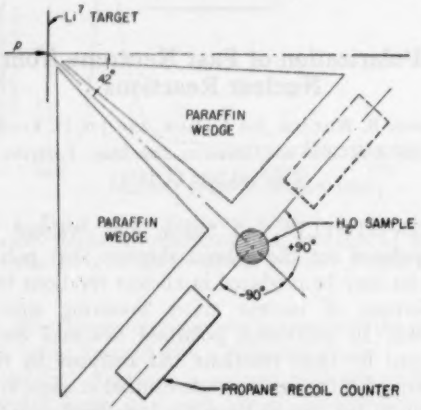

FIG. 1. The geometry for measuring the polarization asymmetry.

is somewhat higher than the measured value, but consistent with the resolution employed (20 kev). The value of $P_2(90°)$ was then computed and is the solid curve in the upper part of Fig. 2 using the left ordinate. The measured values of $P_1(42°)P_2(90°)$ are also plotted in the upper part of Fig. 2 using the right ordinate.

The results are consistent with the known level parameters of the level in O^{17}, and a nearly constant value of $P_1(42°)=0.50\pm0.04$ for the $Li^7(p,n)Be^7$ reaction in this region. This value decreases slowly below 300 kev and above 550 kev. Preliminary measurements[8] which show that this reaction is polarized at 400 kev have been reported, but no value for the polarization is given.

$T(p,n)He^3$ neutrons emitted at $\theta_1=50°$ were also scattered from O^{16}, and the observed value of $P_1(50°)P_2(90°)$ was 0.01 ± 0.04 at 400 kev.

In order to eliminate systematic errors in these measurements, elastic scattering from C^{12}, which has

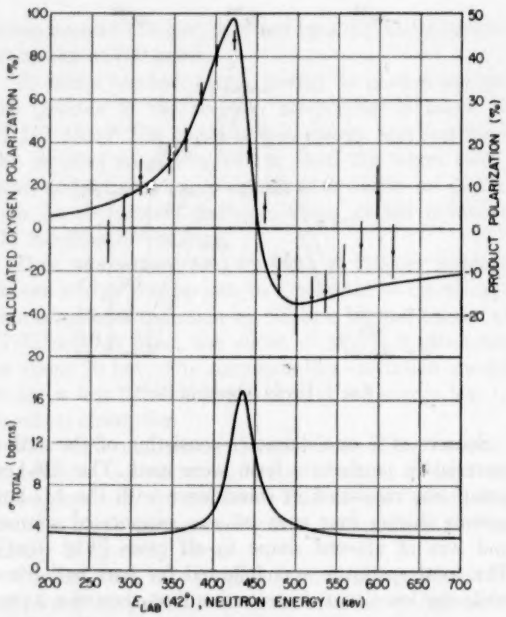

FIG. 2. The lower curve shows the total cross section of O^{16}. The upper curve, using the left ordinate, shows the theoretical polarization for neutrons scattered through 90° by O^{16}. The measured values of the product polarization $P_1(42°)P_2(90°)$ for $Li^7(p,n)Be^7$ neutrons scattered by O^{16} are plotted using the right ordinate.

only *s*-wave interaction in this region, was used as an analyzer and showed no observable asymmetry (4 percent probable error).

The authors are deeply indebted to Dr. Albert Simon of this laboratory for many stimulating discussions on the subject of polarization.

[1] R. J. Blin-Stoyle, Proc. Phys. Soc. (London) **64**, 700 (1951).
[2] A. Simon and T. A. Welton, Phys. Rev. **90**, 1036 (1953).
[3] J. Schwinger, Phys. Rev. **69**, 681 (1946).
[4] F. Ajzenberg and C. Lauritsen, Revs. Modern Phys. **24**, 338 (1952).
[5] C. K. Bockelman, Phys. Rev. **80**, 1011 (1950).
[6] R. K. Adair, Phys. Rev. **92**, 1491 (1954).
[7] Martin Walt, Ph.D. thesis, University of Wisconsin, 1953 (unpublished).
[8] Darden, Fields, and Adair, Phys. Rev. **93**, 931 (1954).

Radiative Decay of the θ^0 Particle*

S. B. TREIMAN
Palmer Physical Laboratory, Princeton University, Princeton, New Jersey
(Received July 16, 1954)

THE production of soft photons in charged particle transformations has been extensively studied in connection with β decay, K capture, charged meson production, and π- and μ-meson decay.[1] The photon emission in such transformations corresponds to the classical radiation which accompanies the sudden acceleration of a charged particle. Indeed, in the limit

of small photon energy, the classically computed photon spectrum is essentially identical with the spectrum obtained from quantum electrodynamics (for particles of spin zero or spin one-half with normal Dirac magnetic moment).[2] Consequently, experimental study of the "inner bremsstrahlung" effect—insofar as it is confined to the low energy portion of the photon spectrum—cannot be expected to yield any new information about the specific quantum mechanical details of the transformations in question. These become significant only at large photon energies, where unfortunately the spectrum is strongly depleted.

Nevertheless, in the case of unstable particles which normally undergo two-body decay, the inner bremsstrahlung effect is of some importance. Consider, for example, the decay of a pion at rest. The emission of a photon of appreciable energy immediately forces itself to one's attention in that the muon secondary comes off with "anomalously" short range.[3] The successful explanation of anomalous pion decays in these terms has (it is to be hoped) eliminated the need to invent new particles or processes to explain the observed effect.[4]

Although statistics are still limited, similar situations can be expected to arise in connection with the newer unstable particles; and one will want to consider whether rare "anomalies" may be explained in terms of radiative decay.

The present note deals with this effect for the decay of the θ^0 particle. The normal mode of decay is $\theta^0\to\pi^+ +\pi^-+Q_0$, where $Q_0=214\pm5$ Mev.[5] In the case of a radiative decay, the Q value obtained by analyzing the event in terms of the normal decay mode would appear to be "anomalous" $[Q(\pi,\pi)\equiv Q<Q_0]$. There have been a number of reports of "anomalous θ^0 events"—events in which $Q(\pi,\pi)<214$ Mev, but which otherwise resemble the normal decay of a θ^0 particle.[6,7] It appears that there are far too many cases where in particular $Q(\pi,\pi)<75$ Mev for these to be explainable in terms of radiative decay of the θ^0 particle. It may be that this class of events actually represents the decay of a neutral counterpart of the τ meson: $\tau^0\to\pi^++\pi^-+\pi^0$.[6] If the τ^0 mass is the same as the $\tau^\pm$ mass, the value of $Q(\pi,\pi)$ for such a decay cannot exceed $\sim$75 Mev. However, there are also a few events where $75<Q(\pi,\pi)<214$ Mev. These too may ultimately have to be ascribed to some new fundamental particle or perhaps to an alternate mode of decay of the θ^0 particle, as for example $\theta^0\to\pi+\mu+\nu$;[7] but insofar as there are still only a very few events of this kind it may be that they can be understood in terms of radiative θ^0 decay. As indicated below, the probability that a θ^0 decay will yield an apparent Q value less than say 194 Mev is about 0.7 percent.

We assume that the matrix element for the normal mode of decay of the θ^0 particle is independent of the 4-momenta of the two pions, so that the momentum dependence in the matrix element for the radiative decay comes entirely from the propagation of the virtual pion. A standard relativistic calculation, to lowest order, yields then the following expression for the probability that a θ^0 particle decaying at rest will emit a photon of energy w:

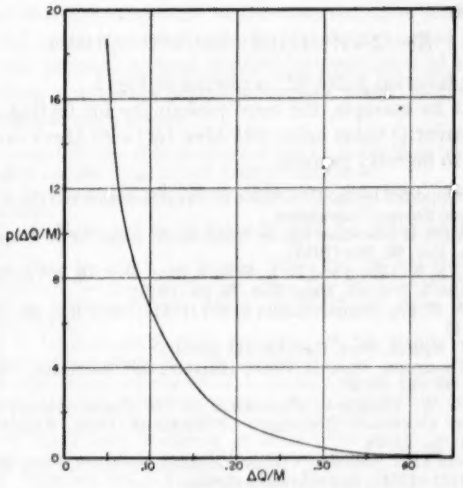

FIG. 1. Relative distribution in θ^0 particle Q value anomalies caused by photon emission.

$$P(w)dw=(2/\pi)(1/137)(1-4m^2/M^2)^{-\frac{1}{2}}f(w)dw/w,$$

$$f(w)=\left(1-\frac{2w}{M}-2\frac{m^2}{M^2}\right)\log\frac{1+B}{1-B}-\left(1-\frac{2w}{M}\right)B,$$

$$B=[1-(4m^2/M^2)(1-2w/M)]^{\frac{1}{2}},$$

where m and M are, respectively, the pion and θ^0 particle rest energies.

The distribution in apparent Q values can now be obtained in the following manner. Let p_0, p_+, p_-, and k denote the respective momentum 4 vectors of the θ^0 particle, the positive and negative pions, and the photon ($p_0^2=M^2$, $p_+^2=p_-^2=m^2$, $k^2=0$). If a radiative decay event is analyzed on the assumption that no photon was emitted, one computes the (apparent) mass M^* of the θ^0 particle from $M^{*2}=(p_++p_-)^2$. Since this quantity is a Lorentz invariant we can evaluate it in the θ^0 rest frame, using $p_0=p_++p_-+k$:

$$M^{*2}=M^2-2Mw.$$

The apparent and true Q values, however, are related by $\Delta Q\equiv Q_0-Q=M-M^*$. Thus,

$$w=(1-\Delta Q/2M)\Delta Q.$$

Making this replacement, we obtain the following expression for the distribution in ΔQ:

$$P(\Delta Q/M)d(\Delta Q/M)=Kp(\Delta Q/M)d(\Delta Q/M),$$

$$p(\Delta Q/M)=f[w(\Delta Q/M)]\frac{1-\Delta Q/M}{1-\Delta Q/2M}\frac{1}{(\Delta Q/M)},$$

where

$$K=(2/\pi)(1/137)(1-4m^2/M^2)^{-\frac{1}{2}}=0.0056.$$

The function $p(\Delta Q/M)$ is plotted in Fig. 1.

As an example, the total probability for finding an apparent Q value below 194 Mev ($\Delta Q=20$ Mev) turns out to be $\sim$0.7 percent.

* Supported by the U. S. Office of Naval Research and the U. S. Atomic Energy Commission.

[1] A list of references can be found in the paper by A. Lenard, Phys. Rev. **90**, 968 (1953).

[2] C. S. W. Chang and D. L. Falkoff, Phys. Rev. **76**, 365 (1949); see also L. I. Schiff, Phys. Rev. **76**, 89 (1949).

[3] W. F. Fry, Nuovo cimento **8**, 590 (1951); Phys. Rev. **83**, 1268 (1951).

[4] T. Eguchi, Phys. Rev. **85**, 943 (1952).

[5] Thompson, Burwell, Cohn, Huggett, and Karzmark, Phys. Rev. **95**, 661 (1954).

[6] R. W. Thompson, *Proceedings of The Fourth Annual Rochester Conference* (University of Rochester Press, Rochester, 1954), pp. 75–79.

[7] Van Lint, Anderson, Cowan, Leighton, and York, Phys. Rev. **94**, 1732 (1954); and references therein.

Photodisintegration of Deuterium by 165-Mev X-Rays*

E. A. Whalin, Jr.
Physics Research Laboratory, University of Illinois, Champaign, Illinois

(Received July 6, 1954)

A LIQUID deuterium target[1] 1.25 in. in diameter with walls of 0.0005-in. brass was exposed to a collimated beam of 165-Mev x-rays from the University of Illinois 320-Mev betatron. The x-ray beam was monitored with an 8-in. diameter flat Cu ion chamber which had been calibrated calorimetrically by Kerst and Edwards.[2] The photoprotons were detected by 600-micron thick Ilford G-5 emulsions mounted on 1-in. by 3-in. glass plates. The plates, which were tipped at an angle of about 10° to the equatorial plane, were placed around the outside of the liquid deuterium target at angles of 30°, 45°, 75°, 120°, and 150° with respect to the direction of the x-ray beam. The number of protons per unit area of the plates and their energies were determined by scanning the plates using Leitz Ortholux binocular microscopes. The energies were obtained from measurements of the range of the protons which stopped and from measurements of the grain density of the tracks of the protons which passed through the emulsions.

Figure 1 shows the angular distributions determined for average center-of-mass energies of 62.9 Mev and 130.6 Mev. The curves shown have the form

$$(A+B\sin^2\theta)(1+2\beta\cos\theta).$$

The angular distributions were smoothed simultaneously with the energy dependence curves so that the two sets of curves coincided at the energy and angle of each data point. It can be seen that the $\sin^2\theta$ component which is appreciable at 62.9 Mev has practically disappeared at 130.6 Mev. Here the angular distribution is characterized primarily by the large fore and aft asymmetry presumably due to a retardation effect.

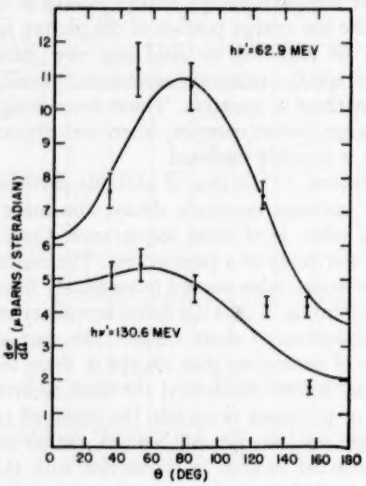

FIG. 1. Angular distributions of the photoprotons in the center-of-mass system for center-of-mass photon energies of 62.9 Mev and 130.6 Mev.

The experimental retardation factor β is shown in Fig. 2, where v_p/c, the ratio of emitted proton velocity to the velocity of light, is also shown for comparison.

Figure 2 also shows the total cross sections calculated from the angular distributions. In addition to the

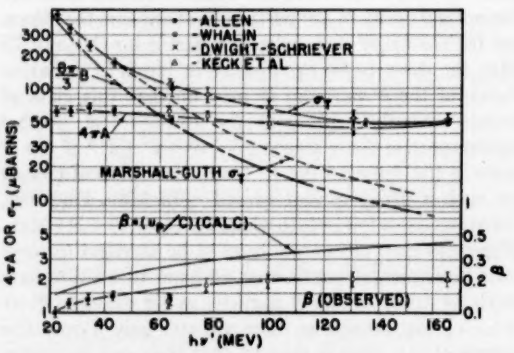

FIG. 2. The experimental total cross section, $\sigma_T=4\pi A+\frac{1}{3}8\pi B$, and $4\pi A$, the isotropic component, and $\frac{1}{3}8\pi B$, the $\sin^2\theta$ component, are shown together with the total cross section calculated by Marshall and Guth. Also shown are the experimental retardation factor β and the ratio of the center-of-mass proton velocity to the velocity of light v_p/c.

data from this experiment, data are plotted which were taken from the work of Allen,[3] Dwight-Schriever,[4] and Keck *et al.*[5]

The similarity between the total cross section of Marshall and Guth[6] and the experimentally determined $\sin^2\theta$ component, $8\pi B/3$, suggests that this component is largely accounted for by their calculations, while the isotropic component $4\pi A$ is mainly due to a specific mesonic effect. Figure 3 shows the difference between

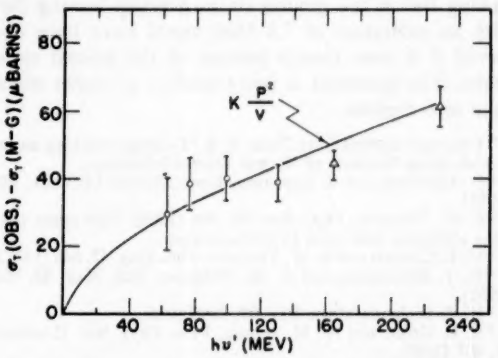

FIG. 3. Difference between the experimental total cross section and the total cross section calculated by Marshall and Guth. P is the momentum and V is the velocity of the photoproton in the center-of-mass system.

the observed total cross section and the total cross section of Marshall and Guth. The difference is a slowly rising quantity which is approximately proportional to the momentum of the emitted proton. This suggests that the matrix element for this part of the cross section is approximately constant. The lack of a distinct difference in the behavior of this component above and below the meson threshold indicates it does not compete with the low-energy photomeson production. This can be understood in terms of an argument of Wilson[7] concerning the absorption of a photon by the meson field in a small volume with a radius less than the pion Compton wavelength. If this volume is occupied by more than one nucleon, nucleons are emitted practically every time because of their much greater statistical weight.

Two more specific mesonic models also seem to show promise of explaining the observed cross sections. The first interaction is suggested by the well known electric dipole transition which is involved in low-energy photopion production. In this transition the photon is absorbed by one of the nucleons flipping its spin and producing an S wave meson. The meson is subsequently absorbed by the other nucleon accompanied by another spin flip producing a final odd-parity state. Such a state could be described as approximately a $^3P_0$ state and would account for the observed isotropic angular distribution.[8] The second interaction involves the interaction magnetic moment and has been considered by Nagahara and Fujimura[9] and also by Bruno and Depken.[10] In this case a P wave meson is emitted by one nucleon, which absorbs the photon. The meson is then absorbed by the other nucleon. These authors show that the magnitude of the observed cross section as well as the angular distribution can be accounted for by this process. A more definite interpretation of the experimental results seems to require more complete theoretical calculations.

* Assisted by the joint program of the U. S. Office of Naval Research and the U. S. Atomic Energy Commission.
[1] E. A. Whalin, Jr., and R. A. Reitz, Rev. Sci. Instr. (to be published).
[2] D. W. Kerst and P. D. Edwards, Rev. Sci. Instr. **24**, 490 (1953).
[3] L. Allen, Jr., and A. O. Hanson, Phys. Rev. **95**, 629 (1954).
[4] Schriever, Whalin, and Hanson, Phys. Rev. **94**, 763 (1954).
[5] Keck, Littauer, O'Neill, Perry, and Woodward, Phys. Rev. **93**, 827 (1954).
[6] J. F. Marshall and E. Guth, Phys. Rev. **78**, 738 (1950).
[7] R. R. Wilson, Phys. Rev. **86**, 125 (1952).
[8] A preliminary calculation of I. Hodes and Y. Yamaguchi indicates that such a transition gives an angular distribution represented by $4+\sin^2\theta$. This transition can also interfere with the usual electric dipole term, producing an effect which might be important at intermediate energies (private communication).
[9] Y. Nagahara and J. Fujimura, Prog. Theoret. Phys. (Japan) **8**, 49 (1952).
[10] B. Bruno and S. Depken, Arkiv Fysik **6**, 177 (1953).

Energy Levels in Be^8 from $Li^7(d,n)Be^8$

CARROLL C. TRAIL* AND C. H. JOHNSON
Oak Ridge National Laboratory, Oak Ridge, Tennessee
(Received July 14, 1954)

SEVERAL low-lying states in Be^8 have been reported in addition to a well-established broad level at 3 Mev.[1] In particular, Titterton[2] has discussed the evidence for levels in Be^8 at 4, 5.3 and 7.5 Mev. Existence of the 4-, 5.3-, and 7.5-Mev levels is suggested[3–9] from $B^{11}(\gamma,t)Be^8$, $B^{10}(\gamma,d)Be^8$, $Li^7(d,n)Be^8$, and $Li^7(p,\gamma\alpha)He^4$. Additional evidence for the 7.5-Mev level is given by the $\alpha-\alpha$ scattering experiment of Steigert and Sampson.[10] The neutron spectrum from $Li^7(d,n)Be^8$ has been obtained previously with photographic plates,[5–8] and the purpose of this investigation was to measure this neutron spectrum with good statistics with a spectrometer described elsewhere.[11]

In a recent article Kunz, Moak, and Good[12] reported the proton spectrum from $Li^6(He^3,p)Be^8$. The spectrum indicates only the 3.0-Mev excited state in Be^8 up to an excitation of 10 Mev. Malm and Inglis[13] observed the α-particle spectrum from $B^{11}(p,\alpha)Be^8$ and found only the 3-Mev excited state up to an excitation of 7 Mev. The $B^{10}(d,\alpha)Be^8$ reaction[14] was found to leave Be^8 in only the ground and 3.0-Mev states.

The spectrometer for this study contains a polyethylene radiator, two proportional counters, and a NaI scintillation counter. Protons which recoil in the forward direction from the radiator pass through the two proportional counters and terminate in the NaI crystal. Triple coincidences produced in this manner gate a twenty-channel pulse sorter which analyzes the pulses in the scintillation counter. The crystal was found to give three percent resolution from 15-Mev protons

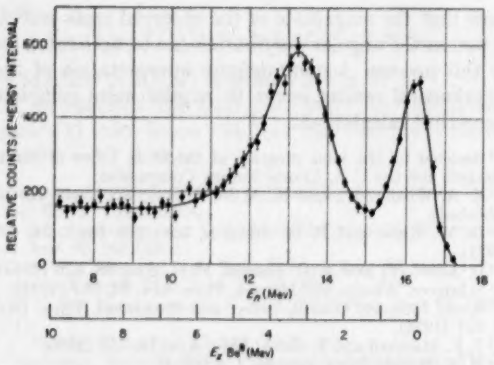

FIG. 1. Neutron spectrum at zero degrees from $Li^7(d,n)Be^8$. The energy of the incident deuteron is 2 Mev.

from the $He^3(d,p)He^4$ reaction. For the $Li^7(d,n)Be^8$ experiment 2-Mev deuterons from the 2.5-Mev Van de Graaff bombarded lithium targets having a stopping power of 300 kev. The targets were prepared from separated metallic Li^7.[15]

The resulting neutron spectrum at zero degrees corrected for the variation of the $n-p$ cross section is shown in Fig. 1. The statistical uncertainties are ten percent up to a neutron energy of 11 Mev and six percent for energies greater than 11 Mev. Backgrounds were determined by observing the difference in counting rates with the radiator in and the radiator out. The radiator was about eight percent thick to recoil protons in the 7-Mev to 11-Mev region and five percent thick to those in the 11-Mev to 17-Mev region.

Figure 1 shows two groups of neutrons corresponding to the formation of Be^8 in the ground state and in an excited state at 3 Mev. Neutron groups leaving Be^8 in an excitation of 4 Mev or 5 Mev would have been resolved if they were ten percent as intense as the group leaving Be^8 in the ground state. A group leaving Be^8 with an excitation of 7.5 Mev would have been observed if it were twenty percent of the ground state group. The spectrum is being studied at angles other than zero degrees.

* Graduate student from Texas A & M College working under an Oak Ridge Institute of Nuclear Studies fellowship.

[1] F. Ajzenberg and T. Lauritsen, Revs. Modern Phys. **24**, 321 (1952).
[2] E. W. Titterton, Phys. Rev. **94**, 206 (1954). This paper contains additional references to previous work.
[3] M. E. Calcraft and E. W. Titterton, Phil. Mag. **42**, 666 (1951).
[4] M. J. Brinkworth and E. W. Titterton, Phil. Mag. **42**, 952 (1951).
[5] H. T. Richards, Phys. Rev. **59**, 796 (1941).
[6] L. L. Green and W. M. Gibson, Proc. Phys. Soc. (London) **62**, 407 (1949).
[7] Trumpy, Grotdal, and Crane, Nature **170**, 1118 (1952).
[8] Catala, Aguilor, and Busquets, Anales real soc. españ. ffs. y quim. (Madrid) **A49**, 131 (1953).
[9] E. K. Inall and A. J. F. Boyle, Phil. Mag. **44**, 1081 (1953).
[10] F. E. Steigert and M. B. Sampson, Phys. Rev. **92**, 660 (1953).
[11] C. C. Trail and C. H. Johnson, Rev. Sci. Instr. (to be published).
[12] Kunz, Moak, and Good, Phys. Rev. **91**, 676 (1953).
[13] R. Malm and D. R. Inglis, Phys. Rev. **92**, 1326 (1953).
[14] P. B. Treacy, Phil. Mag. **44**, 325 (1953).
[15] The separated isotopes were obtained from Stable Isotopes Division, Oak Ridge National Laboratory.

CONTENTS—Continued

Letters to the Editor:

Electron Multiplication in Germanium at Low Temperatures . . . . . E. J. Ryder, I. M. Ross, and D. A. Kleinman 1342

Electron Spin Resonance in Beryllium . . . . . G. Feher and A. F. Kip 1343

Structure of the Intermediate State in Superconductors . . . . . A. L. Schawlow, B. T. Matthias, H. W. Lewis, and G. E. Devlin 1344

Distribution of the Mass Transported from a Collector into a Germanium Crystal by the Forming Process . . . . M. W. Aarons, M. Poberezkin, J. E. Gates, and E. B. Dale 1345

Effect of Chemical Combination on the Characteristic Energy Loss of Electrons . . . . . Lewis B. Leder and L. Marton 1345

Plastic Flow and the Low-Frequency Dispersion in the Alkali Halide Crystal . . . . . Masakazu Ishiguro, Fujio Oda, and Tatsuo Fujino 1347

Small-Angle p-p Cross Sections and Polarization at 340 Mev . . . . . O. Chamberlain, G. Pettengill, E. Segrè, and C. Wiegand 1348

Proton-Proton Scattering Experiments at 370 and 260 Mev . . . . . Owen Chamberlain and John D. Garrison 1349

Small Angle Proton-Proton Scattering at 330 Mev . . . David Fischer and Gerson Goldhaber 1350

Recoil Spectrum in the Beta Decay of He^6 . . . W. Parker Alford and Donald R. Hamilton 1351

Equilibrium Charge Distribution of Stripped 26-Mev Nitrogen Ions . . . . . H. L. Reynolds and A. Zucker 1353

Limits on π^- Meson Mass from Mesonic X-Rays . . . . . M. Stearns, M. B. Stearns, S. DeBenedetti, and L. Leipuner 1353

Decay Scheme of Pb^{203m} . . . . . V. E. Krohn and S. Reboy 1354

Nuclear Magnetic Resonance in Solid Hydrogen with Various Ortho Concentrations . . . . . Tadashi Sugawara, Yoshiki Masuda, Teinosuke Kanda, and Eino Kanda 1355

Spins and Hyperfine Splittings of Ag^{107} and Cs^{133} . . Aaron Lemonick and Francis M. Pipkin 1356

Resonance Absorption of Gamma Radiation by Cs^{137} Nuclei . . . . . J. G. Campbell 1357

Ground State of Re^{187} . . . . . Lee Koerts 1358

Polarization of Fast Neutrons from Nuclear Reactions . . . . . Harvey B. Willard, Joe K. Bair, and Joe D. Kington 1359

Radiative Decay of the θ^0 Particle . . . . . S. B. Treiman 1360

Photodisintegration of Deuterium by 165-Mev X-Rays . . . . . E. A. Whalin, Jr. 1362

Energy Levels in Be^8 from $Li^7(d,n)Be^8$ . . . . . Carroll C. Trail and C. H. Johnson 1363